BEILSTEIN JOURNAL OF NANOTECHNOLOGY

Nanomaterials for photocatalysis and applications in environmental remediation and renewable energy

Edited by Viet Van Pham and Wee-Jun Ong

Imprint

Beilstein Journal of Nanotechnology
www.bjnano.org
ISSN 2190-4286
Email: journals-support@beilstein-institut.de

The *Beilstein Journal of Nanotechnology* is published by the Beilstein-Institut zur Förderung der Chemischen Wissenschaften.

Beilstein-Institut zur Förderung der Chemischen Wissenschaften
Trakehner Straße 7–9
60487 Frankfurt am Main
Germany
www.beilstein-institut.de

BEILSTEIN JOURNAL OF NANOTECHNOLOGY

Nanomaterials for photocatalysis and applications in environmental remediation and renewable energy

Viet Van Pham*[1] and Wee-Jun Ong[2]

Editorial

Open Access

Address:
[1]HUTECH University, 475A Dien Bien Phu Street, Binh Thanh District, Ho Chi Minh City, Vietnam and [2]Xiamen University Malaysia, Jalan Sunsuria, Bandar Sunsuria, 43900 Sepang, Selangor, Malaysia

Email:
Viet Van Pham* - pv.viet@hutech.edu.vn

* Corresponding author

Beilstein J. Nanotechnol. **2023,** *14,* 722–724.
https://doi.org/10.3762/bjnano.14.58

Received: 29 May 2023
Accepted: 07 June 2023
Published: 13 June 2023

This article is part of the thematic issue "Nanomaterials for photocatalysis and applications in environmental remediation and renewable energy".

Editor-in-Chief: G. Wilde

Global warming and climate change are increasing global issues. In the last ten years, the intensity of these issues has drawn significant attention from many countries worldwide. One of the factors that cause climate change are industrial processes which need high power to run, and most countries have used fossil fuels for these processes [1]. The use of fossil fuels generates harmful emissions to the environment, such as carbon dioxide (CO_2), methane (CH_4), nitrous oxide (N_2O), nitric oxide and nitrogen dioxide (together termed NO_x), and fluorinated gases (e.g., hydrofluorocarbons, perfluorocarbons, and sulfur hexafluoride) which are currently considered primary sources of environmental [2]. A Global Warming Potential (GWP) measurement was used to compare the global warming effects of different gases. It has been calculated to reflect how long gases remain in the atmosphere, on average, and how strongly it absorbs energy [3]. Besides, the discharge of persistent organic pollutants (POPs) also contributes to water pollution, increasing global environmental pollution. Recently, the reduction and conversion of CO_2 into fuel as valuable hydrocarbon products has been drawing attention from scientists in materials science, chemical engineering, nanotechnology, and related fields [4]. To reduce contaminants (e.g., air pollution (CO_2, NO_x, SO_2), POPs) there are many routes (e.g., physico-chemical approaches, biological fixation, advanced oxidation process, and photocatalysis [5-8]). Among the aforementioned methods, the photocatalysis route is appropriate for treating pollutants, even in atmospheric conditions [9-11]. Moreover, the photocatalysis method is also a potential solution for environmental remediation, carbon emission reduction, and renewable energy production [12-14].

Combining photocatalysts and sunlight irradiation is a potential strategy for water treatment via the effectively infinite energy from the sun and the photocatalysts. Photocatalysis based on nanostructured semiconductors can significantly contribute to tackling several environmental pollution problems, sustainable synthesis, and energy production [2,15,16]. Semiconducting photocatalyst nanomaterials, such as SnO_2, TiO_2, MoS_2, g-C_3N_4, and Bi-nanostructures have been proven efficient for a range of applications, including organic pollutant removal, NO_x degradation, renewable energy production, and waste-to-energy conversion [15,17,18]. Figure 1 shows a general photocatalysis

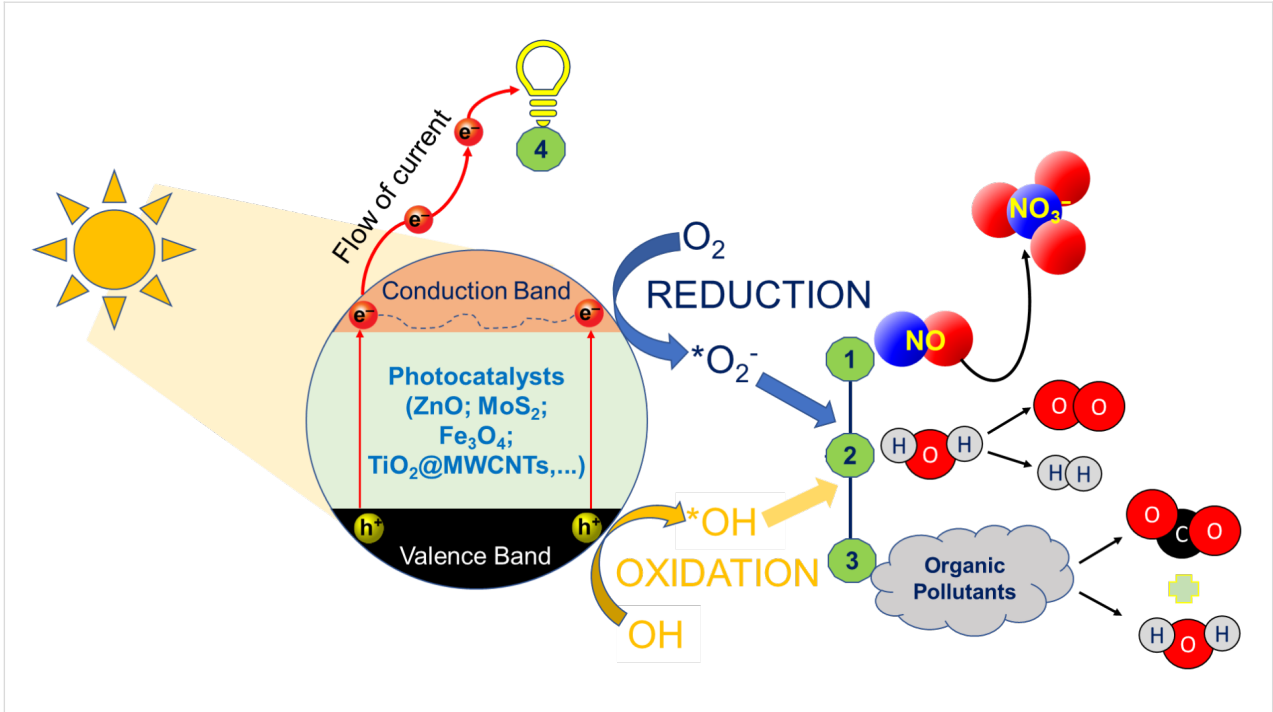

Figure 1: A general photocatalytic mechanism for several possible target processes: (1) NO_x degradation, (2) water splitting for hydrogen and oxygen evolution reactions, (3) degradation of organic pollutants, and (4) solar cell application.

mechanism outlining several possible targets (i.e., NO_x degradation, water splitting, degradation of organic pollutants, and enhancement of electron generation in a solar-cell application).

This Thematic Issue highlights recent experimental and theoretical developments in using light harvesting by semiconductor materials for sustainable applications; for instance, dye solar cells, solar-driven water splitting, NO_x removal, and contaminant degradation. The synthesis of semiconductor nanomaterials published on this thematic issue indicates a wide range of synthetic routes. The as-prepared nanomaterials with various morphologies demonstrated many preeminent features in the above applications. In detail, the MoS2 with a honeycomb-like structure was first synthesized by an electrochemical route and applied in dye-sensitized solar cells [19], which expressed a higher applicability than that of other studies [20-22]. Besides, Nhu et al. [23] used rosin as a green chemical approach to fabricate ZnO nanoparticles, exhibiting a high photocatalytic activity for both methylene blue (100%) and methyl orange (82.78%) decomposition after 210 min under UV radiation. Moreover, the advantages in the development of advanced materials based on semiconductors (i.e., carbon-modified hexagonal boron nitride (MBN), MgO@g-C3N4, and TiO2@MWCNTs) have indicated a highly efficient photocatalytic performance for phenol removal using a low-power visible LED light source. For NO degradation, a visible light source was used whereas for water splitting natural sunlight was used [24-26]. These results are mentioned as scaling up photocatalytic systems to reach net zero emission goals and the next technology to produce green hydrogen energy [14].

Up-to-date trending topics on photocatalysts based on semiconducting nanomaterials, perovskites, or Bi-based nanomaterials are presented to incentivize fine-tuning of current studies and research works on photocatalytic efficiency of nanomaterials [27]. In addition, this Thematic Issue will undoubtedly provide the reader with novel ideas for developing nanomaterials for environmental remediation and sustainable applications; for instance, dye solar cells, solar-driven water splitting, NO_x removal, and contaminant degradation. This Thematic Issue will make a good reference material and be of great use for scientists in nanomaterials fields.

Viet Van Pham and Wee-Jun Ong

Ho Chi Minh City and Sepang, June 2023.

Acknowledgements

We sincerely thank the authors who contributed with quality articles to this Thematic Issue. We also thank the editorial team of the Beilstein Journal of Nanotechnology, especially the support from Dr. Barbara Hissa and Dr. Lasma Gailite for the completion of this Thematic Issue.

ORCID® iDs

Viet Van Pham - https://orcid.org/0000-0002-8697-7095

References

1. Ali, K.; Bakhsh, S.; Ullah, S.; Ullah, A.; Ullah, S. *Environ. Sci. Pollut. Res.* **2021,** *28,* 7515–7527. doi:10.1007/s11356-020-10996-6
2. Ismael, M.; Wu, Y. *Sustainable Energy Fuels* **2019,** *3,* 2907–2925. doi:10.1039/c9se00422j
3. Global Greenhouse Gas Emissions Data. https://www.epa.gov/ghgemissions/global-greenhouse-gas-emissions-data (accessed April 20, 2023).
4. Ezekiel, J.; Ebigbo, A.; Adams, B. M.; Saar, M. O. *Appl. Energy* **2020,** *269,* 115012. doi:10.1016/j.apenergy.2020.115012
5. Muratori, M.; Kheshgi, H.; Mignone, B.; Clarke, L.; McJeon, H.; Edmonds, J. *Int. J. Greenhouse Gas Control* **2017,** *57,* 34–41. doi:10.1016/j.ijggc.2016.11.026
6. Bartolomeu, M.; Neves, M. G. P. M. S.; Faustino, M. A. F.; Almeida, A. *Photochem. Photobiol. Sci.* **2018,** *17,* 1573–1598. doi:10.1039/c8pp00249e
7. Zhai, S.; Rojas, J.; Ahlborg, N.; Lim, K.; Cheng, C. H. M.; Xie, C.; Toney, M. F.; Jung, I.-H.; Chueh, W. C.; Majumdar, A. *Energy Environ. Sci.* **2020,** *13,* 592–600. doi:10.1039/c9ee02795e
8. Salehizadeh, H.; Yan, N.; Farnood, R. *Chem. Eng. J.* **2020,** *390,* 124584. doi:10.1016/j.cej.2020.124584
9. Kondratenko, E. V.; Mul, G.; Baltrusaitis, J.; Larrazábal, G. O.; Pérez-Ramírez, J. *Energy Environ. Sci.* **2013,** *6,* 3112. doi:10.1039/c3ee41272e
10. Ganesh, I. *Renewable Sustainable Energy Rev.* **2014,** *31,* 221–257. doi:10.1016/j.rser.2013.11.045
11. Kumar, B.; Llorente, M.; Froehlich, J.; Dang, T.; Sathrum, A.; Kubiak, C. P. *Annu. Rev. Phys. Chem.* **2012,** *63,* 541–569. doi:10.1146/annurev-physchem-032511-143759
12. Lin, Y.-R.; Dizon, G. V. C.; Yamada, K.; Liu, C.-Y.; Venault, A.; Lin, H.-Y.; Yoshida, M.; Hu, C. *J. Colloid Interface Sci.* **2020,** *567,* 202–212. doi:10.1016/j.jcis.2020.02.017
13. Alkhatib, I. I.; Garlisi, C.; Pagliaro, M.; Al-Ali, K.; Palmisano, G. *Catal. Today* **2020,** *340,* 209–224. doi:10.1016/j.cattod.2018.09.032
14. Isaacs, M.; Garcia-Navarro, J.; Ong, W.-J.; Jiménez-Calvo, P. *Global Challenges* **2023,** *7,* 2200165. doi:10.1002/gch2.202200165
15. Ameta, R.; Solanki, M. S.; Benjamin, S.; Ameta, S. C. Photocatalysis. *Advanced Oxidation Processes for Waste Water Treatment;* 2018; pp 135–175. doi:10.1016/b978-0-12-810499-6.00006-1
16. Meng, X.; Eluagwule, B.; Wang, M.; Wang, L.; Zhang, J. Solar photocatalysis for environmental remediation. *Handbook of Smart Photocatalytic Materials;* 2020; pp 183–195. doi:10.1016/b978-0-12-819049-4.00013-1
17. Iqbal, W.; Yang, B.; Zhao, X.; Rauf, M.; Waqas, M.; Gong, Y.; Zhang, J.; Mao, Y. *Catal. Sci. Technol.* **2018,** *8,* 4576–4599. doi:10.1039/c8cy01061g
18. Chen, Y.; Zhang, G.; Ji, Q.; Liu, H.; Qu, J. *ACS Appl. Mater. Interfaces* **2019,** *11,* 26781–26788. doi:10.1021/acsami.9b05978
19. Mai, L. T. T.; Le, H. V.; Nguyen, N. K. T.; Pham, V. L. T.; Nguyen, T. A. T.; Huynh, N. T. L.; Nguyen, H. T. *Beilstein J. Nanotechnol.* **2022,** *13,* 528–537. doi:10.3762/bjnano.13.44
20. Wei, W.; Sun, K.; Hu, Y. H. *J. Mater. Chem. A* **2016,** *4,* 12398–12401. doi:10.1039/c6ta04743b
21. Liu, W.; He, S.; Yang, T.; Feng, Y.; Qian, G.; Xu, J.; Miao, S. *Appl. Surf. Sci.* **2014,** *313,* 498–503. doi:10.1016/j.apsusc.2014.06.011
22. Lei, B.; Li, G. R.; Gao, X. P. *J. Mater. Chem. A* **2014,** *2,* 3919. doi:10.1039/c3ta14313a
23. Nhu, V. T. T.; Dat, N. D.; Tam, L.-M.; Phuong, N. H. *Beilstein J. Nanotechnol.* **2022,** *13,* 1108–1119. doi:10.3762/bjnano.13.94
24. Mishra, N. S.; Saravanan, P. *Beilstein J. Nanotechnol.* **2022,** *13,* 1380–1392. doi:10.3762/bjnano.13.114
25. Pham, M.-T.; Tran, D. P. H.; Bui, X.-T.; You, S.-J. *Beilstein J. Nanotechnol.* **2022,** *13,* 1141–1154. doi:10.3762/bjnano.13.96
26. Le, A. Q. H.; Nguyen, N. N. T.; Tran, H. D.; Nguyen, V.-H.; Tran, L.-H. *Beilstein J. Nanotechnol.* **2022,** *13,* 1520–1530. doi:10.3762/bjnano.13.125
27. Phang, S. J.; Wong, V.-L.; Tan, L.-L.; Chai, S.-P. *Appl. Mater. Today* **2020,** *20,* 100741. doi:10.1016/j.apmt.2020.100741

License and Terms

BEILSTEIN JOURNAL OF NANOTECHNOLOGY

Tin dioxide nanomaterial-based photocatalysts for nitrogen oxide oxidation: a review

Viet Van Pham*[1], Hong-Huy Tran[1], Thao Kim Truong[1] and Thi Minh Cao[2]

Review

Open Access

Address:
[1]Photocatalysis Research Group (PRG), Faculty of Materials Science and Technology, University of Science, VNU–HCM, 227 Nguyen Van Cu Street, District 5, Ho Chi Minh City, 700000, Viet Nam and [2]HUTECH University, 475A Dien Bien Phu Street, Binh Thanh District, Ho Chi Minh City, 700000, Viet Nam

Email:
Viet Van Pham* - pvviet@hcmus.edu.vn

* Corresponding author

Keywords:
green products; nanomaterials; NO oxidation; photocatalysis; SnO_2

Beilstein J. Nanotechnol. **2022,** *13,* 96–113.
https://doi.org/10.3762/bjnano.13.7

Received: 07 October 2021
Accepted: 30 December 2021
Published: 21 January 2022

This article is part of the thematic issue "Nanomaterials for photocatalysis and applications in environmental remediation and renewable energy".

Associate Editor: C. T. Yavuz

Abstract

Semiconducting SnO_2 photocatalyst nanomaterials are extensively used in energy and environmental research because of their outstanding physical and chemical properties. In recent years, nitrogen oxide (NO_x) pollutants have received particular attention from the scientific community. The photocatalytic NO_x oxidation will be an important contribution to mitigate climate change in the future. Existing review papers mainly focus on applying SnO_2 materials for photocatalytic oxidation of pollutants in the water, while studies on the decomposition of gas pollutants are still being developed. In addition, previous studies have shown that the photocatalytic activity regarding NO_x decomposition of SnO_2 and other materials depends on many factors, such as physical structure and band energies, surface and defect states, and morphology. Recent studies have been focused on the modification of properties of SnO_2 to increase the photocatalytic efficiency of SnO_2, including bandgap engineering, defect regulation, surface engineering, heterojunction construction, and using co-catalysts, which will be thoroughly highlighted in this review.

Review

Introduction

A World Health Organization (WHO) report indicated that 4.2 million deaths every year occur due to exposure to ambient (outdoor) air pollution [1]. This number is much higher than the deaths from the COVID-19 pandemic in the past year. WHO also reported that the emissions of nitrogen oxides in the early 1980s over the world were estimated at approximately 150×10^{12} g/year while the concentration of nitrogen dioxide outdoor can achieve up to 940 μg/m^3 (0.5 ppm) for 30 min and 400 μg/m^3 (0.21 ppm) for 60 min [2]. Nitrogen oxides (NO_x, including NO and NO_2) are poisonous and highly reactive gases. Nitrogen dioxide (NO_2) is associated with respiratory diseases and mortality. NO_x is formed when fuel is burnt at high temper-

atures and emitted by automobiles, trucks, and various non-road vehicles (e.g., construction equipment, boats) and industrial sources such as power plants, industrial boilers, cement kilns, and turbines [3]. In addition, diesel vehicles are considered a primary NO_x emission source causing adversely impacts on environment and human health, such as acid rain, global warming, and respiratory diseases in humans (Figure 1a). NO_x pollution damages lung cells and reacts with molecules in the air when released into the ozone layer. NO_x can aggravate respiratory diseases such as asthma, bronchitis, and cardiovascular diseases. When humans are exposed to NO_2 at concentrations of over 200 μg/m^3, even for periods of time, this will cause adverse effects on the respiratory system. Some studies have shown that NO_2 concentrations over 500 μg/m^3 can cause acute health effects. Although the lowest threshold for NO_2 exposure with a direct effect on lung function in asthmatic subjects was 560 μg/m^3, NO_2 exposure to concentrations over 200 μg/m^3 caused pulmonary responses in asthmatic people [4,5]. Guillaume P. Chossière et al. indicated that reducing NO_x in the air will significantly reduce the risk of death in humans demonstrated through a study on lockdowns during the COVID-19 pandemic in China that led to a reduction of NO_2, O_3, and $PM_{2.5}$ concentrations globally, resulting in ca. 32,000 avoided premature mortalities, including ca. 21,000 in China [6]. Therefore, the control, treatment, and conversion of NO_x to green products greatly interested the scientific community in recent years.

There are many methods for controlling and removing NO_x, such as reducing the burning temperature, reducing the residence time at peak temperature, chemical reduction or oxidation of NO_x, removal of nitrogen from combustion fuels, and sorption, both adsorption and absorption [7,8]. Among them, photocatalytic oxidation is an efficient method of converting NO_x into nitrate (NO_3^-) ions. The removal of NO_3^- ions is easy, efficient, and economic through chemical or biological methods such as the conversion of NO_3^- to N_2 by aerobic microorganisms [9,10]. Figure 1b illustrates the working scheme of semiconductor photocatalysts for NO oxidation. Light generates holes (h^+) in the valence band (VB) and electrons (e^-) in the conduction band (CB) of the photocatalytic material. Electrons at the material surface will react with oxygen molecules to form superoxide radicals ($^{\bullet}O_2^-$, similarly holes react with water to form hydroxyl radicals). Free radicals and strong oxidizing agents react with NO_x to produce NO_3^-, deposited on the photocatalyst surface. The NO_3^- product formed on the surface of the catalyst can be easily separated for further treatment by washing with water due [11] (see Equations 1–10).

$$\text{Semiconductor} + h\nu \rightarrow \text{Semiconductor}\left(h^+_{VB} + e^-_{CB}\right) \quad (1)$$

$$O_2 + e^-_{CB} \rightarrow {}^{\bullet}O_2^- \quad (2)$$

$$H_2O + h^+_{VB} \rightarrow HO^{\bullet} + H^+ \quad (3)$$

$${}^{\bullet}O_2^- + H_2O \rightarrow HO_2^{\bullet} + OH^- \quad (4)$$

$$2\,{}^{\bullet}HO_2 \rightarrow O_2 + H_2O_2 \quad (5)$$

$$HO_2^{\bullet} + H_2O + e^-_{CB} \rightarrow H_2O_2 + OH^- \quad (6)$$

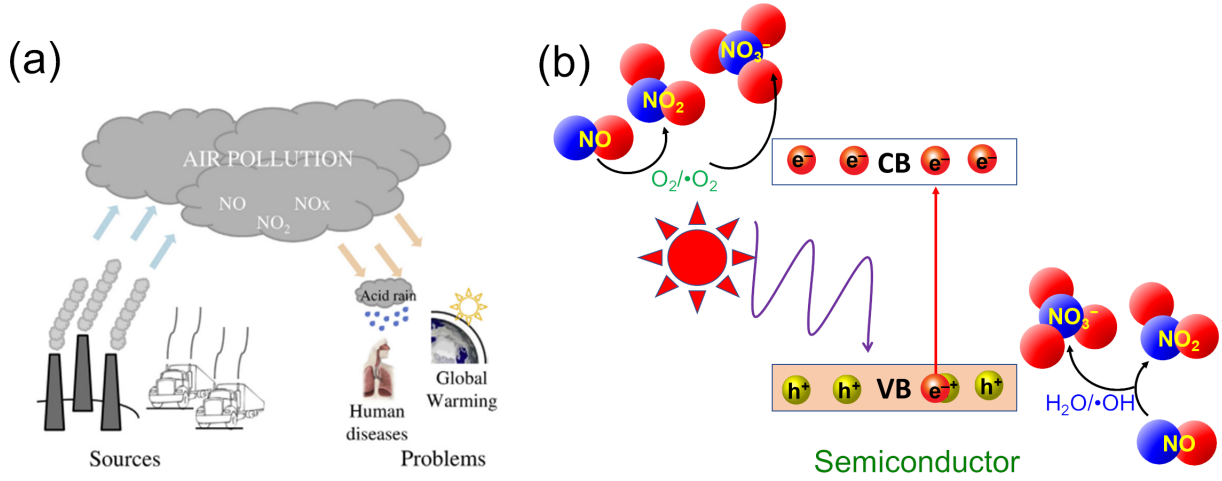

Figure 1: Problems and sources associated with NO_x air pollution (a) and NO photocatalysis over a semiconductor (b). Figure 1a was reprinted from [12], Journal of Environmental Management, vol. 129, by J. Ângelo; L. Andrade; L. M. Madeira; A. Mendes "An overview of photocatalysis phenomena applied to NO_x abatement", pages 522–539, Copyright (2013), with permission from Elsevier. This content is not subject to CC BY 4.0.

$$2^{\bullet}O_2^- + 2H_2O \rightarrow 2H_2O_2 + O_2 \quad (7)$$

$$H_2O_2 + e_{CB}^- \rightarrow {}^{\bullet}OH + OH^- \quad (8)$$

$$NO + {}^{\bullet}O_2^- \rightarrow NO_3^- \quad (9)$$

$$NO + 2HO^{\bullet} \rightarrow NO_2 + H_2O \quad (10)$$

Recently, research on tin dioxide (SnO_2) materials has increased significantly, which expresses the potential of SnO_2 materials for the scientific community (Figure 2a). SnO_2 is one of the most extensively investigated n-type semiconductors. It is known as tin(VI) oxide or stannic oxide (not to be confused with stannous oxide with tin in the oxidation state of 2+ [13], also known as cassiterite [14]. SnO_2 materials have many interesting properties. For instance, the structure and electronic structure can be manipulated easily due to the highly tunable valence state and oxygen vacancy defects (OVs) [15,16]. Therefore, SnO_2 is considered a potential material in various technological fields such as catalysis, optoelectronic devices, rechargeable lithium batteries, electrocatalysis, photocatalysis, solar energy conversion, and gas sensing [17-24]. In the catalytic area, SnO_2 is an emerging material for removing contaminants such as organic dyes, phenolic compounds, and volatile organic compounds (VOCs) due to strongly oxidizing properties thanks to flexible energy band structure, rich defects, good chemical, and high thermal stability, and easily controlled morphology [25-30]. However, pure SnO_2 suffers from some inherent drawbacks that limit its practical applications. With a wide bandgap (3.5–3.7 eV) [31,32], SnO_2 can only be excited by UV irradiation. As a typical oxidation photocatalyst with the CB edge energy level, which is not conducive to the reduction of O_2 to ${}^{\bullet}O_2^-$ [31,33] and the rapid recombination rate of photoinduced electron–hole pairs [34], the photocatalytic ability of SnO_2 is less efficient than that of other semiconductor photocatalysts (Figure 2b). Despite literature relating to the unfavorable CB edge of SnO_2, many reports still proposed its photocatalytic behaviors partly based on ${}^{\bullet}O_2^-$ species via the combination of experimental physicochemical analyses, such as electron spin resonance (ESR) spectroscopy, active species trapping experiments, valence band X-ray photoelectron spectroscopy (XPS), and diffuse reflectance spectroscopy (DRS) [35-40]. This promotes a new avenue for diverse analyses of semiconductor photocatalysts in addition to the traditional theories and conclusions.

Previous studies have shown that the photocatalytic activity of NO_x decomposition of materials in general and SnO_2 depends on many factors, including the structure and energy band, surface and defect states, morphology, etc. For that reason, recent studies are being focused on the modification of properties of SnO_2 to upgrade the photocatalytic efficiency of SnO_2, including bandgap engineering, defect regulation, surface engineering, heterojunction construction, co-catalyst, which will be thoroughly outlined in this review.

Structure and bandgap

SnO_2 has a crystal structure similar to that of rutile TiO_2 [41,42]. The unit cell parameters of rutile SnO_2 are $a = b = 0.47374$ nm and $c = 0.31864$ nm [43]. In one unit cell of rutile SnO_2, a Sn^{4+} ion is bonded to six oxygen ions, and every oxygen atom is coordinated by three Sn^{4+} ions, forming a (6, 3) coordination structure [44]. When SnO_2 materials are prepared as thin films with two to eight layers the bandgap is larger than that of bulk SnO_2 and decreases with increasing film thickness [45]. Zhou et al. indicated that the direct bandgap transition of SnO_2 has an absorption coefficient α and the optical bandgap (E_g) can be determined by the calculation of

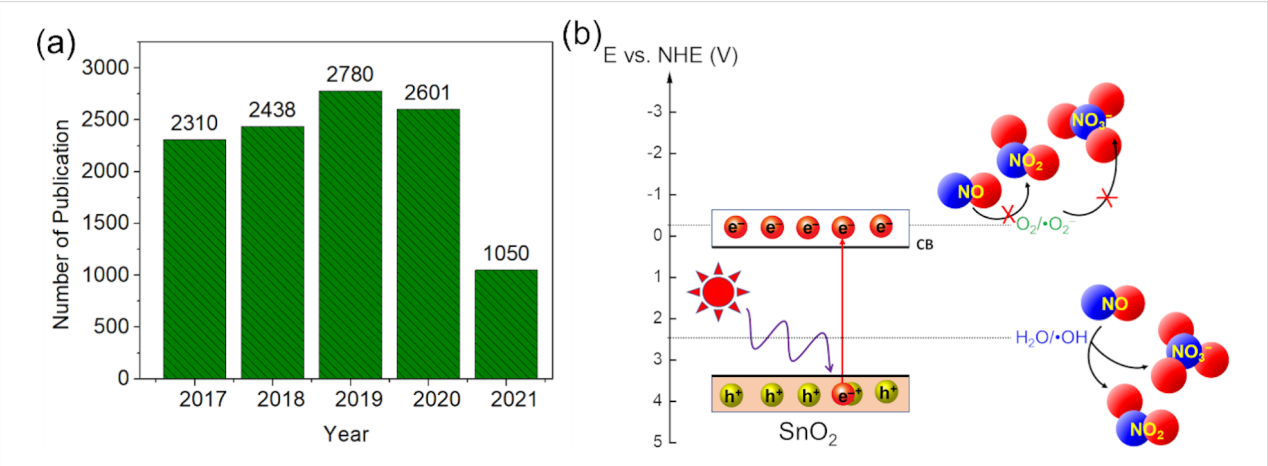

Figure 2: (a) Statistics of publication number on SnO_2 materials (2017–06/2021). Data was extracted from Web of Science, Clarivate Analytics; (b) NO photocatalytic oxidation ability of SnO_2.

$\alpha(h\nu)^2 \propto (h\nu - E_g)^{1/2}/h\nu$, and the plot of $\alpha(h\nu)^2$ vs photon energy $h\nu$, respectively. For example, the bandgap of a SnO_2 thin film with a thickness of about 130 nm is 3.597 eV [42].

The reported bandgap of bulk SnO_2 is 3.6 eV. Changing the morphology, particle size, or the formation of OVs or defects narrow the bandgap. In the study of Babu et al., a redshift of the absorption edge was observed when SnO_2 quantum dots (SQDs) were heated from 200 to 700 °C, which indicated that the bandgap of the SQDs decreased from 3.49 to 2.52 eV (for SQD-700) as shown in Figure 3. These results demonstrated that the redshift is favorable for a photocatalytic activity in the visible light region.

Meanwhile, Fan et al. [47] investigated the bandgap of SnO_2 when changing the self-doping of SnO_2. The change of the color of the powder products and the redshift in the absorption spectra are two quantities that are correlated with each other. Normally, SnO_2 is white and optical absorptions in the visible region arise from changes of the band structure. Moreover, the bandgap of SnO_{2-x} self-doped with Sn^{2+} can be easily determined as follows: A straight line to the x-axis, equaling to the extrapolated value of E_{photon} at $\alpha = 0$, gives the absorption edge energy. This energy parameter corresponds to the bandgap (E_g) of the material [47].

Surface and defect states

Structural defects and lattice imperfections usually bestow most of the properties exploited for applications of SnO_2 materials as they influence various physicochemical properties and reactions on the surface. Most important are defect states of materials, including predominantly point defects, that is, defects associated with one lattice point, such as cation or oxygen ion vacancies. OVs determine the physical and chemical properties of metal oxides. Figure 4a shows the natural crystal structure of SnO_2 synthesized by vapor transport [48]. The (110) plane of rutile SnO_2 is the most common surface, and it is also thermodynamically the most stable [48]. In the rutile phase of SnO_2 in Figure 4b, the (110) plane contains all surface bridging oxygens (1), bridging OVs (2), and oxygen coordinated three- or fivefold (3, 4) with surface tin atoms (Sn 5f). The dual valency of Sn at the surface of SnO_2 plays a role in the reversible transformation of the surface composition from Sn^{4+} cations to Sn^{2+}, which leads to active centers in the surface chemical process [48]. Moreover, the OVs in SnO_2 often appear when it is synthesized by chemical methods such as sol–gel, hydrothermal, and microwave synthesis [49-51]. The formation and concentration of OVs depend on particle size, synthesizing temperature, and morphology of SnO_2. The OVs play the role of an electron donor and provide free electrons, making SnO_2 an n-type semiconductor [52].

Guoliang Xu et al. indicated that NO could be absorbed easily on various SnO_2(110) surfaces, and it is preferentially adsorbed on the OV site through an N-down orientation. Figure 5 shows the calculation of the energy of NO conversion processes on SnO_2(110), SnO_{2-x}(110), and O_2 + SnO_{2-x}(110) surfaces. The oxidation of NO on other surfaces is determined by the reaction energies, as shown in Figure 5. The O_2 + SnO_{2-x}(110) surface is more exothermic and preferable than other surfaces, which leads to an efficient reaction of NO with the SnO_2 surface [54]. Also, Tiya-Djowe et al. [55] indicated that calcined SnO_2 sam-

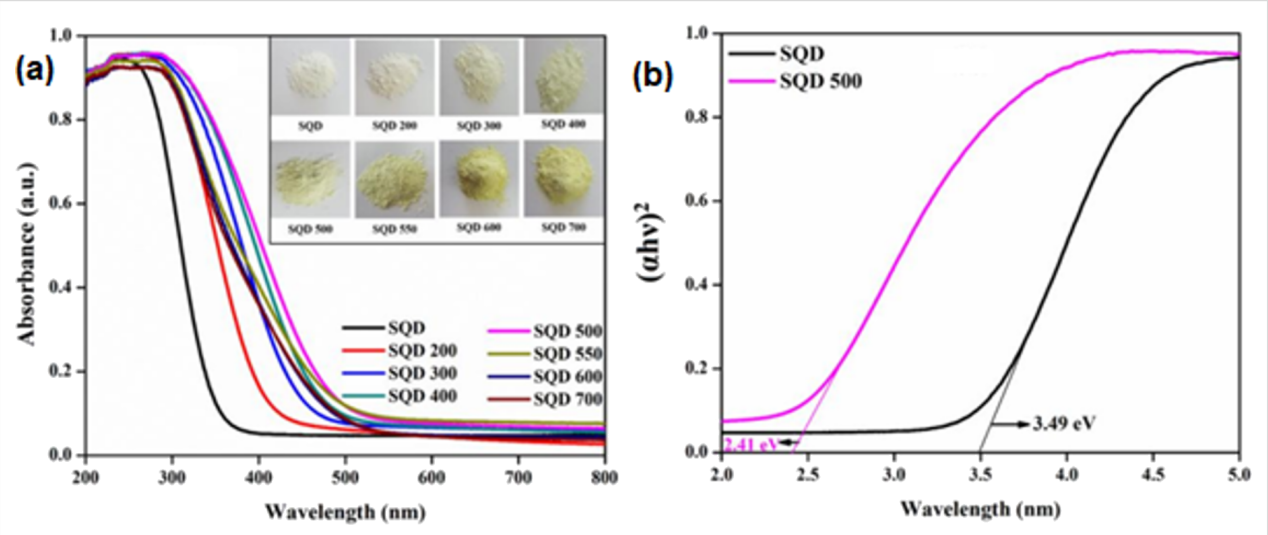

Figure 3: Ultraviolet–visible absorption spectra (a) and corresponding bandgaps of SQDs (b). Figure 3 was reprinted from [46], Materials Letters, vol. 221, by Babu, B.; Neelakanta Reddy, I.; Yoo, K.; Kim, D.; Shim, J. "Bandgap tuning and XPS study of SnO_2 quantum dots", pages 211–215, Copyright (2018), with permission from Elsevier. This content is not subject to CC BY 4.0.

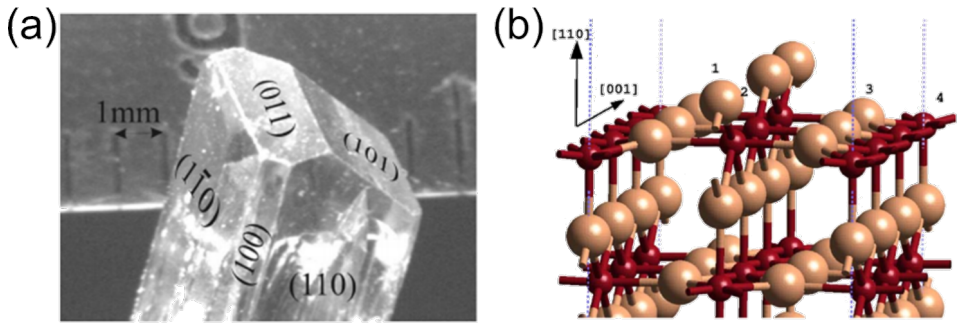

Figure 4: (a) Natural growth faces of SnO_2 are the (110), (100) (equivalent to (010) in rutile), and (101) (equivalent to (011) in rutile) surfaces. Figure 4a was reprinted with permission from [48] (M. Batzill; K. Katsiev; J. M. Burst; U. Diebold; A. M. Chaka; B. Delley, Phys. Rev. B, vol. 72, article no. 165414, 2005). Copyright (2005) by the American Physical Society. This content is not subject to CC BY 4.0; (b) SnO_2(110) surface including a bridging oxygen vacancy (1-bridging oxygen; 2-bridging OV; 3-oxygen coordinated threefold with surface tin (Sn 5f); 4-oxygen coordinated fivefold with surface tin (Sn 5f). Figure 4b was reprinted from [53], Surface Science, vol. 577, by Mäki-Jaskari, M. A.; Rantala, T. T.; Golovanov, V. V. "Computational study of charge accumulation at SnO_2(110) surface", pages 127–138, Copyright (2005), with permission from Elsevier. This content is not subject to CC BY 4.0.

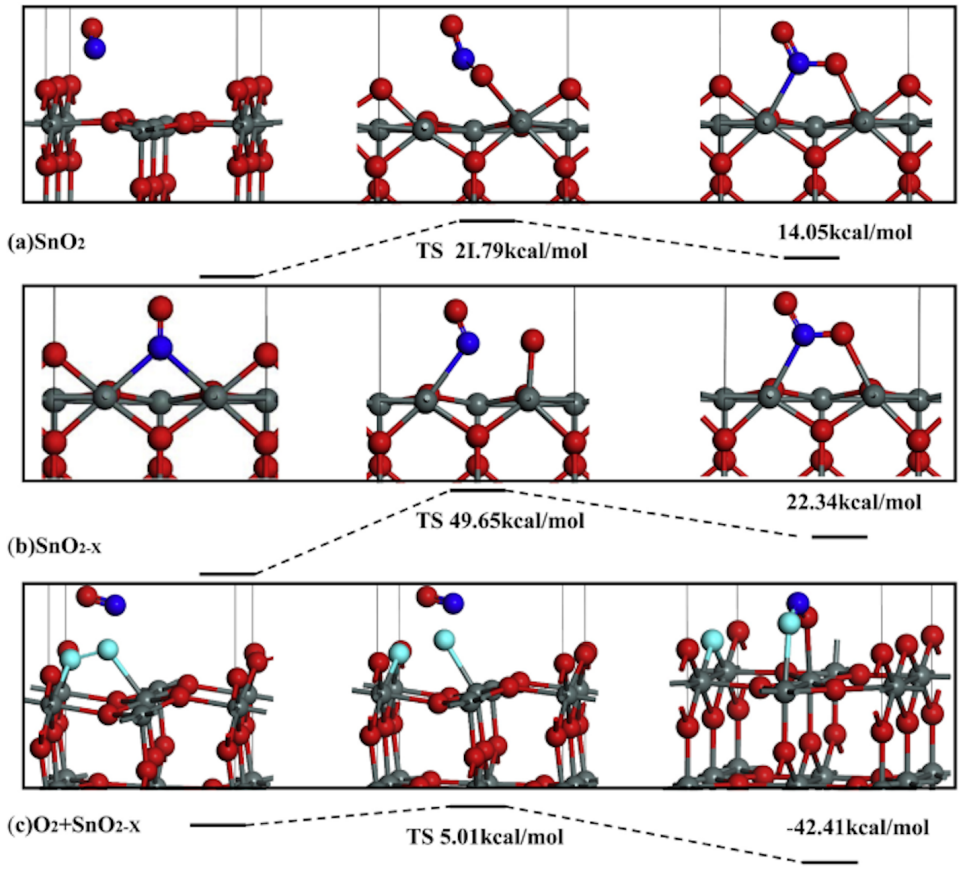

Figure 5: The conversion processes of NO on perfect SnO_2(110), SnO_{2-x}(110) and O_2 + SnO_{2-x}(110) surfaces. Figure 5 was reprinted from [54], Sensors and Actuators B: Chemical, vol. 221, by Xu, G.; Zhang, L.; He, C.; Ma, D.; Lu, Z. "Adsorption and oxidation of NO on various SnO_2(110) surfaces: A density functional theory study", pages 717–722, Copyright (2015), with permission from Elsevier. This content is not subject to CC BY 4.0.

ples with higher OV density showed improved photocatalytic performances. Besides, the OV density contributes to the rise of the valence band maximum and a decrease of the bandgap energy of SnO_2 materials.

Morphology

There are many shapes of SnO_2, for example, nanoparticles, nanocubes, nanorods, nanosheets, nanospheres, nanobelts, and nanotubes. These morphologies can be controllably obtained by

using polyvinylpyrrolidone (PVP), sodium dodecyl sulfonate (SDS), cetyl trimethyl ammonium bromide (CTAB), or tetrapropyl ammonium bromide (TPAB) as surfactants in a hydrothermal method [56-59]. The difference of morphologies will affect the properties of SnO_2 regarding gas sensor activity and optical, electrical, and electrochemical properties [60-63]. The typical properties of SnO_2 are significantly affected by the effective surface area of different nanomaterial morphologies [63-65].

Wang et al. [66] synthesized SnO_2 microspheres on a fluorine-doped tin oxide (FTO) substrate and the SEM images (Figure 6) show SnO_2 microspheres with an average diameter of 2.0–2.5 μm. By using SnO_2 microsphere photocatalysts for the photocatalytic oxidation of NO, Le et al. [67] indicated that 3D hierarchical flower-like SnO_2 microspheres exhibited a photocatalytic activity towards NO decomposition comparable to that of commercial P25 TiO_2. Specifically, SnO_2 microspheres can degrade 57.2% NO (1 ppm of initial concentration) under solar light. However, the photocatalytic mechanism of NO degradation has not been investigated [67]. Zhang et al. [68] found that the crystalline/amorphous stacking structure of SnO_2 microspheres can moderate surface absorption competition between oxygen gas and NO gas, contributing to the generation of reactive oxygen species (ROS) to oxidize NO to NO_3^- ions. Huy et al. [69] synthesized SnO_2 NPs, and this is the first report on using a SnO_2 photocatalyst with NP morphology for the NO degradation. The photocatalytic mechanism of SnO_2 NPs is based on electrons and holes to generate reactive radicals. Figure 7 shows that the photocatalytic NO removal efficacy of SnO_2 NPs achieved 63.37% after 30 min under solar light irradiation, and the conversion efficacy from NO to NO_2 is 1.66%. The high photocatalytic performance and the stability of SnO_2 NPs under solar light is promising for potential application [69].

Recent approaches in the modification of SnO_2 for photocatalytic NO_x oxidation

Many attempts have been made to enhance the photocatalytic activity and take better advantage of SnO_2 for the NO_x abatement, including the combination with other metal oxides [70], organic semiconductors [71], or metallic nanomaterials [72] to form a heterojunction/composite photocatalyst, and self-doping [73] or elemental doping [39,74]. Hybrid or doped photocatalysts ideally exhibit an improved photocatalytic efficacy due to the reduced recombination rate of photogenerated charge carriers and the lower activation energy. However, additional factors considerably affect the overall photocatalytic process. Table 1 shows a comparison of the NO photocatalytic oxidation ability of neat SnO_2 and modified SnO_2 materials. Recent studies on this material system mainly focus on modifying SnO_2 toward the application in the visible light region.

Charge transfer improvement

The combination of SnO_2 with other co-photocatalysts, including inorganic and organic semiconductors, is a practical approach to enhance the charge transfer efficacy for the photocatalytic process. The photocatalytic degradation of NO_x over SnO_2 as a host photocatalyst is reported to be considerably enhanced after the combination with organic semiconductors such as graphitic carbon nitride (g-C_3N_4) [71]. When acting as an auxiliary photocatalyst, SnO_2 promotes the photocatalytic activity of the primary material [38,70,75,76].

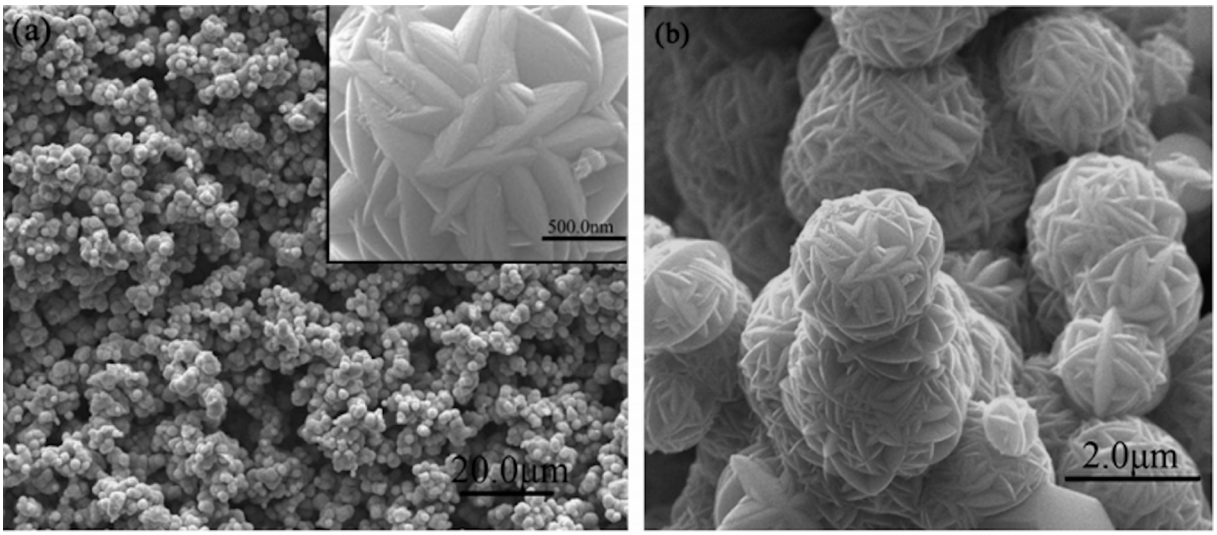

Figure 6: SEM images of SnO_2 microspheres synthesized by a hydrothermal method at 180 °C for 24 h. Figure 6 was reprinted with permission from [66], Copyright 2010 American Chemical Society. This content is not subject to CC BY 4.0.

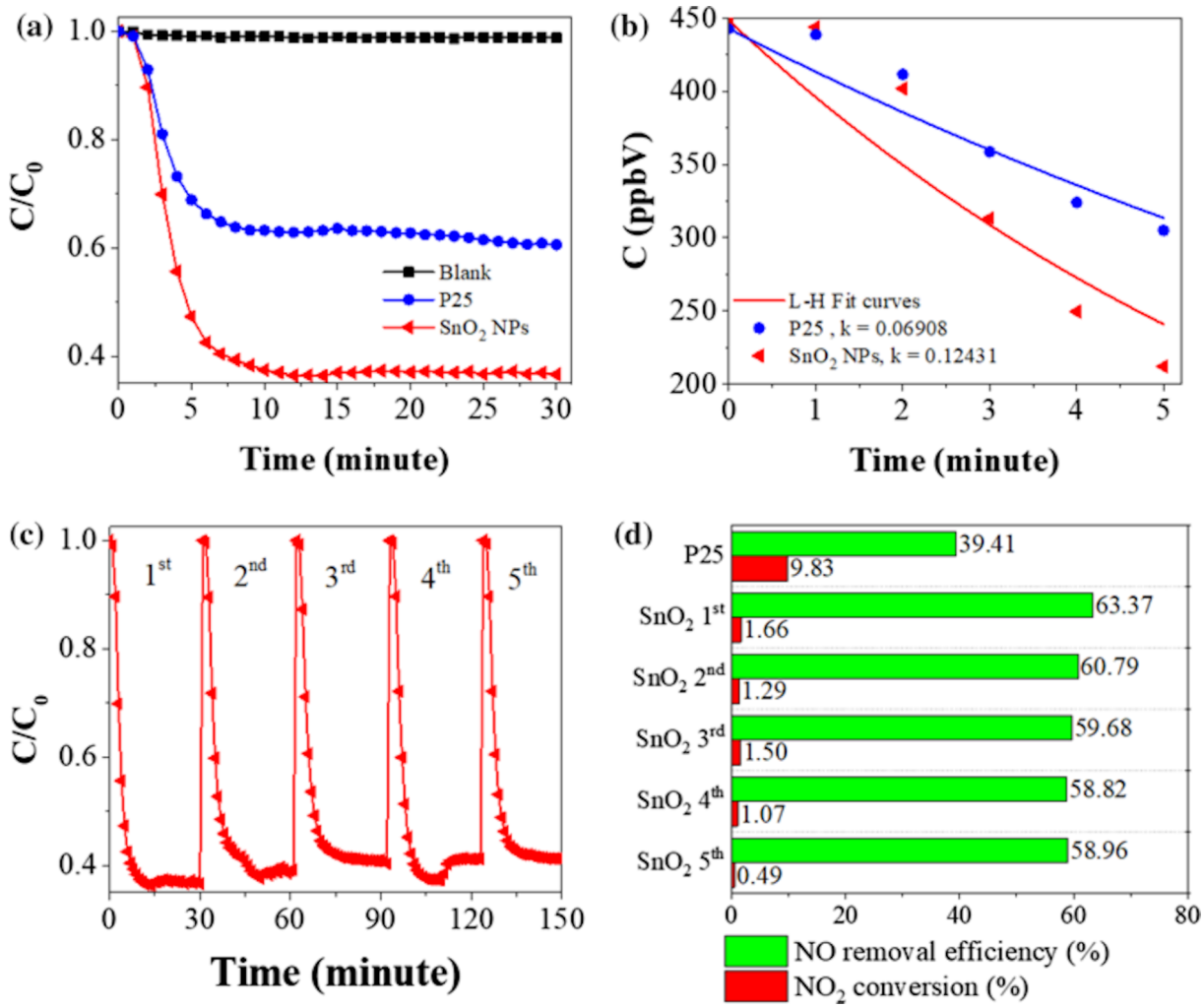

Figure 7: NO photodegradation of materials under solar light (a), the dependence of concentration on irradiation time (b), photochemical stability of SnO_2 NPs (NPs) (c), and NO removal efficacy and NO_2 conversion efficacy (d). Figure 7 is from [69] and was reprinted by permission from Springer Nature from the journal Environmental Chemistry Letters ("High photocatalytic removal of NO gas over SnO_2 nanoparticles under solar light" by T. H. Huy; B. D. Phat; C. M. Thi; P. V. Viet), Copyright 2018 Springer Nature. This content is not subject to CC BY 4.0.

Table 1: A comparison of photocatalytic systems for NO abatement with SnO_2 photocatalyst systems.

Year	Photocatalyst	SnO_2 morphology	Experimental conditions				NO removal (%)	NO_2 yield (%)	Ref.
			Light source	Initial NO conc. (ppb)	Humidity (%)	Sample weight (g)			
2013	SnO_2	microspheres	vis: λ > 510 nm and λ > 400 nm; UV: λ > 290 nm (450 W high-pressure mercury lamp with filters)	10^3	N/A	N/A	57.2 (λ > 290 nm) 11.5 (λ > 400 nm) 4.2 (λ > 510 nm)	N/A	[67]
2017	SnO_2/Zn_2SnO_4/ graphene	unclear shape	vis (3 W LED lamp, λ = 420 ± 10 nm)	600	N/A	0.2	59.3	N/A	[75]

Table 1: A comparison of photocatalytic systems for NO abatement with SnO_2 photocatalyst systems. (continued)

2018	SnO_2	NPs	solar (300 W Xe lamp)	450	70	0.2	63.37	1.66	[69]
2018	SnO_2/TiO_2	NPs	vis (300 W Xe lamp with a UV cutoff filter (λ > 420 nm)	450	70	0.2	59.49	2.58	[38]
2018	SnO_2/graphene	QDs	solar and vis (Xe lamp)	600	N/A	N/A	75 (full spectrum) 57 (vis)	N/A	[36]
2018	SnO_2/polyaniline	NPs	solar (300 W Xe lamp)	450	30	0.2	15	8	[35]
2019	SnO_2/N-doped carbon quantum dots/$ZnSn(OH)_6$	NPs	vis-near-infrared (300 W Xe lamp, λ ≥ 420 nm)	400	30 ± 5	0.2	37	<1.25	[76]
2019	SnO_2/g-C_3N_4	QDs	vis (150 W tungsten halogen lamp with a filter (λ > 420 nm)	600	N/A	0.4	32	8	[37]
2019	Ag@SnO_2	NPs	solar (300 W Xe lamp)	N/A	N/A	0.2	70	4	[72]
2020	Ce doped SnO_2	particles	vis (300 W Xe lamp with a UV filter (λ > 420 nm)	10^4	65	0.4	82	10	[39]
2020	BiOBr/SnO_2	NPs	vis (150 W tungsten halogen lamp with a UV cut-off filter (λ > 420 nm)	600	N/A	0.10	50.3	N/A (NO-to-NO_2 conversion was studied via in situ DRIFTS)	[70]
2021	g-C_3N_4/SnO_2	NPs	vis (300 W solar simulator with a UV filter (λ > 420 nm)	500	70	0.2	44.17	9.29	[71]
2021	SnO_{2-x}/g-C_3N_4	NPs	vis (300 W solar simulator with a UV cut-off filter (λ > 420 nm)	500	N/A	0.2	40.8	7.5	[73]

Wu et al. reported the visible-light-driven elimination of NO over hydrothermally synthesized BiOBr/SnO_2 p–n heterojunction photocatalysts. The as-prepared BiOBr/SnO_2 photocatalyst with a molar ratio of 2:5 between SnO_2 NPs and BiOBr microspheres shows an enhanced NO_x photocatalytic removal of 50.3%, at an initial NO concentration of 600 ppb, and a great stability after four cycles. The generation of toxic NO_2 products was inhibited effectively. The charge movement at the BiOBr/SnO_2 p–n interface was also revealed via theoretical and experimental findings. Electrons in SnO_2 transfer into BiOBr over pre-formed charge migration channels and an internal electric field at the BiOBr/SnO_2 interface, which directs photoinduced electrons from the CB of BiOBr to that of SnO_2, thus prolonging the lifetime of photogenerated electron–hole pairs (Figure 8). The NO-to-NO_2 conversion and intermediates and products were confirmed via in situ diffuse reflectance infrared Fourier transform spectroscopy during NO oxidation [70].

Huy et al. [38] hydrothermally synthesized SnO_2 NPs adhering to TiO_2 nanotubes (SnO_2/TNTs) via a facile one-step method for the photocatalytic abatement of NO under visible light (Figure 9). At a NO concentration of 450 ppb in a continuous flow, SnO_2/TNTs yields a photocatalytic degradation of NO of 59.49%, which is much better than that of bare TiO_2 NTs (44.61%), SnO_2 NPs (39.55%), and a physical blend of SnO_2 NPs and TiO_2 NTs (39.18%). Also, the heterostructured photocatalyst shows an effective reduction of NO_2 generation after 30 min of photocatalytic reaction. The photogenerated electrons and $^{\bullet}O_2^-$ radicals played a primary role in the photocatalytic NO oxidation. Additionally, using photoluminescence (PL) spectroscopy, XPS, active species trapping tests, and ESR spectroscopy, the authors studied the photoinduced charge migration and trapping. They proposed the band structure of the SnO_2/TNTs and pointed out the existence of $^{\bullet}O_2^-$ and $^{\bullet}OH$ radicals as critical factors in the photocatalysis process [38]. These results demonstrated that the SnO_2 NPs could be both a host or an auxiliary material for the NO photocatalytic degradation.

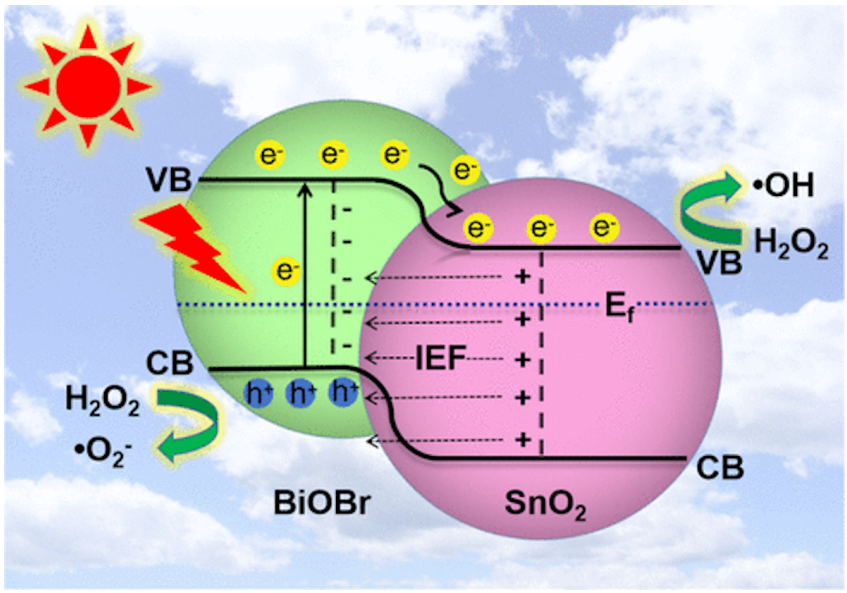

Figure 8: Proposed mechanisms for photocatalytic NO oxidation via interfacial charge migration over BiOBr/SnO_2 p–n heterojunctions. Figure 8 was reprinted with permission from [70], Copyright 2020 American Chemical Society. This content is not subject to CC BY 4.0.

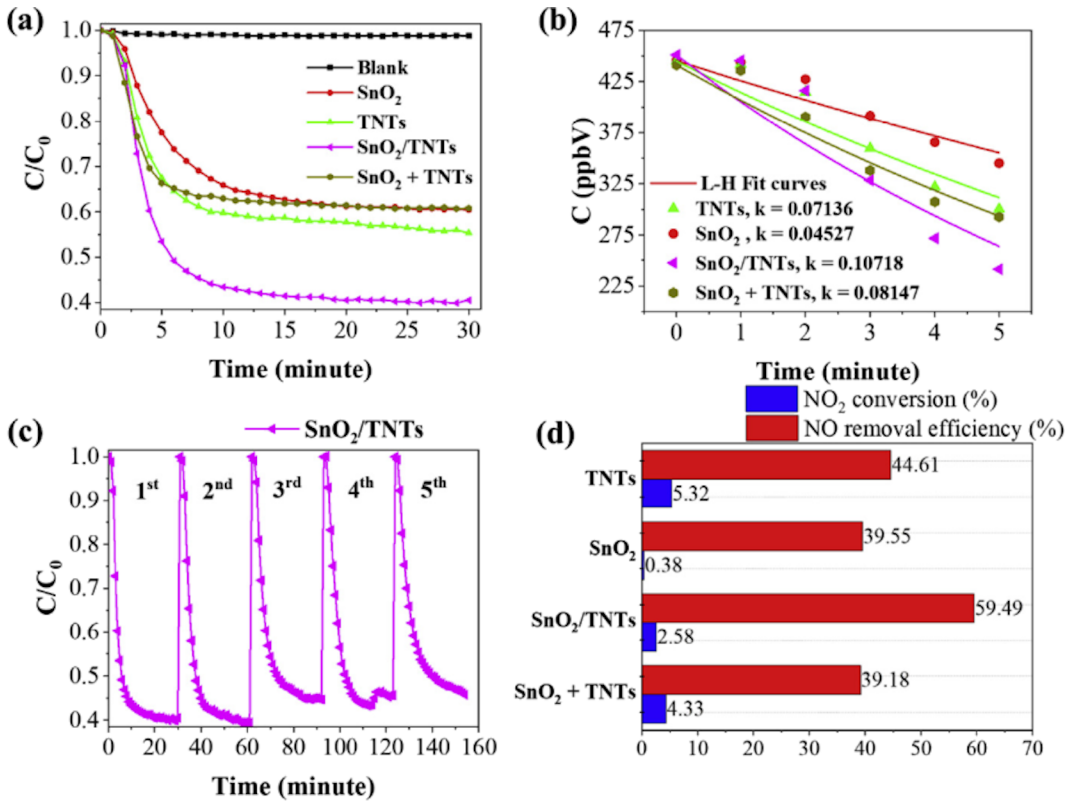

Figure 9: NO photocatalytic degradation of materials under visible light irradiation (a), the dependence of concentration on irradiation time (b), photochemical stability of SnO_2/TNTs (c), and NO removal efficacy and NO_2 conversion efficacy (d). Figure 9 was reprinted from [38], Chemosphere, vol. 215, by Huy, T. H.; Bui, D. P.; Kang, F.; Wang, Y. F.; Liu, S. H.; Thi, C. M.; You, S. J.; Chang, G. M.; Pham, V. V. "SnO_2/TiO_2 nanotube heterojunction: The first investigation of NO degradation by visible-light-driven photocatalysis", pages 323–332, Copyright (2018), with permission from Elsevier. This content is not subject to CC BY 4.0.

Besides the coupling with semiconductor oxides such as TiO_2 and BiOBr, recent works reported the successful combination of SnO_2 nanomaterials with conjugated polymers such as graphitic carbon nitride (g-C_3N_4) and polyaniline (PANI), yielding metal-free visible-light-driven photocatalysts for addressing NO gas pollution. Such combinations hold great potential because they exhibit a wide range of useful properties, including high conductivity, cost-effectiveness, high flexibility and processability, and ease of fabrication. These recent advances are highlighted and discussed in terms of preparation method and photocatalytic mechanism in this review. Regarding g-C_3N_4, Zou et al. successfully deposited SnO_2 quantum dots (QDs) on g-C_3N_4 sheets by a simple physical mixing process. The authors indicated that the SnO_2/g-C_3N_4 photocatalyst had a twice as high NO removal efficacy than bare SnO_2 QDs and a low NO_2 generation upon exposure to visible light for 30 min. This enhancement of the photocatalytic activity was interpreted as the synergistic effect between the high photo-oxidation ability of SnO_2 triggered by the visible light response of g-C_3N_4. Also, the key role of the SnO_2/g-C_3N_4 interface in inhibiting the production of NO_2 facilitates the transition of photogenerated carriers used for the NO removal [37].

Pham et al. showcased a step-scheme (S-scheme) photocatalyst composed of 2D/0D g-C_3N_4 nanosheet-assisted SnO_2 NPs (g-C_3N_4/SnO_2) for removing NO with low NO_2 generation. This work established an S-scheme charge transfer path by combining density functional theory (DFT) calculations, trapping experiments, and electron spin resonance measurements (Figure 10). Thus, the impact of intrinsic OVs within SnO_2 NPs and the resulting S-scheme heterojunction on the band structure, charge transfer, and photocatalytic activity was presented. The

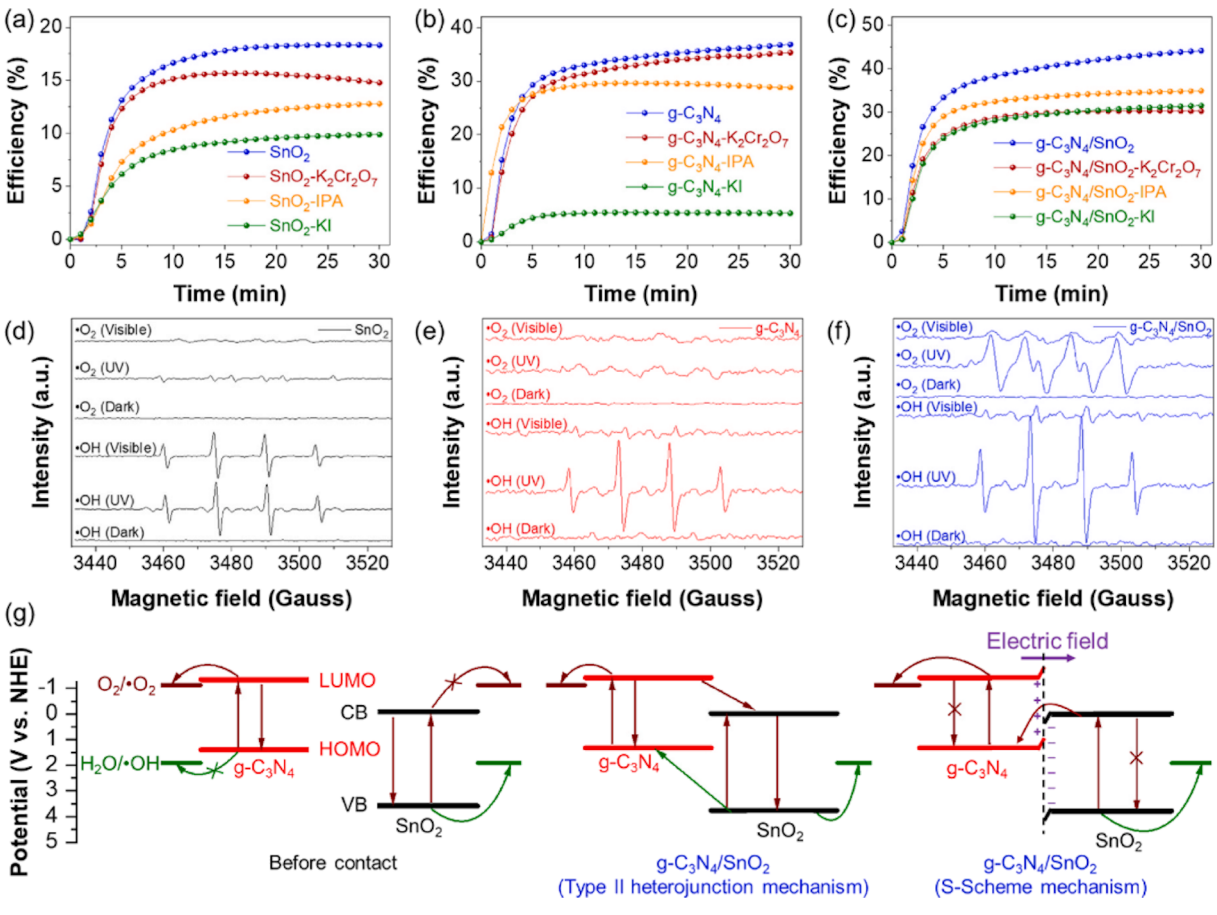

Figure 10: Photocatalytic NO removal efficacy over SnO_2 (a), g-C_3N_4 (b) and g-C_3N_4/SnO_2 (c) with scavengers under visible light ($400 < \lambda < 800$). ESR signals (d) of $^{\bullet}OH$ radicals, and $^{\bullet}O_2^-$ radicals of the materials after 10 min under visible light ($400 < \lambda < 800$). Growth curves of $^{\bullet}OH$ radicals (e) and $^{\bullet}O_2^-$ radicals (f) vs irradiation time of the materials. The charge transfer pathways of the materials (g). $K_2Cr_2O_7$, KI, and isopropyl alcohol (IPA) act as scavengers for electrons, holes, and $^{\bullet}OH$ radicals, respectively. The brown and green arrows indicate the path of electrons and holes, respectively. Figure 10 was reprinted from [71], Environmental Pollution, vol. 286, by Van Pham, V.; Mai, D.-Q.; Bui, D.-P.; Van Man, T.; Zhu, B.; Zhang, L.; Sangkaworn, J.; Tantirungrotechai, J.; Reutrakul, V.; Cao, T. M. "Emerging 2D/0D g-C3N4/SnO2 S-scheme photocatalyst: New generation architectural structure of heterojunctions toward visible-light-driven NO degradation", article no. 117510, Copyright (2021), with permission from Elsevier. This content is not subject to CC BY 4.0.

resulting heterojunction photocatalytically removed 40% NO (initial concentration of 500 ppb) and showed excellent photostability under visible light. The NO_2 production from the photocatalytic reaction was also negligible. The good photocatalytic NO degradation of the 2D/0D g-C_3N_4/SnO_2 catalyst is due to the defects actively trapping electrons and the charge transfer described in the S-scheme model. These factors increase the lifetime of electron–hole pairs and free radicals. The finding of this work enables the generation of a new and innovative structures with S-scheme heterojunctions for environmental treatment [71].

A similar model, a Z-scheme photocatalyst, was reported by Lu et al. who successfully fabricated a ternary nanohybrid consisting of mesoporous SnO_2, nitrogen-doped carbon quantum dots (NCDs), and $ZnSn(OH)_6$ using a simple in situ solvothermal method. This nanohybrid photocatalyst exhibited a broad optical response range and excellent oxidation ability and showed great potential in addressing air pollution. The ternary Z-scheme photocatalyst could remove 37% of NO under visible light and IR without generating NO_2. In addition, this work also discussed the critical role of NCDs in extending the light harvesting range and promoting the separation of photogenerated electrons. A considerable amount of reactive oxygen radicals was produced during the photocatalytic reaction, resulting from the large amount of free surface OH groups. PL, photocurrent response, electrochemical impedance spectroscopy (EIS) data, and the nanosecond-level time-resolved fluorescence decay spectra (Figure 11) demonstrated that the SnO_2/NCDs/ZHS nanohybrid achieved low charge carrier recombination, high photoactivity, and excellent photoinduced charge transfer to the surface of the semiconductor. This study enables new insights into the underlying mechanism of heterojunction photocatalysts, especially those with Z-shaped interfaces [76].

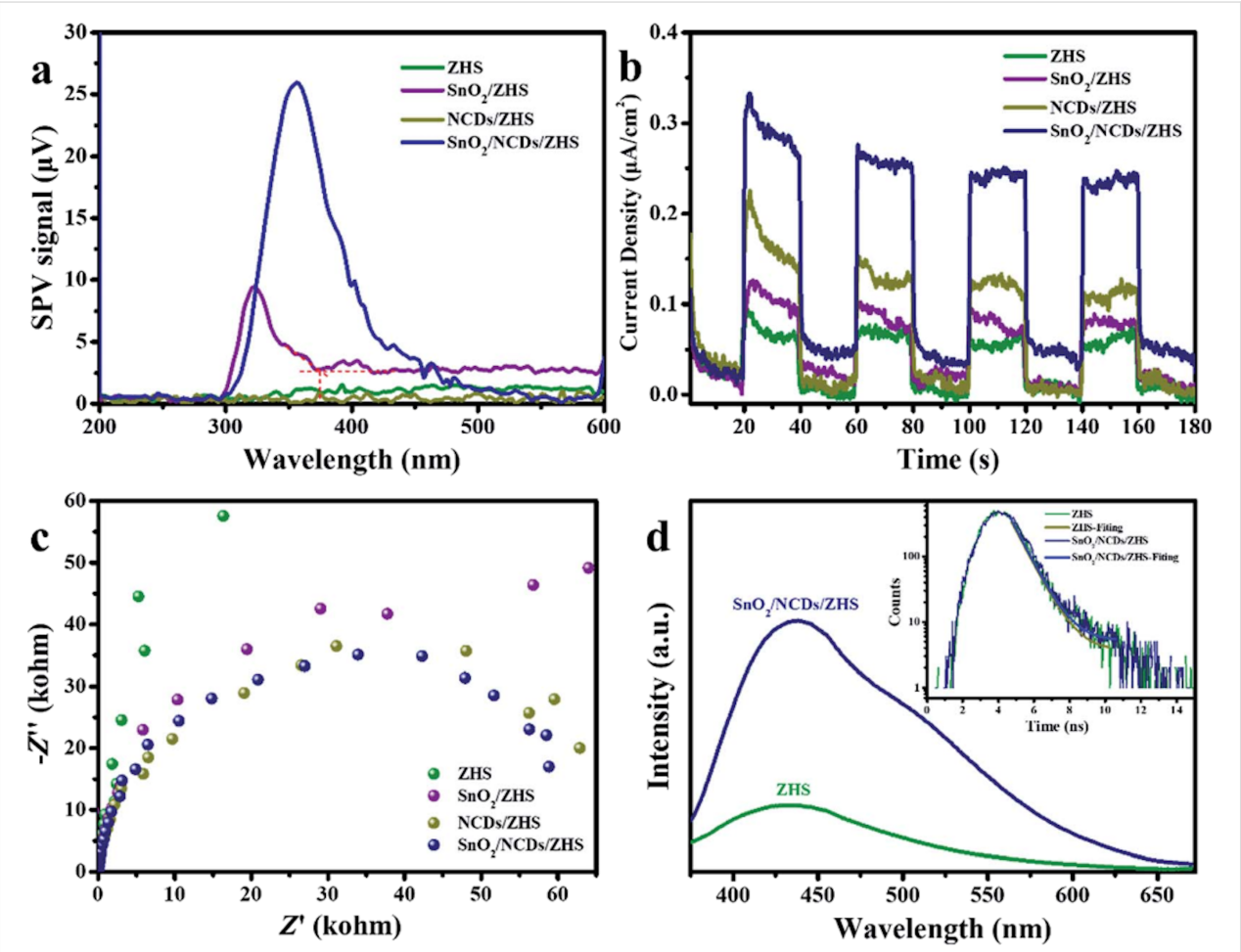

Figure 11: (a) Surface photovoltage spectroscopy, (b) transient photocurrent responses, (c) EIS Nyquist plots of ZHS, SnO_2/ZHS, NCDs/ZHS and SnO_2/NCDs/ZHS samples, and (d) PL spectra (inset: transient fluorescence decay spectra). Figure 11 was republished with permission of The Royal Society of Chemistry from [76] ("Constructing Z-scheme SnO_2/N-doped carbon quantum dots/$ZnSn(OH)_6$ nanohybrids with high redox ability for NO_x removal under VIS-NIR light" by Y. Lu et al., J. Mater. Chem. A, vol. 7, issue 26, © 2019); permission conveyed through Copyright Clearance Center, Inc. This content is not subject to CC BY 4.0.

Polyaniline (PANI) is a conducting polymer and compared to g-C_3N_4, PANI is inexpensive and easy to synthesize. Bui et al. [35] presented a SnO_2/PANI nanocomposite for photocatalytic NO removal under solar light for the first time. Furthermore, they found that the introduction of SnO_2 NPs increases the photostability of PANI during the photocatalytic process, which holds great potential for scalable manufacturing. Also, this work thoroughly discussed the adsorption and photocatalytic mechanisms, and the polymer photodegradation of the resulting nanocomposite using DFT techniques. The results confirmed that the interaction between NO and PANI is indeed a hydrogen bond and photogenerated holes serve as the primary factor of the photocatalytic NO removal [35]. Moreover, this study also indicated that hydrogen bonds between NO and PANI increased the adsorption of NO on the SnO_2/PANI surface, leading to enhanced photocatalysis. However, the photocatalytic stability of SnO_2/PANI is still a challenging problem.

Enesca et al. [29] developed photoactive heterostructures based on SnO_2, TiO_2, and $CuInS_2$ using an automated spray pyrolysis method, which is particularly beneficial for air cleaning applications. This work showed that the surface tension of the material surface directly impacts the photocatalytic activity under humid conditions. Furthermore, introducing $CuInS_2$ enables good UV and vis absorption thus extending the light-responsive range. As a result, such a $CuInS_2/TiO_2/SnO_2$ heterostructure presented one of the highest photocatalytic efficacies (51.7%) in acetaldehyde removal. However, this work also opens some new questions for future studies on optimizing the band structure, which remains critical for studying charge separation [29]. In another study, a SnO_2–Zn_2SnO_4 Z-scheme photocatalyst system was prepared with a graphene modification to create surface vacancy sites in the composite, which contributed to an enhanced photoactivity in the oxidation of NO and acetone [75]. The presence of graphene induces the formation of SnO_2 and introduces Sn vacancies, which supports the electron transfer from the CB of Zn_2SnO_4 to oxygen under visible light irradiation (Figure 12). The authors only used a visible light LED with low power (3 W) and obtained a high efficacy of NO degradation (59.3%) [75]. However, the disadvantage of this study and other studies is that it did not determine the formation of NO_2 after the reaction (see Table 1).

Creation of narrower bandgaps

To narrow the bandgap of SnO_2 is an advanced strategy for enhancing photocatalytic ability. Specifically, reducing the bandgap of SnO_2 will increase the photoresponse in the visible light region, making up 45% of the solar spectrum. Moreover, reducing the bandgap will also create many defect states that can decrease the recombination of photogenerated electron–hole

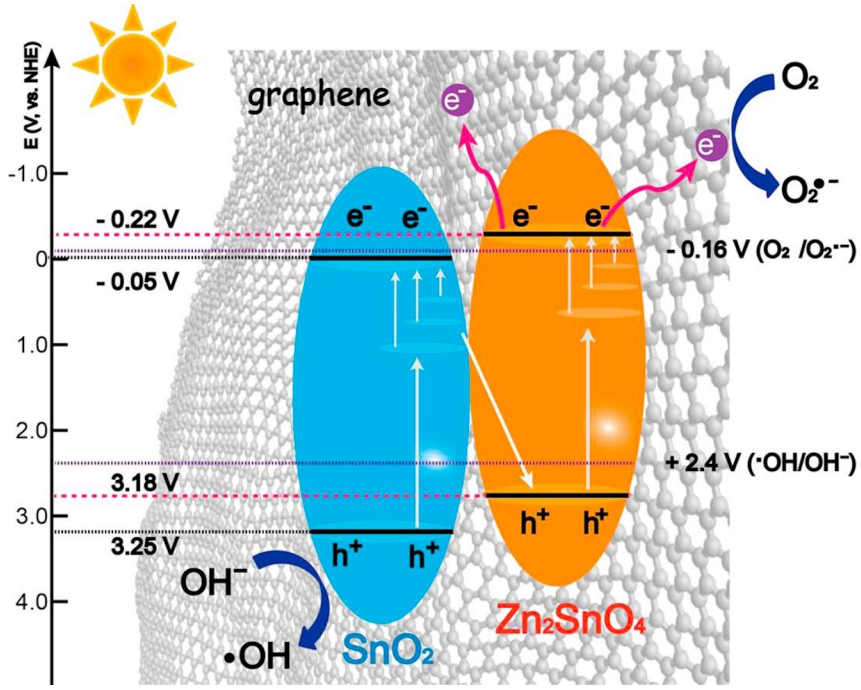

Figure 12: A mechanism of NO photocatalytic oxidation over SnO_2–Zn_2SnO_4/graphene. Figure 12 was reprinted from [75], Chemical Engineering Journal, vol. 336, by Li, Y.; Wu, X.; Ho, W.; Lv, K.; Li, Q.; Li, M.; Lee, S. C. "Graphene-induced formation of visible-light-responsive SnO_2-Zn_2SnO_4 Z-scheme photocatalyst with surface vacancy for the enhanced photoreactivity towards NO and acetone oxidation", pages 200–210, Copyright (2017), with permission from Elsevier. This content is not subject to CC BY 4.0.

pairs. There are many approaches to narrowing the bandgap of SnO_2, such as modifying SnO_2 by noble metal, graphene, or doping, including self-doping SnO_2 (Sn^{2+}-doped SnO_2 or SnO_{2-x}). In general, doping SnO_2 will reduce the bandgap, which enhances the photoactivity in the visible light region for SnO_2. The narrowing of the bandgap by introducing defects in metal oxide semiconductors opens up the possibility of their use in the visible spectrum [77]. Recently, Xie et al. reported using SnO_2/graphene quantum dot (GQD) composites. They showed that the absorption edge of as-prepared SnO_2 (Figure 13a black line) is around 340 nm, equaling to a bandgap of 3.64 eV. The PL peak of SnO_2 was located in the range of 280–485 nm (Figure 13b). The combination of GQDs and SnO_2 did not affect the shape of the PL peak. However, the corresponding PL intensity of the SnO_2/GQDs sample was decreased because of the greatly reduced radiative charge recombination of SnO_2. Moreover, enhanced visible light response and enhanced charge separation in the sample with GQDs have been observed (Figure 13c). The EIS measurements (Figure 13d) indicated that the diameter of the arc radius of SnO_2/GQDs (1%) is much smaller than that of SnO_2, confirming that the GQDs contributed to improving the charge separation, significantly reducing indoor NO under visible light irradiation. The optimized composite removed 57% of the initial NO while generating a negligible amount of NO_2. In addition, this work found that the insertion of graphene quantum dots did not induce any noticeable impact on the structure of the SnO_2 component. Still, its presence strongly enhanced energy harvesting and charge separation in the resulting composite [36].

Regarding the self-doping SnO_2, Pham et al. reported on the fabrication of a SnO_{2-x}/g-C_3N_4 heterojunction, inducing an

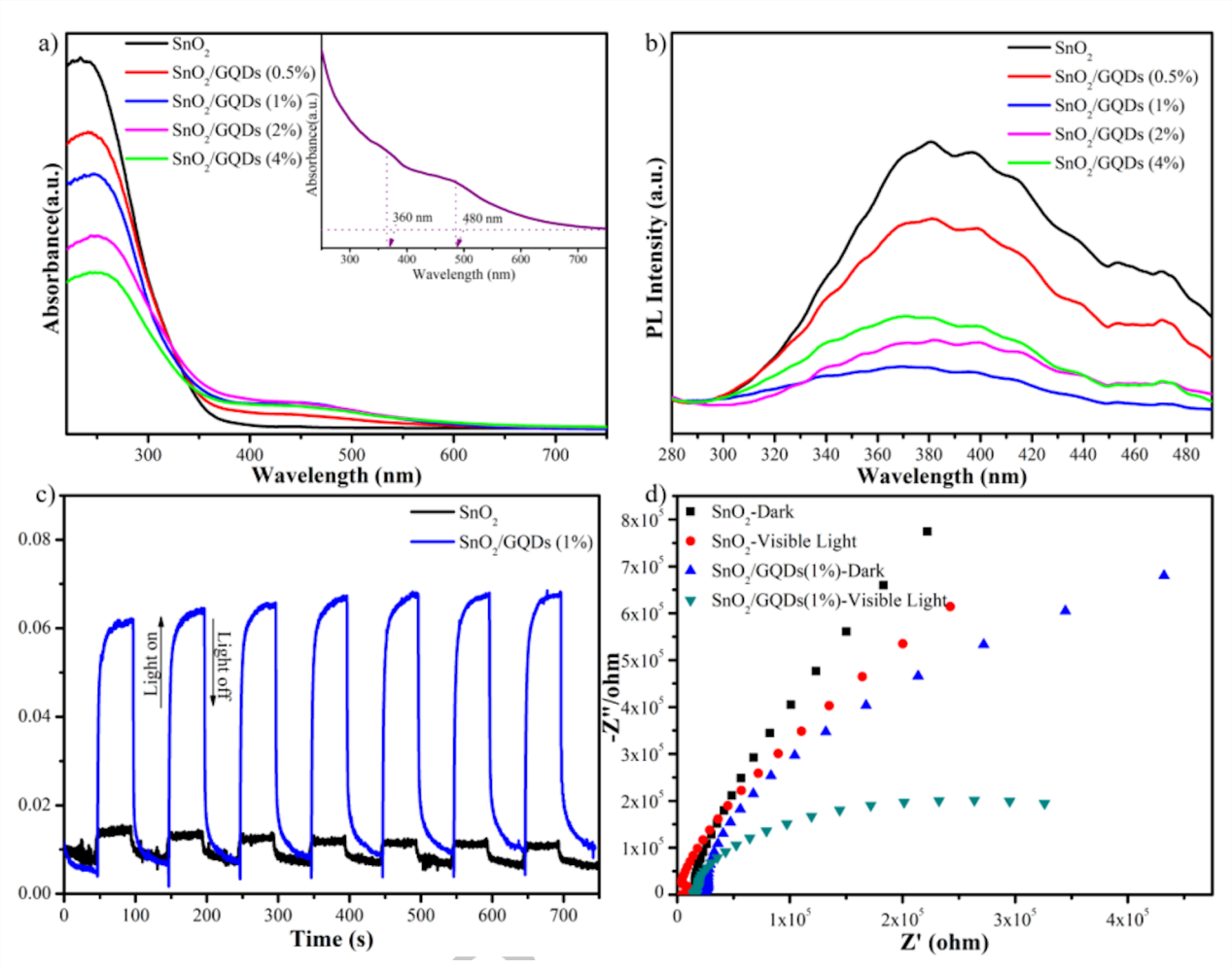

Figure 13: (a) Diffuse reflectance spectra of SnO_2 and SnO_2/GQDs composites. Inset is the absorption spectrum of GQDs dispersed in water. (b) PL spectra of SnO_2 and SnO_2/GQDs composites. Excitation wavelength: 260 nm. (c) Transient photocurrent response and (d) EIS curves of SnO_2 and SnO_2/GQDs (1%) under visible light illumination and in darkness. Figure 13 was reprinted from [36], Applied Surface Science, vol. 448, by Xie, Y.; Yu, S.; Zhong, Y.; Zhang, Q.; Zhou, Y. "SnO_2/graphene quantum dots composited photocatalyst for efficient nitric oxide oxidation under visible light", pages 655–661, Copyright (2018), with permission from Elsevier. This content is not subject to CC BY 4.0.

S-scheme interface, showing impressive photocatalytic NO removal under visible light. In this work, Pham et al. indicated that deep trap centers of OV defects (Figure 14) formed with a very high concentration (36.69%), mainly from $V_{O}^{\bullet}$ and $V_{O}^{\bullet\bullet}$ centers. These OVs reduced the bandgaps of SnO_2 (3.7 eV) and SnO_{2-x} (3.17 eV), significantly impacting the reaction rate during the photocatalytic process, leading to enhanced NO removal under visible light. Also, the reported selectivity of the SnO_{2-x}/g-C_3N_4 heterojunction is three times higher than that of the bare materials. The finding of this work further supports the importance of OVs in the design of photocatalytic materials [73].

Song et al. synthesized Ce-doped SnO_2 materials with a high number of OVs to improve NO oxidation removal efficacy (Figure 15). The results showed that the excellent NO oxidation activity of Ce–SnO_2 materials was based on the OVs, which create a suitable site for the formation of NO^- intermediates to generate nitrite and nitrate products in the photocatalytic reaction processes. Moreover, additional OVs could be readily formed by thermal treatment under argon atmosphere. The work suggested an innovative approach for developing high-performance photocatalysts and a cost-effective, environmentally benign way through heat treatment in different atmospheres [39].

Combining noble metals with SnO_2, such as in Au/SnO_2 [78] or Pd/SnO_2 [79], is an advanced approach yielding an effective performance for gas sensing. However, There is only one report by Bui et al. on using Ag@SnO_2 NPs for removing NO, taking advantage of plasmonic-induced photocatalysis [72]. The Ag@SnO_2 NPs were fabricated by a simple and green approach using hydrothermal growth and photoreduction deposition. The introduction of Ag induced a bending of the band structure of SnO_2 NPs, leading to a change of the Fermi level. As a result, the Ag@SnO_2 NPs showed an impressive photocatalytic NO removal of 70% while generating very little NO_2 (4%) after 30 min. In addition, this work one to understand the

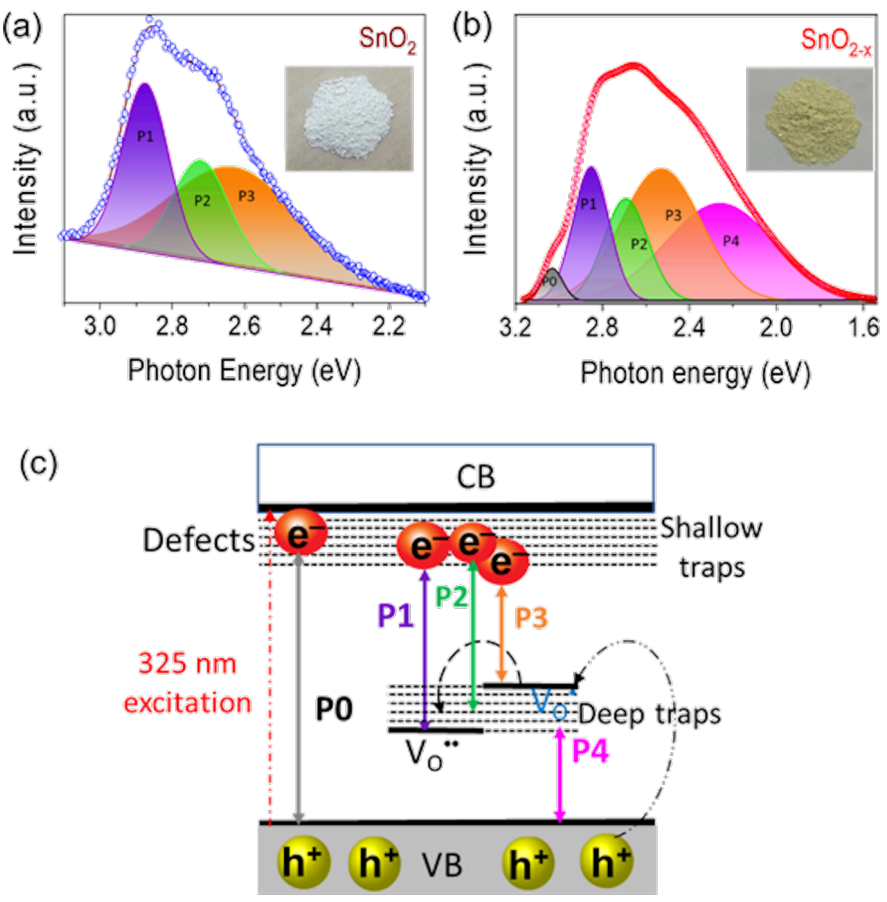

Figure 14: Gaussian fit of PL spectra with inserted images of sample color of SnO_2 (a) and SnO_{2-x} (b); and proposed schematic model for emissions from defects in SnO_2 and SnO_{2-x} (c). Figure 14 was reproduced from [73], © 2021 The Chinese Ceramic Society. Production and hosting by Elsevier B.V. This is an open access article under the CC BY-NC-ND license (http://creativecommons.org/licenses/by-nc-nd/4.0/). This content is not subject to CC BY 4.0.

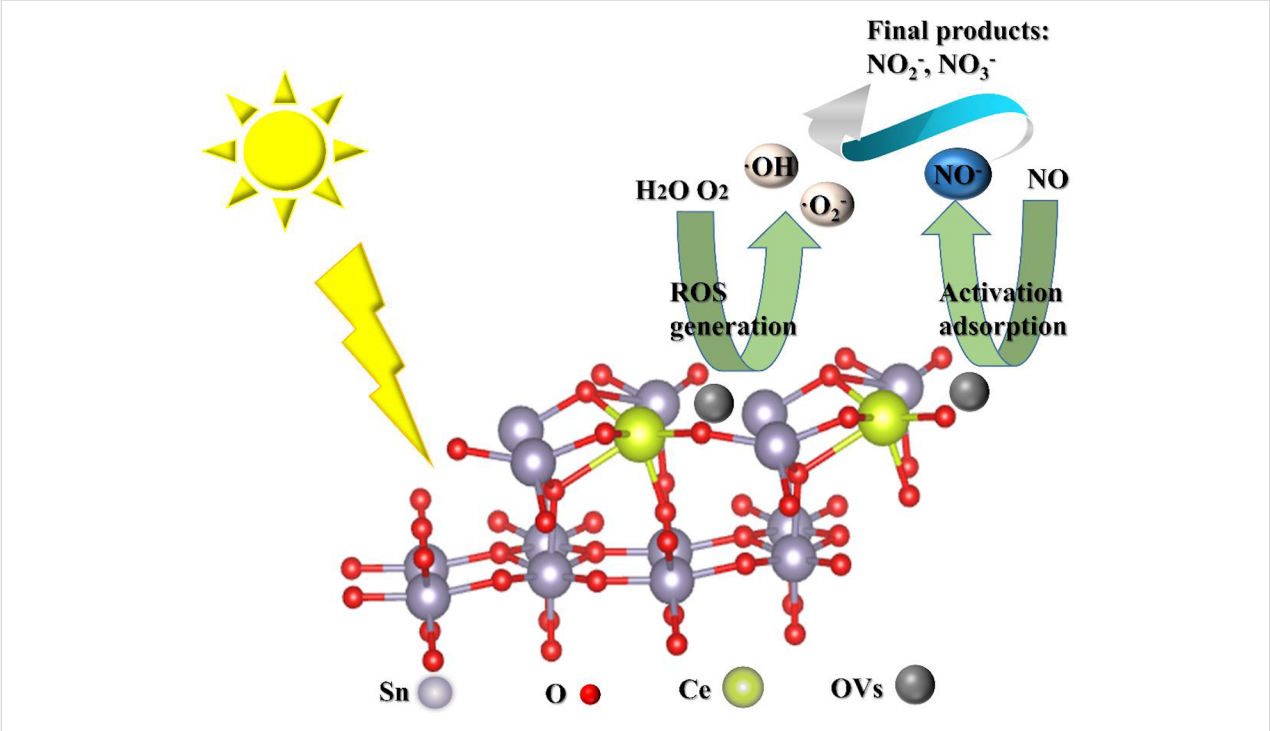

Figure 15: The proposed process of NO + O_2 reaction over Ce–SnO_2 under visible light irradiation. The ROS reacted with the activated NO^- intermediates to nitrates and nitrites. Figure 15 was reprinted from [39], Applied Catalysis B: Environmental, vol. 284, by Song, X.; Qin, G.; Cheng, G.; Jiang, W.; Chen, X.; Dai, W.; Fu, X. "Oxygen defect-induced NO– intermediates promoting NO deep oxidation over Ce doped SnO_2 under visible light", article no. 119761, Copyright (2020), with permission from Elsevier. This content is not subject to CC BY 4.0.

underlying photocatalytic mechanism through the species lifespan obtained from trapping experiments and time-dependent ESR signals (Figure 16). Electrons and holes are equally important for photocatalysis [72].

Conclusion

Regarding the improvement of the photocatalytic NO degradation over SnO_2 nanomaterials there are many developments and approaches, such as BiOBr/SnO_2, g-C_3N_4/SnO_2, SnO_2/NCDs/$ZnSn(OH)_6$, Ce-doped SnO_2, SnO_2 self-doped with Sn^{2+}, and Ag@SnO_2. These systems yielded an enhanced photocatalytic NO_x degradation either through increasing the charge transfer, through structural changes leading to bandgap reduction, or through the generation of favorable surface states for the NO_x decomposition reaction. However, the performance in NO removal is still low (only nearly 60% under visible light and

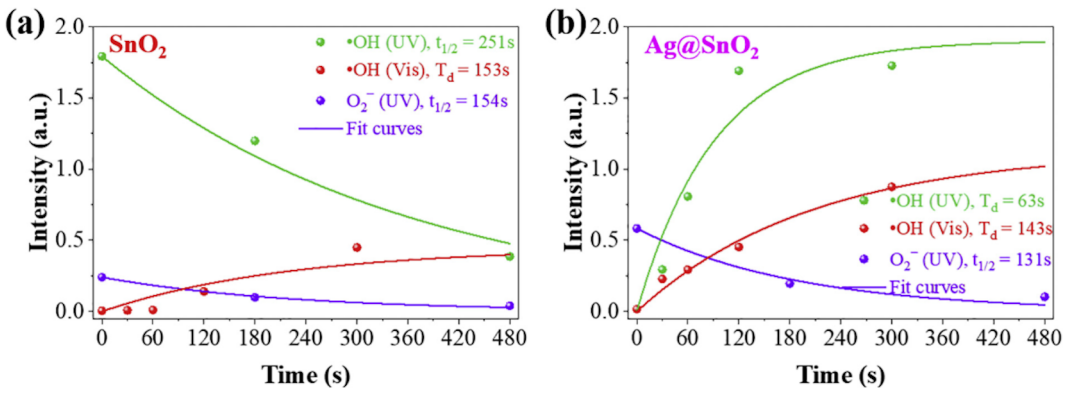

Figure 16: Decay and growth curves of primary ROS versus radiation time of SnO_2 NPs (a) and Ag@SnO_2 (b). Figure 16 was reprinted from [72], Catalysis Communications, vol. 136, by Bui, D. P.; Nguyen, M. T.; Tran, H. H.; You, S.-J.; Wang, Y.-F.; Van Viet, P. "Green synthesis of Ag@SnO_2 nanocomposites for enhancing photocatalysis of nitrogen monoxide removal under solar light irradiation", article no. 105902, Copyright (2019), with permission from Elsevier. This content is not subject to CC BY 4.0.

75% under solar light). Also, the syntheses of the materials are difficult to upscale to an industrial scale. Moreover, the photocatalysts were prepared in powder form, which is not suitable for emerging applications. Based on this review, we suggest the following subjects for future research: (1) improving the NO photocatalytic degradation by combining other favorable bandgap semiconductors; (2) constructing a ternary heterostructure to create double Z-scheme/S-scheme materials, preferably using two redox sites; (3) synthesizing other morphologies of SnO_2 such as nanorods, nanotubes, or 3D structures to increase the specific surface area of the catalyst; (4) upscaling the syntheses and using other synthesis approaches such as sol–gel or chemical vapor deposition to form thin film materials that can replace powder materials, (5) adhering the catalyst materials on commercial films such as polypropylene, polytetrafluoroethylene, or PM2.5 films for real-life applications, such as air filters and NO_x gas treatment membranes; and (6) applying the materials in biological media where the presence of NO/NO_2 is predominant.

Acknowledgements

The authors sincerely thank the Department of Science and Technology, Ho Chi Minh City, the CM Thi Laboratory, and Mr. Sang T. Truong for support. The authors would also like to thank Elsevier, the American Chemical Society, the American Physical Society, and the Royal Society of Chemistry for allowing us to reuse some of the materials in this work.

ORCID® iDs

Viet Van Pham - https://orcid.org/0000-0002-8697-7095
Hong-Huy Tran - https://orcid.org/0000-0002-7883-596X

References

1. WHO Air pollution. https://www.who.int/health-topics/air-pollution#tab=tab_1 (accessed June 23, 2021).
2. WHO Regional Office for Europe. *Chapter 7.1-Nitrogen dioxide;* Copenhagen, Denmark, 2000; pp 1–33.
3. United States Environmental Protection Agency. *Nitrogen Oxides Control Regulations, Ozone Control Strategies, Ground-level Ozone;* New England, 2021.
4. WHO. *Ambient (outdoor) air pollution;* 2021.
5. Health Canada. Residential Indoor Air Quality Guideline: Nitrogen Dioxide. 2015; https://www.canada.ca/en/health-canada/services/publications/healthy-living/residential-indoor-air-quality-guideline-nitrogen-dioxide.html.
6. Chossiere, G. P.; Xu, H.; Dixit, Y.; Isaacs, S.; Eastham, S. D.; Allroggen, F.; Speth, R. L.; Barrett, S. R. H. *Sci. Adv.* **2021,** *7,* eabe1178. doi:10.1126/sciadv.abe1178
7. United States Environmental Protection Agency. *Nitrogen Oxides (NOx), Why and How They Are Controlled;* North Carolina, 1999.
8. Haneda, M.; Ota, Y.; Doi, Y.; Hattori, M. *J. Mater. Sci.* **2016,** *51,* 10949–10959. doi:10.1007/s10853-016-0307-8
9. Rajta, A.; Bhatia, R.; Setia, H.; Pathania, P. *J. Appl. Microbiol.* **2020,** *128,* 1261–1278. doi:10.1111/jam.14476
10. Bogaerts, W. F.; Lampert, C. M. *J. Mater. Sci.* **1983,** *18,* 2847–2875. doi:10.1007/bf00700767
11. Zou, J.; Xu, Y.; Hou, B.; Wu, D.; Sun, Y. *China Particuol.* **2007,** *5,* 206–212. doi:10.1016/j.cpart.2007.03.006
12. Ângelo, J.; Andrade, L.; Madeira, L. M.; Mendes, A. *J. Environ. Manage.* **2013,** *129,* 522–539. doi:10.1016/j.jenvman.2013.08.006
13. Batzill, M.; Diebold, U. *Prog. Surf. Sci.* **2005,** *79,* 47–154. doi:10.1016/j.progsurf.2005.09.002
14. He, Z.; Zhou, J. *Mod. Res. Catal.* **2013,** *02,* 13–18. doi:10.4236/mrc.2013.23a003
15. Savioli, J.; Gavin, A. L.; Lucid, A. K.; Watson, G. W. The structure and electronic structure of tin oxides. In *Tin Oxide Materials;* Orlandi, M. O., Ed.; 2020; pp 11–39. doi:10.1016/b978-0-12-815924-8.00002-5
16. Grządziel, L.; Krzywiecki, M. *Front. Nanosci.* **2019,** *14,* 215–256. doi:10.1016/b978-0-08-102572-7.00008-8
17. Subramanian, V.; Burke, W. W.; Zhu, H.; Wei, B. *J. Phys. Chem. C* **2008,** *112,* 4550–4556. doi:10.1021/jp711551p
18. Xiao, L.; Shen, H.; von Hagen, R.; Pan, J.; Belkoura, L.; Mathur, S. *Chem. Commun.* **2010,** *46,* 6509–6511. doi:10.1039/c0cc01156h
19. Kar, A.; Kundu, S.; Patra, A. *J. Phys. Chem. C* **2011,** *115,* 118–124. doi:10.1021/jp110313b
20. Birkel, A.; Lee, Y.-G.; Koll, D.; Meerbeek, X. V.; Frank, S.; Choi, M. J.; Kang, Y. S.; Char, K.; Tremel, W. *Energy Environ. Sci.* **2012,** *5,* 5392–5400. doi:10.1039/c1ee02115j
21. Priya, S.; Halder, J.; Mandal, D.; Chowdhury, A.; Singh, T.; Chandra, A. *J. Mater. Sci.* **2021,** *56,* 9883–9893. doi:10.1007/s10853-021-05942-x
22. Wang, Z.; Zhi, M.; Xu, M.; Guo, C.; Man, Z.; Zhang, Z.; Li, Q.; Lv, Y.; Zhao, W.; Yan, J.; Zhai, C. *J. Mater. Sci.* **2021,** *56,* 7348–7356. doi:10.1007/s10853-020-05737-6
23. Jiang, S.; Yue, W.; Gao, Z.; Ren, Y.; Ma, H.; Zhao, X.; Liu, Y.; Yang, X. *J. Mater. Sci.* **2013,** *48,* 3870–3876. doi:10.1007/s10853-013-7189-9
24. Li, T.-T.; Xia, L.; Yu, H.; Huang, X.-X. *J. Mater. Sci.* **2020,** *55,* 11949–11958. doi:10.1007/s10853-020-04892-0
25. Anandan, K.; Rajendran, V. *Superlattices Microstruct.* **2015,** *85,* 185–197. doi:10.1016/j.spmi.2015.05.031
26. Bouras, K.; Rehspringer, J.-L.; Schmerber, G.; Rinnert, H.; Colis, S.; Ferblantier, G.; Balestrieri, M.; Ihiawakrim, D.; Dinia, A.; Slaoui, A. *J. Mater. Chem. C* **2014,** *2,* 8235–8243. doi:10.1039/c4tc01202j
27. Yadav, B. C.; Verma, N.; Shukla, T.; Singh, S.; Sabhajeet, S. R. *J. Mater. Sci.: Mater. Electron.* **2016,** *27,* 7852–7863. doi:10.1007/s10854-016-4776-y
28. Malik, R.; Tomer, V. K.; Chaudhary, V.; Dahiya, M. S.; Rana, P. S.; Nehra, S. P.; Duhan, S. *ChemistrySelect* **2016,** *1,* 3247–3258. doi:10.1002/slct.201600634
29. Enesca, A.; Yamaguchi, Y.; Terashima, C.; Fujishima, A.; Nakata, K.; Duta, A. *J. Catal.* **2017,** *350,* 174–181. doi:10.1016/j.jcat.2017.02.015
30. Fan, C.; Song, X.; Yin, Z.; Yu, H.; Sun, S. *J. Mater. Sci.* **2006,** *41,* 5696–5698. doi:10.1007/s10853-006-0067-y
31. Li, D.; Huang, J.; Li, R.; Chen, P.; Chen, D.; Cai, M.; Liu, H.; Feng, Y.; Lv, W.; Liu, G. *J. Hazard. Mater.* **2021,** *401,* 123257. doi:10.1016/j.jhazmat.2020.123257
32. Dawar, A. L.; Kumar, A.; Sharma, S.; Tripathi, K. N.; Mathur, P. C. *J. Mater. Sci.* **1993,** *28,* 639–644. doi:10.1007/bf01151238
33. Kim, S. P.; Choi, M. Y.; Choi, H. C. *Mater. Res. Bull.* **2016,** *74,* 85–89. doi:10.1016/j.materresbull.2015.10.024
34. Al-Hamdi, A. M.; Rinner, U.; Sillanpää, M. *Process Saf. Environ. Prot.* **2017,** *107,* 190–205. doi:10.1016/j.psep.2017.01.022

35. Bui, P. D.; Tran, H. H.; Kang, F.; Wang, Y.-F.; Cao, T. M.; You, S.-J.; Vu, N. H.; Pham, V. V. *ACS Appl. Nano Mater.* **2018,** *1,* 5786–5794. doi:10.1021/acsanm.8b01445
36. Xie, Y.; Yu, S.; Zhong, Y.; Zhang, Q.; Zhou, Y. *Appl. Surf. Sci.* **2018,** *448,* 655–661. doi:10.1016/j.apsusc.2018.04.145
37. Zou, Y.; Xie, Y.; Yu, S.; Chen, L.; Cui, W.; Dong, F.; Zhou, Y. *Appl. Surf. Sci.* **2019,** *496,* 143630. doi:10.1016/j.apsusc.2019.143630
38. Huy, T. H.; Bui, D. P.; Kang, F.; Wang, Y.-F.; Liu, S.-H.; Thi, C. M.; You, S.-J.; Chang, G.-M.; Pham, V. V. *Chemosphere* **2019,** *215,* 323–332. doi:10.1016/j.chemosphere.2018.10.033
39. Song, X.; Qin, G.; Cheng, G.; Jiang, W.; Chen, X.; Dai, W.; Fu, X. *Appl. Catal., B* **2021,** *284,* 119761. doi:10.1016/j.apcatb.2020.119761
40. Islam, M. H.; Hogarth, C. A.; Lott, K. A. *J. Mater. Sci.* **1989,** *24,* 1305–1308. doi:10.1007/pl00020212
41. Dou, M.; Persson, C. *J. Appl. Phys.* **2013,** *113,* 083703. doi:10.1063/1.4793273
42. Zhou, W.; Liu, Y.; Yang, Y.; Wu, P. *J. Phys. Chem. C* **2014,** *118,* 6448–6453. doi:10.1021/jp500546r
43. Yu, H.; Wang, S.; Xiao, C.; Xiao, B.; Wang, P.; Li, Z.; Zhang, M. *CrystEngComm* **2015,** *17,* 4316–4324. doi:10.1039/c5ce00448a
44. Entradas, T.; Cabrita, J. F.; Dalui, S.; Nunes, M. R.; Monteiro, O. C.; Silvestre, A. J. *Mater. Chem. Phys.* **2014,** *147,* 563–571. doi:10.1016/j.matchemphys.2014.05.032
45. Mounkachi, O.; Salmani, E.; Lakhal, M.; Ez-Zahraouy, H.; Hamedoun, M.; Benaissa, M.; Kara, A.; Ennaoui, A.; Benyoussef, A. *Sol. Energy Mater. Sol. Cells* **2016,** *148,* 34–38. doi:10.1016/j.solmat.2015.09.062
46. Babu, B.; Neelakanta Reddy, I.; Yoo, K.; Kim, D.; Shim, J. *Mater. Lett.* **2018,** *221,* 211–215. doi:10.1016/j.matlet.2018.03.107
47. Fan, C.-M.; Peng, Y.; Zhu, Q.; Lin, L.; Wang, R.-X.; Xu, A.-W. *J. Phys. Chem. C* **2013,** *117,* 24157–24166. doi:10.1021/jp407296f
48. Batzill, M.; Katsiev, K.; Burst, J. M.; Diebold, U.; Chaka, A. M.; Delley, B. *Phys. Rev. B* **2005,** *72,* 165414. doi:10.1103/physrevb.72.165414
49. Van Viet, P.; Huy, T. H.; Sang, N. X.; Thi, C. M.; Van Hieu, L. *J. Mater. Sci.* **2018,** *53,* 3364–3374. doi:10.1007/s10853-017-1762-6
50. Van Viet, P.; Thi, C. M.; Hieu, L. V. *J. Nanomater.* **2016,** *2016,* 1–8. doi:10.1155/2016/4231046
51. Nam, V. H.; Van Viet, P.; Van Hieu, L.; Thi, C. M. *Mater. Res. Express* **2016,** *3,* 105901. doi:10.1088/2053-1591/3/10/105901
52. Zhong, Y.; Li, W.; Zhao, X.; Jiang, X.; Lin, S.; Zhen, Z.; Chen, W.; Xie, D.; Zhu, H. *ACS Appl. Mater. Interfaces* **2019,** *11,* 13441–13449. doi:10.1021/acsami.9b01737
53. Mäki-Jaskari, M. A.; Rantala, T. T.; Golovanov, V. V. *Surf. Sci.* **2005,** *577,* 127–138. doi:10.1016/j.susc.2005.01.004
54. Xu, G.; Zhang, L.; He, C.; Ma, D.; Lu, Z. *Sens. Actuators, B* **2015,** *221,* 717–722. doi:10.1016/j.snb.2015.06.143
55. Tiya-Djowe, A.; Dourges, M.-A.; Deleuze, H. *J. Mater. Sci.* **2020,** *55,* 4792–4807. doi:10.1007/s10853-019-04335-5
56. Wang, M.; Gao, Y.; Dai, L.; Cao, C.; Guo, X. *J. Solid State Chem.* **2012,** *189,* 49–56. doi:10.1016/j.jssc.2012.01.021
57. Jain, K.; Shrivastava, A.; Rashmi, R. *ECS Trans.* **2006,** *1* (21), 1–7. doi:10.1149/1.2218985
58. Zhao, Q.; Ju, D.; Deng, X.; Huang, J.; Cao, B.; Xu, X. *Sci. Rep.* **2015,** *5,* 7874. doi:10.1038/srep07874
59. Talebian, N.; Jafarinezhad, F. *Ceram. Int.* **2013,** *39,* 8311–8317. doi:10.1016/j.ceramint.2013.03.101
60. Park, M.-S.; Kang, Y.-M.; Wang, G.-X.; Dou, S.-X.; Liu, H.-K. *Adv. Funct. Mater.* **2008,** *18,* 455–461. doi:10.1002/adfm.200700407
61. Nahirniak, S.; Dontsova, T.; Dusheiko, M.; Smertenko, P.; Kwapinski, W. *J. Mater. Sci.: Mater. Electron.* **2020,** *31,* 21934–21947. doi:10.1007/s10854-020-04697-6
62. Matysiak, W.; Tański, T.; Smok, W.; Polishchuk, O. *Sci. Rep.* **2020,** *10,* 14802. doi:10.1038/s41598-020-71383-2
63. Shen, Y.; Wang, W.; Fan, A.; Wei, D.; Liu, W.; Han, C.; Shen, Y.; Meng, D.; San, X. *Int. J. Hydrogen Energy* **2015,** *40,* 15773–15779. doi:10.1016/j.ijhydene.2015.09.077
64. Chu, D.; Mo, J.; Peng, Q.; Zhang, Y.; Wei, Y.; Zhuang, Z.; Li, Y. *ChemCatChem* **2011,** *3,* 371–377. doi:10.1002/cctc.201000334
65. Pijolat, C.; Riviere, B.; Kamionka, M.; Viricelle, J. P.; Breuil, P. *J. Mater. Sci.* **2003,** *38,* 4333–4346. doi:10.1023/a:1026387100072
66. Wang, Y.-F.; Lei, B.-X.; Hou, Y.-F.; Zhao, W.-X.; Liang, C.-L.; Su, C.-Y.; Kuang, D.-B. *Inorg. Chem.* **2010,** *49,* 1679–1686. doi:10.1021/ic902092e
67. Le, T. H.; Truong, Q. D.; Kimura, T.; Li, H.; Guo, C.; Yin, S.; Sato, T.; Ling, Y.-C. *Solid State Sci.* **2013,** *15,* 29–35. doi:10.1016/j.solidstatesciences.2012.09.004
68. Zhang, L.; Tong, R.; Shirsath, S. E.; Yang, Y.; Dong, G. *J. Mater. Chem. A* **2021,** *9,* 5000–5006. doi:10.1039/d0ta12101k
69. Huy, T. H.; Phat, B. D.; Thi, C. M.; Van Viet, P. *Environ. Chem. Lett.* **2019,** *17,* 527–531. doi:10.1007/s10311-018-0801-0
70. Wu, H.; Yuan, C.; Chen, R.; Wang, J.; Dong, F.; Li, J.; Sun, Y. *ACS Appl. Mater. Interfaces* **2020,** *12,* 43741–43749. doi:10.1021/acsami.0c12628
71. Van Pham, V.; Mai, D.-Q.; Bui, D.-P.; Van Man, T.; Zhu, B.; Zhang, L.; Sangkaworn, J.; Tantirungrotechai, J.; Reutrakul, V.; Cao, T. M. *Environ. Pollut.* **2021,** *286,* 117510. doi:10.1016/j.envpol.2021.117510
72. Bui, D. P.; Nguyen, M. T.; Tran, H. H.; You, S.-J.; Wang, Y.-F.; Van Viet, P. *Catal. Commun.* **2020,** *136,* 105902. doi:10.1016/j.catcom.2019.105902
73. Van Viet, P.; Nguyen, T.-D.; Bui, D.-P.; Thi, C. M. *J. Materiomics* **2022,** *8,* 1–8. doi:10.1016/j.jmat.2021.06.006
74. Zhang, T.; Xu, J.; Qian, J.; Zhang, J. *J. Mater. Sci.* **2020,** *55,* 13605–13617. doi:10.1007/s10853-020-04998-5
75. Li, Y.; Wu, X.; Ho, W.; Lv, K.; Li, Q.; Li, M.; Lee, S. C. *Chem. Eng. J.* **2018,** *336,* 200–210. doi:10.1016/j.cej.2017.11.045
76. Lu, Y.; Huang, Y.; Cao, J.-j.; Li, H.; Ho, W.; Lee, S. C. *J. Mater. Chem. A* **2019,** *7,* 15782–15793. doi:10.1039/c9ta03504d
77. Kamble, V. B.; Umarji, A. M. *AIP Adv.* **2013,** *3,* 082120. doi:10.1063/1.4819451
78. Manjula, P.; Arunkumar, S.; Manorama, S. V. *Sens. Actuators, B* **2011,** *152,* 168–175. doi:10.1016/j.snb.2010.11.059
79. Zhang, K.; Yang, X.; Wang, Y.; Bing, Y.; Qiao, L.; Liang, Z.; Yu, S.; Zeng, Y.; Zheng, W. *Sens. Actuators, B* **2017,** *243,* 465–474. doi:10.1016/j.snb.2016.11.153

BEILSTEIN JOURNAL OF NANOTECHNOLOGY

Influence of thickness and morphology of MoS_2 on the performance of counter electrodes in dye-sensitized solar cells

Lam Thuy Thi Mai[1], Hai Viet Le[*2,3], Ngan Kim Thi Nguyen[2,3], Van La Tran Pham[2,3], Thu Anh Thi Nguyen[1], Nguyen Thanh Le Huynh[2,3] and Hoang Thai Nguyen[2,3]

Full Research Paper

Open Access

Address:
[1]Tra Vinh University, 126 Nguyen Thien Thanh Street, Ward 5, Tra Vinh City 940000, Vietnam, [2]University of Science, VNU-HCM, 227 Nguyen Van Cu Street, District 5, Ho Chi Minh City, 700000, Vietnam and [3]Vietnam National University Ho Chi Minh City, Linh Trung Ward, Thu Duc City, Ho Chi Minh City, 700000, Vietnam

Email:
Hai Viet Le[*] - lvhai@hcmus.edu.vn

* Corresponding author

Keywords:
cyclic voltammetry (CV); dye-sensitized solar cells (DSSCs); electrocatalytic activity; honeycomb-like; molybdenum disulfide (MoS_2); thin film

Beilstein J. Nanotechnol. **2022,** *13,* 528–537.
https://doi.org/10.3762/bjnano.13.44

Received: 22 March 2022
Accepted: 01 June 2022
Published: 17 June 2022

This article is part of the thematic issue "Nanomaterials for photocatalysis and applications in environmental remediation and renewable energy".

Guest Editor: V. V. Pham

Abstract

Non-platinum electrodes for photoelectric devices are challenging and attractive to the scientific community. A thin film of molybdenum disulfide (MoS_2) was prepared on substrates coated with fluorine-doped tin oxide (FTO) to substitute the platinum counter electrode (CE) for dye-sensitized solar cells (DSSCs). Herein, we synthesized layered and honeycomb-like MoS_2 thin films via the cyclic voltammetry (CV) route. Thickness and morphology of the MoS_2 thin films were controlled via the concentration of precursor solution. The obtained results showed that MoS_2 thin films formed at a low precursor concentration had a layered morphology while a honeycomb-like MoS_2 thin film was formed at a high precursor concentration. Both types of MoS_2 thin film were composed of 1T and 2H structures and exhibited excellent electrocatalytic activity for the I_3^-/I^- redox couple. DSSCs assembled using these MoS_2 CEs showed a maximal power conversion efficiency of 7.33%. The short-circuit value reached 16.3 mA·cm^{-2}, which was higher than that of a conventional Pt/FTO CE (15.3 mA·cm^{-2}). This work reports for the first time the possibility to obtain a honeycomb-like MoS_2 thin film morphology by the CV method and investigates the effect of film structure on the electrocatalytic activity and photovoltaic performance of CEs for DSSC application.

Introduction

Since Grätzel's first report in 1991, dye-sensitized solar cells (DSSCs) have been the subject of much research due to the easy fabrication process and respectable efficiency [1]. This promising third generation of solar cells contains a dye-adsorbed TiO_2 photoanode, an iodide/triiodide electrolyte, and a platinum-based cathode, also known as the counter electrode (CE). How-

ever, the high cost of platinum has prevented the real-world application of DSSCs, which has led researchers to explore efficient cathode materials for DSSCs beyond platinum. To date, Pt replacement materials are divided into three categories, namely carbonaceous materials [2-5], conductive polymers [5], and transition metal compounds [6-8]. Transition metal compounds are considered a potential approach due to the high activity and acceptable price. Molybdenum disulfide (MoS_2) has recently gained a lot of attention due to its layered structure, cost efficiency, and superior catalytic activity [9-16]. MoS_2 exhibits layered structures with three types of crystal phase, that is, trigonal (1T), hexagonal (2H), and rhombohedral (3R). Considering electrocatalytic applications, the 1T metallic phase exhibits a higher catalytic activity than the 2H and 3R semiconductor phases [11,17]. Moreover, it is well known that the electrocatalytic activity of MoS_2 strongly depends on the number of catalytically active sites located at the edge planes [1,18,19]. These unsaturated Mo and S edges of MoS_2 enable the generation of the I_3^-/I^- redox couple, making it a potential CE for DSSCs. So far, MoS_2-based CEs for DSSCs have been fabricated and investigated using various techniques such as chemical bath deposition [1], sputtering [2], hydrothermal synthesis [10-13], wet chemistry [14], thermal reduction [15], and electrodeposition (ED) [20]. Among these methods, ED shows many advances thank to its simplicity and rapidity. Additionally, it allows for the direct deposition of MoS_2 thin films from liquid precursors onto various conducting substrates with easily controlled thickness and morphology.

Several reports have already been published that describe the control of structure and morphology of electrodeposited MoS_2 to maximize its catalytic activity. Li et al. reported the synthesis of MoS_2/graphene composite films on FTO, which were directly used as CE for DSSCs without further thermal treatment. The power conversion efficiency (PCE) of the DSSCs was 8.01%, which was comparable to that of a Pt CE (8.21%) [21]. Quy et al. prepared MoS_2/FTO. The resulting DSSCs showed a PCE of 7.16%, similar to that of a Pt/FTO CE (7.48%). The MoS_2 film was amorphous and contained agglomerated clusters of nanoparticles [22]. Recently, Gurulakshmi et al. reported on DSSCs using a flexible CE fabricated by electrodeposition of a MoS_2 thin film onto a conductive FTO/PET substrate. The PCE of this flexible DSSCs reached 4.84%. The MoS_2 film was composed of sheets with a length of about 6 μm and a thickness of about 500 nm [23]. Another report by Chang et al. mentioned the change in morphology of MoS_2 from sphere-like shapes with large grain size to a uniform thin layer when changing the ED technique from potentiostatic (PS) mode to potential-reversal (PR) mode. This resulted in an improvement in PCE from 6.89% to 8.77% [24]. In general, above studies still have limits such as depositing MoS_2 on graphene or carbon dots, instead of directly developing the FTO substrate. In addition, the effect of thickness and morphology of MoS_2/FTO on the performance of DSSCs was not examined in these studies.

In this work, thin films of MoS_2 with two different shapes (layered and honeycomb-like) were deposited on FTO substrates from an aqueous precursor solution containing $(NH_4)_6Mo_7O_{24}{\cdot}4H_2O$ and Na_2S by cyclic voltammetry (CV). Morphology and thickness of the MoS_2 thin films were controlled by adjusting the concentration of the precursor solution. The electrochemical catalytic activity of the MoS_2 thin films was investigated regarding the I_3^-/I^- redox couple. The as-prepared MoS_2 thin films were directly used as CE for DSSCs. The structure and morphology of the MoS_2 thin films and their corresponding DSSC performance have been carefully evaluated. Furthermore, the effect of MoS_2 film thickness on the performance of DSSCs has also been discussed. It should be noted that this is the first report dealing with the fabrication of MoS_2 honeycomb-like thin films for DSSC application.

Results and Discussion

Electrodeposition of MoS_2 thin films

Electrodeposition of MoS_2 thin films was carried out from precursor solutions containing a mixture of $(NH_4)_6Mo_7O_{24}$ and Na_2S in KCl electrolyte solution. To study the redox behavior of the solution, the CV curves for each component and the mixture solutions were recorded in the potential range from −1.5 V to 1.0 V (Figure 1). The blank KCl electrolyte exhibits a straight line around zero current, while the precursor solutions show redox peaks associated with the oxidation/reduction of the precursor ions on the surface of the FTO electrode. In detail, the CV recorded in Na_2S solution shows a broad anodic peak around −0.50 V due to the oxidation of S^{2-} ions [25,26]. The CV curve of $(NH_4)_6Mo_7O_{24}$ solution exhibited two redox couple peaks at −0.34 V/−0.76 V and −0.77 V/−1.34 V attributed to the redox reactions of $Mo_7O_{24}^{6-}$ and MoO_4^{2-} ions, respectively [27]. The presence of MoO_4^{2-} ions is due to the equilibrium in Equation 3, which occurs in acidic solution of $(NH_4)_6Mo_7O_{24}$ (the pH here is about 4.3). The CV recorded in the mixture solution showed two oxidation peaks at −0.20 V and −0.50 V attributed to the oxidation of $Mo_7O_{24}^{6-}$ and S^{2-} ions, respectively. Moreover, a new reduction peak appeared around −1.20 V related to the reduction of MoS_4^{2-} to form MoS_2 as described in Equation 5. This CV behavior is similar to that of $(NH_4)_2MoS_4$ reported by Falola and co-workers [28]. The formation of MoS_4^{2-} ions in the mixture solution is detailed in Equations 1–4 [27-30]:

$$Na_2S \rightarrow 2Na^+ + S^{2-}, \quad (1)$$

$$(NH_4)_6\,Mo_7O_{24}\cdot 4H_2O \rightarrow Mo_7O_{24}^{6-} + 6NH_4^+ + 4H_2O, \quad (2)$$

$$7MoO_4^{2-} + 8H^+ \rightleftharpoons Mo_7O_{24}^{6-} + 4H_2O, \quad (3)$$

$$MoO_4^{2-} + 6S^{2-} + 12H^+ \rightarrow MoS_4^{2-} + 4H_2, \quad (4)$$

$$MoS_4^{2-} + 6H^+ + 2e^- \rightarrow MoS_2 + 2H_2S + H_2. \quad (5)$$

It should be noted that $(NH_4)_2MoS_4$ is poorly soluble in water. Hence, the in situ synthesis of MoS_4^{2-} from $(NH_4)_6Mo_7O_{24}$ (high solubility) and Na_2S in acidic media (adjusted to pH 6) is very favorable to the preparation of MoS_4^{2-} precursor solution. In this work, the optimal concentration ratio of $(NH_4)_2Mo_7O_{24}$ (mM) to Na_2S (g/L) was found to be 1:6 (data not shown).

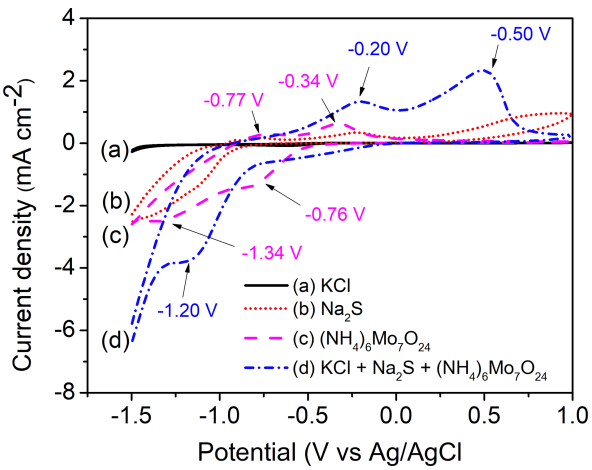

Figure 1: CV curves recorded in the solutions of (a) 0.1 M KCl, (b) 30 g/L Na_2S, (c) 5 mM $(NH_4)_6Mo_7O_{24}$, and (d) a mixture of 30 g/L Na_2S and 5 mM $(NH_4)_6Mo_7O_{24}$ in 0.1 M KCl, pH 6, using an FTO electrode, at scan rate of 100 mV·s^{-1}.

It can be seen from the CV curve of the mixture solution that the reduction of MoS_4^{2-} occurred beginning at a potential of −0.80 V. Electrodeposition of MoS_2 at high overpotential leads to the formation of thick films [28]. To obtain thin films, we limited the deposition potential range of MoS_2 to a range between −1.0 V and 1.0 V and studied the effect of the concentration of the precursor solution on the morphology and the electrocatalytic activity of the MoS_2 thin films. The CVs (10 cycles) for the MoS_2 electrodeposition from solution 2.5 (see Experimental section for the denomination of the sample solutions) are shown in Figure 2a. The comparison of the tenth cycle of the CV recorded in different concentrations of precursor solution (solution 1.25, 2.5, and 5.0) is shown in Figure 2b. The presence of the redox couple peak at −0.2/−0.75 V can be attributed to the redox reactions of $Mo_7O_{24}^{6-}$ ions (the anodic peak is slightly shifted towards the anodic potential compared to that of the $(NH_4)_2Mo_7O_{24}$ solution, see the insert in Figure 2a). The current density of the CV curves increases with the increase of precursor solution concentration. This allows one to predict that the thickness of MoS_2 film will be increased in the order: solution 1.25 < solution 2.5 < solution 5.0.

Morphology and structure of MoS_2 thin films

Morphology and thickness of MoS_2 films prepared on the FTO substrate were analyzed by FE-SEM. The MoS_2 films formed from solutions 1.25 and 2.5 exhibited thin-layered structures, which exposed edge sites (Figure 3a–c). The same structure had been found in the reports of Falola and Lin [24,28]. However, the film thickness of MoS_2 in these reports was thick compared to our results. Interestingly, the formation of MoS_2 film from solution 5.0 showed a homogenous honeycomb-like structure

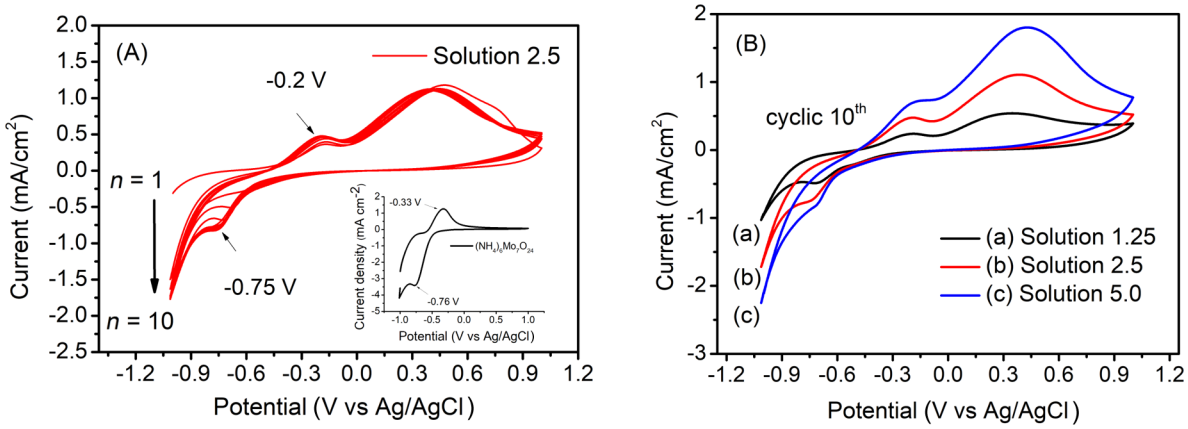

Figure 2: (a) CVs recorded during electrodeposition of MoS_2 from solution 1.25; (b) comparison of the tenth cycle of CVs recorded in solutions 1.25, 2.5, and 5.0; a scan rate of 100 mV·s^{-1} was used.

(Figure 3e). The surface of the film consists of honeycomb grids with a diameter of around 50 nm (see Figure 3e, insert). The roughness of the films was further studied by AFM. The film with the honeycomb-like structure showed the highest average roughness (S_a) and root mean square roughness (S_q) of 24.179 and 30.443 nm, respectively (see Supporting Information File 1, Figure S1 and Table S1). To the best of our knowledge, this is the first report on this type of MoS_2 film synthesized by CV. The potential range of the CV and the concentration of the precursor solution strongly affect the thickness and morphology of the MoS_2 films. The thickness of MoS_2 films was estimated from cross-sectional FE-SEM images. The formation of MoS_2 from solutions 2.5 and 5.0 yielded thicknesses of about 50 nm and 500 nm, respectively (Figure 3d,f).

The phase structure of the electrodeposited MoS_2 thin films was identified by XRD and Raman analyses. The XRD pattern and the Raman spectrum of the MoS_2 thin film deposited from solution 5.0 are presented in Figure 4. The XRD pattern of the MoS_2/FTO samples shows only the peaks of the FTO substrate because the MoS_2 thin film is amorphous or too thin (Figure 4a) [22-24]. Thus, the electrodeposited thin film was further characterized by Raman spectroscopy. The Raman spectrum of the MoS_2/FTO sample showed the characteristic peaks of the 2H

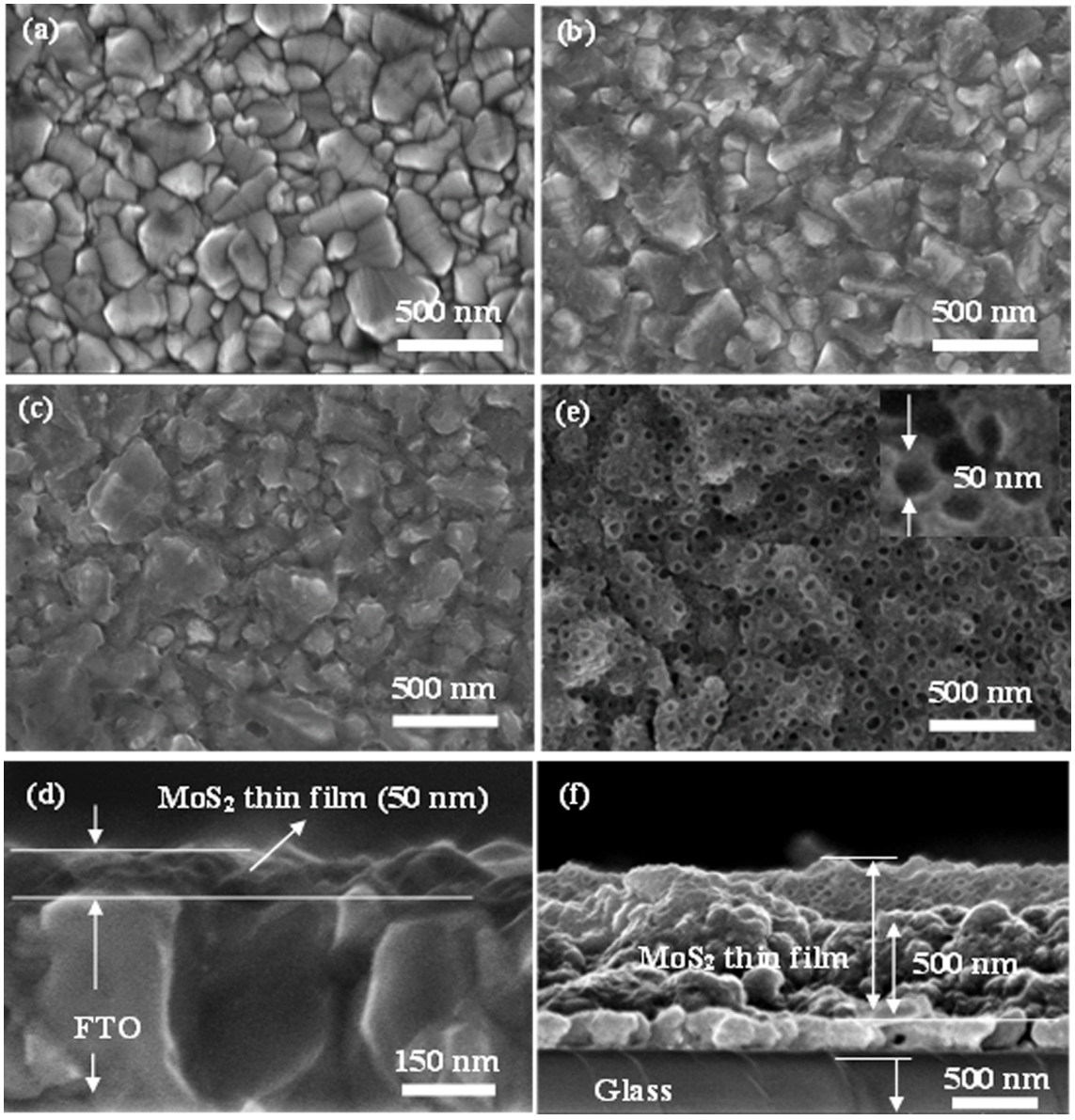

Figure 3: FE-SEM images (top view and cross-sectional view) of (a) FTO and (b–f) MoS_2 deposited on FTO from different precursor solution concentrations: (b) solution 1.25, (c ,d) solution 2.5, and (e, f) solution 5.0.

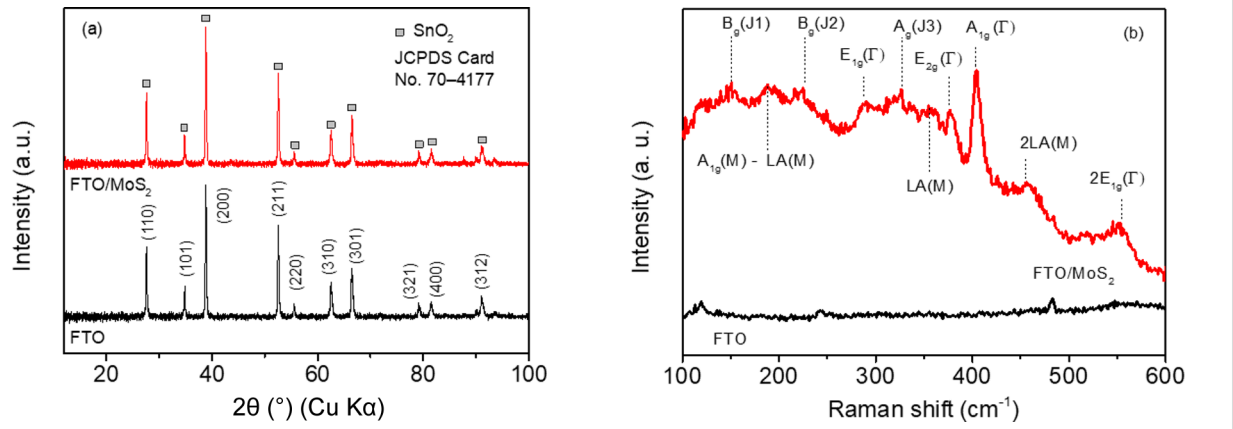

Figure 4: (a) XRD patterns and (b) Raman spectra of the FTO substrate and a thin film of MoS_2 electrodeposited from solution 5.0.

and 1T phases of MoS_2 (Figure 4b). The appearance of the J_1, J_2, and J_3 peaks around 150, 226, and 326 cm^{-1} confirmed the presence of the 1T metallic phase. Whereas the two Raman vibration modes, E_{2g} (in plane) and A_{1g} (out of plane), observed at 376 and 403 cm^{-1}, respectively, are attributed to the 2H semiconductor phase [31-33]. The three first-order Raman modes, A_{1g}, E_{2g}, and E_{1g} (288 cm^{-1}), are attributed to vibrational modes of the S–Mo–S layer. Other well-known multiphonon bands, namely A_{1g}-LA (188 cm^{-1}), LA (355 cm^{-1}), 2LA (455 cm^{-1}), and $2E_{1g}$ (553 cm^{-1}) have also been observed [34-36]. The 1T phase exhibits a higher electroactivity than the 2H phase. Also, the 1T phase tends to transform into the 2H phase at high temperatures (Figure 4b) [1,17,36]. Therefore, the freshly prepared MoS_2/FTO electrodes (without heat treatment) were used to examine the electrocatalytic activity towards the I_3^-/I^- redox couple as well as directly used as CEs for DSSCs.

Electroactivity of MoS_2 CEs

The electrocatalytic activity of MoS_2 CEs towards the I_3^-/I^- redox couple was investigated and compared to that of a Pt CE. As can be seen in Figure 5, there are two redox pairs (Ox_1/Red_1) and (Ox_2/Red_2). These redox peaks were well defined as the oxidation and reduction of iodide and triiodide ($3I^- - 2e^- \rightarrow I_3^-$ (Ox_1), $I_3^- + 2e^- \rightarrow 3I^-$ (Red_1) and $2I_3^- - 2e^- \rightarrow 3I_2$ (Ox_2), $3I_2 + 2e^- \rightarrow 2I_3^-$ (Red_2) [6-9].

Since the reduction of I_3^- to I^- on the CE plays a vital role in the regeneration of the oxidized dye molecules on the photoanode of the DSSCs, the electrocatalytic behavior of MoS_2 CEs was further evaluated regarding the first redox couple (Ox_1/Red_1). Various parameters including anode/cathode peak potentials (E_{pOx1}, E_{pRed1}), peak-to-peak voltage separation (E_{pp}), and anode/cathode peak current densities (J_{Ox1}, J_{Red1}) were calculated and presented in Table 1. The E_{pp} value for MoS_2 CEs was slightly larger than that of Pt CE

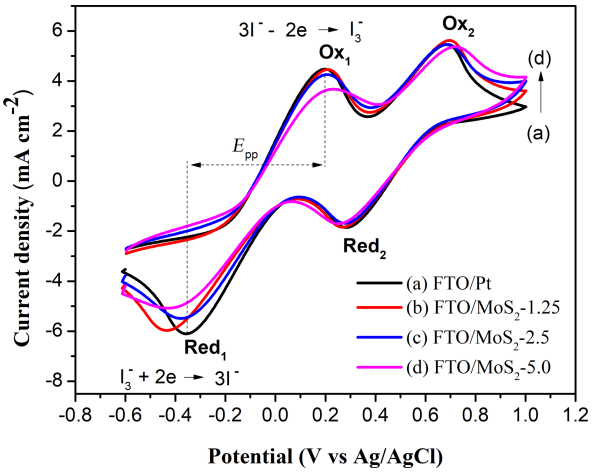

Figure 5: CV curves of MoS_2 CEs prepared with different concentrations of reaction precursors compared to that of Pt CE, recorded in ACN solution of 10 mM I_2, 20 mM KI, and 0.1 M $LiClO_4$; a scan rate of 100 $mV{\cdot}s^{-1}$ was used.

confirming their excellent electrocatalytic activity. The J_{Red1} values of MoS_2 CEs decreased in the order: MoS_2-1.25 ≈ Pt > MoS_2-2.5 > MoS_2-5.0 (see Table 1). This demonstrated that increasing the concentration of the precursor solution resulted in the increase in the thickness of the MoS_2 film and, thus, reduced the electrocatalytic activity.

Further study of the electrocatalytic behavior of the MoS_2 CEs was carried out by using the EIS technique under dark conditions using full cells assembled from different MoS_2/FTO CEs or a Pt/FTO CE. The Nyquist plots for these cells exhibited two semicircles as presented in Figure 6. The first semicircle in the high-frequency region is associated with the reduction of I_3^- at the cathode (CE/electrolyte), while the second one in the low-frequency region is attributed to electron transport in the TiO_2

Table 1: Electrochemical parameters from CV measurements of MoS_2 and Pt CEs.

CE	E_{pOx1} (V)	E_{pRed1} (V)	E_{pp} (V)	J_{Ox1} (mA·cm^{-2})	J_{Red1} (mA·cm^{-2})
Pt	0.195	−0.355	0.550	4.450	−6.059
MoS_2-1.25	0.208	−0.432	0.640	4.476	−5.965
MoS_2-2.5	0.208	−0.373	0.581	4.257	−5.511
MoS_2-5.0	0.226	−0.415	0.641	3.695	−5.057

film in the back reaction at the TiO_2/electrolyte interface (TiO_2/dye/electrolyte). EIS data were fitted using an equivalent-circuit model including the series resistances of electrolyte and FTO substrate (R_s) and the charge-transfer resistances on the CE/electrolyte and TiO_2/dye/electrolyte interfaces (R_{ct1} and R_{ct2}) associated with the corresponding constant phase elements (CPE1 and CPE2) as described in Figure 6 (Figure 6, insert).

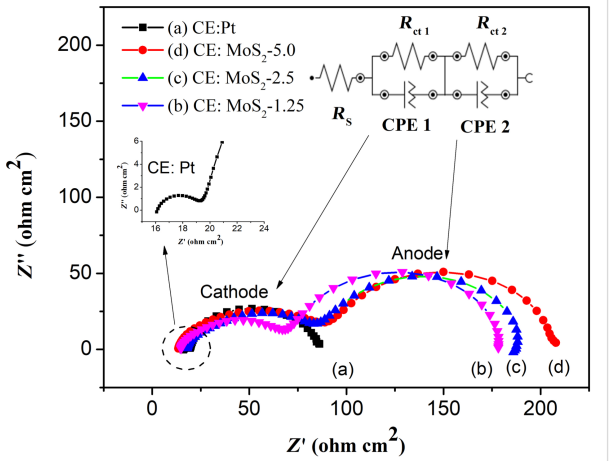

Figure 6: Nyquist plots of DSSCs using different MoS_2/FTO and Pt/FTO CEs, the inset shows the equivalent circuit model.

The fit values for R_s and R_{ct1} reflect the catalytic behavior of CEs in DSSCs and are presented in Table 2. The R_s value for MoS_2 CE-based DSSCs slightly increased with the thickness of the films and is comparable to that of Pt CE-based DSSCs. This is due to the high conductivity of the metallic 1T phase of MoS_2 and is in good agreement with Raman analysis. Under dark conditions, the R_{ct1} value for MoS_2 CE-based DSSCs (from 52.6 to 78.5 Ω·cm^2) was found to be significantly higher than that of Pt CE-based DSSCs (3.6 Ω·cm^2), indicating slower charge transfer kinetics at the MoS_2/electrolyte interface compared to the Pt/electrolyte interface. The high peak current density value for I_3^- reduction from CV analysis obtained for MoS_2-based CEs was therefore attributed to the high number of catalytically active sites located on the edge planes of the MoS_2 films.

DSSC performance

To further evaluate the effect of MoS_2 morphology and thickness on the performance of the DSSCs, the photovoltaic performance of DSSCs using different MoS_2 CEs was investigated under illumination. The *J*–*V* curves and the corresponding photovoltaic parameters of DSSCs are given in Figure 7 and Table 2, respectively. The DSSC using MoS_2-1.25/FTO CE displayed an excellent photovoltaic performance compared to that with a Pt/FTO a CE. In particular, the obtained value of 16.3 mA·cm^{-2} for the short-circuit photocurrent (J_{sc}) was found to be higher than that of Pt/FTO CE (15.3 mA·cm^{-2}). This is attributed to the high number of catalytically active sites together with the low resistance of this MoS_2 film.

Although the electrocatalytic ability regarding the reduction of I_3^- of MoS_2 was lower than that of Pt, other parameters including an open-circuit voltage (V_{oc}) of 0.69 V, a fill factor (FF) of 0.66, and a PCE of 7.33% of this MoS_2 CE-based DSSCs were comparable to those of a DSSC based on a Pt CE (V_{OC} = 0.75 V, FF = 0.75, PEC = 8.66%) and to values found in

Table 2: Photovoltaic parameters and EIS data of the DSSCs based on different MoS_2 CEs and a Pt CE.

CE	J_{sc} (mA·cm^{-2})	V_{oc} (V)	FF	η (%)	R_s (Ω·cm^2)	R_{ct1} (Ω·cm^2)	τ (ms)
Pt	15.30	0.75	0.75	8.66	16.1	3.60	23
MoS_2-1.25	16.30	0.69	0.66	7.33	14.8	52.6	30
MoS_2-2.5	14.85	0.68	0.63	6.39	16.6	65.8	31
MoS_2-5.0	14.90	0.67	0.53	5.31	17.5	78.5	40

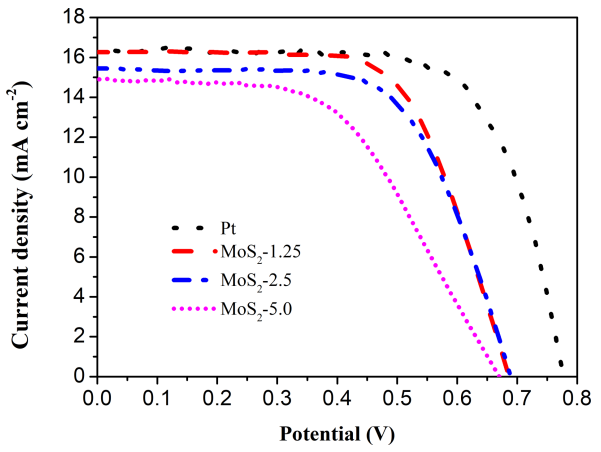

Figure 7: Photovoltaic performance of DSSCs fabricated with different MoS_2/FTO and Pt/FTO CEs.

other reports (Table 3). The PCE for DSSCs using MoS_2 with different thicknesses decreased in the order: MoS_2-1.25 (very thin film) > MoS_2-2.5 (50 nm) > MoS_2-5.0 (500 nm). This is in good agreement with the trend of R_s and R_{ct1} values (see Table 2 and Table 3). The effect of film thickness on the electrical conductivity of the MoS_2 films was also investigated by *I–V* measurements (see Supporting Information File 1, Figure S2 and Table S1). The electrical conductivity of the as-prepared MoS_2 decreased in the order: MoS_2-1.25 (75 mS·cm^{-1}) > MoS_2-2.5 (61 mS·cm^{-1}) > MoS_2-5.0 (46 mS·cm^{-1}). This suggests that the thickness of the MoS_2 film has a significant effect on the catalytic ability and photovoltaic performance of the CE in DSSCs. Additionally, the electron lifetime (τ) indicates the recombination kinetics of electrons in the mesoscopic TiO_2 film of the DSSCs. This parameter can be calculated from the peak frequency (f_{max}) of the low-frequency semicircles ($\tau = 1/2\pi f_{max}$). The τ values measured under dark conditions for DSSCs devices fabricated from various CEs are presented in Table 2. The τ values for DSSCs fabricated with MoS_2 CEs were higher than those of a DSSC using a Pt CE and increased in the order: DSSCs-MoS_2-1.25 < DSSCs-MoS_2-2.5 < DSSCs-MoS_2-5.0. A longer electron lifetime indicates a slower recombination process within the DSSCs fabricated with MoS_2/FTO CEs. The stability of the devices was tested by repeating the *I–V* measurements every week (Supporting Information File 1, Figure S3). The PCE value of a DSSC fabricated using MoS_2-1.25 showed a slight decrease of 2.6% and reached stability after two weeks of testing under ambient conditions. This suggested that the MoS_2-1.25/FTO CE has reversible redox activity and electrochemical stability. The electrochemical stability of the MoS_2/FTO CE should provide long-term stability for solar cell devices. However, more work needs to be done to improve the efficiency of this DSSC device [36-39].

Table 3: Performance summary of MoS_2-based CEs for DSSCs.

MoS_2 CE	Method	V_{oc} (V)	J_{sc} (mA·cm^{-2})	FF	η (%)	Ref
MoS_2/FTO	chemical bath deposition	0.73	15.92	0.61	7.14	[1]
MoS_2/FTO	sputtering	0.71	13.17	0.64	6.00	[9]
MoS_2/FTO	hydrothermal	0.70	18.37	0.58	7.41	[10]
1T MoS_2/FTO	hydrothermal	0.73	18.76	0.52	7.08	[11]
2H MoS_2/FTO	hydrothermal	0.73	6.78	0.35	1.72	[11]
MoS_2/FTO	hydrothermal	0.74	16.96	0.66	8.28	[12]
porous MoS_2/FTO	hydrothermal/spin coating	0.76	15.4	0.53	6.35	[13]
flower-shaped MoS_2/FTO	hydrothermal/spin coating	0.70	13.73	0.52	5.23	[13]
MoS_2/FTO	wet-chemical process	0.68	18.46	0.58	7.01	[14]
MoS_2/FTO	spin coating/thermal reduction	0.73	16.91	0.52	6.35	[15]
multilayered MoS_2/FTO	spray coating	0.75	15.81	0.25	2.92	[16]
few-layered MoS_2/FTO	exfoliation of ML-MoS_2 powder and spray coating technique	0.74	14.90	0.16	1.74	[16]
MoS_2 nanoparticles/FTO	thermal decomposition	0.75	14.72	0.49	5.41	[16]
MoS_2/FTO	potentiostatic	0.72	15.68	0.63	7.16	[22]
MoS_2/FTO	potentiostatic	0.78	16.18	0.54	6.89	[24]
MoS_2/FTO	potential reversal	0.76	16.16	0.71	8.77	[24]
layered MoS_2/FTO	cyclic voltammetry	0.69	16.29	0.66	7.33	this work
honeycomb-like MoS_2/FTO	cyclic voltammetry	0.67	14.90	0.53	5.31	this work

Conclusion

We synthesized successfully MoS_2 thin films with layered or honeycomb-like structures onto FTO substrates by the CV route. The morphology and thickness of the MoS_2 films can be effectively controlled by adjusting the concentration of the precursor solution. In detail, MoS_2 formed a layered thin film with a thickness of about 50 nm when the concentration level ratio between $(NH_4)_2Mo_7O_{24}$ and Na_2S was 2.5/15 (solution 2.5, see Experimental section). Honeycomb MoS_2 was formed with a thickness of about 500 nm from solution 5.0 (with a concentration level ratio between $(NH_4)_2Mo_7O_{24}$ and Na_2S of 5/30). In addition, as-prepared MoS_2 films have been used as an alternative CE to Pt in DSSCs. The short-circuit photocurrent (J_{sc}) was higher than that of a Pt/FTO CE. Moreover, the highest performance of solar cells was found with the layered MoS_2 film thank to good electrical conductivity, a high number of catalytically active sites, and the thickness of the MoS_2 film. The MoS_2/FTO films could be applied as non-Pt electrodes for DSSCs in the near future.

Experimental

Materials and reagents

Ammonium molybdate tetrahydrate ($(NH_4)_6Mo_7O_{24}{\cdot}4H_2O$, 99.98%), sodium sulfide nonahydrate ($Na_2S{\cdot}9H_2O$, 99.99%), potassium chloride (KCl, 99%), acetonitrile (ACN, CH_3CN, 99%), dimethyl sulfoxide (DMSO, $(CH_3)_2SO$, 99.5%), ethanol (EtOH, CH_3CH_2OH, 99.8%), guanidinium thiocyanate ($NH_2C(=NH)NH_2{\cdot}HSCN$, 99%), iodine ($I_2$, 99.8%), 1-methyl-3-propylimidazolium iodide ($C_7H_{13}IN_2$, 98%), 4-*tert*-butylpyridine ($C_9H_{13}N$, 98%), valeronitrile ($CH_3(CH_2)_3CN$, 99.5%), chloroplatinic acid hexahydrate ($H_2PtCl_6{\cdot}6H_2O$, ≥37.50% Pt), sulfuric acid (H_2SO_4, 95–98%), polyvinylpyrrolidone (PVP, $(C_6H_9NO)_n$, average M_w 10,000), and sodium borohydride ($NaBH_4$, 99%) were purchased from Sigma-Aldrich (Germany). Low-temperature thermoplastic sealant (Surlyn, 25 μm), 18NR-T transparent titania paste (particle size of 20 nm), 18NR-AO active opaque titania paste (particle sizes of 20 and 450 nm), fluorine-doped tin oxide (FTO, TEC8 glass plates, 8 $\Omega{\cdot}cm^{-2}$, 2.2 mm thickness), and N719 industry standard dye (N719) were purchased from Dyesol (Australia). All commercial chemicals were of analytical grade and were used as supplied without further purification.

Electrodeposition of MoS_2 thin films

Thin films of MoS_2 with different morphologies were electrodeposited onto FTO substrates by the CV method. MoS_2 electrodeposition was carried out using an Autolab 302 N (Eco chemie, Netherlands) connected to a three-electrode cell. Accordingly, a Pt mesh, an Ag/AgCl (ALS, Japan), and the FTO plate (1.5 × 1.5 cm) were used as the counter electrode (CE), the reference electrode (RE), and the working electrode (WE), respectively. Prior to CV electrodeposition, the FTO substrates were first cleaned in a 1% Hellmanex solution at 70 °C for 30 min in an ultrasonic bath, then washed three times in distilled water, dried by nitrogen flow, and finally treated in a UV ozone chamber for 5 min to obtain the cleaned FTO electrode. Precursor solutions were prepared by dissolving $(NH_4)_6Mo_7O_{24}$ (x mM) and Na_2S (y $g{\cdot}L^{-1}$) in distilled water, the pH of the solution was adjusted to 6.0 using a 20% (v/v) H_2SO_4 solution, KCl (0.1 M) was used as the supporting electrolyte. The concentration ratio between $(NH_4)_2Mo_7O_{24}$ and Na_2S was kept constant (x/y = 1:6) with different concentration levels including 1.25:7.5 (solution 1.25), 2.5:15 (solution 2.5), and 5:30 (solution 5.0). The CV measurement was performed under a dynamic potential between −1.0 V and 1.0 V for ten cycles at a scan rate of 100 $mV{\cdot}s^{-1}$ in a nitrogen atmosphere.

Fabrication of DSSCs

DSSCs with an active area of 0.25 cm^2 were assembled using the pre-cleaned FTO plates (1.5 × 1.5 cm) for the fabrication of anode and cathode. For cathode preparation, MoS_2/FTO CEs were prepared with different morphologies from the above MoS_2 samples. The obtained CEs were designated as MoS_2-1.25/FTO, MoS_2-2.5/FTO, and MoS_2-5.0/FTO. For comparison, a Pt-based CE (Pt/FTO) was fabricated by soaking the cleaned FTO glasses in PVP–platinum suspension at 45 °C for 5 min, followed by washing with distilled water. The PVP–platinum suspension was prepared as follows: First, 1.0 g of H_2PtCl_6 was dissolved in 150 mL of distilled water, then 0.5 g PVP was added to the above solution under stirring for 10 min. Finally, to this solution, $NaBH_4$ solution (1.17 g $NaBH_4$ was dissolved in 124.8 mL of distilled water, stirred for 3 min) was added at a rate of 1.5 mL/min until the color of the mixture solution turned into black.

For the fabrication of the photoanodes, the cleaned FTO electrodes were first pretreated by immersion in a 40 mM $TiCl_4$ solution at 70 °C for 30 min and rinsed with distilled water and ethanol. The treated FTO electrodes were then successively coated with a transparent 18NR-T titania paste (three layers) and an active opaque 18NR-AO titania paste (one outer layer) by the screen-printing method using 43T mesh. The printed electrodes were dried at room temperature for 5 min, then at 120 °C for 5 min after each printed layer, and finally heated at 450 °C under airflow for 30 min. When the temperature was cooled down to 70 °C, the electrodes were dipped in N719 dye (0.3 M N719 in the mixture DMSO/EtOH, v/v = 1:9) for 12 h to obtain the photoanodes.

For cell assembly, the DSSCs were fabricated in a nitrogen atmosphere using a glove box. Typically, the photoanode and the MoS_2-based CE were sealed together by a hot-melt Surlyn film

using a thermopress, pressed at 170 °C for 15 s. The electrolyte solution (0.1 M guanidinium thiocyanate, 0.03 M iodine, 1 M 1-methyl-3-propylimidazolium iodide, 0.5 M 4-*tert*-butylpyridine in a mixture of valeronitrile/acetonitrile with a volume ratio of 0.15:0.85) was then injected into the cell through predrilled holes on the CE. The holes were then covered with a thin glass slide using the same thermopress method as described above to obtain DSSC devices. DSSCs assembled using the CE fabricated from precursor solutions 1.25, 2.5, and 5.0 were denoted as DSSCs-MoS_2-1.25, DSSCs- MoS_2-2.5, and DSSCs-MoS_2-5.0, respectively. For comparison, DSSCs based on Pt/FTO CE (DSSCs-Pt) were also fabricated under the same conditions.

Characterizations of MoS_2 thin films

X-ray diffraction (XRD) analysis was carried out using a D8 Advance (Bruker, Germany) with a copper anode ($\lambda_{K\alpha}$ = 1.54 Å). Raman spectroscopy measurements were performed on a LabRAM HR 800 Raman Spectrometer (HORIBA Jobin Yvon) with an excitation laser source at 532 nm. The morphology of MoS_2 thin films was analyzed by an ultrahigh-resolution field-emission scanning electron microscope (FE-SEM, Hitachi SU-8010, Japan). The electrochemical catalytic activity of the MoS_2-based CEs was studied regarding the I_3^-/I^- redox couple (prepared with 10 mM I_2, 20 mM KI, and 0.1 M $LiClO_4$ in acetonitrile) and compared to that of a FTO/Pt CE by CV.

DSSC characterizations

Photoelectrochemical measurements were performed using an Oriel Sol1A class ABB solar simulator (Oriel-Newport-USA, Model No. 94061A). Simulated sunlight of 100 mW·cm^{-2} (1 sun) was generated and corrected by a 1000 W Xe lamp and an AM 1.5 filter. The photocurrent density–voltage (J–V) curves of the DSSCs were measured using a Keithley model 2400 multisource meter. Electrochemical impedance spectroscopy (EIS) of the fabricated DSSCs was carried out using an Autolab 302 N equipped with a FRA 32M module. The EIS measurements were carried out at open-circuit voltage with an alternating voltage amplitude of 10 mV under dark conditions in a frequency range between 0.01 Hz and 100 kHz. The efficiency of the DSSCs was analyzed and reported as the average of three cells.

Supporting Information

Supporting Information File 1

Additional experimental data.
[https://www.beilstein-journals.org/bjnano/content/supplementary/2190-4286-13-44-S1.pdf]

Acknowledgements

We thank Professor Tzu-Chien Wei, Department of Chemical Engineering, National Tsing Hua University, Taiwan, for his great help on EIS, AFM and Raman measurements.

Funding

This research was fully funded by Tra Vinh University under grant contract number 140/HĐ.HĐKH-ĐHTV

ORCID® iDs

Hai Viet Le - https://orcid.org/0000-0001-7480-806X

References

1. Vikraman, D.; Patil, S. A.; Hussain, S.; Mengal, N.; Kim, H.-S.; Jeong, S. H.; Jung, J.; Kim, H.-S.; Park, H. J. *Dyes Pigm.* **2018,** *151,* 7–14. doi:10.1016/j.dyepig.2017.12.037
2. Roy-Mayhew, J. D.; Bozym, D. J.; Punckt, C.; Aksay, I. A. *ACS Nano* **2010,** *4,* 6203–6211. doi:10.1021/nn1016428
3. Chen, J.; Li, K.; Luo, Y.; Guo, X.; Li, D.; Deng, M.; Huang, S.; Meng, Q. *Carbon* **2009,** *47,* 2704–2708. doi:10.1016/j.carbon.2009.05.028
4. Yang, Z.; Chen, T.; He, R.; Guan, G.; Li, H.; Qiu, L.; Peng, H. *Adv. Mater. (Weinheim, Ger.)* **2011,** *23,* 5436–5439. doi:10.1002/adma.201103509
5. Lee, K. S.; Lee, H. K.; Wang, D. H.; Park, N. G.; Lee, J. Y.; Park, O. O.; Park, J. H. *Chem. Commun.* **2010,** *46,* 4505–4507. doi:10.1039/c0cc00432d
6. Li, C.-T.; Lee, C.-P.; Li, Y.-Y.; Yeh, M.-H.; Ho, K.-C. *J. Mater. Chem. A* **2013,** *1,* 14888–14896. doi:10.1039/c3ta12603j
7. Wu, M.; Wang, Y.; Lin, X.; Yu, N.; Wang, L.; Wang, L.; Hagfeldt, A.; Ma, T. *Phys. Chem. Chem. Phys.* **2011,** *13,* 19298–19301. doi:10.1039/c1cp22819f
8. Liu, C.-J.; Tai, S.-Y.; Chou, S.-W.; Yu, Y.-C.; Chang, K.-D.; Wang, S.; Chien, F. S.-S.; Lin, J.-Y.; Lin, T.-W. *J. Mater. Chem.* **2012,** *22,* 21057–21064. doi:10.1039/c2jm33679k
9. Hussain, S.; Shaikh, S. F.; Vikraman, D.; Mane, R. S.; Joo, O.-S.; Naushad, M.; Jung, J. *ChemPhysChem* **2015,** *16,* 3959–3965. doi:10.1002/cphc.201500644
10. Al-Mamun, M.; Zhang, H.; Liu, P.; Wang, Y.; Cao, J.; Zhao, H. *RSC Adv.* **2014,** *4,* 21277–21283. doi:10.1039/c4ra00583j
11. Wei, W.; Sun, K.; Hu, Y. H. *J. Mater. Chem. A* **2016,** *4,* 12398–12401. doi:10.1039/c6ta04743b
12. Liang, J.; Li, J.; Zhu, H.; Han, Y.; Wang, Y.; Wang, C.; Jin, Z.; Zhang, G.; Liu, J. *Nanoscale* **2016,** *8,* 16017–16025. doi:10.1039/c6nr03635j
13. Liu, W.; He, S.; Yang, T.; Feng, Y.; Qian, G.; Xu, J.; Miao, S. *Appl. Surf. Sci.* **2014,** *313,* 498–503. doi:10.1016/j.apsusc.2014.06.011
14. Patil, S. A.; Kalode, P. Y.; Mane, R. S.; Shinde, D. V.; Doyoung, A.; Keumnam, C.; Sung, M. M.; Ambade, S. B.; Han, S.-H. *Dalton Trans.* **2014,** *43,* 5256–5259. doi:10.1039/c3dt53356e
15. Lin, C.-H.; Tsai, C.-H.; Tseng, F.-G.; Yu, Y.-Y.; Wu, H.-C.; Hsieh, C.-K. *Nanoscale Res. Lett.* **2015,** *10,* 446. doi:10.1186/s11671-015-1156-0
16. Lei, B.; Li, G. R.; Gao, X. P. *J. Mater. Chem. A* **2014,** *2,* 3919–3925. doi:10.1039/c3ta14313a
17. Liu, Z.; Gao, Z.; Liu, Y.; Xia, M.; Wang, R.; Li, N. *ACS Appl. Mater. Interfaces* **2017,** *9,* 25291–25297. doi:10.1021/acsami.7b05775

18. Li, G.; Zhang, D.; Qiao, Q.; Yu, Y.; Peterson, D.; Zafar, A.; Kumar, R.; Curtarolo, S.; Hunte, F.; Shannon, S.; Zhu, Y.; Yang, W.; Cao, L. *J. Am. Chem. Soc.* **2016,** *138,* 16632–16638. doi:10.1021/jacs.6b05940
19. Jaramillo, T. F.; Jørgensen, K. P.; Bonde, J.; Nielsen, J. H.; Horch, S.; Chorkendorff, I. *Science* **2007,** *317,* 100–102. doi:10.1126/science.1141483
20. Aliyev, A. S.; Elrouby, M.; Cafarova, S. F. *Mater. Sci. Semicond. Process.* **2015,** *32,* 31–39. doi:10.1016/j.mssp.2015.01.006
21. Li, S.; Min, H.; Xu, F.; Tong, L.; Chen, J.; Zhu, C.; Sun, L. *RSC Adv.* **2016,** *6,* 34546–34552. doi:10.1039/c6ra02494g
22. Quy, V. H. V.; Vijayakumar, E.; Ho, P.; Park, J.-H.; Rajesh, J. A.; Kwon, J.; Chae, J.; Kim, J.-H.; Kang, S.-H.; Ahn, K.-S. *Electrochim. Acta* **2018,** *260,* 716–725. doi:10.1016/j.electacta.2017.12.023
23. Gurulakshmi, M.; Meenakshamma, A.; Siddeswaramma, G.; Susmitha, K.; Venkata Subbaiah, Y. P.; Narayana, T.; Raghavender, M. *Sol. Energy* **2020,** *199,* 447–452. doi:10.1016/j.solener.2020.02.047
24. Chang, C.-Y.; Anuratha, K. S.; Lin, Y.-H.; Xiao, Y.; Hasin, P.; Lin, J.-Y. *Sol. Energy* **2020,** *206,* 163–170. doi:10.1016/j.solener.2020.06.001
25. Ghayad, I. M.; Al Kharafi, F. M.; Saad, A. Y.; Ateya, B. G. *Mod. Appl. Sci.* **2010,** *4,* 2–11. doi:10.5539/mas.v4n3p2
26. Wang, L.; Lu, P.; Liu, C.; Wang, L. *Int. J. Electrochem. Sci.* **2015,** *10,* 8374–8384.
27. You, J.; Wu, D.; Liu, H. *Polyhedron* **1986,** *5,* 535–537. doi:10.1016/s0277-5387(00)84960-8
28. Falola, B. D.; Wiltowski, T.; Suni, I. I. *J. Electrochem. Soc.* **2016,** *163,* D568–D574. doi:10.1149/2.0011610jes
29. Ponomarev, E. A.; Neumann-Spallart, M.; Hodes, G.; Lévy-Clément, C. *Thin Solid Films* **1996,** *280,* 86–89. doi:10.1016/0040-6090(95)08204-2
30. Ghosh, S. K.; Bera, T.; Karacasu, O.; Swarnakar, A.; Buijnsters, J. G.; Celis, J. P. *Electrochim. Acta* **2011,** *56,* 2433–2442. doi:10.1016/j.electacta.2010.10.065
31. Tan, S. J. R.; Sarkar, S.; Zhao, X.; Luo, X.; Luo, Y. Z.; Poh, S. M.; Abdelwahab, I.; Zhou, W.; Venkatesan, T.; Chen, W.; Quek, S. Y.; Loh, K. P. *ACS Nano* **2018,** *12,* 5051–5058. doi:10.1021/acsnano.8b02649
32. Sharma, C. H.; Surendran, A. P.; Varghese, A.; Thalakulam, M. *Sci. Rep.* **2018,** *8,* 12463. doi:10.1038/s41598-018-30867-y
33. Nayak, A. P.; Pandey, T.; Voiry, D.; Liu, J.; Moran, S. T.; Sharma, A.; Tan, C.; Chen, C.-H.; Li, L.-J.; Chhowalla, M.; Lin, J.-F.; Singh, A. K.; Akinwande, D. *Nano Lett.* **2015,** *15,* 346–353. doi:10.1021/nl5036397
34. Windom, B. C.; Sawyer, W. G.; Hahn, D. W. *Tribol. Lett.* **2011,** *42,* 301–310. doi:10.1007/s11249-011-9774-x
35. Livneh, T.; Spanier, J. E. *2D Mater.* **2015,** *2,* 035003. doi:10.1088/2053-1583/2/3/035003
36. Blanco, É.; Afanasiev, P.; Berhault, G.; Uzio, D.; Loridant, S. *C. R. Chim.* **2016,** *19,* 1310–1314. doi:10.1016/j.crci.2015.08.014
37. Rashidi, S.; Rashidi, S.; Heydari, R. K.; Esmaeili, S.; Tran, N.; Thangi, D.; Wei, W. *Prog. Photovoltaics* **2021,** *29,* 238–261. doi:10.1002/pip.3350
38. Akman, E.; Akin, S.; Ozturk, T.; Gulveren, B.; Sonmezoglu, S. *Sol. Energy* **2020,** *202,* 227–237. doi:10.1016/j.solener.2020.03.108
39. Akman, E. *J. Mol. Liq.* **2020,** *317,* 114223. doi:10.1016/j.molliq.2020.114223

License and Terms

BEILSTEIN JOURNAL OF NANOTECHNOLOGY

Solar-light-driven $LaFe_xNi_{1-x}O_3$ perovskite oxides for photocatalytic Fenton-like reaction to degrade organic pollutants

Chao-Wei Huang*[1], Shu-Yu Hsu[2], Jun-Han Lin[2], Yun Jhou[2], Wei-Yu Chen[3], Kun-Yi Andrew Lin[4], Yu-Tang Lin[5] and Van-Huy Nguyen*[6]

Full Research Paper

Open Access

Address:
[1]Department of Engineering Science, National Cheng Kung University, Tainan 70101, Taiwan, [2]Department of Chemical and Materials Engineering, National Kaohsiung University of Science and Technology, Kaohsiung 80778, Taiwan, [3]Department of Materials Engineering, National Pingtung University of Science and Technology, No.1, Xuefu Rd., Neipu Township, Pingtung County 912, Taiwan, [4]i-Center for Advanced Science and Technology (iCAST), Innovation and Development Center of Sustainable Agriculture, Department of Environmental Engineering, National Chung Hsing University, Taichung 402227, Taiwan, [5]Department of Chemical and Biological Engineering, University of Colorado Boulder, Boulder, Colorado 80309, United States and [6]Chettinad Hospital and Research Institute, Chettinad Academy of Research and Education (CARE), Chengalpattu district, Kelambakkam, Tamil Nadu, 603103, India

Email:
Chao-Wei Huang* - huangcw@gs.ncku.edu.tw; Van-Huy Nguyen* - vhnguyen.ChE@gmail.com

* Corresponding author

Keywords:
$LaFeO_3$; $LaNiO_3$; methylene blue (MB); perovskite oxides; photocatalyst

Beilstein J. Nanotechnol. **2022,** *13,* 882–895.
https://doi.org/10.3762/bjnano.13.79

Received: 28 May 2022
Accepted: 16 August 2022
Published: 05 September 2022

This article is part of the thematic issue "Nanomaterials for photocatalysis and applications in environmental remediation and renewable energy".

Guest Editor: V. V. Pham

Abstract

$LaFe_xNi_{1-x}O_3$ perovskite oxides were prepared by the sol–gel method under various conditions, including different pH values (pH 0 and pH 7) and different calcination temperatures (500–800 °C) as well as different Fe/Ni ratios (1/9, 3/7, 5/5, 7/3, 9/1). The samples were examined by XRD, DRS, BET, and SEM to reveal their crystallinity, light-absorption ability, specific surface area, and surface features, respectively. The photocatalytic Fenton reaction was conducted using various $LaFe_xNi_{1-x}O_3$ perovskite oxides to decompose the methylene blue molecules. Accordingly, the synthesis condition of pH 0, calcination temperature at 700 °C, and Fe/Ni ratio = 7/3 could form $LaFe_{0.7}Ni_{0.3}O_3$ perovskite oxides as highly efficient photocatalysts. Moreover, various conditions during the photocatalytic degradation were verified, such as pH value, catalyst dosage, and the additional amount of H_2O_2. $LaFe_{0.7}Ni_{0.3}O_3$ perovskite oxides could operate efficiently under pH 3.5, catalyst dosage of 50 mg/150 mL, and H_2O_2 concentration of 133 ppm to decompose the MB dye in the 1st order kinetic rate constant of 0.0506 s^{-1}.

Introduction

With the advancement of science and technology, the world's population is increasing, leading to the fact that factories are consuming more and more resources. Water inevitably plays a vital role in industrial development among the demanded resources. According to the World Resources Institute (WRI), the demand for freshwater has continued to rise since the 1960s [1]. The inseparable relationship between water and human urban economic activities has been strong. Particularly, agricultural irrigation and animal husbandry have consumed the world's largest water. As the global population increases, the water demand for agricultural planting also increases yearly [2]. Moreover, there is abundant industrial wastewater produced [3]. It originates from the increased demand for electricity, fuels, textiles, and other related industries that consume water [4]. However, it leads to a severe environmental issue due to a large amount of discharged wastewater. For example, domestic wastewater mainly includes organic pollutants from excrement, clothing, cleaning lotion, etc. On the other hand, wastewater discharged from the industry often contains biological drugs, such as antibiotics and pesticides. These drug residues in various industries would enter the drinking water source. It threatens human health and makes bacteria and viruses resistant to drugs, significantly impacting the environment [5]. Notably, wastewater without proper solutions would eventually significantly affect natural ecology and people's quality of life.

Dyes are widely used in various living areas, such as paint, leather, textiles, oil wax, etc. Accordingly, a large amount of dye wastewater is produced every day. Dye wastewater refers to dyes remaining in the aqueous solution during the textile process. The amount of dye wastewater is enormous and has gradually become the main wastewater discharged in the industry [6]. At present, dyes are mainly divided into azo dyes, thiazine dyes, acridine dyes, and aryl methane dyes. Due to their complex chemical structure and high chromophore, it is not conducive to most biological and physical treatments. Thus, wastewater is regarded as a threat to the environment and health. As environmental awareness is gradually increasing, many countries are currently starting to control the use of harmful azo dyes [7].

On the other hand, pharmaceuticals' personal care products (PPCPs) are also sources of organic pollutants in wastewaters. PPCPs cover prescription drugs, nutritious foods, and personal health products that may cause environmental impacts. Among the medicines, tetracycline is antibiotics, which belong to a subcategory of natural or semi-synthetic polyketides. Tetracycline consists of a linear tetracycline nucleus, exhibiting antibacterial activity, which may affect the biological system after discharging [8]. As the population has become dense, vigorous industrial activities, and the animal husbandry industry is relatively developed nowadays, leading to the wide use of antibiotics and drugs. However, most of these substances are eventually released into rivers or oceans, considerably impacting the domestic water and aquatic environments [9].

Several methods deal with wastewater with organic pollutants, such as adsorption, coagulation, filtration, and chemical and biochemical oxidation [10,11]. Advanced oxidation processes (AOPs) have recently attracted attention due to their simple operation, low cost, and potentially high effectiveness. AOPs are the technologies that use various chemical methods to treat wastewater to purify water quality, such as electrochemical oxidation [12], Fenton method [13], ozonation [14], and photocatalysis [15]. They can achieve a fast reaction rate and extremely high organic removal ratio under average temperature and pressure to remove or decompose organic substances in wastewater [16]. Among these procedures, the Fenton method causes numerous interests due to its convenience and effectiveness. Notably, the Fenton method can produce many hydroxyl radicals (·OH) by introducing divalent iron solution and hydrogen peroxide, as shown in Equation 1 below.

$$Fe^{2+} + H_2O_2 \rightarrow Fe^{3+} + OH^- + OH^{\cdot} \quad (1)$$

The Fenton method exhibits high oxidation capability and low selectivity for removing most organic substances. It can decompose organic pollutants into smaller organic molecules and generate carbon dioxide, water, and inorganic ions [17]. Generally, the ferrous ion employed in the Fenton reaction is from ferrous sulfate ($FeSO_4$), which can provide a uniform reaction system due to its high solubility. Unfortunately, it might cause two severe shortcomings in the Fenton reaction process. First, ferric ions (Fe^{3+}) formed in the Fenton reaction will interact with the excess hydroxide ion (OH^-) to produce $Fe(OH)_3$ precipitation, which is called iron sludge. It might decrease the activity and lead to the termination of the Fenton reaction. Second, ferric ions might easily cause complicated chain reactions with organic matters, resulting in the formation of Fe^{3+} complexes or other intermediate products. Such complexes might compete with the hydroxyl radicals, eliciting a degradation of the reaction performance [18].

In recent years, the Fenton method has gradually developed into a new scenario of oxidation method, called photo-Fenton, which is facilitated or driven by the light source. Compared with a typical Fenton reaction, a photo-Fenton reaction excited by ultraviolet light or visible light can achieve a faster reaction rate

and a complete degree of oxidation [19]. Besides, it shows a positive relationship between light intensity and photocatalytic activity. With the assistance of light irradiation, the hydrogen peroxide can be remarkably transformed into redox radicals, followed by destroying the organic pollutants. Meanwhile, the remaining divalent iron complexes in the system can return to the circulation of hydrogen peroxide reaction and continuously form new hydroxide radicals [20]. Therefore, based on our knowledge of photocatalysis [21,22], the benefits of Fenton reaction and photocatalysis are combined to develop a conceptual catalytic design to expand the photocatalytic pathway of Fenton oxidation, called photocatalytic Fenton-like reaction or heterogeneous photo-Fenton-like reaction [23].

$LaFeO_3$ perovskite oxides are promising materials to conduct Fenton-like oxidation to decompose organic pollutants with light irradiation. Some literature exhibits the capability of $LaFeO_3$ perovskite oxides as photocatalysts to degrade organic contaminants. Li et al. prepared intrinsic $LaFeO_3$ or $SmFeO_3$ nanoparticles via the sol–gel method to decompose rhodamine-B under visible light irradiation. With the assistance of H_2O_2, it shows a synergistic effect between photocatalytic reaction and heterogeneous photo-Fenton-like reaction [23]. Furthermore, the strategies of being loaded over supports (such as g-C_3N_4 [24], carbon spheres [25], BiOBr [26], and Ag_2CrO_4 [27]) to form heterojunction structures or doping other atoms into $LaFeO_3$ [28] are comprehensively developed. For instance, Orak et al. impregnated $LaFeO_3$ or $LaTi_{0.15}Fe_{0.85}O_3$ on the monolithic cordierite structure, which could provide light transmittance and suitable surface area for degrading methylparaben. Although Ti-doped catalyst was expected as a semiconductor to enhance the photocatalytic efficiency, pure $LaFeO_3$ still revealed the better performance of methylparaben photodegradation than $LaTi_{0.15}Fe_{0.85}O_3$ [28]. On the contrary, Garcia-Muñoz et al. attempted to substitute Ti to Fe within $LaFeO_3$ as the mediator of heterogeneous Fenton-like reaction to remove 4-chlorophenol in water. The network with Ti substitution (Ti/Fe molar ratio = 0.21) provided stronger robustness, resulting in lower iron release and higher activity enhancement [29]. Ti-doped, Mn-doped [30], and Cu-doped [31] $LaFeO_3$ were investigated to conduct a photocatalytic Fenton-like reaction. Jauhar et al. demonstrated that Mn substituting Fe within $LaFeO_3$ with the molar ratio of 0.1–0.5 displayed the effect of being used as a heterogeneous photocatalyst for dye degradation. Though it was proven that Mn-doped $LaFeO_3$ could enhance the activity of heterogeneous photo-Fenton-like reactions, the influence of Mn content on the activity was not significant [30]. Phan et al. verified that Cu-doped $LaFeO_3$ exhibited physicochemical properties to decolorize methlyorgane, methylene blue, and rhodamine B under visible light irradiation. Their optimal sample was $LaFe_{0.85}Cu_{0.15}O_3$, which could remove dyes much more efficiently due to more generation of hydroxyl radicals than pure $LaFeO_3$ [31].

Ni-doped $LaFeO_3$ was ubiquitously employed as a photo/thermal catalyst or a catalyst precursor for VOCs combustion [32], hydrogen production from ethanol [33], hydrocarbon fuels production from CO_2 and H_2O [34], syngas production from dry reforming [35], steam reforming of methane [36], or combined reforming of methane with CO_2 and O_2 [37]. Meanwhile, $LaNiO_3$ photocatalysts also played an essential role in photocatalytic reactions for wastewater [38]. Fe doping of $LaNiO_3$ revealed the potential of tuning bandgap and boosting the light absorption to degrade RhB [39]. However, little literature comprehensively and systematically discusses the effect of different doping ratios on photocatalytic reactions. Moreover, $LaNiO_3$ revealed broad absorption in the visible light range [38], so the Ni doping was expected to improve the visible light harvesting of $LaFeO_3$. Accordingly, little literature explored the effect of Ni substitution to $LaFeO_3$ on the performance of photocatalytic Fenton-like reaction to degrade dye pollutants in water. Therefore, in this study, various contents of Ni-doped $LaFeO_3$ were examined to remove organic pollutants under simulated solar light irradiation. Methylene blue is the representative compound of thiazine dyes and tetracycline is the indicator pollutant to represent the antibiotics of PPCPs accordingly.

Results and Discussion

Material characterization of various photocatalysts

X-ray powder diffraction (XRD) was used to reveal the structure of the materials. In the synthesis step of $LaNiO_3$, the calcination temperature was set to 500, 600, 700, and 800 °C, respectively, and the samples were named $LaNiO_3$-500, $LaNiO_3$-600, $LaNiO_3$-700, $LaNiO_3$-800 in sequence. The uncalcined sample was noted as $LaNiO_3$-NC. As shown in Figure 1, there was no crystalline $LaNiO_3$ signal for the sample of $LaNiO_3$-NC, but there were other signals for other samples indicating the presence of La_2NiO_4 (42.8°, JCPDS Card #011-0557), NiO (37.3°, 43.3°, JCPDS Card #04-0835), and $La_2O_2CO_3$ (13.1°, 22.8°, 29.6°, 31.3°, JCPDS Card #23-0322) signals, respectively [40]. The sample calcined at 500 °C exhibited the more apparent signals belonging to $La_2O_2CO_3$ and NiO. The signal of $LaNiO_3$ did not appear for $LaNiO_3$-500, indicating that the temperature of 500 °C was not enough to form $LaNiO_3$. With the increase of temperature up to 600 °C, some obvious 2θ signals of $LaNiO_3$ crystalline appeared, including 23.3°, 32.8°, 41.2°, 47.3°, 58.6°, and 68.8°. These peaks indicated the crystal planes (012), (110), (202), (024), (211), and (220) of $LaNiO_3$, respectively, conforming to JCPDS Card #033-0711 [41]. $LaNiO_3$-700 and $LaNiO_3$-800 performed similar peak positions

with higher intensity of signals. Accordingly, the crystal diameter of $LaNiO_3$ was calculated by Scherrer's equation [42]. The crystal diameters of $LaNiO_3$-600, $LaNiO_3$-700, and $LaNiO_3$-800 were 8.5 nm, 11.9 nm, and 14.6 nm, respectively. It could be seen that the higher the calcination temperature, the higher the crystal size will form.

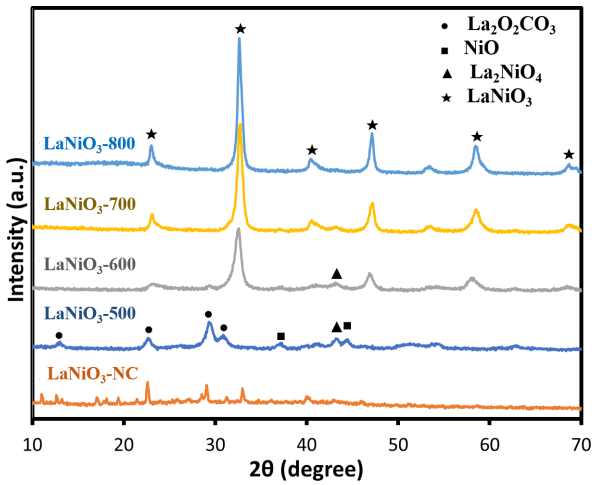

Figure 1: The characteristic XRD patterns of $LaNiO_3$ at different calcination temperatures.

Similarly, $LaFeO_3$ samples with different calcination temperatures of uncalcined, 500, 600, 700, and 800 °C were noted as $LaFeO_3$-NC, $LaFeO_3$-500, $LaFeO_3$-600, $LaFeO_3$-700, and $LaFeO_3$-800, respectively. In Figure 2, there was no signal for the uncalcined sample. While the calcination temperature was set at 500 °C, the signals of the $LaFeO_3$ crystalline phase appeared. The diffraction peak of $LaFeO_3$ became stronger as the calcination temperature increased. As shown in Figure 2, the 2θ peaks of 22.6°, 32.2°, 39.6, 46.3°, 57.4°, and 67.4° indicated the crystal planes of (101), (121), (220), (202), (240), and (242), according to JCPDS Card #037-1493 [43]. With the increase in calcination temperature, the higher crystal diameters of $LaFeO_3$ calculated by Scherrer's equation were obtained. The crystal diameters was 18.5 nm, 25.4 nm, 29.1 nm, 35.0 nm for $LaFeO_3$-500, $LaFeO_3$-600, $LaFeO_3$-700, $LaFeO_3$-800, respectively, suggesting higher calcination temperature caused higher crystallinity for $LaFeO_3$. Moreover, all $LaFeO_3$ samples revealed higher crystal diameters than $LaNiO_3$, indicating $LaFeO_3$ tended to grow crystal than $LaNiO_3$ at a certain calcination temperature. However, high temperature might cause particle aggregation, leading to the lower surface area. Therefore, a moderate temperature of 700 °C was selected to obtain the perovskite materials. On the other hand, the XRD of $LaFeO_3$-800 indicated the appearance of Fe_2O_3 at 2θ peaks of 32.9°, 38.3°, 47.3° (JCPDS Card #39-0238) and La_2O_3 at 2θ peaks of 25.3°, 52.0°, 54.1° (JCPDS Card #40-1281). Especially, the peak of 32.9° for $LaFeO_3$-800 was much clearer than that of $LaFeO_3$-700, suggesting that the calcination temperature was too high and caused the formation of Fe_2O_3.

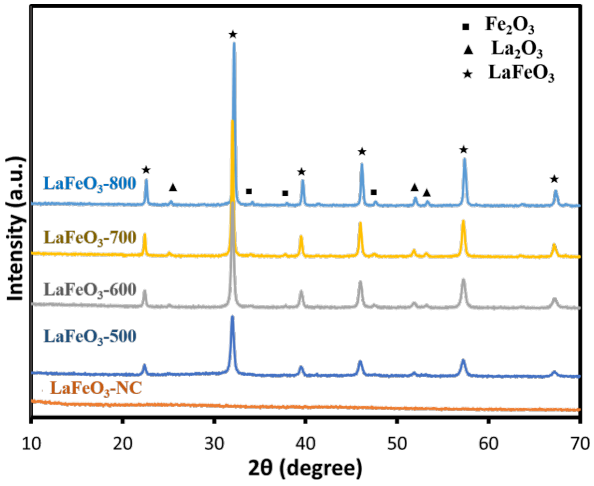

Figure 2: The characteristic XRD patterns of $LaFeO_3$ at different calcination temperatures.

In addition, samples with various doping proportions of Fe/Ni, including 0.1/0.9, 0.3/0.7, 0.5/0.5, 0.7/0.3, and 0.9/0.1 were synthesized. The pH value was adjusted at 0 during synthesis, and the calcination temperature was fixed at 700 °C. The samples were named $LaFeO_3$, $LaFe_{0.9}Ni_{0.1}O_3$, $LaFe_{0.7}Ni_{0.3}O_3$, $LaFe_{0.5}Ni_{0.5}O_3$, $LaFe_{0.3}Ni_{0.7}O_3$, $LaFe_{0.1}Ni_{0.9}O_3$, $LaNiO_3$ to represent the different Fe/Ni doping ratios. In Figure 3, the signals of $LaFeO_3$ and $LaNiO_3$ were identified by JCPDS Card #037-1493 [43] and JCPDS Card #033-0711 [41], respectively. Among these peaks, the main characteristic peak around 32° was slightly shifted for different Fe/Ni doping ratios, indicating that Fe and Ni were successfully doped into the structure of perovskite oxides. It is interesting to note that $LaFe_{0.7}Ni_{0.3}O_3$ had a stronger signal than other doped samples. The crystal diameters of samples with various Fe/Ni doping ratios were also calculated by Scherrer's equation, as shown in Figure 4, which ranged from 9.5 to 31.3 nm. When the Fe/Ni ratio was manipulated at 7/3, the sample had the largest crystal diameter of 31.3 nm. The better crystallinity caused less recombination of electron-and-hole pairs, and subsequent reactions might occur more effectively [44]. On the other hand, The unit cell parameters and cell volume were also estimated from the XRD patterns and summarized in Supporting Information File 1, Table S2. Since the peaks of $LaFe_{0.5}Ni_{0.5}O_3$, $LaFe_{0.7}Ni_{0.3}O_3$, and $LaFe_{0.9}Ni_{0.1}O_3$ were closed to $LaFeO_3$, the unit cell parameters and interplanar spacing were calculated based on the model of orthorhombic $LaFeO_3$ (JCPDS card: 037-1493) using Bragg's

law [45]. Meanwhile, $LaFe_{0.5}Ni_{0.5}O_3$, $LaFe_{0.3}Ni_{0.7}O_3$, and $LaFe_{0.1}Ni_{0.9}O_3$ were also calculated based on the model of hexagonal $LaNiO_3$. As a result, the lattice constant and cell volume were slightly expanded. It was interesting to note that $LaFe_{0.7}Ni_{0.3}O_3$ revealed a relatively larger expansion, which had a higher cell volume, suggesting a better separation of photo-induced electron and hole pairs.

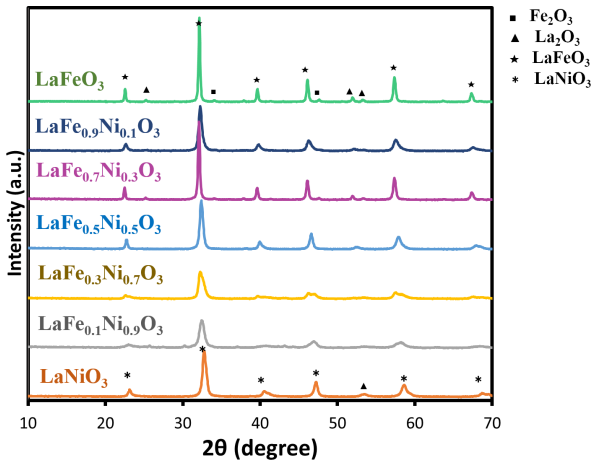

Figure 3: The characteristic XRD patterns of $LaFe_xNi_{1-x}O_3$.

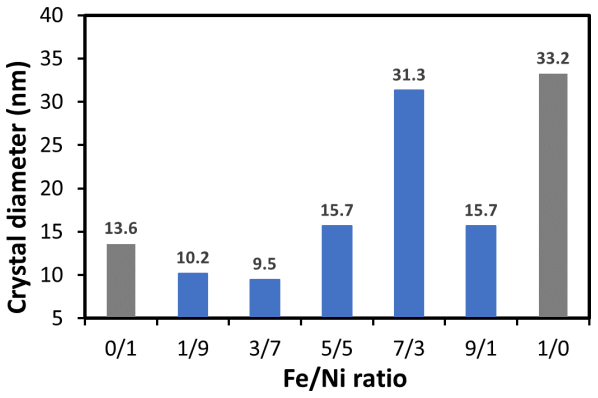

Figure 4: The crystal diameters of samples with various Fe/Ni doping ratios.

The UV–vis absorption capability with diffuse reflectance spectroscopy (DRS) and photographs of various $LaFe_xNi_{1-x}O_3$ perovskite oxides with different proportions were shown in Figure 5a and 5b. Except for $LaFeO_3$, which was brown, the rest of the perovskite oxides doped with Ni became black. Since pristine $LaNiO_3$ was black, it exhibited the total absorption in the ultraviolet–visible light spectrum, consistent with the literature comparison [46]. For comparison, $LaFeO_3$ revealed an apparent absorption shoulder between 500 and 600 nm in Figure 5a, similar to the previous study [47]. To enhance the light absorption of $LaFeO_3$, it was an effective method to dope Ni into the perovskite oxides. Accordingly, the samples were doped with Ni to form $LaFe_xNi_{1-x}O_3$ perovskite oxides that could absorb the most visible and ultraviolet light spectrum. Thus, the prepared Ni-doped $LaFeO_3$ perovskite oxides were presented as black, as shown in Figure 5b. They successfully increased the absorption efficiency of visible light and utilized more visible light effectively.

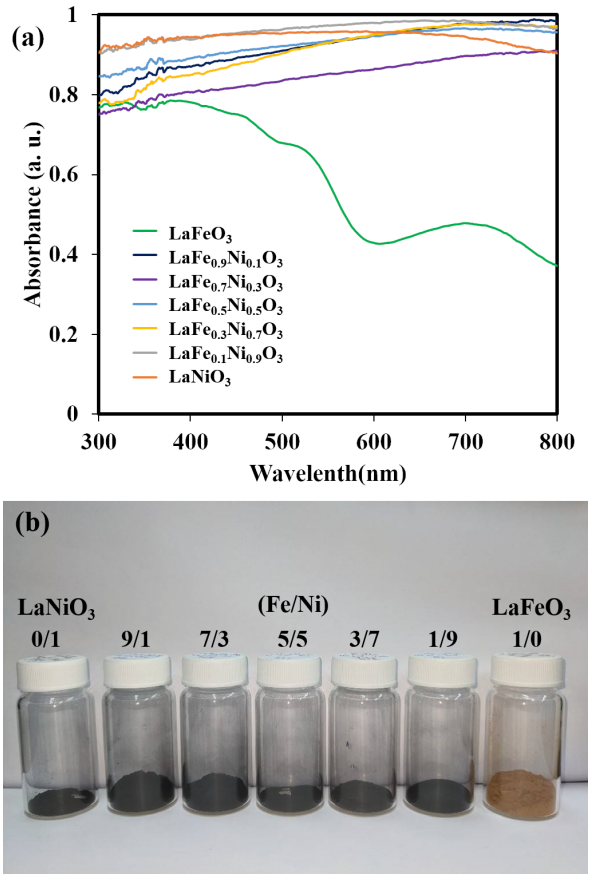

Figure 5: (a) The DRS spectrum and (b) the pictures of samples with various Fe/Ni doping ratios.

In order to determine the specific surface area, pore size, and pore volume of the prepared perovskite oxides, the analysis of nitrogen adsorption and desorption was performed. As shown in Supporting Information File 1, Figure S1, all $LaFe_xNi_{1-x}O_3$ perovskite oxides were in line with Type IV isotherm according to their hysteresis phenomenon. The Brunauer–Emmett–Teller (BET) result of the pristine $LaFeO_3$ and $LaNiO_3$ corresponded to the result in the literature [48,49]. The pore size distribution of the samples was shown in Figure S2. The distribution between 2 and 50 nm indicated that the prepared perovskite oxides were mesoporous. The summary of the

specific surface area, pore size, and pore volume for all the samples with different Fe/Ni ratios was presented in Table S1. In Figure 6, it could be found that the $LaFe_{0.7}Ni_{0.3}O_3$ with the Fe/Ni ratio of 7/3 had the highest specific surface area, pore volume, and pore size, suggesting there was more possibility for $LaFe_{0.7}Ni_{0.3}O_3$ to adsorb and react with the molecules on the surface. On the other hand, the prepared samples might also be considered non-porous materials with inter-particle pore voids, since their low surface area might come from the external surface, indicating that $LaFe_{0.7}Ni_{0.3}O_3$ had the highest external surface area for reaction.

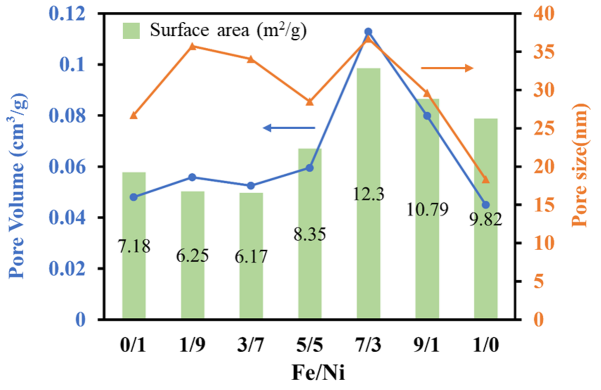

Figure 6: Specific surface area, pore size, and pore volume of the samples with different Fe/Ni ratios.

Figure 7 revealed the field emission scanning electron microscopy (FESEM) images at the magnification of 100,000×, the surface of the samples with different Fe/Ni ratios were irregular and slightly different from each other. The grain surfaces of the pure $LaNiO_3$ and $LaFeO_3$ were chestnut-like. The observed appearance was also similar to the literature situation [50]. With the increased Fe content, some small lumps formed on the surface. When Fe/Ni ratio reached 7/3, relatively abundant small particles were generated than other samples. Small particles of $LaFe_{0.7}Ni_{0.3}O_3$ would increase the surface area, which was consistent with the trend of the results detected by BET. On the other hand, it is interesting to note that the pH value during synthesis could affect the appearance of $LaFe_xNi_{1-x}O_3$. The samples prepared at pH 0 showed more uniform than that at pH 7 (shown in Supporting Information File 1, Figure S3). It indicated that the protons in the sol–gel solution could help the separation of $LaFe_xNi_{1-x}O_3$ crystals, leading to less particle aggregation. Moreover, the elemental analysis of the samples was also carried out using energy dispersive spectroscopic (EDS). The Fe contents of the samples with different Fe/Ni atomic ratios were identified. EDS detection showed that the synthesized samples exhibited the accurate Fe/Ni atomic ratios as designed. The detailed EDS data was provided in Table S3. The lanthanum, nickel, iron, and oxygen were analyzed from the samples, and the carbon was detected from the carbon tape.

MB removal test using various photocatalysts prepared at pH 0 or pH 7

The standard concentration of MB aqueous solution was prepared at 20 ppm. Various $LaFe_xNi_{1-x}O_3$ perovskite oxides prepared at pH 0 were examined for dark adsorption and photocatalytic degradation. First, dark adsorption was not significant for all perovskite oxides since their specific surface areas were low. After 30 min, to confirm the achievement of dark adsorption-desorption equilibrium, the photocatalytic reaction occurred under the irradiation of simulated AM 1.5G solar light with adding H_2O_2. By monitoring the C/C_0 of MB, the performance of all perovskite oxides prepared at pH 0 or pH 7 were depicted in Figure 8a and 8b, respectively. $LaFeO_3$ had the highest content of Fe^{3+} ions so that it could generate more hydroxyl radicals with H_2O_2 in the solution, resulting in the best performance of MB degradation. $LaFeO_3$ could completely degrade MB after 45 min of simulated solar light irradiation due to the Fenton effect of Fe^{3+} [51]. On the contrary, $LaNiO_3$ did not conduct the Fenton-like effect; therefore, it exhibited poor photocatalytic ability. Fe's phenomenon revealed better catalytic activity than Ni, similar to the previous study [52]. It might result from Ni's apparent activation energy being higher than Fe's for producing oxidizing species [53]. Although Fe was attempted to be doped into $LaNiO_3$, $LaFe_{0.1}Ni_{0.9}O_3$ and $LaFe_{0.3}Ni_{0.7}O_3$ still exhibited low photocatalytic capability. Until Fe doped amount was up to 50% for replacing Ni, the photocatalytic performance of $LaFe_{0.5}Ni_{0.5}O_3$ was enhanced much more apparent than that of $LaFe_{0.3}Ni_{0.7}O_3$. It indicated that Fe^{3+} plays a vital role in involving MB degradation. As the Fe doped content increased, $LaFe_{0.7}Ni_{0.3}O_3$ reached the highest photocatalytic capability, originating from its largest surface area and crystal diameters. A larger surface area would enhance the surface reaction with the aqueous solution, and larger crystal diameters could decrease the possibility of recombining electron-and-hole pairs. However, while the Fe doped content was set at 90%, replacing Ni, the photocatalytic capability was reduced due to the lower surface area and smaller pore size. The above inference was consistent with the cases of the samples prepared at pH 0 and pH 7. Interestingly, the performance of the perovskite oxide prepared at pH 0 was much better than that prepared at pH 7. It was derived from the fact that more uniform structural features of the perovskite oxide prepared at pH 0 were achieved than the condition at pH 7. Moreover, the photocatalytic performance of physically mixed 70% $LaFeO_3$ and 30% $LaNiO_3$ could be estimated based on the result of MB degradation using 70% $LaFeO_3$ (since $LaNiO_3$ showed no MB degradation). The degradation of 70% $LaFeO_3$ in 30 min was approximately 60.0%. Considering the light shading effect by $LaNiO_3$, the MB photo-

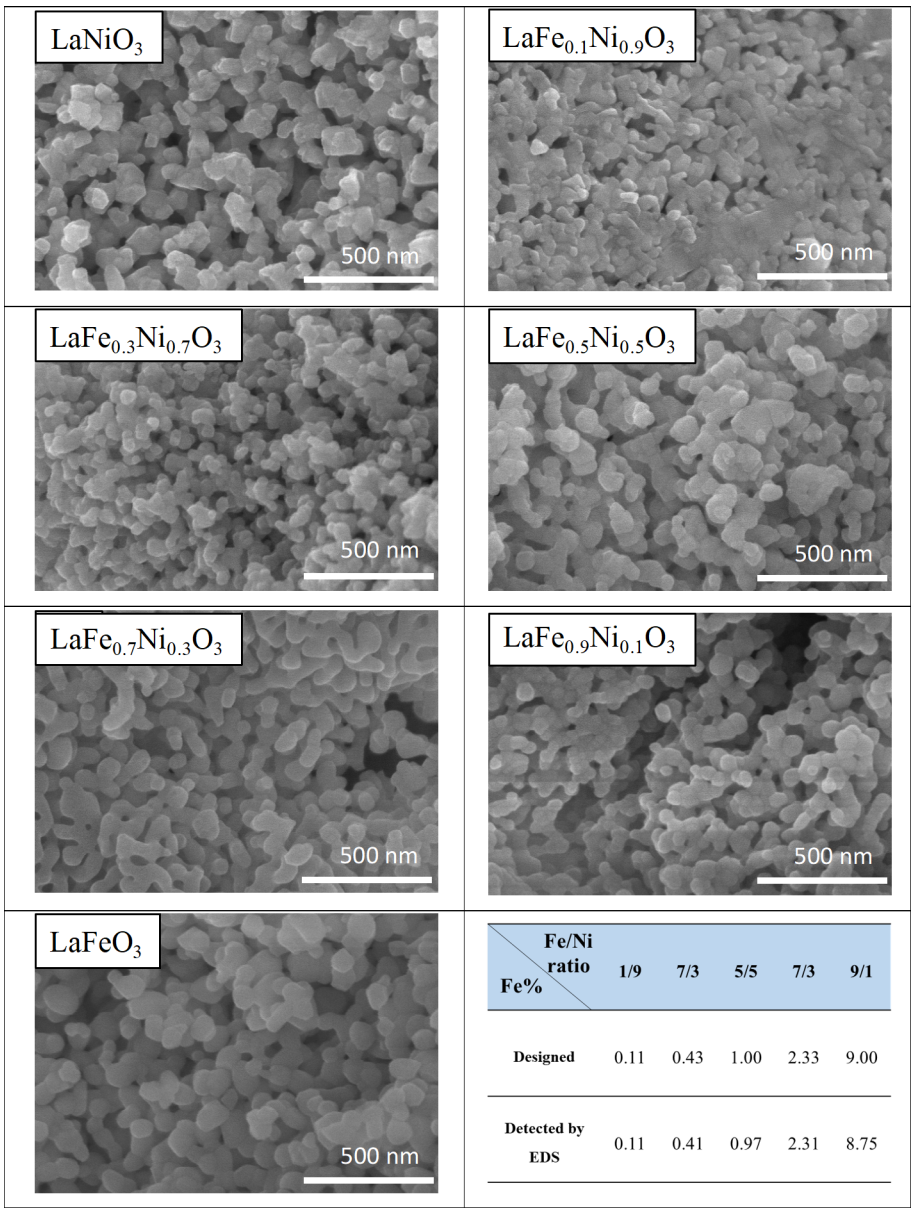

Fe% \ Fe/Ni ratio	1/9	7/3	5/5	7/3	9/1
Designed	0.11	0.43	1.00	2.33	9.00
Detected by EDS	0.11	0.41	0.97	2.31	8.75

Figure 7: The FESEM images of $LaFe_xNi_{1-x}O_3$ prepared at pH 0 (at the magnification of 100,000×).

degradation of physically mixed 70% $LaFeO_3$ and 30% $LaNiO_3$ might be lower. On the contrary, the $LaFe_{0.7}Ni_{0.3}O_3$ showed 78.5% of MB degradation in 30 min. Therefore, we believed there would be a benefit of doping Ni to improve the photodegradation.

In Figure 9, by taking the negative natural logarithmic value of C/C_0, it was observed that all the degradation trends were in line with first-order kinetics:

$$-\ln\frac{C}{C_0} = kt$$

where k was the rate constants of MB degradation reaction; t was the reaction duration in min. As shown in Table 1, for photocatalytic Fenton-like reaction to decompose MB dye, $LaFeO_3$ had the fastest degradation rate (k = 0.1072 prepared at pH 0; k = 0.0086 prepared at pH 7). It might be due to the higher content of Fe ion for $LaFeO_3$ than $LaFe_{0.7}Ni_{0.3}O_3$. However, we would like to focus on the doping effect on photocatalytic reaction so that $Fe_{0.7}Ni_{0.3}O_3$ was the target material to be further analyzed and characterized. Comparing the samples co-doped with Fe and Ni, $LaFe_{0.7}Ni_{0.3}O_3$ exhibited a higher k value of 1st order reaction than other co-doped samples. $LaFe_{0.7}Ni_{0.3}O_3$ had a larger crystal diameter and higher specif-

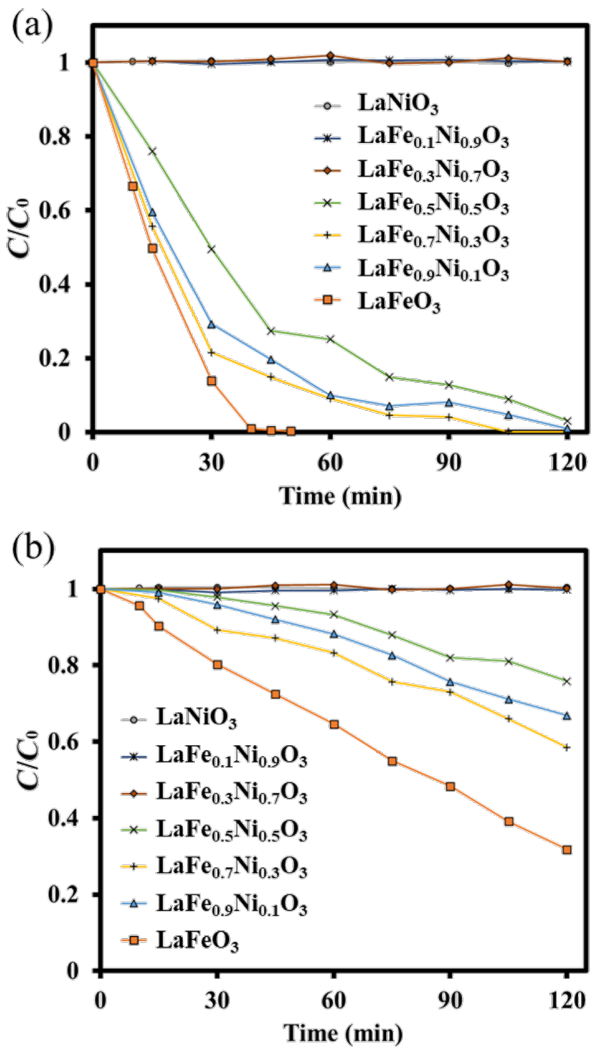

Figure 8: MB degradation experiments using various $LaFe_xNi_{1-x}O_3$ with different Fe/Ni ratios prepared at (a) pH 0; (b) pH 7.

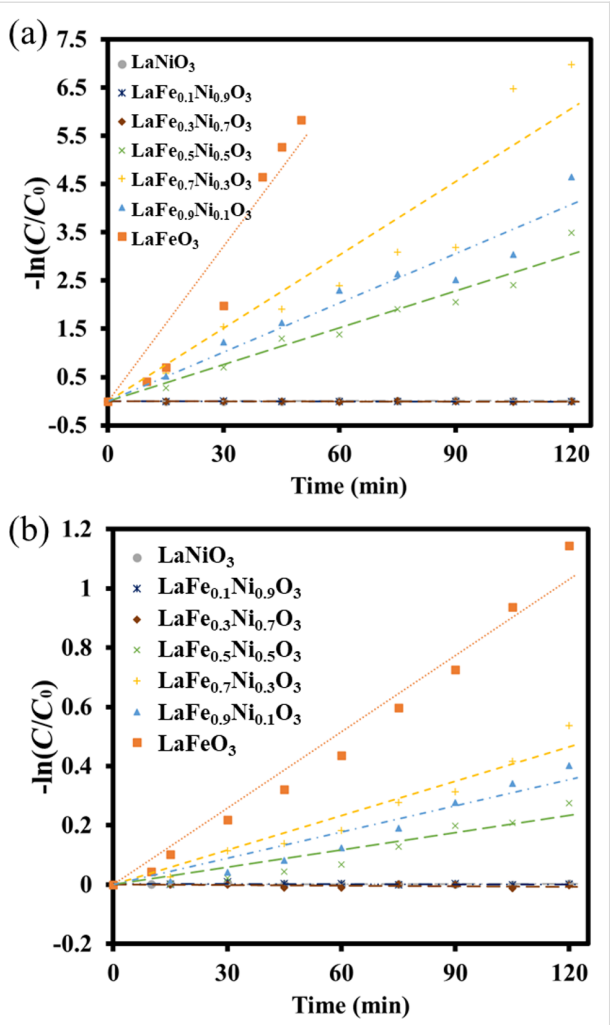

Figure 9: Kinetic analysis of MB degradation experiments using various $LaFe_xNi_{1-x}O_3$ with different Fe/Ni ratios at (a) pH 0 and (b) pH 7.

ic surface, which improved the separation of photogenerated charge carriers and the efficiency of the surface reaction. For comparison, the second-order kinetics analysis was also conducted for the samples prepared at pH 0 in Table 1. However, the R^2 values were too low to represent their kinetic model. Therefore, 1st order reaction kinetics was more suitable for describing the kinetic model of $LaFe_xNi_{1-x}O_3$.

Table 1: The kinetic analysis of $LaFe_xNi_{1-x}O_3$ perovskite oxides prepared at pH 0 and pH 7.

pH value	Reaction kinetics analysis		$LaFeO_3$	$LaFe_{0.9}Ni_{0.1}O_3$	$LaFe_{0.7}Ni_{0.3}O_3$	$LaFe_{0.5}Ni_{0.5}O_3$
pH 0	1st order	k	0.1072	0.0339	0.0506	0.0254
		R^2	0.9616	0.9808	0.9584	0.9876
	2nd order	k	0.8043	0.0313	0.4098	0.0125
		R^2	0.6892	0.4846	0.5404	0.6184
pH 7	1st order	k	0.0086	0.003	0.0039	0.002
		R^2	0.9903	0.9691	0.9838	0.9517

MB removal test under different conditions using $LaFe_{0.7}Ni_{0.3}O_3$ prepared at pH 0

The pH value of the solution was a strong effect on photocatalytic degradation [54]. Accordingly, different pH values of solution using $LaFe_{0.7}Ni_{0.3}O_3$ perovskite oxides prepared at pH 0 were examined for photocatalytic degradation. Thus, the MB aqueous solution was adjusted to pH 1.5, 3.5, and 5.5. The performance of the photocatalytic Fenton degradation was measured at different pH values in Figure 10. After 120 min of simulated solar light irradiation, the degradation performance at 1.5, 3.5, and 5.5 were 97.9%, 100%, and 25.2%, respectively. The pH value at 3.5 revealed the highest photocatalytic performance, in which MB pollutants were completely degraded within 105 min. Based on the 1st order kinetic analysis, the reaction rate constants (k) at pH 1.5, 3.5, and 5.5 were 0.0254, 0.0506, and 0.002, respectively. While the pH value was too high, the hydrogen peroxide in the solution was easily decomposed into oxygen and water [55]. On the other hand, when the pH value was too low, the solution tended to generate too many hydrogen ions, which would react with hydrogen peroxide to form water, leading to a decrease in the photocatalytic degradation performance [56]. Therefore, the operating condition of the pH value was set at 3.5.

After manipulating the operating pH value, the pH of the solution was fixed at 3.5. The dosages of $LaFe_{0.7}Ni_{0.3}O_3$ perovskite oxides were further examined. In this study, the amount of the MB solution was 150 mL, and various $LaFe_{0.7}Ni_{0.3}O_3$ perovskite oxides, including 30 mg (200 ppm), 50 mg (333 ppm), 80 mg (533 ppm), and 100 mg (666 ppm) of catalyst were put into the reactor for photocatalytic degradation reaction. As shown in Figure 11a, the degradation performances after 120 min photocatalytic reaction were 55.7%, 100%, 98.8%, and 97.3%, respectively. Comparing the condi-

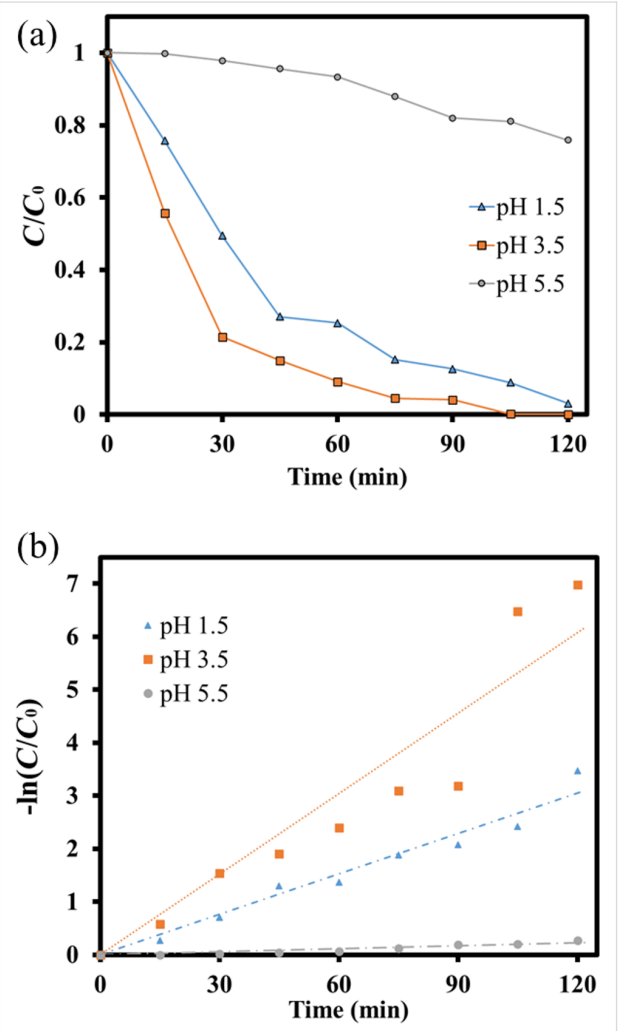

Figure 10: (a) The C/C_0 and (b) 1st order kinetic analysis of the MB photodegradation using $LaFe_{0.7}Ni_{0.3}O_3$ operating at different pH values.

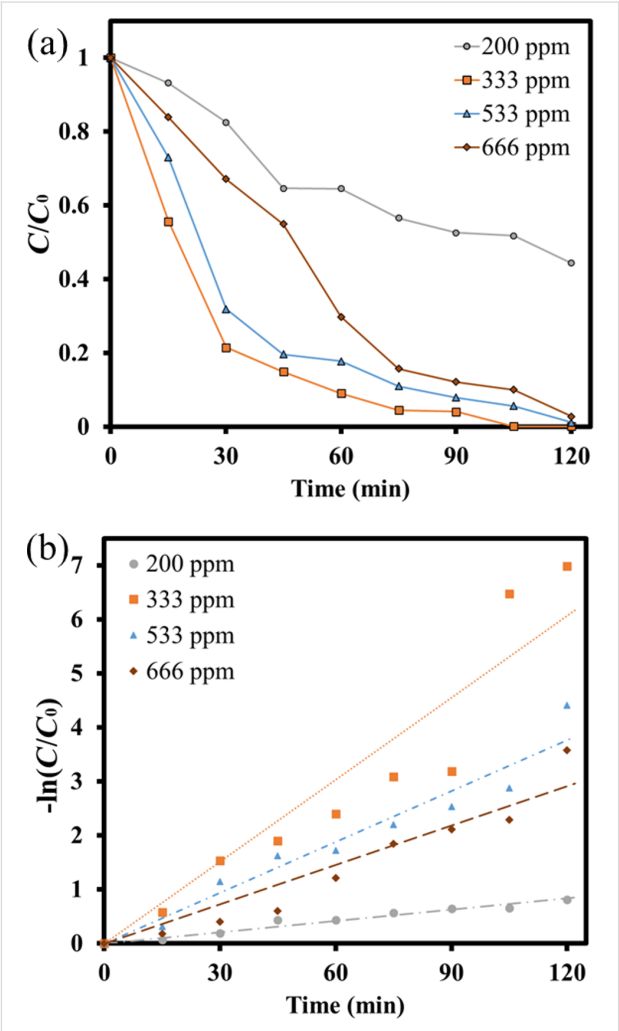

Figure 11: (a) The C/C_0 and (b) 1st order kinetic analysis of the MB photodegradation using $LaFe_{0.7}Ni_{0.3}O_3$ operating at different catalyst dosages.

tions of 30 mg (200 ppm) and 50 mg (333 ppm), it could be found that if more $LaFe_{0.7}Ni_{0.3}O_3$ perovskite oxides were added to the solution, a better photocatalytic degradation performance would be obtained. However, while too many $LaFe_{0.7}Ni_{0.3}O_3$ perovskite oxides were added, the excess catalyst would inhibit light penetration into the suspension. Thus, the availability of light energy was reduced, resulting in a reduction of the photocatalytic degradation capability [30]. Accordingly, the degradation performance was calculated by the 1st order kinetics, as shown in Figure 11b. It could be known that when the catalyst dosage was 30 mg (200 ppm), 50 mg (333 ppm), 80 mg (533 ppm), and 100 mg (666 ppm), their reaction rate constants *k* were 0.007, 0.0242, 0.0314, and 0.0506, respectively. Therefore, the pH of the solution was 3.5, and the catalyst dosage was 50 mg for the following examination.

Moreover, the amount of hydrogen peroxide added was manipulated in advance. Similarly, the amount of contaminant solution was 150 mL. The pH value of the solution was fixed at 3.5, the catalyst dosage was 50 mg, and hydrogen peroxide was added in various amounts, such as 5 µL (33 ppm), 10 µL (66 ppm), 20 µL (133 ppm) and 60 µL (400 ppm), respectively. The photocatalytic degradation experiment results were shown in Figure 12a. With the increase of hydrogen peroxide addition, the degradation capability after 120 min simulated solar light irradiation was 69.4%, 97.2%, 100%, and 99.9%, respectively. Then, their 1st order kinetics analysis was also depicted in Figure 12b. The reaction rate constants *k* of various conditions by adding different amounts of H_2O_2 were obtained as 0.0086, 0.0251, 0.0326, and 0.0506, respectively. It could be concluded that adding more H_2O_2 could increase the hydroxyl radicals in the aqueous solution and improve the performance of photocatalytic degrading pollutants. However, when too many hydroxyl radicals were generated, the hydroxyl radicals in the aqueous solution would combine with excess H_2O_2 to form superoxide hydrogen radicals and water [56], reducing the degradation capability.

Accordingly, the optimal operating conditions were summarized together: (1) the pH value of the aqueous solution was 3.5; (2) the amount of catalyst added was 50 mg in 150 mL solution (333 ppm); (3) the amount of hydrogen peroxide added was 20 µL. The MB removals contributed to the photocatalytic reactions and the Fenton reactions simutaneously. In order to further understand the effect of the photocatalysis and the Fenton reaction in the degradation reaction, some degradation tests were also carried out as controlling experiments for comparison, including: (1) without adding photocatalyst (No catalyst), (2) without light (No light), and (3) without adding H_2O_2 (No H_2O_2), as shown in Supporting Information File 1, Figure S4a. It could be observed that in the case of no catalyst added, the

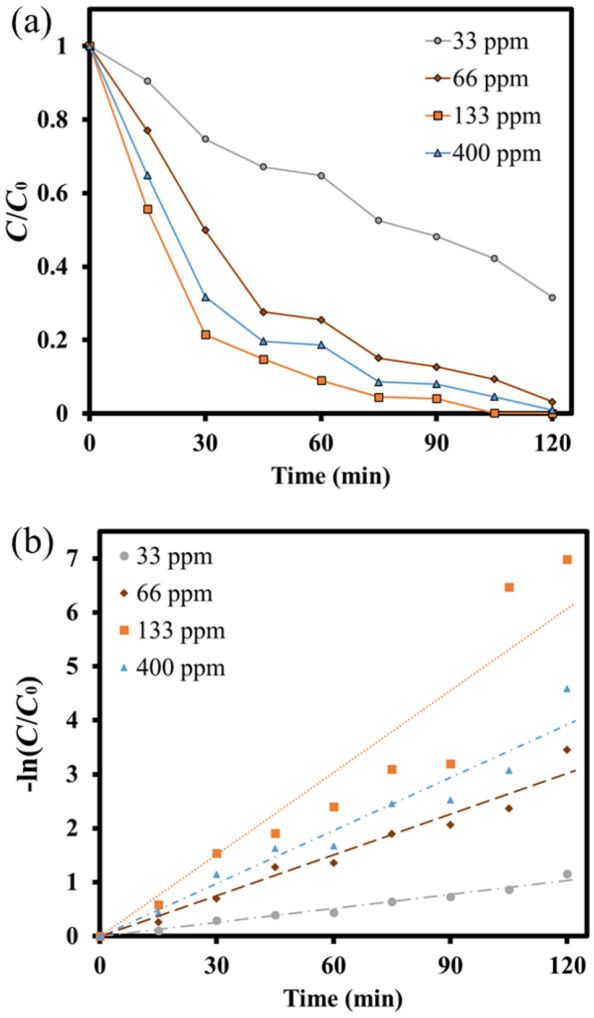

Figure 12: (a) The C/C_0 and (b) 1st order kinetic analysis of the photodegradation using $LaFe_{0.7}Ni_{0.3}O_3$ operating at different H_2O_2 addition.

degradation was only 2.2% after 120 min, suggesting that H_2O_2 might not be easy to form ·OH radicals under visible light irradiation to carry out the degradation reaction. Then, the degradation of the case without adding H_2O_2 was approximately 4.9% after 120 min. It indicated that the heterogeneous Fenton reaction might play a more critical role than the photocatalytic reaction. Another possibility, even though $LaFe_{0.7}Ni_{0.3}O_3$ was a visible-light-driven photocatalyst, its electron–hole recombination was still too severe, resulting in relatively poor performance of MB removal. Next, the result of the case without light indicated the Fenton reaction was carried out without light. After 120 min, it was found that the degradation reached 69.2%. $LaFe_{0.7}Ni_{0.3}O_3$ catalyst contained iron ions, which could certainly convert H_2O_2 into ·OH and achieve a certain degree of degradation. Finally, compared with the above-mentioned controlling cases, the degradation under original conditions (All) reached 100% at 120 min, attributed mainly to the Fenton

reaction and the photocatalysis, which could multiply the function of hydroxyl radicals. Their performances of MB degradation were calculated by 1st order kinetics, as shown in Figure S4b. The reaction rate constants k of different conditions: (1) No cat., (2) No H_2O_2, (3) No light, and (4) All, were 0.0002, 0.0005, 0.0096, and 0.0506, respectively. Moreover, the comparison of the prepared $LaFe_{0.7}Ni_{0.3}O_3$ with other materials from the literature was also listed in Table S4. It showed that $Fe_{0.7}Ni_{0.3}O_3$ samples revealed comparable photodegradation performance to other composite materials.

Moreover, the degradation of TC using $LaFe_{0.7}Ni_{0.3}O_3$ prepared at pH 0 was also carried out under the optimal conditions of pH 3.5, catalyst = 333 ppm, and H_2O_2 = 20 µL as shown in Supporting Information File 1, Figure S5a. The TC concentration could drop by nearly 93.3% in 30 min of light irradiation compared with the initial concentration (20 ppm). The TC was degraded entirely in 60 min. Since there were multiple polar groups (hydroxyl group) within the chemical structure of TC [57], it was easy to attract the hydroxyl radicals in the TC solution, resulting in a better photocatalytic performance than MB. The kinetic rate constant of TC degradation was also calculated, as shown in Figure S5b. Accordingly, the reaction rate constants k of photodegrading TC and MB were 0.10991 and 0.0506, respectively, indicating $LaFe_{0.7}Ni_{0.3}O_3$ revealed a great potential to decompose other organic pollutants.

Conclusion

In this experiment, $LaFe_xNi_{1-x}O_3$ perovskite oxides were successfully synthesized by the sol–gel method. The calcination temperature and the pH value were manipulated during synthesizing $LaFe_xNi_{1-x}O_3$ photocatalysts. Through XRD, it could be found that the calcination temperature must be higher than 700 °C to reveal the clear crystal phase. Moreover, the $LaFe_xNi_{1-x}O_3$ photocatalysts prepared at pH 0 exhibited higher photocatalytic performance than at pH 7 due to more uniform structural features for the condition of pH 0. On the other hand, the Fe/Ni doping ratio during the synthesis was detected by XRD, indicating that the sample with the Fe/Ni ratio of 7/3 could obtain the largest crystal diameter with a better crystallinity. Meanwhile, the perovskite oxides with the Fe/Ni ratio of 7/3 had the highest specific surface area according to the BET BET measurement, which was conducive to photocatalysis. Furthermore, with changing the conditions during degradation, the pH value of the solution, the amount of catalyst dosage, and the amount of H_2O_2 added were examined. A higher pH value in the solution would cause hydrogen peroxide quickly decompose into oxygen and water. When the pH value was too low, the solution tended to produce too many hydrogen ions, which would combine with hydroxyl radicals to form water. An unsuitable pH value would decrease the photocatalytic degradation capability so that the operating pH was set at 3.5. Similarly, the catalyst could perform better with the increase of the additional amount. However, excess catalysts would inhibit light penetration and decrease light availability. Accordingly, the catalyst dosage was set at 50 mg. On the other hand, H_2O_2 could enhance the generation of the hydroxyl radicals in the aqueous solution. Unfortunately, when excess H_2O_2 produced too many hydroxyl radicals, the hydroxyl radicals would combine with H_2O_2 to form hydrogen peroxide radicals and water, reducing the poor photocatalytic degradation. The amount of H_2O_2 added was suggested at 20 µL. To sum up, the $LaFe_xNi_{1-x}O_3$ perovskite oxides could be the photocatalysts to conduct the photocatalytic Fenton reaction to decompose the MB pollutants under the irradiation of simulated AM 1.5G solar light. It could be seen that the $LaFe_xNi_{1-x}O_3$ perovskite oxides could be used as an environmentally to catalyze the photocatalytic degradation of pollutants.

Experimental

Materials

The precursors of $LaFe_xNi_{1-x}O_3$ for La, Fe, and Ni were lanthanum nitrate hexahydrate (99.9%, $La(NO_3)_3{\cdot}6H_2O$, Alfa Aesar), ferric nitrate nonahydrate (≥98.0%, $Fe(NO_3)_3{\cdot}9H_2O$, J.T. Baker), and nickel nitrate hexahydrate (98.0%, $Ni(NO_3)_2{\cdot}6H_2O$, Showa), respectively. The citric acid (95.0%, $C_6H_8O_7$) and ammonia (28.0–30.0%, NH_4OH) were both obtained from J.T. Baker Chemicals. Ethanol (95.0%, C_2H_5OH) was purchased from Echo Chemical. Hydrochloric acid (>37%, HCl) and hydrogen peroxide (50%, H_2O_2) were acquired from Honeywell Research Chemicals and OCI company, respectively. Model compounds, including methylene blue (≥98.0%, MB, $C_{16}H_{18}N_3SCl$) and tetracycline (≥98.0%, TC, $C_{22}H_{24}N_2O_8$), were provided from Sigma-Aldrich. Commercial tungsten oxide (99.8%, WO_3) was bought from Alfa Aesar.

Synthesis of $LaFe_xNi_{1-x}O_3$

The $LaFe_xNi_{1-x}O_3$ catalysts were synthesized via the sol–gel method with citric acid crosslinking reaction, followed by self-propagating high-temperature synthesis. First, 0.02 mol lanthanum nitrate hexahydrate ($La(NO_3)_3{\cdot}6H_2O$), ferric nitrate nonahydrate ($Fe(NO_3)_3{\cdot}9H_2O$), and nickel nitrate hexahydrate ($Ni(NO_3)_2{\cdot}6H_2O$) were dissolved in deionized water to form the mixed solution. Various photocatalysts with different molar ratios of Fe/Ni were manipulated at 0.1/0.9, 0.3/0.7, 0.5/0.5, 0.7/0.3, and 0.9/0.1. Accordingly, the chemical stoichiometric ratios of Fe and Ni were noted as x and $1-x$, respectively. Second, 0.1 mol citric acid ($C_6H_8O_7$) was also dissolved into the mixed solution as the cross-linking agent to gradually form the gel solution with light brown color. The pH value was adjusted to pH 0 or pH 7 with ammonia (NH_4OH). The total volume of the brown solution was controlled at 100 mL, fol-

lowed by being heated at 110 °C for 60 min with continuous stirring to remove water. Citric acid acted as a chelating agent during the dehydration process, so condensation and polymerization reactions occurred between citric acid and nitrate to chelate metal ions. Subsequently, the gel was formed and transferred to a high-temperature furnace for pre-calcination by self-propagating combustion in an air environment of 300 °C. The combustion duration was 20 min to remove the excess colloid of the gel and generate loose powders. After that, the obtained powder was ground with an agate grinder evenly and calcined under the air environment at different temperatures (500 °C, 600 °C, 700 °C, 800 °C) for 5 h. With further grinding uniformly, the $LaFe_xNi_{1-x}O_3$ perovskite oxides were prepared ultimately.

Photocatalysts characterization

The $LaFe_xNi_{1-x}O_3$ photocatalysts were characterized by D8 advance (Bruker, Germany) to reveal the X-ray powder diffraction (XRD) patterns. The Cu Kα target was facilitated under 40 kV to generate the X-ray with λ = 0.15406 nm. The 2θ diffracting angle was set from 10° to 70° with a scan rate of 4 °/min. The crystalline sizes of the $LaFe_xNi_{1-x}O_3$ perovskite oxides were further obtained by Scherrer's equation. To obtain the morphologies of the prepared samples, S-4800 (Hitachi, Japan) was employed to conduct field emission scanning electron microscopy (FESEM). The light absorption spectra of the perovskite oxides were inspected using V-670 (Jasco, Japan) to examine the UV–vis absorption capability with diffuse reflectance spectroscopy (DRS) from 200 to 800 nm. The nitrogen adsorption–desorption analyzer, ASAP 2020 PLUS (ASAP, USA), was applied to determine the specific surface area of the as-synthesized samples via the BET (Brunauer–Emmett–Teller) method. The calcination temperature of the perovskite oxides was determined via a Thermogravimetric Analyzer (SDT 2960, TA Instruments, USA).

Photocatalytic MB and tetracycline degradation

The photocatalytic activity of $LaFe_xNi_{1-x}O_3$ photocatalysts was examined by evaluating the performance of photocatalytic MB degradation. 300 W Xe-lamp equipped with AM 1.5G filter (Newport Corporation, USA) was used as the light source in the degradation experiment. The light intensity was adjusted to 100 mW/cm^2 calibrated with a light intensity meter Model 1919-R (Newport Corporation, USA). First, 150 mL of 20 ppm MB solution was prepared and transferred to a quartz reactor. Perovskite oxide photocatalysts with 30 mg, 50 mg, 80 mg, and 100 mg were placed into the reactor. Furthermore, different amounts of 50% H_2O_2 (5 μL, 10 μL, 20 μL, and 60 μL) were also transferred into the reactor via micropipettes. The pH of the reactor solution was adjusted to 1.5, 3.5, and 5.5 by adding hydrochloric acid. Then, the photocatalysts were deposited into the reactor with the magnet stirring at 600 rpm. Before light irradiation, the MB concentration reached adsorption–desorption equilibrium in 30 min in the dark, which was recorded (C_0). After that, the simulated AM 1.5G solar light was turned on, and the photocatalytic reaction occurred. The MB concentrations (C) were monitored every 15 min by sampling 5 mL of solution, then filtering the samples through a 0.22 μm needle filter. The MB concentrations were evaluated using the UV–vis spectrometer U-2910 (HITACHI, Japan). The detection range was set from 200 to 800 nm. The scanning rate was 400 nm/min. The maximum absorption peaks of MB and TC solution were at 664 nm and 356 nm, respectively.

Supporting Information

Figure S1: The nitrogen adsorption and desorption curves of the samples with different Fe/Ni synthesis ratios at pH 0. Figure S2: Pore size distribution of the samples with different Fe/Ni synthesis ratios. Figure S3: The FESEM images of $LaFe_xNi_{1-x}O_3$ prepared at pH 7 (at the magnification of 100,000×). Figure S4: (a) The C/C_0 and (b) the 1st order kinetic analysis of the photodegradation using $LaFe_{0.7}Ni_{0.3}O_3$ operating at different controlling conditions. Figure S5: (a) The C/C_0 and (b) 1st order kinetic analysis of the MB and TC photodegradation using $LaFe_{0.7}Ni_{0.3}O_3$ operating at the optimal condition. Table S1: The specific surface area, pore size, and pore volume for the samples with different Fe/Ni ratios. Table S2: The unit cell parameters and cell volume for the samples with different Fe/Ni ratios. Table S3: The detailed EDS information of various samples with different Fe/Ni ratios. Table S4: The comparison of photodegradation performance over various $LaFeO_3$-related samples.

Supporting Information File 1

Additional figures and tables.
[https://www.beilstein-journals.org/bjnano/content/supplementary/2190-4286-13-79-S1.pdf]

Funding

The authors would like to sincerely thank the Ministry of Science and Technology (MOST) in Taiwan for providing the funding under MOST 109-2221-E-992 -035 and MOST 110-2221-E-006 -217 -MY3.

ORCID® iDs

Chao-Wei Huang - https://orcid.org/0000-0002-1374-0556
Yu-Tang Lin - https://orcid.org/0000-0003-4644-8567
Van-Huy Nguyen - https://orcid.org/0000-0001-8556-1955

References

1. Otto, B.; Schleifer, L. *Domestic Water Use Grew 600% Over the Past 50 Years*. World Resources Institute, 2020; https://www.wri.org/insights/domestic-water-use-grew-600-over-past-50-years (accessed Aug 15, 2022).
2. Searchinger, T.; Waite, R.; Hanson, C.; Ranganathan, J.; Dumas, P.; Matthews, E. *Creating a Sustainable Food Future;* World Resources Institute, 2018. doi:10.1163/2210-7975_hrd-9927-20180005
3. Lin, Y.-T.; Wang, Y.-H.; Wu, J. C. S.; Wang, X. *Appl. Catal., B* **2021,** *281,* 119517. doi:10.1016/j.apcatb.2020.119517
4. Lin, Y.-T.; Huang, C.-W.; Wang, Y.-H.; Wu, J. C. S. *Top. Catal.* **2020,** *63,* 1240–1250. doi:10.1007/s11244-020-01263-6
5. Gatidou, G.; Kinyua, J.; van Nuijs, A. L. N.; Gracia-Lor, E.; Castiglioni, S.; Covaci, A.; Stasinakis, A. S. *Sci. Total Environ.* **2016,** *563–564,* 633–640. doi:10.1016/j.scitotenv.2016.04.130
6. Rott, U.; Minke, R. *Water Sci. Technol.* **1999,** *40,* 137–144. doi:10.2166/wst.1999.0030
7. Choudhary, S.; Silakari, O. Thiazine: A Versatile Heterocyclic Scaffold for Multifactorial Diseases. *Key Heterocycle Cores for Designing Multitargeting Molecules,* 1st ed.; Elsevier: Amsterdam, Netherlands, 2018; pp 247–284. doi:10.1016/b978-0-08-102083-8.00007-8
8. Zhang, Q.; Jiang, L.; Wang, J.; Zhu, Y.; Pu, Y.; Dai, W. *Appl. Catal., B* **2020,** *277,* 119122. doi:10.1016/j.apcatb.2020.119122
9. Shao, S.; Hu, Y.; Cheng, J.; Chen, Y. *Crit. Rev. Biotechnol.* **2018,** *38,* 1195–1208. doi:10.1080/07388551.2018.1471038
10. Jung, C.; Son, A.; Her, N.; Zoh, K.-D.; Cho, J.; Yoon, Y. *J. Ind. Eng. Chem. (Amsterdam, Neth.)* **2015,** *27,* 1–11. doi:10.1016/j.jiec.2014.12.035
11. Chu, K. H.; Al-Hamadani, Y. A. J.; Park, C. M.; Lee, G.; Jang, M.; Jang, A.; Her, N.; Son, A.; Yoon, Y. *Chem. Eng. J.* **2017,** *327,* 629–647. doi:10.1016/j.cej.2017.06.137
12. Monteil, H.; Pechaud, Y.; Oturan, N.; Trellu, C.; Oturan, M. A. *Chem. Eng. J.* **2021,** *404,* 127048. doi:10.1016/j.cej.2020.127048
13. Kumar, A.; Rana, A.; Sharma, G.; Naushad, M.; Dhiman, P.; Kumari, A.; Stadler, F. J. *J. Mol. Liq.* **2019,** *290,* 111177. doi:10.1016/j.molliq.2019.111177
14. Souza, F. S.; da Silva, V. V.; Rosin, C. K.; Hainzenreder, L.; Arenzon, A.; Féris, L. A. *Environ. Technol.* **2018,** *39,* 549–557. doi:10.1080/09593330.2017.1306116
15. Huang, C.-W.; Sin, W.-C.; Nguyen, V.-H.; Wu, Y.-C.; Chen, W.-Y.; Chien, A. C. *Top. Catal.* **2020,** *63,* 1121–1130. doi:10.1007/s11244-020-01322-y
16. Deng, Y. *Int. J. Environ. Waste Manage.* **2009,** *4,* 366–384. doi:10.1504/ijewm.2009.027402
17. Hakika, D. C.; Sarto, S.; Mindaryani, A.; Hidayat, M. *Catalysts* **2019,** *9,* 881. doi:10.3390/catal9110881
18. Fenton, H. J. H. *J. Chem. Soc., Trans.* **1894,** *65,* 899–910. doi:10.1039/ct8946500899
19. Bauer, R.; Waldner, G.; Fallmann, H.; Hager, S.; Klare, M.; Krutzler, T.; Malato, S.; Maletzky, P. *Catal. Today* **1999,** *53,* 131–144. doi:10.1016/s0920-5861(99)00108-x
20. Zhang, M.-h.; Dong, H.; Zhao, L.; Wang, D.-x.; Meng, D. *Sci. Total Environ.* **2019,** *670,* 110–121. doi:10.1016/j.scitotenv.2019.03.180
21. Do, H.-T.; Phan Thi, L.-A.; Dao Nguyen, N. H.; Huang, C.-W.; Le, Q. V.; Nguyen, V.-H. *J. Chem. Technol. Biotechnol.* **2020,** *95,* 2569–2578. doi:10.1002/jctb.6333
22. Huang, C.-W.; Wu, M.-C. *J. Chem. Technol. Biotechnol.* **2020,** *95,* 2715–2722. doi:10.1002/jctb.6392
23. Li, L.; Wang, X.; Zhang, Y. *Mater. Res. Bull.* **2014,** *50,* 18–22. doi:10.1016/j.materresbull.2013.10.027
24. Ye, Y.; Yang, H.; Wang, X.; Feng, W. *Mater. Sci. Semicond. Process.* **2018,** *82,* 14–24. doi:10.1016/j.mssp.2018.03.033
25. Wang, K.; Niu, H.; Chen, J.; Song, J.; Mao, C.; Zhang, S.; Gao, Y. *Appl. Surf. Sci.* **2017,** *404,* 138–145. doi:10.1016/j.apsusc.2017.01.223
26. Guan, S.; Yang, H.; Sun, X.; Xian, T. *Opt. Mater. (Amsterdam, Neth.)* **2020,** *100,* 109644. doi:10.1016/j.optmat.2019.109644
27. Ye, Y.; Yang, H.; Zhang, H.; Jiang, J. *Environ. Technol.* **2020,** *41,* 1486–1503. doi:10.1080/09593330.2018.1538261
28. Orak, C.; Atalay, S.; Ersöz, G. *Sep. Sci. Technol.* **2017,** *52,* 1310–1320. doi:10.1080/01496395.2017.1284866
29. Garcia-Muñoz, P.; Fresno, F.; Lefevre, C.; Robert, D.; Keller, N. *Catal. Sci. Technol.* **2020,** *10,* 1299–1310. doi:10.1039/c9cy02269d
30. Jauhar, S.; Dhiman, M.; Bansal, S.; Singhal, S. *J. Sol-Gel Sci. Technol.* **2015,** *75,* 124–133. doi:10.1007/s10971-015-3682-8
31. Phan, T. T. N.; Nikoloski, A. N.; Bahri, P. A.; Li, D. *J. Ind. Eng. Chem. (Amsterdam, Neth.)* **2018,** *61,* 53–64. doi:10.1016/j.jiec.2017.11.046
32. Pecchi, G.; Reyes, P.; Zamora, R.; Cadús, L. E.; Fierro, J. L. G. *J. Solid State Chem.* **2008,** *181,* 905–912. doi:10.1016/j.jssc.2008.01.020
33. Gallego, J.; Mondragon, F.; Batiot-Dupeyrat, C. *Appl. Catal., A* **2013,** *450,* 73–79. doi:10.1016/j.apcata.2012.10.022
34. Zheng, D.; Wei, G.; Xu, L.; Guo, Q.; Hu, J.; Sha, N.; Zhao, Z. *J. Photochem. Photobiol., A* **2019,** *377,* 182–189. doi:10.1016/j.jphotochem.2019.03.045
35. Provendier, H.; Petit, C.; Estournes, C.; Kiennemann, A. *Stud. Surf. Sci. Catal.* **1998,** *119,* 741–746. doi:10.1016/s0167-2991(98)80520-x
36. Provendier, H.; Petit, C.; Kiennemann, A. *C. R. Acad. Sci., Ser. IIc: Chim.* **2001,** *4,* 57–66. doi:10.1016/s1387-1609(00)01212-3
37. Jahangiri, A.; Aghabozorg, H.; Pahlavanzadeh, H. *Int. J. Hydrogen Energy* **2013,** *38,* 10407–10416. doi:10.1016/j.ijhydene.2013.05.080
38. Ghorai, K.; Panda, A.; Hossain, A.; Bhattacharjee, M.; Chakraborty, M.; Bhattacharya, S. K.; Show, B.; Sarkar, A.; Bera, P.; Kim, H.; Seikh, M. M.; Gayen, A. *J. Rare Earths* **2022,** *40,* 725–736. doi:10.1016/j.jre.2021.04.013
39. Iqbal, S.; Bibi, I.; Majid, F.; Kamal, S.; Alwadai, N.; Iqbal, M. *Opt. Mater. (Amsterdam, Neth.)* **2022,** *124,* 111962. doi:10.1016/j.optmat.2021.111962
40. ZHANG, L.-f.; WANG, Y.-p.; HUANG, Q.-w. *Trans. Nonferrous Met. Soc. China* **2009,** *19,* 1444–1449. doi:10.1016/s1003-6326(09)60048-0
41. Li, Y.; Yao, S.; Wen, W.; Xue, L.; Yan, Y. *J. Alloys Compd.* **2010,** *491,* 560–564. doi:10.1016/j.jallcom.2009.10.269
42. Monshi, A.; Foroughi, M. R.; Monshi, M. R. *World J. Nano Sci. Eng.* **2012,** *2,* 154–160. doi:10.4236/wjnse.2012.23020
43. Gong, S.; Xie, Z.; Li, W.; Wu, X.; Han, N.; Chen, Y. *Appl. Catal., B* **2019,** *241,* 578–587. doi:10.1016/j.apcatb.2018.09.041
44. Wiranwetchayan, O.; Promnopas, S.; Phadungdhitidhada, S.; Phuruangrat, A.; Thongtem, T.; Singjai, P.; Thongtem, S. *Ceram. Int.* **2019,** *45,* 4802–4809. doi:10.1016/j.ceramint.2018.11.175
45. Khan, A.; Hussain, R.; Toufiq, A. M.; Shah, A.; Khan, B. A.; Niaz, Z.; Rahman, S. u. *Mater. Charact.* **2020,** *169,* 110661. doi:10.1016/j.matchar.2020.110661
46. Chen, C.; Zhou, J.; Geng, J.; Bao, R.; Wang, Z.; Xia, J.; Li, H. *Appl. Surf. Sci.* **2020,** *503,* 144287. doi:10.1016/j.apsusc.2019.144287

47. Shi, J.; Chang, Y.; Tang, Y.; Wang, X.; Wang, X.; Zhang, X.; Cao, J. *Ceram. Int.* **2020,** *46,* 5315–5322. doi:10.1016/j.ceramint.2019.10.282
48. Mehdizadeh, P.; Amiri, O.; Rashki, S.; Salavati-Niasari, M.; Salimian, M.; Foong, L. K. *Ultrason. Sonochem.* **2020,** *61,* 104848. doi:10.1016/j.ultsonch.2019.104848
49. Hoseini, A.-A.; Farhadi, S.; Zabardasti, A.; Siadatnasab, F. *RSC Adv.* **2019,** *9,* 24489–24504. doi:10.1039/c9ra04265b
50. Pan, G.-T.; Chong, S.; Pan, K.-L.; Chang, M.-B.; Yang, T. C.-K.; Shukla, P. *Clean Technol. Environ. Policy* **2017,** *19,* 1557–1565. doi:10.1007/s10098-016-1319-4
51. Walling, C. *Acc. Chem. Res.* **1975,** *8,* 125–131. doi:10.1021/ar50088a003
52. Yao, Y.; Chen, H.; Lian, C.; Wei, F.; Zhang, D.; Wu, G.; Chen, B.; Wang, S. *J. Hazard. Mater.* **2016,** *314,* 129–139. doi:10.1016/j.jhazmat.2016.03.089
53. Strlič, M.; Kolar, J.; Šelih, V.-S.; Kočar, D.; Pihlar, B. *Acta Chim. Slov.* **2003,** *50,* 619–632.
54. Taran, O. P.; Ayusheev, A. B.; Ogorodnikova, O. L.; Prosvirin, I. P.; Isupova, L. A.; Parmon, V. N. *Appl. Catal., B* **2016,** *180,* 86–93. doi:10.1016/j.apcatb.2015.05.055
55. Wang, S. *Dyes Pigm.* **2008,** *76,* 714–720. doi:10.1016/j.dyepig.2007.01.012
56. Zong, X.; Wu, G.; Yan, H.; Ma, G.; Shi, J.; Wen, F.; Wang, L.; Li, C. *J. Phys. Chem. C* **2010,** *114,* 1963–1968. doi:10.1021/jp904350e
57. Yu, X.; He, J.; Zhang, Y.; Hu, J.; Chen, F.; Wang, Y.; He, G.; Liu, J.; He, Q. *J. Alloys Compd.* **2019,** *806,* 451–463. doi:10.1016/j.jallcom.2019.07.233

License and Terms

BEILSTEIN JOURNAL OF NANOTECHNOLOGY

Green synthesis of zinc oxide nanoparticles toward highly efficient photocatalysis and antibacterial application

Vo Thi Thu Nhu*[1], Nguyen Duy Dat[1], Le-Minh Tam[1] and Nguyen Hoang Phuong[2]

Full Research Paper

Open Access

Address:
[1]Faculty of Chemical & Food Technology, Ho Chi Minh City University of Technology and Education, 1 Vo Van Ngan, Thu Duc City, Ho Chi Minh City, Vietnam and [2]HUTECH University, 475A Dien Bien Phu Street, Binh Thanh District, Ho Chi Minh City, Vietnam

Email:
Vo Thi Thu Nhu* - nhuvtt@hcmute.edu.vn

* Corresponding author

Keywords:
green synthesis; methylene blue; methyl orange; rosin; ZnO nanoparticles

Beilstein J. Nanotechnol. **2022,** *13,* 1108–1119.
https://doi.org/10.3762/bjnano.13.94

Received: 08 June 2022
Accepted: 15 September 2022
Published: 07 October 2022

This article is part of the thematic issue "Nanomaterials for photocatalysis and applications in environmental remediation and renewable energy".

Guest Editor: V. V. Pham

Abstract

Zinc oxide nanoparticles (ZnO NPs) were successfully synthesized by a green method using rosin and zinc chloride as salt precursors. The phase structure, morphology, and particle size of ZnO were determined by X-ray powder diffraction, field emission scanning electron microscopy, and high-resolution transmission electron microscopy. The fabricated ZnO NP samples are crystalline with a grain size of 30–100 nm. The ZnO NPs were used as catalysts for the photodegradation of methylene blue (MB) and methyl orange (MO) under visible and UV light. The results indicate that the prepared ZnO material excellently removed MB and MO ($c_{initial}$ = 10 mg/L) with efficiencies of 100% and 82.78%, respectively, after 210 min under UV radiation with a ZnO NP dose of 2 g/L. The photocatalyst activity of the synthesized material was also tested under visible light radiation with the same conditions; however, it achieved lower efficiencies. In addition, ZnO NPs were also tested regarding their antibacterial activity, and the results showed that the prepared ZnO samples had the highest (i.e., 100%) antibacterial efficiency against *E. coli*.

Introduction

Currently, industrial development has generated a large number of pollutants which are released into the environment. The textile industry is one of the sources of organic pollution which is harmful to the environment and humans. Various technologies have been proposed to remove organic pollutants from water, including coagulation coupled with sedimentation, biological processes, membrane filtration, adsorption, advanced oxidation, catalysis, and photocatalysis [1-3]. Using semiconductors as photocatalysts has been a widely studied approach for the complete removal of organic pollutants due to their advantages. Semiconductors can act as catalysts for the complete degradation of organic substances when excited by light with an energy value higher than their bandgap. Among many semiconductors, TiO_2 and ZnO are widely used as photocatalysts. ZnO has a higher quantum efficiency than that of TiO_2 since it absorbs more energy in the UV region [4-7]. Further-

more, ZnO is a low-cost photocatalyst with high photocatalytic activity, nontoxicity, light sensitivity, and stability [8-10]. The photodegradation of organic substances by the use of ZnO catalysts occurs when ZnO is illuminated by light. When excited by light with an energy greater than the bandgap of ZnO, electrons from the valence band (VB) are excited to the conduction band (CB) to form photogenerated electrons in the CB and photogenerated holes in the VB [11,12]. These photogenerated electrons and holes migrate to the surface of ZnO to react with H_2O and O_2 to generate $O_2^{\bullet-}$ and $^{\bullet}OH$ radicals, which oxidize organic substances. In addition, ZnO nanoparticles (NPs) have high antibacterial activity against bacteria, high biocompatibility, and are nontoxic to human cells [12,13]. Many studies have proven the antibacterial effect of ZnO [14,15] and also that nanoscale ZnO has a more effective antibacterial activity than that of large ZnO [12,16].

Various approaches for synthesizing nanosized materials have been investigated. Among these approaches, chemical and physical routes have their own disadvantages, such as adverse environmental effects due to the use of environmentally unfriendly chemicals or to the release of heat into the environment [17]. Therefore, the development of green approaches is necessary. The biosynthetic process using plant extracts as an alternative route is a promising method for synthesizing nanomaterials due to its rapid, low-cost protocol, and safety to the environment [18]. Numerous studies applied green methods for the synthesis of ZnO nanoparticles from plants, fruits, plant extracts, and seaweeds [19-22]. Rafaie et al. [23] used *Citrus aurantifolia* extracts to synthesize ZnO NPs with a size range of 50–200 nm. Sangeetha et al. and Gunalan et al. used *Aloe vera* leaves as a precursor to synthesize ZnO with a size range of 25–45 nm [24,25]. Many studies have synthesized nanosized ZnO for antibacterial and photocatalyst applications. Nava et al. [26] prepared ZnO NPs using *Camellia sinensis* extracts and applied ZnO NPs to degrade methylene blue (MB). Ambika et al. [12] synthesized ZnO by a green method using a precursor from the *Vitex negundo* plant extract and zinc nitrate, and antimicrobial properties of ZnO NPs were demonstrated against *E. coli* and *S. aureus* bacteria.

As mentioned previously, plant extracts were used as common precursors for nanomaterial synthesis due to their relatively high levels of the steroids, saponins, carbohydrates, and flavonoids which act as reducing agents and phytoconstituents as capping agents, providing stability to the nanoparticles [27]. Rosin is also a plant-derived material containing different resin acids, especially abietic acid and pimaric acid with a general chemical formula of $C_{20}H_{30}O_2$ ($C_{19}H_{29}COOH$) [28]. It is the inexpensive and eco-friendly solid byproduct obtained after refining turpentine from *Pinus latteri* trees to produce turpentine oil, which is usually used as a precursor for many industrial applications such as paints, inks, adhesives, soap, and glue production [28]. Obviously, there is a high potential of using rosin as a green precursor for nanomaterial synthesis. Lack of information regarding this application has been reported. This is the motivation for this study which is focused on synthesizing nanosized ZnO materials by the sol–gel method using rosin as a green precursor. ZnO NPs were synthesized by a sol–gel two-step method from the green precursor rosin and zinc chloride salt. The antibacterial activity of the synthesized ZnO material against *Escherichia coli* (*E. coli*) was studied. In addition, the study also determined the ability of ZnO NPs to act as photocatalysts and to degrade dyes including MB and methyl orange (MO).

Experimental Design

Materials

Rosin was purchased from a Vietnamese company (Loc Thien Investment development Co., Ltd.), which was produced by distilling turpentine from *Pinus latteri* trees in Vietnam. The rosin used in this study is a clear, hard, brittle solid, which is light yellow to pink in color. Zinc chloride ($ZnCl_2$) and sodium hydroxide (NaOH) were provided by Xilong Scientific Co., Ltd. Methylene blue and methyl orange were purchased from Merck Co., Ltd. Nutrients and agar powder were provided by Titan Co., Ltd. All reagents were of analytical grade. $ZnCl_2$ and NaOH were diluted in DI water with low conductivity (0.06 μS/cm). *Escherichia coli* (*E. coli* VTCC-B-482) was used for the antibacterial experiments and purchased from the Hanoi National University.

Preparation of zinc oxide nanoparticles by green syntheses

The ZnO NPs were synthesized by two steps. Firstly, the saponification reaction of rosin was performed using NaOH to create sodium resinate, and zinc resinate was subsequently synthesized from sodium resinate. Rosin (4 g) was dissolved in 24 mL of 0.5 N NaOH at 90 °C under magnetic stirring for 90 min. Then, 40 mL of $ZnCl_2$ (10%) was added to the mixture which was stirred for 60 min to form zinc resinate. The suspension containing zinc resinate was then filtered and washed with hot distilled water to remove impurities. The zinc resinate was then calcined in a furnace with an increasing temperature rate of 5 °C/min to 600 °C and held for 30 min to obtain pure ZnO nanoparticle powder. The relevant reactions that form zinc resinate are shown in Equation 1 and Equation 2. The schematic illustration of the synthesis of ZnO nanoparticles is shown in Figure 1.

$$C_{19}H_{29}COOH + NaOH \rightarrow C_{19}H_{29}COONa + H_2O \quad (1)$$

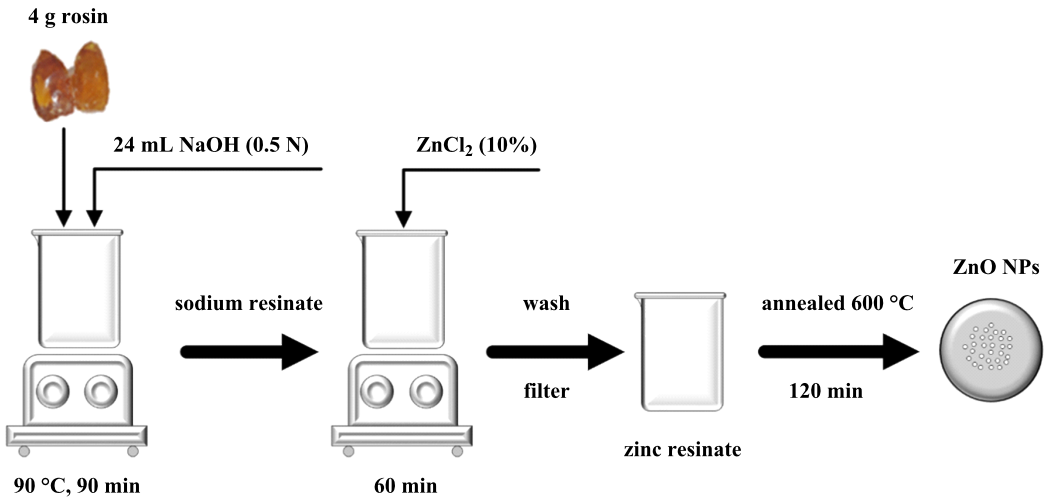

Figure 1: Schematic illustration of the synthesis of ZnO nanoparticles.

$$2C_{19}H_{29}COONa + ZnCl_2 \rightarrow (C_{19}H_{29}COO)_2\,Zn + 2NaCl \quad (2)$$

Methods for determining the characterization of the synthesized material

The phase of the synthesized material was determined by X-ray diffraction (XRD) using a Bruker D8 advanced X-ray diffractometer equipped with Cu Kα radiation (λ = 1.5418 Å). The morphology and size of the synthesized material were determined by field emission scanning electron microscopy (FESEM) on a Hitachi S-4800 at 15 kV and high-resolution transmission electron microscopy (HR-TEM) on a JEOL JEM-2100. The thermal decomposition of zinc resinate to form ZnO NPs were studied by thermal gravimetric analysis (TGA) and differential thermal analysis (DTA) curves using thermal gravimetric analysis (DSC131, LABSYS TG/DSC1600, TMv), by heating up to 1000 °C at a heating rate of 10 °C/min. The zeta potential was measured by analyzing 0.1 g of ZnO in 10 mL of water using a Malvern ZetasizerPro. The solid UV–vis DRS was carried out using a JASCO V550 UV–vis spectrometer.

Photocatalytic degradation reaction

The photocatalytic degradation of a dye solution under visible and UV light using green-synthesized ZnO nanoparticles from rosin and zinc chloride salt was investigated using a batch photocatalytic reactor. Firstly, 0.1 g of ZnO NPs was added to 50 mL of MO or MB solution with an initial concentration of 10 mg/L. The solution was then submitted to magnetic stirring in the dark for 30 min to equilibrate the adsorption. Subsequently, the suspensions were illuminated by a 30 W LED or an 18 W high-pressure mercury lamp. The light source was fixed at a distance of 20 cm from the surface of the reactor. After fixed illumination times, 5 mL was withdrawn and centrifuged at 6000 rpm to measure the dye concentrations. The dye concentration was analyzed by UV–vis spectroscopy (Hitachi U2900) with maximum adsorption wavelengths of MB and MO of 664 nm and 464 nm, respectively [29,30]. The degradation efficiency was calculated using Equation 3.

$$\text{degradation efficiency (\%)} = \frac{c_0 - c_t}{c_0} \times 100\%, \quad (3)$$

where c_0 is the initial dye concentration and c_t is the dye concentration at a given reaction time.

Determination of the antibacterial efficiency against *E. coli*

The experiment was conducted using three different concentrations of ZnO NPs (1, 5, and 10 mg/mL) and two concentrations of *E. coli* ($5{\cdot}10^4$ and $5{\cdot}10^5$ CFU/mL). After adding ZnO NPs into the solutions containing *E. coli*, the suspensions were stirred. Samples were taken out at different contact times of 1, 3, and 6 h to evaluate the influence of time on the antibacterial efficiency. The solution was obtained after being diluted to decimal concentrations of 1/10, 1/100, and so forth. After that, 100 µL of the solution containing *E. coli* was taken using a micropipette and spread on a plate containing the *E. coli* culture medium (consisting of 2.6 g of nutrient broth and 2 g of agar in 200 mL of distilled water). The plate was incubated at 37 °C for 24 h to determine the amount of *E. coli* that survived (i.e., by counting colonies). Each experiment was repeated three times. The *E. coli* inhibition percentage was calculated via Equation 4:

$$E.\,coli \text{ inhibition percentage (\%)} = \frac{c_0 - c_i}{c_0} \times 100\%, \quad (4)$$

where c_0 is the initial number of *E. coli* cells and c_i is the average number of *E. coli* cells/plate.

Results and Discussion

Characteristics of synthesized ZnO NPs

Figure 2 shows the results of DTA/TG analysis of zinc resinate. The TGA curve at a temperature range between 30–300 °C shows an exothermic peak at 172.93 °C and a weight loss of 7%, which corresponds to dehydration of physically adsorbed water. At temperatures between 300–510 °C on the TG curve, a mass decrease of 61% was observed, whereas on the DTA curve, the exothermic peak at 420.62 °C corresponds to the decomposition of an organic compound. Finally, at temperatures in the range of 520–800 °C, the weight loss was found to be 32%. The DTA curve indicated an exothermic peak at 570.54 °C, revealing that the decomposition of organic compounds continues and the oxidation of Zn to form the ZnO crystalline phase occurs completely. From there, the organic matter in the zinc resinate begins to decompose at 300 °C. At a temperature of about 600 °C, the organic matter is almost completely decomposed and only the zinc metal is oxidized to form zinc oxide.

The XRD diagram of ZnO samples (Figure 3) shows diffraction peaks located at 2θ = 31.81°; 34.44°, 36.26°, 47.57°, 56.64°, 62.88°, 66.41°, 67.96°, 69.12°, 72.72°, 77.01° corresponding to the crystal planes (100), (002), (101), (102), (110), (103), (200), (112), (201), (004), (202) which characterize the ZnO wurtzite hexagonal structure (JCPDS card no 36-1451). In addition, there are no characteristic peaks of other crystals. The XRD results are consistent with the results of the DTA mentioned above. Sodium resinate was formed from rosin and sodium hydroxide as shown in Equation 1. Then, the exchange reaction between sodium resinate and zinc salt to produce zinc resinate was conducted as shown in Equation 2. The obtained zinc resinate is heated at 600 °C to be completely decomposed and zinc is oxidized by oxygen to form the ZnO crystalline phase. The ZnO crystal size presented in Table 1 (14–22 nm) was obtained from the XRD spectrum using the Debye–Scherer formula (i.e., Equation 5):

$$L = \frac{k\lambda}{\beta \cos\theta}, \tag{5}$$

where L is the ZnO crystal size (nm), k = 0.9, λ = 0.15418 nm [30], θ is the Bragg angle, and β is the full width at half maximum (FWHM).

The morphology and size of ZnO NPs were illustrated using FESEM and HRTEM. The FESEM image shown in Figure 4 indicates that ZnO NPs have a relatively homogeneous size. The HR-TEM results and particle size distributions obtained from the HR-TEM images are shown in Figure 5. The HR-TEM images in Figure 5a and Figure 5b show the interplanar spacing of 0.251 ± 0.003 nm corresponding to the (101) crystal plane of ZnO. The size of ZnO NPs is in the range of 30–100 nm

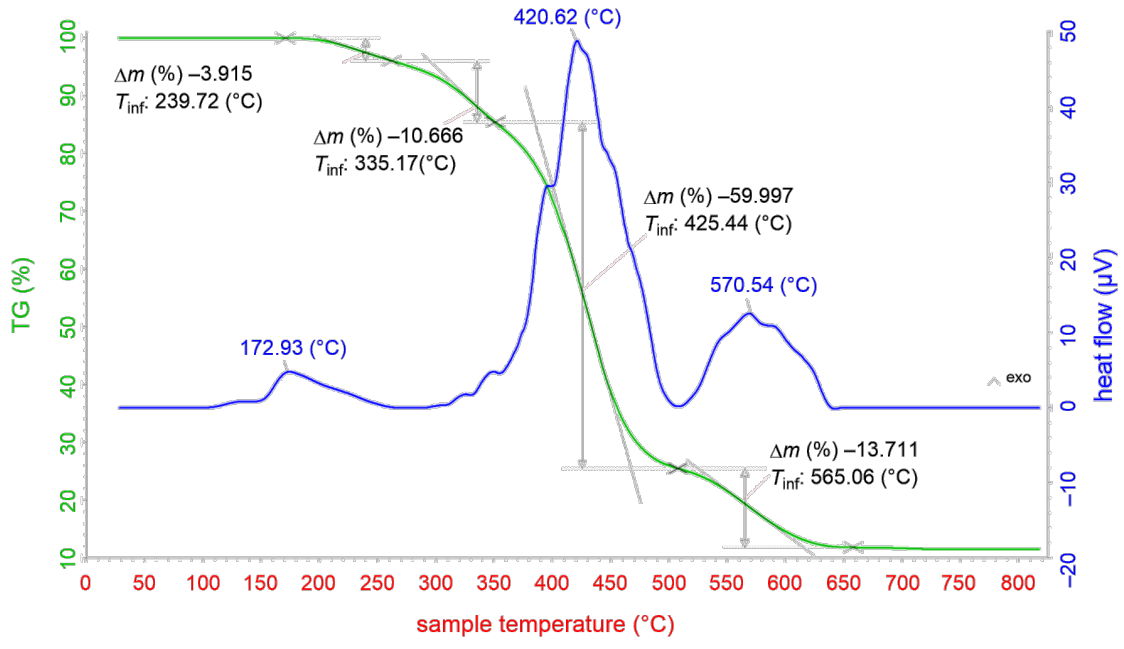

Figure 2: DTA/TG diagram of the zinc resinate sample.

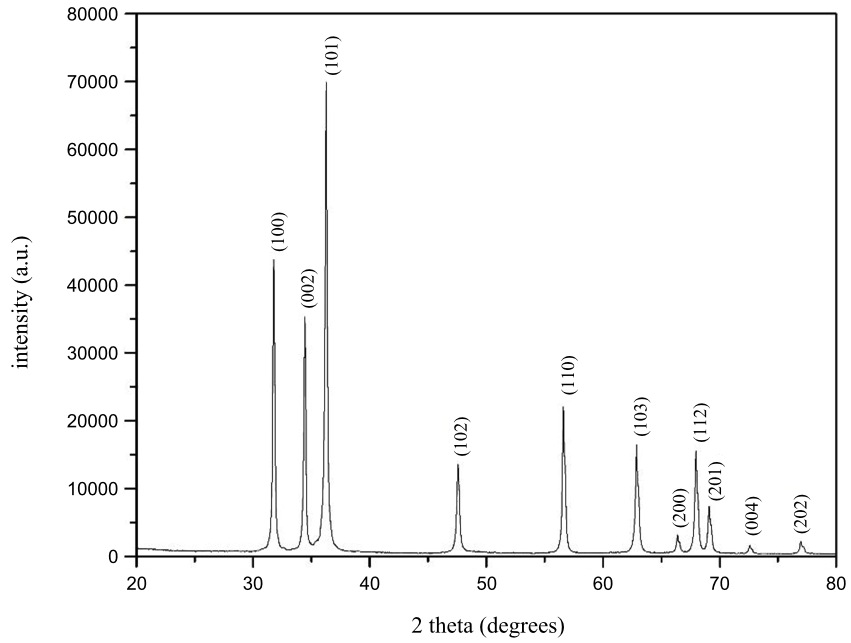

Figure 3: XRD diagram of ZnO NPs.

Table 1: Crystal size of ZnO determined from the Debye–Scherer formula.

Crystal plane	2θ	FWHM (b)	B (rad)	*L* (nm)
(100)	31.81	0.437	0.0076	21.38
(002)	34.44	0.385	0.0067	21.60
(101)	36.26	0.437	0.0076	19.13
(102)	47.57	0.613	0.0107	14.16
(110)	56.64	0.642	0.0112	14.06
(103)	62.88	0.689	0.0120	13.51
(112)	67.96	0.611	0.0110	15.68
(201)	69.12	0.556	0.0097	17.35

(Figure 5c and Figure 5d) and the average size of ZnO NPs from the distribution graph (Figure 5e) was about 60 nm in diameter. Furthermore, the results are in line with those reported by other studies. Stan et al. [31] used plant extracts (garlic, onion, and parsley) to synthesize ZnO NPs and made ZnO NPs of 20–70 nm in size. Hassan et al. [32] synthesized ZnO using *Coriandrum sativum* leaf extract and zinc acetate dihydrate and synthesized ZnO NPs with sizes in the range of 9–18 nm.

UV–vis DRS spectra of ZnO were shown in Figure 6a. ZnO absorbs light in the ultraviolet region. The bandgap energy of synthesized ZnO was determined by extrapolation of the linear part of the curve $(\alpha \cdot h\nu)^2$ as a function of photon energy

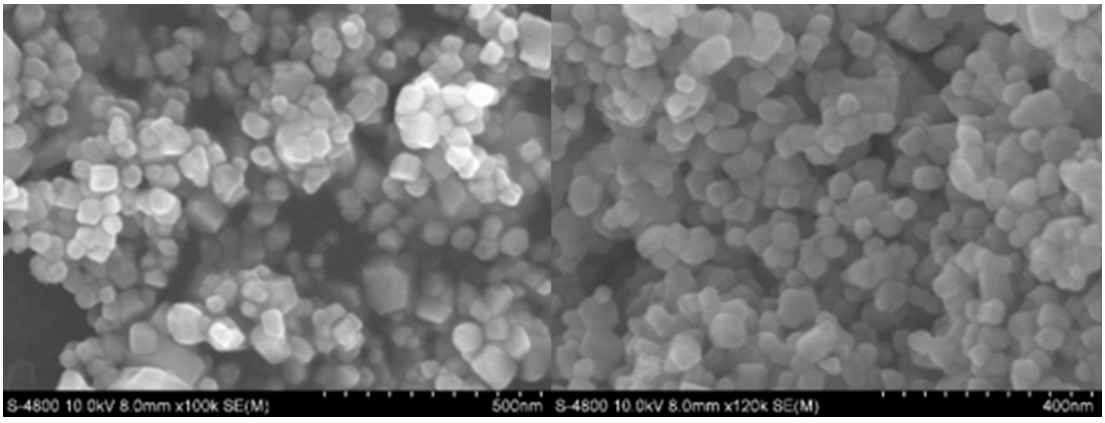

Figure 4: FESEM image of synthesized ZnO NPs.

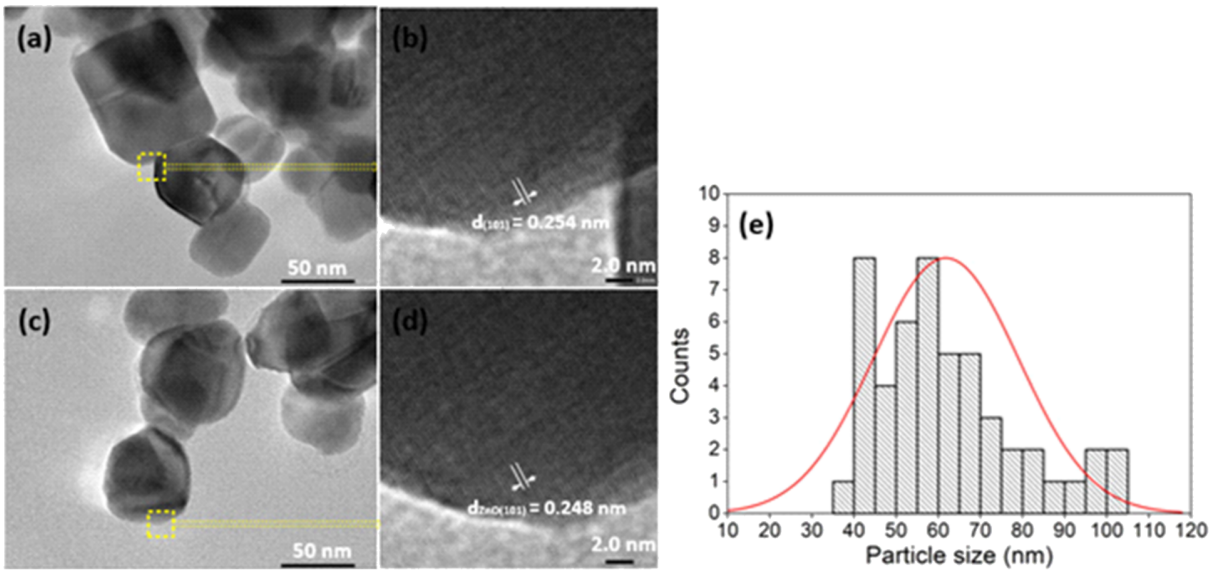

Figure 5: HR-TEM images of synthesized ZnO NPs.

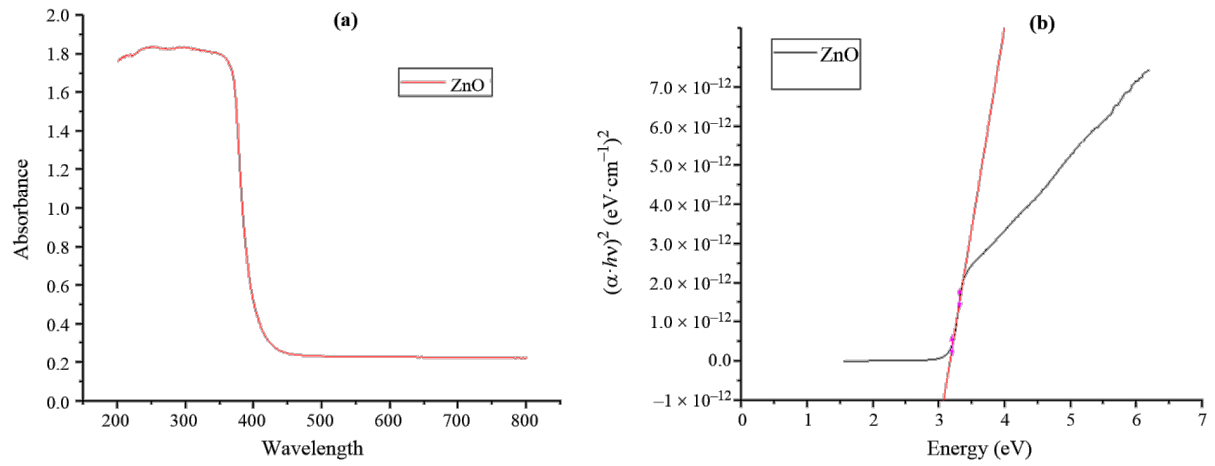

Figure 6: UV–vis DRS spectra (a) and plot of $(\alpha \cdot h\nu)^2$ as a function of photon energy for ZnO NPs (b).

(Figure 6b). The bandgap energy of synthesized ZnO was 3.15 eV, which is close to the bandgap value of 3.2 eV of ZnO shown in a previous report [33]. The zeta potential value displays the surface charge and stability of ZnO NPs. In this study, the zeta potential of ZnO NPs was −19 mV (Figure 7), indicating that ZnO NPs are negatively charged and stable in aqueous solution.

Photocatalytic degradation of dyes

The photocatalytic degradation of ZnO NPs was evaluated through the degradation of methylene blue and methyl orange under visible and UV light and the degradation efficiency was calculated via Equation 3. Figure 8 shows the degradation absorption spectra of MO and MB by synthesized ZnO under visible and UV light for different time intervals. The intensity of the peak decreased with increasing irradiation time. The results in Figure 9 show that the degradation efficiency of MB and MO solutions under UV light was higher than that under visible light. The degradation of MB (10 mg/L) under visible and UV light by ZnO NPs was 50.46% and 100%, respectively, after 210 min of irradiation. The degradation efficiency of MO (10 mg/L) by ZnO was lower than that of MB (10 mg/L). After 210 min of irradiation by visible and UV light, the MO degradation efficiency by ZnO NPs reached 33.56 and 82.78%, respec-

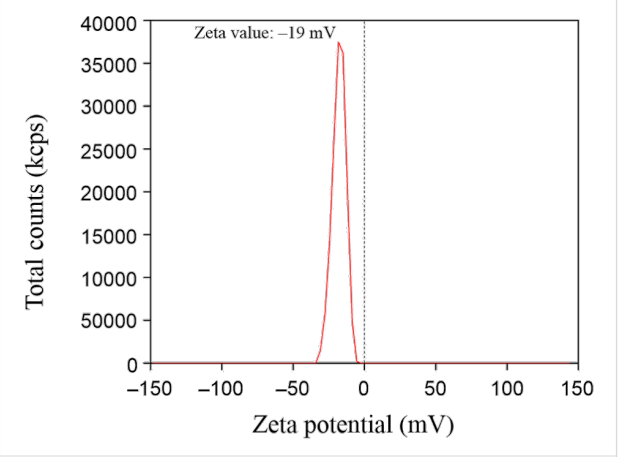

Figure 7: Zeta potential of synthesized ZnO NPs.

tively. ZnO has a rather high bandgap energy; therefore, the degradation efficiency of organic substances under visible light is not as high as that under UV light. Maddu et al. [34] studied the preparation of ZnO NPs with a size of 30 nm. The degradation efficiency of MB (5 mg/L) after 150 min of irradiation by visible and UV light was 40 and 80%, respectively, while synthesized ZnO NPs in this study can degrade more than 90% of MB (10 mg/L) under UV light after 150 min.

Antibacterial performance of synthesized ZnO NPs

The experimental results on antibacterial performance of synthesized materials are presented in Table 2, the *E. coli* inhibition percentage was calculated via Equation 4. Figure 10a shows the results of inhibition efficiency of *E. coli* at an initial concentration of $5{\cdot}10^4$ CFU/mL by ZnO NPs with ZnO NPs doses of 1, 5, and 10 mg/mL and contact time intervals of 1, 3, and 6 h. The ZnO NP concentration of 1 mg/mL is not enough to inhibit all *E. coli* bacteria after 6 h of treatment. By increasing the concentration of ZnO NPs to 5 mg/mL at contact times of 3 and 6 h, the inhibitory efficiency reached 99.83 and 100%, respectively. When the dose of the photocatalyst increased to 10 mg/mL, the *E. coli* inhibition efficiency reached 99.35% with a contact time of 1 h and the efficiency was 100% when

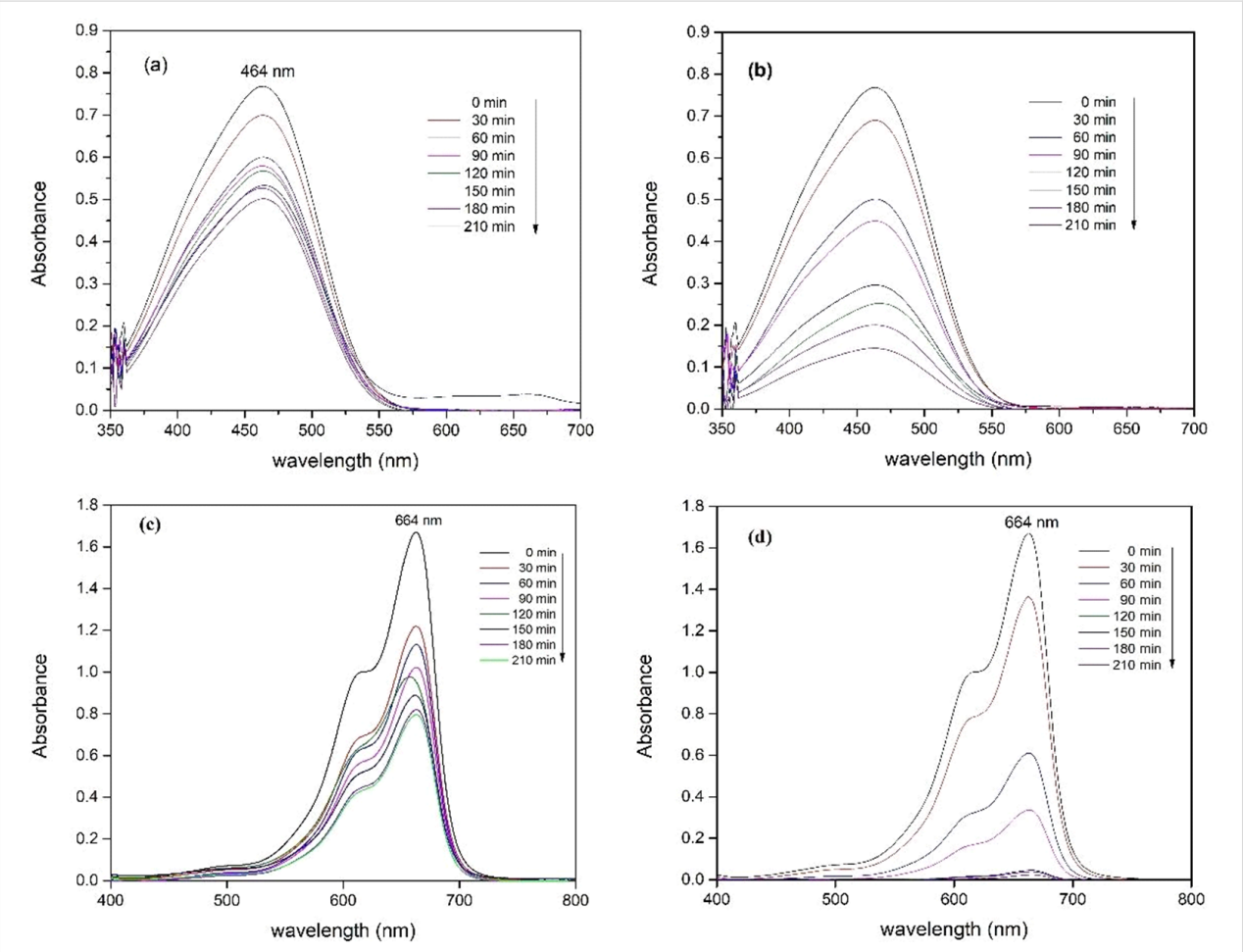

Figure 8: UV–vis spectra of degradation of MO (a, b) and MB (c, d) under visible and UV light.

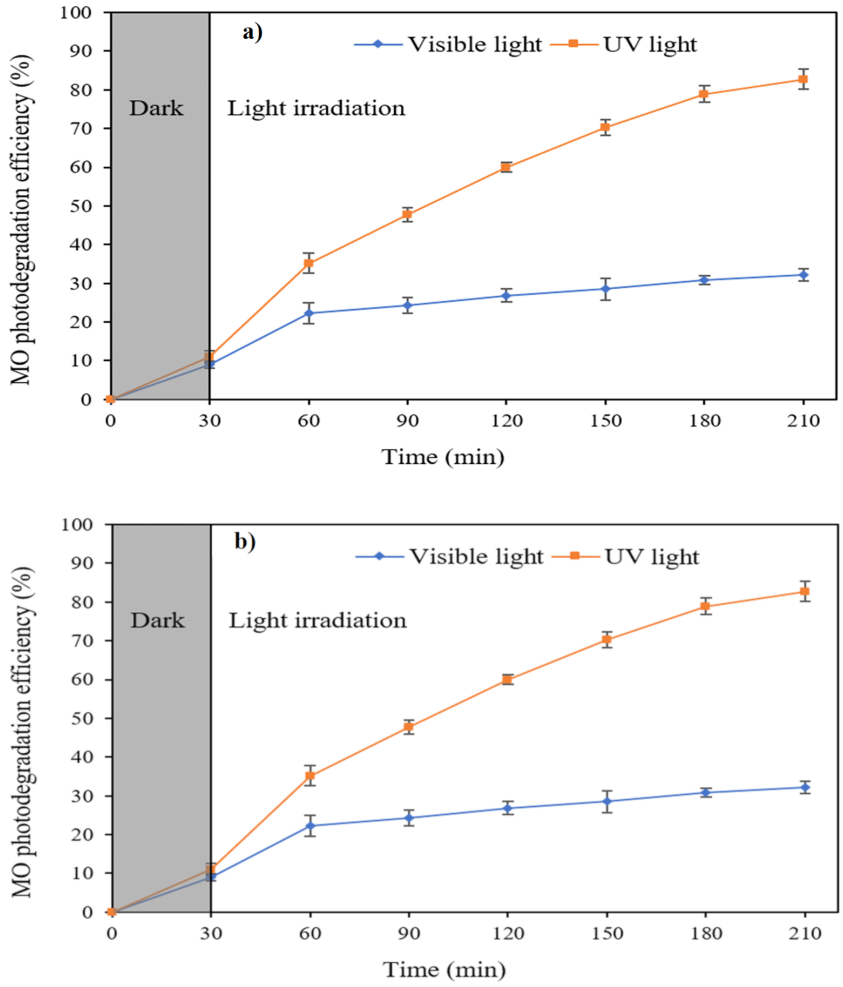

Figure 9: Photodegradation efficiency of MO (a) and MB (b) under visible and UV light.

the contact time was 3 h. The results of *E. coli* bacteria inhibition by ZnO NPs synthesized by the green method when the initial concentration of *E. coli* is increased to $5{\cdot}10^5$ were shown in Figure 10b. When the concentration of ZnO was 1, 5, and 10 mg/mL, the inhibitory efficiency on *E. coli* for 1 h was lower than that on *E. coli* at a concentration of $5{\cdot}10^4$ CFU/mL. When increasing the ZnO NP concentration to 5 mg/mL, the *E. coli* inhibition efficiency reached 99.96% in 6 h and the *E. coli* inhibition efficiency reached 100% when the ZnO NPs dose was increased to 10 mg/mL with a contact time of 6 h.

Proposed mechanism of photocatalytic dye degradation and antibacterial activity against *E. coli* by ZnO NPs

The mechanism of photocatalytic degradation and *E. coli* antibacterial activity by ZnO NPs is illustrated in Figure 11. When ZnO is irradiated with visible or UV light whose energy is equal or greater than the bandgap of ZnO, the electrons from the VB of ZnO NPs are excited to the CB generating holes in VB and electrons in CB. The electrons reduce the oxygen absorbed on the ZnO surface to form $^{\bullet}O_2^-$. These $^{\bullet}O_2^-$ species continue reacting with H_2O to form H_2O_2 and $^{\bullet}OH$. The hole in VB will react with H_2O to produce $^{\bullet}OH$ radicals. These $^{\bullet}OH$ radicals are strong oxidizing radicals and are mainly present in solution which can degraded dyes. These radicals can attract MO and MB molecules, oxidize the dye molecules to degradation products, and finally completely degrade the dyes to CO_2 and H_2O [35,36].

$$H_2O + ZnO\,(h^+_{VB}) \rightarrow ZnO + {}^{\bullet}OH \quad (6)$$

$$O_2 + Zn\,(e^-_{CB}) \rightarrow {}^{\bullet}O_2^- \quad (7)$$

Table 2: Photographs of *E. coli* bacterial culture plates formed after *E. coli* plates were exposed to ZnO NPs at different times.

Content of ZnO NPs	*E. coli* initial concentration: $5{\cdot}10^5$ CFU/mL			*E. coli* initial concentration: $5{\cdot}10^4$ CFU/mL		
	1 h	3 h	6 h	1 h	3 h	6 h
10 mg/mL ZnO	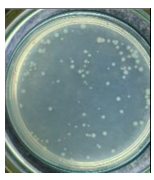	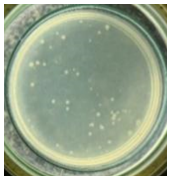		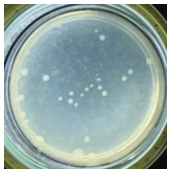	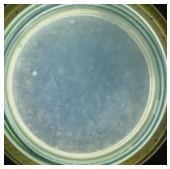	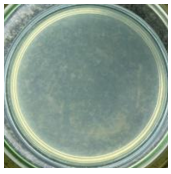
5 mg/mL ZnO	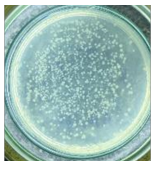	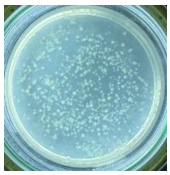	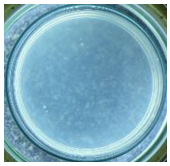		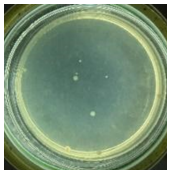	
1 mg/mL ZnO		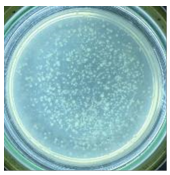		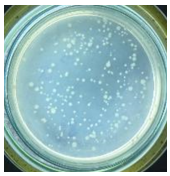	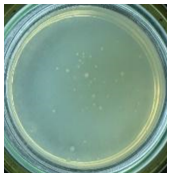	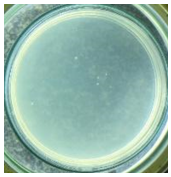

$$^{\bullet}O_2^- + H_2O \rightarrow HO_2^{\bullet} + OH^- \quad (8)$$

$$HO_2^{\bullet} + HO_2^{\bullet} \rightarrow H_2O_2 + O_2 \quad (9)$$

$$^{\bullet}O_2^- + H_2O_2 \rightarrow HO^- + O_2 + {}^{\bullet}OH \quad (10)$$

In addition, when ZnO NPs get in contact with *E. coli*, reactive oxygen species (ROS), such as $^{\bullet}OH$, $^{\bullet}O_2^-$, O_2 formed on the surface of ZnO NPs, will break bacterial cell membranes and enter the cells destroying organelles and ultimately inhibiting and shutting off bacteria metabolism [37,38]. The $^{\bullet}OH$ radical is the most active oxidant which rapidly reacts with bacterial nucleic acids, lipids, proteins, DNA, and amino acids [39-41]. The O_2 causes biomembrane oxidation reactions, damaging tissues [42]. Furthermore, it is reasonable to explain that the additional toxicity that causes bacterial death is due to the fact that zinc solubilization releases Zn^{2+} ions which can infiltrate into bacterial cell membranes, inhibiting amino acid metabolism and disrupting the bacterial cell enzymatic system [43-45].

Conclusion

ZnO nanoparticles were synthesized by a green method using rosin extracted from *Pinus latteri* trees in Vietnam. The XRD diagram of synthesized ZnO showed that ZnO has the hexagonal wurtzite structure form. The HR-TEM image showed the interplanar spacing of 0.251 ± 0.003 nm corresponding to the (101) crystal plane of ZnO, and the size of ZnO NPs is in the range of 30–100 nm. The bandgap energy of synthesized ZnO was 3.15 eV. Synthesized ZnO NPs showed high photocatalytic activity in dye degradation (methylene blue and methyl orange). The photodegradation efficiency of a dye solution by ZnO NPs under UV is greater than that under visible light. ZnO NPs completely degraded a MB solution of 10 mg/L for 210 min under ultraviolet light while the MB degradation efficiency achieved 50.46% under visible light. After 210 min of irradiation, the degradation efficiency values of a MO solution of 10 mg/L under visible and UV light by ZnO NPs were 33.56% and 82.78%, respectively. Furthermore, the synthesized ZnO NPs exhibited high efficiency against *E. coli* Gram-negative bacteria. The *E. coli* bacteria with concentrations of 10^5 and 10^4 CFU/mL was almost completely destroyed after 6 h by ZnO with concentrations of 1, 5, and 10 mg/mL.

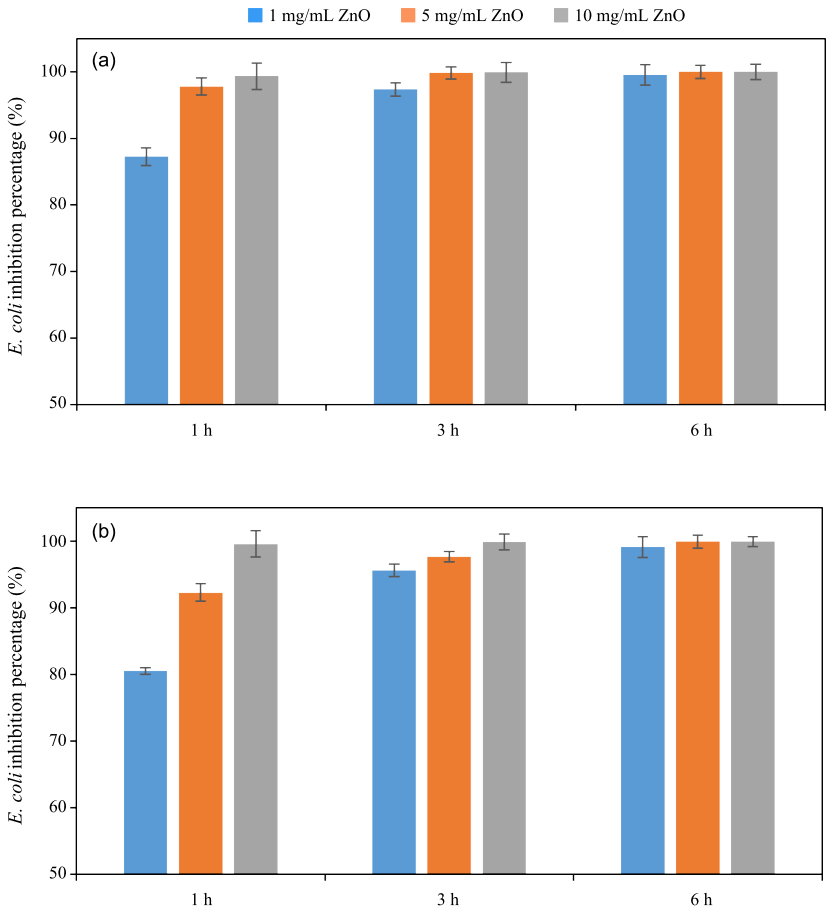

Figure 10: *E. coli* inhibition percentage by ZnO with different amounts of ZnO in various contact time intervals, with *E. Coli* initial concentrations of $5{\cdot}10^4$ CFU/mL (a) and $5{\cdot}10^5$ CFU/mL (b).

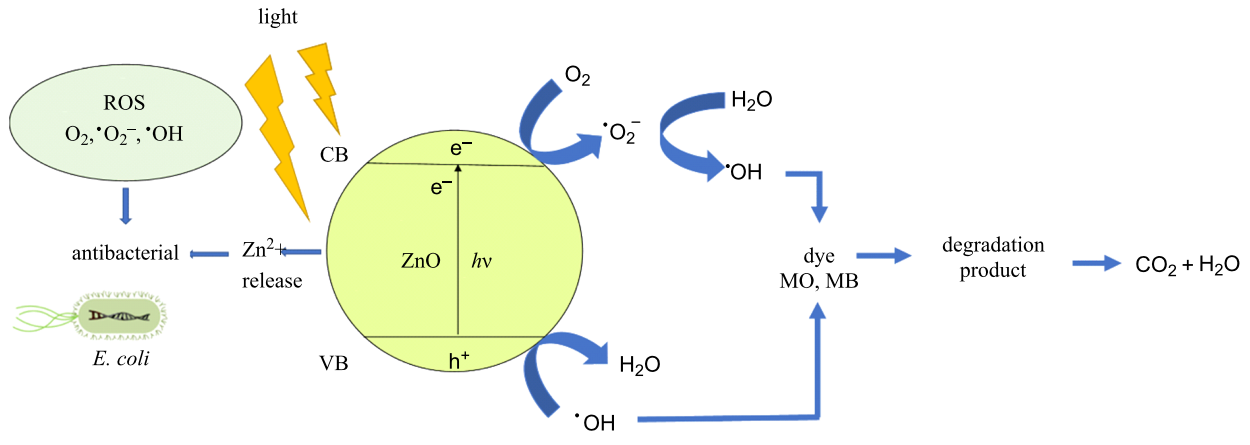

Figure 11: Proposed mechanism of photocatalytic dye degradation and antibacterial activity against *E. Coli* by synthesized ZnO NPs.

Acknowledgements

The authors gratefully acknowledge the Ministry of Education and Training and the Ho Chi Minh City University of Technology and Education for the support regarding instrument and apparatus for doing experiments.

Funding

This work belongs to the project grant No: B2021-SPK-01- HH funded by the Ministry of Education and Training, and hosted by the Ho Chi Minh City University of Technology and Education, Vietnam.

ORCID® iDs

Nguyen Duy Dat - https://orcid.org/0000-0001-5965-2060

References

1. Tijani, J. O.; Fatoba, O. O.; Madzivire, G.; Petrik, L. F. *Water, Air, Soil Pollut.* **2014,** *225,* 2102. doi:10.1007/s11270-014-2102-y
2. Tran, H. N.; Tomul, F.; Thi Hoang Ha, N.; Nguyen, D. T.; Lima, E. C.; Le, G. T.; Chang, C.-T.; Masindi, V.; Woo, S. H. *J. Hazard. Mater.* **2020,** *394,* 122255. doi:10.1016/j.jhazmat.2020.122255
3. Lefebvre, O.; Moletta, R. *Water Res.* **2006,** *40,* 3671–3682. doi:10.1016/j.watres.2006.08.027
4. Hariharan, C. *Appl. Catal., A* **2006,** *304,* 55–61. doi:10.1016/j.apcata.2006.02.020
5. Akyol, A.; Yatmaz, H. C.; Bayramoglu, M. *Appl. Catal., B* **2004,** *54,* 19–24. doi:10.1016/j.apcatb.2004.05.021
6. Colón, G.; Hidalgo, M. C.; Navío, J. A.; Pulido Melián, E.; González Díaz, O.; Doña Rodríguez, J. M. *Appl. Catal., B* **2008,** *83,* 30–38. doi:10.1016/j.apcatb.2008.01.033
7. Lizama, C.; Freer, J.; Baeza, J.; Mansilla, H. D. *Catal. Today* **2002,** *76,* 235–246. doi:10.1016/s0920-5861(02)00222-5
8. Lee, K. M.; Lai, C. W.; Ngai, K. S.; Juan, J. C. *Water Res.* **2016,** *88,* 428–448. doi:10.1016/j.watres.2015.09.045
9. Abbas, K. N.; Bidin, N. *Appl. Surf. Sci.* **2017,** *394,* 498–508. doi:10.1016/j.apsusc.2016.10.080
10. Khademalrasool, M.; Farbod, M.; Iraji zad, A. *J. Alloys Compd.* **2016,** *664,* 707–714. doi:10.1016/j.jallcom.2016.01.028
11. Yu, M.; Ma, Y.; Liu, J.; Li, X.; Li, S.; Liu, S. *Appl. Surf. Sci.* **2016,** *390,* 266–272. doi:10.1016/j.apsusc.2016.08.061
12. Ambika, S.; Sundrarajan, M. *J. Photochem. Photobiol., B* **2015,** *146,* 52–57. doi:10.1016/j.jphotobiol.2015.02.020
13. He, G.; Pearce, E. I. F.; Sissons, C. H. *Arch. Oral Biol.* **2002,** *47,* 117–129. doi:10.1016/s0003-9969(01)00093-0
14. Leung, Y. H.; Xu, X.; Ma, A. P. Y.; Liu, F.; Ng, A. M. C.; Shen, Z.; Gethings, L. A.; Guo, M. Y.; Djurišić, A. B.; Lee, P. K. H.; Lee, H. K.; Chan, W. K.; Leung, F. C. C. *Sci. Rep.* **2016,** *6,* 35243. doi:10.1038/srep35243
15. Rautela, A.; Rani, J.; Debnath Das, M. *J. Anal. Sci. Technol.* **2019,** *10,* No. 5. doi:10.1186/s40543-018-0163-z
16. Hackenberg, S.; Scherzed, A.; Technau, A.; Kessler, M.; Froelich, K.; Ginzkey, C.; Koehler, C.; Burghartz, M.; Hagen, R.; Kleinsasser, N. *Toxicol. In Vitro* **2011,** *25,* 657–663. doi:10.1016/j.tiv.2011.01.003
17. Pal, G.; Rai, P.; Pandey, A. Green synthesis of nanoparticles: A greener approach for a cleaner future. In *Green synthesis, characterization and applications of nanoparticles;* Shukla, A. K.; Iravani, S., Eds.; Micro and Nano Technologies; Elsevier: Amsterdam, Netherlands, 2019; pp 1–26. doi:10.1016/b978-0-08-102579-6.00001-0
18. Roy, S.; Das, T. K. *Int. J. Plant Biol. Res.* **2015,** *3,* 1044.
19. Jafarirad, S.; Mehrabi, M.; Divband, B.; Kosari-Nasab, M. *Mater. Sci. Eng., C* **2016,** *59,* 296–302. doi:10.1016/j.msec.2015.09.089
20. Patil, B. N.; Taranath, T. C. *Int. J. Mycobact.* **2016,** *5,* 197–204. doi:10.1016/j.ijmyco.2016.03.004
21. Salam, H. A.; Sivaraj, R.; Venckatesh, R. *Mater. Lett.* **2014,** *131,* 16–18. doi:10.1016/j.matlet.2014.05.033
22. Vidya, C.; Hiremath, S.; Chandraprabha, M. N.; Antonyraj, M. L.; Gopal, I. V.; Jain, A.; Bansal, K. *Int. J. Curr. Eng. Technol.* **2013,** *1,* 118–120.
23. Rafaie, H. A.; Samat, N. A.; Nor, R. M. *Mater. Lett.* **2014,** *137,* 297–299. doi:10.1016/j.matlet.2014.09.033
24. Sangeetha, G.; Rajeshwari, S.; Venckatesh, R. *Mater. Res. Bull.* **2011,** *46,* 2560–2566. doi:10.1016/j.materresbull.2011.07.046
25. Gunalan, S.; Sivaraj, R.; Rajendran, V. *Prog. Nat. Sci.: Mater. Int.* **2012,** *22,* 693–700. doi:10.1016/j.pnsc.2012.11.015
26. Nava, O. J.; Luque, P. A.; Gómez-Gutiérrez, C. M.; Vilchis-Nestor, A. R.; Castro-Beltrán, A.; Mota-González, M. L.; Olivas, A. *J. Mol. Struct.* **2017,** *1134,* 121–125. doi:10.1016/j.molstruc.2016.12.069
27. Sondi, I.; Salopek-Sondi, B. *J. Colloid Interface Sci.* **2004,** *275,* 177–182. doi:10.1016/j.jcis.2004.02.012
28. Mahendra, V. *Appl. Mech. Mater.* **2019,** *890,* 77–91. doi:10.4028/www.scientific.net/amm.890.77
29. Chen, C.; Liu, J.; Liu, P.; Yu, B. *Adv. Chem. Eng. Sci.* **2011,** *1,* 9–14. doi:10.4236/aces.2011.11002
30. Wafi, M. A. E.; Ahmed, M. A.; Abdel-Samad, H. S.; Medien, H. A. A. *Mater. Sci. Energy Technol.* **2022,** *5,* 217–231. doi:10.1016/j.mset.2022.02.003
31. Stan, M.; Popa, A.; Toloman, D.; Dehelean, A.; Lung, I.; Katona, G. *Mater. Sci. Semicond. Process.* **2015,** *39,* 23–29. doi:10.1016/j.mssp.2015.04.038
32. Hassan, S. S. M.; El Azab, W. I. M.; Ali, H. R.; Mansour, M. S. M. *Adv. Nat. Sci.: Nanosci. Nanotechnol.* **2015,** *6,* 045012. doi:10.1088/2043-6262/6/4/045012
33. Dutta, S.; Chattopadhyay, S.; Jana, D.; Banerjee, A.; Manik, S.; Pradhan, S. K.; Sutradhar, M.; Sarkar, A. *J. Appl. Phys.* **2006,** *100,* 114328. doi:10.1063/1.2401311
34. Maddu, A.; Meliafatmah, R.; Rustami, E. *Pol. J. Environ. Stud.* **2021,** *30,* 273–282. doi:10.15244/pjoes/120156
35. Shinde, S. S.; Shinde, P. S.; Bhosale, C. H.; Rajpure, K. Y. *J. Photochem. Photobiol., B* **2011,** *104,* 425–433. doi:10.1016/j.jphotobiol.2011.04.010
36. Kumar, R.; Kumar, G.; Akhtar, M. S.; Umar, A. *J. Alloys Compd.* **2015,** *629,* 167–172. doi:10.1016/j.jallcom.2014.12.232
37. Thill, A.; Zeyons, O.; Spalla, O.; Chauvat, F.; Rose, J.; Auffan, M.; Flank, A. M. *Environ. Sci. Technol.* **2006,** *40,* 6151–6156. doi:10.1021/es060999b
38. Huang, Z.; Zheng, X.; Yan, D.; Yin, G.; Liao, X.; Kang, Y.; Yao, Y.; Huang, D.; Hao, B. *Langmuir* **2008,** *24,* 4140–4144. doi:10.1021/la7035949
39. Jańczyk, A.; Krakowska, E.; Stochel, G.; Macyk, W. *J. Am. Chem. Soc.* **2006,** *128,* 15574–15575. doi:10.1021/ja065970m
40. Ramos, A. A.; Azqueta, A.; Pereira-Wilson, C.; Collins, A. R. *J. Agric. Food Chem.* **2010,** *58,* 7465–7471. doi:10.1021/jf100082p
41. He, W.; Wu, H.; Wamer, W. G.; Kim, H.-K.; Zheng, J.; Jia, H.; Zheng, Z.; Yin, J.-J. *ACS Appl. Mater. Interfaces* **2014,** *6,* 15527–15535. doi:10.1021/am5043005
42. Yamamoto, O.; Komatsu, M.; Sawai, J.; Nakagawa, Z. *J. Mater. Sci.: Mater. Med.* **2004,** *15,* 847–851. doi:10.1023/b:jmsm.0000036271.35440.36
43. Premanathan, M.; Karthikeyan, K.; Jeyasubramanian, K.; Manivannan, G. *Nanomedicine (N. Y., NY, U. S.)* **2011,** *7,* 184–192. doi:10.1016/j.nano.2010.10.001
44. Li, M.; Zhu, L.; Lin, D. *Environ. Sci. Technol.* **2011,** *45,* 1977–1983. doi:10.1021/es102624t
45. Talebian, N.; Amininezhad, S. M.; Doudi, M. *J. Photochem. Photobiol., B* **2013,** *120,* 66–73. doi:10.1016/j.jphotobiol.2013.01.004

BEILSTEIN JOURNAL OF NANOTECHNOLOGY

Rapid fabrication of MgO@g-C_3N_4 heterojunctions for photocatalytic nitric oxide removal

Minh-Thuan Pham[1,2,3], Duyen P. H. Tran[1,2,3], Xuan-Thanh Bui[4] and Sheng-Jie You[*2,3]

Full Research Paper

Open Access

Address:
[1]Department of Civil Engineering, Chung Yuan Christian University, Taoyuan 32023, Taiwan, [2]Department of Environmental Engineering, Chung Yuan Christian University, Taoyuan 32023, Taiwan, [3]Center for Environmental Risk Management, Chung Yuan Christian University, Taoyuan 32023, Taiwan and [4]Faculty of Environment and Natural Resources, Ho Chi Minh City University of Technology (HCMUT), VNU-HCM, 268 Ly Thuong Kiet Street, District 10, Ho Chi Minh City 700000, Viet Nam

Email:
Sheng-Jie You[*] - sjyou@cycu.edu.tw

* Corresponding author

Keywords:
g-C_3N_4; MgO; nitric oxide; photocatalyst; visible light

Beilstein J. Nanotechnol. **2022,** *13,* 1141–1154.
https://doi.org/10.3762/bjnano.13.96

Received: 27 April 2022
Accepted: 06 October 2022
Published: 18 October 2022

This article is part of the thematic issue "Nanomaterials for photocatalysis and applications in environmental remediation and renewable energy".

Guest Editor: V. V. Pham

Abstract

Nitric oxide (NO) is an air pollutant impacting the environment, human health, and other biotas. Among the technologies to treat NO pollution, photocatalytic oxidation under visible light is considered an effective means. This study describes photocatalytic oxidation to degrade NO under visible light with the support of a photocatalyst. MgO@g-C_3N_4 heterojunction photocatalysts were synthesized by one-step pyrolysis of MgO and urea at 550 °C for two hours. The photocatalytic NO removal efficiency of the MgO@g-C_3N_4 heterojunctions was significantly improved and reached a maximum value of 75.4% under visible light irradiation. Differential reflectance spectroscopy (DRS) was used to determine the optical properties and bandgap energies of the material. The bandgap of the material decreases with increasing amounts of MgO. The photoluminescence spectra indicate that the recombination of electron–hole pairs is hindered by doping MgO onto g-C_3N_4. Also, NO conversion, DeNOx index, apparent quantum efficiency, trapping tests, and electron spin resonance measurements were carried out to understand the photocatalytic mechanism of the materials. The high reusability of the MgO@g-C_3N_4 heterojunction was shown by a five-cycle recycling test. This study provides a simple way to synthesize photocatalytic heterojunction materials with high reusability and the potential of heterojunction photocatalysts in the field of environmental remediation.

Introduction

The rapid development of industrialization has been continuously increasing the combustion of fossil fuels, which leads to a large extent of nitrogen oxide emissions. This particular type of air pollutant leads to environmental damage (e.g., smog and acid) and health problems (e.g., COPD and cardiovascular diseases) [1-3]. Presently, there are different approaches to miti-

gate NO pollution, including catalyst/non-catalyst [4], oxidation [5], bioprocesses [6], adsorption [7], absorption [8], and non-thermal plasma technologies [9]. Photocatalytic oxidation is considered a promising approach due to its ability to degrade various air pollutants with light under ambient conditions [10].

Due to its unique properties, such as high chemical stability and low synthesis cost, graphitic carbon nitride has attracted considerable attention in the realm of environmental remediation [11-13]. It is an organic semiconductor that effectively absorbs visible light due to its small bandgap below 2.7 eV. Because of this, it has been consistently regarded as a catalyst with excellent optical properties [14,15]. Unfortunately, its narrow bandgap leads to rapid recombination of electron–hole (e^-–h^+) pairs, and the valence band potential of g-C_3N_4 (+1.75 eV) is more negative than that of H_2O/•OH (+2.40 eV), reducing the photocatalytic efficiency [16,17]. A well-known approach for overcoming this problem in order to achieve increased photocatalytic performance is to couple two semiconductors with optimal band alignment.

MgO is an alkaline metal oxide with wide bandgap (3.5–5 eV), high availability, non-toxicity, low cost, and native structural defects [18,19]. The large bandgap energy is the limitation of MgO, reducing the photocatalytic performance and applicability of MgO [20]. Various efforts have been made to enhance the absorption in the visible light region, including nonmetal and noble-metal doping, metal deposition, and formation of heterojunctions [21,22]. The construction of heterojunction structures has shown its effectiveness in improving photocatalytic performance by enhancing the separation of charge carriers and optimizing the redox potential by coupling two or more semiconductors [23,24], such as Bi_2MoO_6-based [25-29], BiOCl-based [30,31], g-C_3N_4-based [32-34], ZnO-based [35-37], TiO_2-based [38,39], and MgO-based heterostructured photocatalysts [40]. Among these, the combination of MgO and g-C_3N_4 with a lower bandgap is an efficient process for improving the photocatalytic performance. Li and co-workers reported an improvement in the photocatalytic efficiency of MgO@g-C_3N_4 for the photoreduction of CO_2 under visible light [33]. Similarly, MgO-modified g-C_3N_4 nanostructures enhanced the removal efficiency for NO_x, NO, and NO_2 [12]. However, these studies only focused on the synthesis of MgO from $Mg(NO_3)_2{\cdot}6H_2O$, increasing time and cost of the synthesis process. Commercial MgO as a precursor material for MgO@g-C_3N_4 heterojunctions has not been studied. Furthermore, there are no relevant reports on the fabrication of the MgO@g-C_3N_4 heterojunction via one-step pyrolysis nor on the photocatalytic pathway of the MgO@g-C_3N_4 heterojunction for photocatalytic NO removal under visible light.

In this study, a MgO@g-C_3N_4 heterojunction was synthesized via a one-step pyrolysis method using commercial MgO and urea and, subsequently, characterized. Charge transfer dynamics in the heterojunction and band structure were investigated to understand the effect of the heterojunction on the photocatalytic activity. Finally, the photocatalytic pathway of the MgO@g-C_3N_4 heterojunction was studied via trapping test, electron spin resonance (ESR) measurements, and other methods. This work might be helpful for the development of MgO@g-C_3N_4 heterojunction materials.

Experimental

Synthesis of MgO/g-C_3N_4

For the synthesis of g-C_3N_4, 30 g of urea was ground manually for 30 min and then placed in a 100 mL crucible. Then, the sample was annealed at 550 °C for two hours and let to cool to room temperature.

For preparation of the MgO@g-C_3N_4 heterojunction material, both MgO and urea were mixed, ground, and placed in a 100 mL crucible, followed by annealing at 550 °C for two hours (Figure 1). Then, the samples were let to cool to room temperature naturally. Different mass ratios of MgO and g-C_3N_4 were prepared, that is, 1%, 3% and 5%, named as x-MgO@g-C_3N_4 (x = 1, 3, and 5%).

Characterization

A variety of analytical techniques have been employed to evaluate the morphology and the physical, chemical, and optical properties of the materials. Scanning electron microscopy (SEM) and high-resolution transmission electron microscopy (HR-TEM) were used to assess the morphology of the materials. The crystal phase of the materials was determined by X-ray diffraction (XRD) with a measurement range of 10°–80°. Fourier-transform infrared spectroscopy (FTIR) was used to determine the chemical bond composition of the materials. Differential reflectance spectroscopy (DRS) determined the change in the bandgap of the materials. The elements of the materials were identified by high-resolution X-ray photoelectron spectroscopy (HR-XPS). The photoluminescence (PL) spectra of the materials was carried out in the form of fluorescence analysis with an excitation wavelength range of 200–900 nm. Finally, the photocatalytic mechanism was determined by trapping tests and ESR measurements.

Photocatalytic performance

The photocatalytic activity of as-prepared MgO@g-C_3N_4 was evaluated by monitoring NO degradation. The photocatalytic NO removal experiments were performed using a 4.5 L reaction chamber and a Xenon lamp (300 W) as the visible light source. The initial NO concentration was 500 ppb, the flow rate

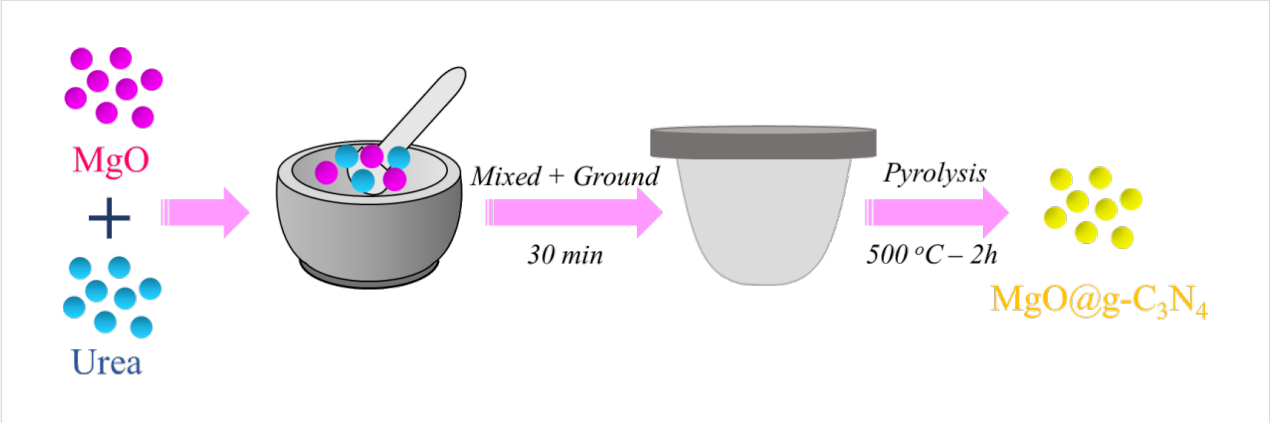

Figure 1: Schematic diagram of pyrolysis synthesis process for MgO@g-C_3N_4 heterojunctions.

was 1.5 L·min^{-1}, and the dosage of catalysts was 0.2 g for all experiments. Before each catalytic experiment, 0.2 g of the sample was dispersed in 10 mL of DI water, evaporated at 80 °C, and placed in the dark to achieve adsorption–desorption equilibrium. Finally, the sample was illuminated by a Xenon lamp (300 W) for 30 min.

Trapping experiments were performed to evaluate the photocatalytic process mechanism for NO degradation. Three trapping agents were used representing different active species, namely isopropyl alcohol (IPA) for the hydroxyl radical (•OH), potassium dichromate ($K_2Cr_2O_7$) for electrons (e^-), and potassium iodide (KI) for holes (h^+). The photocatalytic NO degradation experiments were performed under the previously described conditions.

The photocatalytic NO degradation efficiency (η), the yield of NO_2 conversion (γ), the apparent quantum efficiency (AQE, φ), and the DeNOx index (αDeNOX αDeNOx) were calculated by using Equations 1–4: [41-43]:

$$\eta = \frac{C_{\mathrm{NO,\,i}} - C_{\mathrm{NO,\,f}}}{C_{\mathrm{NO,\,i}}} \cdot 100\%, \tag{1}$$

$$\gamma = \frac{C_{\mathrm{NO_2,\,f}} - C_{\mathrm{NO_2,\,i}}}{C_{\mathrm{NO,\,i}} - C_{\mathrm{NO,\,f}}} \cdot 100\%, \tag{2}$$

$$\varphi_{\mathrm{app}} = \frac{N_{\mathrm{A}} \int_0^t \left(C_{\mathrm{NO,\,i}} - C_{\mathrm{NO,\,f}}\right) V_t}{\text{photon flux} \cdot \text{irradiation area} \cdot t \cdot 1000\,\mathrm{M}} \cdot 100\%, \tag{3}$$

$$\alpha_{\mathrm{DeNOx}} = \eta\left(1 - 3\gamma\right) C_{\mathrm{NO,\,i}}, \tag{4}$$

where C_{NO} is the concentration of NO (ppb), C_{NO2} is the concentration of NO_2 (ppb), the index "i" represents the initial concentration, and the index "f" represents the final concentration. N_A is the Avogadro constant (mol^{-1}), V_t is the flow rate of NO (L·min^{-1}), and M is the molecular weight of NO (g·mol^{-1}). The photon flux in the photocatalytic experiment is 2.72·10^{19} cm^{-2}·min^{-1}, the irradiation area for the 12 cm diameter petri dish is 113.1 cm^2.

In addition, the bandgap energy of materials was calculated by using the Tauc and the Kubelka–Munk equation as described in Equations 5–7 [43]:

$$E = h\nu = \frac{hc}{\lambda}, \tag{5}$$

$$\left(\alpha h\nu\right)^r = B\left(h\nu - E_{\mathrm{g}}\right), \tag{6}$$

$$\left(F\left(R\right)h\nu\right)^r = B\left(h\nu - E_{\mathrm{g}}\right), \tag{7}$$

where E is the photon energy (eV), h is Planck's constant (4.132·10^{-15} eV·s), ν is the photon frequency (s^{-1}), c is the velocity of light (nm·s^{-1}), λ is the wavelength (nm), α is the absorption coefficient, B is a constant, and E_g is the bandgap energy (eV), R is the reflectance value.

Results and Discussion

Photocatalytic performance

The photocatalytic NO removal efficiency of the materials is shown in Figure 2a. The efficiency gradually increased during the first 5 min of the photocatalytic reaction and remains stable until the end of the photocatalytic reaction. The photocatalytic NO removal efficiency values are 0.6%, 62.8%, 16.8%, 68.4%, 75.4%, and 72.1% for the blank sample, g-C_3N_4, MgO, 1%

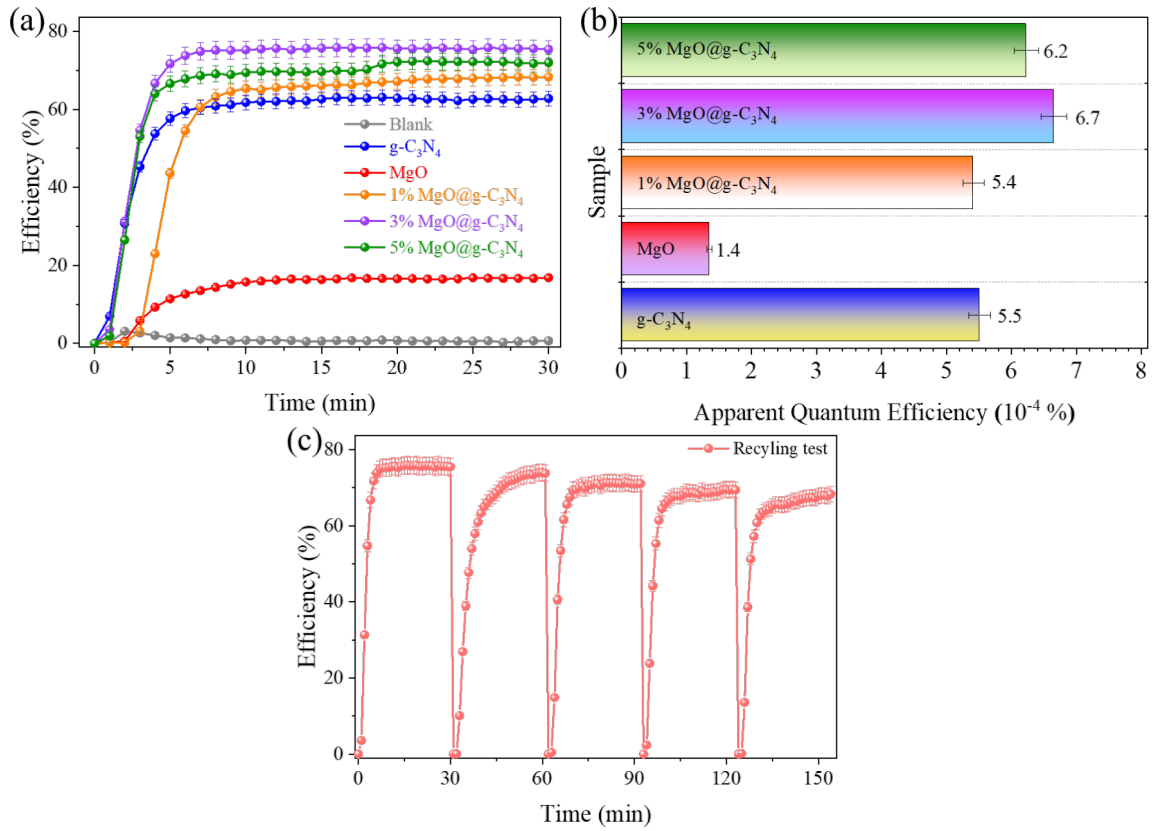

Figure 2: (a) Photocatalytic NO degradation efficiency, (b) apparent quantum efficiency of the materials, and (c) photocatalytic recycling test of 3% MgO@g-C_3N_4.

MgO@g-C_3N_4, 3% MgO@g-C_3N_4, and 5% MgO@g-C_3N_4, respectively. The photocatalytic NO removal efficiency is increased by combining MgO with g-C_3N_4. The results indicate that MgO@g-C_3N_4 heterojunction structures have been successfully synthesized with high photocatalytic NO degradation efficiency under visible light by one-step pyrolysis (see Table 1 for a comparison of the photocatalytic NO removal efficiency values). Also, the AQE has been calculated according to Equation 3. The AQE values (10^{-4}%) of g-C_3N_4, MgO, 1% MgO@g-C_3N_4, 3% MgO@g-C_3N_4, and 5% MgO@g-C_3N_4 are 5.5, 1.4, 5.4, 6.7, and 6.2, respectively. The AQE results show (Figure 2b) that photons are most efficient in 3% MgO@g-C_3N_4. The heterojunction structure has enhanced the photocatalytic activities of the materials [44]. In addition, the photocatalytic reusability of 3% MgO@g-C_3N_4 was shown by a five-cycle recycling test under identical experimental conditions (Figure 2c). The photocatalytic NO degradation efficiency in the recycling test is 75.4%, 73.8%, 71.1%, 69.4%, and 68.3% after five cycles, respectively. The photocatalytic NO degradation efficiency decreased by 7% after five cycles. The FTIR spectra and the XRD patterns of the 3% MgO@g-C_3N_4 before and after the recycling test are shown in Figure S1a and Figure S1b of Supporting Information File 1, respectively. The results indicate the high reusability of 3% MgO@g-C_3N_4 [45].

The conversion rates of NO to NO_2 and by-products have been calculated (Figure 3a). The conversion rates of NO to NO_2 of g-C_3N_4, MgO, 1% MgO@g-C_3N_4, 3% MgO@g-C_3N_4, and 5% MgO@g-C_3N_4 are 34.6%, 9.6%, 34.9%, 21.9%, and 25.8%, respectively. Besides, the rates of converting NO to by-products of g-C_3N_4, MgO, 1% MgO@g-C_3N_4, 3% MgO@g-C_3N_4, and 5% MgO@g-C_3N_4 are 28.2%, 7.3%, 34.4%, 53.5%, and 46.3%, respectively. In this study, the by-products are defined as any nitrogen species (e.g., N_2O_5, N_2O, and NO_3^-) except NO_2, which are unstable and can be absorbed by plants [46]. MgO generates the lowest amount of NO_2 and by-products due to the lowest photocatalytic NO removal efficiency (16.8%). 3% MgO@g-C_3N_4 has the lowest NO_2 (21.9%) and highest

Table 1: Comparison of photocatalytic NO removal of current photocatalyst systems under visible light.

Material	Initial NO concentration (ppb)	Light source	Irradiation time (min)	Dosage (g)	Flowrate ($L \cdot min^{-1}$)	NO removal efficiency (%)	NO_2 generation	Ref.
$BiOIO_3$/ g-C_3N_4	600	xenon 300 W	30	0.1	1.2	57	80 (ppb)	[72]
SnO_2/ g-C_3N_4	600	tungsten halogen 150 W	30	0.4	N/A	32	6%	[73]
Ti_3C_2@TiO_2/ g-C_3N_4	430	xenon-300 W	30	N/A	N/A	29	18.7 (ppb)	[74]
rGO/ Fe-doped g-C_3N_4	1000	metal halide 250 W	30	N/A	N/A	93.4	N/A	[75]
$FAPbBr_3$/g-C_3N_4	600	xenon	60	0.1	1.2	58	0.3 (ppb)	[76]
g-C_3N_4/SnO_2	500	xenon-300 W	30	0.2	0.6	35	2%	[77]
TiO_2@g-C_3N_4	500	xenon-300 W	30	0.2	0.5	90.2	5.3%	[44]
g-C_3N_4@BiOCl/ $Bi_{12}O_{17}Cl_2$	500	tungsten halogen 100 W	30	0.2	1	46.8	N/A	[78]
MoS_2/g-C_3N_4	600	tungsten halogen 150 W	30	0.2	N/A	51.7	N/A	[79]

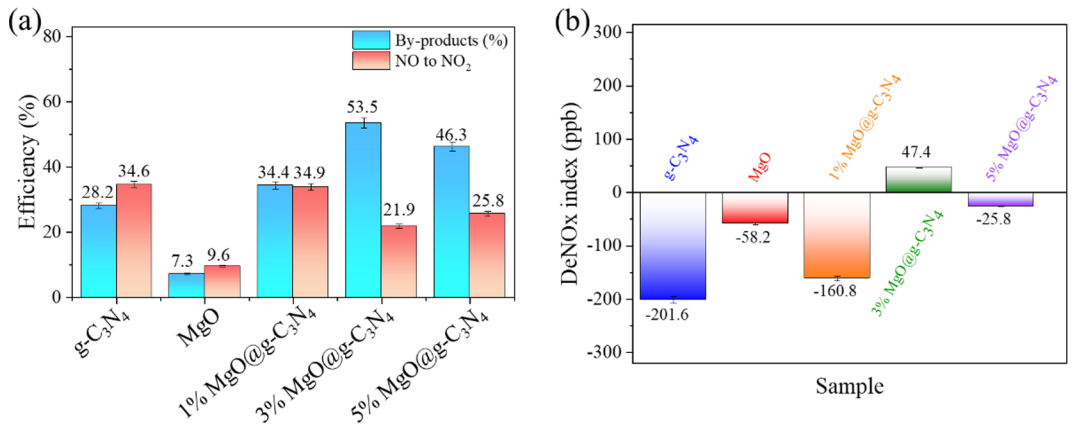

Figure 3: (a) NO conversion and (b) DeNOx index of the materials.

by-product (53.5%) generation. In addition, the NO_2 generation of g-C_3N_4 is almost equal to that of 1% MgO@g-C_3N_4. This can be explained by the low amount of MgO (only 1%). 3% MgO@g-C_3N_4 shows the highest photocatalytic NO removal efficiency with the lowest NO_2 generation, which indicates a possible future application of 3% MgO@g-C_3N_4. Also, the DeNOx index values have been calculated according to Equation 4 [47]. The values of g-C_3N_4, MgO, 1% MgO@g-C_3N_4, 3% MgO@g-C_3N_4, and 5% MgO@g-C_3N_4 are −201.6%, −58.2%, −160.8%, 47.4%, and −25.8%, respectively.

XRD and FTIR analyses

XRD patterns of the synthesized materials are shown in Figure 4a. There are two distinct diffraction peaks at 2θ = 13°

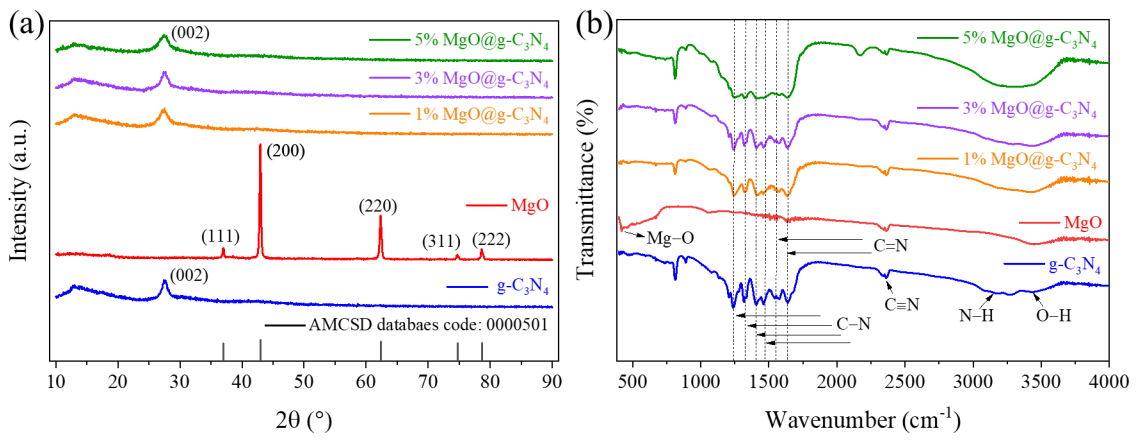

Figure 4: (a) XRD patterns and (b) FTIR spectra of the materials.

and 27.4°, which were assigned to the (100) and (002) planes of g-C_3N_4, respectively [48]. Diffraction peaks of the pure MgO sample are detected at 36.9°, 42.9°, 62.5°, 74.8°, and 78.7°, which were attributed to the (111), (200), (220), (311), and (222) planes, respectively [AMCS: 000501] [49,50]. All MgO@g-C_3N_4 samples show the characteristic peaks of g-C_3N_4. No impurities are detected in the MgO@g-C_3N_4 samples. There are no reflections of MgO in all MgO@g-C_3N_4 samples, due to the low amount of MgO in the MgO@g-C_3N_4 samples. This agrees with previous studies, in which characteristic peaks of MgO were only detected when MgO amounts higher than 5% had been added [33,51].

Figure 4b shows the FTIR spectra of g-C_3N_4, MgO, and MgO@g-C_3N_4. For pure g-C_3N_4, the broad peak in the range of 3000–3600 cm^{-1} was attributed to the stretching vibrations of N–H and O–H bonds, indicating the existence of amino groups and adsorbed water molecules in the material [32,52]. The characteristic peaks at 1240, 1320, 1407, and 1465 cm^{-1} were associated with the stretching vibrations of aromatic C–N bonds, and the typical peaks at 1562 and 1642 cm^{-1} characterize the presence of C=O bonds [53,54]. In addition, the characteristic peak at 810 cm^{-1} matches with the typical breathing mode of triazine. After adding MgO, the distinct peaks of all MgO@g-C_3N_4 heterojunctions are similar to that of pure g-C_3N_4, indicating that the crystal structure of g-C_3N_4 remains unchanged. In addition, the small peak at 419 cm^{-1} proves the presence of MgO in MgO@g-C_3N_4 [55].

SEM and TEM analyses

The morphology of g-C_3N_4, MgO, and 3%MgO@g-C_3N_4 has been determined through SEM and TEM analyses. The typical bulk structure of g-C_3N_4 is shown in Figure 5e,f. The difference between the morphologies of MgO and g-C_3N_4 is difficult to observe by SEM (Figure 5c,d). Figure 5a and Figure 5b show that the morphology of 3%MgO@ g-C_3N_4 is similar to that of pure g-C_3N_4. The results indicate that the morphology of 3% MgO@g-C_3N_4 is identical to that of g-C_3N_4 because the added amount of MgO is very low, as determined by EDS mapping. The EDS mapping images of 3% MgO@g-C_3N_4 are shown in Figure 6 and Figure S2 (Supporting Information File 1). The weight percentages of C, N, Mg, and O are 37, 52, 9, and 2 wt %, respectively. The weight fractions of Mg and O are the lowest, indicating that the amount of MgO in the MgO@g-C_3N_4 sample is too low. The shape of g-C_3N_4 is easy to observe in Figure 7c,d. However, the shape of MgO is complicated to determine by TEM and HR-TEM (Figure 7a,b). These results prove the presence of MgO in the compound.

Chemical state analysis

XPS and HR-XPS have been employed to determine the chemical states of the materials. XPS survey scans of g-C_3N_4 MgO and 3% MgO@ g-C_3N_4 are shown in Figure 8a. The peaks at 87 and 530 eV were assigned to the Mg 2s and O 1s levels of MgO, respectively. The peaks at 287 and 397 eV were assigned to the C 1s and N 1s levels of g-C_3N_4, respectively [12,56,57]. In the MgO sample, the peaks of Mg 2p, Mg KLL, O loss, and O KLL levels are observed at 46, 304, 555, and 978 eV, respectively [58,59]. The HR-XPS of the C 1s level are shown in Figure 8b. The peak at 283 eV was assigned to the C–C coordination in MgO, and the peak at 287 eV was assigned to N–C=N bonds of g-C_3N_4. The latter peak only appears in g-C_3N_4 and 3% MgO@g-C_3N_4. However, the former peak of MgO and g-C_3N_4 occurs only in 3% MgO@g-C_3N_4. The C 1s peaks of

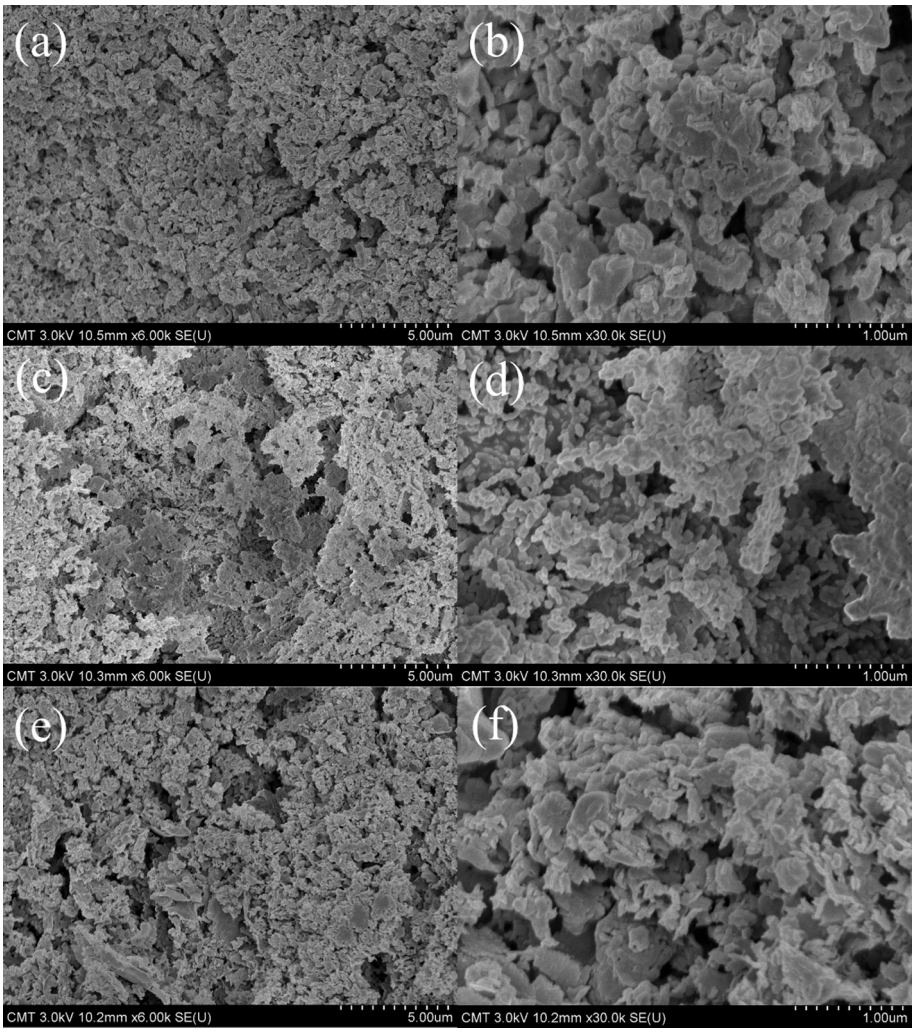

Figure 5: SEM images of (a, b) 3%MgO@g-C_3N_4, (c, d) MgO, and (e, f) g-C_3N_4.

the materials do not change during the pyrolysis. The HR-XPS of the N 1s level of the materials is shown in Figure 8c. The peaks at 397 and 399 eV correspond to the C–N=C bonds and the N–$(C)_3$ structures of g-C_3N_4, respectively [60]. Figure 8d shows the peak of Mg–O bonds in MgO at 398 eV [61]. The Mg 2s peaks of MgO are shown in Figure 8e and Figure 8f. The peaks at 87 eV (Figure 8e) and 88 eV (Figure 8f) confirm the metallic state of Mg [62]. The peaks of the O 1s and Mg 2s levels in 3% MgO@g-C_3N_4 are too weak.

Optical properties

DRS spectra have been measured to understand the optical absorption characteristics of the materials (Figure 9). The g-C_3N_4 sample significantly absorbs light at a peak around 440 nm, corresponding to the direct and the indirect bandgap of 2.83 and 2.68 eV, respectively (Figure 9b,d). MgO with a wide bandgap shows absorption below 400 nm in both Kubelka–Munk and Tauc plots (Figure 9a,c). After adding MgO to g-C_3N_4, the absorption of the MgO@ g-C_3N_4 samples slightly shifts to the visible light region. The optical direct and indirect bandgap energy is slightly reduced, corresponding to the increase in MgO fraction. The indirect bandgap energies of 1% MgO@g-C_3N_4, 3% MgO@g-C_3N_4, and 5% MgO@g-C_3N_4 are 2.79, 2.73, and 2.69 eV, respectively. The trend of the direct bandgap is the same. The bandgap of the materials reduces with increasing amounts of added MgO. The bandgap reduction can be attributed to Mg−N bonds in the MgO@g-C_3N_4 materials, which promote charge transport, thus, increasing the photocatalytic efficiency [33,51]. Generally, smaller bandgaps lead to better light absorption, indicating the high photocatalytic activi-

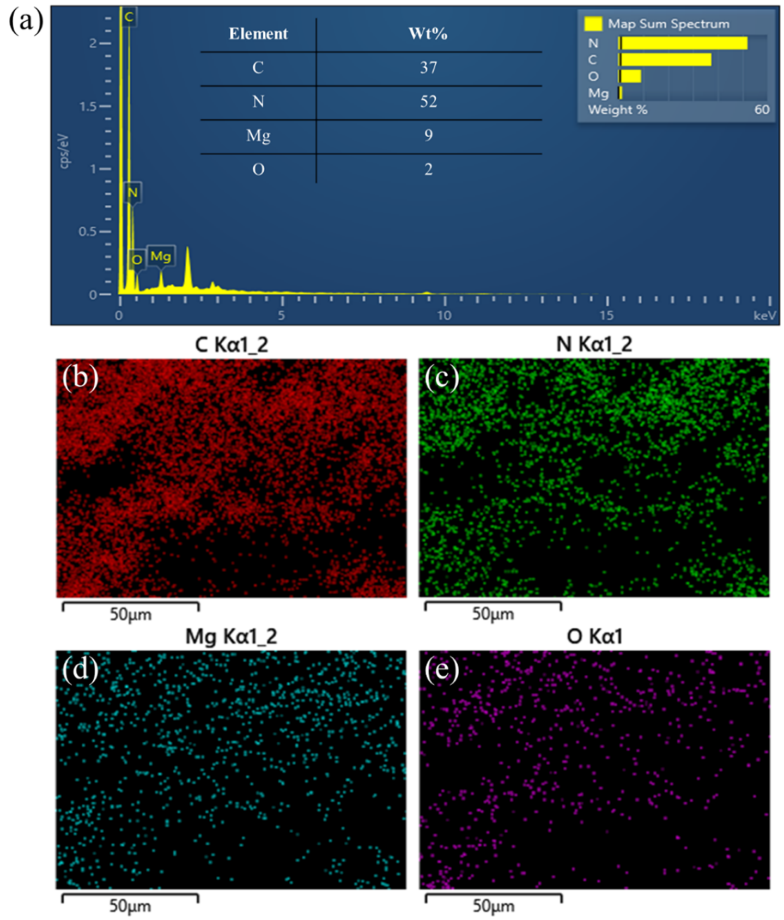

Figure 6: (a) Elemental composition and (b–e) EDS mappings of 3% MgO@g-C_3N_4.

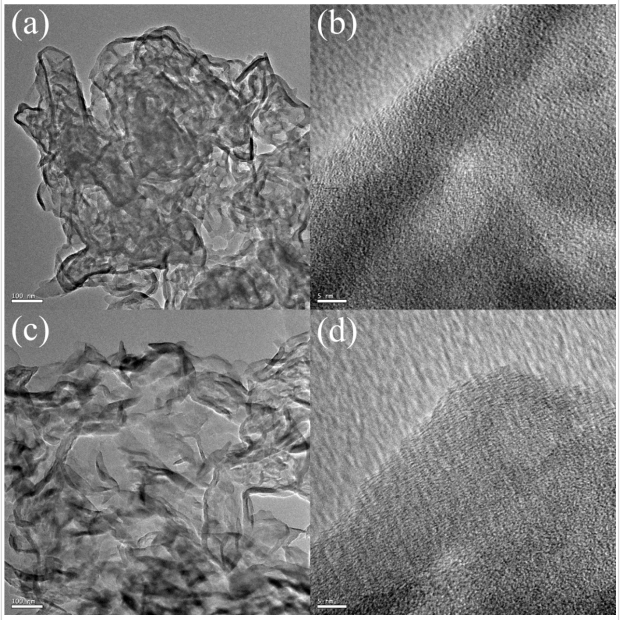

Figure 7: TEM and HR–TEM images of (a, b) MgO@g-C_3N_4 and (c, d) g-C_3N_4.

ty of MgO@g-C_3N_4 under visible light and also the existence of MgO in the MgO@g-C_3N_4 heterojunction materials. However, with a smaller bandgap, the recombination of e^-–h^+ pairs will be faster, which decreases the photocatalytic activity of the materials [63]. As shown in Figure 9a and Figure 9c, the materials mostly absorb in the UV range (200–400 nm), with a sudden decrease in the visible range. The absorbance of 3% MgO@g-C_3N_4 is more substantial than the absorbance of 1% MgO@g-C_3N_4 and 5% MgO@g-C_3N_4 in the UV and visible ranges. These results indicate that the higher photocatalytic NO removal efficiency of the 3% MgO@g-C_3N_4 strongly depends on the optical properties.

Photoluminescence

Fluorescence spectra of MgO and 3% MgO@g-C_3N_4 are shown in Figure 10a and Figure 10b, respectively. MgO shows strong fluorescence at 270 nm with an excitation wavelength (270 nm) in the UV range. MgO also shows another emission wavelength at 380 nm with an excitation wavelength (770 nm) in the visible range, which could be caused by the native structural defects in MgO [18]. 3% MgO@g-C_3N_4 shows intense fluores-

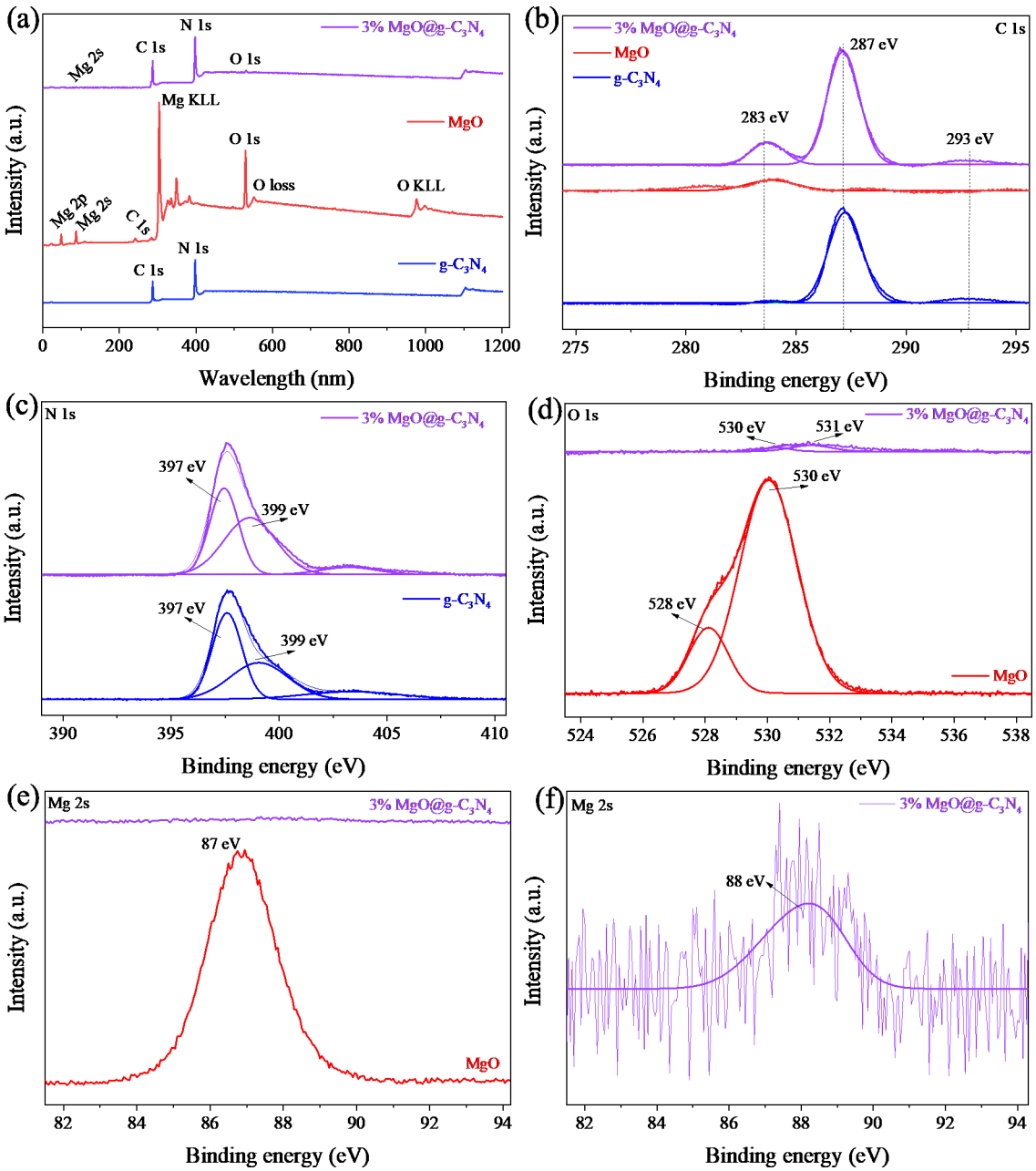

Figure 8: The XPS survey (a), HR–XPS C1s (b), N 1s (c), O 1s (d), C 1s (c), and Mg 2s (e, f) of the materials.

cence at 420 nm via excitation at 850 nm, due to the recombination of charge carriers. The photogenerated electrons from the valance band (VB) of g-C_3N_4 migrate to the conduction band (CB). The excited electrons in the CB of g-C_3N_4 can then return to energy bands between the CB and VB of g-C_3N_4 to produce an emission with an energy of about 1.5 eV. The energy band in g-C_3N_4 can be attributed to transitions between C atoms and N atoms [64-66]. Also, Liang and co-workers reported that the recombination of the e^-–h^+ pairs could be inhibited by doping MgO into g-C_3N_4 [32]. When MgO is added, the defect concentration increases and Mg and O vacancies are generated in MgO@g-C_3N_4. These defects work as the electron traps, which enhance the capacity to separate photogenerated e^-–h pairs in MgO@g-C_3N_4. The photogenerated e^-–h^+ pairs in the defects also contribute to the photocatalytic reaction [67,68].

Photocatalytic mechanism

Trapping experiments were carried out to evaluate the involvement of electrons, holes, and reactive oxygen species. The used trapping agents were KI (h^+), $K_2Cr_2O_7$ (e^-), and IPA (•OH).

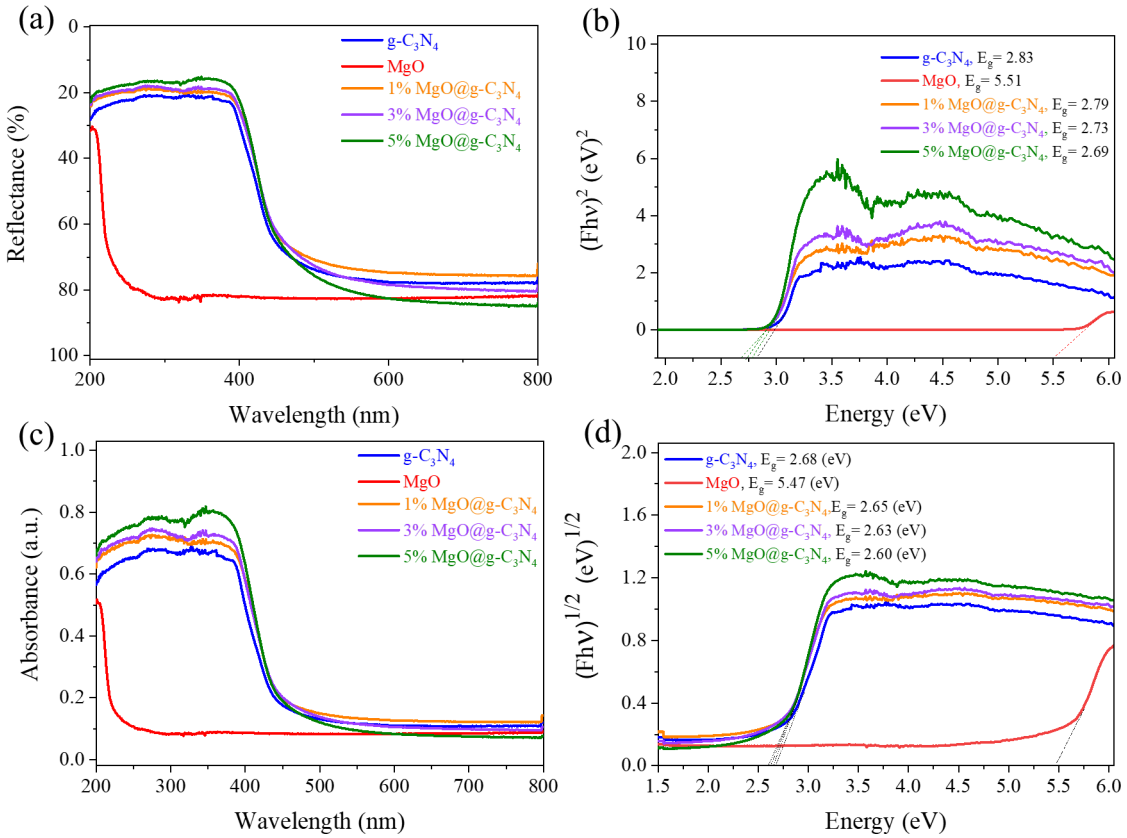

Figure 9: (a) DRS reflectance spectra, (b) direct bandgap, (c) DRS absorbance spectra, and (d) indirect bandgap of the materials.

Figure 11a shows the reduction in efficiency when different scavengers are present. The photocatalytic NO degradation efficiency decreases significantly from 75.4% to 36.4% in the presence of KI. $K_2Cr_2O_7$ as electron scavenger also reduces the NO decomposition by about 1.3 times. The weak contribution of •OH radicals in the NO degradation is clearly shown, with a reduction in efficiency by only about 1%. Hence, electrons and holes are the main contributors to the photocatalytic NO degradation.

Also, ESR was used to determine accurately the reaction mechanism of the material. Figure 11b shows that under visible light and using DMPO–H_2O and DMPO–OH, the material generates •OH and $•O_2$ radicals. In contrast, only •OH radicals are generated in the dark, but to a very low extent. Hence, the generation of $•O_2$ radicals contributes significantly to the photocatalytic NO degradation efficiency.

A photocatalysis mechanism of MgO@g-C_3N_4 is proposed taking into account the results of the DRS and ESR analyses and trapping tests. Because of the large bandgap of MgO, only g-C_3N_4 generates e^-–h^+ pairs under visible light (Equation 8). The holes can degrade NO directly by oxidizing NO into NO_2 (Equations 9 and 10) [47,69]. Simultaneously, at the CB of g-C_3N_4, electrons are excited and react with O_2 to produce $•O_2^-$ radicals. In addition, these electrons also migrate across the CB of MgO, creating excess electrons in MgO and avoiding the recombination at g-C_3N_4. Then, the photogenerated electrons react with O_2 to produce $•O_2^-$ radicals (Equation 11). These $•O_2^-$ radicals decompose NO to NO_3 and prevent the formation of NO_2 (Equation 12). Also, $•O_2^-$ reacts with H_2O to produce $•HO_2$ radicals and OH^- (Equation 13). Then, the $•HO_2$ decomposes NO to form NO_2 and •OH (Equation 14). Also, $•HO_2$ also reacts with H_2O and electrons to produce H_2O_2 (Equation 15). Finally, H_2O_2 generates two •OH radicals to decompose NO (Equations 16–19) [70,71].

$$\text{MgO@g-C}_3\text{N}_4 + h\nu \rightarrow \text{MgO@g-C}_3\text{N}_4\left(\text{e}^-_{(\text{CB})} + \text{h}^+_{(\text{VB})}\right), \quad (8)$$

$$\text{h}^+_{(\text{VB})} + \text{NO} + \text{H}_2\text{O} \rightarrow \text{HNO}_2 + \text{H}^+, \quad (9)$$

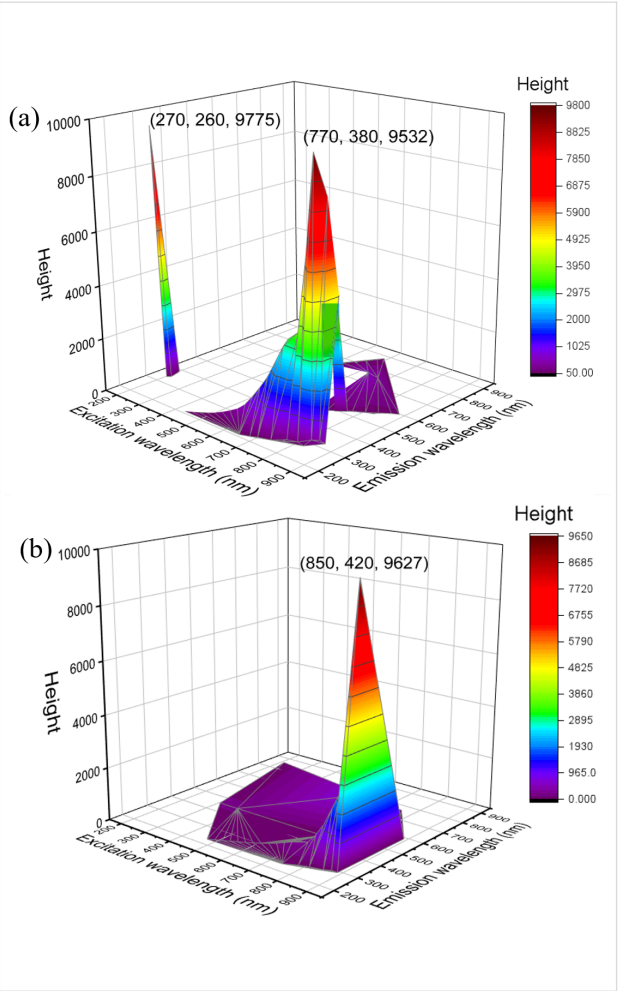

Figure 10: 3D fluorescence scan of (a) MgO and (b) 3% MgO@g-C_3N_4.

$$2HNO_2 \rightarrow NO_2 + NO + H_2O, \quad (10)$$

$$e^-_{(CB)} + O_2 \rightarrow \cdot O_2^-, \quad (11)$$

$$\cdot O_2^- + NO \rightarrow NO_3^-, \quad (12)$$

$$\cdot O_2^- + H_2O \rightarrow \cdot HO_2 + OH^-, \quad (13)$$

$$NO + \cdot HO_2 \rightarrow NO_2 + \cdot OH, \quad (14)$$

$$\cdot HO_2 + H_2O + e^-_{(CB)} \rightarrow H_2O_2 + OH^-, \quad (15)$$

$$H_2O_2 \rightarrow 2 \cdot OH, \quad (16)$$

$$NO + \cdot OH \rightarrow HNO_2, \quad (17)$$

$$HNO_2 + \cdot OH \rightarrow NO_2 + H_2O, \quad (18)$$

$$NO_2 + \cdot OH \rightarrow HNO_3. \quad (19)$$

Conclusion

MgO@g-C_3N_4 heterojunction materials were effectively synthesized by one-step pyrolysis of commercial MgO and urea. The photocatalytic efficiencies of the synthesized materials were increased dramatically by mixing MgO and g-C_3N_4. 3% MgO@g-C_3N_4 possessed the highest photocatalytic NO removal efficiency, reaching 75.4%. In addition, the photocatalytic NO removal efficiency of the MgO@g-C_3N_4 heterojunction materials was decreased when the amount of MgO exceeded 3%. An enhanced apparent quantum efficiency of (6.7×10^{-4})% as well as an extended lifetime of photogener-

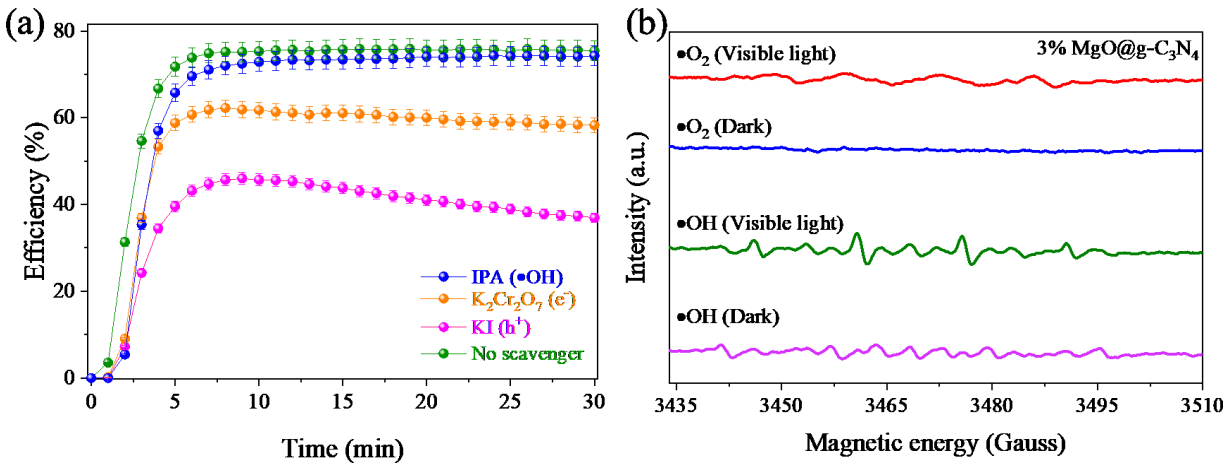

Figure 11: (a) Trapping test results of the materials and (b) detection of radicals over over 3% MgO@g-C_3N_4 by ESR.

ated electrons based on the heterojunction structure were obtained by combining MgO and g-C_3N_4. Moreover, the conversion rates of NO to NO_2 and by-products of the 3% MgO@g-C_3N_4 were the lowest (21.9%) and the highest (53.5%), respectively. Also, 3% MgO@ g-C_3N_4 showed high reusability after a five-cycle recycling test, when the photocatalytic NO removal efficiency decreased only by 7.1%. The results indicated that 3% MgO@g-C_3N_4 could be applied in the future as an excellent photocatalyst with high removal efficiency and low generation of toxic products. FTIR, XPS, and EDS measurements were carried out to confirm the presence of MgO in the MgO@g-C_3N_4 heterojunctions. Although MgO was difficult to determine in the MgO@g-C_3N_4 heterojunctions, the addition of MgO affected the optical properties of the MgO@g-C_3N_4 heterojunctions. The DRS result showed that the bandgap of the MgO@g-C_3N_4 heterojunctions decreased by adding larger amounts of MgO. The light absorption of 3% MgO@g-C_3N_4 was higher than that of 1% MgO@g-C_3N_4 and 5% MgO@g-C_3N_4 in the visible and UV range, which increased the photocatalytic performance under visible light irradiation. The PL results confirmed the presence of vacancies in the MgO@g-C_3N_4 heterojunctions. MgO@g-C_3N_4 is promising for large-scale fabrication via this simple and fast method. This study provides a new way to synthesize a MgO@g-C_3N_4 heterojunction materials and an understanding of the photocatalytic mechanism of the MgO@g-C_3N_4 heterojunction applied in the removal of NO.

Supporting Information

Supporting Information File 1

Additional figures.
[https://www.beilstein-journals.org/bjnano/content/supplementary/2190-4286-13-96-S1.pdf]

Acknowledgements

This work was supported by Department of Civil Engineering Chung Yuan Christian University, Taoyuan City, 32023, Taiwan; Department of Environmental Engineering, Chung Yuan Christian University, Taoyuan City, 32023, Taiwan; Center for Environmental Risk Management, Chung Yuan Christian University, No.200, Taoyuan City, 32023, Taiwan; Faculty of Environment and Natural Resources, Ho Chi Minh City University of Technology (HCMUT), VNU-HCM, Vietnam.

Funding

This research was financially supported by the Chung Yuan Christian University, Taiwan (Project No: 109609432)

ORCID® iDs

Minh-Thuan Pham - https://orcid.org/0000-0002-6069-445X
Duyen P. H. Tran - https://orcid.org/0000-0003-3152-7270
Xuan-Thanh Bui - https://orcid.org/0000-0003-1413-4985
Sheng-Jie You - https://orcid.org/0000-0003-0532-9916

Preprint

A non-peer-reviewed version of this article has been previously published as a preprint: https://doi.org/10.3762/bxiv.2022.30.v1

References

1. Van Viet, P.; Hoang The Vinh, T.; Thi Ngoc Dung, N.; Minh Thi, C. *Chem. Phys. Lett.* **2021,** *775,* 138642. doi:10.1016/j.cplett.2021.138642
2. Zhou, S.; Young, C. J.; VandenBoer, T. C.; Kahan, T. F. *Environ. Sci.: Processes Impacts* **2019,** *21,* 1374–1383. doi:10.1039/c9em00129h
3. Pham, M.-T.; Hussain, A.; Bui, D.-P.; Nguyen, T.-M. T.; You, S.-J.; Wang, Y.-F. *Environ. Technol. Innovation* **2021,** *23,* 101755. doi:10.1016/j.eti.2021.101755
4. Nguyen, V.-H.; Nguyen, B.-S.; Huang, C.-W.; Le, T.-T.; Nguyen, C. C.; Nhi Le, T. T.; Heo, D.; Ly, Q. V.; Trinh, Q. T.; Shokouhimehr, M.; Xia, C.; Lam, S. S.; Vo, D.-V. N.; Kim, S. Y.; Le, Q. V. *J. Cleaner Prod.* **2020,** *270,* 121912. doi:10.1016/j.jclepro.2020.121912
5. Asghar, U.; Rafiq, S.; Anwar, A.; Iqbal, T.; Ahmed, A.; Jamil, F.; Khurram, M. S.; Akbar, M. M.; Farooq, A.; Shah, N. S.; Park, Y.-K. *J. Environ. Chem. Eng.* **2021,** *9,* 106064. doi:10.1016/j.jece.2021.106064
6. Qie, F.; Zhu, J.; Rong, J.; Zong, B. *Bioresour. Technol.* **2019,** *292,* 122037. doi:10.1016/j.biortech.2019.122037
7. Wang, S.; Xu, S.; Gao, S.; Xiao, P.; Jiang, M.; Zhao, H.; Huang, B.; Liu, L.; Niu, H.; Wang, J.; Guo, D. *Sci. Rep.* **2021,** *11,* 11003. doi:10.1038/s41598-021-90532-9
8. Chen, R.; Zhang, T.; Guo, Y.; Wang, J.; Wei, J.; Yu, Q. *Chem. Eng. J.* **2021,** *420,* 127588. doi:10.1016/j.cej.2020.127588
9. Talebizadeh, P.; Babaie, M.; Brown, R.; Rahimzadeh, H.; Ristovski, Z.; Arai, M. *Renewable Sustainable Energy Rev.* **2014,** *40,* 886–901. doi:10.1016/j.rser.2014.07.194
10. He, F.; Jeon, W.; Choi, W. *Nat. Commun.* **2021,** *12,* 2528. doi:10.1038/s41467-021-22839-0
11. Wang, S.; Li, C.; Wang, T.; Zhang, P.; Li, A.; Gong, J. *J. Mater. Chem. A* **2014,** *2,* 2885–2890. doi:10.1039/c3ta14576j
12. Papailias, I.; Todorova, N.; Giannakopoulou, T.; Karapati, S.; Boukos, N.; Dimotikali, D.; Trapalis, C. *Appl. Surf. Sci.* **2018,** *430,* 225–233. doi:10.1016/j.apsusc.2017.08.084
13. Van Pham, V.; Mai, D.-Q.; Bui, D.-P.; Van Man, T.; Zhu, B.; Zhang, L.; Sangkaworn, J.; Tantirungrotechai, J.; Reutrakul, V.; Cao, T. M. *Environ. Pollut.* **2021,** *286,* 117510. doi:10.1016/j.envpol.2021.117510
14. Hoang The Vinh, T.; Minh Thi, C.; Van Viet, P. *Mater. Lett.* **2020,** *281,* 128637. doi:10.1016/j.matlet.2020.128637
15. Zhao, G.-Q.; Zou, J.; Hu, J.; Long, X.; Jiao, F.-P. *Sep. Purif. Technol.* **2021,** *279,* 119769. doi:10.1016/j.seppur.2021.119769
16. Van, K. N.; Huu, H. T.; Nguyen Thi, V. N.; Le Thi, T. L.; Truong, D. H.; Truong, T. T.; Dao, N. N.; Vo, V.; Tran, D. L.; Vasseghian, Y. *Chemosphere* **2022,** *289,* 133120. doi:10.1016/j.chemosphere.2021.133120

17. Mousavi, M.; Habibi-Yangjeh, A.; Pouran, S. R. *J. Mater. Sci.: Mater. Electron.* **2018,** *29,* 1719–1747. doi:10.1007/s10854-017-8166-x
18. Madona, J.; Sridevi, C. *Inorg. Chem. Commun.* **2022,** *138,* 109265. doi:10.1016/j.inoche.2022.109265
19. Huang, Z.; Zhao, X.; Xia, H.; Lu, F.; Hu, L.; Chu, P. K. *J. Environ. Chem. Eng.* **2021,** *9,* 105922. doi:10.1016/j.jece.2021.105922
20. Sharmin, F.; Chandra Roy, D.; Basith, M. A. *Int. J. Hydrogen Energy* **2021,** *46,* 38232–38246. doi:10.1016/j.ijhydene.2021.09.072
21. Qi, K.; Cheng, B.; Yu, J.; Ho, W. *J. Alloys Compd.* **2017,** *727,* 792–820. doi:10.1016/j.jallcom.2017.08.142
22. Murillo-Sierra, J. C.; Hernández-Ramírez, A.; Hinojosa-Reyes, L.; Guzmán-Mar, J. L. *Chem. Eng. J. Adv.* **2021,** *5,* 100070. doi:10.1016/j.ceja.2020.100070
23. Liu, D.; Kelly, T. L. *Nat. Photonics* **2014,** *8,* 133–138. doi:10.1038/nphoton.2013.342
24. Low, J.; Yu, J.; Jaroniec, M.; Wageh, S.; Al-Ghamdi, A. A. *Adv. Mater. (Weinheim, Ger.)* **2017,** *29,* 1601694. doi:10.1002/adma.201601694
25. Li, S.; Wang, C.; Cai, M.; Yang, F.; Liu, Y.; Chen, J.; Zhang, P.; Li, X.; Chen, X. *Chem. Eng. J.* **2022,** *428,* 131158. doi:10.1016/j.cej.2021.131158
26. Yu, H.; Jiang, L.; Wang, H.; Huang, B.; Yuan, X.; Huang, J.; Zhang, J.; Zeng, G. *Small* **2019,** 1901008. doi:10.1002/smll.201901008
27. Wang, C.; Cai, M.; Liu, Y.; Yang, F.; Zhang, H.; Liu, J.; Li, S. *J. Colloid Interface Sci.* **2022,** *605,* 727–740. doi:10.1016/j.jcis.2021.07.137
28. Wang, C.; Li, S.; Cai, M.; Yan, R.; Dong, K.; Zhang, J.; Liu, Y. *J. Colloid Interface Sci.* **2022,** *619,* 307–321. doi:10.1016/j.jcis.2022.03.075
29. Li, S.; Wang, C.; Liu, Y.; Cai, M.; Wang, Y.; Zhang, H.; Guo, Y.; Zhao, W.; Wang, Z.; Chen, X. *Chem. Eng. J.* **2022,** *429,* 132519. doi:10.1016/j.cej.2021.132519
30. Li, S.; Cai, M.; Wang, C.; Liu, Y.; Li, N.; Zhang, P.; Li, X. *J. Mater. Sci. Technol.* **2022,** *123,* 177–190. doi:10.1016/j.jmst.2022.02.012
31. Guo, M.; Zhou, Z.; Yan, S.; Zhou, P.; Miao, F.; Liang, S.; Wang, J.; Cui, X. *Sci. Rep.* **2020,** *10,* 18401. doi:10.1038/s41598-020-75003-x
32. An, W.; Tian, L.; Hu, J.; Liu, L.; Cui, W.; Liang, Y. *Appl. Surf. Sci.* **2020,** *534,* 147518. doi:10.1016/j.apsusc.2020.147518
33. Li, N.; Huang, M.; Zhou, J.; Liu, M.; Jing, D. *Chin. J. Catal.* **2021,** *42,* 781–794. doi:10.1016/s1872-2067(20)63690-7
34. Ge, L.; Peng, Z.; Wang, W.; Tan, F.; Wang, X.; Su, B.; Qiao, X.; Wong, P. K. *J. Mater. Chem. A* **2018,** *6,* 16421–16429. doi:10.1039/c8ta05488f
35. Shelemanov, A. A.; Evstropiev, S. K.; Karavaeva, A. V.; Nikonorov, N. V.; Vasilyev, V. N.; Podruhin, Y. F.; Kiselev, V. M. *Mater. Chem. Phys.* **2022,** *276,* 125204. doi:10.1016/j.matchemphys.2021.125204
36. Panchal, P.; Paul, D. R.; Sharma, A.; Hooda, D.; Yadav, R.; Meena, P.; Nehra, S. P. *J. Photochem. Photobiol., A* **2019,** *385,* 112049. doi:10.1016/j.jphotochem.2019.112049
37. Dhiman, P.; Rana, G.; Kumar, A.; Sharma, G.; Vo, D.-V. N.; Naushad, M. *Environ. Chem. Lett.* **2022,** *20,* 1047–1081. doi:10.1007/s10311-021-01361-1
38. Chen, J.; Xiong, J.; Song, Y.; Yu, Y.; Wu, L. *Appl. Surf. Sci.* **2018,** *440,* 1269–1276. doi:10.1016/j.apsusc.2018.01.228
39. Huang, Y.-C.; Chang, S.-Y.; Jehng, J.-M. *J. Phys. Chem. C* **2017,** *121,* 19063–19068. doi:10.1021/acs.jpcc.7b05806
40. Vaizogullar, A. I. *Kinet. Catal.* **2018,** *59,* 418–427. doi:10.1134/s0023158418040146
41. Guerrand, H.; Pucheault, M.; Vaultier, M. Ionic Liquids. *Green Process Engineering;* CRC Press:: Boca Raton, FL, USA, 2015; pp 267–291.
42. Ohtani, B. *Adv. Inorg. Chem.* **2011,** *63,* 395–430. doi:10.1016/b978-0-12-385904-4.00001-9
43. Bui, D.-P.; Pham, M.-T.; Tran, H.-H.; Nguyen, T.-D.; Cao, T. M.; Pham, V. V. *ACS Omega* **2021,** *6,* 27379–27386. doi:10.1021/acsomega.1c04215
44. Pham, M.-T.; Luu, H. Q.; Nguyen, T.-M. T.; Tran, H.-H.; You, S.-J.; Wang, Y.-F. *Aerosol Air Qual. Res.* **2021,** *21,* 210276. doi:10.4209/aaqr.210276
45. Li, S.; Hu, S.; Jiang, W.; Zhang, J.; Xu, K.; Wang, Z. *J. Colloid Interface Sci.* **2019,** *556,* 335–344. doi:10.1016/j.jcis.2019.08.077
46. Roy, S.; Madras, G. *Curr. Org. Chem.* **2015,** *19,* 2122–2131. doi:10.2174/1385272819666150603235429
47. Pham, M.-T.; Tran, H.-H.; Nguyen, T.-M. T.; Bui, D.-P.; Huang, Y.; Cao, J.; You, S.-J.; Van Viet, P.; Nam, V. H.; Wang, Y.-F. *Acta Mater.* **2021,** *215,* 117068. doi:10.1016/j.actamat.2021.117068
48. Kumar, A.; Singh, S.; Khanuja, M. *Mater. Chem. Phys.* **2020,** *243,* 122402. doi:10.1016/j.matchemphys.2019.122402
49. Xu, L.; Gao, S.; Chen, M.; Wu, Y.; Shinozaki, K. *Mater. Chem. Phys.* **2020,** *253,* 123368. doi:10.1016/j.matchemphys.2020.123368
50. Mohammed, W. M.; Yanilkin, I. V.; Gumarov, A. I.; Kiiamov, A. G.; Yusupov, R. V.; Tagirov, L. R. *Beilstein J. Nanotechnol.* **2020,** *11,* 807–813. doi:10.3762/bjnano.11.65
51. Mao, N.; Jiang, J.-X. *Appl. Surf. Sci.* **2019,** *476,* 144–150. doi:10.1016/j.apsusc.2019.01.049
52. Yuan, Y.; Zhang, L.; Xing, J.; Utama, M. I. B.; Lu, X.; Du, K.; Li, Y.; Hu, X.; Wang, S.; Genç, A.; Dunin-Borkowski, R.; Arbiol, J.; Xiong, Q. *Nanoscale* **2015,** *7,* 12343–12350. doi:10.1039/c5nr02905h
53. Chen, Z.; Sun, P.; Fan, B.; Liu, Q.; Zhang, Z.; Fang, X. *Appl. Catal., B* **2015,** *170-171,* 10–16. doi:10.1016/j.apcatb.2015.01.024
54. Bojdys, M. J.; Müller, J.-O.; Antonietti, M.; Thomas, A. *Chem. – Eur. J.* **2008,** *14,* 8177–8182. doi:10.1002/chem.200800190
55. Dobrucka, R. *Iran. J. Sci. Technol.* **2018,** *42,* 547–555. doi:10.1007/s40995-016-0076-x
56. Li, D.; Xiao, Y.; Pu, M.; Zan, J.; Zuo, S.; Xu, H.; Xia, D. *Mater. Chem. Phys.* **2019,** *231,* 225–232. doi:10.1016/j.matchemphys.2019.04.016
57. Tan, L.; Xu, J.; Zhang, X.; Hang, Z.; Jia, Y.; Wang, S. *Appl. Surf. Sci.* **2015,** *356,* 447–453. doi:10.1016/j.apsusc.2015.08.078
58. Cimino, A. *Mater. Chem. Phys.* **1985,** *13,* 221–241. doi:10.1016/0254-0584(85)90057-4
59. Peng, Q.; Dai, Y.; Liu, K.; Luo, X.; He, D.; Tang, X.; Huang, G. *J. Mater. Sci.* **2020,** *55,* 11267–11283. doi:10.1007/s10853-020-04822-0
60. Wang, P.; Guan, Z.; Li, Q.; Yang, J. *J. Mater. Sci.* **2018,** *53,* 774–786. doi:10.1007/s10853-017-1540-5
61. Vesali-Kermani, E.; Habibi-Yangjeh, A.; Ghosh, S. *J. Ind. Eng. Chem. (Amsterdam, Neth.)* **2020,** *84,* 185–195. doi:10.1016/j.jiec.2019.12.033
62. Gu, W.; Lee, J. T.; Nitta, N.; Yushin, G. *Nanomater. Nanotechnol.* **2014,** *4,* 30. doi:10.5772/59931
63. Lenes, M.; Morana, M.; Brabec, C. J.; Blom, P. W. M. *Adv. Funct. Mater.* **2009,** *19,* 1106–1111. doi:10.1002/adfm.200801514
64. Wei, F.; Liu, Y.; Zhao, H.; Ren, X.; Liu, J.; Hasan, T.; Chen, L.; Li, Y.; Su, B.-L. *Nanoscale* **2018,** *10,* 4515–4522. doi:10.1039/c7nr09660g

65. Li, Y.; Gu, M.; Zhang, X.; Fan, J.; Lv, K.; Carabineiro, S. A. C.; Dong, F. *Mater. Today* **2020,** *41,* 270–303. doi:10.1016/j.mattod.2020.09.004
66. Li, S.; Wang, C.; Liu, Y.; Xue, B.; Jiang, W.; Liu, Y.; Mo, L.; Chen, X. *Chem. Eng. J.* **2021,** *415,* 128991. doi:10.1016/j.cej.2021.128991
67. Mageshwari, K.; Mali, S. S.; Sathyamoorthy, R.; Patil, P. S. *Powder Technol.* **2013,** *249,* 456–462. doi:10.1016/j.powtec.2013.09.016
68. Karthik, K.; Dhanuskodi, S.; Gobinath, C.; Prabukumar, S.; Sivaramakrishnan, S. *J. Photochem. Photobiol., B* **2019,** *190,* 8–20. doi:10.1016/j.jphotobiol.2018.11.001
69. Wang, J.; Yu, J.; Fu, Q.; Yang, H.; Tong, Q.; Hao, Z.; Ouyang, G. *ACS Cent. Sci.* **2021,** *7,* 355–364. doi:10.1021/acscentsci.0c01600
70. Lasek, J.; Yu, Y.-H.; Wu, J. C. S. *J. Photochem. Photobiol., C* **2013,** *14,* 29–52. doi:10.1016/j.jphotochemrev.2012.08.002
71. Nikokavoura, A.; Trapalis, C. *Appl. Surf. Sci.* **2018,** *430,* 18–52. doi:10.1016/j.apsusc.2017.08.192
72. Wang, B.; Chen, D.; Li, N.; Xu, Q.; Li, H.; He, J.; Lu, J. *J. Colloid Interface Sci.* **2020,** *576,* 426–434. doi:10.1016/j.jcis.2020.05.037
73. Zou, Y.; Xie, Y.; Yu, S.; Chen, L.; Cui, W.; Dong, F.; Zhou, Y. *Appl. Surf. Sci.* **2019,** *496,* 143630. doi:10.1016/j.apsusc.2019.143630
74. Zhang, X.; Nie, J.; Rao, F.; Liu, H.; Wang, Y.; Qu, D.; Wu, W.; Zhong, P.; Zhu, G. *Ceram. Int.* **2021,** *47,* 31302–31310. doi:10.1016/j.ceramint.2021.08.003
75. Yang, X.; Cao, X.; Tang, B.; Shan, B.; Deng, M.; Liu, Y. *J. Photochem. Photobiol., A* **2019,** *375,* 40–47. doi:10.1016/j.jphotochem.2019.02.011
76. Xie, B.; Chen, D.; Li, N.; Xu, Q.; Li, H.; He, J.; Lu, J. *Chem. Eng. J.* **2022,** *430,* 132968. doi:10.1016/j.cej.2021.132968
77. Van Viet, P.; Nguyen, H.-P.; Tran, H.-H.; Bui, D.-P.; Hai, L. V.; Pham, M.-T.; You, S.-J.; Thi, C. M. *J. Sci.: Adv. Mater. Devices* **2021,** *6,* 551–559. doi:10.1016/j.jsamd.2021.07.005
78. Zhang, W.; Liang, Y. *Front. Chem. (Lausanne, Switz.)* **2019,** *7,* 664. doi:10.3389/fchem.2019.00664
79. Wen, M. Q.; Xiong, T.; Zang, Z. G.; Wei, W.; Tang, X. S.; Dong, F. *Opt. Express* **2016,** *24,* 10205–10212. doi:10.1364/oe.24.010205

License and Terms

BEILSTEIN JOURNAL OF NANOTECHNOLOGY

Recent trends in Bi-based nanomaterials: challenges, fabrication, enhancement techniques, and environmental applications

Vishal Dutta[1], Ankush Chauhan[*2], Ritesh Verma[3], C. Gopalkrishnan[4] and Van-Huy Nguyen[*2]

Review

Open Access

Address:
[1]School of Advanced Chemical Sciences, Shoolini University, Solan, Himachal Pradesh 173212, India, [2]Chettinad Hospital and Research Institute, Chettinad Academy of Research and Education (CARE), Chengalpattu district, Kelambakkam, Tamil Nadu, 603103, India, [3]University Centre for Research and Development, Chandigarh University, 140413, India and [4]Department of Physics and Nanotechnology, SRM Institute of Science and Technology, Tamil Nadu, 603203, India

Email:
Ankush Chauhan[*] - ankushchauhan18@gmail.com;
Van-Huy Nguyen[*] - vhnguyen.ChE@gmail.com

* Corresponding author

Keywords:
bismuth-based nanomaterials; environmental remediation; heterojunction formation; photocatalysis

Beilstein J. Nanotechnol. **2022,** *13,* 1316–1336.
https://doi.org/10.3762/bjnano.13.109

Received: 15 July 2022
Accepted: 13 October 2022
Published: 11 November 2022

This article is part of the thematic issue "Nanomaterials for photocatalysis and applications in environmental remediation and renewable energy".

Guest Editor: V. V. Pham

Abstract

One of the most enticing approaches to environmental restoration and energy conversion is photocatalysis powered by solar light. Traditional photocatalysts have limited practical uses due to inadequate light absorption, charge separation, and unknown reaction mechanisms. Discovering new visible-light photocatalysts and investigating their modification is crucial in photocatalysis. Bi-based photocatalytic nanomaterials have gotten much interest as they exhibit distinctive geometric shapes, flexible electronic structures, and good photocatalytic performance under visible light. They can be employed as stand-alone photocatalysts for pollution control and energy production, but they do not have optimum efficacy. As a result, their photocatalytic effectiveness has been significantly improved in the recent decades. Numerous newly created concepts and methodologies have brought significant progress in defining the fundamental features of photocatalysts, upgrading the photocatalytic ability, and understanding essential reactions of the photocatalytic process. This paper provides insights into the characteristics of Bi-based photocatalysts, making them a promising future nanomaterial for environmental remediation. The current review discusses the fabrication techniques and enhancement in Bi-based semiconductor photocatalysts. Various environmental applications, such as H_2 generation and elimination of water pollutants, are also discussed in terms of semiconductor photocatalysis. Future developments will be guided by the uses, issues, and possibilities of Bi-based photocatalysts.

Introduction

Nanomaterials photocatalysis is a “green” integrative technique that combines physics, chemistry, and materials science with chemical engineering to catalyze chemical processes and transform constantly recoverable solar energy into productive chemical energy [1]. Various semiconductor nanoparticles have been used as effective photocatalysts in essential photocatalytic applications such as wastewater treatment, water dissociation, and energy conversion/storage due to their reactivity, surface area, and advantageous features compared to their bulk counterparts [2-4]. In recent years, many efforts have increased the photocatalytic performance. However, the relative photocatalytic performance is still deficient, and it does not fulfil the criteria for the practical implementation of photocatalysis techniques. Among many approaches, attention has been paid to altering and modifying the properties of photocatalytic materials [5,6]. Environmental treatment and energy conversion using photocatalytic technology have shown to be cost-effective and environmentally beneficial alternatives [7]. The choice of the photocatalysts is one of the most important steps in attaining high performance in photocatalysis. Semiconductors with bandgaps greater than 3 eV are called wide-bandgap photocatalysts. These semiconductors include oxides (e.g., TiO_2, Bi_2O_3, Bi_2WO_6, and $SrTiO_3$), sulfates (e.g., MoS_2 and Bi_2S_3), selenides (e.g., $MoSe_2$ and CdSe), and phosphates (e.g., Ag_3PO_4) [8-15].

The bandgap of photocatalysts sensitive to visible light is smaller than 3 eV. Wide-bandgap photocatalysts can only be stimulated by ultraviolet light, which makes up less than 5% of the absorbed solar radiation. Hence, developing photocatalysts that react to visible light is essential for photocatalysis since 43% of the total energy from the sun belongs to the visible spectrum [1,16]. Bi-based nanomaterials are photocatalysts that respond to visible light and have adequate bandgaps and performance. Bi_2MO_6 (M = Mo, W), $(BiO)_2CO_3$, Bi_2S_3, BiOX (X = I, Br, Cl), $BiPO_4$, $BiVO_4$, Bi_2O_3, and other Bi-based nanomaterials have been designed and examined for photocatalysis. The vast majority of these compounds have a layered structure, which causes an internal electric field (IEF) between the layers. This electric field allows photogenerated charge carriers to be separated and moved effectively [17-21].

A range of visible-light-active Bi-based photocatalysts has lately raised curiosity among semiconductor photocatalysts. Bi^{3+} has a higher stability than Bi^{5+}. The earlier compounds have been examined more thoroughly than the latter. The overlap of O 2p and Bi 6s orbitals in the valence band (VB) of Bi^{3+}-containing compounds improves photogenerated charge mobility and, hence, improves photocatalytic activity [22,23]. Furthermore, except for BiOF, BiOCl, and $(BiO)_2CO_3$, most Bi-based compounds have bandgaps that may be stimulated by visible light. As a result, much interest in environmental cleanup and energy conversion research has been sparked by Bi compounds [24]. Because of their advanced photocatalytic process, more and more publications on synthesizing and applying a semiconductor photocatalyst have been published in recent years. A survey on bismuth-based nanocomposites with the search keywords "Bismuth-based nanoparticles for environmental remediation" from 2011 to 2021 yields roughly 15,995 articles. This data illustrates the interest of the scientific community in environmental cleanup using bismuth-based nanoparticles (Figure 1). In recent years, an abundance of Bi-based photocatalysts has been reported.

The most commonly used Bi-based photocatalysts include metallic Bi, Bi-based binary oxides, Bi-based oxyhalides, Bi-based multicomponent oxides, and binary Bi sulfides. Bismuth oxyhalides are indirect bandgap semiconductors in which photogenerated electrons and holes rarely recombine. BiOX is an excellent photocatalyst, and it is widely applied due to its small bandgap and high electron density, which are easily adjustable by changing the type of halogen used. The activation of otherwise inert CO_2 and H_2O molecules is greatly aided by the ease with which photoinduced oxygen vacancies (OVs) are produced on the surface [25]. The excellent photocatalytic performance can be attributed to the layered crystal structures and small bandgap energies. Many persistent organic contaminants can be degraded at room temperature through the oxidizing power of VB holes in bismuth oxyhalides [26]. BiOCl, BOI, BiOBr, and composites made from them have been widely reported due to their excellent photocatalytic properties [27-29]. However, the photocatalytic effectiveness of those semiconductors is inadequate for practical environmental and energy conservation applications because of substantial electron–hole recombination and a low capacity for the absorption of visible light. Numerous attempts have been made, with an emphasis on doping, the creation of heterojunctions, crystal plane management, and defect development, to enhance the photocatalytic efficacy of pristine Bi-based photocatalysts [1,30]. The photocatalytic processes of Bi-based photocatalytic applications have received little attention in environmental remediation and energy conversion. The rapidity with which this vital subject is advancing necessitates a thorough examination of recent breakthroughs regarding Bi-based photocatalysts. Consequently, in this work, Bi-based semiconductor photocatalysts and their manufacturing methods are discussed to make use of these photocatalysts in eco-friendly applications on a large scale. Bi-based nanomaterials as semiconductor photocatalysts are one of the study’s primary goals, as is the use of Bi-based nanomaterials for wastewater treatment, hydrogen generation, and photocatalytic degradation. Fabrication methods, reliability analo-

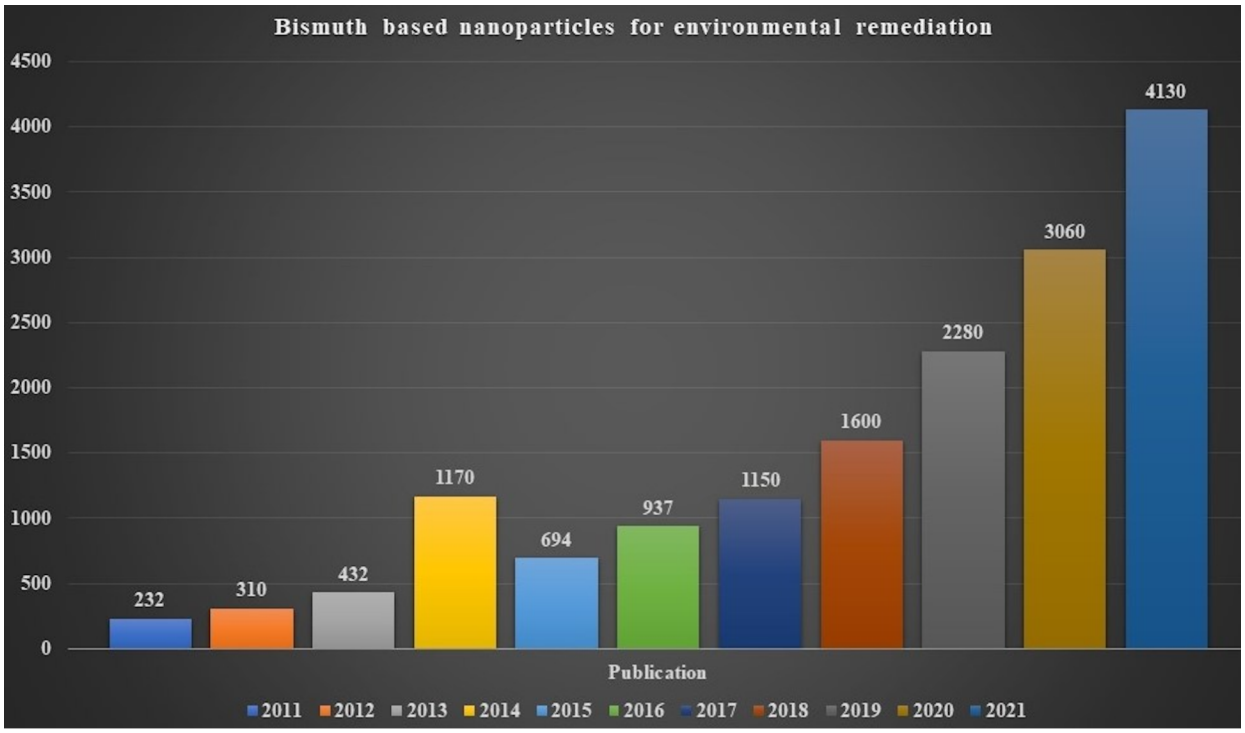

Figure 1: Reported publications from 2011 to 2021 were searched on 6th June 2022 using the keyword "Bismuth-based nanoparticles for environmental remediation". Data was extracted from Web of Science, Clarivate Analytics.

gies, and future challenges of photocatalysts derived from bismuth-based nanomaterials are also discussed. There are many review reports on synthesis and enhancement techniques of Bi-based photocatalysts and the application of these photocatalysts in hydrogen generation, CO_2 reduction, and water purification [31-35]. However, the present report focuses on understanding the role of different Bi-based photocatalysts concerning their synthesis method and enhancement. The mechanism of photocatalysts for different applications has been described for the type or nature of the photocatalyst. Hopefully, this work will help researchers understand how Bi-based nanomaterial photocatalysts may be employed in different environmental remediation systems by understanding the properties of Bi-based nanomaterials photocatalysts.

Review

Photocatalysis

Photocatalysis and its challenges

Photocatalysis can transform solar energy into storable chemical energy. Because of its minimal energy intake and carbon footprint, it is eco-friendly and promising. Two examples are the conversion of CO_2 to hydrocarbons and water splitting to H_2 and O_2 [36,37]. Also, it is essential in domains including pollution degradation, antibiotic treatment, and sterilization [38]. The term "advanced oxidation processes" has become more common recently. In this process, many oxidizing agents (·OH) are created. Electron–hole pairs are formed in AOPs when the VB electrons of semiconductor photocatalysts are driven into the conduction band (CB) through visible light [39]. The holes in the valence band of the catalyst split water to hydroxyl radicals ($^{\bullet}OH$). Electrons in the CB of a semiconductor photocatalyst can generate the superoxide anion ($^{\bullet}O_2^-$) when they interact with oxygen molecules. During the photocatalytic oxidative degradation, the most notable oxidizing species are $^{\bullet}OH$, photogenerated holes, and $^{\bullet}O_2^-$. These species are responsible for the photodegradation of organic and inorganic contaminants in wastewater [40]. To date, it is widely understood that the main limitation of photocatalysts is their low photocatalytic efficiency. The reason is that photogenerated electrons and holes recombine quickly [41]. We use an analogy for a more straightforward comprehension of the recombination timeframe. The force of gravity ensures that any item thrown into the air will return to the Earth below within a few seconds. After being exposed to light, electrons in a single photocatalyst undergo a transition akin to an item thrown into the air. This transition takes place from the VB to the CB [42]. After that, the very powerful Columbic force among photogenerated electrons and holes pulls them together, enabling recombination within a few picoseconds to nanoseconds in bulk or on the photocatalyst surface. It is possible to have a better understanding of the

timescale by contrasting the calculation of the gravitational force with the computation of the Coulomb force. Because the gravitational constant (6.67×10^{-11} N·m^2·kg^{-2}) is significantly smaller than the Coulomb constant (8.99×10^9 N·m^2·C^{-2}), the recombination of the photogenerated electron and hole pairs takes significantly less time than the fall of the object. Within a single photocatalyst, photogenerated electrons and holes cannot withstand the tremendous force, which results in rapid recombination [43]. In addition to a low rate of recombination, other essential qualities of a superior photocatalyst include broad sunlight absorption and enough redox capacity. A small bandgap is desirable regarding a broad light absorption band. However, when redox ability is considered, the catalyst should have a high CB position and a low VB position, resulting in a large bandgap. These two prerequisites are not compatible. As a direct consequence of this, heterojunctions are produced. To create heterojunction photocatalysts, two semiconductor photocatalysts are combined [44,45]. Consequently, researchers focus their attention mainly on heterojunction photocatalysts.

Promising Bi-based nanomaterials

The overwhelming number of Bi-based semiconductors utilized in photocatalysis also have a distinctive layered structure and a bandgap of less than 3.0 eV. The connections between the layers are just van der Waals forces, which are weak [46]. Metal oxides such as TiO_2 only have the O 2p orbital in their VB. In contrast , Bi-based oxide materials have an electronic structure in which O 2p and Bi 6s orbitals are paired in the VB. The bandgap of the semiconductor may be reduced to 3.0 eV thanks to the significant charge carrier dispersion provided by hybrid orbitals involving the Bi 6s orbital, as seen in Figure 2. Photoinduced electron–hole separation and charge carrier transfer in Bi-based materials are facilitated by a unique layered structure that creates an IEF. A magnetic field is generated between layers of Bi-based materials [47]. Many researchers have revealed that Bi-based nanomaterials have an adequate photocatalytic capacity for pollution remediation, water splitting, and the elimination of volatile organic compounds. Bi-based photocatalysts have substantial oxidative capabilities, as illustrated in Figure 2, since their VB potential is much higher than the oxidation potential of H_2O, that is, 0.82 V vs NHE. Unfortunately, due to inadequate CB potential energy, most reduction processes, such as CO_2 reduction, N_2 fixation, and H_2 creation, cannot be catalyzed with Bi-based nanomaterials. However, a few Bi-based semiconductor photocatalysts, such as Bi_2S_3, have a more substantial negative CB potential, making reduction reactions possible [34,48,49]. However, in real applications, the usefulness of Bi_2S_3 is limited because of the quick recombination of electrons and holes. New research has shown that it is possible to generate H_2 or reduce CO_2 by carefully controlling the production procedure of ultrathin photocatalysts based on Bi. Compared to Bi_2WO_6 formed using a solid-state reaction, single-unit-cell layers of Bi_2WO_6, synthesized using a hydrothermal process, offered three times greater CO_2 adsorption and

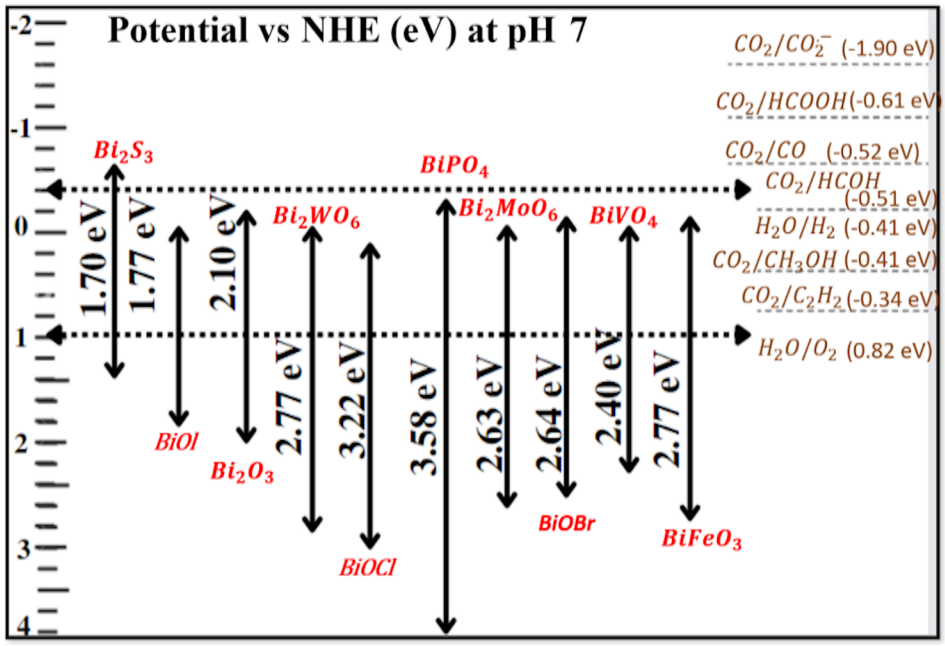

Figure 2: Bi-based photocatalysts exhibit substantial oxidative capabilities for various redox processes.

enhanced light absorption. The enhanced properties were reflected in the photocatalytic activity, resulting in a rate of methanol synthesis of 75 $mol \cdot g^{-1} \cdot h^{-1}$, which was much greater than the rate produced by the unaltered Bi_2WO_6. As a result of the decrease in dimensionality, it was projected that there would be a significant confinement effect and enlarged bandgap energy. Additionally, an upshift of the CB and a downshift of the VB were also measured [48,50]. The preparation process can be used to modify the electrical structure of Bi-based semiconductors. Most Bi-based semiconductors, especially oxide semiconductors such as Bi_2O_3, $BiVO_4$, and Bi_2WO_6, have n-type properties with electrons as the majority carrier. Recent research suggests that the synthesis route can shift the conductivity types of Bi-based materials [45,51].

Fabrication routes

Synthesis approaches affect the topological size and size distribution of semiconductor photocatalysts, substantially influencing adsorption characteristics and photocatalytic efficacy. As well as affecting the environment, synthesis size, and cost, the fabrication method also affects manufacturing safety considerations [52]. Bi-based photocatalysts may currently be synthesized using various methods, the most common of which are hydrothermal synthesis, solid-state reaction, and design and optimization.

Today, $NaBiO_3 \cdot 2H_2O$, Bi_2O_3, $Bi(NO_3)_3 \cdot 5H_2O$, $BiCl_3$, and Bi are the most common Bi-based semiconductor photocatalysts. The hydrothermal process is one of the most frequent and widely utilized synthesis methods. Morphology, facets, size, surface flaws, and dimensionality of Bi-based photocatalysts are all susceptible to change when the synthesis conditions are altered. Generally, the hydrothermal technique yield a higher quality, and the nanoparticles that result from this process are more suited for specific applications than photocatalysts manufactured using dry methods [53]. However, the hydrothermal approach has a noticeable limitation in output yield. The usage of specific autoclaves has resulted in a long manufacturing time and the batch nature of production. For the hydrothermal technique, there is a danger of nanoparticle leakage, primarily in water, and the risk of toxic solvent emissions. Su et al. [54] reported the first hydrothermal fabrication of Bi_5O_7Br. Bi_5O_7Br rods of 50 μm length and 2 μm width were obtained. They found that Bi_5O_7Br effectively converts molecular oxygen to superoxide radicals and hydroxyl radicals in visible light. Under UV–vis irradiation, Bi_5O_7Br showed a higher photocatalytic activity in the degradation of rhodamine B (RhB) dye than BiOBr. The addition of Bi_5O_7Br photocatalysis to the Bi–O–X photocatalytic system improved the system. In this work, they found that the RhB elimination percentage over Bi_5O_7Br is 85% after 120 min of UV–visible-light irradiation, and the reaction rate constant was measured as 1.496 $h^{-1} \cdot m^{-2}$. In contrast, the reaction rate constant for BiOBr was found to be only 0.154 $h^{-1} \cdot m^{-2}$. Additionally, the hydrothermally fabricated Bi_5O_7Br has also excellent stability when exposed to light in aqueous environments. The photocatalytic performance was not much decreased after eight cycles. Recently, Lin et al. fabricated a monoclinic $BiVO_4$ photocatalyst via a surfactant-free hydrothermal technique [55]. According to the results, the pH value has a significant impact on shape, surface area, particle size, and V–O bond length. The grain size was reduced when the pH value was raised, and the crystal structure became more closely stacked. Under visible-light irradiation, the RhB photodegradation efficiency of the coralloid particles produced at pH 7 was about four times greater than that of the sample synthesized at pH 0.5. The increased photocatalytic activity was caused by several factors, such as a synergistic effect of highly exposed (010) grain facets, an increase in the overlap between Bi 6s and O 2p orbitals, a reduced charge transfer route, and strange floating features. In another approach, Huang et al. reported a one-step hydrothermal synthesis of a $BiIO_4/Bi_2MoO_6$ hybrid photocatalyst for photodegradation of RhB dye [56]. Under visible-light irradiation ($\lambda > 420$ nm), photoelectrochemical studies demonstrated that the RhB photodegradation effectiveness and photocurrent density of the $BiIO_4/Bi_2MoO_6$ hybrid composite is much higher than that of the pure components. Because of the successful construction of the $BiIO_4/Bi_2MoO_6$ hybrid, the photocatalytic activity was found to be significantly increased. This improvement was ascribed to the efficient interfacial charge transfer obtained as a consequence of the process. According to the active species trapping study, the photocatalysis process is significantly aided by the presence of photogenerated holes.

It has been shown that the hydrothermal method of fabricating Bi-based semiconductor photocatalysts offers some significant benefits. Nanostructured materials have several advantages, including a more adaptable area for more detailed reconstruction, confinement effects, superior mechanical stability, and large surface area, which make them excellent for photocatalysis. The progress of synthesis processes allows one to change the physical properties as needed.

In order to create economically viable Bi-based photocatalysts, substantial amounts of water are required. Solid-state reaction methods that do not require water are suitable for large-scale synthesis. However, in solid-state reaction methods, there is the risk of a release of nanoparticles into the air; as a result, they are not entirely eco-friendly [57]. He et al. reported the fabrication of a Bi_4NbO_8Br photocatalyst via solid-state synthesis [58]. They found that the temperature used during calcination plays a vital role. A higher calcination temperature results in a more

crystalline morphology with more active sites for photocatalytic activity. The fabricated specimens were utilized for the photodegradation of RhB under visible light. The sample calcinated at 750 °C revealed the highest photocatalytic performance. Hamza et al. fabricated $Bi_2(CrO_4)_3$ nanoparticles via a facile precipitation technique [59]. The photocatalytic activity of the $Bi_2(CrO_4)_3$ nanoparticles was studied under UV, AM 1.5, and visible-light irradiation, and acceptable rates of 522.44, 174.15, and 88.24 $\mu mol \cdot g^{-1} \cdot h^{-1}$, respectively, were reached under these conditions. These rates outperform those of other similar Bi-based semiconductor photocatalysts reported in the literature.

To synthesize Bi-based photocatalysts with high anisotropy, hollow structures, or crystalline multidimensional forms, the template technique is one of several synthesis approaches. Direct manufacturing processes make this almost impossible. Therefore, using templates is a great workaround [60]. Template methods may be characterized either as a "hard templates", "soft templates", or "self-templates". The high cost of template methods results from the lengthy process of creating and removing templates. Also, environmental aspects need to be considered as removing templates such as SiO_2 requires using very corrosive acids or bases [61]. Numerous studies have focused on choosing templates for making nanostructures of functional materials. However, templates were chosen rather based on utility than on cost. The self-template technology does not require additional templates, which leads to less expensive production and increased efficiency. This makes the approach more realistic for practical applications [62]. A very good micro-/nanoscale hierarchical $Bi_7O_9I_3$/NTC photocatalyst was created in a one-step, easy, and environmentally friendly way by Hou et al., who used an in situ ion exchange–recrystallization approach [63]. The used buffer provided a relatively stable environment for producing regular structures. The aqueous NH_3 solution provided OH^- ions for the successful exchange of I^-, and the result was the synthesis of $Bi_7O_9I_3$. The $Bi_7O_9I_3$/NTC has evenly distributed $Bi_7O_9I_3$ nanostructures in the shape of lanterns formed of extremely thin nanosheets with a thickness of less than 10 nm on both the surface and the inside. When exposed to visible light, $Bi_7O_9I_3$/NTC displayed higher photocatalytic activity owing to the synergistic effect of the micro-/nanoscale hierarchical structure, low iodine content, and well-contacted interface. 93.5% methyl orange (MO) and 96.6% RhB were eliminated from solution during in two hours, suggesting a greater photocatalytic effectiveness than that of pure BiOI. To deposit metallic Bi on Bi_2WO_6 nanosheets, an in situ reduction approach using $NaBH_4$ as the reducing agent was used [64]. Compared to pure Bi_2WO_6, Bi-coated Bi_2WO_6 absorbs more visible light, is more sensitive to photocurrent, and has a lower electrochemical impedance rate. This is because of surface plasmon resonances (SPRs) and the electron transport capabilities of Bi. The photocatalytic activity for the breakdown of phenol was significantly improved, compared to pristine Bi_2WO_6 under visible light. Xiao and colleagues have shown a straightforward synthesis approach for fabricating Bi_2WO_6 nanosheet rods [65]. They discovered that the hydrolysis of the precursor $Bi(NO_3)_3$ may quickly result in the formation of $Bi_6O_5(OH)_3(NO_3)_5 \cdot 3H_2O$ nanorods, which then acted as templates for the generation of Bi_2WO_6. It has been observed that the newly generated Bi_2WO_6 has a greater BET surface area and superior charge transfer kinetics. These properties point to an increase in photocatalytic activity. Other Bi-based hollow hierarchical structures, such as $BiVO_4$, have the potential to be synthesized and used as CO_2 reduction photocatalysts. This possibility exists since these structures are hollow. It is anticipated that hierarchical Bi-based photocatalysts produced would have a broad range of applications in environmental science and energy research.

Different preparation methods have been employed for the synthesis of Bi-based photocatalysts. Each method has unique advantages and disadvantages, which are compared and contrasted in Table 1. New strategies are still required to create suitable nanomaterials by overcoming faults and enhancing the synthesis process. The hydrothermal approach is the one that is most often used to produce nanomaterials. This is because it is easy to implement and allows for a complete control over the shape and size of the nanoparticles.

Enhancement techniques

The characteristics of a semiconductor photocatalyst alter as its size is reduced to the nanoscale. Increasing the proportion of atoms or ions exposed on the photocatalyst surface will increase the number of photocatalytically active sites [75]. Under light irradiation, the average amount of time it takes for a photogenerated carrier to diffuse from the bulk to the surface may be calculated as follows: $\tau = r^2/\pi^2 D$, where r is the grain radius and D is the carrier's diffusion coefficient. Consequently, as the particle radius decreases, a higher number of photogenerated carriers can reach the surface, where they might participate in a photocatalytic process [76]. Bismuth is often used as a nanoscale plasmonic photocatalyst. Nanospheres, nanorods, and nanosheets can be synthesized using various techniques. Hydrothermal calcination, template synthesis, precipitation, reverse micro-emulsion, sonochemical procedures, and microwave methods are typical techniques for fabricating Bi-based nanostructures [77]. Recombination of charge carriers and insufficient photon absorption are the two most common problems related to semiconductor photocatalysts. Also, it is necessary to have a wide bandgap to yield an adequate redox ability. However, a moderate bandgap is required to perform photocatalysis

Table 1: Various fabrication techniques, their advantages, and limitations.

No.	Technique	Advantages	Limits	Ref.
1	solid-state technique	high crystallinity, easy operation	phase transition, high temperature, big grain particle, tiny surface area	[66]
2	chemical precipitation	convenient synthesis, low cost, and low energy consumption	aggregation of particles, limited surface area, development of impurities, uncontrolled morphology	[67]
3	sol–gel technique	controllable morphology, nanoparticles, tiny and fine particles	organic residues, high costs, and treatment procedure	[68]
4	hydrolysis	different particles size, easy synthesis conditions, and simple equipment	uncontrollable morphology, solvent-dependent, poor dispersion	[69]
5	hydrothermal	simple operation, high crystallinity, a variety of morphologies, and particle size control	high pressure, different reaction parameter	[70]
6	drop casting method	convenient precipitation, easy operation	time-consuming, unpredictable thickness and homogeneity, and poor adhesion	[71]
7	dip/spin-coating	simple operation, thickness control, homogenous film	inadequate attachment, specialized equipment	[72]
8	spray pyrolysis	quick and easy operation, cost-effective, scalable technique, controlled thickness, complex composites production	high temperature, high cost, unwanted precipitates production, and high resistance	[66]
9	hydrothermal coating	easy synthesis, good conductivity, long durability, and controllable morphology	high pressure, poor yield, complex parameters, and poor dispersion	[68]
10	chemical vapor deposition	regular thickness, minimal porosity, diverse materials, and a high degree of crystallinity	extreme temperatures and specialized equipment	[66]
11	anodization technique	large-scale synthesis, large surface area, and morphological control	applied bias, complex synthesis parameters	[73]
12	electrodeposition technique	thickness control, homogenous film	specific equipment, imposed bias, and treatment procedure	[74]

using visible light. This gap is essential for improving the material's light-harvesting capabilities [78,79]. Consequently, in an attempt to improve the photocatalytic efficiency for water purification and other environmental applications, a variety of techniques, such as defect formation, metal/non-metal doping, heterostructure formation, interface modification, and Bi-content enhancement, have been employed.

Defect formation

Vacancies and defects affect the electrical properties of Bi-based semiconductor photocatalysts and, hence, govern the photocatalytic efficacy. Rao et al. reported an N_2-assisted heat treatment approach for the in situ synthesis of a series of oxygen-vacancy (OV)-rich Bi^0/Bi-based photocatalysts [80]. A new understanding of how Bi^0 nanoparticles and OVs are created in situ in Bi-based photocatalysts has been reported. Compared to other Bi-based photocatalysts, Bi^0/OV–$(BiO)_2CO_3$ showed high photocatalytic performance and stability for the photooxidative elimination of NO. The ohmic interaction between OV–$(BiO)_2CO_3$ and Bi^0 has been shown to promote the synthesis of $^{\bullet}O_2^-$ and $^{\bullet}OH$ species. It was found that $^{\bullet}O_2^-$ had a significant impact on the photocatalytic elimination of NO.

In another approach, Huang et al. reported that BiOI microspheres served as self-sacrificing templates for in situ phase transformation and formation of phase junctions [81]. Different bismuth oxyiodides were formed as a result of this. Hierarchical BiOI, $Bi_4O_5I_2$, $Bi_4O_5I_2$–Bi_5O_7I phase-junction, and Bi_5O_7I may be synthesized from bismuth oxyiodides at different temperatures (Figure 3a). The photoabsorption wavelength of these bismuth oxyiodides has been tuned between 400 and 700 nm. Also, these compounds have a distinctive microstructure and a controllable band structure. (Figure 3b). The breakdown of antibiotics and pollutants such as tetracycline hydrochloride, bisphenol A (BPA), and RhB was used to measure the photocatalytic activity of the bismuth oxyiodides. The activity decreased in the sequence $Bi_4O_5I_2$–Bi_5O_7I > $Bi_4O_5I_2$ > BiOI, which is linked to charge separation efficiency and band structure. Engineered Bi vacancies in monolayered Bi_2WO_6 nanosheets with a thickness of 1.0 nm have recently been shown [82]. The Bi defects were shown to promote the adsorption and activation of reactant molecules, which reduced the energy barrier even more. The photocatalytic performance corroborated this. The presence of divacancies may help increase charge carrier separation by capturing photogenerated electrons close to the divacancies. In comparison, pure Bi_2WO_6 nano-

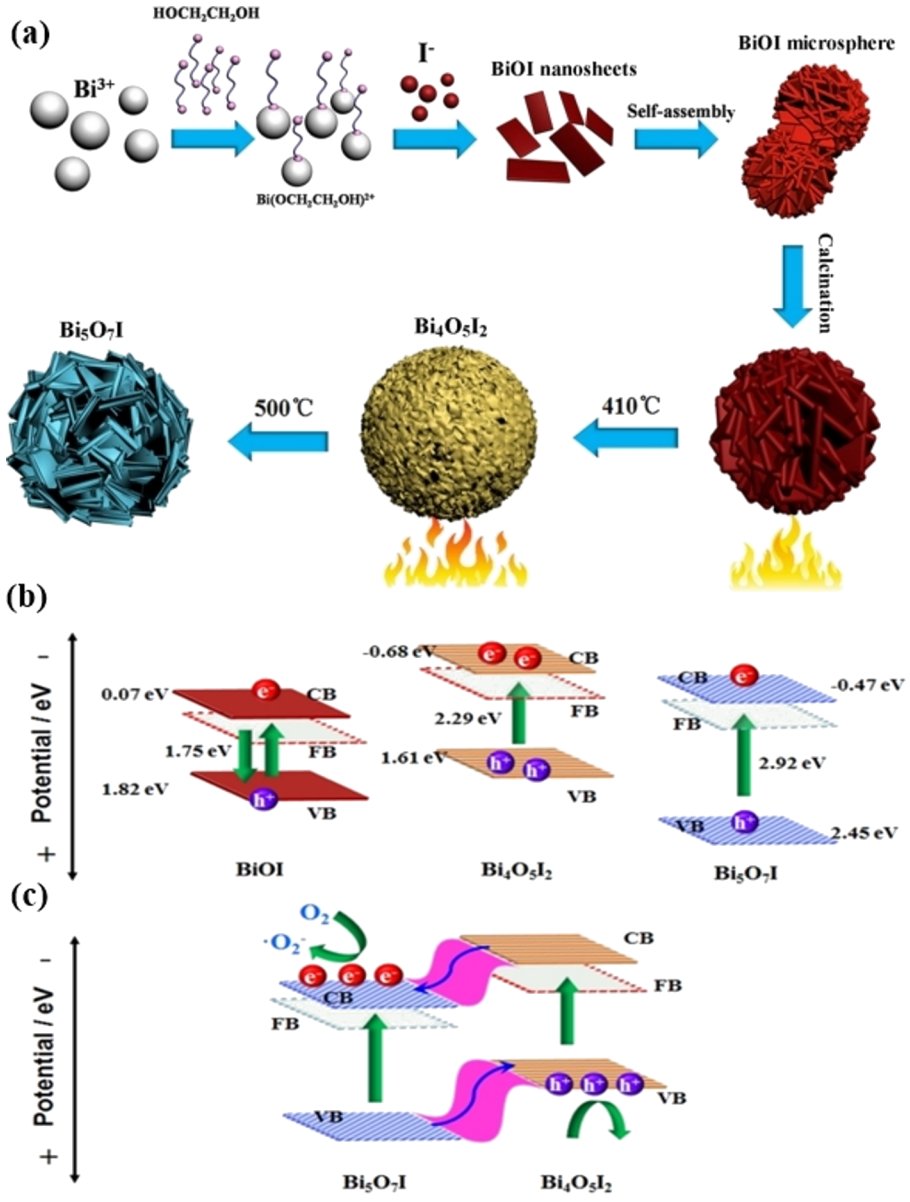

Figure 3: (a) The hierarchical structures of BiOI, $Bi_4O_5I_2$, $Bi_4O_5I_2$–Bi_5O_7I composite, and Bi_5O_7I are shown in this diagram. A schematic description of the charge segregation and transfer process for (b) the single photocatalyst of BiOI, $Bi_4O_5I_2$, and Bi_5O_7I, and (c) $Bi_4O_5I_2$–Bi_5O_7I phase junction. Figure 3a–c were reprinted from [81]. This article was published in Applied Catalysis B: Environmental, vol. 203, by H. Huang; K. Xiao; T. Zhang; F. Dong; Y. Zhang, "Rational design on 3D hierarchical bismuth oxyiodides via in situ self-template phase transformation and phase-junction construction for optimizing photocatalysis against diverse contaminants", pages 879–888, Copyright Elsevier (2016). This content is not subject to CC BY 4.0.

sheets had a photocatalytic performance 32 times lower for the elimination of gaseous toluene when exposed to visible light.

Recently, Zou et al. proposed a simple hydrothermal synthesis for preparing 2D BiOCl nanosheets [83]. This was accomplished by altering the pH value of the precursor solution and using of dulcitol ($C_6H_{14}O_6$) as surfactant. The pH value substantially influenced the thickness of the nanosheets and the fraction of exposed (001) facets. The sample synthesized at pH 4 demonstrated outstanding visible-light photocatalytic performance regarding the degradation of RhB. This was due to the low thickness, exposed (001) facets, and an appropriate number of oxygen vacancies. This work proposed that revolutionary photoexcitation mechanisms were found on oxygen vacancies. Irradiation with visible light excites the electrons in the VB to transition into defect states. In addition, photogenerated defect states cannot readily recombine with photogenerated holes because oxygen vacancies operate as electron traps. Because of this, electrons trapped inside the oxygen vacancies have a longer lifetime than those in the CB. Therefore, electrons in

defect states have the potential to react with oxygen that has been adsorbed by oxygen vacancies, which results in the production of superoxide $^{\bullet}O_2^-$ radicals. These may subsequently be employed to drive photocatalytic processes. The absence of a metal atom would considerably affect the amount of absorbed light, the rate of charge transfer, and the number of reactive surface sites.

Metal/non-metal doping

Photocatalysts based on bivalent cations may be enhanced by doping them with additional elements. Self-doping and deposition and doping of metals and non-metallic elements are the most common doping methods. Metal ions modify the crystal structure of the Bi-based semiconductor photocatalysts or induce defects. Also, the photocatalytic properties may be altered by doping or deposition of metallic components [84,85]. Using a straightforward hydrothermal procedure, Hu et al. produced iron-doped Bi_2WO_6 nanocomposites [84].

In comparison to pristine Bi_2WO_6, Fe-doped Bi_2WO_6 exhibits superior visible-light photoabsorption, a considerably increased number of oxygen vacancies, and a noticeably improved capacity for separating photogenerated electrons and holes. As a result of the Fe doping, an impurity energy level was produced close to the VB, and an imperfection (oxygen vacancy) energy level was produced close to the CB. Both of these energy levels are in a position to potentially accept photoinduced holes and electrons, which significantly improves the electron–hole pair splitting. When Fe^{3+} substitutes W^{6+}, the structure of the crystal is not compromised in any way; nevertheless, numerous additional oxygen vacancies are produced. The increased electron–hole pair separation is the driving factor behind the improved photocatalytic activity of the Fe-doped Bi_2WO_6 compound. When exposed to visible light, Fe-doped Bi_2WO_6 exhibited photocatalytic degradation rates that were 11.9 and 8.0 times higher than those of pristine Bi_2WO_6. This material was also found to be superior to the majority of modified Bi_2WO_6 photocatalysts that had been reported in the past. In addition to this, Fe-doped Bi_2WO_6 has a high degree of stability. The results of this study provide new information on boosting the photoactivity of Fe-doped Bi_2WO_6.

The SPR effect can be obtained by the deposition of metallic elements on a semiconductor surface. SPRs can potentially boost quantum yield by broadening the spectral response range of semiconductors. Fe, Au, Co, Ag, Ni, Bi, Al, and other metallic elements are often deposited and doped. For example, a nanostructure composite based on plasmonic Ag metal nanoclusters and monoclinic $BiVO_4$ nanoparticles was fabricated using high-energy ball milling [86]. Ag clusters (5–10 nm) were homogeneously distributed on the flocculated $BiVO_4$ particles (50–100 nm). The structure of the Ag-doped $BiVO_4$ nanocomposite would promote the efficiency of the photodegradation of acid blue dyes. Huang and co-workers observed that a Bi-Bi_2WO_6 composite successfully degraded RhB and 4-chlorophenol under visible light [87]. They reported that the formed heterojunction yielded a two times higher RhB photodegradation and a three times higher 4-chlorophenol photodegradation than bare Bi_2WO_6.

Using nonmetal doping, doping energy levels may be created between CB and VB of Bi-based photocatalysts. This can increase light absorption, and charge transfer may be improved to enhance electron–hole segregation and reduce recombination. It is not uncommon to see nonmetals atoms replaced with heteroatoms, such as N (C), B (S), X (F, Cl), Br (I). Dong et al. [88] reported the fabrication of boron-doped Bi_3O_4Cl ultrathin nanosheets via a solvothermal technique, which were found to have enhanced solar absorption and efficient electron–hole separation. The B atoms enhance the photocatalytic performance via (1) producing mid-gap states to widen the light response region significantly up to 557 nm and (2) functioning as electron capture centers to accelerate charge carrier separation. According to ESR measurements, B-doped Bi_3O_4Cl can create more $^{\bullet}O_2^-$ and $^{\bullet}OH$ radicals. Consequently, the B-doped sample has a 3-fold and 2.1-fold better degradation efficiency for, respectively, BPA and ciprofloxacin than pristine Bi_3O_4Cl. This study offers fresh perspectives on photocatalyst design and underlines the importance of electronic structure modification in catalytic activity adjustment.

Self-doping is a novel approach for introducing intermediates from the synthesis process into photocatalysts to alter the energy band structure and increase photocatalytic activity [89]. A simple two-step technique was used to develop a novel compound photocatalyst of Bi/BiOBr-Bi^{5+} [90]. X-ray diffraction, field-emission transmission electron microscopy, and X-ray photoelectron spectroscopy revealed the coexistence of self-doped Bi^{5+} and in situ deposited Bi(M). Compared to Bi/BiOBr or BiOBr–Bi^{5+}, the photocatalytic activity of Bi/BiOBr-Bi^{5+} regarding RhB degradation under visible light was significantly increased. OVs helped in separating photoexcited carriers, and SPRs enhanced the ability to absorb visible light. The photocatalytic activity of Bi(M) was further enhanced by the exposure of (010) facets (Figure 4a). Bi^{5+} reduced the bandgap of BiOBr, which led to an increase in the density of carriers. Examining electron transfer channels and identifying the most active species led to a credible mechanism for RhB degradation (Figure 4b,c).

It has been shown that the carrier combination centers may easily get doped at a deep level, considerably lowering photo-

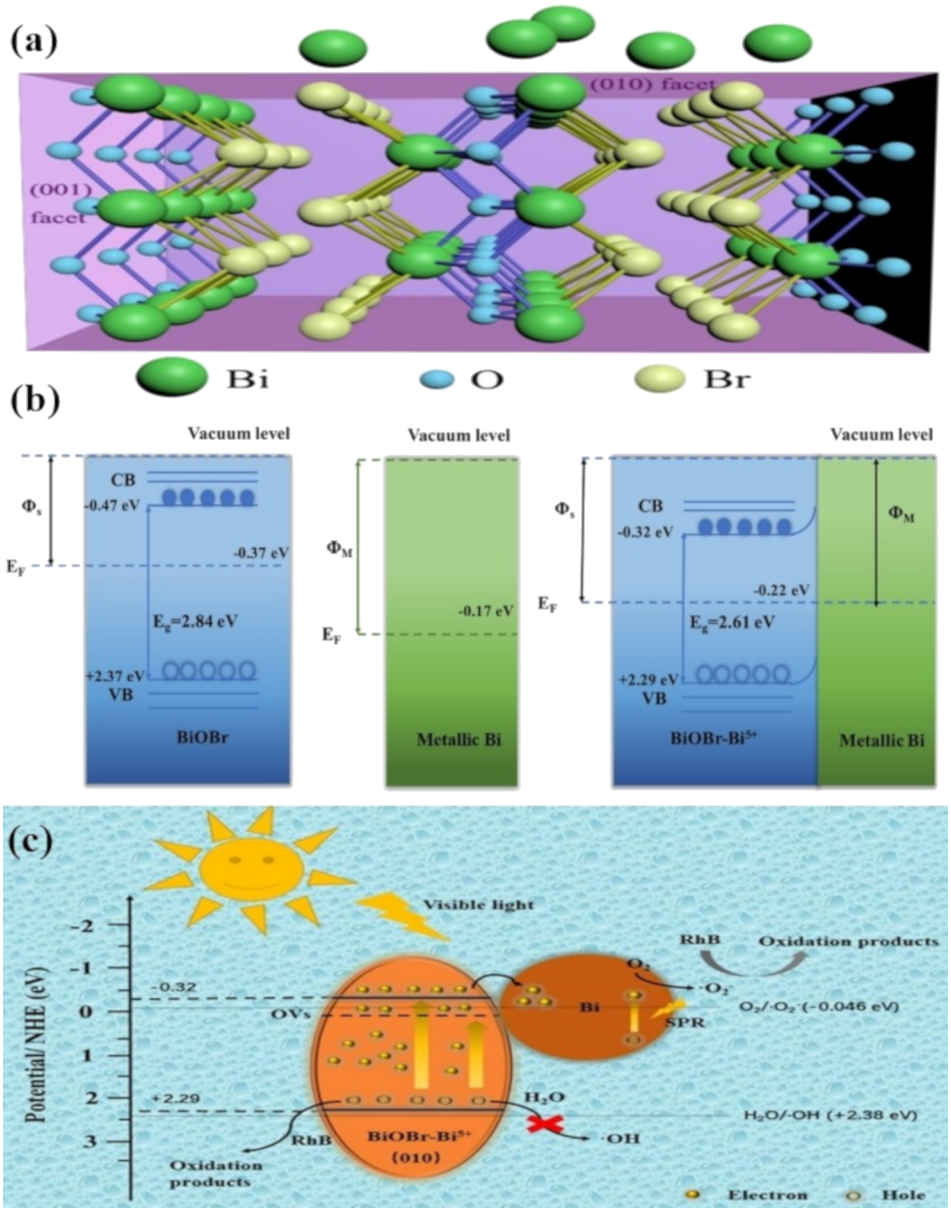

Figure 4: (a) Crystal structure of self-doped Bi/BiOBr–Bi^{5+}, (b) band structure, and (c) RhB degradation of Bi/BiOBr–Bi^{5+} in visible light. Figure 4a–c were adapted from [90]. This article was published in Separation and Purification Technology, vol. 253, by Q. Wu; S. Chai; H. Yang; Z. Gao; R. Zhang; L. Wang; L. Kang, "Enhancing visible-light driven photocatalytic performance of BiOBr by self-doping and in situ deposition strategy: A synergistic effect between Bi^{5+} and metallic Bi", article no. 117388, Copyright Elsevier (2020). This content is not subject to CC BY 4.0.

catalytic activity. As a result, optimizing the electrical configuration by using suitable dopants and concentrations will increase photocatalytic activity. Photogenerated electron–hole separation efficiency and light absorption ability are critical functions that can be improved by appropriate doping.

Heterojunction formation

In general, for a photocatalyst to function appropriately, it is necessary to use a semiconductor with the following characteristics: a bandgap suitable for light harvesting, effective charge carrier separation capabilities, and suitable VB and CB edge potentials [91,92]. It is challenging to meet these requirements with only one single Bi-based photocatalyst. Constructing semiconductor heterojunctions may be an effective technique for addressing the difficulties of individual Bi-based photocatalysts. This may be due to the changeable band structure and effective photoinduced electron–hole separation, which bestows them with higher capabilities [93]. It is possible to improve absorption of visible light, charge carrier segregation, and charge transport effectiveness by combining heterojunction and nano-

materials in photocatalysts constructed with care. As a result, this technique offers much potential for photocatalysis applications [94]. The band arrangement shown in Figure 5a may be used to classify the heterojunctions between semiconductors as either a straddling gap (type I), an uneven gap (type II), or a broken gap (type III). Type-II heterojunctions have garnered the most interest because of the improved photogenerated electron–hole separation they offer. They include n–n heterojunctions, p–n heterojunctions, p–p heterojunctions, and Z-scheme-based heterojunctions (Figure 5b). By using heterojunctions, it is possible to exert control over the electronic components of the photocatalyst to increase light absorption and photoinduced separation and migration [95,96]. Photoinduced holes in n-type semiconductors are transported to p-type semiconductors by an electric field at the interface, whereas photoinduced electrons from p-type semiconductors are transported to n-type semiconductors (Figure 5b).

Using simple and cost-effective experimental conditions, Sang et al. reported the fabrication of nanoflower-like Bi_2O_3/Bi_2S_3 heterojunctions via a one-step hydrothermal technique [97]. In the photocatalytic elimination of RhB and Cr(VI) under visible-light irradiation, the photocatalytic activity of this Bi_2O_3/Bi_2S_3 heterojunctions outperforms that of pristine Bi_2O_3 and Bi_2S_3. They found that photoinduced holes were the main oxidative species for eliminating RhB, whereas photogenerated electrons were responsible for the photoreduction of Cr(VI). Typically, the Fermi energy level of n-type Bi_2O_3 is quite close to the VB, while the Fermi energy level of p-type Bi_2S_3 is somewhat close to the CB. In a heterojunction from n-type Bi_2O_3 and p-type Bi_2S_3, electrons flow from n-type Bi_2O_3 to p-type Bi_2S_3, and holes flow from p-type Bi_2S_3 with a low Fermi level to n-type Bi_2O_3 with a high Fermi level. As a consequence of this, negative charges build up in Bi_2S_3 near the interface, which leads to an electric field. Also, the Fermi level of Bi_2O_3 goes down, while the level of Bi_2S_3 goes up. Along the Fermi level, the energy bands of both Bi_2O_3 and Bi_2S_3 are moving simultaneously in a downward and an upward direction. An equilibrium state, in which the Fermi levels of Bi_2O_3 and Bi_2S_3 equilibrate at the p–n junction, was also proposed. Bi_2S_3, which has a smaller bandgap than Bi_2O_3, is excited when it is exposed to visible light, while Bi_2O_3 is not. The photogenerated holes stay in the p-type Bi_2S_3 VB, while the excitons in the p-type Bi_2S_3 CB migrate to the n-type Bi_2O_3 CB. In the Bi_2O_3/Bi_2S_3 photocatalytic system, electrons and holes participate directly in the redox process. In another reported work, a $BiOI/Bi_2O_2CO_3$/graphene ternary composite was fabricated via a facile and economic hydrothermal technique [98]. In order to assess the newly constructed semiconductor heterojunction, tetracycline and RhB were degraded using visible light. Better photocatalytic activity can be achieved with $BiOI/Bi_2O_2CO_3$ photocatalysts instead of just using BiOI alone. This is because in $BiOI/Bi_2O_2CO_3$ photocatalysts, an electric field emerges at the p–n heterojunction, which in turn helps to foster the movement of photogenerated carriers. Furthermore, the high photocatalytic activity of the $BiOI/Bi_2O_2CO_3$/RGO composite can be attributed to the fact that the positively charged $BiOI/Bi_2O_2CO_3$ was electrostatically paired with the negatively charged graphite oxide (GO) to form interlayer contacts. This caused the photocatalytic reaction sites to boost, the light response to broaden,

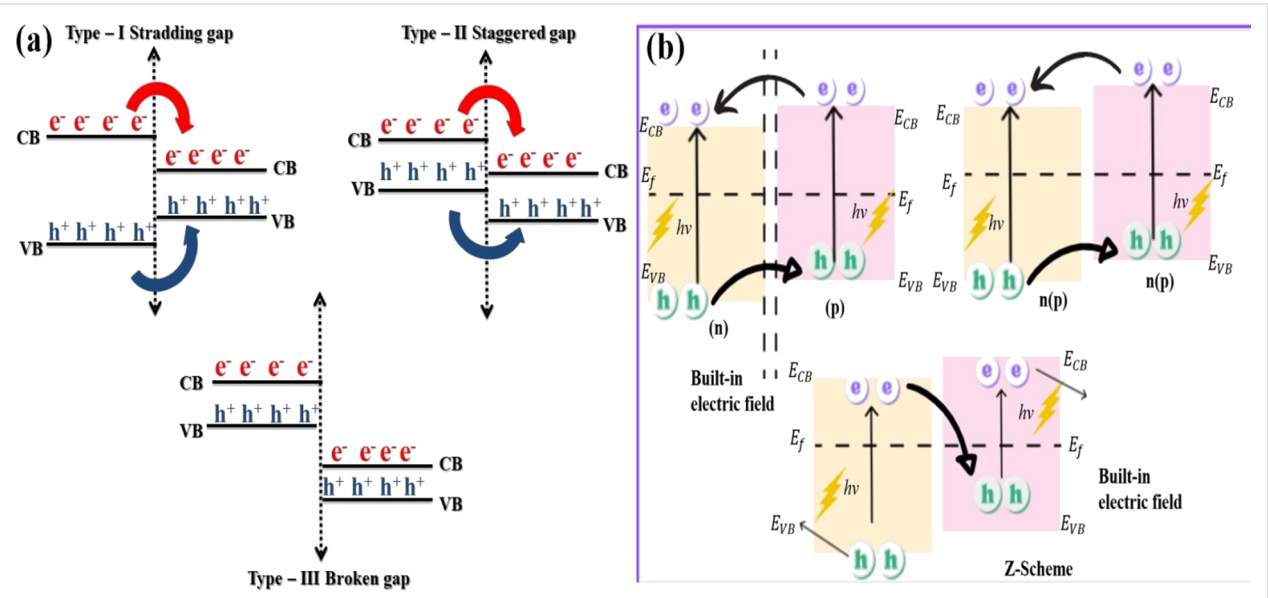

Figure 5: (a) Band diagrams representing three different semiconductor heterojunctions, (b) band diagrams for p–n, n–n (p–p), and Z-scheme-based heterostructures.

and the separation of photoinduced charge to improve. Lv et al. [99] fabricated a p–n heterojunction-based novel CuS/Bi_2WO_6 semiconductor photocatalyst with 2D interfacial connections of CuS over the surface of Bi_2WO_6. The hydrothermal method was used, and it was discovered that the produced CuS/Bi_2WO_6 semiconductor photocatalyst had increased photocatalytic performance for the breakdown of glyphosate when exposed to visible light. Enhanced photocatalytic activity, excellent recyclability, high stability of CuS/Bi_2WO_6 photocatalysts may be primarily due to the presence of an electrical potential at the interface, which is responsible for both the enhanced visible light absorption and the efficient segregation of photoinduced charges. This study introduced a unique 2D interfacial coupling for the production and design of efficient photocatalysts. It also demonstrated that CuS may be used as an effective semiconductor in heterostructures, which is a concept that may be extended to other functional nanomaterials based on bismuth.

The most important heterojunctions are known as Z-scheme heterojunctions and have a band energy structure comparable to type-II heterojunctions. However, there are many alternative pathways open for charge carrier movement (Figure 6), including mediator-free or direct (Figure 6a), solid mediator (Figure 6b), and redox pair mediator (Figure 6c) [43,100]. A "mediator" is often employed to offer an intermediary conduit for electrons to flow from the CB of semiconductor II (SC II) to the VB of semiconductor I (SC I), making the charge transfer easier [38]. A solid substance or a redox couple in solution may serve as a mediator in the Z-scheme. This dual absorber system has the potential to get excited, which would result in the generation of photogenerated holes and electrons in CB and VB, respectively. Photogenerated electrons in the CB of SC II may migrate to the VB of SC I, where they may merge with photogenerated holes. This design is favorable for the electrons in the CB of SC I and the holes in the VB of SC II to keep their optimum and original redox potentials (Figure 6a). This method of electron transmission resembles the letter Z. As a result, the structure of this heterojunction is referred to as the direct Z-scheme [43,101]. Fu et al. [102] demonstrated the synthesis of a new direct Z-scheme photocatalyst made of ultrathin Bi_2O_3 and Bi_2MoO_6 microspheres. For the effective production of Bi_2O_3/Bi_2MoO_6 nanocomposites, researchers adopted a simple in situ alkali treatment of Bi_2MoO_6 followed by calcination. As a substrate for the production of Bi_2O_3 sheets, Bi_2MoO_6 microspheres were used. The 2D morphological properties of the Bi_2O_3 sheets resulted in enhanced charge carrier transfer. The relative mass ratio of Bi_2MoO_6 and Bi_2O_3 may be fine-tuned by adjusting the alkali dose (i.e., NaOH or KOH). Using phenol degradation and hydrogen generation as a test, the 1.5% Bi_2O_3/Bi_2MoO_6 sample was shown to be the most photocatalytically active. An easy hierarchical Z-scheme system with a $ZnIn_2S_4$/$BiVO_4$ heterojunction has been proposed by Hu and co-workers [103]. This system can precisely regulate redox centers at the $ZnIn_2S_4$/$BiVO_4$ heterojunction by expediting the detachment and mobility of photoinduced charges. This, in turn, increases the ability of holes and electrons to undergo oxidation and reduction, respectively. As a consequence of this, the $ZnIn_2S_4$/$BiVO_4$ heterojunction has unusual photocatalytic activity. It has an H_2 evolution rate much higher than pure $ZnIn_2S_4$, with a value of 5.944 $mol \cdot g^{-1} \cdot h^{-1}$. This value is over five times higher. In addition, this heterojunction has excellent stability and the capacity to be recycled, making it a promising photocatalyst for the formation of H_2. Ternary composite heterojunction photocatalysts have been also reported. The Fenelon group successfully fabricated SnO_2 and Bi_2S_3–Bi_{25} composites via a facile hydrothermal technique followed by thermal breakdown [27].

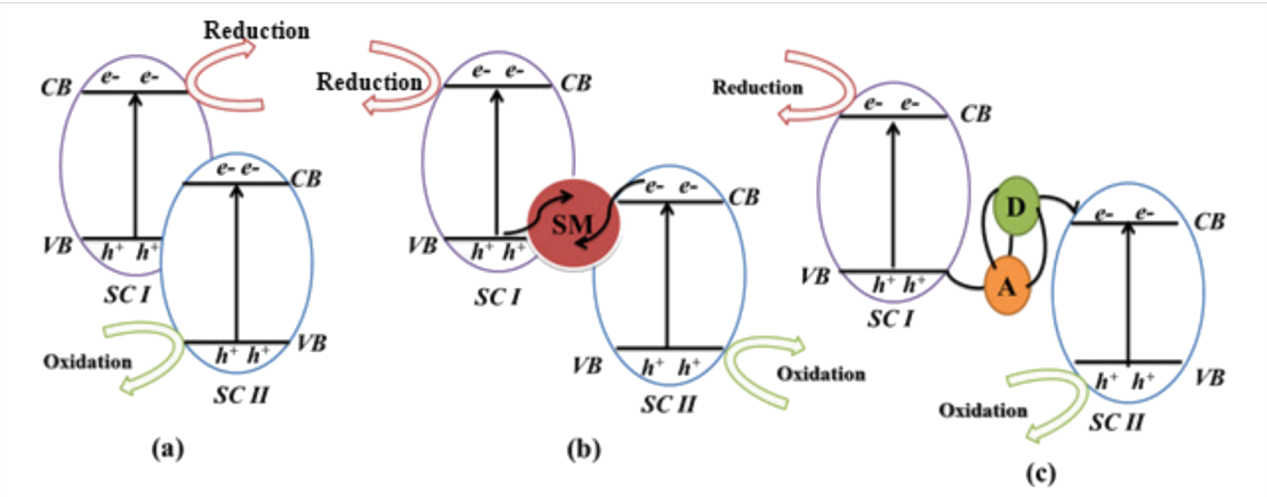

Figure 6: Different charge transfer Z-scheme types: (a) Mediator-free or direct, (b) solid mediator, and (c) redox pair mediator. Abbreviation lists: semiconductor I (SC I), semiconductor II (SC II), valence band (VB), and conduction band (CB).

The photocatalytic performance of the fabricated ternary composite photocatalyst was 2.75 times higher than that of pristine Bi_2S_3 for the photodegradation of RhB under visible light. Their research also revealed that 15% SnO_2 precursor solution was the most effective concentration for achieving a photocatalytic degradation efficiency of 80% after 180 min of exposure to visible light. Photogenerated holes were found to be responsible for the oxidation and breakdown of the pollutant during the photocatalytic reaction.

One of the most popular ways to create an effective heterojunction structure is by combining two semiconductors with matching band alignment. When it comes to understanding the mechanisms behind the enhanced photocatalytic performance of heterojunction photocatalysts, researchers have recently proposed an S-scheme heterojunction [45]. Separating photoinduced electrons and holes with an S-scheme heterojunction efficiently preserves the promising redox properties of semiconductors. It is common for electrons to flow from the CB of one semiconductor to the VB of the other in an S-scheme heterojunction photocatalyst due to an IEF that typically exists at the interface of the two semiconductors [104]. Lately, Xu et al. reported the fabrication of a $MoS_2/BiVO_4$ heterojunction via solvothermal and electrospinning techniques [105]. Without any additional agent, the fabricated heterojunction completely degraded a RhB dye solution within 20 min. $BiVO_4$ nanorods photogenerated hydroxyl radicals rather than super oxides because of the more positive oxidation potential of $BiVO_4$ (2.31 V). MoS_2 sheets favored the photogeneration of superoxide radicals because of the more negative CB position (−1.39 V). This finding demonstrated the spatial distribution of oxidation sites ($BiVO_4$) and reduction sites (MoS_2) via an S-scheme charge transfer path and significantly aided in the inactivation of bacteria under illumination. In another work, a simple hydrothermal technique was applied by Liu et al. to modify $BiVO_4$ heterojunctions with carbon quantum dots [106]. Exceptional photocatalytic performance for the degradation of RhB dye under visible light was exhibited by CNQDs-ms/tz-$BiVO_4$ and NCQDs-ms/tz-$BiVO_4$ composites. The reason for their increased photocatalytic efficiency was the formation of heterojunctions together with the loading of quantum dots, which enhanced the light-harvesting efficiency and promoted the separation and migration of photogenerated carriers. The fabricated composites followed the S-scheme charge transfer mechanism, efficiently contributing to enhanced photocatalytic performance. Another research group reported that photoreduction and hydrothermal techniques were used to successfully synthesize a new 2D/2D Bi_2MoO_6/g-C_3N_4 S-scheme composite including Au as a co-catalyzer [107]. Bi_2MoO_6/g-C_3N_4/Au had a photocatalytic activity in RhB degradation that was 9.7 times and 13.1 times higher than that of Bi_2MoO_6 and g-C_3N_4, respectively. In the Bi_2MoO_6/g-C_3N_4/Au system, the higher photocatalytic activity can be attributed to the abundance of active sites and the enhanced separation efficiency of photogenerated carriers. The potential role of Au nanoparticles in the S-scheme heterostructure is noteworthy. They serve as a co-catalyst for improving electron separation and transmission due to the photogenerated potential.

By forming heterojunctions, the visible-light absorption as well as the carrier separation efficiency of Bi-based nanophotocatalysts can be improved, which in turn increases the photocatalytic activity. The zonal organization of several crystalline surfaces made from the same material may significantly increase charge separation. It can be used to create classic heterojunctions in addition to surface heterojunctions, which can be created using the same method. Surface heterojunctions have recently emerged as a novel concept that has garnered much interest. As a direct consequence of this, it is possible that in the not-too-distant future, it will be possible to construct and analyze further Bi-based surface heterojunction photocatalysts. Table 2 below provides an in-depth explanation of several different strategies that may be used to improve Bi-based nanocomposites.

Environmental applications

The use of Bi-based photocatalysts in power production and environmental remediation is widespread. Sewage treatment, environmental monitoring, disinfection, and sterilization are all areas where the photocatalytic breakdown of contaminants is used. Primary energy uses included photocatalytic hydrogen production from carbon dioxide, conversion of carbon dioxide to specific molecular organic matter, and nitrogen fixation [1,108,109]. Photocatalysts with Bi-based photocatalysts are discussed in this section in more depth.

Photocatalytic hydrogen generation

At the moment, humanity's existence greatly depends on the consumption finite fossil fuels. Thus, finding long-term renewable energy sources is critical. Hydrogen is produced primarily by the electrolysis of water, in parts using solar energy, and the reformation of fossil fuels [110]. The conversion of water into hydrogen by using solar energy is considered the best way to produce hydrogen [111]. Photocatalysts still face the following issues regarding efficient water splitting. First, the quantum efficiency deteriorates as one moves into the visible region. Second, photocatalysts such as sulfides and nitrogen oxides in the visible region have poor stability and are frequently inactivated by photocorrosion. Third, the removal of O_2 from the surface of a semiconductor photocatalyst is complex, which is why a h^+-capturing substance is frequently added to the system to promote the production of H_2 [112]. Pt, Pd, Au, and other

precious metals, as well as photocatalysts containing Cd, Pb, and other elements (such as CdS), are some of the costliest and environmentally hazardous high-performance photocatalysts on the market. CdS is a more ecologically friendly alternative to other photocatalysts [113]. To improve the efficiency of photocatalytic water breakdown from the perspective of catalytic reaction kinetics, one method that is both practical and effective is to design photocatalysts in such a way as to change the processes involved in photocatalytic reaction kinetics.

For example, Cao et al. reported the fabrication of a bismuth-based $Bi/Bi_2MoO_6/TiO_2$ nanocomposite photocatalytic material using a facile one-step solvothermal technique [114]. To reduce metal Bi on the surface of Bi_2MoO_6, they employed glucose as a reducing agent. To test the photocatalytic activity, they exposed the as-prepared materials to simulated solar irradiation and measured the degradation efficiency of RhB (7.321%), MB (92.98%), and Cr(VI) (70.54%). The highest hydrogen generation rate was 173.41 $mol{\cdot}h^{-1}{\cdot}cm^{-2}$, and after four cycles with the same parameters, there was no noticeable decrease in the hydrogen production of the $Bi/Bi_2MoO_6/TiO_2$ system. The development of Bi_2MoO_6/TiO_2 heterojunctions, the SPR effect of Bi, and synergistic effect may be responsible for the enhanced photocatalytic activity and hydrogen generation rate (Figure 7a). Developing semiconductor photocatalysts that are both low-cost and highly efficient is essential for the practical conversion of solar energy into fuel. A $Ag–C_3N_4$-modified $(BiO)_2CO_3$ semiconductor photocatalyst was synthesized using an in situ thermal approach in [115]. The activity of the $(BiO)_2CO_3/g\text{-}C_3N_4$ heterojunction reached 965 $\mu mol{\cdot}h^{-1}{\cdot}cm^{-2}$ after 5 h. This is almost three times the activity of pristine $g\text{-}C_3N_4$ or any other modified $g\text{-}C_3N_4$ nanomaterial (337 $\mu mol{\cdot}h^{-1}{\cdot}cm^{-2}$). An increase in photocatalytic activity has been found due to the usage of a direct Z-scheme system

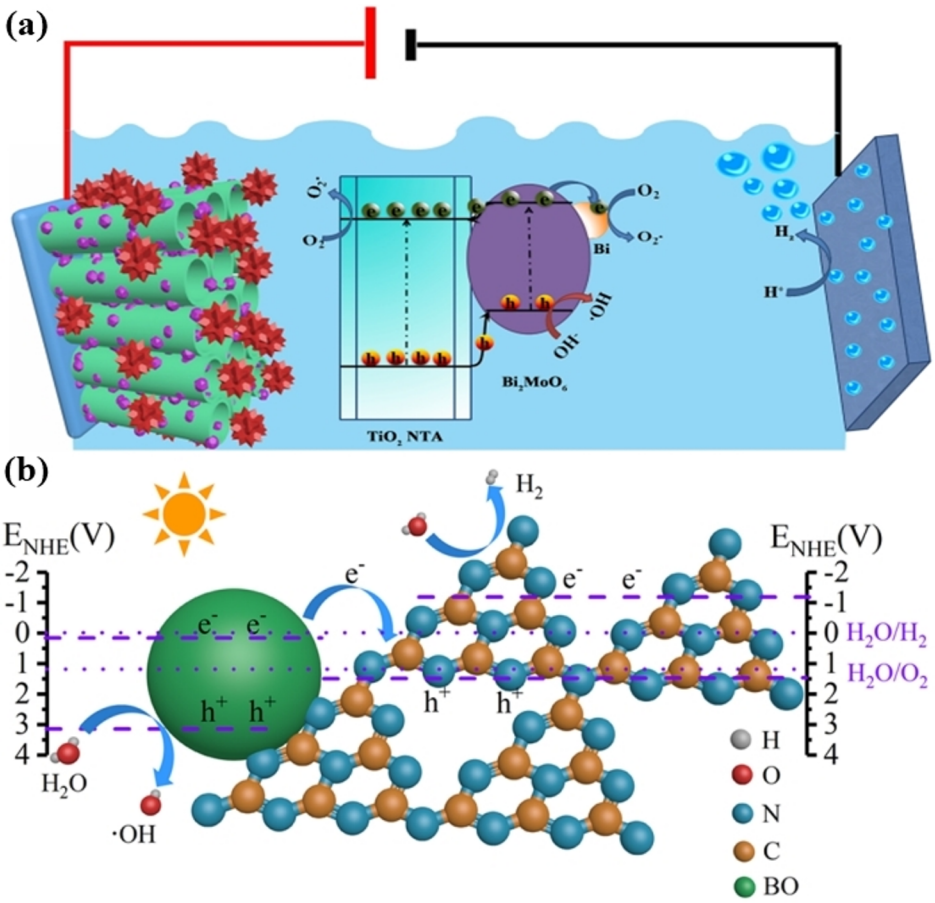

Figure 7: Graphical representation of the proposed charge transfer mechanism of (a) the $Bi/Bi_2MoO_6/TiO_2$ nanocomposite and (b) the $(BiO)_2CO_3/g\text{-}C_3N_4$ heterojunction. Figure 7a was reprinted from [114]. This article was published in Separation and Purification Technology, vol. 250, by D. Cao; Q. Wang; Y. Wu; S. Zhu; Y. Jia; R. Wang, "Solvothermal synthesis and enhanced photocatalytic hydrogen production of Bi/Bi_2MoO_6 co-sensitized TiO_2 nanotube arrays", article no. 117132, Copyright Elsevier (2020). This content is not subject to CC BY 4.0. Figure 7b was reprinted with permission from [115], Copyright 2019 American Chemical Society. This content is not subject to CC BY 4.0.

(Figure 7b). Theoretical simulations showed that charge carriers were redistributed at the junction between $(BiO)_2CO_3$ and g-C_3N_4.

Photocatalytic elimination of water pollutants

A wide variety of contaminants in water, such as heavy metal ions, pharmaceuticals, and pesticides, have been used as models substances for photocatalytic degradation. Reactive oxygen species (ROSs) such as $^{\bullet}O_2^-$ and $^{\bullet}OH$ are critical to the photocatalytic removal of environmental pollutants.

Malathi et al. reported the photocatalytic and photoelectrochemical performance of $BiFeWO_6$/BiOI nanohybrids, which were fabricated by wet impregnation, under visible-light irradiation [116]. Within 90 min, the composite degraded 92% of RhB. Similarly, Priya et al. used a simple wet-chemical method to make $BiFeWO_6/WO_3$ nanocomposites [117]. A 250 W tungsten halogen lamp was used to carry out the photoexcitation of the catalysts for RhB degradation. After a period of 60 min, the composite yielded a 83% breakdown of RhB. The multiferroic single-phase material known as nanoscale zero-valent iron-doped bismuth ferrite (NZVI@$BiFeO_3$) displays concurrent ferroelectric, ferromagnetic, and ferroelastic properties. $BiFeO_3$ has the ability to be utilized in heterogeneous photocatalysis when exposed to light from the sun. The NZVI@$BiFeO_3$/g-C_3N_4 nanocomposite was produced using a straightforward hydrothermal process [118]. The composite was employed for the photodegradation of RhB. The generated composite could degrade 97% of the RhB dye when exposed to solar light. Compared to pure $BiFeO_3$, the NZVI@$BiFeO_3$/g-C_3N_4 composite has a better optical responsiveness, which contributes to the improved photocatalysis of the material. According to the theorized dye degradation mechanism, the composite provides efficient reactive species trapping sites. Because of this, the NZVI@$BiFeO_3$/g-C_3N_4 nanocomposite has the potential to be utilized to oxidize a wide range of organic and inorganic contaminants that are found in wastewater.

Recently, Chava et al. proposed the solvothermal method for preparing 1D/0D CdS/Bi heterostructures [119]. To evaluate their potential photocatalytic performance toward photodegradation of the organic pollutants, tetracycline was used as model substance. The 1D/0D CdS/Bi heterostructures exhibited excellent catalytic activity, compared to pure CdS. It was expected that 1D/0D CdS/Bi could act as an effective photocatalyst for the treatment of other organic pollutants in wastewater, such as organic dyes and pharmaceuticals. The enhanced photocatalytic degradation efficiency may be due to doped Bi^{3+} species, the SPR effect in the metallic Bi quantum dots, and increased photoinduced charge carrier separation. In another study, a visible-light-sensitive heterostructure made of $InVO_4/Bi_2WO_6$ nanoflakes was synthesized using an in situ hydrothermal process [120]. The photocatalytic degradation of tetracycline was successfully investigated. Notably, the $InVO_4/Bi_2WO_6$ semiconductor photocatalyst manufactured with 5.0 mg of Bi_2WO_6 exhibits the highest tetracycline degradation rate, that is, 97.42% in 72 min. Following the findings of quenching studies, hydroxyl radicals and holes prevail throughout the photocatalytic process. In addition, the improved nanocomposite does not lose its stability after being exposed to light for four cycles, highlighting the excellent reusability and photostability of the photocatalyst.

Photoreduction of carbon dioxide

The CO_2 content in the atmosphere has risen from 280 to 408 ppm since the late 1800s. Officials and scholars are now concentrating their efforts on devising strategies that would significantly reduce atmospheric CO_2 concentrations. The photochemical reduction of carbon dioxide to convert it to hydrocarbon fuels is one of the most promising options that have been found. Energy may be obtained from sustainable solar energy, which can be used directly or indirectly in this process, resulting in carbon recycling that lives up to its name since it can be conducted outside at ambient temperature and atmospheric pressure [121,122]. Therefore, using photocatalysis to remove excess CO_2 from the atmosphere is of the utmost significance.

However, the photocatalytic reduction of CO_2 is difficult for several reasons. First, breaking the bonds in CO_2 requires significant energy. Second, reducing CO_2 to methanol or methane requires processes involving the transfer of, respectively, six or eight electrons. These processes are far more intricate than the process transferring four electrons during the breakdown of water. Third, transforming carbon dioxide into methanol and other fuels requires complex, multi-step intermediate processes, such as proton transfer and hydroxylation. Fourth, in a system that exists in a liquid phase, the reduction of CO_2 is typically followed by a competitive reaction (proton reduction) [123]. Furthermore, CO_2 reduction produces a range of by-products, making catalyst selectivity crucial.

Among the candidates for CO_2 photoreduction, bismuth-based photocatalysts have received enormous attention [124]. They offer many advantages, such as excellent bandgap features and a unique electronic structure. The vacancy defects in Bi-based photocatalysts could facilitate the adsorption and activation of CO_2, resulting in further enhancing the efficiency of CO_2 reduction. Moradi et al. combined sol–gel and photodeposition processes to fabricate Pt@Bi-TiO_2 photocatalysts for converting CO_2 [125]. As expected, methane production was noticeably improved over the Pt@Bi-TiO_2 photocatalyst. Its

methane yield was about 6.2 times greater than that of pure TiO_2. The enhanced activity might be attributed to the efficient charge separation facilitated via Pt nanoparticles, and the increase of CO_2 adsorption on phases containing Bi. Lui et al. [126] reported that a simple in situ one-step combustion approach was used to prepare $Bi_2Al_4O_9$/β-Bi_2O_3 heterojunction. Urea was employed as the fuel for the reaction, while bismuth nitrate pentahydrate was used as a source of $Bi_2Al_4O_9$ and β-Bi_2O_3. A transfer pathway of the photogenerated charges was suggested. Enhancement in CO yield was ascribed to oxygen vacancies, which improved the adsorption activation of CO_2, and the photogenerated charge carriers effectively separated in the heterostructure. The CO_2 photoreduction performance of the heterojunction of 0.14 $Bi_2Al_4O_9$/β-$Bi_2O_3$was determined to be the highest. In contrast to the 1.5 μmol·g^{-1} CO yield on β-Bi_2O_3, the sample of 0.14 $Bi_2Al_4O_9$/β-Bi_2O_3 gave 13.2 μmol·g^{-1} CO. Bi integration into TiO_2 and subsequent loading of Pt on its surface led to a significant rise in methane generation. Methane yields were about 6.2 times higher with modified TiO_2, which included 3 wt % Bi and 1.5 wt % Pt, compared to pure TiO_2. Pt nanoparticles facilitated charge separation and boosted CO_2 adsorption on phases containing Bi, which increased CO_2 conversion activity.

Photocatalytic nitrogen fixation

Regarding the synthesis of NH_3, photocatalytic N_2 fixation ($2N_2 + 6H_2O$ + light → $4NH_3 + 3O_2$) is a promising concept. To further promote N_2 photofixation, many studies have focused to develop effective photocatalysts.

Rong et al. proposed a Bi_2Te_3/BiOCl heterostructure as an effective candidate for N_2 photofixation [127]. An NH_3 release rate of 315.9 μmol·L^{-1}·h^{-1} under UV-light irradiation was achieved. The improvement might be attributed to the effective prevention of hole–electron recombination. Bi_2Te_3 is a highly active semiconductor with a bandgap of 0.15 eV; however, its reduction potential of 0.57 eV is less than that of N_2/NH_3 (0.092 eV). As its CB potential (1.1 eV) is more negative than that of N_2/NH_3 (0.092 eV), BiOCl may photogenerate electrons and holes under UV light. So, the electrons photogenerated from BiOCl were crucial to the N_2 photofixation. The photocatalytic activity of BiOCl is severely hampered by the recombination of photogenerated holes and charges. The photogenerated charges from the excitation of Bi_2Te_3 effectively suppress the recombination of photogenerated holes and electrons of BiOCl, which extends the lifetime of electrons in the CB of BiOCl. Without the presence of light or photocatalysts, no NH_3 was measured. Fei et al. utilized graphene quantum dots and Bi_2WO_6 to construct a heterostructure for photocatalytic nitrogen fixation [128]. The photocatalytic performance was, respectively, 33.8 and 8.88 times better than that of pristine graphene quantum dots and Bi_2WO_6. Zhou et al. used an in situ bismuth reduction technique on Bi_2WO_6 [129]. Metallic Bi was used as a lattice junction to build Bi_2WO_6, which was highly oriented on the lattice structure. The directed interface and transfer channels made separating photogenerated carriers possible, leading to successful nitrogen fixation. In another work, Zhang et al. coated Bi_2WO_6 with cyclized polyacrylonitrile (c-PAN), which yielded active sites for N_2 absorption and activation because the pyridinic N atom in c-PAN shifted into an unsaturated state to interact with small molecules and to transfer electrons to the small molecules [130].

Photocatalytic microbial disinfection

Heat and UV light are two methods to kill bacteria and viruses. Photocatalytic technology has also been used to disinfect and sterilize air, with positive results compared to traditional methods. Compared to TiO_2 and ZnO, bismuth-based photocatalysts have a small bandgap and better visible light absorption [131]. Wang et al. reported a hydrothermally synthesized monoclinic dibismuth tetraoxide (m-Bi_2O_4) with a small bandgap of 2.0 eV and mixed valence states (Bi^{3+} and Bi^{5+}) [132]. After 120 min of visible light irradiation, the m-Bi_2O_4 nanorods inactivated *E. coli* with a substantially better photocatalytic efficiency and photostability than CdS and Bi_2O_3. The primary ROS responsible for photocatalytic disinfection was found to be $^{\bullet}OH$. This research also suggested that bismuth-based nanomaterials might be effective, stable, and long-lasting semiconductor photocatalysts for water disinfection under visible light. In another study, Liang et al. reported the fabrication of AgI/AgBr/$BiOBr_{0.75}I_{0.25}$ nanocomposites via solvothermal technique [133]. The fabricated semiconductor photocatalyst was used to deactivate *Escherichia coli* under visible light. A concentration of 80 mg/L AgI/AgBr/$BiOBr_{0.75}I_{0.25}$ was able to totally inactivate 3×10^7 CFU·mL^{-1} *E. coli* cells in 30 min. Furthermore, the bactericidal processes were thoroughly explored. The bactericidal activity of Ag^+ ions generated from the nanocomposite was negligible, whereas active species such as h^+, e^-, and $^{\bullet}O_2^-$ played critical roles in the disinfection. Direct interaction between bacterial cells and nanoparticles was discovered to be necessary for both the production of $^{\bullet}O_2^-$ and disinfection processes. *E. coli* cells were inactivated by disrupting the cell membrane and releasing cytoplasm. Furthermore, even after four repeated cycles, AgI/AgBr/$BiOBr_{0.75}I_{0.25}$ showed excellent antibacterial activity against *E. coli*. A novel Z-scheme AgI/$BiVO_4$ heterojunction was synthesized via the chemical deposition–precipitation technique [134]. *E. coli* disinfection and the decomposition of oxytetracycline hydrochloride (OTC-HCl) were used to measure the photocatalytic activity under visible-light irradiation. The Z-scheme heterojunction took 50 min to kill bacteria and degraded OTC-HCl by 80% via photocatalysis, exhibiting high photocatalytic performance and

photostability. h^+ and $^{\bullet}O_2^-$ were shown to be the major reactive species during photoinactivation, with K^+ permeability playing an important role in cell membrane collapse and bacterial deactivation. It was shown that the AgI/$BiVO_4$ photocatalyst is an effective nanomaterial for wastewater treatment, specifically with extremely high concentrations of pathogenic microorganisms and antibiotics. Table 2 lists a Bi-based nanomaterials that have been studied for environmental applications.

Conclusion and Future Perspectives

There is great potential for Bi-based photocatalysts in the remediation of polluted environments and converting visible light into usable energy. In this study, we demonstrated that nanoscale Bi-based materials could be used for various photocatalytic ecological applications due to their distinctive electrical capabilities, crystal structure, and chemical attributes. These nanomaterials were obtained using various synthetic methods. Since there are constraints on employing just one Bi-based material as a photocatalyst, subsequent developments of Bi-based photocatalysts are explored in depth. The disadvantages are discussed in this article. We considered the most up-to-date research on Bi-based photocatalysts in our study. These developments stemmed from improvements in system design, microstructure management, and the synthesis of Bi-based composites. To further investigate the photocatalytic process, we analyzed the impact of several methods. The improved efficiency of photocatalysis based on Bi-valent cations was also covered.

Bi-based photocatalysts hold promise for environmental applications, but there is still much work to be done to improve the photocatalytic efficacy. Essential criteria in this field include the following: (1) Consideration must be given to the environmental and workplace safety and the economic impacts of the design process to overcome the "energy trilemma" when developing and building Bi-based photocatalysts. (2) The most difficult issue to address is obtaining and preserving the optimal

Table 2: Different roles of Bi-based semiconductor photocatalysts in various environmental remediation applications.

No	Photocatalyst	Enhancement strategy	Environmental Application	Role of photocatalyst	Ref.
1	BiOBr	facet-dependent	bacterial disinfection	enhanced photocatalytic generation of radical	[135]
2	Bi_2O_4/BiOBr nanosheets	facet-dependent	MO dye degradation, microbial disinfection	enhanced light absorption, efficient photoinduced e^-/h^+ pair separation, boosted surface-adsorbed ability	[136]
3	BiO_{2-x}	Z-scheme heterojunction	O_2 evolution	increased IEF	[137]
4	Bi_2MoO_6/g-C_3N_4	heterojunction formation	H_2 evolution, microbial disinfection	enhanced reduction capabilities	[138]
5	BiOI/BiOBr	heterojunction structure	bacteriostatic activity	advance separation of the photoinduced holes	[139]
6	AgI/Bi_2MoO_6	Z-scheme	water disinfection	strong redox potential and enhanced separation of photogenerated charge carriers	[140]
7	MoS_2/Bi_2WO_6	p–n junction formation	water detoxification	generated electric field, efficient separation of photogenerated charges	[141]
8	BiOCl	surface defects	CO_2 photoreduction	increased surface adsorption	[142]
9	$Bi_4O_5Br_2$	Bi-rich strategy	CO_2 photoreduction	efficiently improved surface properties	[143]
10	Bi_2WO_6/$CuBi_2O_4$	Z-scheme formation	tetracycline dye degradation	increased surface oxygen vacancy	[144]
11	$BiPO_4$/$BiOCl_{0.9}I_{0.1}$	Z-scheme	phenol and RhB dye degradation	boosted redox ability increased charge transfer	[145]
12	Bi_2S_3/$SnIn_4S_8$	heterojunction formation	microbial disinfection, RhB dye degradation	advanced redox ability	[146]
13	g-C_3N_4/Bi_2WO_6/AgI	Z-scheme	environmental decontamination	enhanced the separation and transfer of photoinduced charges	[147]
14	Bi_2WO_6/CdS	heterojunction formation	H_2 evolution, RhB dye degradation	enhanced electrochemical properties	[148]
15	β-Bi_2O_3@g-C_3N_4	Z-scheme	tetracycline dye degradation	enhanced separation ability and prolonged lifespan of photogenerated charges	[149]

nanostructure and morphology. (3) Thorough knowledge on reaction circumstances depending on structural traits is crucial. (4) Only there are only few studies on Bi-based photocatalysts in energy photocatalysis, such as H_2 production, CO_2 reduction, and selective organic transformation, because of the restricted number of photogenerated electrons from the less negative CB edge. (5) One of the most effective approaches to research reduction applications is to use Z-scheme heterojunctions with larger negative CB and photocatalytic Bi-based materials. (6) The stability of photocatalysts plays a vital role in large-scale application. Substantial research work has been already reported on it, but more ways to stabilize and recover a used Bi-based photocatalyst need to be found. Hence, more studies on the durability and renewability of Bi-based photocatalysts need to be carried out.

ORCID® iDs

Vishal Dutta - https://orcid.org/0000-0002-8423-5370
Ankush Chauhan - https://orcid.org/0000-0001-7707-1032
Van-Huy Nguyen - https://orcid.org/0000-0001-8556-1955

References

1. He, R.; Xu, D.; Cheng, B.; Yu, J.; Ho, W. *Nanoscale Horiz.* **2018,** *3,* 464–504. doi:10.1039/c8nh00062j
2. Liu, G.; Zhen, C.; Kang, Y.; Wang, L.; Cheng, H.-M. *Chem. Soc. Rev.* **2018,** *47,* 6410–6444. doi:10.1039/c8cs00396c
3. Di, J.; Xia, J.; Li, H.; Liu, Z. *Nano Energy* **2017,** *35,* 79–91. doi:10.1016/j.nanoen.2017.03.030
4. Xiong, J.; Song, P.; Di, J.; Li, H.; Liu, Z. *J. Mater. Chem. A* **2019,** *7,* 25203–25226. doi:10.1039/c9ta10144f
5. Dou, W.; Peng, X.; Kong, L.; Hu, X. *Sci. Total Environ.* **2022,** *824,* 153909. doi:10.1016/j.scitotenv.2022.153909
6. Wang, Z.; Mi, B. *Environ. Sci. Technol.* **2017,** *51,* 8229–8244. doi:10.1021/acs.est.7b01466
7. Navalón, S.; Dhakshinamoorthy, A.; Álvaro, M.; Garcia, H. *ChemSusChem* **2013,** *6,* 562–577. doi:10.1002/cssc.201200670
8. Parzinger, E.; Miller, B.; Blaschke, B.; Garrido, J. A.; Ager, J. W.; Holleitner, A.; Wurstbauer, U. *ACS Nano* **2015,** *9,* 11302–11309. doi:10.1021/acsnano.5b04979
9. Jin, J.; He, T. *Appl. Surf. Sci.* **2017,** *394,* 364–370. doi:10.1016/j.apsusc.2016.10.118
10. Chahkandi, M.; Zargazi, M. *J. Hazard. Mater.* **2019,** *380,* 120879. doi:10.1016/j.jhazmat.2019.120879
11. Zhang, L.-W.; Wang, Y.-J.; Cheng, H.-Y.; Yao, W.-Q.; Zhu, Y.-F. *Adv. Mater. (Weinheim, Ger.)* **2009,** *21,* 1286–1290. doi:10.1002/adma.200801354
12. Ouyang, S.; Tong, H.; Umezawa, N.; Cao, J.; Li, P.; Bi, Y.; Zhang, Y.; Ye, J. *J. Am. Chem. Soc.* **2012,** *134,* 1974–1977. doi:10.1021/ja210610h
13. Hsieh, P.-L.; Naresh, G.; Huang, Y.-S.; Tsao, C.-W.; Hsu, Y.-J.; Chen, L.-J.; Huang, M. H. *J. Phys. Chem. C* **2019,** *123,* 13664–13671. doi:10.1021/acs.jpcc.9b02081
14. Yu, H.; Jiang, L.; Wang, H.; Huang, B.; Yuan, X.; Huang, J.; Zhang, J.; Zeng, G. *Small* **2019,** *15,* 1901008. doi:10.1002/smll.201901008
15. Zhang, Z.; Wang, W.; Shang, M.; Yin, W. *J. Hazard. Mater.* **2010,** *177,* 1013–1018. doi:10.1016/j.jhazmat.2010.01.020
16. Yan, X.; Yuan, K.; Lu, N.; Xu, H.; Zhang, S.; Takeuchi, N.; Kobayashi, H.; Li, R. *Appl. Catal., B* **2017,** *218,* 20–31. doi:10.1016/j.apcatb.2017.06.022
17. Li, H.; Shang, J.; Ai, Z.; Zhang, L. *J. Am. Chem. Soc.* **2015,** *137,* 6393–6399. doi:10.1021/jacs.5b03105
18. Dong, C.; Lu, S.; Yao, S.; Ge, R.; Wang, Z.; Wang, Z.; An, P.; Liu, Y.; Yang, B.; Zhang, H. *ACS Catal.* **2018,** *8,* 8649–8658. doi:10.1021/acscatal.8b01645
19. Di, J.; Chen, C.; Zhu, C.; Ji, M.; Xia, J.; Yan, C.; Hao, W.; Li, S.; Li, H.; Liu, Z. *Appl. Catal., B* **2018,** *238,* 119–125. doi:10.1016/j.apcatb.2018.06.066
20. Zhao, Z.-Y.; Dai, W.-W. *Inorg. Chem.* **2015,** *54,* 10732–10737. doi:10.1021/acs.inorgchem.5b01714
21. Tan, C.; Cao, X.; Wu, X.-J.; He, Q.; Yang, J.; Zhang, X.; Chen, J.; Zhao, W.; Han, S.; Nam, G.-H.; Sindoro, M.; Zhang, H. *Chem. Rev.* **2017,** *117,* 6225–6331. doi:10.1021/acs.chemrev.6b00558
22. Di, J.; Xia, J.; Li, H.; Guo, S.; Dai, S. *Nano Energy* **2017,** *41,* 172–192. doi:10.1016/j.nanoen.2017.09.008
23. Xu, K.; Wang, L.; Xu, X.; Dou, S. X.; Hao, W.; Du, Y. *Energy Storage Mater.* **2019,** *19,* 446–463. doi:10.1016/j.ensm.2019.03.021
24. Dutta, V.; Sharma, S.; Raizada, P.; Khan, A. A. P.; Asiri, A. M.; Nadda, A.; Singh, P.; Van Le, Q.; Huang, C.-W.; Nguyen, D. L. T.; Pansambal, S.; Nguyen, V.-H. *Surf. Interfaces* **2021,** *25,* 101273. doi:10.1016/j.surfin.2021.101273
25. Ren, X.; Gao, M.; Zhang, Y.; Zhang, Z.; Cao, X.; Wang, B.; Wang, X. *Appl. Catal., B* **2020,** *274,* 119063. doi:10.1016/j.apcatb.2020.119063
26. Arthur, R. B.; Ahern, J. C.; Patterson, H. H. *Catalysts* **2018,** *8,* 604. doi:10.3390/catal8120604
27. Fenelon, E.; Bui, D.-P.; Tran, H. H.; You, S.-J.; Wang, Y.-F.; Cao, T. M.; Van Pham, V. *ACS Omega* **2020,** *5,* 20438–20449. doi:10.1021/acsomega.0c02461
28. Xue, L.; An, F.; Yang, Y.; Ma, Y. *J. Mater. Res.* **2020,** *35,* 153–161. doi:10.1557/jmr.2019.401
29. Ding, S.; Han, M.; Dai, Y.; Yang, S.; Mao, D.; He, H.; Sun, C. *ChemCatChem* **2019,** *11,* 3490–3504. doi:10.1002/cctc.201900529
30. Ma, H.; He, Y.; Chen, P.; Wang, H.; Sun, Y.; Li, J.; Dong, F.; Xie, G.; Sheng, J. *Chem. Eng. J.* **2021,** *417,* 129305. doi:10.1016/j.cej.2021.129305
31. Sivasubramanian, P.; Chang, J.-H.; Nagendran, S.; Dong, C.-D.; Shkir, M.; Kumar, M. *Chemosphere* **2022,** *307,* 135652. doi:10.1016/j.chemosphere.2022.135652
32. Anku, W. W.; Oppong, S. O. B.; Govender, P. P. Bismuth-Based Nanoparticles as Photocatalytic Materials. In *Bismuth - Advanced Applications and Defects Characterization;* Zhou, Y.; Dong, F.; Jin, S., Eds.; IntechOpen: London, UK, 2018. doi:10.5772/intechopen.75104
33. Yang, C.; Chai, J.; Wang, Z.; Xing, Y.; Peng, J.; Yan, Q. *Chem. Res. Chin. Univ.* **2020,** *36,* 410–419. doi:10.1007/s40242-020-0069-3
34. Bhat, S. S. M.; Jang, H. W. *ChemSusChem* **2017,** *10,* 3001–3018. doi:10.1002/cssc.201700633
35. Shahbazi, M.-A.; Faghfouri, L.; Ferreira, M. P. A.; Figueiredo, P.; Maleki, H.; Sefat, F.; Hirvonen, J.; Santos, H. A. *Chem. Soc. Rev.* **2020,** *49,* 1253–1321. doi:10.1039/c9cs00283a
36. Kudo, A.; Miseki, Y. *Chem. Soc. Rev.* **2009,** *38,* 253–278. doi:10.1039/b800489g
37. Meng, A.; Zhang, L.; Cheng, B.; Yu, J. *Adv. Mater. (Weinheim, Ger.)* **2019,** *31,* 1807660. doi:10.1002/adma.201807660

38. Low, J.; Yu, J.; Jaroniec, M.; Wageh, S.; Al-Ghamdi, A. A. *Adv. Mater. (Weinheim, Ger.)* **2017,** *29,* 1601694. doi:10.1002/adma.201601694
39. Hasija, V.; Kumar, A.; Sudhaik, A.; Raizada, P.; Singh, P.; Van Le, Q.; Le, T. T.; Nguyen, V.-H. *Environ. Chem. Lett.* **2021,** *19,* 2941–2966. doi:10.1007/s10311-021-01231-w
40. Nosaka, Y.; Nosaka, A. Y. *Chem. Rev.* **2017,** *117,* 11302–11336. doi:10.1021/acs.chemrev.7b00161
41. Deng, Y.; Zhao, R. *Curr. Pollut. Rep.* **2015,** *1,* 167–176. doi:10.1007/s40726-015-0015-z
42. Huang, C. P.; Dong, C.; Tang, Z. *Waste Manage. (Oxford, U. K.)* **1993,** *13,* 361–377. doi:10.1016/0956-053x(93)90070-d
43. Xu, Q.; Zhang, L.; Yu, J.; Wageh, S.; Al-Ghamdi, A. A.; Jaroniec, M. *Mater. Today* **2018,** *21,* 1042–1063. doi:10.1016/j.mattod.2018.04.008
44. Serpone, N.; Maruthamuthu, P.; Pichat, P.; Pelizzetti, E.; Hidaka, H. *J. Photochem. Photobiol., A* **1995,** *85,* 247–255. doi:10.1016/1010-6030(94)03906-b
45. Xu, Q.; Zhang, L.; Cheng, B.; Fan, J.; Yu, J. *Chem* **2020,** *6,* 1543–1559. doi:10.1016/j.chempr.2020.06.010
46. He, R.; Cao, S.; Zhou, P.; Yu, J. *Chin. J. Catal.* **2014,** *35,* 989–1007. doi:10.1016/s1872-2067(14)60075-9
47. Dutta, V.; Sharma, S.; Raizada, P.; Kumar, R.; Thakur, V. K.; Nguyen, V.-H.; Asiri, A. M.; Khan, A. A. P.; Singh, P. *J. Environ. Chem. Eng.* **2020,** *8,* 104505. doi:10.1016/j.jece.2020.104505
48. Kwolek, P.; Szaciłowski, K. *Electrochim. Acta* **2013,** *104,* 448–453. doi:10.1016/j.electacta.2012.10.001
49. Sharma, K.; Dutta, V.; Sharma, S.; Raizada, P.; Hosseini-Bandegharaei, A.; Thakur, P.; Singh, P. *J. Ind. Eng. Chem. (Amsterdam, Neth.)* **2019,** *78,* 1–20. doi:10.1016/j.jiec.2019.06.022
50. Liang, L.; Lei, F.; Gao, S.; Sun, Y.; Jiao, X.; Wu, J.; Qamar, S.; Xie, Y. *Angew. Chem., Int. Ed.* **2015,** *54,* 13971–13974. doi:10.1002/anie.201506966
51. Wu, X.; Toe, C. Y.; Su, C.; Ng, Y. H.; Amal, R.; Scott, J. *J. Mater. Chem. A* **2020,** *8,* 15302–15318. doi:10.1039/d0ta01180k
52. Chou, S.-Y.; Chen, C.-C.; Dai, Y.-M.; Lin, J.-H.; Lee, W. W. *RSC Adv.* **2016,** *6,* 33478–33491. doi:10.1039/c5ra28024a
53. Liu, F.-Y.; Dai, Y.-M.; Chen, F.-H.; Chen, C.-C. *J. Colloid Interface Sci.* **2020,** *562,* 112–124. doi:10.1016/j.jcis.2019.12.006
54. Su, Y.; Ding, C.; Dang, Y.; Wang, H.; Ye, L.; Jin, X.; Xie, H.; Liu, C. *Appl. Surf. Sci.* **2015,** *346,* 311–316. doi:10.1016/j.apsusc.2015.04.021
55. Lin, Y.; Lu, C.; Wei, C. *J. Alloys Compd.* **2019,** *781,* 56–63. doi:10.1016/j.jallcom.2018.12.071
56. Huang, H.; Liu, L.; Zhang, Y.; Tian, N. *J. Alloys Compd.* **2015,** *619,* 807–811. doi:10.1016/j.jallcom.2014.08.262
57. Le, M. T.; Van Well, W. J. M.; Van Driessche, I.; Hoste, S. *Appl. Catal., A* **2004,** *267,* 227–234. doi:10.1016/j.apcata.2004.03.007
58. He, Y.; Zhang, Y.; Huang, H.; Tian, N.; Guo, Y.; Luo, Y. *Colloids Surf., A* **2014,** *462,* 131–136. doi:10.1016/j.colsurfa.2014.07.034
59. Hamza, M. A.; El-Shazly, A. N.; Tolba, S. A.; Allam, N. K. *Chem. Eng. J.* **2020,** *384,* 123351. doi:10.1016/j.cej.2019.123351
60. Tian, N.; Zhang, Y.; Huang, H.; He, Y.; Guo, Y. *J. Phys. Chem. C* **2014,** *118,* 15640–15648. doi:10.1021/jp500645p
61. Dong, F.; Li, Q.; Sun, Y.; Ho, W.-K. *ACS Catal.* **2014,** *4,* 4341–4350. doi:10.1021/cs501038q
62. Dong, F.; Xiong, T.; Sun, Y.; Huang, H.; Wu, Z. *J. Mater. Chem. A* **2015,** *3,* 18466–18474. doi:10.1039/c5ta05099e
63. Hou, J.; Wei, R.; Wu, X.; Tahir, M.; Wang, X.; Butt, F. K.; Cao, C. *Dalton Trans.* **2018,** *47,* 6692–6701. doi:10.1039/c8dt00570b
64. Yu, S.; Zhang, Y.; Li, M.; Du, X.; Huang, H. *Appl. Surf. Sci.* **2017,** *391,* 491–498. doi:10.1016/j.apsusc.2016.07.028
65. Xiao, L.; Lin, R.; Wang, J.; Cui, C.; Wang, J.; Li, Z. *J. Colloid Interface Sci.* **2018,** *523,* 151–158. doi:10.1016/j.jcis.2018.03.064
66. Jamkhande, P. G.; Ghule, N. W.; Bamer, A. H.; Kalaskar, M. G. *J. Drug Delivery Sci. Technol.* **2019,** *53,* 101174. doi:10.1016/j.jddst.2019.101174
67. Rajput, N. *Int. J. Adv. Eng. Technol.* **2015,** *7,* 1806–1811. doi:10.7323/ijaet/v7_iss6
68. Rane, A. V.; Kanny, K.; Abitha, V. K.; Thomas, S. Methods for synthesis of nanoparticles and fabrication of nanocomposites. *Synthesis of inorganic nanomaterials;* Woodhead Publishing: Duxford, UK, 2018; pp 121–139. doi:10.1016/b978-0-08-101975-7.00005-1
69. Cipolatti, E. P.; Valério, A.; Henriques, R. O.; Moritz, D. E.; Ninow, J. L.; Freire, D. M. G.; Manoel, E. A.; Fernandez-Lafuente, R.; de Oliveira, D. *RSC Adv.* **2016,** *6,* 104675–104692. doi:10.1039/c6ra22047a
70. Zhu, X. H.; Hang, Q. M. *Micron* **2013,** *44,* 21–44. doi:10.1016/j.micron.2012.06.005
71. Abbas, A.; Amin, H. M. A. *Microchem. J.* **2022,** *175,* 107166. doi:10.1016/j.microc.2021.107166
72. Trino, L. D.; Bronze-Uhle, E. S.; George, A.; Mathew, M. T.; Lisboa-Filho, P. N. *Colloids Surf., A* **2018,** *546,* 168–178. doi:10.1016/j.colsurfa.2018.03.019
73. Nasr, M.; Eid, C.; Habchi, R.; Miele, P.; Bechelany, M. *ChemSusChem* **2018,** *11,* 3023–3047. doi:10.1002/cssc.201800874
74. Welch, C. M.; Compton, R. G. *Anal. Bioanal. Chem.* **2006,** *384,* 601–619. doi:10.1007/s00216-005-0230-3
75. Zhang, L.; Wang, W.; Zhou, L.; Xu, H. *Small* **2007,** *3,* 1618–1625. doi:10.1002/smll.200700043
76. Hagfeldt, A.; Graetzel, M. *Chem. Rev.* **1995,** *95,* 49–68. doi:10.1021/cr00033a003
77. Wang, Z.; Jiang, C.; Huang, R.; Peng, H.; Tang, X. *J. Phys. Chem. C* **2014,** *118,* 1155–1160. doi:10.1021/jp4065505
78. Ma, D.; Zhao, J.; Chu, R.; Yang, S.; Zhao, Y.; Hao, X.; Li, L.; Zhang, L.; Lu, Y.; Yu, C. *Adv. Powder Technol.* **2013,** *24,* 79–85. doi:10.1016/j.apt.2012.02.004
79. Ma, D.; Zhao, J.; Li, Y.; Su, X.; Hou, S.; Zhao, Y.; Hao, X.; Li, L. *Colloids Surf., A* **2010,** *368,* 105–111. doi:10.1016/j.colsurfa.2010.07.022
80. Rao, F.; Zhu, G.; Zhang, W.; Gao, J.; Zhang, F.; Huang, Y.; Hojamberdiev, M. *Appl. Catal., B* **2021,** *281,* 119481. doi:10.1016/j.apcatb.2020.119481
81. Huang, H.; Xiao, K.; Zhang, T.; Dong, F.; Zhang, Y. *Appl. Catal., B* **2017,** *203,* 879–888. doi:10.1016/j.apcatb.2016.10.082
82. Xie, T.; Zhang, Y.; Yao, W.; Liu, Y.; Wang, H.; Wu, Z. *Catal. Sci. Technol.* **2019,** *9,* 1178–1188. doi:10.1039/c8cy02344a
83. Zou, Z.; Xu, H.; Li, D.; Sun, J.; Xia, D. *Appl. Surf. Sci.* **2019,** *463,* 1011–1018. doi:10.1016/j.apsusc.2018.09.025
84. Hu, T.; Li, H.; Du, N.; Hou, W. *ChemCatChem* **2018,** *10,* 3040–3048. doi:10.1002/cctc.201701965
85. Zhou, S.; Zhang, Q.; Zhao, D.; Zong, W.; Fan, Z.; Sun, Y.; Xu, X. *Appl. Organomet. Chem.* **2018,** *32,* e4230. doi:10.1002/aoc.4230
86. Merupo, V. I.; Velumani, S.; Oza, G.; Tabellout, M.; Bizarro, M.; Coste, S.; Kassiba, A. H. *ChemistrySelect* **2016,** *1,* 1278–1286. doi:10.1002/slct.201600090

87. Huang, Y.; Kang, S.; Yang, Y.; Qin, H.; Ni, Z.; Yang, S.; Li, X. *Appl. Catal., B* **2016,** *196,* 89–99. doi:10.1016/j.apcatb.2016.05.022
88. Dong, Y.; Xu, D.; Wang, Q.; Zhang, G.; Zhang, Q.; Zhang, Z.; Lv, L.; Xia, Y.; Ren, Z.; Wang, P. *Appl. Surf. Sci.* **2021,** *542,* 148521. doi:10.1016/j.apsusc.2020.148521
89. Huang, H.; Li, X.; Wang, J.; Dong, F.; Chu, P. K.; Zhang, T.; Zhang, Y. *ACS Catal.* **2015,** *5,* 4094–4103. doi:10.1021/acscatal.5b00444
90. Wu, Q.; Chai, S.; Yang, H.; Gao, Z.; Zhang, R.; Wang, L.; Kang, L. *Sep. Purif. Technol.* **2020,** *253,* 117388. doi:10.1016/j.seppur.2020.117388
91. Xiong, T.; Wen, M.; Dong, F.; Yu, J.; Han, L.; Lei, B.; Zhang, Y.; Tang, X.; Zang, Z. *Appl. Catal., B* **2016,** *199,* 87–95. doi:10.1016/j.apcatb.2016.06.032
92. Zhou, F. Q.; Fan, J. C.; Xu, Q. J.; Min, Y. L. *Appl. Catal., B* **2017,** *201,* 77–83. doi:10.1016/j.apcatb.2016.08.027
93. He, Z.; Shi, Y.; Gao, C.; Wen, L.; Chen, J.; Song, S. *J. Phys. Chem. C* **2014,** *118,* 389–398. doi:10.1021/jp409598s
94. Wang, S.; Yang, X.; Zhang, X.; Ding, X.; Yang, Z.; Dai, K.; Chen, H. *Appl. Surf. Sci.* **2017,** *391,* 194–201. doi:10.1016/j.apsusc.2016.07.070
95. Zou, X.; Dong, Y.; Zhang, X.; Cui, Y.; Ou, X.; Qi, X. *Appl. Surf. Sci.* **2017,** *391,* 525–534. doi:10.1016/j.apsusc.2016.06.003
96. Yi, J.; Jiao, C.; Mo, H.; Chen, Q.; She, Q.; Li, Z. *Ceram. Int.* **2018,** *44,* 22102–22107. doi:10.1016/j.ceramint.2018.08.320
97. Sang, Y.; Cao, X.; Dai, G.; Wang, L.; Peng, Y.; Geng, B. *J. Hazard. Mater.* **2020,** *381,* 120942. doi:10.1016/j.jhazmat.2019.120942
98. Zhao, Q.; Lu, L.; Wang, B.; Jiang, T. *React. Kinet., Mech. Catal.* **2021,** *132,* 581–597. doi:10.1007/s11144-020-01916-3
99. Lv, Y.-R.; He, R.-K.; Chen, Z.-Y.; Li, X.; Xu, Y.-H. *J. Colloid Interface Sci.* **2020,** *560,* 293–302. doi:10.1016/j.jcis.2019.10.064
100. Bard, A. J. *J. Photochem.* **1979,** *10,* 59–75. doi:10.1016/0047-2670(79)80037-4
101. Wang, Y.; Zhang, Z.; Zhang, L.; Luo, Z.; Shen, J.; Lin, H.; Long, J.; Wu, J. C. S.; Fu, X.; Wang, X.; Li, C. *J. Am. Chem. Soc.* **2018,** *140,* 14595–14598. doi:10.1021/jacs.8b09344
102. Fu, F.; Shen, H.; Xue, W.; Zhen, Y.; Soomro, R. A.; Yang, X.; Wang, D.; Xu, B.; Chi, R. *J. Catal.* **2019,** *375,* 399–409. doi:10.1016/j.jcat.2019.06.033
103. Hu, J.; Chen, C.; Zheng, Y.; Zhang, G.; Guo, C.; Li, C. M. *Small* **2020,** *16,* 2002988. doi:10.1002/smll.202002988
104. Bao, Y.; Song, S.; Yao, G.; Jiang, S. *Sol. RRL* **2021,** *5,* 2100118. doi:10.1002/solr.202100118
105. Xu, A.; Tu, W.; Shen, S.; Lin, Z.; Gao, N.; Zhong, W. *Appl. Surf. Sci.* **2020,** *528,* 146949. doi:10.1016/j.apsusc.2020.146949
106. Liu, Y.; Liu, C.; Shi, C.; Sun, W.; Lin, X.; Shi, W.; Hong, Y. *J. Alloys Compd.* **2021,** *881,* 160437. doi:10.1016/j.jallcom.2021.160437
107. Li, Q.; Zhao, W.; Zhai, Z.; Ren, K.; Wang, T.; Guan, H.; Shi, H. *J. Mater. Sci. Technol.* **2020,** *56,* 216–226. doi:10.1016/j.jmst.2020.03.038
108. Kong, X. Y.; Choo, Y. Y.; Chai, S.-P.; Soh, A. K.; Mohamed, A. R. *Chem. Commun.* **2016,** *52,* 14242–14245. doi:10.1039/c6cc07750a
109. Jin, X.; Ye, L.; Xie, H.; Chen, G. *Coord. Chem. Rev.* **2017,** *349,* 84–101. doi:10.1016/j.ccr.2017.08.010
110. Wang, Z.; Li, C.; Domen, K. *Chem. Soc. Rev.* **2019,** *48,* 2109–2125. doi:10.1039/c8cs00542g
111. Maeda, K.; Domen, K. *J. Phys. Chem. Lett.* **2010,** *1,* 2655–2661. doi:10.1021/jz1007966
112. Zou, Z.; Ye, J.; Sayama, K.; Arakawa, H. *Nature* **2001,** *414,* 625–627. doi:10.1038/414625a
113. Martinez Suarez, C.; Hernández, S.; Russo, N. *Appl. Catal., A* **2015,** *504,* 158–170. doi:10.1016/j.apcata.2014.11.044
114. Cao, D.; Wang, Q.; Wu, Y.; Zhu, S.; Jia, Y.; Wang, R. *Sep. Purif. Technol.* **2020,** *250,* 117132. doi:10.1016/j.seppur.2020.117132
115. Yang, C.; Xue, Z.; Qin, J.; Sawangphruk, M.; Rajendran, S.; Zhang, X.; Liu, R. *J. Phys. Chem. C* **2019,** *123,* 4795–4804. doi:10.1021/acs.jpcc.8b10604
116. Malathi, A.; Arunachalam, P.; Grace, A. N.; Madhavan, J.; Al-Mayouf, A. M. *Appl. Surf. Sci.* **2017,** *412,* 85–95. doi:10.1016/j.apsusc.2017.03.199
117. Priya, A.; Arunachalam, P.; Selvi, A.; Madhavan, J.; Al-Mayouf, A. M. *Colloids Surf., A* **2018,** *559,* 83–91. doi:10.1016/j.colsurfa.2018.09.031
118. Rahman, M. U.; Qazi, U. Y.; Hussain, T.; Nadeem, N.; Zahid, M.; Bhatti, H. N.; Shahid, I. *Opt. Mater. (Amsterdam, Neth.)* **2021,** *120,* 111408. doi:10.1016/j.optmat.2021.111408
119. Chava, R. K.; Son, N.; Kang, M. *Chemosphere* **2022,** *300,* 134570. doi:10.1016/j.chemosphere.2022.134570
120. Sreeram, N.; Aruna, V.; Koutavarapu, R.; Lee, D.-Y.; Shim, J. *Chemosphere* **2022,** *299,* 134477. doi:10.1016/j.chemosphere.2022.134477
121. Larimi, A.; Rahimi, M.; Khorasheh, F. *Renewable Energy* **2020,** *145,* 1862–1869. doi:10.1016/j.renene.2019.07.105
122. Lee, J. H.; Lee, H.; Kang, M. *Mater. Lett.* **2016,** *178,* 316–319. doi:10.1016/j.matlet.2016.04.193
123. Li, L.; Li, P.; Wang, Y.; Lin, L.; Shah, A. H.; He, T. *Appl. Surf. Sci.* **2018,** *452,* 498–506. doi:10.1016/j.apsusc.2018.04.256
124. Li, X.; Zhuang, Z.; Li, W.; Pan, H. *Appl. Catal., A* **2012,** *429-430,* 31–38. doi:10.1016/j.apcata.2012.04.001
125. Moradi, M.; Khorasheh, F.; Larimi, A. *Sol. Energy* **2020,** *211,* 100–110. doi:10.1016/j.solener.2020.09.054
126. Liu, Y.; Guo, J.-g.; Wang, Y.; Hao, Y.-j.; Liu, R.-h.; Li, F.-t. *Green Energy Environ.* **2021,** *6,* 244–252. doi:10.1016/j.gee.2020.04.014
127. Rong, X.; Mao, Y.; Xu, J.; Zhang, X.; Zhang, L.; Zhou, X.; Qiu, F.; Wu, Z. *Catal. Commun.* **2018,** *116,* 16–19. doi:10.1016/j.catcom.2018.07.018
128. Fei, T.; Yu, L.; Liu, Z.; Song, Y.; Xu, F.; Mo, Z.; Liu, C.; Deng, J.; Ji, H.; Cheng, M.; Lei, Y.; Xu, H.; Li, H. *J. Colloid Interface Sci.* **2019,** *557,* 498–505. doi:10.1016/j.jcis.2019.09.011
129. Zhou, S.; Zhang, C.; Liu, J.; Liao, J.; Kong, Y.; Xu, Y.; Chen, G. *Catal. Sci. Technol.* **2019,** *9,* 5562–5566. doi:10.1039/c9cy00972h
130. Zhang, Y.; Yu, L.; Tang, L.; Zhu, M.; Jin, Y.; Wang, Z.; Li, L. *Engineering (Irvine, CA, U. S.)* **2021,** *7,* 11–13. doi:10.1016/j.eng.2020.03.006
131. Ning, S.; Lin, H.; Tong, Y.; Zhang, X.; Lin, Q.; Zhang, Y.; Long, J.; Wang, X. *Appl. Catal., B* **2017,** *204,* 1–10. doi:10.1016/j.apcatb.2016.11.006
132. Wang, W.; Chen, X.; Liu, G.; Shen, Z.; Xia, D.; Wong, P. K.; Yu, J. C. *Appl. Catal., B* **2015,** *176-177,* 444–453. doi:10.1016/j.apcatb.2015.04.026
133. Liang, J.; Deng, J.; Li, M.; Tong, M. *Colloids Surf., B* **2016,** *138,* 102–109. doi:10.1016/j.colsurfb.2015.11.060
134. Guan, D.-L.; Niu, C.-G.; Wen, X.-J.; Guo, H.; Deng, C.-H.; Zeng, G.-M. *J. Colloid Interface Sci.* **2018,** *512,* 272–281. doi:10.1016/j.jcis.2017.10.068

135. Wu, D.; Wang, B.; Wang, W.; An, T.; Li, G.; Ng, T. W.; Yip, H. Y.; Xiong, C.; Lee, H. K.; Wong, P. K. *J. Mater. Chem. A* **2015,** *3,* 15148–15155. doi:10.1039/c5ta02757h
136. Wu, D.; Ye, L.; Yue, S.; Wang, B.; Wang, W.; Yip, H. Y.; Wong, P. K. *J. Phys. Chem. C* **2016,** *120,* 7715–7727. doi:10.1021/acs.jpcc.6b02365
137. Wang, M.; Tan, G.; Zhang, D.; Li, B.; Lv, L.; Wang, Y.; Ren, H.; Zhang, X.; Xia, A.; Liu, Y. *Appl. Catal., B* **2019,** *254,* 98–112. doi:10.1016/j.apcatb.2019.04.044
138. Li, J.; Yin, Y.; Liu, E.; Ma, Y.; Wan, J.; Fan, J.; Hu, X. *J. Hazard. Mater.* **2017,** *321,* 183–192. doi:10.1016/j.jhazmat.2016.09.008
139. Wang, Y.; Lin, L.; Li, F.; Chen, L.; Chen, D.; Yang, C.; Huang, M. *Photochem. Photobiol. Sci.* **2016,** *15,* 666–672. doi:10.1039/c5pp00406c
140. Liang, J.; Liu, F.; Deng, J.; Li, M.; Tong, M. *Water Res.* **2017,** *123,* 632–641. doi:10.1016/j.watres.2017.06.060
141. Meng, X.; Li, Z.; Zeng, H.; Chen, J.; Zhang, Z. *Appl. Catal., B* **2017,** *210,* 160–172. doi:10.1016/j.apcatb.2017.02.083
142. Gong, S.; Zhu, G.; Wang, R.; Rao, F.; Shi, X.; Gao, J.; Huang, Y.; He, C.; Hojamberdiev, M. *Appl. Catal., B* **2021,** *297,* 120413. doi:10.1016/j.apcatb.2021.120413
143. Ye, L.; Jin, X.; Liu, C.; Ding, C.; Xie, H.; Chu, K. H.; Wong, P. K. *Appl. Catal., B* **2016,** *187,* 281–290. doi:10.1016/j.apcatb.2016.01.044
144. Yuan, X.; Shen, D.; Zhang, Q.; Zou, H.; Liu, Z.; Peng, F. *Chem. Eng. J.* **2019,** *369,* 292–301. doi:10.1016/j.cej.2019.03.082
145. Yue, P.; Zhang, G.; Cao, X.; Wang, B.; Zhang, Y.; Wei, Y. *Sep. Purif. Technol.* **2019,** *213,* 34–44. doi:10.1016/j.seppur.2018.12.003
146. Shi, H.; Zhao, Y.; Fan, J.; Tang, Z. *Appl. Surf. Sci.* **2019,** *465,* 212–222. doi:10.1016/j.apsusc.2018.09.164
147. Xue, W.; Huang, D.; Li, J.; Zeng, G.; Deng, R.; Yang, Y.; Chen, S.; Li, Z.; Gong, X.; Li, B. *Chem. Eng. J.* **2019,** *373,* 1144–1157. doi:10.1016/j.cej.2019.05.069
148. Arif, M.; Min, Z.; Yuting, L.; Yin, H.; Liu, X. *J. Ind. Eng. Chem. (Amsterdam, Neth.)* **2019,** *69,* 345–357. doi:10.1016/j.jiec.2018.09.026
149. Hong, Y.; Li, C.; Yin, B.; Li, D.; Zhang, Z.; Mao, B.; Fan, W.; Gu, W.; Shi, W. *Chem. Eng. J.* **2018,** *338,* 137–146. doi:10.1016/j.cej.2017.12.108

License and Terms

BEILSTEIN JOURNAL OF NANOTECHNOLOGY

LED-light-activated photocatalytic performance of metal-free carbon-modified hexagonal boron nitride towards degradation of methylene blue and phenol

Nirmalendu S. Mishra and Pichiah Saravanan*§

Full Research Paper

Open Access

Address:
Environmental Nanotechnology Laboratory, Department of Environmental Science and Engineering, Indian Institute of Technology (ISM), Dhanbad-826004, Jharkhand, India

Email:
Pichiah Saravanan* - saravananpichiah@iitism.ac.in

* Corresponding author
§ Tel: +91-326-2235995

Keywords:
carbon modification; hexagonal boron nitride (HBN); LED light; phenol; photocatalysis

Beilstein J. Nanotechnol. **2022,** *13,* 1380–1392.
https://doi.org/10.3762/bjnano.13.114

Received: 30 July 2022
Accepted: 02 November 2022
Published: 22 November 2022

This article is part of the thematic issue "Nanomaterials for photocatalysis and applications in environmental remediation and renewable energy".

Guest Editor: V. V. Pham

Abstract

The present study outlines the transformation of non-photoresponsive hexagonal boron nitride (HBN) into a visible-light-responsive material. The carbon modification was achieved through a solid-state reaction procedure inside a tube furnace under nitrogen atmosphere. In comparison to HBN (bandgap of 5.2 eV), the carbon-modified boron nitride could efficiently absorb LED light irradiation with a light harvesting efficiency of ≈90% and a direct bandgap of 2 eV. The introduction of carbon into the HBN lattice led to a significant change in the electronic environment through the formation of C–B and C–N bonds which resulted in improved visible light activity, lower charge transfer resistance, and improved charge carrier density (2.97×10^{19} cm^{-3}). This subsequently enhanced the photocurrent density (three times) and decreased the photovoltage decay time (two times) in comparison to those of HBN. The electronic band structure (obtained through Mott–Schottky plots) and charge trapping analysis confirmed the dominance of e^-, $O_2^{-\bullet}$, and $^\bullet OH$ as dominant reactive oxygen species. The carbon modification could effectively remove 93.83% of methylene blue (MB, 20 ppm solution) and 48.56% of phenol (10 ppm solution) from the aqueous phase in comparison to HBN which shows zero activity in the visible region.

Introduction

Hexagonal boron nitride (HBN) commonly known as white graphene belongs to a class of two-dimensional layered crystalline materials. It comprises boron (B) and nitrogen (N) atoms in equal stoichiometry in a honeycomb-like arrangement comparable to that of graphene [1-3]. Its interlayer stacking consists of a sandwich-type arrangement of B and N atoms. The N atom is more electronegative than the B atom, leading to polarization and localization of electrons in the HBN lattice. This results in photoinactivity due to a wider bandgap (5.5 eV) and limits its applicability to adsorption, drug delivery, insulators,

flame retardants, hydrogen storage, among others [3-9]. This dictates the development of various innovative approaches to make it as a light-driven nanomaterial owing to its potential capabilities.

The light-driven ability of HBN can be achieved through multiple strategies. These include varying the structural morphology, heterojunction formation with a suitable photocatalyst, and doping with heteroatoms. The variation in the structural morphology results in development of multiple active sites that ensure adsorption and effective charge transfer [10]. On the other hand, HBN has been utilised as a support material in the formation of heterojunctions owing to its large surface area and separation of charge carriers due to appropriate positioning of edge potentials with respect to the synergised photocatalyst [11-13]. The process of doping includes introduction of heteroatoms such as sulphur, oxygen, and carbon into the HBN lattice. The doping of oxygen into the HBN lattice results in the generation of nitrogen vacancies and formation of energy sub-bands which help in overall reduction of the bandgap energy (E_g) [14]. At the same time, the incorporation of carbon into the HBN lattice results in the delocalization of electrons with simultaneous reduction in bandgap and is directly dependent upon the percentage of carbon introduced. This demonstrates the potential of HBN to be used as a photocatalytic material. However the studies in the sense of exploring its photocatalytic ablity intented for environmental applications is very limited [15-17]. This has motivated us to extend our study on the specified subject.

The present study discusses LED light-responsive modified boron nitride (MBN) towards its photocatalytic application. The HBN was modified by introducing carbon through the solid-state reaction method. Such introduction of carbon into the HBN lattice transformed it into a good light-responsive material with improved charge carrier density (2.97×10^{19} cm^{-3}). The LED light harvesting properties were analysed through various established characterization techniques and the photocatalysis was verified by eliminating the aqueous phase methylene blue (MB: 93.83%) and phenol (48.56%) moieties. The mechanistic insights on the transfer and separation of charge carriers along with the photodegradation performance and reactive oxygen species (ROS) trapping have been enunciated in detail. The apparent quantum efficiency (AQE) further substantiated the potential of MBN to be used as a visible light photocatalyst.

Materials and Methods

Chemicals required

Boric acid (H_3BO_3), melamine, glucose, hexagonal boron nitride nanopowder (BET surface area: 19 m^{-2} g^{-1}), MB, and phenol were purchased from Alfa Aesar and TCI chemicals. All the purchased chemicals were high purity analytical grade reagents and utilized without any further purification.

Synthesis procedure

The modified HBN was synthesized through a solid-state reaction approach with various modifications to the process described in Wang et al. [17]. An equimolar mix (0.1 M) of melamine, boric acid, and glucose was finely grounded in an agate mortar pestle to form a uniform white mixture. The bandgap could be regulated by the amount of carbon substituted into the lattice sites, with higher concentration of C atoms leading to better light harvesting and electronic properties [17,18]. Thus, the amount of glucose utilized for this study was fixed at 80 wt %. The obtained mixture was placed in a boat-type alumina crucible and subjected to heat treatment in a tube furnace at 900 °C for 3 h with a heating ramp rate of 5 °C/min under nitrogen atmosphere. Finally, the obtained MBN was naturally cooled to room temperature, washed multiple times with DI water, and dried overnight at 60 °C. The commercially available HBN was used as a control sample.

Characterization techniques

A Rigaku Smart Lab high-resolution X-ray diffractometer (HR-XRD) equipped with a HyPix-3000 detector and Cu anode emitting Kα radiation was employed to obtain the crystallographic characterization. The morphology of the obtained nanostructures was captured by high-resolution transmission electron microscopy (HRTEM, Talos F200X G2, Thermo Scientific). The optical properties were characterized with a Shimadzu UV 2600 UV–vis spectrophotometer with an integrating sphere attachment using $BaSO_4$ as the standard. The electronic arrangement of the studied materials was revealed through a PHI 5000 versa probe III high-resolution X-ray photoelectron spectroscope (HR-XPS). The mineralization efficiency was estimated through the variation in the total organic carbon content by using a Shimadzu TOC-L CSH analyser. The surface area and pore characteristics were characterized by a Micromeritics (3FLEX 3500) gas sorption analyser. The surface charge was analysed through a Zeta-Meter 4.0 (Zeta-Meter, Inc, USA). The electron paramagnetic resonance (EPR) experiments were performed by utilizing an EMX micro A200-9.5/12/S/W, Bruker Biospin, Germany.

Photoelectrochemical study

The photoelectrochemical properties of the studied materials were evaluated through a CHI 650 electrochemical workstation comprising a three-electrode system with Pt and Ag/AgCl as counter and reference electrodes, respectively. The setup consists of a 0.5 M Na_2SO_4 electrolyte/hole-scavenger solution along with LED lamps as a visible light source. The working electrode was fabricated through an ITO-PTFE electrode

(dimensions: 1 cm × 1 cm) drop casted with a slurry of the studied materials, isopropanol and Nafion solution. The Mott–Schottky (MS) analysis was performed at a frequency of 1 kHz while the electrochemical impedance spectroscopy (EIS) studies were conducted at 0 V DC under a frequency range of 10^5 to 100 Hz. The open circuit potential as a function of time (OCPT) was performed under alternating light and dark conditions. The linear sweep voltammetry (LSV) studies were conducted under both dark and light conditions with a scanning speed of 5 mV/s.

Photocatalytic activity

The LED-light-driven photocatalysis experiments were performed in a 250 mL conical flask containing 50 mg of the as-synthesized material and 200 mL of a solution containing 20 ppm of MB and 10 ppm of phenol under continuous stirring. All the batches were subjected to a dark reaction until adsorption–desorption equilibrium was achieved. A control experiment in the absence of photocatalysts was performed to study the removal percentage due to photolysis of H_2O_2. Aliquots were drawn at regular intervals, ultracentrifuged at 7500 rpm, and then subjected to quantification of residual concentration of pollutants using a spectrophotometer (UV 2600 SHIMADZU, Japan). The intermediates formed during the photodegradation of phenol were analysed through a gas chromatograph coupled with a mass spectrometer (GC–MS, Thermo Fisher Scientific) by taking aliquots at 150 min and 330 min. The photocatalytic degradation and mineralization efficiencies were calculated by utilizing the following equations [19]:

$$E = \left\{\frac{\left[\left[1-\mathrm{Abs}(t)\right]\right]}{\mathrm{Abs}(0)}\right\} * 100\%, \quad (1)$$

$$\text{Mineralization} = \left\{\frac{1-\mathrm{TOC}(t)}{\mathrm{TOC}(0)}\right\} * 100\%, \quad (2)$$

where Abs(0) symbolizes the initial absorbance, Abs(t) represents the absorbance of the samples at varied time intervals, TOC(0) represents the initial TOC, and TOC(t) denotes TOC at varied time intervals.

Apparent quantum efficiency

The photon harvesting ability of the as-synthesized MBN was evaluated by the apparent quantum efficiency (AQE) parameter. The AQE was evaluated by using Equation 3 [20]:

$$\mathrm{AQE} = \frac{\text{Rate of reaction of the species } \left(K(s)\right)}{\text{Rate of photon absorption } \left(I(s)\right)}. \quad (3)$$

The intensity of the incident radiant energy was determined through a radiometer and found to be 0.05 W/cm^2.

Results and Discussion

Crystallographic information and morphological analysis

The crystallographic information obtained for MBN is shown in Figure 1a. The HR-XRD pattern demonstrates characteristic diffraction peaks at 26.14° and 42° corresponding to (002) and (100) planes of HBN, respectively. The interlayer distance (002) for MBN was found to be 0.346 nm which is considerably greater than that of HBN (0.334 nm). This indicates the turbostratic and poor crystalline nature of the as-synthesized MBN. The characteristic peak shift and widening can be attributed to the surface modification through simultaneous replacement of nitrogen atoms with larger carbon atoms [18,21,22]. The surface morphology of HBN, MBN-25, MBN-50, and MBN-80 samples have been depicted in Figure 1b–f. Furthermore, the atomic microstructure of MBN-80 demonstrates a sheet-like porous structure with a homogeneous distribution of mesopores and can be visualized through the HRTEM images in Figure 1g–m. The formation of mesopores could be attributed to the bubbling of various gases (NH_3, CO_2, H_2O) generated during the synthesis process [3,23].

Elemental characteristics and surface area

The XPS binding energy (BE) survey spectrum for MBN and its constituent elements have been depicted in Figure 2a. The existence of B 1s, N 1s, and C 1s in the BE spectra clearly indicates the formation of the BN framework along with the introduction of carbon. The B 1s spectra seen in Figure 2b could be further deconvoluted into three subpeaks at 191.30 (B–N), 189.81 (B–C), and 192.60 eV (B–O) in MBN. The relative peak intensity of the B–N bond in the B 1s spectra was found to be higher than that of B–C/B–O bonds, indicating that MBN retained the principal BN framework. Further, the N 1s spectrum (Figure 2c) could be deconvoluted into three subpeaks at 397.3, 398.78, and 399.66 eV corresponding to N–B, N–C, and N–H bonds, respectively. The C 1s peak from MBN was deconvoluted into four subpeaks at 283.66 (C–B), 284.96 (C–C), 287.4 (C–N), and 288.55 eV (C=O) respectively and has been depicted in Figure 3d. The XPS analysis also validates the equal stoichiometry of B/N in the as-synthesized MBN. Furthermore, the C content in MBN was found to be 37.4% which is noticeably higher. The O 1s Be spectrum has been demonstrated in Figure 2e. Thus, the previous observations strongly indicate the successful introduction of carbon into the BN network [17,24].

Additionally, the as-synthesized MBN-80 nanopowder had a lower BET surface area of 5.12 m^2 g^{-1} with a pore volume of

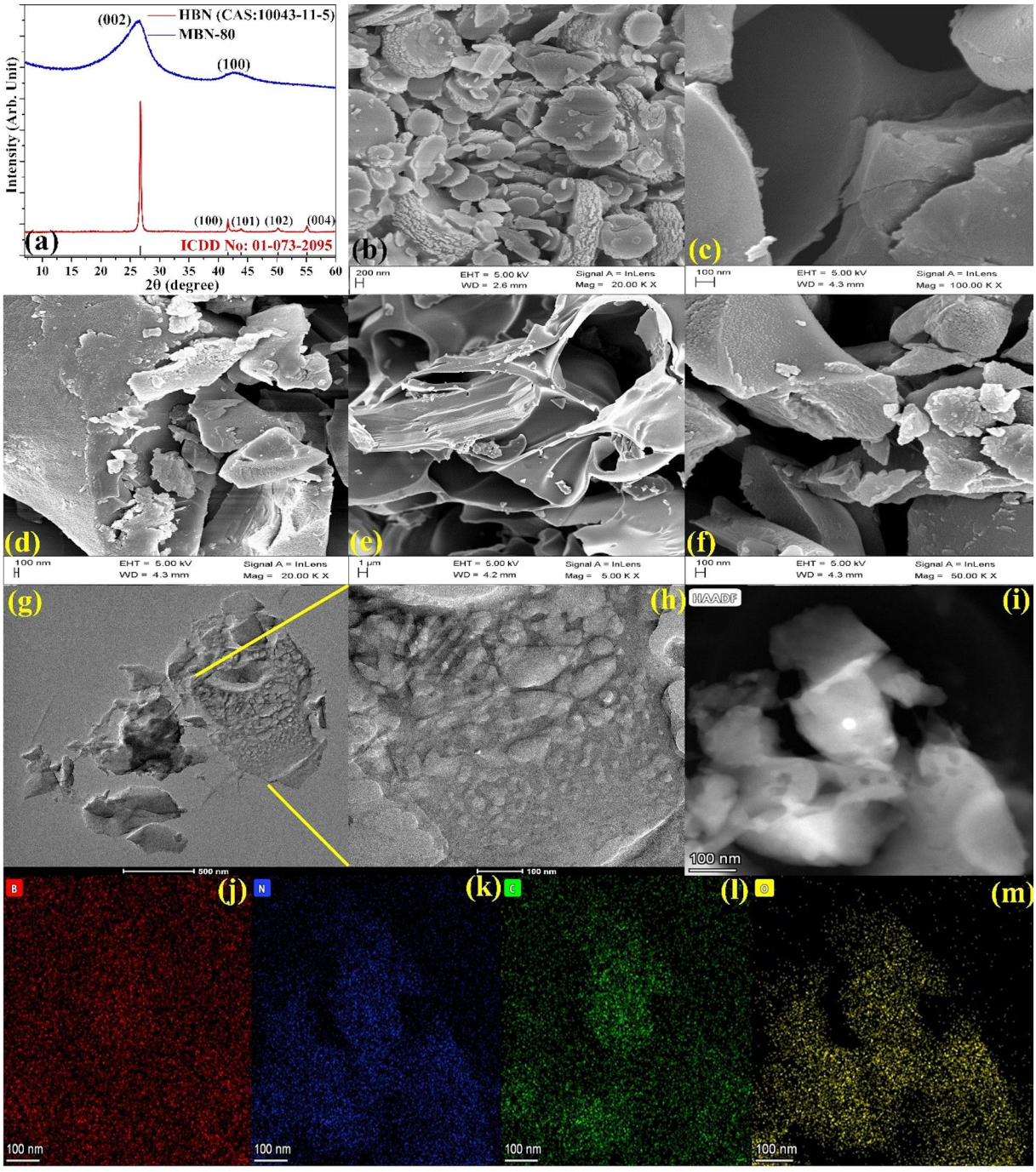

Figure 1: (a) HR-XRD plots for HBN and MBN-80, (b–d) SEM images for HBN, MBN-25, MBN-50, and (e, f) MBN-80. HRTEM images for (g, h) MBN-80 nanosheets, (i) HAADF STEM image, and (j–m) elemental mapping of B, N, C, and O in MBN-80.

0.0073 cm^3 g^{-1}. The BJH adsorption pore size distribution indicated the dominance of mesopores (2 nm < d < 50 nm) with an average pore size of 4.42 nm. The N_2 adsorption–desorption isotherm demonstrated a H4 type hysteresis curve indicating narrow slit-like pores in the as-synthesized sample. In comparison, the HBN nanopowder had a BET surface area of 19.14 m^2 g^{-1} with a pore volume of 0.0385 cm^3 g^{-1}. The BJH adsorption pore size distribution indicated an average pore size of 3.63 nm with dominance of mesopores (1.54 nm < d < 60 nm). The BJH adsorption pore size distribution along with the BET adsorption–desorption hysteresis for HBN and MBN-80 have been schematized in Figure 4. The BET surface area and pore volume decreased in MBN-80 and could be attributed to the structural pore collapse or excess carbon aggregation

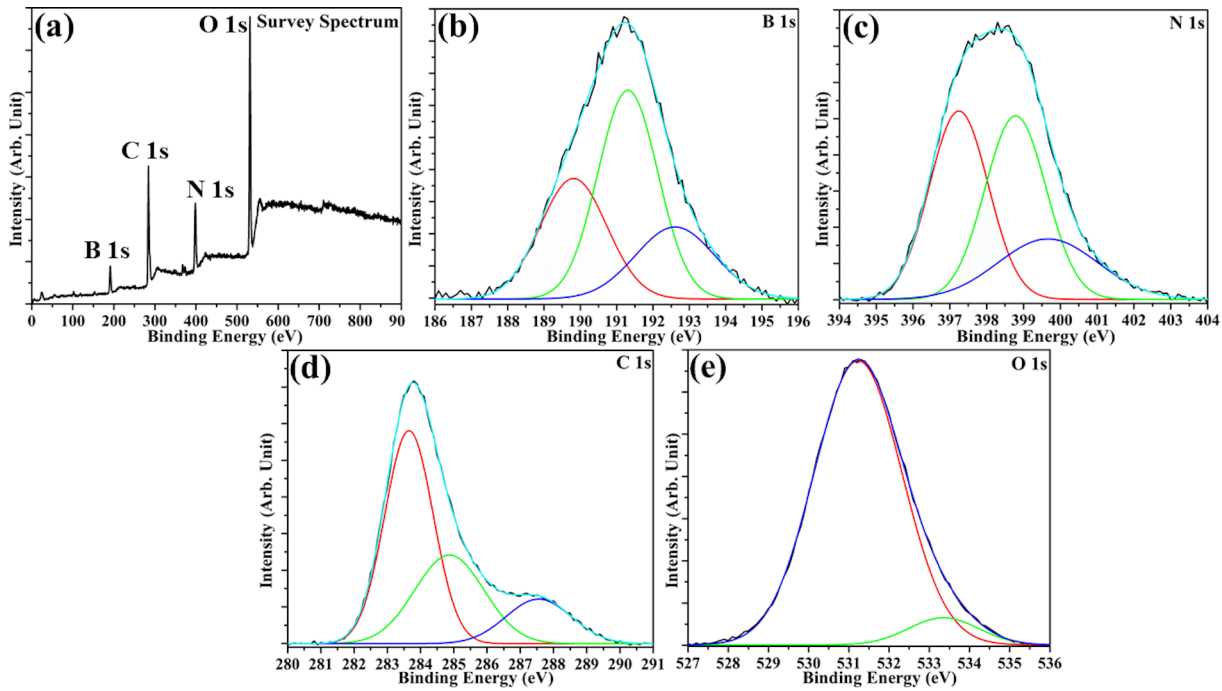

Figure 2: XPS binding energy spectrum for constituent elements from MBN. (a) Survey scan, (b) B 1s, (c) N 1s, (d) C 1s, and (e) O 1s.

[25]. However, the increase in carbon content contributed to the improvised light utilization property.

Electronic properties and zeta potential

The electronic properties exhibited by as-synthesized samples were also studied through light-induced EPR measurements. The Figure 4a demonstrates EPR spectra of MBN-25, MBN-50, and MBN-80. The samples exhibit single Lorentzian lines which can be attributed to the unpaired electrons. The MBN-80 sample shows the highest EPR spin intensity, meaning greater concentration of unpaired electrons along with higher electron delocalization which are highly favourable towards enhanced separation and generation of charge carriers [26,27]. Additionally, surface charge is an important parameter which governs the adsorption of the pollutant moiety over the photocatalyst. Thus, it becomes very important to study the variation of surface charge of the MBN-80. The variation of surface charge over MBN-80 in terms of pH value and isoelectric point of the solution was studied through zeta potential analysis (depicted in Figure 4b). It was observed that the surface of MBN-80 is positively charged at lower pH values which gradually increases with the increase in pH range. The isoelectric point was determined to be at pH 5.08. The MBN-80 was found to be negatively charged with a zeta potential of −20 mV at a neutral pH. This implies that the surface of MBN-80 is negatively charged above pH 5.08 which results in better adsorptive ability towards positively charged pollutant moieties and vice-versa.

Optical studies

The UV–vis light harvesting characteristics (absorbance, bandgap (E_g), RI, and light harvesting efficiency (LHE)) of HBN and as-synthesized MBN materials were obtained in the spectral wavelength of 200 to 900 nm and are illustrated in Figure 5. The E_g for HBN, MBN-25, MBN-50, and MBN-80 were extracted from the UV-DRS absorbance spectra through the Kubelka–Munk function by utilizing the Tauc plot mentioned in Equation 3. The obtained values were depicted in Figure 5a–e. The enhanced light absorption properties could be attributed to the grey/black colour of MBN and enhanced charge transfer attained due to the change in the electronic structure through the formation of C–N moieties in the BN framework [16].

$$(\alpha E)^{\frac{n}{2}} = A\left(E - E_g\right), \tag{4}$$

$$E = \frac{hc}{\lambda}, \tag{5}$$

where h, α, c, E denote the Planck's constant, absorption coefficient derived from the Lambert's equation, speed of light (3×10^8 m s^{-1}), and energy, respectively. The value of n (n = 4 for direct bandgap and n = 1 for indirect bandgap) depends upon the nature of the electronic transition within the semiconductor. The HBN exhibited an absorption edge at about 220 nm

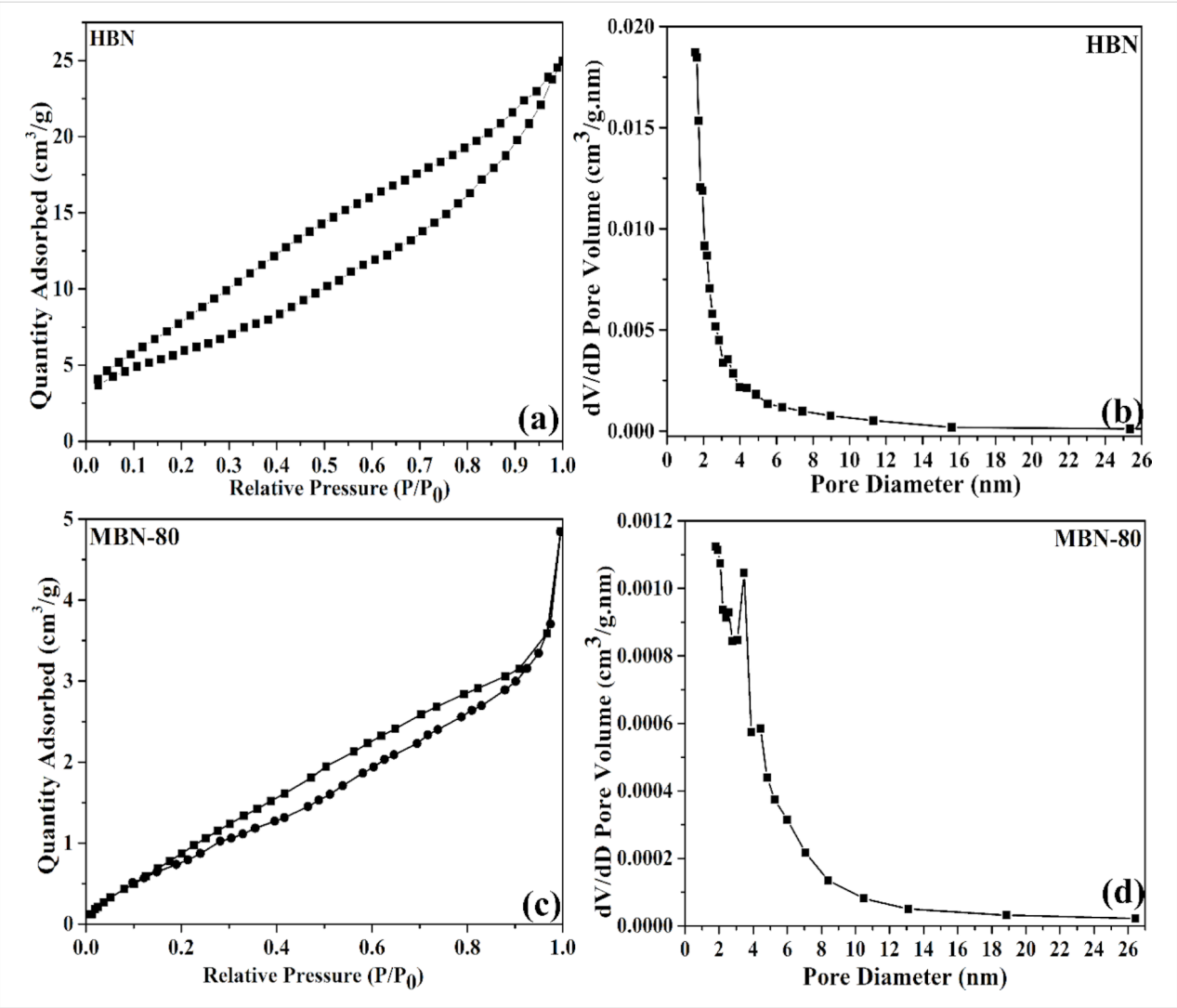

Figure 3: BET adsorption–desorption isotherm and BJH pore distribution for (a) HBN and (b) MBN-80.

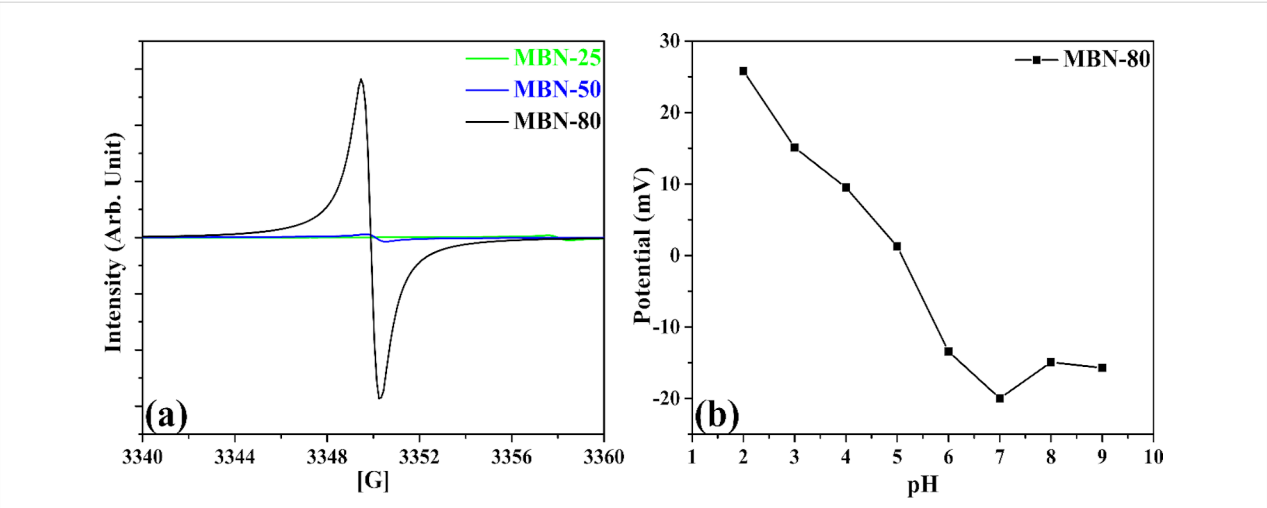

Figure 4: (a) EPR plot for the studied materials, (b) zeta potential study.

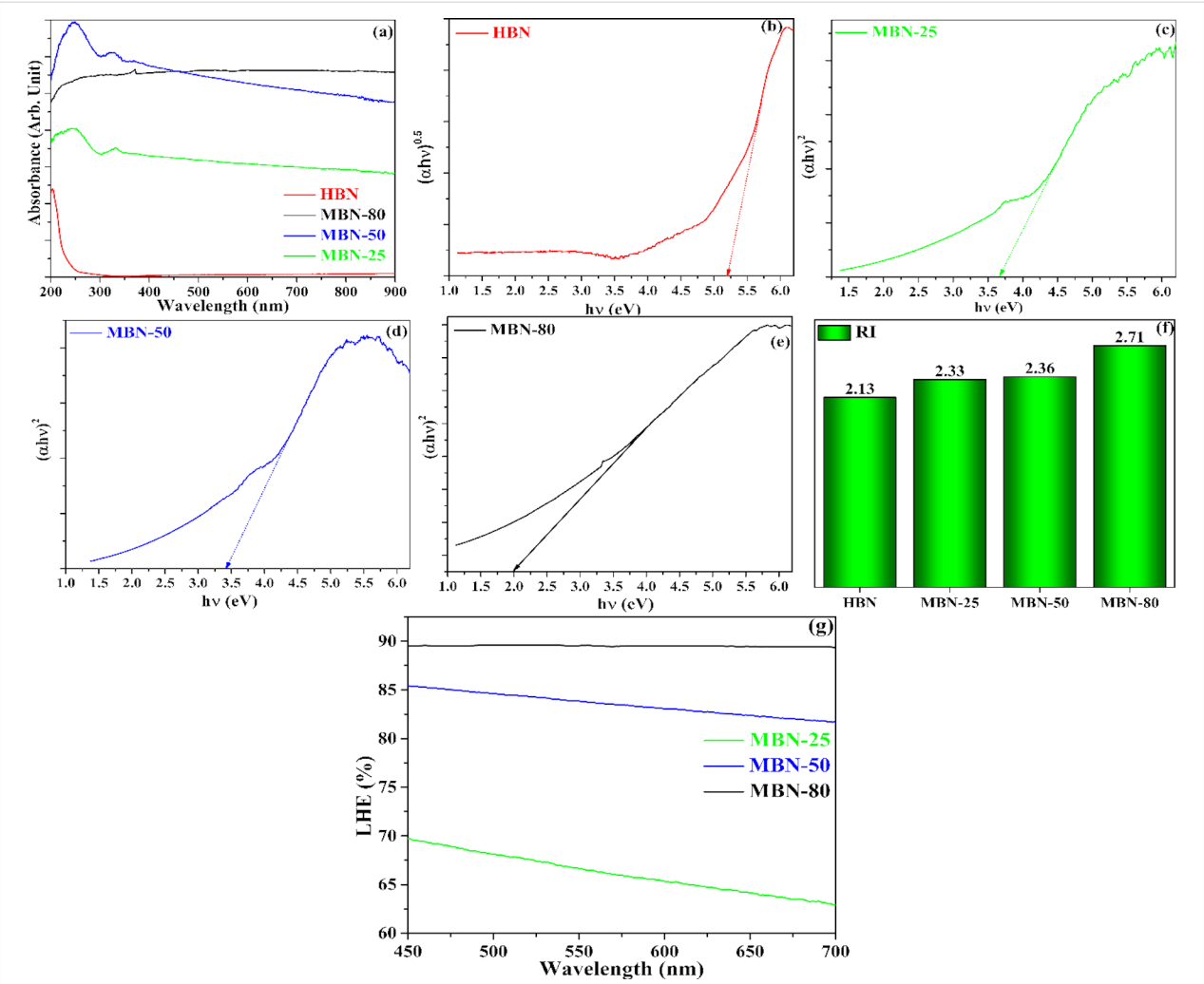

Figure 5: (a–e) UV-DRS and Tauc plot, (f) RI plot, and (g) LHE plot for the studied materials.

corresponding to a bandgap (E_g) of 5.2 eV, whereas the bandgap of MBN materials was found to be 3.68, 3.41, and 2 eV for MBN-25, MNB-50, and MBN-80, respectively.

The material capability to interact with incident photons and light utilization were analysed by calculating the refractive index of the studied materials through the Moss relation (Equation 6) and was depicted in Figure 5f. In Equation 6, E_g denotes the calculated band energy from UV-DRS analysis and R is the refractive index [28].

$$E_g R^4 = 108 \text{ eV}. \quad (6)$$

Additionally, the photon harvesting ability of the studied photocatalysts was also evaluated by determining the light harvesting efficiency (LHE). The LHE of the material was determined from the following equation and has been demonstrated in Figure 5g [29].

$$\text{LHE\%} = 100 - T - R, \quad (7)$$

where T and R denote the transmittance and reflectance for the specified materials, respectively. It was observed that the MBN had an enhanced LHE (90%) in comparison to that of HBN with zero activity in the visible range, 85% (MBN-50), and 70% (MBN-25).

Electrochemical analysis

The EIS analysis provides further evidence on the enhanced performance of MBN-80 by providing in-depth information on the charge transfer kinetics, and the obtained Nyquist plots are depicted in Figure 6a. The charge transfer resistance at the electrode–electrolyte interface can be interpreted through the arc radius from the Nyquist plot [30].

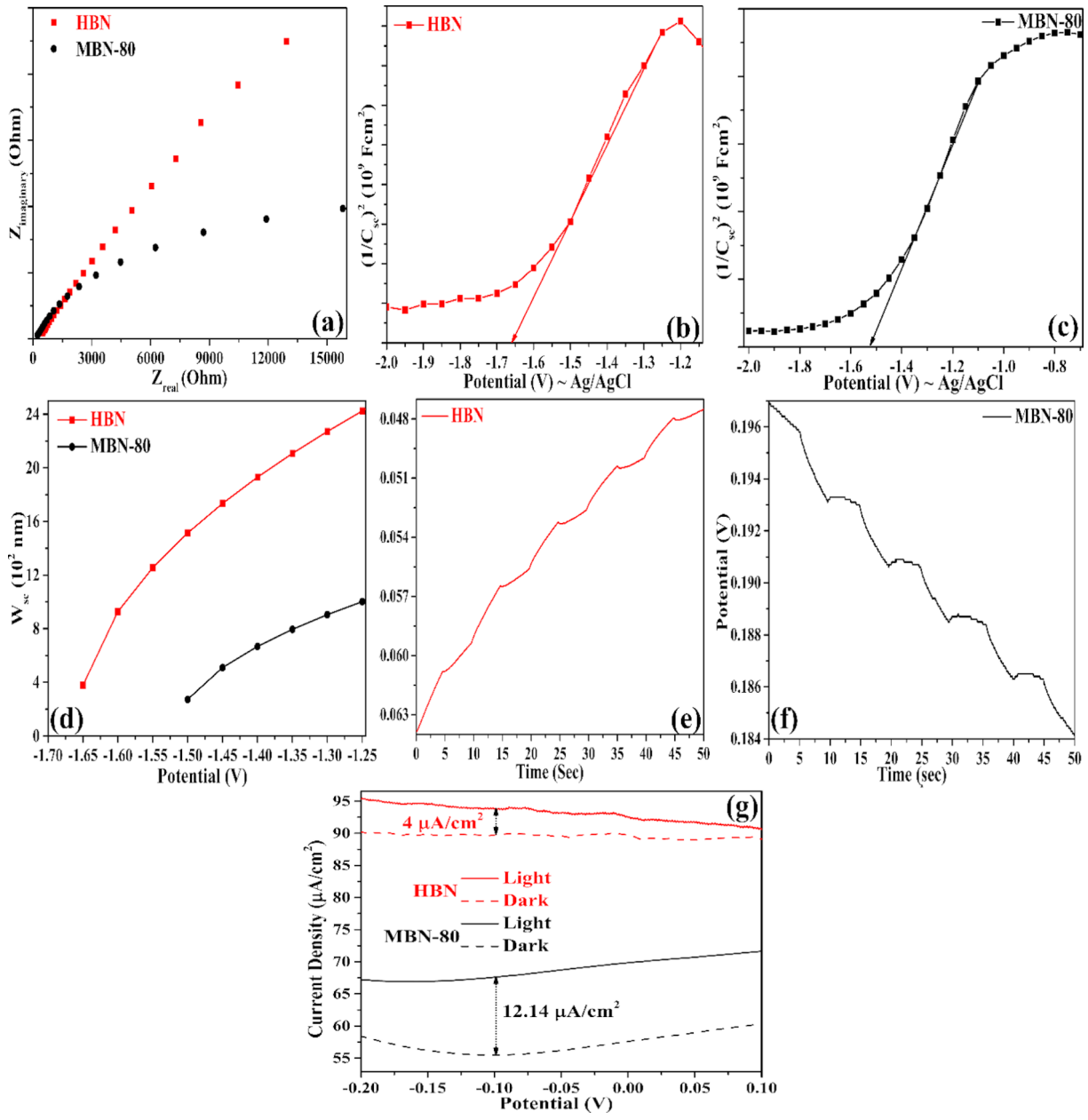

Figure 6: (a) Nyquist plot for HBN and MBN-80, (b, c) MS-plot, (d) W_{sc} analysis for HBN and MBN-80, (e, f) OCPT, and (g) LSV plots for HBN and MBN-80.

The lower Nyquist radius for MBN-80 thus demonstrates the enhanced electrochemical performance and lower charge transfer resistance. This mainly means an enhanced electron transfer from MBN-80 for a favourable visible light photocatalysis.

Additionally, the capacitance of the electrical double layer generated at the semiconductor–electrolyte interface was measured as a function of the applied potential (E_{appl}) and enunciated through Equation 8. Furthermore, the band structure, Debye length (L_{DB}), density of charge carriers (N_d), and width of the space charge region (W_{sc}) pertaining to MBN-80 could also be calculated from the Mott–Schottky analysis through the following equations [28,31,32].

$$\frac{1}{C_{sc}^2} = \frac{2}{eA^2 N_d \varepsilon\varepsilon_0}\left(E_{appl} - E_{FB} - \frac{k_B T}{e}\right) \quad (8)$$

$$N_d = \frac{2}{e\varepsilon\varepsilon_0 A^2} \frac{1}{\frac{d}{dE_{appl}}\left(\frac{1}{C_{sc}^2}\right)} \quad (9)$$

$$L_{Debye} = \sqrt{\frac{\varepsilon\varepsilon_0 k_B T}{e^2 N_d}} \quad (10)$$

$$W_{sc} = \sqrt{\frac{2\varepsilon\varepsilon_0\left(E_{appl} - E_{FB}\right)}{eN_d}} \quad (11)$$

where C_{sc}, e, A, ε, ε_0, k_B, and T indicate the capacitance of the space charge region, charge of an electron, active area of the electrode, dielectric constant, permittivity of free space, Boltzmann's constant, and absolute temperature, respectively.

The MS plots for the studied materials is depicted in Figure 6b,c. The n-type nature of the materials was confirmed through the occurrence of a positive slope. Subsequently, the flat band potential (E_{FB}) was determined by extrapolating the linear portion of the MS plot [33]. The E_{FB} values for HBN and MBN-80 were determined to be −1.66 V and −1.52 V, respectively. The respective potentials vs Ag/AgCl were converted to NHE.

The CB_{MBN} shifted to a lower edge potential (by 0.14 V) due to the interaction with the adjacent nitrogen/boron atoms through C–B and C–N bonds [17]. Furthermore, this also increased the availability of charge carriers in MBN-80 (N_d: 2.97×10^{19} cm^{-3}) which was found to be significantly greater than that in HBN (N_d: 7.38×10^{18} cm^{-3}). The increased charge density in MBN could be attributed to the accumulation of electrons over the carbon atom which aids in the photocatalytic process [24]. The MBN-80 also exhibited a lower L_{DB} and charge transit time through the depletion layer (charge transit time $\propto (L_{Debye})^2$), meaning a lower recombination of the charge carriers leading to an enhanced photocatalytic activity [29]. The same could again be justified through the width reduction of the space charge region as seen in Figure 6d. Such reduction results in rapid transport and separation of the charge carriers in comparison to HBN.

The electrochemical and potentiodynamic characteristics of MBN-80 were studied by analysing LSV and OCPT data. The LSV response for MBN-80 was studied under both visible and dark conditions, whereas the OCPT studies were performed under a constant voltage and discrete light illumination cycles [34]. The LSV and OCPT plots were depicted in Figure 6e–g. It was observed that the illumination of MBN-80 generated electron–hole pairs which resulted in a voltage buildup which subsequently decayed upon quenching of the light source [31]. The obtained photovoltage plots were subsequently fitted with an exponential decay curve. The MBN-80 demonstrated a reduced decay time (4.55 s) in comparison to that of HBN (2.65 s) emphasizing an efficient charge separation. The photovoltage was measured to be 0.198 V for MBN-80 which is about 3.3 times more than that of HBN (0.06 V), depicting the superiority of MBN-80. Further, it generated a photo current density of 12.14 μA/cm^2 which is three times greater than that of HBN (4 μA/cm^2).

Photocatalytic study of modified boron nitride

Photocatalytic study

Figure 7a–g depicts the adsorption and photocatalytic degradation performance of MBN-80 towards MB (20 ppm) and phenol (10 ppm) accomplished through LED irradiation. Specifically, it removed 78.87% of MB (20 ppm solution) which was further enhanced to 93.83% in the presence of 0.05 M H_2O_2. The photocatalysis process followed a pseudo-first-order reaction kinetics with a rate constant (K) of 0.016 min^{-1} (for the aqueous phase MB) and 0.0204 min^{-1} (for the aqueous phase MB in the presence of H_2O_2) with a TOC removal of 54.55% and 70%, respectively. On the other hand, the photocatalytic degradation of phenol demonstrated a removal rate of 0.0015 min^{-1} with 48.56% removal and a mineralization efficiency of 20.17%. The AQE for phenol/H_2O_2 system was found to be at 2.67%. A negligible removal percentage in the order of 4% for MB and 6% for phenol over a period of 140 min and 330 min, respectively, was observed for control experiments.

The photocatalytic degradation of MB was found to be dependent on the solution pH value with greater removal at higher pH values. The variation in the photocatalytic degradation as a function of pH was depicted in Figure 7b. The high removal rate towards MB could be ascribed to a better adsorption boosted through electrostatic interactions (cationic MB and negatively charged surface of MBN-80) and the synergy obtained through the photoactivity of MBN-80 and dye sensitization through MB moieties. The photosensitization of MB dye moieties generates additional photo-excited electrons which are transferred into the CB of MBN-80, resulting in enhanced charge carrier density and generation of $^{\bullet}OH$ via the O_2 reduction pathway, thus enhancing dye degradation.

Conversely, the photocatalytic degradation of phenol showed a 48.56% removal with a mineralization efficiency of 20.17% and AQE of 2.67%. This could be explained by the fact that the interaction of the photocatalyst with a specified pollutant varies with respect to its chemical behaviour. In the case of MB, an

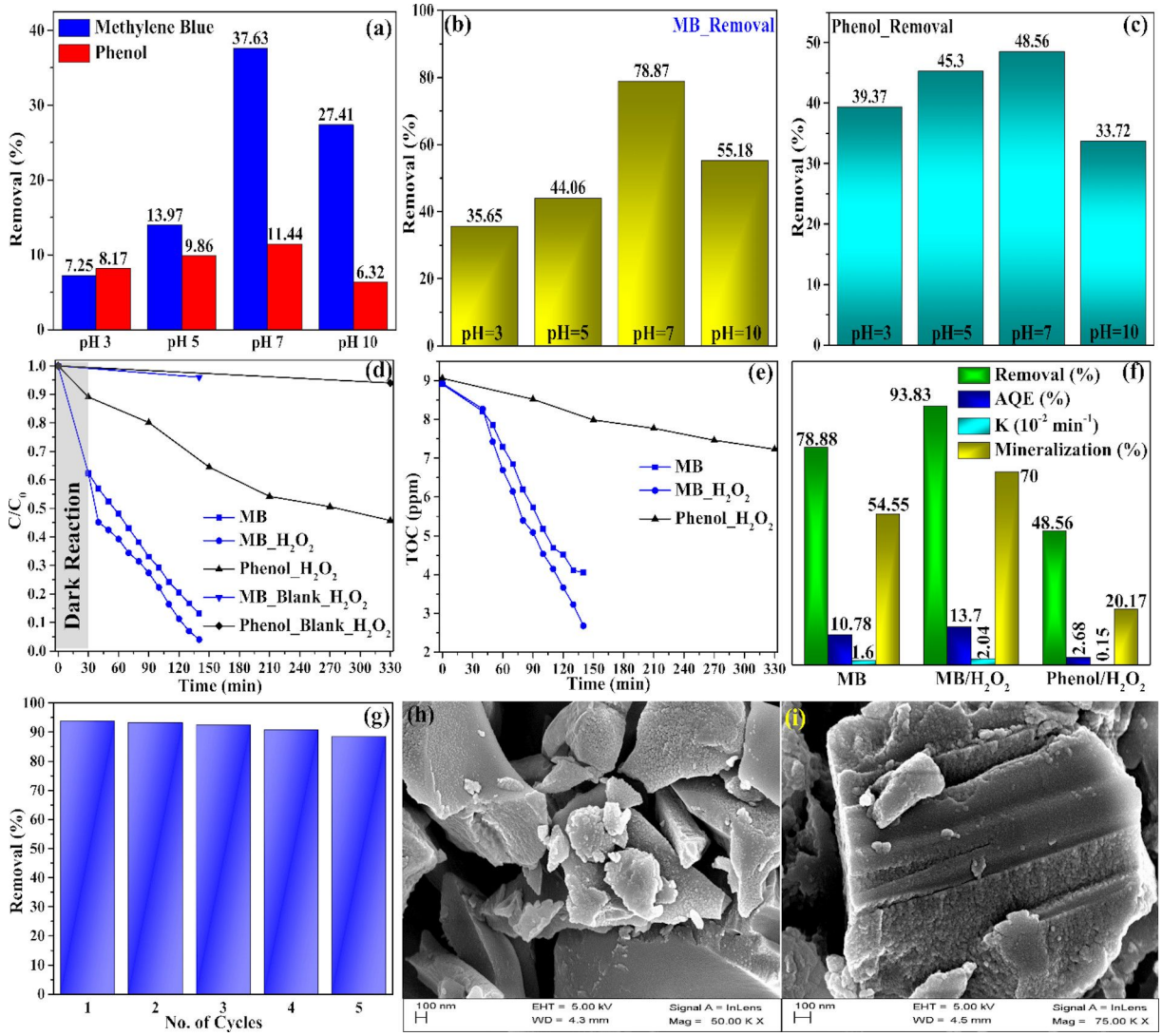

Figure 7: (a) Adsorption of MB and phenol at varied pH values. (b) The effect of pH variation on photocatalytic degradation of MB. (c) The effect of pH variation on photocatalytic degradation of phenol. (d) LED photocatalysis over MBN-80 on MB (20 ppm) and phenol (10 ppm). (e) Mineralization of MB and phenol, (f) degradation (%), AQE, rate constant (*K*) and mineralization efficiency (%), and (g) photocatalytic performance of MB up to five cycles. (h, i) SEM images of MBN-80 before and after five reuse cycles.

electrostatic interaction was observed (owing to the negatively charged MBN-80 and positively charged MB dye moieties) and that triggered the photocatalysis reaction.

In the case of phenol, it contains a phenyl group ($–C_6H_5$) with a neutral charge and thus the interaction between this group and the photocatalyst is limited. Also, the phenol is not a photosensitizing compound as MB. The variation in the photocatalytic degradation as a function of pH was depicted in Figure 7c. It can be clearly observed that the degradation efficiency decreases at higher pH values (pH 10) due to changes in surface charges of the phenol moieties (P_{ka} = 9.3) [35]. Nevertheless, the obtained MBN-80 was found to be a potential photocatalyst which can be activated with LED light and has a limited spectrum as compared to solar light. The SEM images of MBN-80 before and after five reuse cycles is depicted in Figure 7e,f. A comparison between the photocatalytic performance of MBN-80 and other photocatalytic materials reported in the literature is discussed in Table 1.

Photocatalytic mechanism

The detailed photocatalytic mechanism is explained in Figure 8a,b. The CB potential of MBN-80 (−1.7 V vs NHE) is more negative than that of $O_2/O_2^{-\bullet}$ (−0.33 V vs NHE) [44]. Conversely, the VB potential of MBN (0.3 V vs NHE) is less positive than that of $H_2O/^{\bullet}OH$ (2.32 V vs NHE) [45].

Table 1: A comparison of the photocatalytic performance of MBN-80 with previously published photocatalytic materials.

Sl.No	Photocatalyst	Light source	Pollutant/degradation efficiency	Ref.
1	BCN-80	300 W xenon lamp with 420 nm cutoff filter	U (VI)/97.40%	[17]
2	Ag_2CrO_4 / BN composite photocatalyst	visible light	rhodamine B/96.70%	[12]
3	$Bi_4O_5I_2$/3 wt % BN composite photocatalyst	300 W xenon lamp	rhodamine B/80% bisphenol-A/97%	[36]
4	0.9 % g-BN/g-C_3N_4 composite photocatalyst	300 W xenon lamp with 420 nm cutoff filter	BPA/91.9%	[37]
5	HBN-S	300 W xenon lamp	2,4-dichlorophenol/77%	[38]
6	rGO/Fe_3O_4/ZnO composite photocatalyst	tungsten halogen	methylene violet/83%	[39]
7	Fe_3O_4/ZnO/pumice composite photocatalyst	green LED	rhodamine B/72%	[40]
8	Fe_3O_4/ZnO/$CoWO_4$ composite photocatalyst	LED	MB/99%	[41]
9	HBN/titania composite photocatalyst	UV light with a wavelength of 365 nm	rhodamine B/98% MB/92%	[42]
10	5 wt % hBN/Fe_eO_3 composite photocatalyst	250 W tungsten-halogen lamp	MB/91%	[11]
11	$CaTiO_3$/BNQDs composite photocatalyst	sunlight	tetracycline/88.5%	[43]
12	MBN-80	LED light	MB/93.83% phenol/48.56%	present study

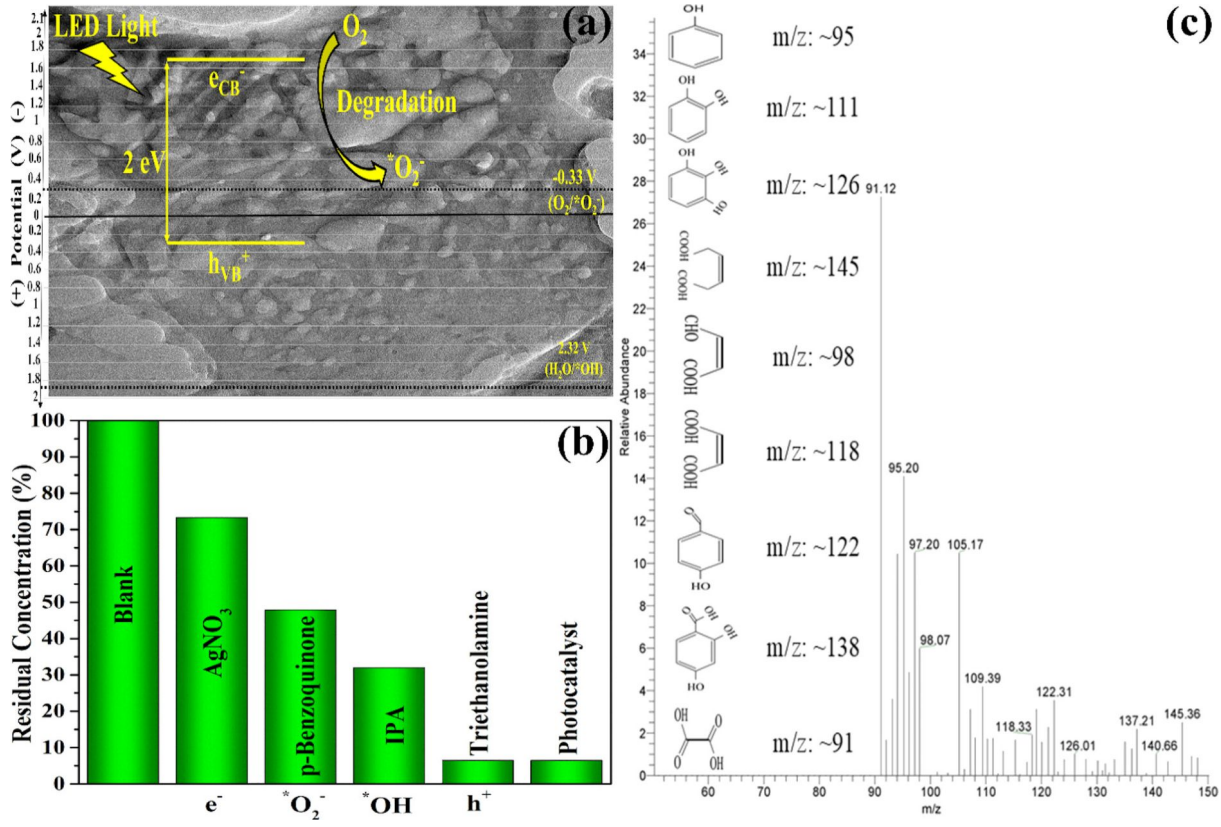

Figure 8: (a) Electronic band structure demonstrating the edge potentials for MBN. (b) Charge trapping analysis using various quenching reagents and (c) GC–MS analysis for the obtained intermediates.

This implies that the degradation could be dependent upon e^-, h^+ and $O_2^{-\bullet}$ as the predominant ROS species. Thus, the charge trapping analysis (CTA) was conducted to determine the dominant ROS species taking part in the degradation mechanism.

The CTA was achieved by taking 1 mmol of p-benzoquinone, isopropyl alcohol (IPA), $AgNO_3$, and triethanolamine (TEA) as quenching agents to trap $O_2^{-\bullet}$, $^\bullet OH$, e^-, and h^+, respectively [46]. The outcome of CTA was depicted in Figure 8b. The addition of TEA demonstrated an insignificant effect on the photocatalytic efficiency, which means no participation of h^+ in the degradation process. Further, the addition of IPA also affected the degradation performance suggesting the contribution of the $^\bullet OH$ radical (from photolysis of H_2O_2) in the photocatalytic process. Furthermore, a substantial reduction in the photocatalytic activity was observed when $AgNO_3$ and p-benzoquinone were added into the reaction system. The introduction of $AgNO_3$ resulted in the capture of electrons from the reaction mixture which disrupts the generation of $O_2^{-\bullet}$ through the $O_2/O_2^{-\bullet}$ reduction pathway. The same can also be observed during the addition of p-benzoquinone, which leads to a significant decrease in the photo catalytic efficiency due to scavenging of $O_2^{-\bullet}$. Further, the byproducts of phenol degradation analysed through GC–MS is depicted Figure 8c. The intermediate products were identified as catechol (*m*/*z*: 111), 4-hydroxybenzaldehyde (*m*/*z*: 122), salicylic acid (*m*/*z*: ≈138), benzene-1,2,3-triol (*m*/*z*: ≈126), maleic acid (*m*/*z*: ≈118), (*Z*)-4-oxobut-2-enoic acid (*m*/*z*: ≈98), (*Z*)-hex-3-enedioic acid (*m*/*z*: ≈146), and oxalic acid (*m*/*z*: ≈91) [47,48].

Conclusion

The comprehensive analysis of the obtained experimental outcomes substantiates MBN as a superior photoactive material with enhanced LHE, charge carrier generation, and reduced exciton recombination in comparison to HBN. The introduction of carbon into the HBN lattice sites boosted the overall photocatalytic performance through changes in the electronic structure by the formation of C–B and C–N moieties. This also led to the delocalization of electrons and accumulation of additional electrons from the graphitic carbon leading to an increase in charge carrier density within MBN-80. The removal of MB and phenol demonstrated LED-light-driven photocatalytic activity of MBN-80 over the nonresponsive photoinactive HBN.

Funding

Dr P. Saravanan thanks the Science and Engineering Research Board, Department of Science and Technology (DST-SERB) for the financial support received under IMPRINT with the grant code IMP/2019/000286.

Acknowledgements

Dr P. Saravanan appreciates the help from Prof. Gopinath, the head of Centre of Nanotechnology, IIT Roorkee for performing the EPR analysis.

ORCID® iDs

Pichiah Saravanan - https://orcid.org/0000-0001-8302-9586

References

1. Yu, S.; Wang, X.; Pang, H.; Zhang, R.; Song, W.; Fu, D.; Hayat, T.; Wang, X. *Chem. Eng. J.* **2018,** *333,* 343–360. doi:10.1016/j.cej.2017.09.163
2. Pakdel, A.; Bando, Y.; Golberg, D. *Chem. Soc. Rev.* **2014,** *43,* 934–959. doi:10.1039/c3cs60260e
3. Mishra, N. S.; Saravanan, P. *ChemistrySelect* **2018,** *3,* 8023–8034. doi:10.1002/slct.201801524
4. Yin, L.; Gong, K.; Zhou, K.; Qian, X.; Shi, C.; Gui, Z.; Qian, L. *J. Colloid Interface Sci.* **2022,** *608,* 853–863. doi:10.1016/j.jcis.2021.10.056
5. Kalay, S.; Yilmaz, Z.; Sen, O.; Emanet, M.; Kazanc, E.; Çulha, M. *Beilstein J. Nanotechnol.* **2015,** *6,* 84–102. doi:10.3762/bjnano.6.9
6. Weng, Q.; Kvashnin, D. G.; Wang, X.; Cretu, O.; Yang, Y.; Zhou, M.; Zhang, C.; Tang, D.-M.; Sorokin, P. B.; Bando, Y.; Golberg, D. *Adv. Mater. (Weinheim, Ger.)* **2017,** *29,* 1700695. doi:10.1002/adma.201700695
7. Cassabois, G.; Valvin, P.; Gil, B. *Nat. Photonics* **2016,** *10,* 262–266. doi:10.1038/nphoton.2015.277
8. Ba, K.; Jiang, W.; Cheng, J.; Bao, J.; Xuan, N.; Sun, Y.; Liu, B.; Xie, A.; Wu, S.; Sun, Z. *Sci. Rep.* **2017,** *7,* 45584. doi:10.1038/srep45584
9. Guo, Y.; Wang, R.; Wang, P.; Rao, L.; Wang, C. *ACS Appl. Mater. Interfaces* **2018,** *10,* 4640–4651. doi:10.1021/acsami.7b15638
10. Ng, Y. H.; Lightcap, I. V.; Goodwin, K.; Matsumura, M.; Kamat, P. V. *J. Phys. Chem. Lett.* **2010,** *1,* 2222–2227. doi:10.1021/jz100728z
11. Shenoy, M. R.; Ayyasamy, S.; Bhojan, V.; Swaminathan, R.; Raju, N.; Senthil Kumar, P.; Sasikumar, M.; Kadarkarai, G.; Tamilarasan, S.; Thangavelu, S.; J, S.; Reddy, M. V. *J. Mater. Sci.: Mater. Electron.* **2021,** *32,* 4766–4783. doi:10.1007/s10854-020-05215-4
12. Wu, X.-f.; Zhao, Z.-h.; Sun, Y.; Li, H.; Zhang, C.-x.; Wang, Y.-j.; Liu, Y.; Wang, Y.-d.; Yang, X.-y.; Gong, X.-d. *J. Nanopart. Res.* **2017,** *19,* 193. doi:10.1007/s11051-017-3892-9
13. Singh, B.; kaur, G.; Singh, P.; Singh, K.; Sharma, J.; Kumar, M.; Bala, R.; Meena, R.; Sharma, S. K.; Kumar, A. *New J. Chem.* **2017,** *41,* 11640–11646. doi:10.1039/c7nj02509b
14. Singh, R. S.; Tay, R. Y.; Chow, W. L.; Tsang, S. H.; Mallick, G.; Teo, E. H. T. *Appl. Phys. Lett.* **2014,** *104,* 163101. doi:10.1063/1.4872318
15. Shentu, Q.; Wu, Z.; Song, W.; Pan, S.; Zhou, Z.; Lv, W.; Song, C.; Yao, Y. *Chem. Eng. J.* **2022,** *446,* 137274. doi:10.1016/j.cej.2022.137274
16. Lu, Q.; An, J.; Duan, Y.; Luo, Q.; Shang, Y.; Liu, Q.; Tang, Y.; Huang, J.; Tang, C.; Yin, R.; Wang, D. *Catalysts* **2022,** *12,* 555. doi:10.3390/catal12050555
17. Wang, Y.; Chen, G.; Weng, H.; Wang, L.; Chen, J.; Cheng, S.; Zhang, P.; Wang, M.; Ge, X.; Chen, H.; Huang, W.; Lin, M. *Chem. Eng. J.* **2021,** *410,* 128280. doi:10.1016/j.cej.2020.128280
18. Li, H.; Zhu, S.; Zhang, M.; Wu, P.; Pang, J.; Zhu, W.; Jiang, W.; Li, H. *ACS Omega* **2017,** *2,* 5385–5394. doi:10.1021/acsomega.7b00795

19. Ahmadi, M.; Seyed Dorraji, M. S.; Rasoulifard, M. H.; Amani-Ghadim, A. R. *Sep. Purif. Technol.* **2019,** *228,* 115771. doi:10.1016/j.seppur.2019.115771
20. Li, Y.-X.; Fu, H.; Wang, P.; Zhao, C.; Liu, W.; Wang, C.-C. *Environ. Pollut.* **2020,** *256,* 113417. doi:10.1016/j.envpol.2019.113417
21. Matović, B.; Luković, J.; Nikolić, M.; Babić, B.; Stanković, N.; Jokić, B.; Jelenković, B. *Ceram. Int.* **2016,** *42,* 16655–16658. doi:10.1016/j.ceramint.2016.07.096
22. Lian, J.; Kim, T.; Liu, X.; Ma, J.; Zheng, W. *J. Phys. Chem. C* **2009,** *113,* 9135–9140. doi:10.1021/jp9004136
23. Chen, S.; Li, P.; Xu, S.; Pan, X.; Fu, Q.; Bao, X. *J. Mater. Chem. A* **2018,** *6,* 1832–1839. doi:10.1039/c7ta08515j
24. Ma, C.; Zhang, Y.; Yan, S.; Liu, B. *Appl. Catal., B* **2022,** *315,* 121574. doi:10.1016/j.apcatb.2022.121574
25. Xiong, J.; Zhu, W.; Li, H.; Yang, L.; Chao, Y.; Wu, P.; Xun, S.; Jiang, W.; Zhang, M.; Li, H. *J. Mater. Chem. A* **2015,** *3,* 12738–12747. doi:10.1039/c5ta01346a
26. Leong, K. H.; Tan, Z. Z.; Sim, L. C.; Saravanan, P.; Bahnemann, D.; Jang, M. *ChemistrySelect* **2017,** *2,* 84–89. doi:10.1002/slct.201601490
27. Zhao, X.; Zhao, Y.; Tan, H.; Sun, H.; Qin, X.; Ho, W.; Zhou, M.; Lin, J.; Li, Y. *Sci. Bull.* **2021,** *66,* 1764–1772. doi:10.1016/j.scib.2021.05.007
28. Kuila, A.; Saravanan, P.; Bahnemann, D.; Wang, C. *Appl. Catal., B* **2021,** *293,* 120224. doi:10.1016/j.apcatb.2021.120224
29. Sahoo, P.; Sharma, A.; Padhan, S.; Udayabhanu, G.; Thangavel, R. *Sol. Energy* **2019,** *193,* 148–163. doi:10.1016/j.solener.2019.09.045
30. Zhang, R.; Zeng, K. *Diamond Relat. Mater.* **2021,** *115,* 108343. doi:10.1016/j.diamond.2021.108343
31. Baram, N.; Ein-Eli, Y. *J. Phys. Chem. C* **2010,** *114,* 9781–9790. doi:10.1021/jp911687w
32. Lv, F.; Huang, W. *Cell Rep. Phys. Sci.* **2021,** *2,* 100652. doi:10.1016/j.xcrp.2021.100652
33. Adán-Más, A.; Silva, T. M.; Guerlou-Demourgues, L.; Montemor, M. F. *Electrochim. Acta* **2018,** *289,* 47–55. doi:10.1016/j.electacta.2018.08.077
34. Su, J.; Liu, C.; Liu, D.; Li, M.; Zhou, J. *ChemCatChem* **2016,** *8,* 3279–3286. doi:10.1002/cctc.201600767
35. Tri, N. L. M.; Thang, P. Q.; Van Tan, L.; Huong, P. T.; Kim, J.; Viet, N. M.; Phuong, N. M.; Al Tahtamouni, T. M. *J. Water Process Eng.* **2020,** *33,* 101070. doi:10.1016/j.jwpe.2019.101070
36. Ji, M.; Xia, J.; Di, J.; Liu, Y.; Chen, R.; Chen, Z.; Yin, S.; Li, H. *Chem. Eng. J.* **2018,** *331,* 355–363. doi:10.1016/j.cej.2017.08.100
37. Xu, H.; Wu, Z.; Wang, Y.; Lin, C. *J. Mater. Sci.* **2017,** *52,* 9477–9490. doi:10.1007/s10853-017-1167-6
38. Feng, C.; Tang, L.; Deng, Y.; Zeng, G.; Wang, J.; Liu, Y.; Chen, Z.; Yu, J.; Wang, J. *Appl. Catal., B* **2019,** *256,* 117827. doi:10.1016/j.apcatb.2019.117827
39. Thangavel, S.; Thangavel, S.; Raghavan, N.; Krishnamoorthy, K.; Venugopal, G. *J. Alloys Compd.* **2016,** *665,* 107–112. doi:10.1016/j.jallcom.2015.12.192
40. Taheri-Ledari, R.; Valadi, K.; Gharibi, S.; Maleki, A. *Mater. Res. Bull.* **2020,** *130,* 110946. doi:10.1016/j.materresbull.2020.110946
41. Shekofteh-Gohari, M.; Habibi-Yangjeh, A. *J. Ind. Eng. Chem. (Amsterdam, Neth.)* **2016,** *44,* 174–184. doi:10.1016/j.jiec.2016.08.028
42. Sheng, Y.; Yang, J.; Wang, F.; Liu, L.; Liu, H.; Yan, C.; Guo, Z. *Appl. Surf. Sci.* **2019,** *465,* 154–163. doi:10.1016/j.apsusc.2018.09.137
43. Bilgin Simsek, E. *Ceram. Int.* **2022,** *48,* 26487–26498. doi:10.1016/j.ceramint.2022.05.343
44. Kumar, A.; Schuerings, C.; Kumar, S.; Kumar, A.; Krishnan, V. *Beilstein J. Nanotechnol.* **2018,** *9,* 671–685. doi:10.3762/bjnano.9.62
45. Li, J.; Jiang, M.; Zhou, H.; Jin, P.; Cheung, K. M. C.; Chu, P. K.; Yeung, K. W. K. *Global Challenges* **2019,** *3,* 1800058. doi:10.1002/gch2.201800058
46. Zhong, J.; Jiang, H.; Wang, Z.; Yu, Z.; Wang, L.; Mueller, J. F.; Guo, J. *Environ. Sci. Ecotechnology* **2021,** *5,* 100079. doi:10.1016/j.ese.2021.100079
47. Azevedo, E. B.; Radler de AquinoNeto, F.; Dezotti, M. *Appl. Catal., B* **2004,** *54,* 165–173. doi:10.1016/j.apcatb.2004.06.014
48. Rani, M.; Shanker, U. *Colloids Surf., A* **2018,** *553,* 546–561. doi:10.1016/j.colsurfa.2018.05.071

License and Terms

BEILSTEIN JOURNAL OF NANOTECHNOLOGY

A TiO_2@MWCNTs nanocomposite photoanode for solar-driven water splitting

Anh Quynh Huu Le[1], Ngoc Nhu Thi Nguyen[2,3], Hai Duy Tran[1], Van-Huy Nguyen[*4] and Le-Hai Tran[*2,3]

Full Research Paper

Open Access

Address:
[1]Ho Chi Minh City University of Natural Resource and Environment, 236B Le Van Sy street, Tan Binh District, Ho Chi Minh City, Vietnam, [2]Faculty of Chemical Engineering, Ho Chi Minh City University of Technology (HCMUT), 268 Ly Thuong Kiet street, District 10, Ho Chi Minh City, Vietnam, [3]Vietnam National University Ho Chi Minh City, Linh Trung Ward, Thu Duc City, Ho Chi Minh City, Vietnam and [4]Faculty of Allied Health Sciences, Chettinad Hospital and Research Institute, Chettinad Academy of Research and Education, Kelambakkam-603103, Tamil Nadu, India

Email:
Van-Huy Nguyen* - vhnguyen.ChE@gmail.com; Le-Hai Tran* - tranlehai@hcmut.edu.vn

* Corresponding author

Keywords:
multi-wall carbon nanotubes (MWCNTs); nanomaterials; photoelectrochemical; TiO_2; water splitting

Beilstein J. Nanotechnol. **2022,** *13,* 1520–1530.
https://doi.org/10.3762/bjnano.13.125

Received: 09 August 2022
Accepted: 22 November 2022
Published: 14 December 2022

This article is part of the thematic issue "Nanomaterials for photocatalysis and applications in environmental remediation and renewable energy".

Guest Editor: V. V. Pham

Abstract

A TiO_2@MWCNTs (multi-wall carbon nanotubes) nanocomposite photoanode is prepared for photoelectrochemical water splitting in this study. The physical and photoelectrochemical properties of the photoanode are characterized using field emission-scanning electron microscopy, transmission electron microscopy, X-ray diffraction, and linear sweep voltammetry. The results show that the TiO_2@MWCNTs nanocomposite has an optical bandgap of 2.5 eV, which is a significant improvement in visible-light absorption capability compared to TiO_2 (3.14 eV). The cyclic voltammograms show that incorporating TiO_2 with the MWCNTs leads to a decrease in the electrical double layer, thereby facilitating the electron transfer rate in the TiO_2@MWCNTs electrode. Moreover, the current density of the photoelectrochemical electrode formed by TiO_2@MWCNTs under solar irradiation is significantly higher than that prepared by TiO_2 (vs Ag/AgCl). The low charge capacity of the TiO_2@MWCNTs electrode–electrolyte interface hinders the recombination of the photogenerated electrons and holes, which contributes to the enhancement of the solar-to-hydrogen (STH) conversion efficiency. The average STH conversion efficiency of the TiO_2@MWCNTs electrode under solar exposure from 6 AM to 5 PM is 11.1%, 8.88 times higher than that of a TiO_2 electrode. The findings suggested TiO_2@MWCNTs is a feasible nanomaterial to fabricate the photoanode using photoelectrochemical water splitting under solar irradiation.

Introduction

TiO_2 is an excellent photochemical catalyst for environmental and chemical applications due to its good activity regarding numerous reduction and oxidation reactions. As a wide-bandgap (ca. 3.2 eV) semiconductor, TiO_2 is a promising photocatalyst for degrading a massive range of high-molecular-weight organic pollutants under UV radiation [1]. Because of high specific surface, nanoscale TiO_2 as grains or tubes can absorb UV light more substantially than mesoscale TiO_2 [2,3]. This results in an improvement of the photon efficiency of TiO_2 nanoparticles. Reducing the dimension of the photocatalyst favors not only a bandgap shift to the visible-light region but, unfortunately, also the recombination of photogenerated electrons and holes (e^-/h^+), which limits the photocatalytic performance [4,5].

Because TiO_2 only exhibits photochemical activity under UV excitation, which accounts for a small fraction (ca. 4%) of the solar energy, numerous modification methods such as doping with nonmetals, coupling with other catalysts, and attaching to supports have been developed to increase the absorption of visible solar light [6,7]. Notably, carbon nanotubes (CNTs) are a promising material for visible-light absorption [8]. A combination of TiO_2 with CNTs can effectively enhance the separation of e^-/h^+ pairs based on the high electric conductivity of CNTs. This approach improves solar water splitting performance [7,9]. However, an excess amount of CNTs can deteriorate the photoactivity of TiO_2 nanoparticles because CNTs block and cover the surface of TiO_2 [9].

There are three categories of water splitting techniques applying photocatalysts, namely photocatalytic, photoelectrochemical, and photovoltaic–photoelectrochemical systems. The features and the operating mechanism of photoelectrochemical water splitting are detailed in [10,11]. Photoelectrochemical water splitting has attracted much research interest because it has some outstanding advantages. The research focuses on synthesizing and modifying photocatalysts for photoanodes and photocathodes for photoelectrochemical water splitting [11]. Several TiO_2-based photocatalysts have been developed and applied in photoelectrochemical water splitting. The results showed that the solar-to-hydrogen (STH) conversion efficiency of TiO_2-based photoanodes (0.2–0.42%) is lower than that of TiO_2/CNT anodes (4.4%), which is attributed to a wider bandgap of the TiO_2 photocatalyst and the lesser extent of e^-/h^+ pair recombination [12]. Dai et al. prepared a MWCNTs/TiO_2 (MWCNTs = multi-wall carbon nanotubes) nanocomposite by sol–gel method for visible-light-induced photocatalytic hydrogen evolution [8]. The photocatalyst consisted of dense TiO_2 particles covering functionalized MWNTs and exhibited good photoactivity under visible light ($\lambda > 420$ nm), but the photoelectrochemical water splitting showed a low hydrogen evolution of 450 $\mu mol \cdot h^{-1}$. Reddy et al. loaded TiO_2 particles on MWCNTs via a simple hydrothermal method [13]. However, the MWNTs/TiO_2 nanocomposite showed photoactivity only under UV irradiation due to the high bandgap of 3.1 eV.

To the best of our knowledge, there are only a few studies on TiO_2@MWCNTs nanocomposites as photoanode material for photoelectrochemical water splitting. Furthermore, the preparation of TiO_2/MWCNTs nanocomposite derived from TiO_2 precursors and functionalized MWCMTs for photoelectrochemical water splitting is based on complicated and time-consuming hydrothermal and sol–gel methods. Herein, a TiO_2@MWCNTs nanocomposite photocatalyst is synthesized via a simple hydrolysis method. The coupling of TiO_2 and MWCNTs aims to limit the recombination of photogenerated electrons and holes, to improve the visible-light absorption of the photoanode under solar irradiation, and to enhance the hydrogen evolution. The morphology and photoelectrochemical properties of the TiO_2@MWCNTs electrode are systematically studied, and the efficiency of the electrode in photoelectrochemical water splitting is also demonstrated.

Experimental

Materials

Multi-wall carbon nanotubes (purity >99.5%), synthesized via chemical vapor deposition were supplied by Vinanotech (Vietnam). Titanium tetrachloride (purity >99%) was purchased from Sigma-Aldrich (USA), and pure potassium hydroxide and potassium chloride (purity >85%) were provided from Merck (Germany). All other chemical reagents used in this study were of reagent grade.

Preparation of photocatalyst and photoelectrode

TiO_2 powders

TiO_2 powders were simply prepared from a violent hydrolysis reaction of $TiCl_4$ vapor in humid air. Precipitated fine TiO_2 particles were collected before thermal treatment at 350 °C for 60 min.

TiO_2@MWCNTs nanocomposite

First, 1.0 g of MWCNTs are added to 25 mL of $TiCl_4$ in a glass beaker under an inert atmosphere. Following, MWCNTs are dispersed in $TiCl_4$ under ultrasound for 15 min. After that, an excessive amount of deionized water is slowly dropped into the mixture. Then, the obtained solid phase is filtered and washed with water to neutralize. Finally, it is treated at 350 °C within 60 min to form the TiO_2@MWCNTs nanocomposite photocatalyst.

Photoelectrochemical electrode

1.0 g of the obtained photocatalyst is dispersed in a 25 mL solution containing 0.1 M of polyaniline and 0.3 M of oxalic acid. A plastic bar (15 × 35 × 3 mm^3 of width × height × thickness) as the support for the electrode is immersed in the as-prepared mixture. The catalyst mixture is assembled on the plastic bar under ultrasound for 1 min. Finally, the photoelectrochemical electrode is obtained after drying at 60 °C for 15 min.

TiO_2@MWCNTs nanocomposite characterizations

The surface morphology of MWCNTs and the TiO_2@MWCNTs nanocomposite is characterized by using field-emission scanning electron microscopy (FE-SEM, S4800) and transmission electron microscopy (TEM, JEOL-1400). The crystallization behavior of the catalysts is analyzed by X-ray diffraction (XRD, D2 PHASER). The chemical structure of the samples is characterized using Fourier-transform infrared spectroscopy (FTIR, Brucker 27). The electrochemical measurements are carried out on a MPG2 Biologic system with a three-electrode cell controlled by ECLab® software. Diffuse reflectance spectra (DRS) are recorded with a spectrophotometer (FL-1039, HORIBA) using a 450 W xenon lamp. A portable Luxmeter (MW700, Milwaukee) and a pyranometer (SR30, Huseflux) are used for sunlight intensity and irradiance measurements.

Photoelectrochemical measurements

Electrochemical measurements are performed in 0.1 M KCl solution at a scan rate of 50 $mV{\cdot}s^{-1}$ with a three-electrode cell using Ag/AgCl and Pt wire as the reference and counter electrodes, respectively. The prepared TiO_2@MWCNTs electrode is used as the working electrode. The measurement is carried out in a lab under 350 ± 10 lux of naturally luminous emittance. The relation of current and potential is recorded under dark (D) and light (L) conditions corresponding to the sunlight intensity below 10 lux and around 100 lux.

Photoelectrochemical water splitting performance experiments are carried out under natural sunlight using a two-electrode cell, including the photoanode and a Cu-based cathode. Hydrogen evolution at the cathode and the solar irradiance is recorded at 60 min intervals. The prepared photoelectrochemical electrode is wholly immersed in KOH electrolyte before each photoelectrochemical measurement. Only one electrode surface with a size of 1.5 × 2.0 cm^2 is irradiated. A schematic of the experimental apparatus is described in Figure 1.

Results and Discussion

Characterization of the TiO_2@MWCNTs nanocomposite catalyst

FE-SEM images of the morphology of the MWCNTs, TiO_2 powder, and the TiO_2@MWCNTs nanocomposite are shown in Figure 2. They confirm that the TiO_2@MWCNTs nanocomposite catalyst is successfully prepared via the hydrolysis reaction. It can be seen from Figure 2a that the morphology of MWCNTs is incoherent, curved, interlaced, and with little branching. Furthermore, a non-uniform decoration of TiO_2 clusters is observed on the surface of the MWCNTs (Figure 2c).

Figure 3 shows TEM images of the MWCNTs, TiO_2 powder, and the TiO_2@MWCNTs nanocomposite. Figure 3a shows that the pristine MWCNTs are uniform and possess an external diameter of less than 50 nm with a wall thickness of roughly 10 nm. Moreover, the non-smooth walls of the MWCNTs indicates the presence of defects such as vacancies, dangling bonds, interstitials, and pentagons [14]. Figure 3b shows the irregular

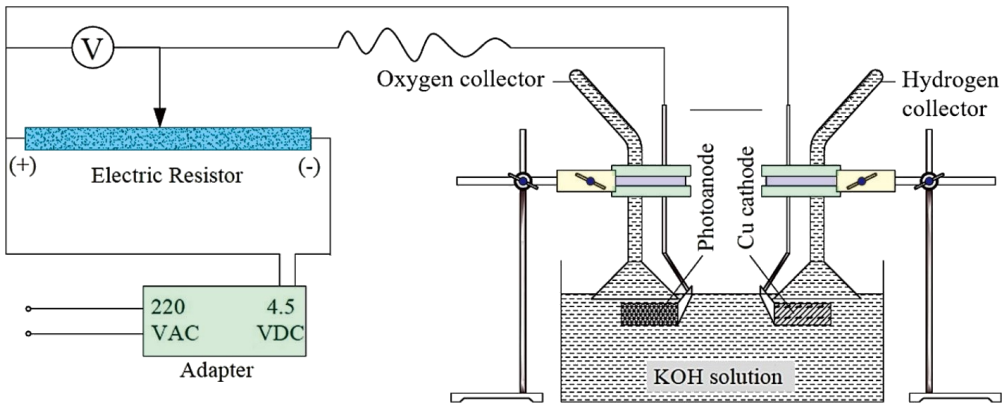

Figure 1: Schematic of the photoelectrochemical water splitting experimental apparatus.

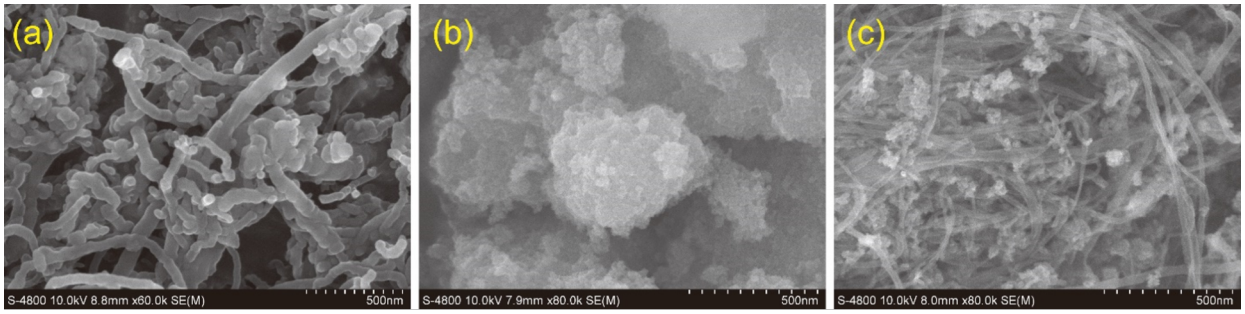

Figure 2: SEM images of (a) MWCNTs, (b) TiO_2, and (c) the TiO_2@MWCNTs nanocomposite.

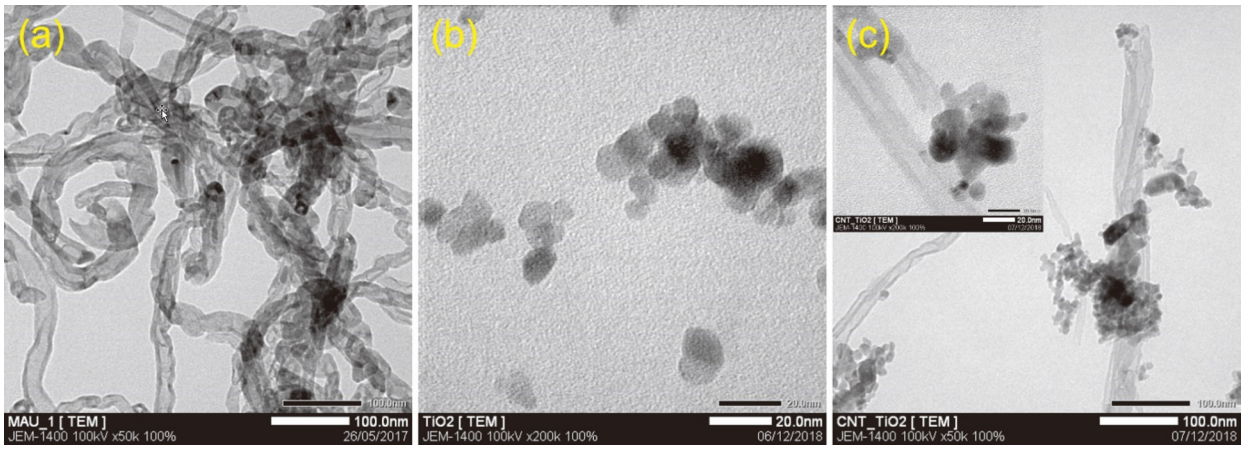

Figure 3: TEM images of (a) MWCNTs, (b) TiO_2, and (c) the TiO_2@MWCNTs nanocomposite.

shape of TiO_2 particles smaller than 20 nm and their non-uniform distribution. In Figure 3c, some MWCNTs link with TiO_2 clusters as conjunctional bridges. TiO_2 particles deposit only on the outside wall surface of the MWCNTs. Additionally, an agglomeration of TiO_2 particles is only observed at the branching points, zigzag regions, and the end of MWCNTs where the defects are identified. However, the observation differs from previous studies, in which the TiO_2 particles are uniformly attached to CNTs by layer-by-layer coating or sol–gel methods [15-17]. Notably, the defects on the wall surface of MWCNTs, which enable π–π interactions, could be the active sites to generate the TiO_2 agglomerations via hydroxy groups and, thus, enhance the photoelectrochemical activity in aqueous environment [18-20].

Figure 4 shows the EDX spectra of MWCNTs and the TiO_2@MWCNTs nanocomposite. The EDX spectrum for TiO_2@MWCNTs confirms the presence of Ti, which accounts for 28.76 wt %. Small amounts of Fe, Al, and Si exists in as-synthesized MWCNTs and TiO_2@MWCNTs, which could result from the catalyzed synthesis of MWCNTs [14].

Raman spectroscopy is applied for phase characterization of MWCNTs and TiO_2@MWCNTS, as shown in Figure 5. The peaks at 178, 424, and 609 cm^{-1} are characteristic of the TiO_2 phase in the TiO_2@MWCNTs catalyst [21]. In the Raman spectrum of MWCNTs, there are two bands, that is, the D band at 1324 cm^{-1} and the G band at 1585 cm^{-1}, which are ascribed to the defect structure and the ordered graphitic structure of the MWCNTs, respectively. The ratio between the D band and G band intensities (I_D/I_G) of the TiO_2@MWCNTs catalyst is 1.45, higher than that for MWCNTs with 1.23. This observation indicates that TiO_2 is a functional group on the outside wall of MWCNTs [22]. The ratios of $I_{G'}/I_D$ and $I_{G'}/I_G$ of TiO_2@MWCNTs are 0.67 and 0.93, respectively. These ratios are higher than that for MWCNTs, with 0.41 and 0.51, respectively. The results reveal that TiO_2 contributes to an increased number of defects on TiO_2@MWCNTs [20]. Nevertheless, the intensities of the G bands belonging to the MWCNTs and the TiO_2@MWCNTs nanocomposite, ascribed to the structure of the MWCNTs, are only slightly different. This reveals that the defects in the initial MWCNTs are hardly affected by the TiO_2 nanoparticles. The TEM image also confirms that TiO_2 nano-

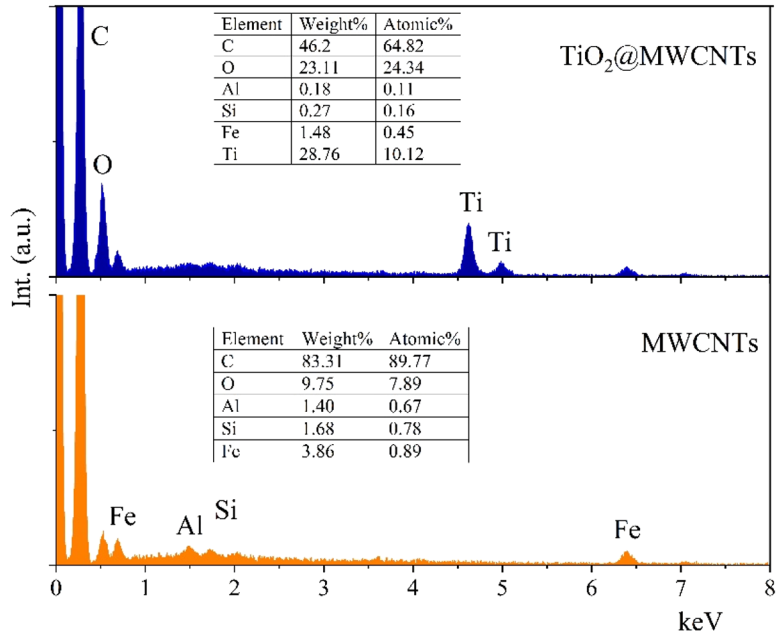

Figure 4: EDX spectra of MWCNTs and TiO_2@MWCNTs.

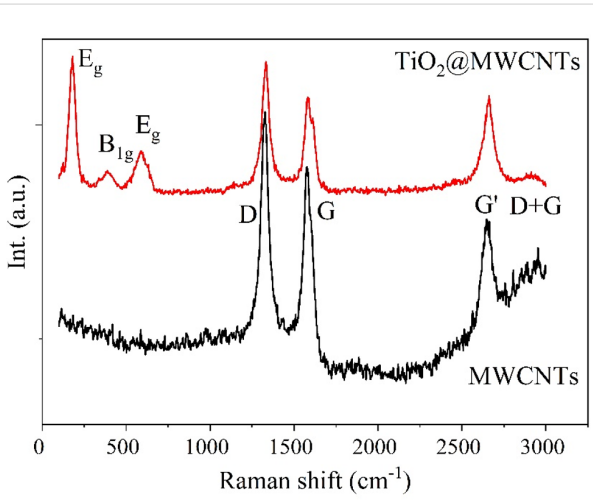

Figure 5: Raman spectra of MWCNTs and TiO_2@MWCNTs.

particles only attach to some defects on the MWCNTs (Figure 3c) [17].

FTIR spectra of MWCNTs, TiO_2, and the TiO_2@MWCNTs nanocomposite are shown in Figure 6a. Regarding the spectrum of MWCNTs, a typical peak at 1559 cm^{-1} is attributed to the vibration of C=C groups, whereas the peaks at 536, 1343, and 3394 cm^{-1} correspond to the C–O–C, C–C–O, and OH groups, respectively, on the MWCNTs [23]. For TiO_2, a broad peak at 3404 cm^{-1} is attributed to the OH stretching, and another broad peak at 621 cm^{-1} is assigned to the Ti–O and Ti–O–Ti stretching of TiO_2 [24]. In addition, the spectrum of TiO_2@MWCNTs shows the characteristic peak at 972 cm^{-1} of the vibration of Ti–O–C groups, indicating the formation of a covalent bond between TiO_2 and MWCNTs [24].

The UV–vis diffuse reflectance spectra of the prepared catalysts are shown in Figure 6b. The optical absorption of TiO_2 is in the UV region, while the light absorption edge of TiO_2@MWCNTs redshifts to the visible-light region. As seen from the Tauc plots (inset of Figure 6b), the optical band gap of TiO_2 and TiO_2@MWCNTs catalysts are calculated as 3.14 and 2.51 eV, respectively. The results show that the lower bandgap of TiO_2@MWCNTs catalyst could derive from vacancies on the MWCNTs or the interaction between TiO_2 and MWCNTs [25]. Moreover, the C–O–Ti linkages on the TiO_2@MWCNs contribute to the extension of the absorption of light at a longer wavelength [26]. Accordingly, the low bandgap of TiO_2@MWCNTs indicates improved visible-light absorption.

XRD analysis is performed to confirm the crystalline structure and phase composition of TiO_2, MWCNTs, and the TiO_2@MWCNTs nanocomposite as described in Figure 7. Diffraction peaks at 26.1° and 42.6° correspond to the *d*-spacing between graphene sheets and the lateral correlation of graphite layers, which is presentative for MWCNTs [27]. Additionally, the XRD pattern of TiO_2 exhibits peaks at 25.4° and 48.2°, ascribed to the anatase phase, while the other peaks at 27.6° and 36.2° are attributed to the rutile phase [28]. The weight fraction of anatase/rutile (*f*) relating to the intensity of the most substan-

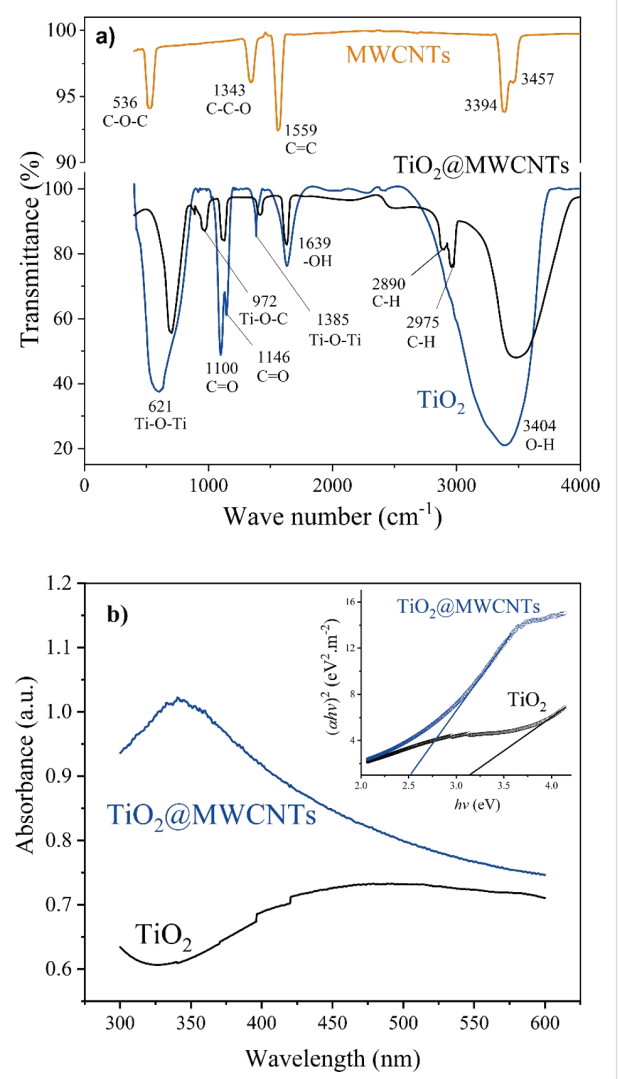

Figure 6: FTIR spectra of (a) MWCNTs, TiO_2, and TiO_2@MWCNTs, and (b) UV–vis DRS of TiO_2 and TiO_2@MWCNTs (Inset: Tauc plots).

tial peaks (25.4° for anatase (I_A) and 27.6° for rutile (I_R)) is calculated to be 73.8 % using the estimated model $f = 1/(1 + 1.26I_R/I_A)$ [29]. The overlap of the prominent peak at 26.1° for MWCNTs with that at 25.4° for anatase TiO_2 results in a problematic identification for each component. Moreover, the rutile phase increases 3.5 times based on the intensity of the primary diffraction peak at 27.6° of TiO_2@MWCNTs compared to that of TiO_2. The observation indicates that anatase TiO_2 transforms into rutile. This could be due to the carbon components on the MWCNTs acting as a robust reducing agent for facilitating the transformation from anatase to rutile TiO_2 by forming oxygen vacancies [30].

Generally, the capacitance of the photoelectrochemical electrode is associated with the photoelectrochemical processes occurring at the interface between electrode and electrolyte

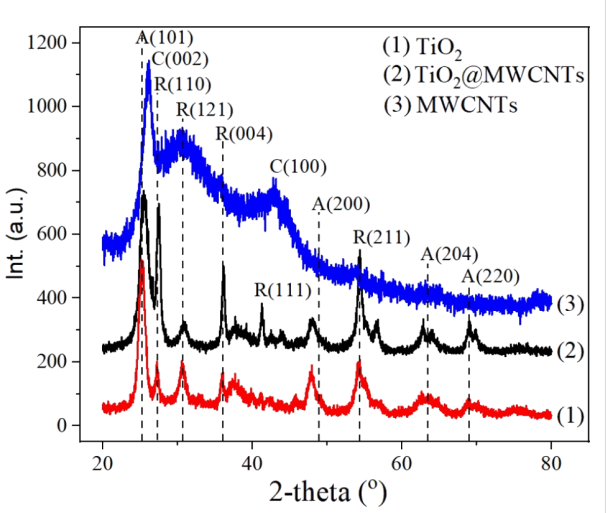

Figure 7: XRD patterns of MWCNTs, TiO_2 and TiO_2@MWCNTs nanocomposite.

[31]. Cyclic voltammetry measurements are utilized to analyze the characteristics of charge and discharge of the photoelectrochemical electrodes. Figure 8a shows the cyclic voltammograms (CVs) generated using the prepared TiO_2, MWCNTs, and TiO_2@MWCNTs electrodes as working electrodes in 0.1 M KCl electrolyte at a sweep rate of 50 mV/s. In Figure 8a, oxidation and reduction peaks are not observed in the CVs in the scanned potential range from −1.0 to +0.2 V. In the CV of the TiO_2 electrode, the current decreases significantly at a potential below −0.3 V, which could be due to the electron trap energy [32]. Moreover, the width of the CV for the MWCNTs electrode is more larger than that for TiO_2 and TiO_2@MWCNTs electrodes, indicating that the MWCNTs electrode possesses a porous surface and high capacitance derived from a thick electrical double layer (EDL) [33]. However, incorporating TiO_2 onto the MWCNTs leads to a decrease of the EDL, increasing the electron transfer rate in the TiO_2@MWCNTs electrode [34]. Puthirath et al. proved that the EDL has a significant influence on the hydrogen evolution reaction of the electrode [35]. Based on the cyclic voltammetry results, it could be suggested that the TiO_2@MWCNTs electrode is superior regarding photoelectrochemical application compared to TiO_2 and MWCNTs electrodes.

Electrochemical impedance spectroscopy (EIS) is applied to characterize the electron-transfer property of the electrodes through Nyquist plots, as shown in Figure 8b. The MWCNTs electrode has the lowest arc radius among the prepared electrodes, indicating the fast charge transport on this electrode [36]. A contrastive result is observed for the TiO_2 electrode, which could be due to the poor electrical conductivity of TiO_2 [37].

Table 1 shows the EIS parameters obtained from fitting the measured results with equivalent circuits. The R_1 values illustrate a low electrical resistance of the 0.1 M KCl solution, while the R_2 values show that the TiO_2 electrode has the highest resistance among the prepared electrodes [38]. The results reveal a significant improvement in the electrical conductivity for the TiO_2@MWCNTs electrode. The result agrees well with a previous study on TiO_2@graphene composite electrodes [37]. Among the electrodes, the EDL capacitance (C_2) at the TiO_2 electrode surface is the lowest (1.32 μF), whereas that on the MWCNTs surface is the highest (29.64 μF). The EDL on the photoelectrochemical electrode surface contributes to the prevention of a fast carrier recombination and, hence, could improve the performance [39]. However, a thick EDL is detrimental to the photoelectrochemical performance because free electrons can shift to the trap state, resulting in a potential difference in the interface between the electrolyte and the electrode [40]. The Warburg element (W_3) in the equilibrium circuit, indicating the contribution of diffusion to the overall charge transfer on the electrode, is not found in the TiO_2 and TiO_2@MWCNTs electrodes [41]. The EIS spectrum shows that the Voigt circuit is found to fit the TiO_2 electrode. In contrast, the EIS spectrum of the TiO_2@MWCNTs electrode, including two semicircle parts, demonstrates different responses of the electrode at low and high frequencies [42,43]. Additionally, the equivalent circuit fitted to the TiO_2@MWCNTs electrode indicates that electron and ion transfers and the electrode material contribute to the overall charge transfer [43]. The results suggest synergies of TiO_2 nanoparticles and MWCNTs in the TiO_2@MWCNTs electrode.

Effect of KOH concentration on photoelectrochemical water splitting

Figure 9a shows the effect of KOH concentration on the activation voltage for the water redox reaction at the photoelectrochemical electrodes. The increase in KOH concentration leads to a decrease in the resistance of the electrolyte, thereby decreasing the activation voltage for water splitting or water redox reaction of the photoelectrochemical electrodes (Figure 9a) [44]. Notably, the activation voltage for water splitting of the TiO_2@MWCNTs electrode is lower than that of the TiO_2 electrode at all KOH concentrations. Furthermore, a KOH concentration higher than 3 M insignificantly affects the activation voltage of the TiO_2@MWCNTs photoelectrochemical electrode.

The increase in KOH concentration could improve the electrical conductivity and the photocurrent of the photoelectrochemical electrode [44,45]. As seen in Figure 9b, the water splitting performance was significantly enhanced with increasing KOH concentration. However, the difference in the photoelectrochemical performance between KOH concentrations of 3 and 4 M is negligible. Furthermore, using high KOH concentrations for the electrolyte is not recommended to avoid corrosion of the electrodes [44]. Accordingly, it is suggested that the 3 M KOH electrolyte is suitable for the photoelectrochemical electrolyte.

Photoelectrochemical behavior

The relationships between the applied potential and the current density of TiO_2 and TiO_2@MWCNTs electrodes under dark (D) and light (L) conditions (luminous emittance values in the

Table 1: Parameters from fitting EIS results.

Electrode	Best fit circuit	Parameters	Values	Dev.
TiO_2	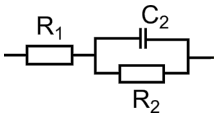	R_1, Ω	3.457	0.2782
		C_2, μF	1.324	27.18×10^{-9}
		R_2, Ω	84.04	0.3206
MWCNTs	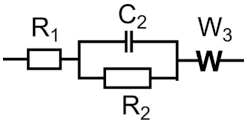	R_1, Ω	1.385	0.2425
		C_2, μF	29.64	2.971×10^{-6}
		R_2, Ω	17.84	0.3985
		W_3, Ω	202	1.27
TiO_2@MWCNTs	$R_1 + C_2/(R_2 + C_3/R_3)$	R_1, Ω	1.666	0.2652
		C_2, μF	12.47	1.516×10^{-6}
		R_2, Ω	21.32	1.49
		C_3, mF	0.493	0.175×10^{-3}
		R_3, Ω	13.78	1.661

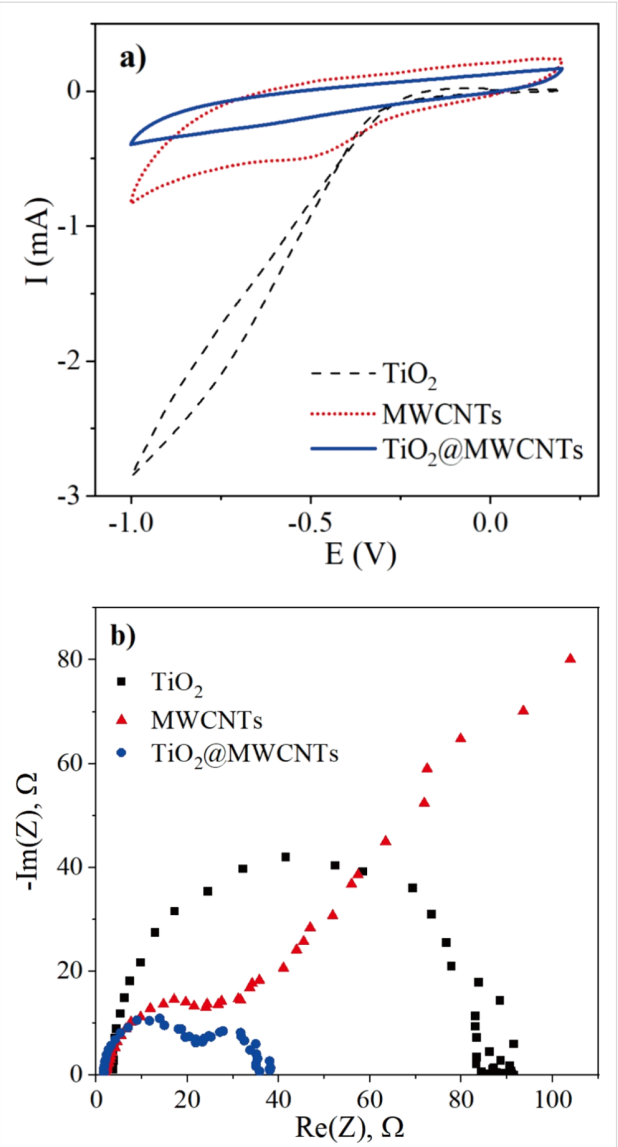

Figure 8: (a) Cyclic voltammograms in 0.1 M KCl at 50 mV/s of scan rate, (b) Nyquist plots from EIS measurements in 0.1 M KCl.

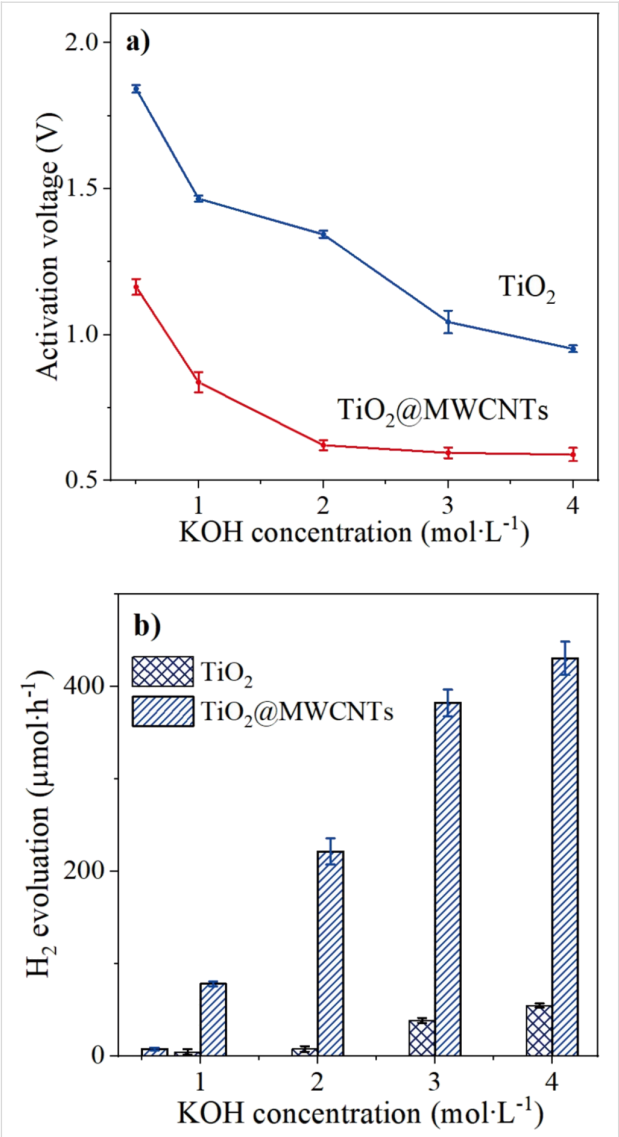

Figure 9: Effect of KOH concentration on (a) water splitting activation voltage and (b) rate of H_2 evolution at a voltage of 1.0 V; measurements under sunlight with 85 ± 5 klux of illuminance.

range of 20–40 and 50–60 klux, respectively) are shown in Figure 10a. The results show that the current density of both electrodes tested under light condition is more higher than that in the dark. The TiO_2 electrode exhibits insignificant photocatalytic activity in the studied potential window. This confirms that the combination of TiO_2 and MWCNTs enhances the visible-light absorption of the nanocomposite, even under weak light illuminance (dark conditions), which leads to the enhancement of the current density of the TiO_2@MWCNTs electrode. At 1.0 V of voltage, the current density of the TiO_2@MWCNTs electrode is about 30 times (D) and 10 times (L) higher than that of the TiO_2 one. The results reveal that the TiO_2@MWCNTs-based photoelectrochemical electrode is an effective photoelectrochemical catalyst under visible-light irradiation.

Figure 10b shows the hydrogen production and the average light intensity as a function of the time of the day from 6:00 AM to 5:00 PM. In Figure 10b, the sunlight illuminance peaks from 10:00 AM to 2:00 PM correlate with the highest hydrogen production of the TiO_2@MWCNTs electrode. The TiO_2 electrode exhibits poor hydrogen production under sunlight irradiation. It could be explained by the 3.14 eV optical band gap of TiO_2, which absorbs only UV light. In addition, the fast recombination of the photogenerated (h^+/e^-) pairs contributes to the poor photochemical catalysis activity of the TiO_2 electrode [46]. For the TiO_2@MWCNTs nanocomposite, the TiO_2 agglomerates attached to the MWCNTs are found to prevent the recombination of the h^+/e^- pairs and the H^+/O^- couples.

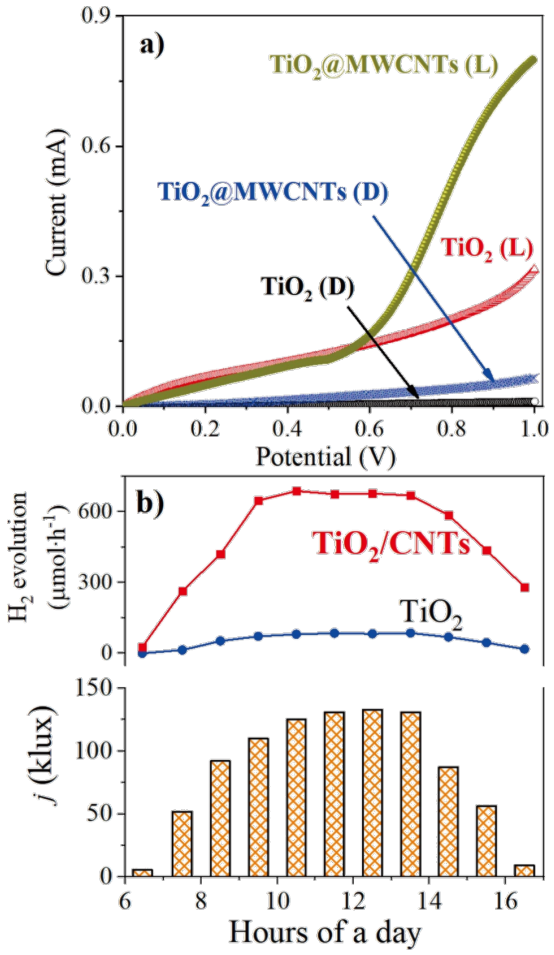

Figure 10: (a) Voltammograms of the TiO_2 and the TiO_2@MWCNTs electrode under dark (D) and light (L) conditions. (b) Dependence of luminous intensity and H_2 evolution on the time of the day; electrolyte: 3 M KOH.

Furthermore, excitons in the MWCNT structure can absorb visible-light irradiation and accordingly produce a sub-cathode current [8], which significantly improves the rate of hydrogen evolution (Figure 10b). From 6:00 AM to 5:00 PM, the average rate of hydrogen evolution generated from the TiO_2@MWCNTs electrode is 8.88 times higher than that from the TiO_2 electrode. In particular, the feature increases 15 and 18 times at 7:00 AM and 4:00 PM, respectively, while identical sunlight spectra are revealed in the morning and in the afternoon [47]. The observation suggests that the photoactivity of the photoelectrochemical water splitting catalyst depends on photon energy and luminous emittance [9,46]. Furthermore, illumination higher than 100 klux solar allows the photoelectrochemical electrode to generate H_2 at the highest rates.

The STH conversion efficiency is the ratio between the hydrogen production rate and the solar energy input [10,11]. Assuming a mean illuminance of the solar irradiation of 88.9% [48], the average STH conversion efficiency of the TiO_2@MWCNTs electrode from 6 AM to 5 PM is 11.1%, as shown in Table 2. The photoelectrochemical water splitting performance of the TiO_2@MWCNTs photoanode is superior compared to electrodes in previous studies [48].

Conclusion

A TiO_2@MWCNTs nanocomposite photocatalyst is successfully synthesized via a simple hydrolysis method to fabricate the photoanode for photoelectrochemical water splitting. The TiO_2@MWCNTs nanocomposite with a bandgap of 2.5 eV enables visible-light absorption of the electrode. Additionally, the coupling of TiO_2 and MWCNTs hinders the recombination

Table 2: Photoelectrochemical water splitting performance of various TiO_2-based catalysts.[a]

Photoanode (E_g, eV)	Photocathode (E_g, eV)	Light/source	Applied potential, V	STH conversion efficiency, %	n/p electrolyte	Ref. (year)
TiO_2-SWCNTs	SCE	UV–vis/150 W Xe lamp	0	0.2	1 M KOH	[12] (2007)
TiO_2 (3 eV)	GaP (2.35 eV)	UV–vis/450 W Xe lamp	0.96	0.25	0.2 N H_2SO_4	[49] (1976)
TiO_2	Cu-Ti-O NT	UV–vis/300 W Xe lamp	0.3	0.30	0.1 M KOH/0.1 M $NaHPO_4$	[50] (2008)
TiO_2	np^+Si	UV–vis/Xe lamp	0.0	0.39	1.0 M KOH/1.0 M H_2SO_4	[51] (2015)
C doped TiO_2 NTs (2.75 eV)	RHE	vis/150 W Xe lamp	1.5	0.42	1.0 M KCl	[52] (2019)
Ag/TiO_2/CNTs (2.8 eV)	Ag/AgCl	UV–vis/20 $W{\cdot}cm^{-2}$	1.0	4.4	0.5 M H_2SO_4	[53] (2016)
TiO_2@MWCNTs (2.5 eV)	Cu	sunlight	1.0	11.1	3 M KOH	this work

[a]NTs: nanotubes; SCE: saturated calomel electrode; RHE: reversible hydrogen electrode; CNTs: carbon nanotubes; SWCNTs: single-wall CNTs; MWCNTs: multi-wall CNTs.

of photogenerated h^+/e^- pairs and, thus, improves the hydrogen evolution of the electrode. The average rate of hydrogen evolution of the TiO_2@MWCNTs electrode is 8.88 times higher than that of a TiO_2 electrode operating under sunlight illuminance from 6 AM to 5 PM, demonstrating the superior photoelectrochemical performance of the TiO_2@MWCNTs electrode for water splitting.

Acknowledgements

We acknowledge Ho Chi Minh City University of Technology (HCMUT), VNU-HCM for supporting this study.

Conflict of Interest

The authors declare no conflict of interest.

ORCID® iDs

Hai Duy Tran - https://orcid.org/0000-0002-0103-8866
Van-Huy Nguyen - https://orcid.org/0000-0001-8556-1955

References

1. Kumar, A.; Pandey, G. *Mater. Sci. Eng. Int. J.* **2017,** *1,* 106–114. doi:10.15406/mseij.2017.01.00018
2. Areerachakul, N.; Sakulkhaemaruethai, S.; Johir, M. A. H.; Kandasamy, J.; Vigneswaran, S. *J. Water Process Eng.* **2019,** *27,* 177–184. doi:10.1016/j.jwpe.2018.12.006
3. Lin, H.; Huang, C.; Li, W.; Ni, C.; Shah, S. I.; Tseng, Y.-H. *Appl. Catal., B* **2006,** *68,* 1–11. doi:10.1016/j.apcatb.2006.07.018
4. Ye, Y.; Feng, Y.; Bruning, H.; Yntema, D.; Rijnaarts, H. H. M. *Appl. Catal., B* **2018,** *220,* 171–181. doi:10.1016/j.apcatb.2017.08.040
5. Retamoso, C.; Escalona, N.; González, M.; Barrientos, L.; Allende-González, P.; Stancovich, S.; Serpell, R.; Fierro, J. L. G.; Lopez, M. *J. Photochem. Photobiol., A* **2019,** *378,* 136–141. doi:10.1016/j.jphotochem.2019.04.021
6. Amano, F.; Ishinaga, E.; Yamakata, A. *J. Phys. Chem. C* **2013,** *117,* 22584–22590. doi:10.1021/jp408446u
7. Tachan, Z.; Hod, I.; Zaban, A. *Adv. Energy Mater.* **2014,** *4,* 1301249. doi:10.1002/aenm.201301249
8. Dai, K.; Zhang, X.; Fan, K.; Zeng, P.; Peng, T. *J. Nanomater.* **2014,** 694073. doi:10.1155/2014/694073
9. Chen, P.; Wang, L.; Wang, P.; Kostka, A.; Wark, M.; Muhler, M.; Beranek, R. *Catalysts* **2015,** *5,* 270–285. doi:10.3390/catal5010270
10. Ahmed, M.; Dincer, I. *Int. J. Hydrogen Energy* **2019,** *44,* 2474–2507. doi:10.1016/j.ijhydene.2018.12.037
11. Jiang, C.; Moniz, S. J. A.; Wang, A.; Zhang, T.; Tang, J. *Chem. Soc. Rev.* **2017,** *46,* 4645–4660. doi:10.1039/c6cs00306k
12. Kongkanand, A.; Martínez Domínguez, R.; Kamat, P. V. *Nano Lett.* **2007,** *7,* 676–680. doi:10.1021/nl0627238
13. Ramesh Reddy, N.; Mamatha Kumari, M.; Cheralathan, K. K.; Shankar, M. V. *Int. J. Hydrogen Energy* **2018,** *43,* 4036–4043. doi:10.1016/j.ijhydene.2018.01.011
14. Padilha, J. E.; Amorim, R. G.; Rocha, A. R.; da Silva, A. J. R.; Fazzio, A. *Solid State Commun.* **2011,** *151,* 482–486. doi:10.1016/j.ssc.2010.12.031
15. Cha, Y. L.; Park, I. H.; Moon, K. H.; Kim, D. H.; Jung, S. I.; Yoon, Y. S. *J. Korean Ceram. Soc.* **2018,** *55,* 618–624. doi:10.4191/kcers.2018.55.6.09
16. Ahmad, A.; Razali, M. H.; Mamat, M.; Kassim, K.; Amin, K. A. M. *Arabian J. Chem.* **2020,** *13,* 2785–2794. doi:10.1016/j.arabjc.2018.07.009
17. Zhang, X.; Cao, S.; Wu, Z.; Zhao, S.; Piao, L. *Appl. Surf. Sci.* **2017,** *402,* 360–368. doi:10.1016/j.apsusc.2017.01.096
18. Kim, K. J.; Huh, M.-Y.; Kim, W.-S.; Song, J.-H.; Lee, H. S.; Kim, J.-Y.; Lee, S.-R.; Seo, W. S.; Yang, S.-M.; Park, Y. S. *Carbon Lett.* **2018,** *26,* 95–101. doi:10.5714/cl.2018.26.095
19. Eder, D.; Windle, A. H. *J. Mater. Chem.* **2008,** *18,* 2036–2043. doi:10.1039/b800499d
20. Chaudhary, D.; Khare, N.; Vankar, V. D. *Ceram. Int.* **2016,** *42,* 15861–15867. doi:10.1016/j.ceramint.2016.07.056
21. Zhao, Y.; Hu, Y.; Li, Y.; Zhang, H.; Zhang, S.; Qu, L.; Shi, G.; Dai, L. *Nanotechnology* **2010,** *21,* 505702. doi:10.1088/0957-4484/21/50/505702
22. Mohan, S.; Oluwafemi, O. S.; Songca, S. P.; Rouxel, D.; Miska, P.; Lewu, F. B.; Kalarikkal, N.; Thomas, S. *Pure Appl. Chem.* **2016,** *88,* 71–81. doi:10.1515/pac-2015-0602
23. Dias, M. R. G.; de Pauloveloso, A.; do Amaral, L. F. M.; Betim, R. T.; Nascimento, M. G.; Pilissão, C. *J. Braz. Chem. Soc.* **2018,** *29,* 1876–1884. doi:10.21577/0103-5053.20180063
24. Koo, Y.; Littlejohn, G.; Collins, B.; Yun, Y.; Shanov, V. N.; Schulz, M.; Pai, D.; Sankar, J. *Composites, Part B* **2014,** *57,* 105–111. doi:10.1016/j.compositesb.2013.09.004
25. Chuang, H.-Y.; Chen, D.-H. *Int. J. Hydrogen Energy* **2011,** *36,* 9487–9495. doi:10.1016/j.ijhydene.2011.05.093
26. MamathaKumari, M.; Praveen Kumar, D.; Haridoss, P.; DurgaKumari, V.; Shankar, M. V. *Int. J. Hydrogen Energy* **2015,** *40,* 1665–1674. doi:10.1016/j.ijhydene.2014.11.117
27. Rodríguez, L. A. A.; Pianassola, M.; Travessa, D. N. *Mater. Res. (Sao Carlos, Braz.)* **2017,** *20* (Suppl. 1), 96–103. doi:10.1590/1980-5373-mr-2017-0406
28. Haider, A. J.; Jameel, Z. N.; Taha, S. Y. *Eng. Technol. J.* **2015,** *33,* 761–771.
29. Spurr, R. A.; Myers, H. *Anal. Chem. (Washington, DC, U. S.)* **1957,** *29,* 760–762. doi:10.1021/ac60125a006
30. Hanaor, D. A. H.; Triani, G.; Sorrell, C. C. *Surf. Coat. Technol.* **2011,** *205,* 3658–3664. doi:10.1016/j.surfcoat.2011.01.007
31. Asha, K.; Satsangi, V. R.; Shrivastav, R.; Kant, R.; Dass, S. *RSC Adv.* **2020,** *10,* 42256–42266. doi:10.1039/d0ra07870k
32. Ansón-Casaos, A.; Hernández-Ferrer, J.; Rubio-Muñoz, C.; Santidrian, A.; Martínez, M. T.; Benito, A. M.; Maser, W. K. *ChemElectroChem* **2017,** *4,* 2300–2307. doi:10.1002/celc.201700321
33. Frackowiak, E.; Metenier, K.; Bertagna, V.; Beguin, F. *Appl. Phys. Lett.* **2000,** *77,* 2421–2423. doi:10.1063/1.1290146
34. Gusmão, R.; Browne, M. P.; Sofer, Z.; Pumera, M. *Electrochem. Commun.* **2019,** *102,* 83–88. doi:10.1016/j.elecom.2019.04.004
35. Puthirath, A. B.; Shirodkar, S.; Fei, M.; Baburaj, A.; Kato, K.; Saju, S. K.; Prasannachandran, R.; Chakingal, N.; Vajtai, R.; Yakobson, B. I.; Ajayan, P. M. *Nanoscale* **2020,** *12,* 1790–1800. doi:10.1039/c9nr08102j
36. Liu, H.; Cheng, S.; Wu, M.; Wu, H.; Zhang, J.; Li, W.; Cao, C. *J. Phys. Chem. A* **2000,** *104,* 7016–7020. doi:10.1021/jp000171q
37. E, T.; Ma, Z.; Yang, S.; Li, Y.; Ma, D.; Xing, Z.; Li, Y. *J. Alloys Compd.* **2020,** *827,* 154280. doi:10.1016/j.jallcom.2020.154280
38. Lei, L.; Sang, L.; Zhang, Y.; Gao, Y. *ACS Omega* **2020,** *5,* 3522–3532. doi:10.1021/acsomega.9b03847

39. Liu, J.; Shahid, M.; Ko, Y.-S.; Kim, E.; Ahn, T. K.; Park, J. H.; Kwon, Y.-U. *Phys. Chem. Chem. Phys.* **2013,** *15,* 9775–9782. doi:10.1039/c3cp51053k
40. Schneider, J.; Bahnemann, D.; Ye, J.; Li Puma, G.; Dionysiou, D. D., Eds. *Photocatalysis: fundamentals and perspectives;* Royal Society of Chemistry: Cambridge, UK, 2016. doi:10.1039/9781782622338
41. Yang, T.; Liu, J.; Finklea, H.; Lee, S.; Epting, W. K.; Mahbub, R.; Hsu, T.; Salvador, P. A.; Abernathy, H. W.; Hackett, G. A. *Int. J. Hydrogen Energy* **2018,** *43,* 15445–15456. doi:10.1016/j.ijhydene.2018.06.076
42. Lukács, Z.; Kristóf, T. *Electrochim. Acta* **2020,** *363,* 137199. doi:10.1016/j.electacta.2020.137199
43. Péter, L. *J. Solid State Electrochem.* **2013,** *17,* 3075–3081. doi:10.1007/s10008-013-2158-4
44. Becker, J.-P.; Urbain, F.; Smirnov, V.; Rau, U.; Ziegler, J.; Kaiser, B.; Jaegermann, W.; Finger, F. *Phys. Status Solidi A* **2016,** *213,* 1738–1746. doi:10.1002/pssa.201533025
45. Schalenbach, M.; Zeradjanin, A. R.; Kasian, O.; Cherevko, S.; Mayrhofer, K. J. J. *Int. J. Electrochem. Sci.* **2018,** *13,* 1173–1226. doi:10.20964/2018.02.26
46. Haldorai, Y.; Rengaraj, A.; Lee, J.-B.; Huh, Y. S.; Han, Y.-K. *Synth. Met.* **2015,** *199,* 345–352. doi:10.1016/j.synthmet.2014.12.014
47. Barolet, D.; Christiaens, F.; Hamblin, M. R. *J. Photochem. Photobiol., B* **2016,** *155,* 78–85. doi:10.1016/j.jphotobiol.2015.12.014
48. Robledo, L.; Soler, A. *Energy* **2001,** *26,* 669–677. doi:10.1016/s0360-5442(01)00025-1
49. Nozik, A. J. *Appl. Phys. Lett.* **1976,** *29,* 150–153. doi:10.1063/1.89004
50. Mor, G. K.; Varghese, O. K.; Wilke, R. H. T.; Sharma, S.; Shankar, K.; Latempa, T. J.; Choi, K.-S.; Grimes, C. A. *Nano Lett.* **2008,** *8,* 1906–1911. doi:10.1021/nl080572y
51. Shaner, M. R.; McDowell, M. T.; Pien, A.; Atwater, H. A.; Lewis, N. S. *J. Electrochem. Soc.* **2016,** *163,* H261–H264. doi:10.1149/2.0141605jes
52. Gwag, E. H.; Moon, S. Y.; Mondal, I.; Park, J. Y. *Catal. Sci. Technol.* **2019,** *9,* 688–694. doi:10.1039/c8cy02226g
53. Chaudhary, D.; Singh, S.; Vankar, V. D.; Khare, N. *Int. J. Hydrogen Energy* **2017,** *42,* 7826–7835. doi:10.1016/j.ijhydene.2016.12.036

License and Terms

BEILSTEIN JOURNAL OF NANOTECHNOLOGY

Non-stoichiometric magnetite as catalyst for the photocatalytic degradation of phenol and 2,6-dibromo-4-methylphenol – a new approach in water treatment

Joanna Kisała*[1], Anna Tomaszewska[2] and Przemysław Kolek[3]

Full Research Paper

Open Access

Address:
[1]Department of Biology, Institute of Biology and Biotechnology, University of Rzeszow, Pigonia 1, PL-35-310 Rzeszow, Poland, [2]Department of Biotechnology, Institute of Biology and Biotechnology, University of Rzeszow, Pigonia 1, PL-35-310 Rzeszow, Poland and [3]Institute of Physics, University of Rzeszow, 1 Pigonia Street, PL-35-310, Rzeszów, Poland

Email:
Joanna Kisała* - jkisala@ur.edu.pl

* Corresponding author

Keywords:
magnetite; ozonolysis; persistent organic pollutants; photocatalysis; water treatment

Beilstein J. Nanotechnol. **2022,** *13,* 1531–1540.
https://doi.org/10.3762/bjnano.13.126

Received: 08 September 2022
Accepted: 24 November 2022
Published: 15 December 2022

This article is part of the thematic issue "Nanomaterials for photocatalysis and applications in environmental remediation and renewable energy".

Guest Editor: V. V. Pham

Abstract

Phenol and 2,6-dibromo-4-methylphenol (DBMP) were removed from aqueous solutions by ozonolysis and photocatalysis. The properties and structural features of the catalysts and the organic compounds are discussed, as well as their influence on the degradation reaction rates. The degradation efficiency in photocatalytic processes was higher for DBMP (98%) than for phenol (approximately 50%). This proves the high efficiency of magnetite in the photocatalytic degradation of halogenated aromatic pollutants. The particularly high degradation efficiency regarding halogen-containing DBMP molecules and the yield of bromide ions indicate that DBMP degradation follows a mixed reduction–oxidation mechanism. DBMP molecules interact with the magnetite surface, enabling them to react with the available electrons, and, as a result, bromide ions can be released. The results confirm that magnetite is an effective photocatalyst in the degradation of halogenated aromatic pollutants.

Introduction

Water is one of the most important natural resources on Earth. It helps to maintain environmental balance, but most of all, it is essential for human life and health. Although water covers more than 70% of our planet's surface, only 2.5% is freshwater and less than 1% is accessible [1,2]. In the context of water consumption, there is an environmental indicator called the water footprint, which represents the sum of direct water consumption and virtual consumption (i.e., the amount of water needed to produce food and other consumer goods) [3]. Water consumption calculated in this way may amount to thousands of

liters per person per year. Therefore, the use of water in a closed circuit is a major technological challenge. It is essential to design and develop new technologies for wastewater treatment and water recovery.

Bromophenols (BPs) are widely used as flame retardants (brominated flame retardants, BFRs), wood preservatives, and components in the polymer industry [4,5]. Bromophenols from various industries can cause severe contamination of soil, sediment, and water [6,7]. The United States Environmental Protection Agency (US EPA) has listed BPs as hazardous waste with strict environmental regulations to them [8]. Consequently, there is a growing need to develop processes for removing BPs from wastewater. In recent decades, much attention has been paid to advanced oxidation processes (AOPs) in the research and development of wastewater treatment technologies [7,9]. Processes such as cavitation, ozonation, Fenton chemistry, and photocatalysis have been successfully used to remove persistent organic pollutants (POPs) or as a pre-treatment in conventional or biological methods [10]. Ozonation is an AOP technique that has been widely used to remove organic compounds such as drugs, pesticides, petroleum constituents, and volatile organic compounds. Furthermore, the rate of ozonation is accelerated in alkaline media because hydroxide ions catalyze the decomposition of ozone and produce hyperactive hydroxyl radicals ($^{\bullet}$OH).

Photocatalysis is a promising technique for removing POPs from water using solar radiation as an energy source [11]. The photocatalysts are activated by radiation and produce highly reactive photo-induced charge carriers, which can react with the contaminants adsorbed on the surface of the catalyst. Understanding the properties of the photocatalyst material is critical to designing an effective photocatalytic process. The factors that influence photocatalytic efficiency include the photocatalyst bandwidth, the recombination rate of photogenerated electron–hole pairs, the use of solar energy, and problems with catalyst degradation.

Magnetite is a common auxiliary mineral in igneous and metamorphic rocks [12]. It is also found in sediments and soils. Magnetite has the smallest energy gap, the highest conductivity, and one of the lowest reduction potentials among natural minerals. It is an important reducer of heavy metals and organic pollutants in aquatic environments. Due to the mixed and variable valency of iron in its structure ($(Fe(III)_{tet}[Fe(II),Fe(III)]_{oct}O_4$), this oxide has unique properties [13,14]. At room temperature, magnetite is an inverse spinel conductor with Fe^{3+} on the tetrahedral sites and Fe^{2+} and Fe^{3+} on the octahedral sites. Electron hopping along the octahedral iron chain handles its conductivity and redox properties, causing the magnetite to initialize oxidation/reduction reactions. Fe_3O_4 nanoparticles have been used as a photocatalyst for the degradation of azo dyes [15], for wastewater treatment [16,17], for water decomposition, and for Cr(VI) reduction [18].

The study investigated the degradation of aqueous solutions of phenol (PhOH) and 2,6-dibromo-4-methylphenol (DBMP) via two processes, namely photocatalysis and ozonolysis. Two types of magnetite (M1 and M2) were used as catalysts in the photocatalysis process. The same type of magnetite catalysts has been investigated by us in our previous article [17] as photocatalysts for the degradation of 4,4′-isopropylidenebis(2,6-dibromophenol) in comparison with ozonolysis. Magnetite was chosen as a photocatalyst because of its low cost, interesting electron properties, and indisputably low environmental impact. The progress of the reaction was monitored by measuring the organic compound concentration. In order to determine the efficiency of the photocatalytic process, the organic compounds were also degradated through ozonolysis.

Results and Discussion

The selected catalysts were characterized by SEM, X-ray diffraction, and ultraviolet–visible (UV–vis) analysis. The XRD and UV–vis results were published in our previous article [17]. We present this data again in this article as it is necessary for the discussion of the results. Zeta potential measurements were also presented in another previous publication of ours [19]. The absorption spectra of the catalysts showed noticeable differences (Figure 1b). Using the absorption spectra, the electron gap energies for M1 and M2 were determined to be 0.11 V and 1.75 V, respectively (Table 1) [20].

Phase identification of the magnetite structure was performed using a powder X-ray diffractometer (Figure 1a). The XRD spectra revealed that the diffraction peaks at 2θ = 30.2°, 35.3°, 43.7°, 53.9°, 57.1°, and 62.7° (Figure 1a) correspond to those of Fe_3O_4 (reference code COD 01-089-3854); they belong to a cubic structure system corresponding to the facets (220), (311), (400), (422), (511), and (440) of Fe_3O_4, respectively [21]. The absence of the (210) and (211) peaks confirms that the catalysts were indeed magnetite. The mean size of the catalyst crystallites (*D*) was calculated from the high-reflection X-ray diffraction profiles by measuring the full width at half maximum (FWHM), using the Scherrer equation (Equation 1) [22,23]:

$$D = \frac{0.89\lambda}{B\cos\theta}, \quad (1)$$

where λ is the X-ray wavelength in nanometers, *B* is the width at half peak-height in radians, and θ is the angle between the incident and diffracted beams in angular degrees.

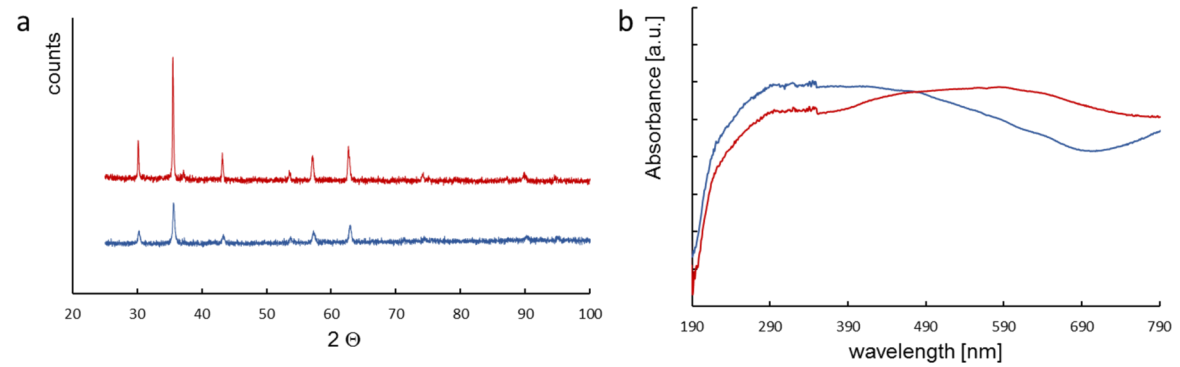

Figure 1: X-ray diffraction measurements of M1 (red), M2 (blue) (a), and UV–vis absorption spectra of M1 (red) and M2 (blue) (b). Figure 1a and 1b were adapted from [17] (© 2022 J. Kisała et al., distributed under the terms of the Creative Commons Attribution 4.0 International License, https://creativecommons.org/licenses/by/4.0).

Table 1: Catalyst parameters.

Oxide	Size declared[a] [nm]	Size measured[b] [nm]	a[c] [Å]	x[d]	E_{bg} [eV]
M1	<5000	46	8.3845	0.4094	0.11
M2	<50	28	8.3595	0.1829	1.75

[a]Size declared by the vendor; [b]XRD measurements; [c]length of the edge of the magnetite unit cell; [d]$x = Fe^{2+}/Fe^{3+}$.

Magnetite oxidation (determined as the parameter $x = Fe^{2+}/Fe^{3+}$) can range from 0.5 (stoichiometric magnetite $Fe(III)_{tet}[Fe(II),Fe(III)]_{oct}O_4$) to 0 (completely oxidized; maghemite, γ-Fe_2O_3) [24]. A magnetite with x values in the range of $0 < x < 0.5$ is defined as non-stoichiometric or partially oxidized magnetite. Stoichiometric magnetite and maghemite are significantly different. Magnetite is a conductor (bandgap of 0.1 eV), while maghemite is a semiconductor (bandgap of approx. 2.0 eV) [12]. The unit cell parameter of magnetite is slightly larger (ca. 8.40 Å) than that of maghemite (ca. 8.34 Å). A combination of these properties is what characterizes non-stoichiometric magnetite. The length of the edge of the magnetite unit cell is linearly related to the stoichiometry (for $x = 0$, $a = 8.3390$ Å; for $x = 0.25$, $a = 8.3662$ Å; for $x = 0.5$, $a = 8.3942$ Å) [25]. Knowing the cell length from the XRD measurements makes it possible to determine x for the catalysts under study (Table 1). The determined x-values indicate that the catalysts were non-stoichiometric magnetites. M1 with a larger grain diameter is less oxidized while M2 is highly oxidized. This is also reflected in the electron bandgap energy. These values show that the tested catalysts were semiconductors rather than conductors.

The morphology of the Fe_3O_4 catalysts is shown in Figure 2. The images show nanocrystal agglomerates with particle sizes of 100–400 nm for M1 and of 25–100 nm for M2 (Figure 2). The aggregation of M2 particles is much stronger than that of M1. Hence, M2 forms a porous structure.

There is a disparity in the particle sizes measured with SEM and XRD, because the particle sizes detected using these two techniques are not in the same orientation, and the terms "particle size" and "crystal size" refer to different concepts (a particle may contain several or only one crystallite) [26]. The particle size can be calculated from the XRD measurements using the Scherrer equation (Equation 1). The sizes of the crystal structures are determined by analyzing the diffraction intensity of the X-ray beams. The lines in a powder diffraction pattern have a finite width, but the lines are wider than usual if the particles are small (widening decreases as the particle size increases). Line broadening is used to estimate the mean particle size, but peak broadening may have many causes other than crystal size. Widening of the diffraction peaks can result from both instrument constraints and the sample (all types of crystal imperfections would lead to an additional widening of the XRD peak due to microstrain, resulting in a lower apparent crystal size value). This means that the Scherrer equation is an extremely rough estimate of the minimal size of crystals whereas SEM reveals the maximum size of the particles.

The catalytic activity of commercially available M1 and M2 was evaluated through the photocatalytic degradation of phenol

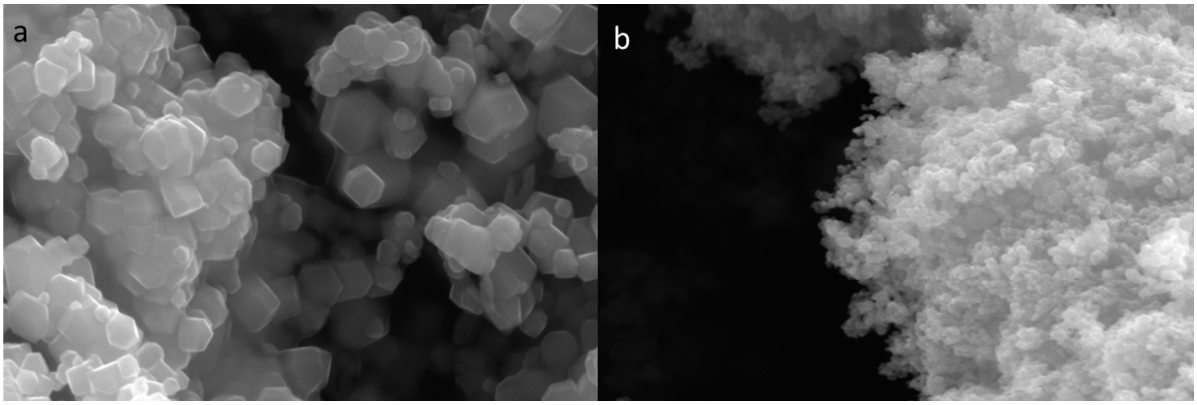

Figure 2: SEM images of M1 (a), and M2 (b) catalysts.

and DBMP. The photocatalytic activity was compared with the efficiency of ozonolysis. The photocatalytic efficiency is improved by the adsorption of organic compounds onto the surface of the catalyst. The sorption power depends largely on the properties of the organic molecule in question, as well as on the properties of the catalyst's surface. The test reactions were carried out in aqueous solution at pH 8 (due to the hydrolytic stability of the catalysts). Under acidic conditions, magnetite dissolves according to Equation 2:

$$Fe_3O_4 + 2H^+ \rightarrow Fe^{2+} + \gamma\text{-}Fe_2O_3 + H_2O. \quad (2)$$

At pH > 7, however, the effect of hydrolysis is expected to be negligible [27]. The molar fractions of the ionic forms of organic compounds present in the solution at pH 8 were calculated using the software CurTiPot [28] based on the published pK_a values for solutes (Figure 3). The resulting values were as follows: DBMP (0.112); $DBMP^-$ (0.888); PhOH (0.987); and PhO^- (0.013).

The properties of the catalyst's surface are essential in photocatalysis. Adsorption of organic compounds on the surface of the catalyst is strongly affected by the surface charge. The point of zero charge (PZC) is defined as the pH value at which the catalyst exhibits a net zero surface charge. At pH values below the PZC, the surface of the catalyst is protonated and has a positive net surface charge. In turn, the net surface charge becomes negative at pH values above the PZC.

As expected, the curves of the final pH as a function of the initial pH of the catalysts in 0.1 mol·L^{-1} NaCl show an intersec-

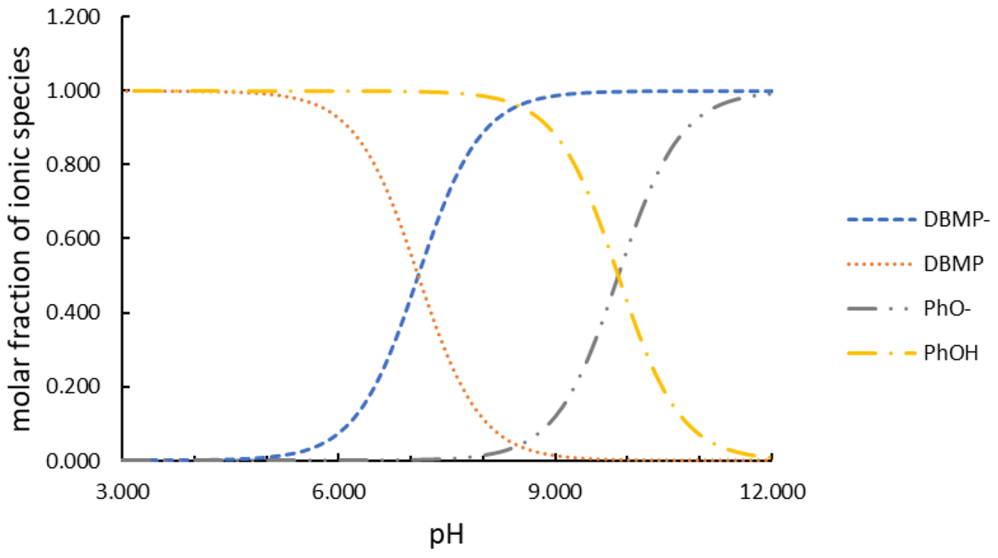

Figure 3: Molar fractions of ionic species as functions of the pH value.

tion with the line $y = x$, which corresponds to the PZC of the sample (Figure 4). The measurement of the PZC exhibits a higher pH_{PZC} value for M1 (8.0) than for M2 (6.2) (Figure 4). The differences in these pH_{PZC} values may result from the oxidation levels of M1 and M2, the latter having a positively charged surface because it is more oxidized and the former being negatively charged due to a lower oxidation level (see the x value, in Table 1). As a result, at pH 8 the surfaces of these two magnetite catalysts have opposite charges, which was shown in the zeta potential measurements of the catalysts (−0.37 mV and +14.4 mV for M1 and M2, respectively). These findings are in line with those previously observed by Hou et al. [29] on analogous samples.

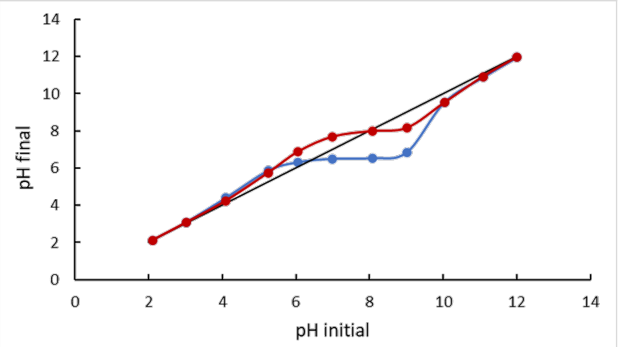

Figure 4: Determination of pH_{PZC} for M1 (red) and M2 (blue).

It is believed that, at the catalyst–solution interface, the phenoxy group binds specifically to surface sites (Equations 3 and 4):

$$\equiv \mathrm{Fe(II,III)OH} + \mathrm{S}^{n-} \rightarrow \equiv \mathrm{Fe(II,III)OH}\cdots\mathrm{S}^{n-} \quad (3)$$

$$\equiv \mathrm{Fe(II,III)O}^{-} + \mathrm{S} \rightarrow \equiv \mathrm{Fe(II,III)O}^{-}\cdots\mathrm{S} \quad (4)$$

S – undissociated organic compound; S^{n-} - dissociated organic compound

This means that DBMP is more likely to interact with the catalyst surface than PhOH. The distribution of species shows that only approximately 0.013 molecules of phenol will react with the protonated catalyst surface, while 0.888 molecules of DBMP could interact with the catalyst surface by Coulombic forces and a further 0.112 via hydrogen bonds.

The apparent degradation rate constant (k_{app}) was determined (for each degradation system) according to Equation 5, assuming that the reactions occurring were of pseudo-first order.

$$\ln\left(C_t/C_0\right) = -k_{app}\, t, \quad (5)$$

where C_0 and C_t are the initial concentration and the concentration at time t, respectively. The dependence of $\ln(C_t/C_0)$ on time is represented by straight lines, as shown in Figure 5b,d. Therefore, the degradation kinetics are consistent with the pseudo-first-order kinetic model ($R^2 > 0.95$). The results demonstrate that the photocatalytic processes were very efficient and more efficient than degradation by ozonolysis. The values of the degradation rate constants and the half-lives are summarized in Table 2. Significant differences in reactivity were observed for phenol and DBMP. The dissociation constant (pK_a) of DBMP is approx. 7.21, hence, almost 90% of the DBMP was dissociated at pH 8, while phenol was mainly (98%) undissociated (Figure 3). The high amount of the ionic form results in rapid direct photolysis. Direct photolysis of aqueous DBMP was mainly initiated by photolytic cleavage of the bromine–carbon bond and the formation of bromide ions. The half-lives of direct photolysis for phenol and DBMP were 1732.9 and 22 min, respectively. These results indicate that the bromine substituent facilitated the direct photolysis of the phenols. The apparent rate constant of DBMP degradation during direct photolysis and through photocatalysis were, respectively, 31.5×10^{-3} min^{-1} and 149×10^{-3} min^{-1} for M1 and 220×10^{-3} min^{-1} for M2. As a result, approximately 50% and 98% of DBMP was degraded via direct photolysis and photocatalysis, respectively (after 60 min). The efficiency of phenol photocatalysis was low (ca. 40% for M1 and ca. 30% for M2, after 60 min). This may be due to the lack of interaction between the catalysts' surfaces and phenol.

The hydroxyl radicals (•OH) generated during water ozonation are described by the SBH model [30-32] for neutral pH or the TFG model [33-35] for pH > 7. Considering the process conditions during the study (pH 8), we are interested in the TFG model. The rate constants used in the model were determined by Chelkowska et al. [36]. The TFG model includes the following reactions:

$$\mathrm{O_3 + OH^- \rightarrow HO_2^- + O_2} \qquad k_6 = 120\ \mathrm{M^{-1}\ s^{-1}} \quad (6)$$

$$\mathrm{HO_2^- + O_3 \rightarrow O_2^{\cdot -} + HO^{\cdot} + O_2} \qquad k_7 = 1.5 \times 10^6\ \mathrm{M^{-1}\ s^{-1}} \quad (7)$$

$$\mathrm{O_2^{\cdot -} + O_3 \rightarrow O_3^{\cdot -} + {}^{\cdot}O_2} \qquad k_8 = 1.6 \times 10^9\ \mathrm{M^{-1}\ s^{-1}} \quad (8)$$

$$\mathrm{O_3^{\cdot -} + H_2O \rightarrow {}^{\cdot}OH + OH^- + O_2} \qquad k_9 = 15\ \mathrm{M^{-1}\ s^{-1}} \quad (9)$$

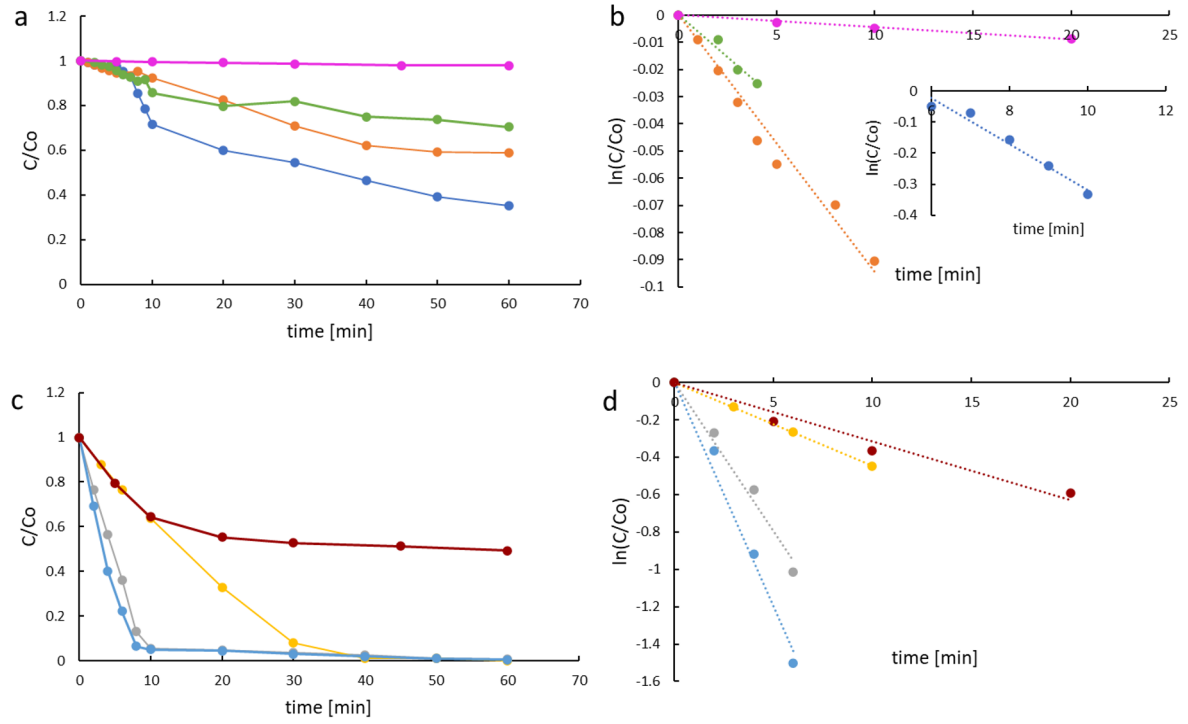

Figure 5: (a) Substrate decay rate of PhOH/O_3 (blue), PhOH/M1 (orange), PhOH/M2 (green), and PhOH/photolysis (pink); (b) plot of ln(C_t/C_0) vs irradiation time for phenol; (c) substrate decay rate of DBMP/O_3 (yellow), DBMP/M1 (grey), DBMP/M2 (light blue), and DBMP/photolysis (red); (d) plot of ln(C_t/C_0) vs irradiation time for DBMP.

Table 2: Kinetic parameters of the reaction systems under study.

Reaction system	k_{app} [min^{-1}]	$t_{1/2}$ [min]	R^2	k_{app} [min^{-1}] bromide formation	R^2
PhOH/O_3	73.6×10^{-3}	15.4	0.97	—	—
PhOH/M1	11.0×10^{-3}	63.0	0.99	—	—
PhOH/M2	6.2×10^{-3}	111.8	0.97	—	—
PhOH/photolysis	4.0×10^{-4}	1732.9	0.99	—	—
DBMP/O_3	44.6×10^{-3}	15.5	0.99	197.3×10^{-3}	0.83
DBMP/M1	159.7×10^{-3}	4.3	0.98	354.2×10^{-3}	0.99
DBMP/M2	239.7×10^{-3}	2.9	0.99	409.7×10^{-3}	0.91
DBMP/photolysis	31.5×10^{-3}	22.0	0.96	50.7×10^{-3}	0.99

The reaction in Equation 6 shows that the ozone decomposition process is initiated by hydroxy anions. Two-electron transfer of the oxygen atom produces the $^{-}$OOH anion, which is necessary for the generation of hydroxyl radicals. The low value of the reaction rate constant (Equation 6) indicates that it is a limiting process of the phenol ozonolysis, hence the observed delay in the rate of phenol degradation in ozonolysis in Figure 5a,b. Because the reaction in Equation 6 is slow, the reaction conditions are not stationary at the initial stage of the ozonolysis process. After reaching static conditions (about 6 min from the start of gas purging), the process proceeds according to the pseudo-first-order kinetic model. The determination of the apparent rate constant of phenol ozonolysis after obtaining steady-state process conditions is shown in the insert in Figure 5b.

The degradation of phenol at pH 8 in both ozonolysis and photocatalysis is oxidative (reaction with hydroxyl, superoxide, and hydroperoxide radicals). When comparing the apparent degradation rate constants (k_{app}) of phenol for ozonolysis

(73.6×10^{-3} min^{-1}) and for photocatalysis (11×10^{-3} min^{-1} for M1 and 6.2×10^{-3} min^{-1} for M2), a higher k_{app} value can be observed for ozonolysis.

As shown in Figure 6, bromide ions were released from the benzene ring by the ozonation reaction. The bromide ion concentration increased with an increasing level of degradation of DBMP, which suggests that degradation generates brominated intermediates that are subsequently decomposed to release bromine atoms. The normalized concentration of bromide ions (with DBMP degradation efficiency close to 95%; Figure 7) is about 0.9 (where 1 is the theoretical complete release of bromide; Figure 6). However, a normalized bromide ion concentration smaller than 0.5 for ozonolysis may denote the production of brominated organic by-products. Release yields of bromine in the form of bromide ions as high as 90% showed eventual mineralization. The half-live of DBMP in photocatalytic processes was 4.6 min (M1) or 3.2 min (M2); for ozonolysis, it was 15.5 min, suggesting a faster degradation of DMBP in photocatalytic processes than in ozonolysis. The apparent rate constants of bromide generation for all processes in the study are summarized in Table 2. The results are consistent with those for degradation. The degradation activity of DBMP was in the order of M2 > M1 > O_3 > photolysis, and the same order was observed for the generation of bromide anions (Figure S2, Supporting Information File 1). The higher yields of bromides in the case of photocatalysis revealed the contribution of the reduction process to the photocatalytic degradation of DBMP.

Figure 7 shows the degradation efficiency regarding phenol and DBMP. Phenol degradation reached approx. 65% after 60 min of ozonation whereas the degradation of DBMP was 95%. This is related to the ionic forms of these compounds under the given reaction conditions (89% of DBMP was dissociated vs only 13% of phenol). The presence of hydroxyl radicals in the solution and a higher reactivity of phenoxide ions compared to that of undissociated forms contributed to a higher degradation efficiency of DBMP in ozonolysis. DBMP is easier to oxidize than phenol. This is also because of the substitution of two hydrogen

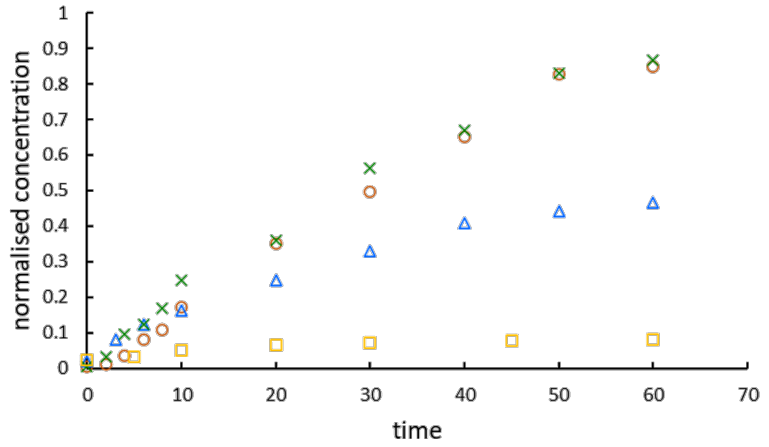

Figure 6: Bromide ion production as a function of the time (circles – M1, crosses – M2, triangles – ozonation, squares – photolysis).

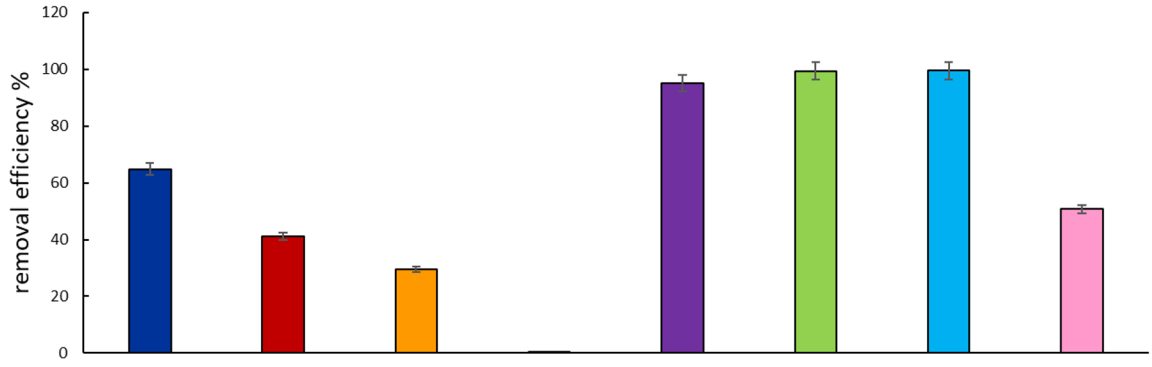

Figure 7: Substrate removal efficiency of PhOH/O_3 (dark blue), PhOH/M1 (red), PhOH/M2 (orange), PhOH/photolysis (black), DBMP/O_3 (violet), DBMP/M1 (green), DBMP/M2 (light blue), and DBMP/photolysis (pink).

atoms by two electron donors (–Br) in the DBMP molecule, which activates the aromatic ring. The degradation efficiency in photocatalysis was higher for DBMP than for phenol, reaching 98%.

Excitation of the catalyst with energies higher than the bandgap energy generates holes and electrons, which, after moving to the catalyst surface, may participate in redox processes. In a basic medium, the photocatalytic process may proceed by oxygen reduction at the surface of the particles (electron transfer only) [37]. A similar electron transfer can occur during the adsorption of organic compounds on magnetite. In the presence of adsorbed aryl halogenated compounds on the catalyst surface, the accumulated electrons are available to activate carbon–halogen bonds via dissociative electron transfer [38,39]. The electron from the catalyst conduction band is injected into the unoccupied orbital of halogenated aromatics, resulting in the breaking of carbon–halogen bonds.

For the Fe^{2+} and Fe^{3+} ions on the octahedral sites, electron transfer between these ions is feasible without substantial excess energy [40]. Therefore, electrons could be transferred with very low activation energy among iron ions on the octahedral sites. As we showed above, DBMP interacts with the magnetite surface, thus, it can react with the generated electrons. The following reaction path for DBMP degradation is proposed to explain our observations (a detailed description of DBMP reactions can be found in Figure S3, Supporting Information File 1):

$$Fe_3O_4 + h\nu \rightarrow Fe_3O_4\left(h^+ + e^-\right)$$

$$Fe_3O_4\left(h^+\right) + H_2O \rightarrow Fe_3O_4 + {}^{\cdot}OH + H^+$$

$$Fe_3O_4\left(h^+\right) + {}^{-}OH \rightarrow Fe_3O_4 + {}^{\cdot}OH$$

$$H^+ + e^- \rightarrow {}^{\cdot}H$$

$$2H^{\cdot} \rightarrow H_2$$

$$O_2 + e^- \rightarrow O_2^{-\cdot}$$

$$DBMP^- + e^- \rightarrow DBMP^{-\cdot} + Br^-$$

$$DBMP^- + {}^{\cdot}H \rightarrow \left[DBMP\right]^{-\cdot} + HBr$$

$$DBMP^{-\cdot} + {}^{\cdot}H \rightarrow \left[DBMPH\right]^-$$

$$DBMP^{-\cdot} + {}^{\cdot}OH \rightarrow \left[DBMPOH\right]^-$$

$$DBMP^- + {}^{\cdot}OH \rightarrow \left[DBMPOH\right]^- + {}^{\cdot}Br$$

$$O_2 + DBMP^{-\cdot} \rightarrow \left[DBMPO_2\right]^{-\cdot}$$

$$O_2^{-\cdot} + DBMP^{-\cdot} \rightarrow \left[DBMPO_2\right]^{2-}$$

The results demonstrate the effectiveness of magnetite in the photocatalytic degradation of halogenated aromatic pollutants.

Conclusion

In the present study, two types of magnetite (M1 and M2) were investigated as possible photocatalysts. The morphology, optical properties, and structural properties of the M1 and M2 samples were investigated. The stoichiometry of magnetite noticeably impacted the optical and surface properties.

Direct photolysis indicated that the bromine substituent facilitated the degradation of phenols. In the ozonation process, the degradation of phenol reached approximately 65% after 60 min, while the degradation of the DBMP reached 95% after the same time. The kinetic results showed that photocatalytic processes were more effective than DBMP degradation by ozonolysis. Phenol degradation occurs mainly via oxidation, as indicated by comparable rate constants for all the degradation processes studied. In the case of photocatalysis, the degradation rate increases with increasing values of the catalyst's zeta potential. This indicates that the apparent rate constant values are influenced by the interaction between the DBMP molecule and the magnetite surface. When bonded to the catalyst's surface, molecules can react with the electrons being generated. Therefore, we postulate a mixed reductive–oxidative mechanism of DBMP degradation on magnetite.

In conclusion, magnetite can be an efficient and low-cost material suitable for removing halogenated aryl compounds from aqueous solutions.

Experimental

Materials

The 2,6-dibromo-4-methylphenol (97%) was purchased from Alfa Aesar, phenol (>99%) was obtained from Riedel-de-Haen. The magnetite samples were obtained from Sigma-Aldrich: Fe_3O_4 micro-powder (M1, particle size under 5 μm, d = 4.8–5.1 g·cm^{-3}, 95% purity estimated from trace metal analysis); Fe_3O_4 nano-powder (M2, particle size under 50 nm, d = 3.9 g·cm^{-3}, >98% purity estimated from trace metal analysis). All chemicals were of analytical grade and were used without prior purification.

Characterization of the photocatalysts

The PZC of catalysts was measured according to Kocharova and co-workers [41]. For the determination of pH_{PZC}, eleven vials were filled with 0.1 mol·L^{-1} NaCl solution. The pH of each vial was adjusted with NaOH and HCl solutions to pH 2–12. Next, 10 mg of catalyst was dispersed in each vial. The solution was constantly agitated at 240 rpm for 3 h at ambient temperature to reach equilibrium. The equilibrium pH value was measured with a multimeter (CPC 411, Elmetron, Poland) and the values were plotted against the initial pH values for both series. The PZC value was then obtained from the point at which the curve showing final pH vs initial pH intersected the $y = x$ line on the graph. The morphology of the catalysts was observed with a field-emission scanning electron microscope (Zeiss Ultra 55, Oberkochen, Germany). The crystalline phases were analyzed with a Cu Kα powder diffractometer (D8 Advance, Bruker, Ettlingen, Germany) operating at 40 kV and 36 mA (λ = 0.154056 nm). The optical characterization of the catalysts was performed by using a spectrophotometer (Cary Series UV-Vis-NIR, Agilent Technologies) in the wavelength range of 190–800 nm.

Photocatalytic degradation of phenols

The photocatalytic activity of M1 and M2 was evaluated by the photocatalytic degradation of PhOH and DBMP. First, 750 cm^3 (1.064×10^{-3} mol·L^{-1}) of aqueous phenol solution was placed into the reactor. The pH of the solution was adjusted to 8 ± 0.1 with 0.1 mol·L^{-1} NaOH. Then, 0.67 g·L^{-1} of the catalyst powder was dispersed in the phenol solution. The resulting suspension was stirred for 30 min in the dark (until adsorption/desorption equilibrium was reached). Photocatalytic degradation was carried out using a glass photoreactor (Heraeus LRS2, Hanau, Germany) in air. The irradiation was performed with a TQ150 excimer lamp (150 W, with forced water cooling to 25 °C, 47 W light energy flux of power density 4.7 mW·cm^{-2} measured by a Peak Tech digital lux meter) immersed in the continuously stirred reaction suspension. The photocatalytic reaction was performed for 60 min. During the reaction, 2 mL samples were collected from the reactor at regular time intervals (from the first to the tenth minute, every 2 min, then every 10 min up to 1 h), then filtered through a 0.22 μm syringe filter. The organic compound concentrations were evaluated by using HPLC.

Ozonolysis of phenols

For the ozonolysis experiment , the aqueous phenol solution (1.064×10^{-3} mol·L^{-1}, 750 cm^3, pH 8 ± 0.1, adjusted with 0.1 mol·L^{-1} NaOH) was continuously purged with gas (ozone solution in air). The ozonolysis reaction was performed using an ozone generator (Viaken Vairo-2186, Krakow, Poland). The ozone concentration in the gas stream was determined by the iodometric method [42] to be 12.73 mg·L^{-1}·h^{-1}. The ozonolysis reaction was performed for 60 min, during which samples were collected from the reactor at regular time intervals (from the first to the tenth minute, every 3 min, then every 10 min up to 1h). The organic compound concentrations were evaluated by using HPLC.

Analysis

Changes in phenol concentration were determined by a high-performance liquid chromatography system (Shimadzu, Japan) equipped with a UV detector (SPD-10AV) and a C18 column (Knauer 250 × 4.6 mm, Eurospher II 100-5 C18 H, with precolumn). The analysis conditions were as follows: mobile phase: 70% acetonitrile and 30% water; flow rate: 1.0 cm^3·min^{-1}; injection volume: 20×10^{-3} cm^3; absorbance detection: 270 and 310 nm for PhOH and DBMP, respectively. External standards of seven concentration levels ranging from 1×10^{-4} to 1×10^{-2} mol·L^{-1} were used to quantify PhOH and DBMP.

The concentration of dissolved bromide ions was determined potentiometrically with a bromide ion-selective electrode (EBr-01, Hydromet, Poland) with a silver chloride electrode (RL-100, Hydromet, Poland) as a reference electrode and a multimeter (CPC 411, Elmetron, Poland). External standards of seven concentration levels ranging from 1×10^{-5} to 1×10^{-3} mol·L^{-1} were used to quantify bromide ions.

Supporting Information

Figure S1: Kubelka–Munk plots of M1 (red) and M2 (blue); Figure S2: Establishing the apparent rate constant for bromide generation; Figure S3: DBMP reactions with reactive species generated during photocatalysis.

Supporting Information File 1

Supplementary information.
[https://www.beilstein-journals.org/bjnano/content/supplementary/2190-4286-13-126-S1.pdf]

ORCID® iDs

Joanna Kisała - https://orcid.org/0000-0003-0014-0866
Anna Tomaszewska - https://orcid.org/0000-0003-2548-0568
Przemysław Kolek - https://orcid.org/0000-0003-3838-5172

References

1. Kaminski, W.; Marszalek, J.; Tomczak, E. *Desalination* **2018,** *433,* 89–93. doi:10.1016/j.desal.2018.01.014

2. What Percent of Earth is Water?. https://www.universetoday.com/65588/what-percent-of-earth-is-water (accessed March 6, 2022).
3. Hoekstra, A. Y.; Chapagain, A. K. *Water Resour. Manage.* **2007,** *21,* 35–48. doi:10.1007/s11269-006-9039-x
4. Nichkova, M.; Germani, M.; Marco, M.-P. *J. Agric. Food Chem.* **2008,** *56,* 29–34. doi:10.1021/jf0721848
5. Sim, W.-J.; Lee, S.-H.; Lee, I.-S.; Choi, S.-D.; Oh, J.-E. *Chemosphere* **2009,** *77,* 552–558. doi:10.1016/j.chemosphere.2009.07.006
6. Michałowicz, J.; Włuka, A.; Bukowska, B. *Sci. Total Environ.* **2022,** *811,* 152289. doi:10.1016/j.scitotenv.2021.152289
7. Koc-Jurczyk, J.; Jurczyk, Ł.; Balawejder, M.; Kisała, J. *Desalin. Water Treat.* **2022,** *246,* 1–11. doi:10.5004/dwt.2022.28035
8. U.S. Environmental Protection Agency. *Ground water and drinking water. National Primary Drinking Water Standards. EPA-816-F-03-016;* USEPA, Office of Water: Washington, DC, USA, 2003.
9. Ma, D.; Yi, H.; Lai, C.; Liu, X.; Huo, X.; An, Z.; Li, L.; Fu, Y.; Li, B.; Zhang, M.; Qin, L.; Liu, S.; Yang, L. *Chemosphere* **2021,** *275,* 130104. doi:10.1016/j.chemosphere.2021.130104
10. Ganiyu, S. O.; Sable, S.; Gamal El-Din, M. *Chem. Eng. J.* **2022,** *429,* 132492. doi:10.1016/j.cej.2021.132492
11. Liu, H.; Wang, C.; Wang, G. *Chem. – Asian J.* **2020,** *15,* 3239–3253. doi:10.1002/asia.202000895
12. Cornell, R. M.; Schwertmann, U. *Iron Oxides in the Laboratory;* Wiley-VCH: Weinheim, Germany, 2003. doi:10.1002/3527602097
13. Bradley, M. J.; Tratnyek, P. G. *ACS Earth Space Chem.* **2019,** *3,* 688–699. doi:10.1021/acsearthspacechem.8b00200
14. Nguyen, M. D.; Tran, H.-V.; Xu, S.; Lee, T. R. *Appl. Sci.* **2021,** *11,* 11301. doi:10.3390/app112311301
15. Solomon, R. V.; Lydia, I. S.; Merlin, J. P.; Venuvanalingam, P. *J. Iran. Chem. Soc.* **2012,** *9,* 101–109. doi:10.1007/s13738-011-0033-8
16. Bogacki, J.; Marcinowski, P.; Bury, D.; Krupa, M.; Ścieżyńska, D.; Prabhu, P. *Catalysts* **2021,** *11,* 9. doi:10.3390/catal11010009
17. Kisała, J.; Tomaszewska, A.; Barylyak, A.; Bobitski, Y.; Balawejder, M. *Int. J. Mol. Sci.* **2022,** *23,* 3438. doi:10.3390/ijms23073438
18. Mishra, P. M.; Naik, G. K.; Nayak, A.; Parida, K. M. *Chem. Eng. J.* **2016,** *299,* 227–235. doi:10.1016/j.cej.2016.04.052
19. Kisała, J.; Tomaszewska, A.; Pogocki, D. *J. Photocatal.* **2020,** *1,* 61–66. doi:10.2174/2665976x01999200607181110
20. Makuła, P.; Pacia, M.; Macyk, W. *J. Phys. Chem. Lett.* **2018,** *9,* 6814–6817. doi:10.1021/acs.jpclett.8b02892
21. Kabekkodu, S., Ed. *PDF-4+ 2015 (Database);* International Centre for Diffraction Data: Newtown Square, PA, USA, 2015.
22. Langford, J. I.; Wilson, A. J. C. *J. Appl. Crystallogr.* **1978,** *11,* 102–113. doi:10.1107/s0021889878012844
23. Scherrer, P. *Nachr. Ges. Wiss. Goettingen, Math.-Phys. Kl.* **1918,** *2,* 98–100.
24. Gorski, C. A.; Scherer, M. M. *Am. Mineral.* **2010,** *95,* 1017–1026. doi:10.2138/am.2010.3435
25. Górski, C. A. Redox behavior of magnetite in the environment: moving towards a semiconductor model. Ph.D. Thesis, University of Iowa, Iowa City, IA, USA, 2009. http://ir.uiowa.edu/etd/365
26. Zhou, W.; Greer, H. F. *Eur. J. Inorg. Chem.* **2016,** 941–950. doi:10.1002/ejic.201501342
27. White, A. F.; Peterson, M. L.; Hochella, M. F., Jr. *Geochim. Cosmochim. Acta* **1994,** *58,* 1859–1875. doi:10.1016/0016-7037(94)90420-0
28. Gutz, I. G. R. *pH Calculation and Acid-Base Titration Curves - Freeware for Data Analysis and Simulation*. http://www.iq.usp.br/gutz/Curtipot_.html (accessed April 6, 2020).
29. Hou, L.; Liang, Q.; Wang, F. *RSC Adv.* **2020,** *10,* 2378–2388. doi:10.1039/c9ra08517c
30. Buehler, R. E.; Staehelin, J.; Hoigné, J. *J. Phys. Chem.* **1984,** *88,* 2560–2564. doi:10.1021/j150656a026
31. Staehelin, J.; Hoigné, J. *Environ. Sci. Technol.* **1982,** *16,* 676–681. doi:10.1021/es00104a009
32. Staehelin, J.; Hoigné, J. *Environ. Sci. Technol.* **1985,** *19,* 1206–1213. doi:10.1021/es00142a012
33. Nemes, A.; Fábián, I.; Gordon, G. *Ozone: Sci. Eng.* **2000,** *22,* 287–304. doi:10.1080/01919510008547212
34. Nemes, A.; Fábián, I.; Gordon, G. *Inorg. React. Mech.* **2000,** *2,* 327–341.
35. Tomiyasu, H.; Fukutomi, H.; Gordon, G. *Inorg. Chem.* **1985,** *24,* 2962–2966. doi:10.1021/ic00213a018
36. Chelkowska, K.; Grasso, D.; Fábián, I.; Gordon, G. *Ozone: Sci. Eng.* **1992,** *14,* 33–49. doi:10.1080/01919519208552316
37. Jolivet, J.-P.; Chanéac, C.; Tronc, E. *Chem. Commun.* **2004,** 481–483. doi:10.1039/b304532n
38. Wang, Y.; Wei, Y.; Song, W.; Chen, C.; Zhao, J. *ChemCatChem* **2019,** *11,* 258–268. doi:10.1002/cctc.201801222
39. Mohamed, H. H.; Bahnemann, D. W. *Appl. Catal., B* **2012,** *128,* 91–104. doi:10.1016/j.apcatb.2012.05.045
40. Domingo, A.; Angeli, C.; de Graaf, C.; Robert, V. *J. Comput. Chem.* **2015,** *36,* 861–869. doi:10.1002/jcc.23871
41. Kocharova, N.; Ääritalo, T.; Leiro, J.; Kankare, J.; Lukkari, J. *Langmuir* **2007,** *23,* 3363–3371. doi:10.1021/la0631522
42. *Standard Methods for the Examination of Water and Wastewater,* 20th ed.; American Water Works Association: Washington, DC, USA, 2005.

License and Terms

BEILSTEIN JOURNAL OF NANOTECHNOLOGY

Photoelectrochemical water oxidation over TiO_2 nanotubes modified with MoS_2 and g-C_3N_4

Phuong Hoang Nguyen[1], Thi Minh Cao[1], Tho Truong Nguyen[1], Hien Duy Tong[*2] and Viet Van Pham[*1]

Full Research Paper

Open Access

Address:
[1]HUTECH University, 475A Dien Bien Phu Street, Binh Thanh District, Ho Chi Minh City, 700000, Vietnam and [2]Faculty of Engineering, Vietnamese-German University (VGU), Le Lai Street, Hoa Phu Ward, Thu Dau Mot City, Binh Duong Province, Vietnam

Email:
Hien Duy Tong[*] - hien.td@vgu.edu.vn;
Viet Van Pham[*] - pv.viet@hutech.edu.vn

* Corresponding author

Keywords:
band structure; g-C_3N_4/TiO_2; MoS_2/TiO_2; photoelectrochemical; water splitting

Beilstein J. Nanotechnol. **2022,** *13,* 1541–1550.
https://doi.org/10.3762/bjnano.13.127

Received: 07 July 2022
Accepted: 25 November 2022
Published: 16 December 2022

This article is part of the thematic issue "Nanomaterials for photocatalysis and applications in environmental remediation and renewable energy".

Associate Editor: W.-J. Ong

Abstract

TiO_2 nanotube arrays (TNAs) have been studied for photoelectrochemical (PEC) water splitting. However, there are two major barriers of TNAs, including a low photo-response and the fast charge carrier recombination in TNAs, leading to poor photocatalytic efficiency. Through a comparison of MoS_2/TNAs and g-C_3N_4/TNAs, it was found that TNAs modified with MoS_2 and g-C_3N_4 exhibited a current density of, respectively, 210.6 and 139.6 μA·cm^{-2} at an overpotential of 1.23 V vs RHE, which is 18.2 and 12 times higher than that of pure TNAs under the same conditions. The stability of the MoS_2/TNAs heterojunction is higher than that of g-C_3N_4/TNAs.

Introduction

Hydrogen energy has become a target pursued in the energy development strategies of many countries and regions. Hydrogen is often synthesized via hydrocarbon compounds or water electrolysis [1]. Methods to produce hydrogen via electrochemical or photo-electrochemical (PEC) water splitting are considered a future direction of renewable fuel development [2-4]. The use of solar energy to activate catalytic materials to separate water for creating clean fuels has been developed for about a decade [5,6]. Water splitting is carried out in solutions rich in H^+ ions to the conduct hydrogen evolution reaction (HER) process or in rich OH^- solutions for the oxygen evolution reaction (OER) process [7-9]. However, the electrode material must be extremely durable and nearly chemically inert to be able to withstand highly acidic or basic environments. Therefore, noble metals such as Pt, Pd, Au and Ag with suitable chemical properties, such as inertness, good resistance against corrosion and good electrical conductivity have been widely used in water splitting reactions [10,11]. However, noble metals are still rare

and expensive materials, and their application as electrode materials is considered to be not optimal [10]. Therefore, the study of a materials with high-performance in PEC water splitting, which could replace noble metals are a research interest.

Photocatalytic technology uses semiconductors for effective approaches to the degradation of dyes and antibiotics, the removal of pollutant gases, and water splitting to produce hydrogen using solar energy [12-17]. Among such semiconductors, TiO_2 nanotube arrays (TNAs) of 2–100 nm in diameter and 1–2 μm in length, are often used for efficient PEC applications exploiting advantages such as chemical stability, less toxicity and suitable cost [18-21]. However, there are two disadvantages affecting directly their photocatalytic ability. (i) TNAs only respond to ultraviolet (UV) light [22-24], and (ii) they exhibit fast carrier recombination [25]. Recently, the development of new heterojunction architectures through coupling TNAs with other semiconductor materials, especially low-bandgap semiconductors, led to a reduction of the required amounts of noble metals and materials such as CdS or ZnS [26-29]. There are many low-bandgap semiconductors that were coupled with TNAs, including MoS_2, WS_2, $MoSe_2$, g-C_3N_4, Cu_2O, and CuO. MoS_2 is a semiconductor with a narrow bandgap (1.9 eV at room temperature) exhibiting unique chemical, thermal, and charge transport properties, which can shift the light absorption of TiO_2 to the visible region [29-32]. An emerging new material in optoelectronics is g-C_3N_4 (bandgap of 2.65–2.7 eV) because it has an appropriate band structure with suitable energy levels regarding TiO_2, which can improve the charge transfer states [33,34]. These two low-bandgap semiconductors improved considerably the PEC water splitting efficiency [35,36]. However, the fabrication of MoS_2/TNAs and g-C_3N_4/TNAs has many disadvantages such as high synthesis temperatures, the requirement of a binder, or expensive synthesis equipment [29,36-38].

In this study, we compare properties and PEC water splitting efficiency of TNAs combined with the typical 2D materials MoS_2 and g-C_3N_4 obtained with the same synthesis procedure. Insightful studies about optical and electronic properties have been conducted to explain clearly the difference between these composite materials

Experimental

Materials and chemicals

Chemicals and materials for the synthesis and characterization include Ti foil (1 cm × 2 cm), hydrochloric acid (HCl), sodium hydroxide (NaOH), DI water, acetone ($(CH_3)_2CO$), ethanol (C_2H_5OH), ammonium fluoride (NH_4F), *N*-acetyl-L-cysteine, ammonium heptamolybdate ($(NH_4)_6Mo_7O_{24}$), thiourea (CH_4N_2S), nitrogen gas, melamine, and nafion solution. All chemicals and materials were purified and used without further treatment.

Preparation of materials

The individual materials including TNAs, MoS_2, and g-C_3N_4 were synthesized as described earlier [39-41]. To combine with TNAs, 5 mg of MoS_2 or g-C_3N_4 powder was dispersed in 2 mL of a solution containing 50 vol % ethanol and 50 vol % nafion solution as described in [40]. The solution was stirred for 30 min before ultrasonic treatment for 3 h to obtain a homogeneous solution. Next, 0.2 mL of either of these solutions was used to coat the surface of TNAs via spin coating. The samples were denoted as MoS_2/TNAs and g-C_3N_4/TNAs. Then, the samples were annealed in nitrogen gas at 60 °C for 12 h to obtain a stable electrode for the investigation processes.

Characterization of materials

The morphology, the phase, and the vibrational characteristics of the surface functional groups of the materials were observed by field-emission scanning electron microscopy (FESEM), X-ray diffraction (XRD), and Fourier-transform infrared spectroscopy (FTIR). Diffuse reflectance spectroscopy (DRS) was carried out to measure the optical bandgap of the semiconductor materials through the Tauc method using the absorption coefficient α of the material, according to Equation 1 [42]:

$$\left(\alpha h\nu\right)^{\frac{1}{\gamma}} = B\left(h\nu - E_g\right), \quad (1)$$

where h, ν, E_g, and B are the Planck constant, the frequency of the photon, the bandgap energy, and a constant, respectively; γ = 1/2 for materials with direct bandgap and γ = 2 for semiconductor materials with an indirect bandgap.

PEC activity evaluation

The PEC water splitting efficiency of the materials was evaluated through a three-electrode PEC cell using a Biologic SP-200 potentiostat. The three electrodes were a Pt counter electrode, a Ag/AgCl 3 M reference electrode, and a MoS_2/TNAs or g-C_3N_4/TNAs working electrode in a 1 M Na_2SO_4 (pH 7.4) electrolyte solution. The light source used in this study was a 150 W Xe lamp (ABET Instruments) with a calibrated luminous intensity of 100 mW·cm^{-2} and a UV filter cutting at 380 nm.

Results and Discussion

Characterizations of materials

Figure 1a displays the morphology of TNAs, which have a uniform distribution of nanotubes with average diameters ranging from 80–100 nm and a length of 500 nm (Figure 1b). The MoS_2 material exhibits the stacked layers of 2D materials

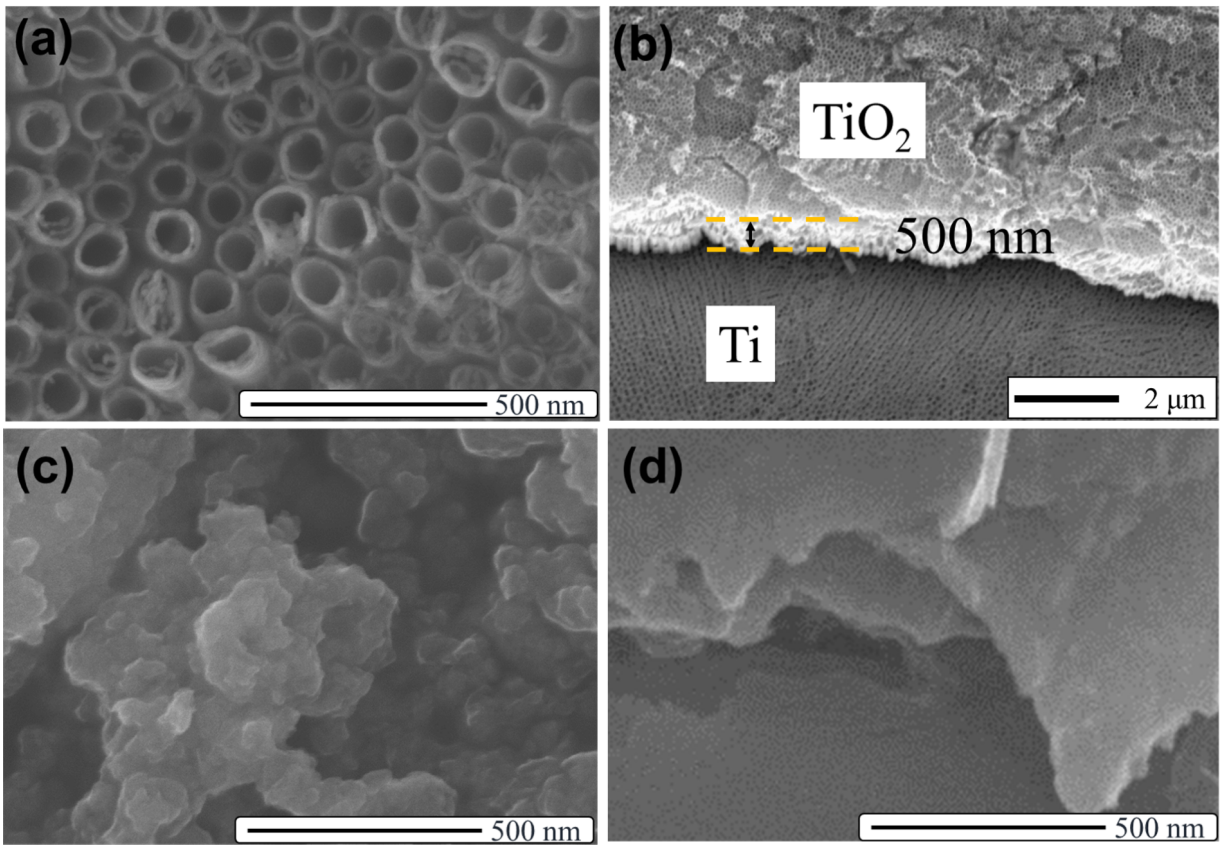

Figure 1: SEM images of TNAs (a, b), MoS_2 (c), and g-C_3N_4 (d).

(Figure 1b). This agrees with the results of previous publications in which hydrothermal methods were applied [24-26]. The SEM image of the g-C_3N_4 material shows the uniform nanosheets that were fabricated by the melamine pyrolysis method (Figure 1c).

After the deposition of 2D materials MoS_2 and g-C_3N_4 onto the TNAs substrate, we examined the morphology of these heterostructures by using SEM (Figure 2). There are some small pieces that are randomly distributed on the surface of TNAs in Figure 2a, which were attributed to be MoS_2. There is a similar

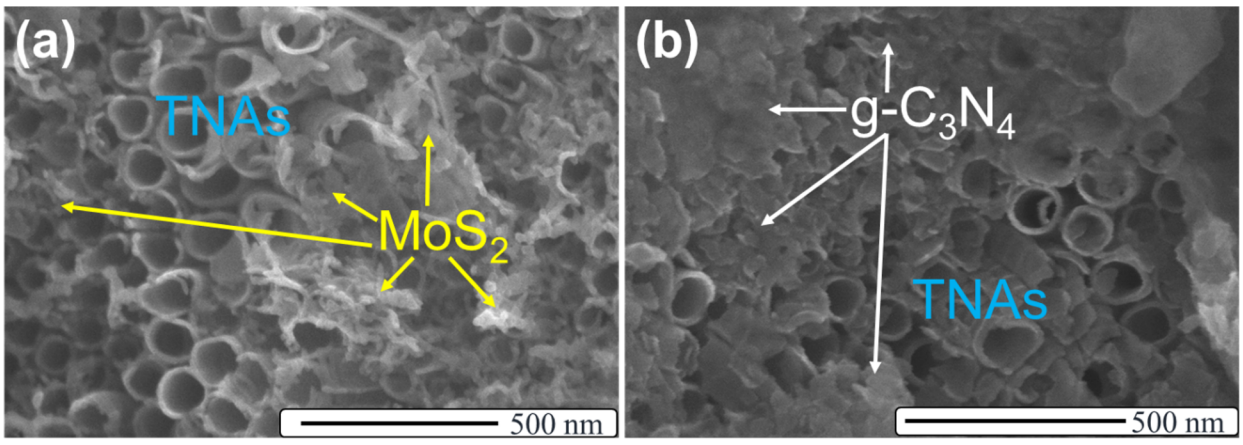

Figure 2: SEM images of MoS_2/TNAs (a), and g-C_3N_4/TNAs (b).

result in the SEM image of g-C_3N_4/TNAs in Figure 2b. However, the distribution of g-C_3N_4 on the surface of the TNAs is denser than that of MoS_2. Besides, the morphology of the TNAs did not change. The appearance of MoS_2 and g-C_3N_4 has also been confirmed by EDS measurements and element mapping (Figure S1 and Figure S2, Supporting Information File 1).

Figure 3a shows that diffraction peaks of TNAs at 2θ = 25.45°, 37.07°, 39.24°, 54.10°, and 55.25°, attributed to the (101), (103), (004), (112), (105), and (211) planes of TiO_2, respectively [JCPDS No. 21-1272]. Besides, the XRD pattern of MoS_2 exhibits diffraction peaks at 13.97°, 33.56°, 40.24°, and 59.25°, corresponding to the (002), (100), (103), and (110) planes, respectively, of the 2H phase of MoS_2 [JCPDS No. 37-1492]. The pristine g-C_3N_4 shows two distinct characteristic peaks at 2θ = 12.9° and 27.45°, assigned to the (100) and (002) planes, respectively [43,44]. The XRD diffraction results show the simultaneous appearance of diffraction peaks at 2θ = 25.45°, typical for the (101) planes of TNAs, and at 33.56° for the (001) planes of MoS_2. Besides, the diffraction peak at 2θ = 16.45° characterizes the semi-crystalline structure of perfluorocarbon chains from nafion films [45]. Notably, the diffraction peak of the MoS_2 material at 2θ = 13.97°, which is typical for the (002) lattice plane, is lost after the formation of the MoS_2/TNAs heterostructure. This could be explained by the very small amount of MoS_2 (5 mg) loaded onto the TNAs. Therefore, it will be difficult to identify the MoS_2 phase in the composite from the XRD pattern of MoS_2/TNAs. The (002) plane indicates the multilayer structure of MoS_2 materials, the (001) plane indicates a monolayer structure of MoS_2 [37,46]. Therefore, the disappearing (002) reflection and the remaining (001) reflection show that the ultrasonic treatment peeled the MoS_2 material into thinner layered structures. This is in agreement with the SEM images, in which material with rather small and thinner structures scattered on the surface of TNAs was observed.

The functional groups and chemical bonds of the as-prepared materials were determined by using FTIR spectroscopy, as shown in Figure 3b. The formation of TiO_2 on the Ti foil is indicated by the vibrations of the Ti–O bond in the wavenumber region from 450 to 750 cm^{-1} [47]. The bonding characteristics in the MoS_2 material are presented by Mo–S vibration peaks between 1620 and 420 cm^{-1} [48]. Also, FTIR spectroscopy is used as an extremely effective technique for studying the vibrational states of organic bonds in g-C_3N_4 materials using the vibrational peaks of C–N bonds between 1640 and 1200 cm^{-1}. A very strong absorption peak at 807.2 cm^{-1} characterizes the fluctuation of tri-s-triazine of g-C_3N_4. Vibrational peaks in the 3200 cm^{-1} region attributed to fluctuations of the C–N group also appeared [49]. Figure 3b shows the bonding states in the MoS_2/TNAs and g-C_3N_4/TNAs heterostructures. The results show that, in addition to the typical bonding of the TNAs substrate such as Ti–O bonds, there are vibrations of composites of TNAs with MoS_2 (between 420 and 1620 cm^{-1}) and g-C_3N_4

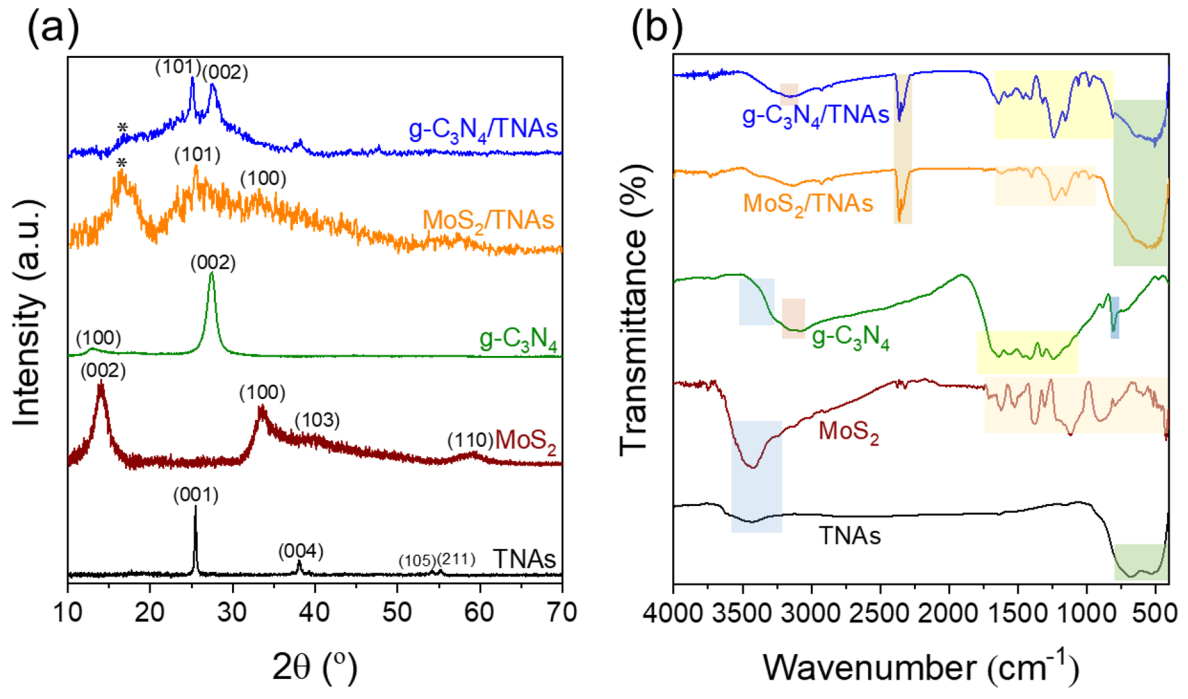

Figure 3: XRD pattern (a) and FTIR spectra (b) of as-synthesized samples.

(between 1200 and 1640 cm^{-1} for C–N bonds and 807 cm^{-1} for tri-s-triazine subunit). The peaks in the wavenumber range between 3400 and 1625 cm^{-1} of all samples are typical for stretching vibrations of the O–H bonds, which are caused by air humidity.

To confirm the ability of the heterojunctions to enhance absorption in the visible-light region, the DRS spectra and Tauc plots were recorded and are presented in Figure 4. It can be easily observed in Figure 4a that the TNAs show a strong absorption edge at 393 nm. This means that TNAs are only activated by near-UV irradiation. In contrast, the g-C_3N_4 sample shows an absorption edge at 464 nm. Meanwhile, MoS_2 exhibits strong absorption from the UV region extending to the entire visible-light region. It can be seen that the loading of both MoS_2 and g-C_3N_4 on the TNAs surface extended the absorption to the visible-light range. Specifically, the absorption edge of the g-C_3N_4/TNAs and MoS_2/TNAs samples shifted to 442 and 425 nm, respectively. Besides, a remarkable feature of the DRS spectrum of MoS_2 is a superior absorption ability in the whole visible-light range in comparison to that of the remaining samples. To evaluate the optical bandgap energy of TNAs and g-C_3N_4, Tauc plots were extrapolated in Figure 4b. The bandgap values of TNAs, g-C_3N_4, and MoS_2 were calculated as about 3.15, 2.67, and 1.47 eV, respectively. These results are agreement with previous publications [50-52].

Figure 5 shows the results of electrochemical impedance spectroscopy (EIS), that is, Nyquist and Mott–Schottky plots of the materials, which give information about the charge transfer mechanism at the interface. In Figure 5a, the Nyquist plots of the samples all exhibit only single semicircular shape, which shows the charge transfer resistance equivalent to the polarization resistance. This result also demonstrates a unique interaction of the electrode surface and the electrolyte solution. Furthermore, the g-C_3N_4 sample shows the semicircle with the largest radius, followed by TNAs and MoS_2, which indicates the low interaction of these materials with the electrolyte. However, after coupling, the g-C_3N_4/TNAs sample shows a semicircle with smaller radius compared than that of g-C_3N_4 or TNAs. The Nyquist plot of the MoS_2/TNAs sample shows the smallest semicircle radius of all samples. This result indicates an increase in carrier density during the reaction with the electrolyte solution, leading to a decrease in resistance of the g-C_3N_4/TNAs and MoS_2/TNAs samples. This could be explained by the enhanced optical interaction, causing an increase of the carrier concentration in MoS_2/TNAs sample such in Figure 4.

The mechanism for the enhanced activity of the heterojunctions can be explained by the Mott–Schottky results in Figure 5b,c. Generally, all samples show positive slopes, which proves that they are n-type semiconductors [53]. Equation 2 shows the Mott–Schottky relationship involving the apparent capacitance as a function of the potential under depletion conditions [54]:

$$C^{-2} = \frac{2}{e\varepsilon\varepsilon_0 N_d A^2}\left(V_a - V_{fb} - \frac{kT}{e}\right), \quad (2)$$

where C, ε, ε_0, N, A, V_a, V_{fb}, k, and T are the capacitance of the space charge region, the dielectric constant of the semiconductor, the vacuum permittivity, the donor density, the area of interface or the electrode, the applied and flat band potentials, the Boltzmann constant, and the temperature, respectively.

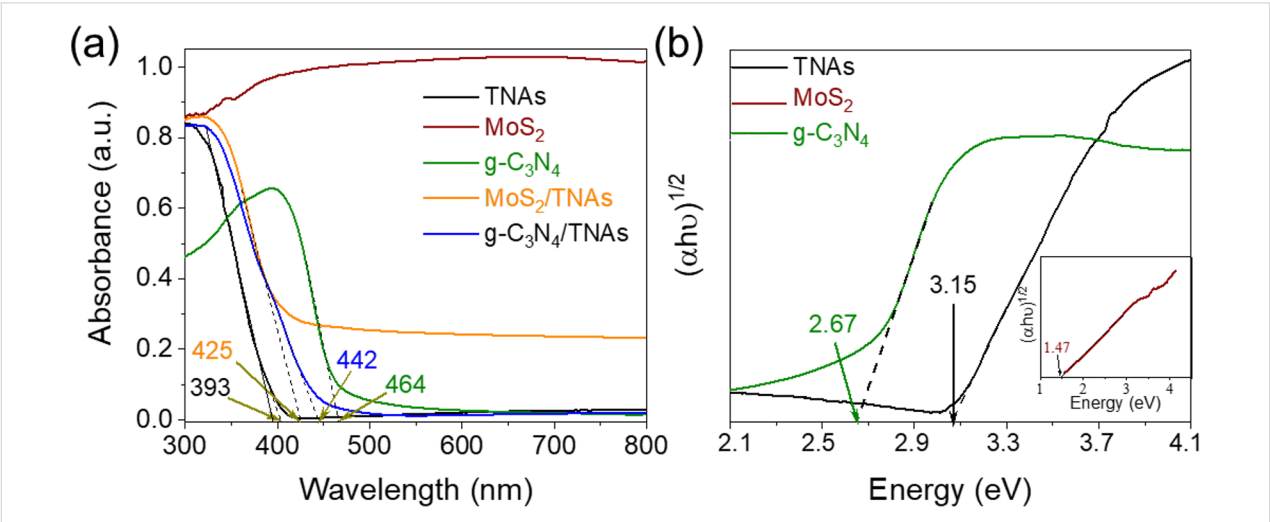

Figure 4: Comparison of the optical properties of as-synthesized materials through DRS spectra (a) and Tauc plots (b).

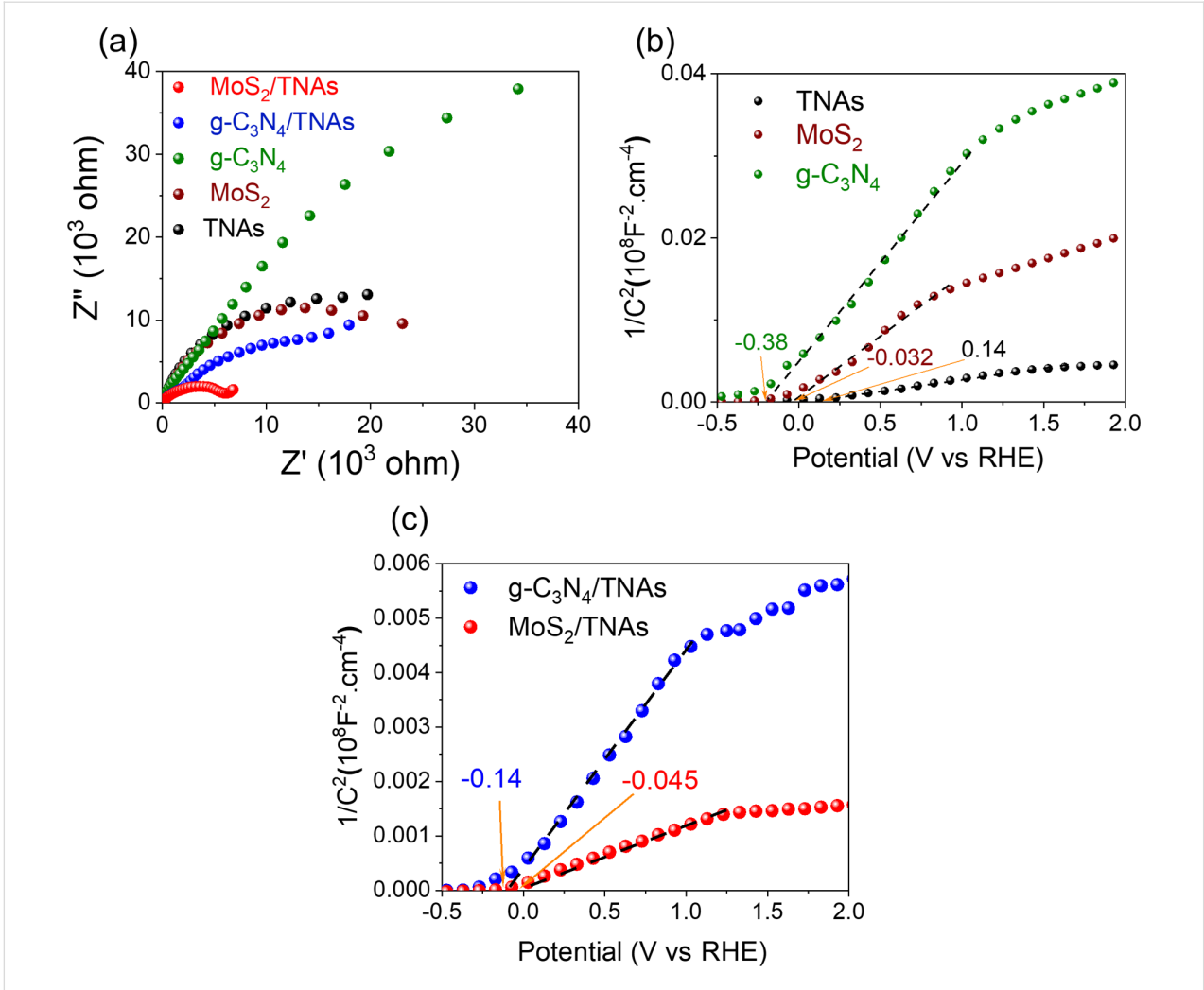

Figure 5: EIS spectra (a), Mott–Schottky plots of pristine materials (b) and heterostructures (c).

The plot of $1/C^2$ vs V shows an intercept of the x-axis, which corresponds to the flat band potential (E_{fb}), that is, the conduction band maximum (CBM) level of the material. The Mott–Schottky plots of TNAs, g-C_3N_4, and MoS_2 samples yield E_{fb} (or CBM) values of 0.14, −0.38, and −0.032 V vs RHE, respectively. It can be found that the E_{fb} values of g-C_3N_4 and MoS_2 are significantly more negative than that of TNAs, which can facilitate the migration of electrons from g-C_3N_4 and MoS_2 to TNAs. Furthermore, the E_{fb} values of g-C_3N_4/TNAs and MoS_2/TNAs are shifted to −0.14 and −0.045 V vs RHE (Figure 5c). The heterostructures express much more negative E_{fb} values than pristine TNAs, which is attributed to the enhanced electron density, the depletion of the E_{fb}, and electron–hole recombination [55].

PEC characterizations of materials

Figure 6 shows the linear sweep voltammetry (LSV) curves, Tafel slopes, and the photo-response of the samples. Figure 6a shows that the current density of all materials is grows linearly with the applied potential under visible-light excitation. The onset potentials of the of TNAs, g-C_3N_4, and MoS_2 are 0.08, 0.16, and 0.14 V vs RHE, respectively. Further, for the OER (1.23 V vs RHE), the current densities of TNAs, g-C_3N_4, and MoS_2 are 11.5, 4.2, and 31.2 μA/cm^2, respectively. The onset potential values of g-C_3N_4/TNAs and MoS_2/TNAs are significantly shifted to −0.76 and 0.008 V, respectively. In addition, the current density also exhibited an improvement with values of 139.6 and 210.6 μA/cm^2 at 1.23 V for g-C_3N_4/TNAs and MoS_2/TNAs, respectively, which shows their superiority in the PEC water oxidation reaction. The LSV results are also consistent with the previous results from EIS analysis and the Mott–Schottky results (Figure 5). The PEC activity of MoS_2/TNAs in this study is higher than that of MoS_2/TNAs synthesized by using a PVA binder agent in [36]. However, the direct combination of g-C_3N_4 with TNAs at a relatively high fabrication temperature (500 °C for 2 h) in [35] yielded better results

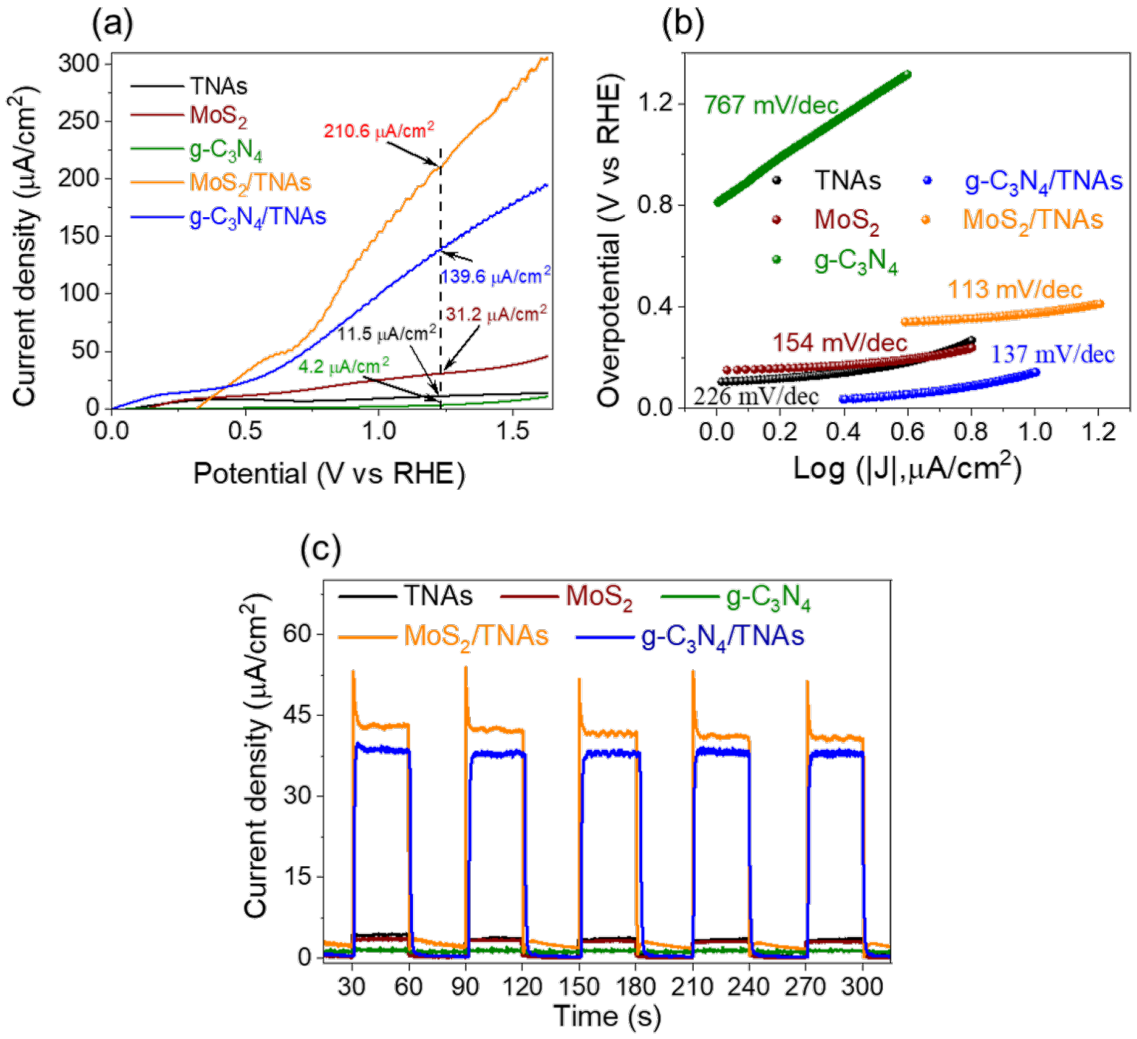

Figure 6: LSV plots (a), Tafel slopes (b), and photo-response (c) of the materials.

better than those of this study. The investigation of the stability of the PEC electrodes from MoS_2/TNAs and g-C_3N_4/TNAs is described in Figure S3, Supporting Information File 1. After every PEC test cycle, we immersed the PEC electrode in DI water for 1 h and let it dry completely before the next test. We can conclude that the stability of the MoS_2/TNAs heterojunction is higher than that of the g-C_3N_4/TNAs heterojunction. The decrease in catalytic activity of the PEC electrodes is explained by the leaching of the catalysts MoS_2 and g-C_3N_4 after each activity measurement.

The Tafel slope is considered as an important parameter to evaluate the PEC activity in water splitting. A smaller Tafel slope value indicates a more rapid increase in the reaction rate of the electrode. Figure 6b shows the high Tafel slope values of the individual materials, TNAs, g-C_3N_4, and MoS_2, of 226, 767, and 154 mV/dec, respectively. After the modification, the Tafel slope value of g-C_3N_4/TNAs is only about 137 mV/dec, while the best Tafel slope value of MoS_2/TNAs is only 113 mV/dec. Furthermore, the photocurrent of the materials was evaluated through the assessment of the photo-response under visible-light irradiation at 0.63 V in Figure 6c. A current density of about 38.6 μA/cm^2 was obtained with the g-C_3N_4/TNAs even after five cycles, which is nearly ten times higher than that of pure TNAs. The current density of MoS_2/TNAs is even higher than that of g-C_3N_4/TNAs reaching 43.4 μA/cm^2 after five cycles. These results indicate that enhancement of the optical interaction in MoS_2/TNAs heterostructures is stronger than that in g-C_3N_4/TNAs [56,57]. Further, the current density increases sharply and decreases rapidly within a few seconds for MoS_2/TNAs under light, which can be explained as follows: The photocurrent density of MoS_2/TNAs promptly increased because of the efficient separation of the e^-–h^+ pairs at the interfaces between TNAs and MoS_2 [58] and the rapid transfer

of the photo-induced electrons from MoS_2 to the TNAs electrode [59]. This result is in agreement with the EIS results in Figure 5a, where the arc radius of the Nyquist plot of MoS_2/TNAs was the smallest, indicating that MoS_2/TNAs effectively decreased the resistance of the TNAs and, thus, speeded up the charge transfer on the photoelectrode. These arguments are consistent with results previously published in [58].

Figure 7 presents the energy band diagram structure of the MoS_2/TNAs and g-C_3N_4/TNAs heterojunctions based on the DRS and Mott–Schottky analysis results, which are summarized in Table 1.

Table 1: The CBM and E_g values of the materials.

Sample	CBM level (V vs RHE, pH 7.3)	E_g (eV)
TNAs	0.14	2.99
MoS_2	−0.032	1.47
g-C_3N_4	−0.38	2.63

It is easily observed from Figure 7 that the heterostructures formed upon incorporation of TNAs with MoS_2 and g-C_3N_4 are all of type II. Type-II heterostructures promote the migration of h^+ and e^- under visible-light irradiation. Electrons can move from the conduction band (CB) of MoS_2 or g-C_3N_4 to the CB of TNAs in MoS_2/TNAs or g-C_3N_4/TNAs, respectively. In contrast, holes will migrate from the valence band (VB) of TNAs to the VB of MoS_2 or g-C_3N_4. Therefore, the recombination of the photo-generated e^-–h^+ pairs is reduced. In this contribution, the PEC water splitting reactions take place in a neutral media, which is well known to occur via two processes, including the oxidation and reduction reactions at, respectively, the anode and cathode described by Equation 3 and Equation 4.

Oxidation reaction at the anode:

$$2OH^- + 2h^+_{VB} \rightarrow 2H^+ + O_2 + 2e^-. \quad (3)$$

Reduction reaction at the cathode:

$$2H^+ + 2e^- \rightarrow H_2. \quad (4)$$

Carrying out the reactions in a neutral medium also contributes to the increased durability of the electrodes. However, the lack of initial H^+ concentration can reduce the efficiency of the H_2 production. For an effective water splitting process, the oxidation reaction of OH^- ions in the electrolyte needs to take place at the anode to generate e^- and H^+ ions along with O_2. The e^- current will immediately migrate to the cathode to perform reduction reactions. At that time, H^+ will also be reduced at the cathode to form H_2. The higher the efficiency of the oxidation reaction, the more e^- are generated and the stronger the H^+ reduction reaction will be. Preventing recombination of photo-generated e^-–h^+ pairs in the MoS_2/TNAs and g-C_3N_4/TNAs heterojunction structures has also been shown to increase the efficiency of PEC water splitting.

Conclusion

MoS_2/TNAs and g-C_3N_4/TNAs heterojunctions have been successfully fabricated for PEC water splitting. The role of g-C_3N_4 and MoS_2 in mitigating the recombination of e^-–h^+ pairs has been demonstrated. The ability to enhance the optical interaction of the heterostructures was presented through the reduction of the bandgap energy. The outstanding application performance of g-C_3N_4/TNAs and MoS_2/TNAs combinations was presented. In detail, the excellent water-splitting ability of g-C_3N_4/TNAs and MoS_2/TNAs heterojunctions achieved about 139.6 and 210.6 μA/cm^2. In addition, the PEC reaction rate was

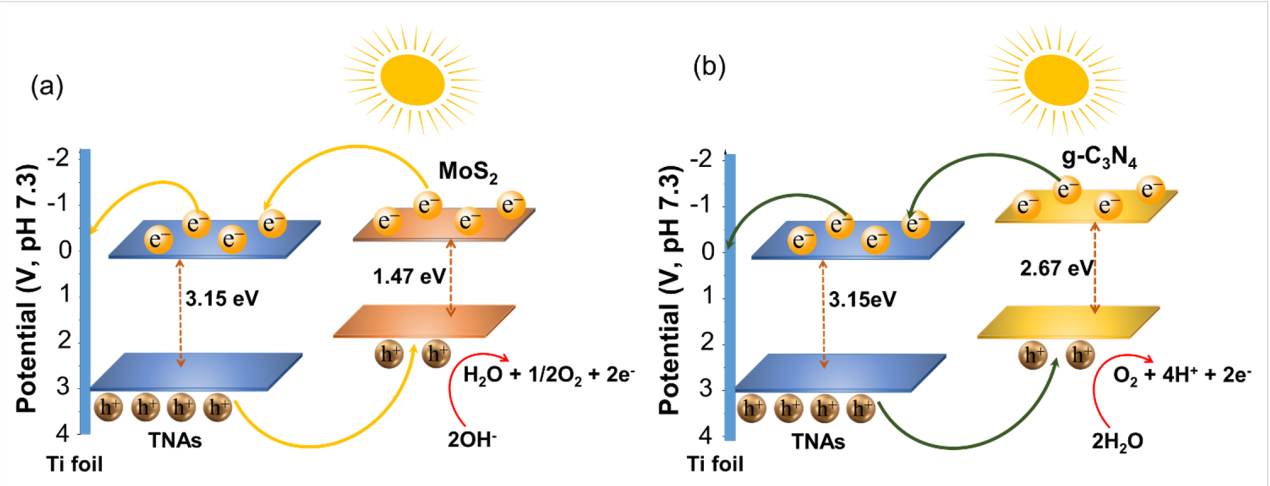

Figure 7: Proposed band diagram of MoS_2/TNAs (a) and g-C_3N_4/TNAs (b).

evaluated by the Tafel slope value, indicating a faster rate for the MoS_2/TNAs heterojunction compared to the g-C_3N_4/TNAs heterojunction. Moreover, the photocurrent density of MoS_2/TNAs is higher than that of g-C_3N_4/TNAs due to the strong optical interaction of the MoS_2/TNAs heterostructure.

Supporting Information

Supporting Information File 1

Additional figures.
[https://www.beilstein-journals.org/bjnano/content/supplementary/2190-4286-13-127-S1.pdf]

Acknowledgements

We sincerely thank the CM Thi Laboratory (HUTECH University) for supporting the facilities in this study.

ORCID® iDs

Viet Van Pham - https://orcid.org/0000-0002-8697-7095

References

1. Lubitz, W.; Tumas, W. *Chem. Rev.* **2007,** *107,* 3900–3903. doi:10.1021/cr050200z
2. Atilhan, S.; Park, S.; El-Halwagi, M. M.; Atilhan, M.; Moore, M.; Nielsen, R. B. *Curr. Opin. Chem. Eng.* **2021,** *31,* 100668. doi:10.1016/j.coche.2020.100668
3. Dincer, I. *Int. J. Hydrogen Energy* **2012,** *37,* 1954–1971. doi:10.1016/j.ijhydene.2011.03.173
4. Chen, W.-H.; Lee, J. E.; Jang, S.-H.; Lam, S.-S.; Rhee, G. H.; Jeon, K.-J.; Hussain, M.; Park, Y.-K. *Int. J. Energy Res.* **2022,** *46,* 5467–5477. doi:10.1002/er.7552
5. Liu, J.; Zou, Y.; Jin, B.; Zhang, K.; Park, J. H. *ACS Energy Lett.* **2019,** *4,* 3018–3027. doi:10.1021/acsenergylett.9b02199
6. Vozniuk, O.; Tanchoux, N.; Millet, J.-M.; Albonetti, S.; Di Renzo, F.; Cavani, F. Chapter 14 - Spinel Mixed Oxides for Chemical-Loop Reforming: From Solid State to Potential Application. In *Studies in Surface Science and Catalysis;* Albonetti, S.; Perathoner, S.; Quadrelli, E. A., Eds.; Elsevier, 2019; Vol. 178, pp 281–302. doi:10.1016/b978-0-444-64127-4.00014-8
7. Suryanto, B. H. R.; Wang, Y.; Hocking, R. K.; Adamson, W.; Zhao, C. *Nat. Commun.* **2019,** *10,* 5599. doi:10.1038/s41467-019-13415-8
8. Ros, C.; Andreu, T.; Morante, J. R. *J. Mater. Chem. A* **2020,** *8,* 10625–10669. doi:10.1039/d0ta02755c
9. Marx, D.; Tuckerman, M. E.; Hutter, J.; Parrinello, M. *Nature* **1999,** *397,* 601–604. doi:10.1038/17579
10. Xu, G.-R.; Hui, J.-J.; Huang, T.; Chen, Y.; Lee, J.-M. *J. Power Sources* **2015,** *285,* 393–399. doi:10.1016/j.jpowsour.2015.03.131
11. He, Y.; Liu, L.; Zhu, C.; Guo, S.; Golani, P.; Koo, B.; Tang, P.; Zhao, Z.; Xu, M.; Zhu, C.; Yu, P.; Zhou, X.; Gao, C.; Wang, X.; Shi, Z.; Zheng, L.; Yang, J.; Shin, B.; Arbiol, J.; Duan, H.; Du, Y.; Heggen, M.; Dunin-Borkowski, R. E.; Guo, W.; Wang, Q. J.; Zhang, Z.; Liu, Z. *Nat. Catal.* **2022,** *5,* 212–221. doi:10.1038/s41929-022-00753-y
12. Vesborg, P. C. K.; Seger, B.; Chorkendorff, I. *J. Phys. Chem. Lett.* **2015,** *6,* 951–957. doi:10.1021/acs.jpclett.5b00306
13. Li, S.; Cai, M.; Wang, C.; Liu, Y.; Li, N.; Zhang, P.; Li, X. *J. Mater. Sci. Technol.* **2022,** *123,* 177–190. doi:10.1016/j.jmst.2022.02.012
14. Wang, C.; Li, S.; Cai, M.; Yan, R.; Dong, K.; Zhang, J.; Liu, Y. *J. Colloid Interface Sci.* **2022,** *619,* 307–321. doi:10.1016/j.jcis.2022.03.075
15. Li, S.; Wang, C.; Liu, Y.; Cai, M.; Wang, Y.; Zhang, H.; Guo, Y.; Zhao, W.; Wang, Z.; Chen, X. *Chem. Eng. J.* **2022,** *429,* 132519. doi:10.1016/j.cej.2021.132519
16. Viet, P. V.; Sang, T. T.; Hien, N. Q.; Thi, C. M.; Hieu, L. V. *Nucl. Instrum. Methods Phys. Res., Sect. B* **2018,** *429,* 14–18. doi:10.1016/j.nimb.2018.05.023
17. Bui, D.-P.; Pham, H.; Cao, T.; Pham, V. *J. Chem. Technol. Biotechnol.* **2020,** *95,* 2707–2714. doi:10.1002/jctb.6466
18. Fujishima, A.; Honda, K. *Nature* **1972,** *238,* 37–38. doi:10.1038/238037a0
19. Gao, B.; Sun, M.; Ding, W.; Ding, Z.; Liu, W. *Appl. Catal., B* **2021,** *281,* 119492. doi:10.1016/j.apcatb.2020.119492
20. Palmas, S.; Mais, L.; Mascia, M.; Vacca, A. *Curr. Opin. Electrochem.* **2021,** *28,* 100699. doi:10.1016/j.coelec.2021.100699
21. Kalamkarov, A. L.; Georgiades, A. V.; Rokkam, S. K.; Veedu, V. P.; Ghasemi-Nejhad, M. N. *Int. J. Solids Struct.* **2006,** *43,* 6832–6854. doi:10.1016/j.ijsolstr.2006.02.009
22. Chiarello, G. L.; Selli, E. Photocatalytic production of hydrogen. In *Advances in Hydrogen Production, Storage and Distribution;* Basile, A.; Iulianelli, A., Eds.; Woodhead Publishing, 2014; pp 216–247. doi:10.1533/9780857097736.2.216
23. de Brito, J. F.; Tavella, F.; Genovese, C.; Ampelli, C.; Zanoni, M. V. B.; Centi, G.; Perathoner, S. *Appl. Catal., B* **2018,** *224,* 136–145. doi:10.1016/j.apcatb.2017.09.071
24. Cui, W.; Bai, H.; Shang, J.; Wang, F.; Xu, D.; Ding, J.; Fan, W.; Shi, W. *Electrochim. Acta* **2020,** *349,* 136383. doi:10.1016/j.electacta.2020.136383
25. Chai, B.; Peng, T.; Mao, J.; Li, K.; Zan, L. *Phys. Chem. Chem. Phys.* **2012,** *14,* 16745–16752. doi:10.1039/c2cp42484c
26. Yang, J.; Zhang, X.; Liu, H.; Wang, C.; Liu, S.; Sun, P.; Wang, L.; Liu, Y. *Catal. Today* **2013,** *201,* 195–202. doi:10.1016/j.cattod.2012.03.008
27. Verbruggen, S. W. *J. Photochem. Photobiol., C* **2015,** *24,* 64–82. doi:10.1016/j.jphotochemrev.2015.07.001
28. Khan, H.; Jiang, Z.; Berk, D. *Sol. Energy* **2018,** *162,* 420–430. doi:10.1016/j.solener.2018.01.055
29. He, H.; Lin, J.; Fu, W.; Wang, X.; Wang, H.; Zeng, Q.; Gu, Q.; Li, Y.; Yan, C.; Tay, B. K.; Xue, C.; Hu, X.; Pantelides, S. T.; Zhou, W.; Liu, Z. *Adv. Energy Mater.* **2016,** *6,* 1600464. doi:10.1002/aenm.201600464
30. Chi, Z.; Zhao, J.; Zhang, Y.; Yu, H.; Yu, H. *Green Energy Environ.* **2022,** *7,* 372–393. doi:10.1016/j.gee.2021.05.002
31. Chhowalla, M.; Shin, H. S.; Eda, G.; Li, L.-J.; Loh, K. P.; Zhang, H. *Nat. Chem.* **2013,** *5,* 263–275. doi:10.1038/nchem.1589
32. Tacchini, I.; Terrado, E.; Anson, A.; Martinez, M. T. *Micro Nano Lett.* **2011,** *6,* 932–936. doi:10.1049/mnl.2011.0460
33. Steinhoff, A.; Kim, J.-H.; Jahnke, F.; Rösner, M.; Kim, D.-S.; Lee, C.; Han, G. H.; Jeong, M. S.; Wehling, T. O.; Gies, C. *Nano Lett.* **2015,** *15,* 6841–6847. doi:10.1021/acs.nanolett.5b02719
34. Zhu, D.; Zhou, Q. *Appl. Catal., B* **2021,** *281,* 119474. doi:10.1016/j.apcatb.2020.119474

35. Nguyen, T. T.; Tran, H.-H.; Cao, T. M.; Pham, V. V. *Korean J. Chem. Eng.* **2022,** *39,* 2523–2531. doi:10.1007/s11814-022-1132-1
36. Nguyen, T. T.; Cao, T. M.; Balayeva, N. O.; Pham, V. V. *Catalysts* **2021,** *11,* 857. doi:10.3390/catal11070857
37. Hu, K. H.; Hu, X. G. *Mater. Sci. Technol.* **2013,** *25,* 407–414. doi:10.1179/174328408x269259
38. Liang, Z.; Shen, R.; Ng, Y. H.; Zhang, P.; Xiang, Q.; Li, X. *J. Mater. Sci. Technol.* **2020,** *56,* 89–121. doi:10.1016/j.jmst.2020.04.032
39. Tho, N. T.; Thi, C. M.; Van Hieu, L.; Van Viet, P. *J. Aust. Ceram. Soc.* **2020,** *56,* 849–857. doi:10.1007/s41779-019-00405-8
40. Liu, Y.; Xu, X.; Zhang, J.; Zhang, H.; Tian, W.; Li, X.; Tade, M. O.; Sun, H.; Wang, S. *Appl. Catal., B* **2018,** *239,* 334–344. doi:10.1016/j.apcatb.2018.08.028
41. Nivetha, M. r. S.; Kumar, J. V.; Ajarem, J. S.; Allam, A. A.; Manikandan, V.; Arulmozhi, R.; Abirami, N. *Environ. Res.* **2022,** *209,* 112809. doi:10.1016/j.envres.2022.112809
42. Budai, J.; Hanyecz, I.; Szilágyi, E.; Tóth, Z. *Thin Solid Films* **2011,** *519,* 2985–2988. doi:10.1016/j.tsf.2010.12.073
43. Jiang, J.; Zou, J.; Wee, A. T. S.; Zhang, W. *Sci. Rep.* **2016,** *6,* 34599. doi:10.1038/srep34599
44. Wang, J.; Wang, S. *Coord. Chem. Rev.* **2022,** *453,* 214338. doi:10.1016/j.ccr.2021.214338
45. Zhang, W.; Yue, P.-L.; Gao, P. *Langmuir* **2011,** *27,* 9520–9527. doi:10.1021/la201047k
46. Zhang, Z.; Wu, S.; Cheng, J.; Zhang, W. *Energy Storage Mater.* **2018,** *15,* 65–74. doi:10.1016/j.ensm.2018.03.013
47. Kumar, P. M.; Badrinarayanan, S.; Sastry, M. *Thin Solid Films* **2000,** *358,* 122–130. doi:10.1016/s0040-6090(99)00722-1
48. Zhao, J.; Zhang, Z.; Yang, S.; Zheng, H.; Li, Y. *J. Alloys Compd.* **2013,** *559,* 87–91. doi:10.1016/j.jallcom.2013.01.067
49. Wen, Y.; Qu, D.; An, L.; Gao, X.; Jiang, W.; Wu, D.; Yang, D.; Sun, Z. *ACS Sustainable Chem. Eng.* **2019,** *7,* 2343–2349. doi:10.1021/acssuschemeng.8b05124
50. Yao, Y.; Sun, M.; Zhang, Z.; Lin, X.; Gao, B.; Anandan, S.; Liu, W. *Int. J. Hydrogen Energy* **2019,** *44,* 9348–9358. doi:10.1016/j.ijhydene.2019.02.100
51. Thang, N. Q.; Sabbah, A.; Chen, L.-C.; Chen, K.-H.; Hai, L. V.; Thi, C. M.; Viet, P. V. *Chem. Eng. Sci.* **2021,** *229,* 116049. doi:10.1016/j.ces.2020.116049
52. Chen, Y.; Huang, S.; Ji, X.; Adepalli, K.; Yin, K.; Ling, X.; Wang, X.; Xue, J.; Dresselhaus, M.; Kong, J.; Yildiz, B. *ACS Nano* **2018,** *12,* 2569–2579. doi:10.1021/acsnano.7b08418
53. Resasco, J.; Zhang, H.; Kornienko, N.; Becknell, N.; Lee, H.; Guo, J.; Briseno, A. L.; Yang, P. *ACS Cent. Sci.* **2016,** *2,* 80–88. doi:10.1021/acscentsci.5b00402
54. Almora, O.; Aranda, C.; Mas-Marzá, E.; Garcia-Belmonte, G. *Appl. Phys. Lett.* **2016,** *109,* 173903. doi:10.1063/1.4966127
55. Bhat, S. S. M.; Pawar, S. A.; Potphode, D.; Moon, C.-K.; Suh, J. M.; Kim, C.; Choi, S.; Patil, D. S.; Kim, J.-J.; Shin, J. C.; Jang, H. W. *Appl. Catal., B* **2019,** *259,* 118102. doi:10.1016/j.apcatb.2019.118102
56. Li, S.; Wang, C.; Cai, M.; Liu, Y.; Dong, K.; Zhang, J. *J. Colloid Interface Sci.* **2022,** *624,* 219–232. doi:10.1016/j.jcis.2022.05.151
57. Li, S.; Cai, M.; Liu, Y.; Zhang, J.; Wang, C.; Zang, S.; Li, Y.; Zhang, P.; Li, X. *Inorg. Chem. Front.* **2022,** *9,* 2479–2497. doi:10.1039/d2qi00317a
58. Li, T.; Wang, Z.; Liu, C.; Tang, C.; Wang, X.; Ding, G.; Ding, Y.; Yang, L. *Nanomaterials* **2018,** *8,* 666. doi:10.3390/nano8090666
59. Cao, S.; Chen, Y.; Liu, X.; Zhou, J.; Liu, J.-t. *Inorg. Chem. Commun.* **2021,** *133,* 108862. doi:10.1016/j.inoche.2021.108862

License and Terms

BEILSTEIN JOURNAL OF NANOTECHNOLOGY

Bismuth-based nanostructured photocatalysts for the remediation of antibiotics and organic dyes

Akeem Adeyemi Oladipo* and Faisal Suleiman Mustafa

Review

Open Access

Address:
Polymeric Materials Research Laboratory, Chemistry Department, Faculty of Arts and Science, Eastern Mediterranean University, TR North Cyprus, Famagusta, via Mersin 10, Turkey

Email:
Akeem Adeyemi Oladipo* - akeem.oladipo@emu.edu.tr

* Corresponding author

Keywords:
advanced oxidation processes; emerging contaminants; low-dimensional nanomaterials; pharmaceutical by-products; Schottky junction

Beilstein J. Nanotechnol. **2023,** *14,* 291–321.
https://doi.org/10.3762/bjnano.14.26

Received: 30 September 2022
Accepted: 10 February 2023
Published: 03 March 2023

This article is part of the thematic issue "Nanomaterials for photocatalysis and applications in environmental remediation and renewable energy".

Guest Editor: V. V. Pham

Abstract

A serious threat to human health and the environment worldwide, in addition to the global energy crisis, is the increasing water pollution caused by micropollutants such as antibiotics and persistent organic dyes. Nanostructured semiconductors in advanced oxidation processes using photocatalysis have recently attracted a lot of interest as a promising green and sustainable wastewater treatment method for a cleaner environment. Due to their narrow bandgaps, distinctive layered structures, plasmonic, piezoelectric and ferroelectric properties, and desirable physicochemical features, bismuth-based nanostructure photocatalysts have emerged as one of the most prominent study topics compared to the commonly used semiconductors (TiO_2 and ZnO). In this review, the most recent developments in the use of photocatalysts based on bismuth (e.g., $BiFeO_3$, Bi_2MoO_6, $BiVO_4$, Bi_2WO_6, Bi_2S_3) to remove dyes and antibiotics from wastewater are thoroughly covered. The creation of Z-schemes, Schottky junctions, and heterojunctions, as well as morphological modifications, doping, and other processes are highlighted regarding the fabrication of bismuth-based photocatalysts with improved photocatalytic capabilities. A discussion of general photocatalytic mechanisms is included, along with potential antibiotic and dye degradation pathways in wastewater. Finally, areas that require additional study and attention regarding the usage of photocatalysts based on bismuth for removing pharmaceuticals and textile dyes from wastewater, particularly for real-world applications, are addressed.

Review

Introduction

Worldwide, water pollution is rising, endangering the economic potential and development objectives of severely polluted areas because of the detrimental effects on human health and aquatic ecosystems. The improper disposal of industrial and agricultural pollutants (such as organic dyes, pesticides, and pharmaceutical residues) in water systems is becoming more and more of a global health threat. Over two billion people live in water-stressed countries, according to the World Health Organization

(WHO, 2020), and it is anticipated that this situation will get worse in some areas because of the increased industrial discharge of contaminated water, population growth, and climate change [1]. According to current projections, 57% of the world's population will experience water shortages by 2050 if sustained and coordinated efforts are not made [2,3]. The estimate provided in [2,3] might have been too low. The projections for water consumption, availability, and quality are affected by a variety of unreliable geopolitical factors. Nevertheless, there is a growing need for the efficient removal of environmental pollutants and the proper treatment of industrial wastes to allowable discharge limits, which are crucial for preserving human life and protecting the environment.

Numerous techniques have been employed to treat contaminated water and wastewater, including adsorption, bioremediation, precipitation, electrocoagulation, filtration, membrane separation, flocculation, centrifugation, advanced oxidation processes based on photocatalysis, and chemical coagulation [4-11]. Each of these techniques has demonstrated varying levels of effectiveness and drawbacks that restrict their widespread use. For instance, due to deficiencies such as the formation of harmful by-products and incomplete removal of organic pollutants, traditional water treatment methods such as sedimentation, filtration, and precipitation, in particular, are believed to be ineffective [4,11]. As a result of the non-biodegradable and persistent nature of the majority of organic contaminants, some physicochemical treatment techniques, such as adsorption, are ineffective in removing them from water resources [11]. Because of their flexible design and low cost, biological approaches have been used for the treatment of various contaminated effluents. However, the process is time-consuming, can be ineffective when toxic recalcitrant pollutants are present, and may even be irreparably harmful to the environment.

Among the water treatment technologies, advanced oxidation processes (AOPs) are regarded as a practical, efficient, and fiercely competitive technology for water treatment for the removal of a variety of toxic and bio-recalcitrant organic pollutants and for the inactivation of pathogen microorganisms that cannot be treated by conventional methods [11-14]. For the oxidation of organic molecules, AOPs rely on the in situ generation of potent oxidants (reactive oxygen species, ROS) such as hydroxyl or sulfate radicals. AOPs have been broadly categorised in terms of how ROS are produced, including non-photochemical techniques, such as chemical, radiation-induced, cavitation, electrochemical techniques, and photochemical processes [11,15-17].

One of the AOPs, photocatalysis, uses natural light – a resource that is both clean and recyclable – to completely degrade a variety of organic pollutants and inactivate pathogens. The term "photocatalysis" refers to chemical reactions that use light and a photocatalyst (basically a semiconductor). A few of the requirements that an effective photocatalyst system should satisfy include high sunlight absorption, an appropriate gap (1.5–2.8 eV), long-term charge carrier separation, high photo-transporter mobility, appropriate physical and chemical properties, sufficient band alignment to meet the kinetic requirements of the target reaction, and anti-corrosion stability in reactive environments [18-20].

Figure 1 depicts the mechanism of the photocatalyst. In a nutshell, when exposed to light of the desired wavelength (enough energy), an electron (e^-) in the photocatalyst's valence band absorbs photon energy and is excited to the conduction band on a femtosecond scale. This results in the formation of a hole (h^+) in the valence band and a charge carrier pair (e^- and h^+) on the surface of the photocatalyst. Three possibilities exist at this point: (a) The generated charge carriers recombine and generate heat, (b) the generated interfacial charge carriers simultaneously reduce and oxidise contaminants, or (c) the generated charge carrier and an electron donor or acceptor on the surface of the photocatalyst may continue to interact. Nothing happens in the first scenario. In the second scenario, an electron or hole interacts with dissolved oxygen or water to produce ROS (e.g., $^{\bullet}OH$, $O_2^{\bullet-}$). These ROS play a significant role in the photo-oxidation/reduction reaction, along with other species such as oxygen, hydrogen peroxide, and persulfate. This excited electron reduces an acceptor, and the acceptor's hole oxidises donor molecules. What happens to the excited electron and hole depends on the relative positions of conduction band and valence band of the semiconductor as well as the redox levels of the substrate [11,21].

One of the main barriers preventing photocatalysis from being used in practical applications is the lack of suitable semiconductor photocatalysts. The commonly used nanometre-sized photocatalysts are metal oxides or sulfides (binary compounds: TiO_2, CuO, CdS, MoO_3; ternary compounds: $Bi_2Mo_3O_{12}$, $ZnFe_2O_4$; quaternary compounds: $Ni_{0.5}Zn_{0.5}Fe_2O_4$, $Bi_4Nb_xTa_{1-x}O_8I$) [19-26]. Because of its distinct features, TiO_2 is the most extensively investigated photocatalytic semiconductor. However, it barely absorbs 4–5% of the ultraviolet light in the solar spectrum due to its broad bandgap of 3.2 eV, which limits the use of visible light. Because of this, the potential photocatalytic use of TiO_2 is constrained and the photocatalytic effectiveness is reduced [19,20,25]. Table 1 compares some of the salient characteristics of some of the bismuth-based photocatalysts with some of the typical metal oxide-based photocatalysts. Some of these important variables and values have been extracted from articles that have been published [27-38].

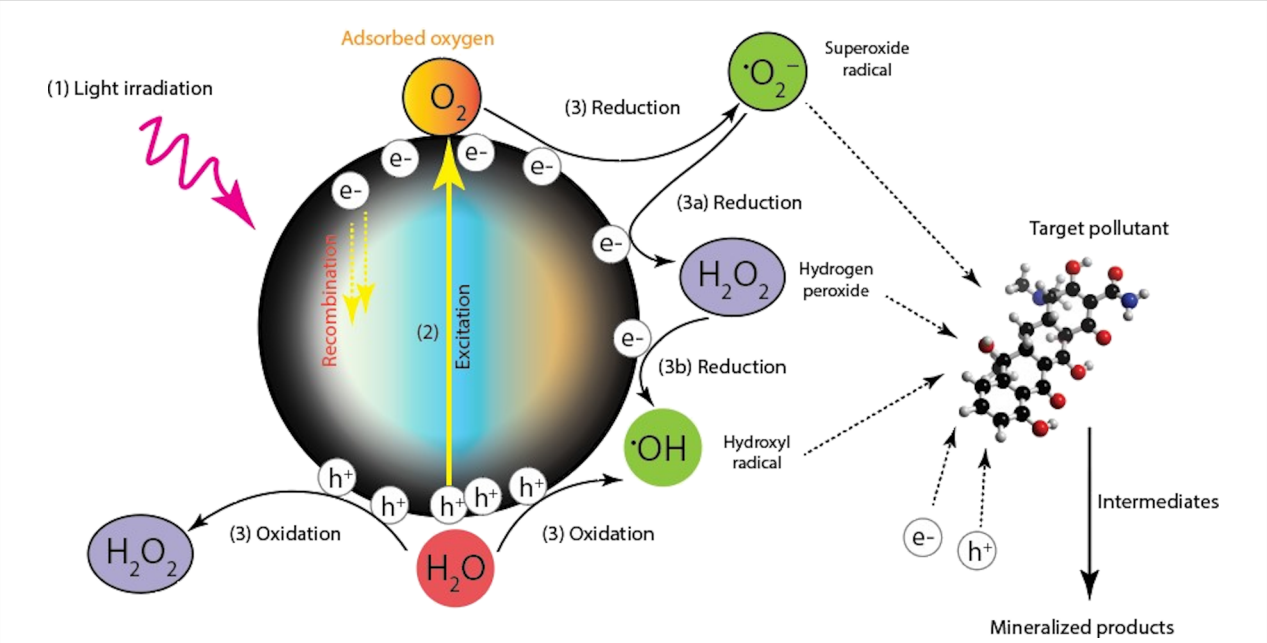

Figure 1: Mechanism of the photocatalytic process used to treat water contaminated with organic pollutants.

Table 1: Comparison of nanometre-sized metal oxide-based and bismuth-based photocatalysts.

Features	Metal oxides		
	TiO_2	ZnO	SnO_2
bandgap (eV)	3.0–3.4	3.10–3.37	3.76–4.24
performance based on the light source	very active in UV light	very active in UV light	very active in UV light
semiconductor type	n-type	n-type	n-type
crystal structure	anatase (tetragonal), brookite (orthorhombic), rutile (tetragonal)	hexagonal wurtzite (most stable at ambient conditions) and cubic zincblende	tetragonal
stability	photostable in solution and resistant to corrosion	readily dissolves in water, photocorrosion under UV	good stability
toxicity	nontoxic	low-toxicity	relatively non-toxic
photon absorption efficiency and quantum yield	high	higher than TiO_2	moderate
cost	low	low	low
electron–hole pairs recombination rate	high	fast	high
magnetic properties	no	no	no
	Bismuth-based		
	$BiFeO_3$	Bi_2WO_6	Bi_2S_3
bandgap (eV)	2.0–2.5	2.6–2.9	1.4–1.6
performance based on the light source	both visible and UV light	both visible and UV light	both visible and UV light
semiconductor type	n-type	n-type	n-type
crystal structure	rhombohedral distorted perovskite structure	orthorhombic	orthorhombic

Table 1: Comparison of nanometre-sized metal oxide-based and bismuth-based photocatalysts. (continued)

stability	sufficiently stable	superior stability	highly stable
toxicity	low toxicity	nontoxicity	low toxicity
photon absorption efficiency and quantum yield	very high	moderately high	high
cost	low	low	low
electron–hole pairs recombination rate	high	fast	moderate
magnetic properties	ferromagnetic at low temperatures and superparamagnetic at room temperature. (multiferroic behaviour)	no	no
	Bismuth-based		
	BiOBr	Bi_2O_3	Bi_3O_4Cl
bandgap (eV)	2.69–2.99	1.5–2.8	2.6–2.8
performance based on the light source	both visible and UV light	both visible and UV light	both visible and UV light
semiconductor type	p-type	p-type	n-type
crystal structure	tetragonal (PbFCl-type structure)	monoclinic (room temperature), tetragonal β-phase or body-centred γ-phase (intermediate temperature), cubic (very high temperature)	cubic (Silleń structure)
stability	good chemical stability	highly chemically stable and photostable in solution	good stability
toxicity	nontoxic	low toxicity	nontoxic
photon absorption efficiency and quantum yield	moderately high	very high	moderate
cost	low	low	low
electron–hole pairs recombination rate	moderate	low	moderate
magnetic properties	no	paramagnetic behaviour	no

As an alternative to TiO_2 for photocatalysis, nanometre-sized photocatalysts based on bismuth have recently been investigated and evaluated, because the majority of bismuth-based photocatalysts have a bandgap below 3.0 eV, making them usable in visible light. Additionally, their electrical structure produces a valence band with hybrid O 2p and Bi 6s orbitals, as opposed to the valence band of TiO_2, which is made up entirely of O 2p orbitals. The mobility of the photogenerated charge carriers is increased by the well-dispersed Bi 6s orbital. Due to their distinctive structure, Bi-based photocatalysts exhibit a steeper absorption edge in the visible-light spectrum. Additionally, the reverse bond between the cation and anion is more favourable for the production and transportation of holes, which facilitates photocatalytic activity. Because of this, significant efforts have been made to synthesise bismuth-based nanomaterials ($BiVO_4$, Bi_5O_7I-MoO_3, Bi_2O_3, $BiFeO_3$, Bi_2WO_6, $Bi_2Mo_3O_{12}$, Bi_2MoO_6, and BiOI [24,25,39-45]) using a variety of techniques to tailor their size, morphology, and optoelectrical properties to improve their photocatalytic performance and to better understand the factors influencing their performance. Different materials based on bismuth have been developed and used for a range of environmental remediation applications. For instance, Mu et al. [46] synthesised a Bi_2S_3/Bi_4O_7 heterostructure via an in situ sulfidation approach and utilised it for the degradation of rhodamine B dye under visible-light exposure. Since the oxidation rate is still up to 96.3% after four cycles, the photocatalyst showed great performance and stability in the photocatalytic oxidation of the dye.

This review provides an overview of the recent nanostructured photocatalytic materials based on bismuth that are employed in the photocatalytic degradation of organic dyes and antibiotics in water. The general synthesis of nanometre-sized photocatalytic materials based on bismuth employing energy-efficient techniques is examined. A critical review is also given of ways to improve the photocatalytic activity of the photocatalysts. An extensive critical evaluation is given of recent findings on the photocatalysis of nanostructured materials based on bismuth and

doped bismuth for the remediation of textile and pharmaceutical wastewater.

Antibiotics and organic dyes in the environment and their toxicological consequences

Antibiotics are administered therapeutically to cure/prevent pathogen infections in people, animals, or both, as well as to increase livestock yields. However, since 50–80% of the antibiotic compounds that are taken are typically eliminated through urine and faeces, there are growing concerns regarding their excessive consumption and how they affect the environment. The widespread use of pharmaceuticals, especially antibiotics, has made them prevalent in the environment, and nearly everyone in the world now acknowledges their existence in both artificial and natural systems. Particularly, it has been claimed that antibiotic residues or metabolites have contaminated groundwater, soil, sediment, tap water, sludge, wastewater, and surface water.

Chemical manufacturing facilities, effluents from wastewater treatment facilities, and animal husbandry and aquaculture are the three main entry points for antibiotics into fresh waters [47-49]. According to the paper of Wise in the year 2002 [50], nearly 200,000 tons of antibiotics are consumed globally each year, with roughly 50% being utilized for veterinary medication and growth stimulants. Notably, between the years 2000 and 2010, the amount of antibiotics consumed by humans alone increased by 36% globally, demonstrating the ongoing problem of antibiotics pollution [51].

According to a recent study by Browne et al. [52], which covered 204 nations from 2000 to 2018, the rate of antibiotic consumption worldwide grew by 46% during the last 20 years. The report offers a comparative analysis of global human consumption rates of all antibiotics, expressed in defined daily doses (DDD) per 1000 population per day, a WHO metric. In contrast to the very low rates of consumption in sub-Saharan Africa and several regions of Southeast Asia, high rates of antibiotic usage were seen in the Middle East, Europe, and North America. The regions of South Asia (116% rise) and North Africa and the Middle East (111% rise) experienced the biggest increases in antibiotic usage rates. Specifically, in South Asia, third-generation cephalosporin consumption rates surged 37-fold and fluoroquinolone consumption rates increased 1.8-fold over the course of the study.

Different geographical areas have different levels of antibiotics in the environment. For instance, aus der Beek et al. [53] reported ofloxacin and sulfamethoxazole at 17.7 µg/L and 14.3 µg/L, respectively, and sulfamethazine has been reported with a concentration of 19 ng/L in Vietnam [54]. Sulfamethoxazole was lastly detected in Africa, where it was found at 53.8 ng/L in Mozambique [55] and 38.9 ng/L in Kenya [56]. Nalidixic acid and ciprofloxacin quantities of 23 µg/L and 14 µg/L, respectively, were found in South African streams and rivers [57]. While it is critical to understand the presence and levels of antibiotics in freshwater environments, it is maybe even more crucial to understand whether the residues or metabolites of the antibiotics have any impact on the various species that live there. The concentration necessary to produce a 50% effect after a given exposure time is known as the EC_{50}. Chemicals having an EC_{50} between 10 and 100 mg/L are classified as hazardous, those from 1 to 10 mg/L as toxic, and those below 1 mg/L are classified as extremely toxic to aquatic life by the Commission of the European Communities [58]. The Wikipharma statistics [59] show that EC_{50} values were less than 1 mg/L in 25% of all research assessing the effects of antibiotics on eukaryotic, single-celled algae and that EC_{50} was even less than 100 µg/L in twelve investigations.

Once these antibiotics are released into the environment, non-target species are unavoidably exposed [47]. The development of antibiotic resistance, which has reduced the therapeutic capacity against human and animal infections, is the most significant issue associated with the release of antibiotics into the environment. It is not true that antibiotic resistance has never been observed in the natural environment; rather, it had previously only been linked to a small number of bacterial strains, but recent research has discovered antibiotic resistance genes in many other bacterial strains, raising serious health concerns. Antibiotic resistance is brought on by a high concentration of antibiotics that enter aquatic systems and interact with native species [47,60-62]. For instance, it may start to alter the genetic makeup and structure of the microbial community [47]. Antibiotic-resistant microbes (algae, fungi, and bacteria) pose a threat to both human and ecological health. The active ingredients of antibiotics and their fragments may cause kidney and liver cell damage in humans if they are exposed to antibiotic residues for an extended time [63-65]. Additionally, it has been noted that prolonged exposure to antibiotic-contaminated water might result in several allergic and respiratory conditions [62-65]. Additionally, an overabundance of antibiotics in the environment causes structural changes in the ecosystem, disruptions in ecological function, and impacts the processes of sulfate reduction, methanogenesis, and nitrogen conversion [61,63].

Antibiotics are persistent for long periods of time in natural environment. It is important to note that bacteria that develop resistance to one antibiotic also exhibit resistance to other drugs and chemicals. For example, Dickinson et al. [64] reported that the focal strain isolates from pond sediments in the northwest of the United Kingdom exhibited resistance to heavy metals and

antibiotics (trimethoprim, oxacillin, and cefotaxime) where the *intI1* gene was involved. A growing body of research indicates that parent antibiotics and their metabolites, which are released into the environment in low concentrations (micrograms per litre to nanograms per litre), are persistent and bioactive, potentially posing a threat to the food chain.

Macrolides, fluoroquinolones, and tetracycline also have an impact on the synthesis of mitochondrial proteins and chloroplasts in plants [48,66]. Fluoroquinolones have a detrimental impact on the morphology and photosynthesis of plants, as well as on the ability of eukaryotic cells to synthesise DNA and replicate plastids. Streptomycin prevents *Hordeum vulgare* from producing chlorophyll, while ciprofloxacin, enrofloxacin, and sulfadimethoxine considerably slow down plant growth. Additionally, tetracyclines have phytotoxic effects that may result in chromosomal abnormalities and the reduction of plant growth. Although β-lactams are thought to be less harmful, they also have an impact on the plastid division in lower plants [48,67].

The textile industry, in addition to the pharmaceutical sector, is another sector that supports global economic expansion. It is one of the major sources of global pollution, although its importance cannot be disputed. Due to its high water demand when producing textiles and the limitations of conventional wastewater treatment techniques, the textile industry is causing concern. The direct release of textile waste into bodies of water without proper treatment to an acceptable level has a negative impact on its aesthetic quality. The presence of organic dyes in bodies of water, even in minute amounts, raises the chemical and biochemical oxygen demand and inhibits photosynthesis. Additionally, the uptake of dye molecules or their by-products in excess may be mutagenic, teratogenic, or carcinogenic [68,69]. Myocardial depression and hypertension are reportedly exacerbated by oral exposure to methylene blue dye. Additionally, some dyes, such as xanthene and erythrosine, have been related to allergic reactions, neurotoxins, and DNA damage in both humans and animals [70]. An eco-friendly, practical, and efficient treatment method is urgently needed because of the increasing pollution and health and ecological concerns of excess antibiotics and dyes in the environment. This article discusses the use of nanomaterials based on bismuth for the remediation of persistent organic pollutants.

Bismuth and bismuth-based nanostructured photocatalysts

Bismuth (Bi) is a semimetal and a member of the p-block with a d^{10} configuration ($6s^2 6p^3$) in the sixth period of group V of the periodic table. Because of their intriguing optical, catalytic, electrical, ferroelectric, and piezoelectric properties, bismuth-based nanostructures are used in several significant fields, including optoelectronics, pollutant sensing [71], and environmental remediation via photocatalysis [25]. Bi-based semiconductors, in particular, are thought to be able to surpass the limitation of the solar light-harvesting capacity of TiO_2-based photocatalytic materials because of their smaller bandgaps. Because of its highly anisotropic Fermi surface charge, low carrier density, small electron effective mass, long electron mean free path, and extremely low band overlap energy, bismuth can transition from a semimetal to a semiconductor by shrinking its crystallite size [25,71-77].

To hasten the separation of photogenerated charges and, hence, increase photocatalytic activity, metallic bismuth can function as a direct plasmonic photocatalyst (similar to Au and Ag) or a co-catalyst [77]. Also, the unique layered crystal structure of Aurivillius-type bismuth oxide-based semiconductors allows for the induction of an internal static electric field, which effectively aids in the separation and transfer of photogenerated carriers. Bulk Bi and Bi-based nanostructure morphologies can also be easily altered using a variety of synthesis techniques due to their unique electrical and optical properties, which are directly tied to the plasmonic and photocatalytic properties. The typical and most recently applied bismuth-based nanostructure photocatalysts are depicted in Figure 2.

Structural, optoelectronic, and magnetic properties

Bismuth's peculiar optical, electronic, and more recently discovered photocatalytic and plasmonic properties have attracted the interest of a large community of scientists. With a low melting point of just above 544 K, Bi is less toxic than its neighbours in the periodic table, antimony, lead, and polonium. The structure of the bismuth crystal, which has rhombohedral symmetry, is typical of the group-V semimetals. Bi atoms form puckered bilayers of atoms perpendicular to the rhombohedral plane with three equidistant nearest neighbours and three equidistant next-nearest neighbours that are slightly farther away.

Bi is widely used in photocatalysis, in part because of its quantum confinement effect, which is important for electronic transport and semimetal-to-semiconductor transition, as well as its highly anisotropic Fermi surface (with an electron and hole Fermi energies of 27.2 and 10.8 meV, respectively), which results in an extremely low carrier density of around 3×10^{17} cm^{-3} [78] and very little overlap between the T-point band (valence) and the L-point band (conduction) [76-78]. Note that a reduction of the crystallite size below a critical value can result in a semimetal-to-semiconductor transition [77-80]. For instance, according to Qi et al. [81], indirect bandgap semiconductors were visible in Bi nanowires with a diameter of around

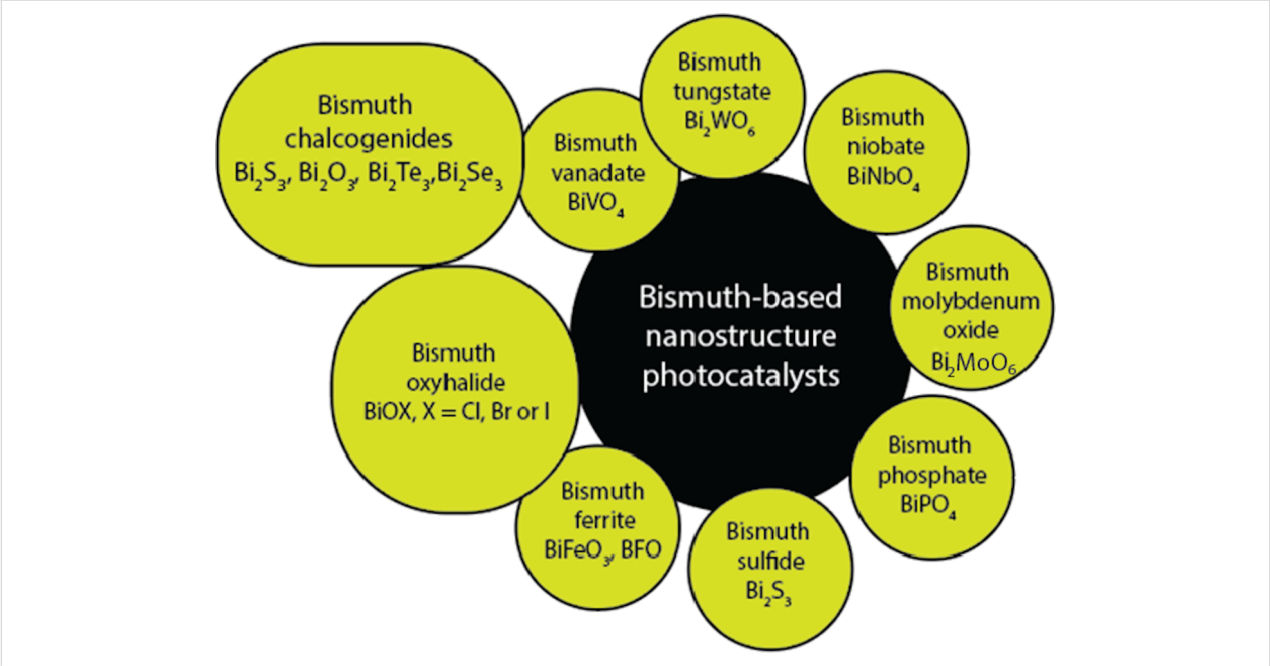

Figure 2: Most recently studied and common bismuth-based nanostructured photocatalysts.

1–3 nm, but as the diameter increased, they became less visible because of the intense quantum confinement effect.

In addition to the electronic properties of Bi, its outstanding optical properties have a big impact on how effective it is as a photocatalyst. Bulk Bi exhibits high interband electronic transition rates that result in a negative ultraviolet–visible permittivity and a large infrared refractive index. Numerous investigations have shown that the quantum confinement effect affects the optical properties of Bi [25,71-80]. Furthermore, nanostructured materials exhibit unique optical properties that set them apart from the corresponding bulk materials as a result of this quantum confinement. Also, note that the optical responses of Bi nanoparticles are strongly influenced by their size, morphology, bandgap structure, shape, and environment. If these parameters are adjusted, the optical responses of Bi nanoparticles can be tuned from the near-ultraviolet to the near-infrared region.

According to Figure 3, the bandgap of different bismuth-based photocatalysts has been observed to fall between 1.30 and 3.85 eV. From an optoelectronic structure standpoint, the majority of bismuth-based photocatalysts have a bandgap below

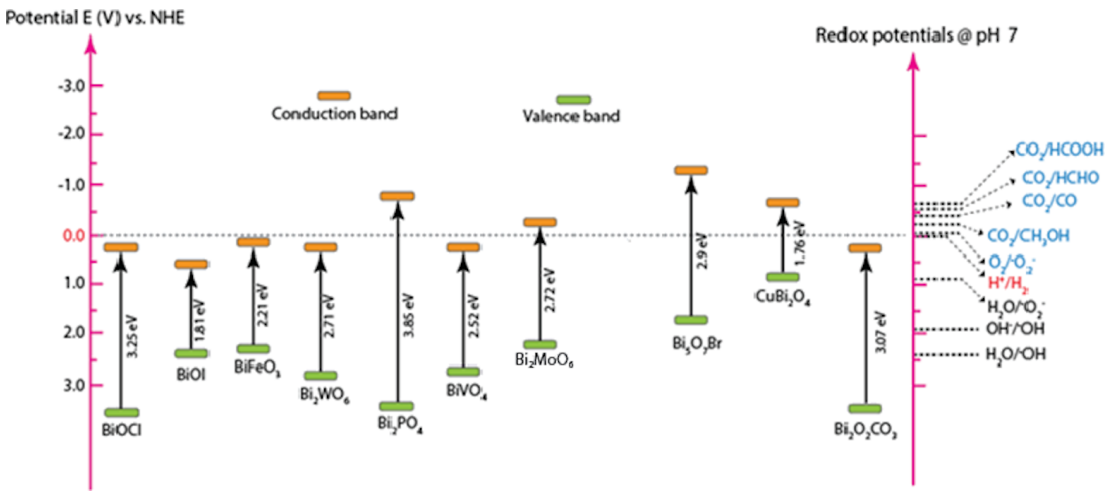

Figure 3: Bandgaps of some bismuth-based photocatalysts extracted from various research articles [27,35-37,83-86].

3.0 eV, which qualifies them for use in visible light. The hybridisation of the O 2p orbital and the 6s orbital in Bi is thought to be the cause of the narrow bandgap [82]. The valence band electrons are elevated by the hybridisation, which benefits the separation of photogenerated electron–hole pairs and the rate of charge carrier migration. Numerous visible-light photocatalysts based on bismuth have been used for the degradation of micropollutants because of their appropriate bandgap and non-toxic nature.

$BiFeO_3$, one of those Bi-based photocatalysts, has been the subject of intensive research in recent years because it is the only naturally occurring magnetoelectric material with ferromagnetic and ferroelectric properties at room temperature [39,75,87-89]. Bismuth ferrite has a distorted rhombohedral perovskite structure (ABO_3), where A is a corner cation, B is a body-centred middle atom, and O is an oxygen atom or anions attached to the crystal faces. $BiFeO_3$ has strong magnetic and multiferroic, and sufficient photocatalytic properties due to this unique structure. $BiFeO_3$ is an effective photocatalyst in the visible-light region, because in contrast to other semiconductors such as TiO_2, it has a very narrow bandgap (Figure 3) and slow electron–hole recombination.

As 44% of solar radiation falls within the visible-light spectrum, $BiFeO_3$ can be activated by direct sunlight, further lowering the cost of treatment. Aside from its magnetic and optical properties, $BiFeO_3$ also exhibits piezoelectric characteristics, photovoltaic effects, switchable ferroelectric diode effects, and spontaneous polarisation enhancement. It is also sensitive to epitaxial strain [88]. Given its intriguing properties, a lot of researchers [90] have used bismuth ferrite to efficiently degrade organic pollutants, as shown in Table 2.

Bi_2WO_6 is a typical Aurivillius-phase material, that is, a type of perovskite denoted by $Bi_2X_{n-1}Y_nO_{3n+3}$, where X is a large

Table 2: Treatment of water containing antibiotics and dyes by bismuth ferrite nanoparticles ($BiFeO_3$).

Particle size (nm)	Target pollutant	Source of light	Experimental conditions	Degradation (%)	Ref.
Remarks on the synthesis and main findings					
5.5	rhodamine B dye	visible light (high-power LEDs)	catalyst dosage: 1.25 g/L; solution pH 2; reaction time: 50 min; initial concentration of rhodamine B: 5 mg/L; observed bandgap: 2.07 eV	100.0	[75]
Monodisperse $BiFeO_3$ nanoparticles were synthesised using a nanocasting approach, and they outperformed $BiFeO_3$ nanoparticles prepared using other synthetic techniques in terms of photocatalytic efficiency and stability when exposed to visible light. When compared to particles of comparable size, the photocatalytic activity of the nanocast $BiFeO_3$ particles is significantly higher. A low density of surface defects and few local strains contributed to this higher performance.					
35	rhodamine B dye	visible light (500 W Xe lamp)	catalyst dosage: 2 g/L; solution pH 0.5; reaction time: 60 min; initial concentration of rhodamine B: 10^{-5} mol/L; observed bandgap: 2.06 eV	100.0	[91]
By using a rapid sol–gel calcination approach, multiferroic $BiFeO_3$ nanoparticles with rhombohedral crystal structures were synthesised, and they had stronger photocatalytic activity than the bulk. Mild room-temperature ferromagnetism was shown by the $BiFeO_3$ nanoparticles.					
150–200	methyl orange dye	visible light (70 W 365 nm UV lamp)	with a catalyst loading of 6.4 mmol/L, the initial concentration of the methyl orange dye was 20 mg/L; the optimum reaction time was 260 min; the bandgap of the catalyst is 2.10 eV.	92.0	[92]
Chemical co-precipitation was used to synthesise the $BiFeO_3$ nanoparticles, and analysis of the samples reveals that they have a perovskite structure that is distorted rhombohedrally and belongs to the polar $R3c$ space group (no. 161). The nanoparticles' bandgap energy was lower than that of the bulk $BiFeO_3$ (2.5 eV) due to the thinness of the sample.					
128	methylene blue dye	simulated solar light (Xe lamp 500 W)	catalyst concentration: 5 ppm; initial concentration of the dye: 1 ppm; pH 1–2; optimum reaction time: 50 min; the bandgap of the 1D nanofiber is 2.38 eV.	nanofiber 98.0 nanoparticulate 68.0	[93]
Electrospinning and the sol–gel method were used to synthesise $BiFeO_3$ nanofibers and nanoparticles, respectively. According to the XRD findings, the $BiFeO_3$ phase exhibits a rhombohedral structure with average crystallite sizes of 60 and 24 nm for $BiFeO_3$ nanoparticles and nanofibers, respectively. Due to 1-dimensional confinements in the $BiFeO_3$ nanofiber, its valence band edge position showed a shift toward higher energy, increasing its charge separation energy.					

Table 2: Treatment of water containing antibiotics and dyes by bismuth ferrite nanoparticles ($BiFeO_3$). (continued)

5–50	congo red dye	visible light (Xe lamp, 500 W)	catalyst dosage: 2 g/L; initial concentration of the dye: 10 mg/L; optimum reaction time: 120 min; bandgap: 2.10–2.19 eV	95.0	[94]
The hydrothermal approach was used to synthesise the nanostructured $BiFeO_3$ particles, which showed a single-phase perovskite structure. With a reduction in crystalline size, the band-gap energy of the nanoparticles increased.					
342–5560	tetracycline	visible light (500 W xenon lamp)	catalyst dosage: 0.5 g/L; initial concentration of the antibiotic: 10 mg/L; pH 8; optimum reaction time: 120 min; bandgap: 1.97 eV	77.0	[95]
According to the XRD data, the $BiFeO_3$ particles showed a perovskite phase after being synthesised using a facile hydrothermal approach.					
20–150	oxytetracycline hydrochloride	visible light (300 W xenon lamp)	catalyst dosage: 1 g/L; initial concentration of the antibiotic: 20 mg/L; 10 g/L potassium peroxymonosulfate; pH 6.5; optimum reaction time: 10 min; bandgap: 1.78–1.95 eV	40.0–97.3	[96]
Through a mild one-pot hydrothermal procedure and a bath-ultrasound-aided dissolving technique, a multiferroic $BiFeO_3$ photocatalyst was synthesised. The XRD analysis showed that the perovskite structure of the $BiFeO_3$ nanocatalyst, which is composed of evenly spaced bimodal mesopores and nanoparticles smaller than 50 nm, was present.					
not given	cefixime trihydrate	direct sunlight	catalyst dosage: 20 mg/L; initial concentration of the antibiotic: 1 mg/L; pH 3 and 9; optimum reaction time: 30 min; bandgap: 1.72–2.25 eV	75.0–94.0	[97]
The combustion synthesis approach was used to synthesise the rhombohedral crystal structure in the bismuth ferrite nanoparticles. The typical crystallite size of the nanoparticles ranged from 24 to 48 nm, with various bandgaps.					
20	tetracycline	visible light (300 W mercury lamp)	catalyst dosage: 2 g/L; oxidant dosage (H_2O_2): 9.8 mmol/L; initial concentration of the antibiotic: 40 mg/L; pH 4; optimum reaction time: 210 min; bandgap: 2.1 eV	$BiFeO_3$ alone 54.0 $BiFeO_3$ + H_2O_2 100.0	[98]
Sol–gel synthesis and calcination were used to synthesise the bismuth ferrite nanoparticles. The perovskite phase of bismuth ferrite was present in the nanoparticles, which were made up of almost rhombic nanoscale particles and showed no secondary contamination. The saturation magnetization value of 12.5 emu/g allowed the nanoparticles to be recovered and reused.					
17.4–929.6	doxorubicin	UV lamp	initial concentration of the antibiotic: 2 mg/L; optimum reaction time: 180 min; bandgap: 2.1 eV	79.0	[99]
Through the thermolysis of the coordination compound of bismuth ferrioxalate and calcination, bismuth ferrite particles were successfully produced. According to the XRD data, the bismuth ferrite nanopowders have a perovskite structure with rhombohedrally deformed (space group R_3c) crystallites that range in size from 17.6 to 118.3 nm on average.					
9–16	ciprofloxacin and levofloxacin	simulated sunlight (500 W Hg Xe lamp)	catalyst dosage: 0.3 g/L; pH 3.5; initial concentration of the antibiotic: 10 mg/L; optimum reaction time: 240 min; bandgap: 1.18–1.95 eV	80.0 ciprofloxacin 79.0 levofloxacin	[100]
The $BiFeO_3$ nanoparticles were synthesised at 160 °C by a simple high-pressure hydrothermal method and then doped with 10% gadolinium to facilitate the separation of electron or hole trapping sites and modify the band structures of the $BiFeO_3$.					

(12-coordinate, such as Ba, Bi, Sr, or Ca) cation and Y is a small (6-coordinate, such as Ti, W, Mo, or Fe) cation. It is another visible-light-driven n-type bismuth-based semiconductor and has received a lot of attention because of its distinctive layered structure, eco-friendliness, high photochemical and thermal stability, and benign visible-light photocatalytic activity [101-104]. Bi_2WO_6 has an orthorhombic structure, a high Curie temperature of about 900 °C, and a narrow bandgap of 2.6–2.8 eV [103]. Other desirable physical and chemical characteristics of Bi_2WO_6 include comparatively low toxicity, piezoelectricity, non-linear dielectric susceptibility, ferroelectricity, photostability and useful electrical properties [102-105]. The highest visible-light photocatalytic activity among bismuth-based oxides with a similar structure has been observed for

Bi_2WO_6, which can be attributed to its distinctive structure [103,104].

It is important to note that several review articles [102-108] have covered in great detail different techniques used to synthesise Bi_2WO_6, its photocatalytic activities, strategies for altering its structure to increase photocatalytic performances, and its applications in environmental remediation. However, the goal of this review is to comprehend the most recent developments in the degradation of various textile dyes and antibiotics in wastewater using photocatalysts based on Bi_2WO_6. The use of Bi_2WO_6-based photocatalysts for the degradation of dyes and antibiotics has attracted great interest over the last eight years, as shown in Table 3.

Although Bi_2WO_6, $BiFeO_3$, and other nanostructured photocatalysts [118-123] based on bismuth have been widely used in wastewater remediation and have demonstrated remarkable performance, their industrial/field application still faces some difficulties, including fast electron–hole pair recombination rate and challenges in separating them from the reaction system. Recently, a variety of methods have been used to enhance the

Table 3: Bi_2WO_6-based nanostructured materials for remediation of antibiotics and dyes.

Morphology	Target pollutant	Source of light	Experimental conditions	Degradation (%)	Ref.
Remarks on the synthesis and main findings					
nanocrystals have uneven, rod-like, nanoplate, and nanoflower morphologies	ceftriaxone sodium	simulated sunlight (300 W Xe lamp)	catalyst dosage: 1 g/L; solution pH 2; optimum reaction time: 240 min; initial concentration antibiotic: 10 mg/mL; observed bandgap: 2.62 eV	70.18	[108]
By varying pH values (from 1 to 11), solvents (ethylene glycol and distilled water), and temperature (160–180 °C), different Bi_2WO_6 nanostructured materials were synthesised using a simple hydrothermal procedure. The findings showed that the morphologies effectively affected the photocatalytic activity of the samples. Due to its large surface area and improved light harvesting, the 3D flower-like structure made of ordered nanoplates provided the best antibiotic degradation efficiency.					
irregular nanocrystals with agglomerated nanocuboid morphology	levofloxacin	visible light (150 W Philips CFL bulb)	catalyst dosage: 0.75 g/L; solution pH 7.14; optimum reaction time:150 min; initial concentration of antibiotic: 10 mg/L; observed bandgap 2.61 eV	80.0	[109]
Bi_2WO_6 was synthesised using a hydrothermal process assisted by ultrasonication at 170 °C for 20 h yielding nanocuboids and orthorhombic phase crystal planes. The performance of the nanocuboids photocatalyst was enhanced by the presence of metal atom defects, crystal defects, or oxygen vacancies. The catalyst performs well at different pH values, although at natural pH, the maximum degradation was observed under visible light.					
flower-like microstructure morphologies with surfaces enriched with nanosized pores	norfloxacin and ciprofloxacin	visible light (300 W Xe bulb, CEL-HXF300)	initial concentration of antibiotic: 10 mg/L; catalyst dosage: 1 g/L; optimum reaction time: 150 min; observed bandgap: 2.36 eV	72.98–74.84	[110]
The Bi_2WO_6 photocatalyst was synthesised using the traditional hydrothermal process and autoclaved at 160 °C for 12 h. Superoxide radicals and photogenerated carriers (e^- and h^+) are the main contributors to the degradation of antibiotics, while hydroxyl radicals have a very minor impact. Metal doping of the Bi_2WO_6 produced nanospherical structures with increased specific surface area, a narrower bandgap, and enhanced photocatalytic activity.					
flower-like, rod-like and lamellar-like nanostructures morphologies	enrofloxacin and norfloxacin	visible light (300 W Xenon arc lamp)	initial concentration of antibiotic: 10 mg/L; catalyst dosage: 0.5 g/L; solution pH 3; optimum reaction time: 75 min; observed bandgap: 2.57–2.85 eV	92.95–94.58	[111]
The Bi_2WO_6 nanorods were synthesised using a solvothermal process with ultrasonic assistance at 180 °C for 12 h, followed by 3 h of calcination at 350–550 °C. The calcination enhanced the crystallinity of the sample by producing nanocrystals with a greater ability to absorb visible light. The active species quench experiments revealed that h^+ was the most significant active species in this study and that $^{\bullet}O_2^-$ had a stronger degrading effect than $^{\bullet}OH$.					

Table 3: Bi_2WO_6-based nanostructured materials for remediation of antibiotics and dyes. (continued)

a hierarchical structure like a persimmon cake, with ultrathin nanoflakes of uniform size and morphology	norfloxacin	visible light (Xe bulb, CEL-HXF300)	initial concentration of antibiotic: 20 mg/L; catalyst dosage: 1 g/L; solution pH 9; optimum reaction time: 120 min; observed bandgap: 2.69–2.76 eV	95.0	[112]
A hydrothermal method was used to synthesise Bi_2WO_6 in a pH range of 4 to 11. Because of its higher specific area and rapid photogenerated carrier separation rate, ultrathin nanoflakes of Bi_2WO_6 produced at pH 4 demonstrated outstanding photodegradation effectiveness toward norfloxacin. The variations in the degradation rate were attributed to the different hierarchical structures of Bi_2WO_6.					
spherical shape aggregated perovskite nanoparticles	erichrome black T dye	simulated solar light (150 W Xe lamp)	initial concentration of antibiotic: 30 mg/L; catalyst dosage: 0.2 g/L; optimum reaction time: 180 min; observed bandgap: 2.7–2.9 eV	64.0–74.0	[113]
Using a one-pot solvothermal technique, Bi_2WO_6 nanoparticles were synthesised by changing the reaction temperature for 20 h between 120 and 180 °C. Because of the synergistic effects of small crystallite size, high surface area, presence of oxygen vacancies, and minimal electron recombination rate, the Bi_2WO_6 produced at 140 °C demonstrated maximum photocatalytic activity.					
sharp geometric corners and zigzag edges with nanoflakes morphology	Coomassie brilliant blue dye	visible light	initial concentration of antibiotic: 0.15 g/L; catalyst dosage: 0.75 g/L; optimum reaction time: 300 min	100.0	[114]
The hydrothermal method was used to synthesise orthorhombic Bi_2WO_6 nanoflakes for 24 h at 180 °C. The reaction temperature significantly affected the Bi_2WO_6's morphology, as non-uniform morphology was seen at 180 °C. The well-defined nanoflakes were generated by continuing the reaction for longer periods of time.					
spherical, uniform, and well-developed 2D nanosheets with flower-like morphology	rhodamine B dye	—	initial concentration of antibiotic: 10 mg/L; catalyst dosage: 1.25 g/L; optimum reaction time: 40 min; ultrasound pulse mode: 9 s on/1 s off	99.5	[115]
The hierarchical Bi_2WO_6 nanostructures with a high surface area were synthesised using a hydrothermal technique at 180 °C for 2 h assisted by ultrasonication. Preparation temperature and time were crucial for the crystal development.					
disordered, flake-like nanocrystals	rhodamine B dye	UV light, visible light and simulated sunlight	initial concentration of antibiotic: 5 mg/L; catalyst dosage: 1 g/L; optimum reaction time: 180 min; bandgap: 2.97–3.0 eV	58.4–87.9	[116]
Bi_2WO_6 nanocrystals with an orthorhombic structure were synthesised by a hydrothermal method over a 24 h period at 200 °C. The as-prepared catalyst was loaded with $NaBH_4$ solution (0.01–0.1 M) to enhance its structure and performance, and the optimized sample (0.03 M-Bi_2WO_6) showed the maximum photocatalytic activity. The Bi_2WO_6 nanoflakes have little photocatalytic activity when exposed to visible light because of their wide bandgap (3.0 eV), but are photocatalytically active when exposed to UV light. While exposed to UV and visible light, 0.03 M-Bi_2WO_6 (2.97 eV) exhibits increased photocatalytic activity. Due to its unique layered crystal structure of perovskite-like units $(WO_4)^{2-}$ positioned between $(Bi_2O_2)^{2+}$ layers, Bi_2WO_6 nanoparticles exhibit strong photocatalytic performance.					
homogenous, bundle-like nanostructured morphology	methylene blue dye	visible light (tungsten lamp 250 W)	initial concentration of antibiotic: 5 ppm; catalyst dosage: 0.4 g/L; optimum reaction time: 180 min; solution pH 4; bandgap: 2.8–2.93 eV	79.1–87.7	[117]
By using a simple combustion process and jackfruit extract, Bi_2WO_6 nanoparticles were synthesised, which were subsequently calcined at 400 °C for 3 h. The synthesised nanocatalyst displayed an orthorhombic phase with a bundle-like structure and showed strong photoluminescence, photocatalytic, and antioxidant activity. Holes and hydroxyl radicals contributed significantly toward the degradation of the dye.					

photocatalytic activity. These methods include engineering their morphologies through various synthesis techniques, metal/non-metal doping, introducing heterojunctions, and combining them with other materials.

Synthesis approaches and performance enhancement

The majority of the reported photocatalysts have been used in laboratory settings. Several fundamental requirements must be met to produce an efficient photocatalyst that can be applied industrially for the remediation of a variety of pollutants in contaminated water. First, photocatalytic activity is significantly influenced by the morphology (e.g., nanoplates, nanotubes, nanowires, nanorods, nanocuboids, nanoflakes, nanosheets, nanocapsules, nanocasts, or nanodots), dimension, and particle size of the photocatalyst.

Functional properties such as bandgap, optoelectronic properties, surface area, photoresponse, and magnetic properties depend on particle size and morphology of Bi-based photocatalysts. For instance, the charge diffusion path can be decreased by using photocatalysts with extremely small or thin structures, effectively separating the photogenerated electrons and holes. Bi-based photocatalysts in zero to three dimensions have been developed recently [102,106].

Low-dimensional (0-D and 1-D) nanomaterials have been extensively used in the field of photocatalysis over the past few years due to their distinct optical and electronic characteristics [42,88,106]. Simple strain relaxation and short diffusion paths are benefits of 1-D nanostructured materials and are advantageous for the separation of photogenerated carriers [102]. 1-D spindle-like $BiVO_4$ nanostructures with oriented carrier transport, high optical performance, and a short carrier diffusion length, for instance, were prepared by Li and co-workers [42]. The photodegradation rates of ciprofloxacin and tetracycline were, respectively, 94.8% and 81.1% after 1 h. Additionally, Lin et al. [122] prepared 1-D Bi_2WO_6 nanofibers with a flower-like morphology by using a hydrothermal process for the degradation of rhodamine B dye. Under visible-light irradiation, the 1-D nanofiber photocatalyst reached a degradation rate of 78.2% after 50 min.

Because of their extraordinarily small size, 0-D nanomaterials are steadily dispersed in solvents. There are very few published reports on 0-D Bi-based nanomaterials and these materials exhibit several quantum confinement effects. 3-D nanostructured Bi-based materials have drawn a lot of attention due to their intriguing architecture and properties. Numerous techniques have been developed to synthesise 3-D Bi-based nanostructures with different morphologies, including solvothermal/hydrothermal and sol–gel processes, mechanical exfoliation, solid-state reactions, chemical vapour deposition, and microwave-assisted techniques [106].

These 3-D photocatalysts have shown adequate photocatalytic activity, a large specific surface area, and an abundance of channels, all of which are advantageous for photocatalysis. For instance, Dang et al. [123] used a microwave-assisted method to synthesise 3-D nanostructured Bi_2WO_6 nanoparticles and reported 92% methylene blue dye degradation after 180 min under visible-light irradiation. 2-D nanostructured materials are thought to function more effectively in photocatalytic processes than 3-D nanostructured photocatalysts [88,102,106,124]. This is because photogenerated carriers in a 2-D structure can rise from a deeper layer of the structure more quickly than those in a 3-D structure.

It is important to note that an effective photocatalyst should have the following properties: (a) strong absorption both of UV and visible light (i.e., a suitable bandgap value, usually less than 3.0 eV); (b) thermal, chemical, and mechanical stability against photocorrosion; (c) high efficiency in quantum conversion; (d) fast generation and efficient transfer of photocarriers (e^- and h^+); and (e) slow recombination rate of photogenerated charge carriers. The nanopowder photocatalysts must also exhibit easy and rapid recovery from the solution with adequate reusability, that is, without noticeable loss of efficiency. Several strategies are currently used to achieve the listed features, including tuning of size, morphology, and particle dimensions. Also, the composition of the photocatalyst is varied yielding core–shell structures, element substitutions, intercalation compounds, plasmon sensitization, heterojunctions, and composites [72,110,118,119]. Several synthesis techniques have been used as summarised in Figure 4.

Several synthesis procedures for bismuth-based photocatalysts have already been published [25,88,119-124], so they are not covered in this review. In general, top-down approaches or bottom-up approaches can be used to synthesise Bi-based nanostructured materials using traditional solid-state methods as well as wet-chemical methods. Solid-state methods are typically high-energy methods.

The final product might have some impurities, relatively large particles, and only a small degree of homogeneity. Large volumes of nanopowder can be produced using a relatively simple apparatus via solid-state routes. Wet-chemical methods (such as electrospinning, sol–gel, hydrothermal, ultrasound, co-precipitation, and aerosol-spraying) have been widely used for the synthesis of various nanostructured materials due to their low cost, low energy requirements, and ease of control of the

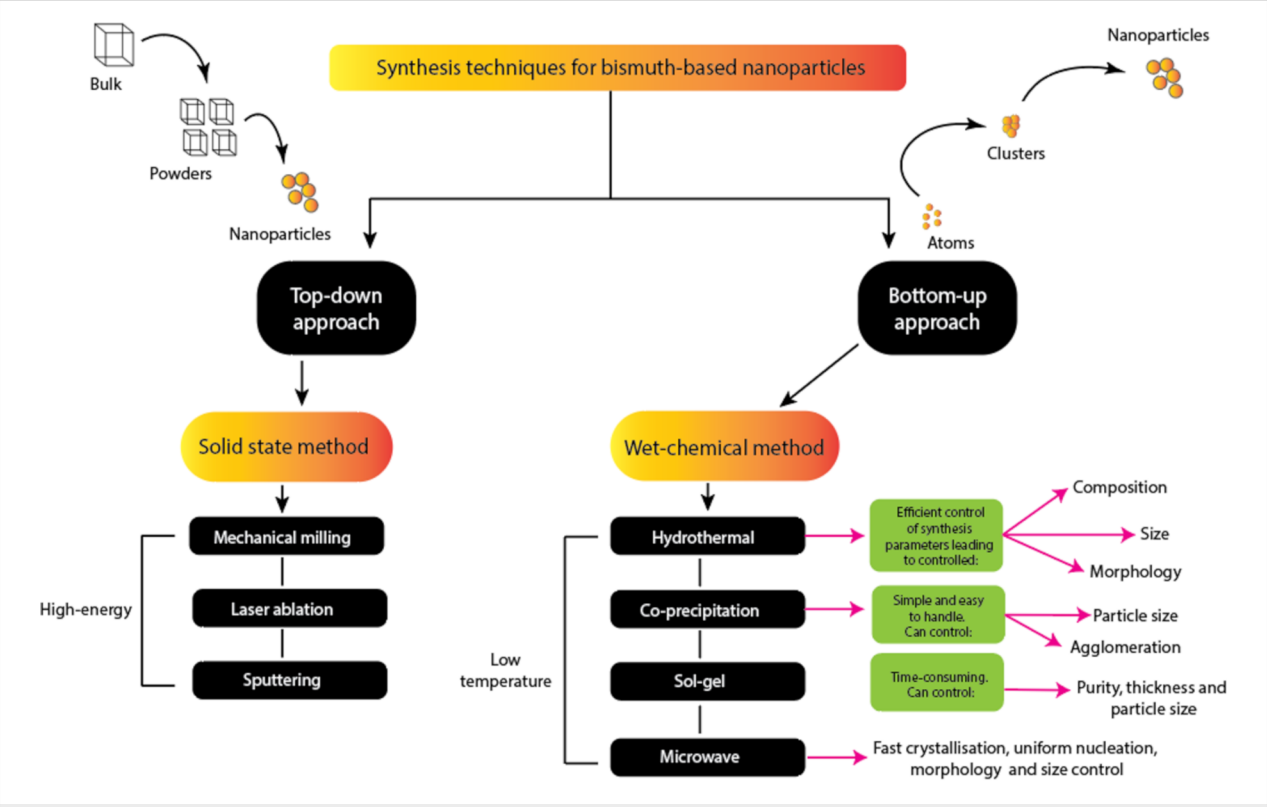

Figure 4: Summary of the commonly used synthesis methods for bismuth-based nanostructured photocatalysts.

solution parameters to meet the growing demand for efficient photocatalysts that can be produced on a large industrial scale at a lower cost. The most frequently used wet-chemical techniques are hydrothermal and co-precipitation techniques. Morphology, particle size, and composition can be easily adjusted using hydrothermal methods, whereas agglomeration and particle size can be controlled using the co-precipitation method. Thus, the combination of both techniques enables the customization of particle properties for particular applications.

It is worth noting that some recently published review articles have paid attention to ways of controlling the morphologies, dimensions, and even the nanoscale modulation as well as ways of enhancing the photocatalytic activities of Bi-based photocatalysts. Bi-based nanostructured materials have been used to treat water and wastewater that contained a variety of antibiotics (e.g., fluoroquinolones, tetracycline and sulfonamides). Table 4 and Table 5 discuss the results of a few studies that used undoped/non-composite Bi-based nanostructured photocatalysts to degrade textile dyes and antibiotics.

Even though different Bi-based photocatalysts have demonstrated impressive photocatalytic performance, pristine and bulk Bi-based photocatalysts still have some drawbacks such as

Table 4: Undoped Bi-based nanostructured photocatalysts for antibiotic remediation.

Photocatalyst	Target antibiotic	Optimum conditions	Source of light	Degradation (%)	Ref.
Remarks on active species					
BiOCl	ofloxacin, norfloxacin, ciprofloxacin	initial concentration of antibiotics: 10 mg/L; catalyst dosage: 0.25 g/L; optimum reaction time: 240 min	UV	95.0, 90.0, and 72.0	[125]
$^{\bullet}OH$ radicals and h^+ played key roles in the degradation process.					
$BiVO_4$	ciprofloxacin	initial concentration of antibiotic: 10 mg/L; optimum reaction time: 120 min	visible light	58.6	[126]
While e^- and $^{\bullet}O_2^-$ were the most active species, h^+, $^{\bullet}OH$ and $^{\bullet}O_2^-$ all took part in the degradation of the antibiotics.					

Table 4: Undoped Bi-based nanostructured photocatalysts for antibiotic remediation. (continued)

Bi_2WO_6	levofloxacin	catalyst dosage: 0.75 g/L; initial concentration of antibiotic: 10 mg/L; solution pH 7.14; optimum reaction time: 150 min	visible light	80.0	[109]
Antibiotics were degraded into simpler molecules as a result of the main active species, that is, radical $^{\bullet}O_2^-$, h^+, e^- and $^{\bullet}OH$.					
Bi_2WO_6	norfloxacin, ciprofloxacin	optimum reaction time: 150 min; dosage of catalyst: 1 g/L; initial concentration of antibiotics: 10 mg/L	visible light	73, 70	[110]
$^{\bullet}O_2^-$ and holes (h^+) played key roles in the degradation of the antibiotics.					
$BiVO_4$	tetracycline	optimum reaction time: 60 min; dosage of catalyst: 1 g/L; initial concentration of antibiotic: 10 mg/L	visible light	monoclinic scheelite: 60.2 tetragonal zircon: 17.3 monoclinic-tetragonal: 80.5	[127]
Hydroxyl radicals and holes (h^+) contributed to the degradation process					
BiOBr	ciprofloxacin	optimum reaction time: 60 min; dosage of catalyst: 0.5 g/L; initial concentration of antibiotic: 15 mg/L	visible light	43.7	[128]
While $^{\bullet}OH$ is only involved to a small extent in the antibiotic photodegradation, h^+ and $^{\bullet}O_2^-$ play a critical role.					
BiOCl	sulfamethoxazole	optimum reaction time: 60 min; dosage of catalyst: 0.2 g/L; initial concentration of antibiotic: 25 mg/L	visible light (Xe)	36.8	[129]
The main reactive species identified through scavenging tests were $^{\bullet}O_2^-$ and $^{\bullet}OH$.					

Table 5: Undoped Bi-based nanostructured photocatalysts for remediation of dye pollution.

Photocatalyst	Target dye pollutant	Optimum experimental conditions	Source of light	Degradation (%)	Ref.
Remarks on active species					
BiOI, Bi_2O_4	rhodamine B	treatment time: 32 min; dosage of catalyst: 0.5 g/L; initial concentration of dye: 10 mg/L	visible light (LED)	10.0, 67.0	[130]
$^{\bullet}O_2^-$ and h^+ were the main active species during the photocatalytic degradation process.					
$Bi_4Ti_3O_{12}$	rhodamine B	treatment time: 120 min; dosage of catalyst: 0.1 g/L; initial concentration of dye: 10 mg/L	visible light (Xenon lamp)	100.0	[131]
$^{\bullet}O_2^-$ and h^+ contributed mostly to the degradation process.					
$BiVO_4$	alizarin red S	treatment time: 180 min; dosage of catalyst: 0.5 g/L; initial concentration of dye: 10 mg/L	UV (365 nm)	99.6	[132]
The degradation of the dye was mainly attributed to the contribution of $^{\bullet}OH$ radicals.					
BiOCl	rhodamine B	treatment time: 100 min; dosage of catalyst: 1 g/L; initial concentration of dye: 9.6 mg/L	visible light	22.0	[133]
The photogenerated electrons converted the adsorbed oxygen into $^{\bullet}O_2^-$, which played a key role together with h^+ in the degradation process.					
Bi_2O_3	acid yellow 29, Coomassie brilliant blue, Acid Green 25	treatment time: 120 min; dosage of catalyst: 1 g/L; initial concentration of Acid Yellow 29: 0.1425×10^{-3} mg/L, of Coomassie brilliant blue: 0.427×10^{-4} mg/L, and of Acid Green 25: 0.156×10^{-3} mg/L	visible light (Halogen lamp)	Acid Yellow 29: 58.0, Coomassie brilliant blue and Acid Green 25: 57.0	[134]
$^{\bullet}O_2^-$ and $^{\bullet}OH$ radicals were the key species while h^+ contributed to the production of more $^{\bullet}OH$ radicals.					

Table 5: Undoped Bi-based nanostructured photocatalysts for remediation of dye pollution. (continued)

$Bi_2O_2CO_3$	rhodamine B	treatment time: 45 min; dosage of catalyst: 0.666 g/L; initial concentration of dye: 10 mg/L	visible light	13.0	[135]
$^{\bullet}O_2^-$ and $^{\bullet}$OH radicals were the dominant species during the photocatalytic degradation process.					
$BiOCl_{0.7}I_{0.3}$	methyl orange	treatment time: 50 min; dosage of catalyst: 2 g/L; initial concentration of dye: 20 mg/L	visible light	100.0	[136]
—					
Bi_2WO_6	rhodamine B	treatment time: 100 min; dosage of catalyst: 1 g/L; initial concentration of dye: 4.8 mg/L	visible light (Xe light)	98.2	[137]
e^- and h^+ contributed to the degradation process.					
BiOCl	methylene blue	treatment time: 120 min; dosage of catalyst: 1 g/L; initial concentration of dye: 20 mg/L	sunlight	36.0	[138]
$^{\bullet}O_2^-$ and $^{\bullet}$OH radicals contributed to the photocatalytic process.					
BiOI	methyl orange	treatment time: 30 min; dosage of catalyst: 1 g/L; initial concentration of dye: 10 mg/L	visible light (300 W Xe lamp)	35.2	[139]
$^{\bullet}O_2^-$ and h^+ were the dominant species while the $^{\bullet}$OH radicals played a minor role in the degradation reaction.					
$BiVO_4$	rhodamine B	treatment time: 180 min; initial concentration of dye: 10 mg/L	visible light (tungsten halogen lamp)	90.0	[140]
$^{\bullet}O_2^-$ and $^{\bullet}$OH were the dominant species.					
BiOI	rhodamine B	treatment time: 240 min; dosage of catalyst: 0.25 g/L; initial concentration of dye: 10 mg/L	direct sunlight	100.0	[125]
The $^{\bullet}$OH radicals and h^+ played key roles in the degradation process.					
Bi_2O_3	methyl orange	treatment time: 240 min; initial concentration of dye: 10 mg/L	visible light	94.8	[141]
—					
$BiFeO_3$	rhodamine B	treatment time: 180 min; dosage of catalyst: 0.2 g/L; initial concentration of dye: 10 mg/L	visible light	94.0	[142]
e^- converted O_2 to $^{\bullet}O_2^-$, which contributed actively to the degradation process alongside h^+.					
$Bi_2WO_6/AgIO_3$	rhodamine B	treatment time: 180 min; dosage of catalyst: 0.5 g/L; initial concentration of dye: 10 mg/L	visible light	100	[143]
The active species were $^{\bullet}O_2^-$ and h^+.					

limited light absorption, weaker charge separation, and poor charge carrier mobility. Researchers are concentrating on several strategies, such as doping, heterojunction formation, induction of the surface plasmon resonance effect, and the formation of Z-schemes, Schottky junctions, and engineered composites, for modifying the optoelectronic and other properties of these Bi-based nanomaterials.

Doping of Bi-based nanostructured materials: To improve the electrical, optical, and magnetic properties of the host materials, doping (rare earth elements, metal, or non-metal ions) is a common technique [20,72,104,110,144-150]. Doping reduces the bandgap energy, introduces intermediate energy levels to overcome constraints, creates trap sites to capture photogenerated charge carriers, and increases the absorption of visible light. Additionally, after doping, oxygen vacancies or/and surface defects are created without destroying the crystal structure (though it might be distorted), effectively separating photogenerated carriers. Doping with metallic (Mg, Ag, Ni, Fe, Li, Co, and Ni) and non-metallic ions (F, C, N, and O), can introduce an intraband close to the conduction band of the host material, enhancing charge carrier dynamics [20,146].

In contrast to undoped Bi_2WO_6, visible light-driven 3-D hierarchical Ag-doped Bi_2WO_6 nanoparticles showed improved photocatalytic performance by destroying 95% of tetracycline in only 70 min, according to Shen and co-workers [147]. The increased performance was caused by the following factors: (a) surface plasmon resonance caused by the Ag dopant; (b) a decrease in the rate at which photoinduced carriers recombined; (c) high Schottky barriers between the Ag dopant and the host material; and (d) an increase in the visible-light absorption range. In addition to improving the photocatalytic properties of the Bi-based host materials, doping them with rare earth elements may also give them special ferroelectric and ferromagnetic properties, as well as electrochemical and luminescent properties.

To produce an Er-doped Bi_2WO_6 nanostructured photocatalyst for the degradation of antibiotics, Qiu et al. [145] used a hydrothermal technique. The bandgap of Bi_2WO_6 decreased from 2.80 to 2.35 eV after Er^{3+} doping, and the specific surface area of the doped Bi_2WO_6 was nearly 2.5 times higher than that of the undoped Bi_2WO_6. In comparison to pure Bi_2WO_6 (82.8%), the dopant significantly increased the tetracycline-degrading activity, which reached 94.6% within 1 h of visible light irradiation. Additionally, Irfan et al. [148] used a bi-solvent sol–gel technique to synthesise porous bismuth ferrite nanostructures with various morphological structures. They discovered that the surface area increased from 3.3 to 9 m^2/g with a significant reduction in bandgap from 2.08 to 1.49 eV when La^{3+} and Mn^{2+} ions were co-doped into the $BiFeO_3$ host material.

Within 120 min of exposure to visible light, the co-doped photocatalyst degraded Congo red dye by about 97%. The research on doped and co-doped Bi-based nanostructured materials using different dopants for dye and antibiotic degradation is summarised in Table 6 and Table 7.

The use of doping generally enhances the photocatalytic activity of photocatalysts. The most important variables to take into account are the quantity and type of dopant. The photocatalytic performance may be impacted if the amount of dopant is greater than the optimum value because it may act as a recombination site for photoinduced charge carriers. Additionally, doping has some drawbacks such as thermal instability and carrier trapping [72]. Other modifications, such as heterojunctions, Schottky junctions, p–n junctions, Z-schemes, and homojunctions, have been used to overcome these problems and boost the effectiveness of photocatalysts.

Table 6: Doped Bi-based nanostructured photocatalysts for antibiotic remediation.

Photocatalyst	Target antibiotic	Optimum experimental conditions	Source of light	Degradation (%)	Ref.
Remarks on active species					
Mg-, Fe-, Cu-, and Zn-doped Bi_2WO_6[a]	norfloxacin, ciprofloxacin	treatment time: 150 min; dosage of catalyst: 1 g/L; initial concentration of antibiotic: 10 mg/L.	visible light	70.0–99.0	[110]
$^{\bullet}O_2^-$ and h^+ were the dominant species while $^{\bullet}OH$ radicals contributed slightly to the degradation of the antibiotics.					
Al/BiOCl	tetracycline	treatment time: 60 min; dosage of catalyst: 0.4 g/L; initial concentration of antibiotic: 100 mg/L.	simulated sunlight	91.1	[149]
e^-, $^{\bullet}OH$ and h^+ played a minor role while $^{\bullet}O_2^-$ was the main active species during the degradation process.					
Cu-doped BiOBr	norfloxacin	treatment time: 30 min; dosage of catalyst: 1 g/L; initial concentration of antibiotic: 10 ppm.	visible light (200 W Hg, Xe arc lamp)	46.5–82.6	[150]
The degradation of norfloxacin was mostly mediated by direct h^+ oxidation; $^{\bullet}O_2^-$ and $^{\bullet}OH$ radicals were not the predominant reactive species.					
Fe/BiOCl	levofloxacin	optimum reaction time: 60 min; dosage of catalyst: 0.5 g/L; initial concentration of antibiotic: 361 mg/L.	visible light	95.0	[151]
Both $^{\bullet}SO_4^-$ and $^{\bullet}OH$ contributed little to the degradation of the antibiotic. $^{\bullet}O_2^-$ and h^+ were the main active species.					
Ti/BiOI	diclofenac	optimum reaction time: 90 min; dosage of catalyst: 0.25 g/L; initial concentration of drug: 10 mg/L; pH 5.9.	visible light	99.2	[152]
$^{\bullet}O_2^-$ and h^+ were the key active species, while $^{\bullet}OH$ play a minor role during the degradation process.					

[a]The metals were doped individually.

Table 7: Doped Bi-based nanostructured photocatalysts for remediation of dye pollution.

Photocatalyst	Target dye pollutant	Optimum experimental conditions	Source of light	Degradation (%)	Ref.
Remarks on active species					
Ag-BiOCl	rhodamine B	treatment time: 100 min; dosage of catalyst: 1 g/L; initial concentration of dye: 9.6 mg/L	visible light	99	[133]
The photogenerated electrons converted adsorbed oxygen into $^{\bullet}O_2^-$ radicals and with h^+ contributed to the degradation process.					
Ce/Bi_2O_3, Nd/Bi_2O_3	Acid Yellow 29, Coomassie brilliant blue (G250), Acid Green 25	Reaction time: 120 min; dosage of catalyst: 1 g/L; the initial concentration of Acid Yellow 29: 0.1425×10^{-3} mg/L., of Coomassie brilliant blue (G250): 0.427×10^{-4} mg/L, and of Acid Green 25: 0.156×10^{-3} mg/L	visible light (halogen lamp)	82.0–88.0, 74.0–84.0	[134]
$^{\bullet}O_2^-$, h^+ and $^{\bullet}OH$ were the active species during the degradation process.					
B/BiOBr	rhodamine B	optimum reaction time: 30 min; dosage of catalyst: 1 g/L; initial concentration of dye: 15 mg/L	visible light	99.3	[153]
$^{\bullet}OH$ played the main role in the degradation of rhodamine B.					
B/BiOCl	rhodamine B	optimum reaction time: 100 min; dosage of catalyst: 0.4 g/L; initial concentration of dye: 20 mg/L	visible light	81.5	[154]
$^{\bullet}O_2^-$ played the main role in the degradation of rhodamine B.					
C/BiOI	methyl orange	optimum reaction time: 60 min; dosage of catalyst: 0.1 g/L; initial concentration of dye: 10 mg/L.	visible light	99.8	[155]
$^{\bullet}O_2^-$ and holes played the main role in the degradation of methyl orange.					
In-BiOI	methyl orange	optimum reaction time: 120 min; dosage of catalyst: 0.1 g/L; initial concentration of dye: 10 mg/L.	visible light	96.0	[150]
$^{\bullet}O_2^-$ and holes played the main role in the degradation of methyl orange.					

Heterojunctions, Schottky junctions, Z-schemes and surface plasmon resonance effect: Heterojunctions, which are the interfaces between two different semiconductors, increase the charge carrier separation efficiency with increased kinetics and strong redox ability. This enhances the photocatalytic capabilities of photocatalysts [101,119,156-161]. Depending on how the semiconductors are connected, heterojunctions can be divided into three types, namely type-I staggered gaps, type-II straddling gaps, and type-III broken gaps. In a broken gap, the bands do not overlap whereas in a staggered gap, the bandgaps of two semiconductors overlap and may cause band discontinuity. The straddling gap heterojunction system is recognised as the standard heterojunction system where the band edges of one semiconductor are lower than those of the second semiconductor [119,156]. The conduction band position of semiconductor Y is highly negative relative to semiconductor X in type-II heterojunction systems. Conversely, the valence band potential of semiconductor X is highly positive. After being exposed to visible light, electrons from semiconductor Y's conduction band move to semiconductor X's conduction band while holes from semiconductor X's valance band move to semiconductor Y's valance band, effectively separating the photogenerated carriers [162].

According to Chae et al. [163], a heterojunction WO_3-$BiVO_4$ composite demonstrated excellent photocatalytic activity with optical properties that were more effective than those of the pure individual components. Li et al. [164] also created a core–shell heterojunction nanocomposite made of $BiFeO_3$ and TiO_2 for the degradation of textile dye. The authors reported a 70% degradation of Congo red dye after 70 min of visible-light irradiation, which they attributed to an improvement in quantum efficiency caused by the efficient separating of holes and electrons. Charge carriers are oxidised and reduced at sites with reduced electric potential when they are separated by type-II heterojunctions, which, according to Low et al. [165], decreases the charge carrier separation efficiency and the redox ability of the photocatalyst.

The shortcomings of heterojunction systems have been overcome by Z-scheme photocatalysis systems, surface plasmon resonance effect, and Schottky junctions. An innovative method for further enhancing sunlight-driven photocatalytic performance in comparison to conventional heterojunction composites is to develop a Z-scheme photocatalytic system. Li et al. [42] constructed spindle-shaped $BiVO_4$-RGO-*g*-C_3N_4 Z-scheme photocatalysts for the highly effective degradation of antibiotics. The 1-D Z-scheme ternary nanocomposites had a very high photooxidation response. According to the authors, ciprofloxacin and tetracycline were degraded by 94.8% and 81.1% after 1 h, respectively.

Another strategy for overcoming constraints such as low charge migration and the unpredictable direction of charge diffusion is the construction of a Schottky junction. A Schottky junction can be created at the interface between the semiconductor and a noble metal with an appropriate work function. A unidirectional charge transfer is enabled by the Schottky potential barrier, increasing charge density and separation [72]. Shen et al. [166] created a Schottky junction by synthesising $NiSe_2$ nanosheets on top of $BiVO_4$ nanosheets using a facile solvothermal technique. An intrinsic electric field is created at the interface as a result of the active migration of electrons from $BiVO_4$ to $NiSe_2$. This improves the separation efficiency of the photogenerated carriers, and the interaction at the interface lowers the bandgap of $BiVO_4$, which in turn improves the photocatalytic activity of the nanocomposites.

Additionally, to maximise the effectiveness of the transfer/separation of photogenerated carriers, noble metals (such as Pt, Ag, and Au) are typically used to induce surface plasmon resonance effects in photocatalysts [146]. However, using noble metals in small or medium-sized industrial water treatment plants will be rather expensive. Recently, bismuth demonstrated a clear surface plasmon resonance effect, indicating the possibility of substituting it for noble metals. Because of the intrinsic photocatalytic characteristics of bismuth, other semiconductors can be used with it to achieve better performance. In a recent study, Chava et al. [167] synthesised bismuth quantum dots anchored to 1-D cadmium sulfide as a plasmonic photocatalyst using a facile solvothermal procedure. To create heterostructure nanorods, Schottky contacts between 1-D CdS and 0-D Bi components were developed. The bandgap values were altered, and the absorption in the visible-to-infrared range was enhanced after the deposition of Bi quantum dots on CdS. To degrade the antibiotic tetracycline, a Bi/CdS heterostructure photocatalyst was used. The optimised photocatalyst showed a maximum photocatalytic degradation activity of 90% under visible-light irradiation in 1 h, which is higher than the 52% achieved by pure CdS under the same conditions. The improved photocatalytic degradation efficiency is attributed to the surface plasmon resonance effect, doped Bi^{3+} ions, the Schottky potential barrier, and efficiently separated photoinduced charge carriers. Table 8 provides a summary of the research on heterojunction photocatalysts for the degradation of antibiotics.

Table 8: Bi-based nanocomposite/heterojunction photocatalysts for antibiotic remediation.

Photocatalyst Remarks on active species	Target antibiotic	Optimum experimental conditions	Source of light	Degradation (%)	Ref.
Azadirachta indica leaf extraction/$BiOBr_{0.2}I_{0.8}$	amoxicillin trihydrate	optimum reaction time: 300 min; dosage of catalyst: 1 g/L; initial concentration of antibiotic: 20 mg/L	visible light	93.2	[168]
The prime active species are h^+ and $^{\bullet}O_2^-$ while $^{\bullet}OH$ radicals play a minor role during the photocatalytic process.					
Bi_2WO_6/C-dots/TiO_2	levofloxacin	optimum reaction time: 90 min; dosage of catalyst: 0.075 g/L; initial concentration of antibiotic: 10 mg/L	sunlight	99.0	[169]
The $^{\bullet}OH$ radicals play a key role in the degradation process while h^+ and e^- contributed to the production of the active species.					
Ag/AgBr/$BiVO_4$	ciprofloxacin	optimum reaction time: 120 min; initial concentration of antibiotic: 10 mg/L	visible light	91.4	[126]
Hydroxyl radicals, h^+, and $^{\bullet}O_2^-$ were the main species that contributed to the degradation process					
$BiVO_4$/TiO_2/RGO	tetracycline, chlortetracycline, oxytetracycline, doxycycline	optimum reaction time: 120 min; initial concentration of antibiotic: 10 mg/L, pH 3	visible light	96.2, 97.5, 98.7, 99.6	[170]
Both $^{\bullet}O_2^-$ and $^{\bullet}OH$ were the key species that participated in the photocatalytic degradation process.					

Table 8: Bi-based nanocomposite/heterojunction photocatalysts for antibiotic remediation. (continued)

g-C_3N_4/BiOBr on carbon fibre	tetracycline	optimum reaction time: 120 min; g-C_3N_4 nanosheets (thickness: ca. 30 nm, diameter: 0.4–1.0 μm) and BiOBr layer (thickness: ca. 25 nm, diameter: 200–500 nm); carbon fiber: (area: 5 × 5 cm^2, weight: 0.15 g); initial concentration of antibiotic: 20 mg/L	visible light	86.1	[171]
$^{\bullet}OH$, h^+ and $^{\bullet}O_2^-$ were revealed to have participated in tetracycline degradation.					
Bi_2O_3–TiO_2/activated carbon	sulfamerazine	optimum reaction time: 120 min; dosage of catalyst: 1 g/L; initial concentration of antibiotic: 20 mg/L	visible light	95.5	[172]
h^+ and $^{\bullet}O_2^-$ participated in sulfamerazine degradation.					
biochar@$ZnFe_2O_4$/BiOBr, biochar@BiOBr, $ZnFe_2O_4$/BiOBr	ciprofloxacin	optimum reaction time: 60 min; dosage of catalyst: 0.5 g/L; initial concentration of antibiotic: 15 mg/L	visible light	65.26, 47.1, 48.76	[128]
The results from the scavenger experiments revealed that radical h^+, $^{\bullet}OH$, and $^{\bullet}O_2^-$ radicals contributed to the photocatalytic degradation process.					
AgI/$Bi_4V_2O_{11}$	sulfamerazine	optimum reaction time: 60 min; dosage of catalyst: 1 g/L; initial concentration of antibiotic: 10 mg/L	visible light	91.47	[173]
$^{\bullet}OH$, h^+ and $^{\bullet}O_2^-$ were all involved in sulfamerazine degradation.					
BiOCl/*g*-C_3N_4/Cu_2O/Fe_3O_4, BiOCl/g-C_3N_4/Cu_2O, BiOCl/Cu_2O/Fe_3O_4, BiOCl/g-C_3N_4/Fe_3O_4, BiOCl/g-C_3N_4, BiOCl/Cu_2O	sulfamethoxazole	optimum reaction time: 120 min; dosage of catalyst: 0.2 g/L; initial concentration of antibiotic: 25 mg/L	visible light (Xe) and sunlight	Xe: 99.5; sunlight: 92.1, 85.3, 83.8, 80.7, 63.5, 59.4	[129]
The main reactive species identified through scavenging tests were $^{\bullet}O_2^-$ and $^{\bullet}OH$.					
Bi_2WO_6/g-C_3N_4	ceftriaxone sodium	optimum time: 120 min; dosage of catalyst: 1 g/L; initial concentration of antibiotic: 10 mg/L	visible light	94.5	[174]
h^+ and $^{\bullet}O_2^-$ radicals played a more significant role in the photocatalytic process then $^{\bullet}OH$.					
AgI/$BiOIO_3$	tetracycline, chlortetracycline	optimum reaction time: 350 min; dosage of catalyst: 0.5 g/L; initial concentration of antibiotic: 10 mg/L	visible light	tetracycline: 45.3, chlortetracycline: 39.1	[175]
From $BiOIO_3$, h^+ cannot sufficiently oxidise H_2O molecules to form $^{\bullet}OH$ radicals. While the h^+ in AgI oxidises OH^- to produce $^{\bullet}OH$ radicals, the electrons in AgI converted O_2 to radical $^{\bullet}O_2^-$. All contributed to the degradation.					
BiOBr/Bi_2S_3, BiOBr	ciprofloxacin, ofloxacin	optimum reaction time: 60 min; dosage of catalyst: 1 g/L; initial concentration of antibiotic: 20 mg/L	indoor fluorescent light	97.2, 89.28, 52.1, 44.21	[176]
$^{\bullet}O_2^-$ and h^+ were shown to be the primary degrading species in scavenger experiments.					

Bismuth nanocomposites: A nanocomposite is a multiphase material (typically a solid) with one to three dimensions of less than 100 nm, where one of the phases has different properties due to differences in chemistry and structure. Following the formation of the nanocomposite, its properties are often enhanced and significantly different from those of the components. Fascinatingly, nanocomposite photocatalysts allow for the integration of multiple functions derived from various types of nanocatalysts, such as semiconductor nanoparticles, plasmonic metals, and carbon-based and magnetic oxides, into the same host matrix. This enables effective tuning of the photocatalytic characteristics of the final nanocomposite by extending the lifetime of the photogenerated carriers. It makes the catalysts recoverable by using external magnets and extends the range of absorption to the visible region for photocatalysis.

According to [177-180], a junction between carbon-based and semiconductor materials can effectively prevent charge carriers from recombining, increasing the photoactivity of $BiFeO_3$. For instance, Wang et al. [180] synthesised spindle-like g-C_3N_4/$BiFeO_3$ nanosheets, and the nanocomposite successfully degraded methyl orange by 75% under visible light, which is better than g-C_3N_4 or $BiFeO_3$ alone. $BiFeO_3$-graphene nanocomposites were made using a hydrothermal process by Lam and co-workers [177]. Under visible-light photocatalysis, the nanocomposite efficiently degraded Congo red dye. The improved performance was attributed to the altered bandgap between graphene oxide and $BiFeO_3$. Table 9 provides a summary of the research on Bi-based nanocomposite photocatalysts for the degradation of dyes.

Operational parameters influencing the photocatalytic efficiency of bismuth-based nanomaterials

In addition to the structure and properties of the photocatalysts used in pollution remediation, other crucial operational factors affect how well they perform. These parameters need to be investigated and optimised to scale up the process to design a

Table 9: Bi-based nanocomposite/heterojunction photocatalysts for remediation of dye pollution.

Photocatalyst	Target dye pollutant	Optimum experimental conditions	Source of light	Degradation (%)	Ref.
Remarks on active species					
$BiOI/Bi_2O_4$	rhodamine B	optimum reaction time: 32 min; dosage of catalyst: 0.5 g/L; initial concentration of dye: 10 mg/L	visible light	97.3	[130]
$^{\bullet}O_2^-$ and h^+ were the main active species during the photocatalytic degradation process.					
$Bi_4Ti_3O_{12}/C_3N_4$	rhodamine B	optimum reaction time: 120 min; dosage of catalyst: 0.1 g/L; initial concentration of dye: 10 mg/L	visible light (xenon lamp)	100	[131]
$^{\bullet}O_2^-$ and h^+ were the main active species during the photocatalytic degradation process.					
$Bi_2O_2CO_3$/g-C_3N_4	rhodamine B	optimum reaction time: 45 min; dosage of catalyst: 0.7 g/L; initial concentration of dye: 10 mg/L	visible light	91	[135]
h^+ and $^{\bullet}OH$ were the main active species during the degradation process while $^{\bullet}O_2^-$ had only a small effect.					
Azadirachta indica leaf extract/$BiOBr_{0.2}I_{0.8}$	methyl orange	optimum reaction time: 80 min; dosage of catalyst: 1 g/L; initial concentration of dye: 20 mg/L	visible light	100	[168]
$^{\bullet}O_2^-$ and h^+ were the main active species during the photocatalytic degradation process.					
Callistemon viminalis extract/$BiVO_4$	methylene blue	optimum reaction time: 300 min	visible light	82	[181]
$^{\bullet}O_2^-$, h^+ and $^{\bullet}OH$ were the main active species during the photocatalytic degradation process.					
$BiOCl_{0.6}/ZnO_{0.4}$	rhodamine B	optimum reaction time: 140 min; dosage of catalyst: 1 g/L; initial concentration of dye: 40 mg/L	visible light (halogen lamp)	100	[182]
The main active species during the photocatalytic degradation process were $^{\bullet}O_2^-$ and $^{\bullet}OH$.					
BiOBr–BiOI	rhodamine B	optimum reaction time: 60 min; dosage of catalyst: 1 g/L; initial concentration of dye: 14.4 mg/L	visible light	90	[183]
The main active species during the photocatalytic degradation process were $^{\bullet}O_2^-$ and $^{\bullet}OH$.					
TiO_2/Bi_2O_3	orange II	optimum reaction time: 180 min; dosage of catalyst: 1 g/L; initial concentration of dye: 5 mg/L	visible light (halogen tungsten lamp)	94.7	[184]
The main active species during the photocatalytic degradation process were $^{\bullet}O_2^-$ and $^{\bullet}OH$.					

Table 9: Bi-based nanocomposite/heterojunction photocatalysts for remediation of dye pollution. (continued)

$BiOCl-Bi/TiO_2$	methylene blue	optimum reaction time: 120 min; dosage of catalyst: 1 g/L; initial concentration of dye: 20 mg/L	sunlight	97	[138]
Hydroxyl radicals, h^+, and $^•O_2^-$ played key roles during the photocatalytic degradation process.					
$BiOI/AgI/g-C_3N_4$	methyl orange	optimum reaction time: 30 min; dosage of catalyst: 1 g/L; initial concentration of dye: 10 mg/L	visible light	95.2	[139]
Hydroxyl radicals, h^+, and $^•O_2^-$ played key roles during the photocatalytic degradation process.					
$Ag_8W_4O_{16}/AgBiW_2O_8/Bi_2WO_6$, $AgBiW_2O_8/Bi_2WO_6$	methylene blue	optimum reaction time: 40 min; dosage of catalyst: 1 g/L; initial concentration of dye: 10 mg/L	UV	82.5, 60	[185]
Considering the values of the potentials of the conduction and valance bands, e^-, h^+, and $^•OH$ contributed to the degradation process.					
$Au-BiVO_4$	methylene blue	optimum reaction time: 360 min; dosage of catalyst: 40 mL suspended nanoparticles/L; initial concentration of dye: 0.5 mg/L	UV–vis light	95	[186]
—					
$Bi_2WO_6/g-C_3N_4$	rhodamine B, methyl orange, methylene blue	optimum reaction time: 80 min; dosage of catalyst: 1 g/L; initial concentration of dye: 10 mg/L	visible light	99.9, 99.8, 99.8	[174]
h^+ and $^•O_2^-$ contributed more to the photocatalytic process than $^•OH$.					
$AgI/BiOIO_3$	methyl orange	optimum reaction time: 150 min; dosage of catalyst: 0.5 g/L; initial concentration of dye: 6.6 mg/L	UV and visible light	94.7, 48	[175]
Because the valence band of $BiOIO_3$ has a lower potential than the redox potential of $^•OH/H_2O$ (2.38 eV), h^+ cannot sufficiently oxidise H_2O molecules to form $^•OH$ radicals. While the h^+ in AgI oxidises OH^- to produce $^•OH$ radicals, the electrons in AgI can convert O_2 to a radical $^•O_2^-$, which took part in the degradation.					

system that is cost-effective, energy-efficient, and effective in treating water. Some of the factors that can affect the performance of the photocatalysts include the pH value of the effluent, the dosage of the photocatalyst, the initial concentration of the target pollutant, the dosage of oxidants, and the type of light source.

To lower the overall cost of water treatment, the photocatalyst must be effective under all types of light, including direct sunlight, UV light, and simulated sunlight. Several Bi-based photocatalysts are visible-light-driven because of the bandgap, making them useful in a variety of situations. The solution pH value is a critical parameter when it comes to the photocatalytic degradation of textile dyes and antibiotics. The point of zero charge (pH_{pzc}) of the photocatalysts, the effluent matrices, and the speciation of the target pollutants at various pH values all affect how well the photocatalytic process degrades pollutants. To avoid additional cost associated with pH adjustment of the effluent, an effective photocatalyst needs to function excellently at all pH values. For instance, electrostatic repulsion may reduce the effectiveness of the degradation process if the photocatalytic experiment is carried out at a pH value at which photocatalyst and pollutant species have the same surface charge.

For instance, lower removal efficiencies for both ciprofloxacin and ofloxacin were recorded at a highly basic pH [187] using a magnetic Bi_2WO_6-biochar composite with a pH_{pzc} of 6.75. The best performance was at pH 7. Since both antibiotics and photocatalyst were negatively charged at a basic pH, electrostatic repulsion between them was thought to be the cause of this. A higher degradation efficiency was noted at basic pH using Bi_2WO_6 to degrade norfloxacin under simulated sunlight [188]. The higher removal was attributed to a potential reaction between the photogenerated holes and hydroxyl ions at basic pH, which may have produced more hydroxyl radicals, enhancing the photocatalytic reaction. These results unequivocally demonstrate the significance of the pH value in the degradation process and the necessity to fine-tune the photocatalysts to make them functional at all pH values.

The removal effectiveness and rate of photocatalytic degradation processes are significantly influenced by the amount of photocatalyst added to the effluent solution before treatment. In general, as the dosage of the photocatalyst is increased, the photocatalytic degradation efficiency rises as well, until an optimum point is reached where adding more photocatalysts has no further effect on the degradation efficiency. More active sites are provided in the effluent solution with the addition of more photocatalysts to the treatment reactor, which favours the production of more photoinduced carriers. The turbidity of the solution as well as the light scattering effect of the photocatalyst, however, may cause a decrease in the degradation efficiency when the amount of photocatalyst is above the optimal dose [157-162]. In addition to achieving maximum efficiency, using the optimum photocatalyst dose will also be very cost-effective.

Lower concentrations of antibiotics (nanograms per litre to micrograms per litre) have been found in environmental media, whereas the majority of textile effluents contain multiple pollutants at varying concentrations. Therefore, the photocatalyst and treatment system must be efficient to treat water with varying concentrations of contaminants. Both the effectiveness and kinetics of the photocatalytic processes are significantly influenced by the initial concentration of pollutants. Both direct and inverse relationships between the initial concentrations of the pollutants and the degree of their removal have been reported. Anwar et al. [189], for instance, reported that the photocatalytic degradation performance of both pollutants decreases with increasing initial concentrations of paracetamol and methylene blue dye. The decrease in the removal was attributed to the fact that high concentrations prevent light dispersion into the solution. An increase in the concentration of pollutant molecules adsorbed on the catalyst surface while the catalyst dosage is unchanged and the generation of reactive species is constant could be another factor causing the decrease in photocatalytic degradation rate with increasing concentrations.

A similar trend was reported by Huang and co-workers [190]. According to the authors, the percentage of photocatalytic degradation using a hierarchical Z-scheme AgBr-Bi_2WO_6 photocatalyst decreased from 88% to 54% when the concentration of tetracycline was increased from 20 to 60 mol/L. The decrease in efficiency was attributed to two causes: First, it is more difficult for photons to reach the photocatalyst at higher concentrations, which resulted in a decrease in the production of oxidant radicals and, as a result, a decrease in the degradation performance. Second, the number of intermediate products formed at higher concentrations increased, competing with tetracycline molecules and decreasing the efficiency of the photocatalytic reaction. To design a water treatment system that works effectively, the aforementioned parameters must be studied at both laboratory and industrial-scale reactors.

Photocatalysis mechanism for bismuth-based photocatalyst and degradation pathway of target pollutant molecule

Understanding the degradation mechanism and the degradation pathway of the pollutants is crucial for designing an efficient photocatalyst and photocatalytic water treatment system. A less efficient and unstable photocatalyst may cause the nanocatalyst to leak into the environment and more hazardous intermediates to be produced. To understand the photocatalytic mechanism and speculate on potential heterojunction configurations for the photocatalysts, it is crucial to understand their optical characteristics, surface chemistry, and energy band structures. The structure of the molecule, the type and strength of its molecular bonds, the pH of the solution, the nature of reactive oxygen radicals, and the type of other pollutants in the system will all affect the degradation pathway.

Several simultaneous or sequential processes take place during the degradation of organic pollutants. The most frequently noticed reactions include the oxidative degradation of ring structures, hydration, dimerization, electron or charge transfer, hydroxylation, replacement, transformation, and rearrangement. In general, active reactive oxygen species (ROS) or photogenerated charge carriers may first remove a proton from a pollutant molecule or replace leaving groups such as halides for hydroxyl groups. Second, the bonds in organic pollutants that are particularly susceptible to degradation or those with less stereohindrance can be attacked by ROS or photogenerated charge carriers. Furthermore, smaller rings or cyclic structures, including three- to six-membered monocyclic compounds, are rapidly destroyed by ROS attacks due to the high ring strains. Radicals can combine to produce more resistant chemical species or unstable chemical species that can be further attacked by ROS to yield mineralized products.

For additional clarification, Figure 5 shows how typical antibiotics undergo bond breaking and degradation in bismuth-based photocatalysis. The antibiotic sulfamethoxazole, as an example, has a 4-aminobenzenesulfonamido group at the oxazole moiety's third position and a methyl substituent at the fifth position. The S–N bond is thought to be particularly susceptible to $^{\bullet}O_2^-$ attack (indicated as route 1), and ROS attack can readily disintegrate the oxazole ring (marked as route 2). Meanwhile, numerous reports have also been made on the hydroxylation of the benzene ring and the associated NH_2 (routes 3 and 4) [191,192].

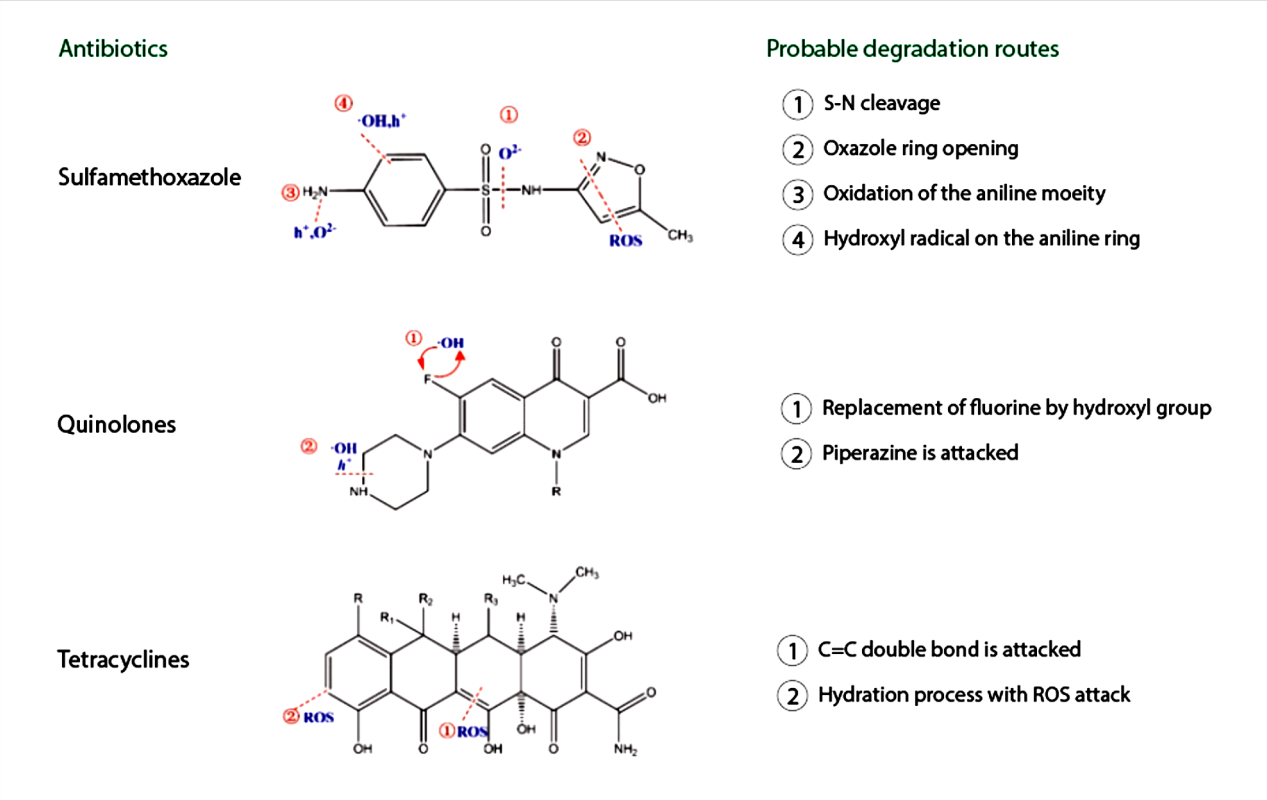

Figure 5: Photocatalytic degradation pathways of antibiotics by bismuth-based photocatalyst. (Adapted from [191], Environmental Research, Vol. 199, by K. Qin; Q. Zhao; H. Yu; X. Xia, J. Li; S. He; L. Wei; T. An, "A review of bismuth-based photocatalysts for antibiotic degradation: Insight into the photocatalytic degradation performance, pathways and relevant mechanisms ", Article No. 111360, Copyright (2021), with permission from Elsevier. This content is not subject to CC BY 4.0.)

$Bi_2WO_6/AgIO_3$ nanosheets were synthesised using a two-step hydrothermal process, according to recent research by Liu et al. [143] for the photocatalytic degradation of rhodamine B dye. The researchers stated that the degradation of rhodamine B dye by $Bi_2WO_6/AgIO_3$ nanosheets follows an S-scheme heterojunction mechanism (Figure 5a) during based on the electron spin resonance spectroscopy (ESR) result and relative energy band structure (valence and conduction bands).

The degradation mechanism may involve type-II heterojunctions, S-scheme heterojunctions, or Z-scheme heterojunctions, depending on the direction of electron–hole transmission. Specifically, when the Bi_2WO_6 and $AgIO_3$ are activated by visible-light irradiation, electrons are transported from the valence band to the conduction band, leaving an equivalent number of holes in the valence band. The electrons in the conduction band (CB) of Bi_2WO_6 were moved to the CB of $AgIO_3$ because its CB is more negative than that of $AgIO_3$. In contrast, the position of the $AgIO_3$ CB is greater than that of $O_2/{}^{\bullet}O_2^-$ (−0.33 eV vs NHE). Based on this finding, $AgIO_3$ CB electrons are unable to convert O_2 to ${}^{\bullet}O_2^-$, which is a limitation. However, the ESR results and radical trapping tests revealed that the major reactive radical in the photocatalytic experiments is ${}^{\bullet}O_2^-$. Hence, $Bi_2WO_6/AgIO_3$ is not compatible with the type-II heterojunction mechanism but with the S-scheme heterojunction mechanism. As seen in Figure 6a, when both semiconductors are in contact, the Bi_2WO_6 electrons migrate over the interface to $AgIO_3$ until the Fermi energy levels are equal. At the interface, an intrinsic electric field is created to stop further electron transmission. As a result, the S-scheme heterojunction mechanism boosted the redox capability of the $Bi_2WO_6/AgIO_3$ heterojunction, which greatly aided the photocatalytic decomposition of rhodamine B.

The degradation pathways for fluoroquinolone antibiotics (ciprofloxacin and norfloxacin) utilizing a metal-doped Bi_2WO_6 photocatalyst were identified by LC-MS/MS in another investigation by Zhu and co-workers [110]. In addition to additional peripheral moieties, ciprofloxacin has a quinolone moiety as its main functional group. The photocatalytic degradation of ciprofloxacin followed two pathways as depicted in Figure 6b and resulted in the identification of seven major intermediates by the authors. The loss of the $–C_2H_3N$ group, the fluorine atom, and the formaldehyde group, as well as the oxidation of the cyclopropyl and piperazine groups, served as indicators of the intermediates.

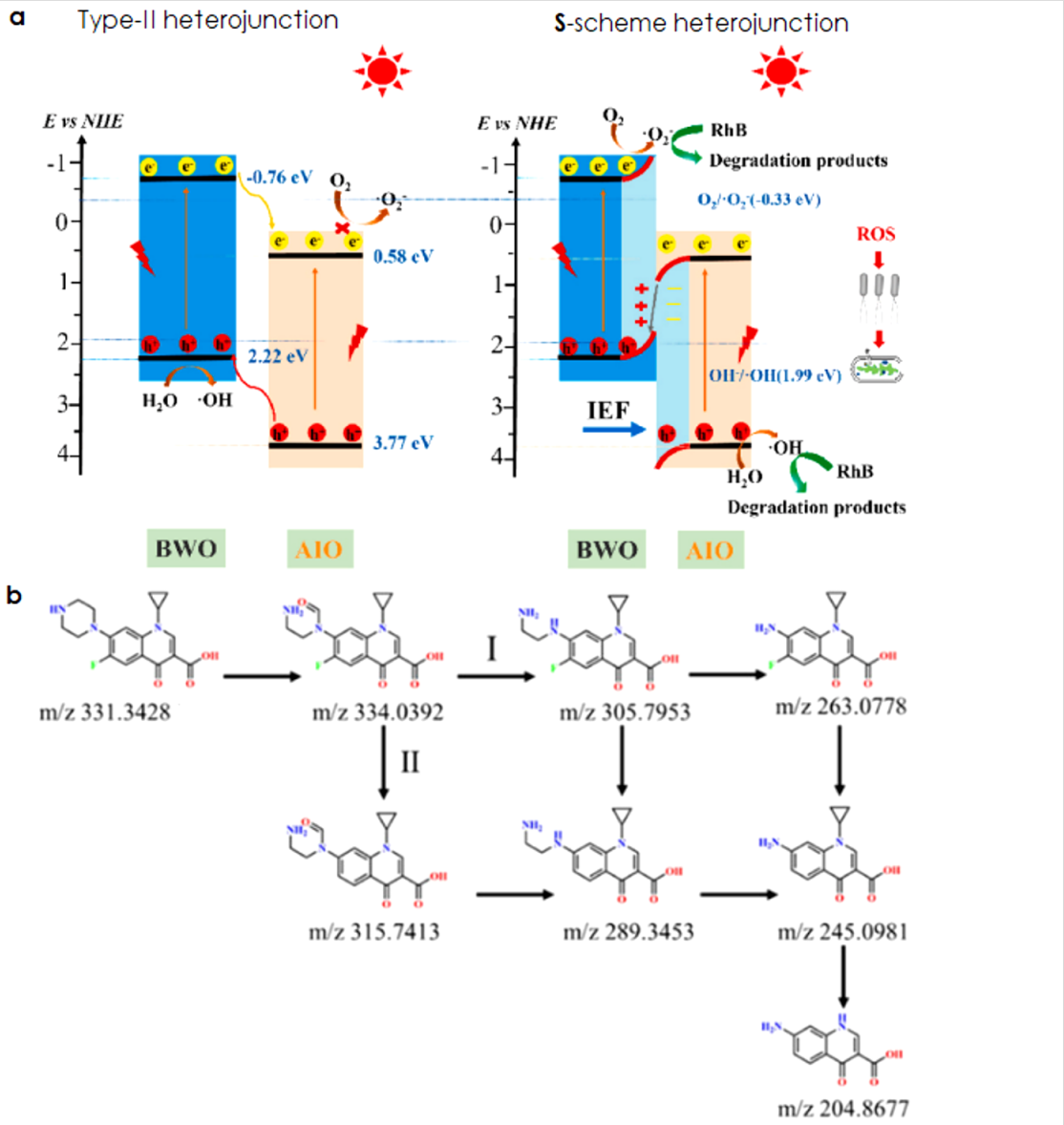

Figure 6: (a) Photocatalysis mechanisms of bismuth-based nanosheets via S-scheme heterojunction and type-II heterojunction systems (Figure 6a was adapted from [143], Ceramics International, Vol. 48, Issue 17, by Z. Liu; H. Wang; J. Duan; B. Hou, "An S-scheme heterojunction of Bi_2WO_6/$AgIO_3$ nanocomposites that enhances photocatalytic degradation of Rhodamine B and antifouling properties", Pages 24777–24787, Copyright (2022), with permission from Elsevier. This content is not subject to CC BY 4.0.). (b) The degradation pathways of ciprofloxacin by Mg-doped Bi_2WO_6 (Figure 6b was adapted from [110], Chemosphere, Vol. 252, by F. Zhu; Y. Lv; J. Li; J. Ding; X. Xia; L. Wei; J. Jiang; G. Zhang; Q. Zhao, "Enhanced visible light photocatalytic performance with metal-doped Bi_2WO_6 for typical fluoroquinolones degradation: Efficiencies, pathways and mechanisms", Article No. 126577, Copyright (2020), with permission from Elsevier. This content is not subject to CC BY 4.0.)

The majority of studies on the degradation of dyes or antibiotics showed that these pollutants were effectively destroyed by the active species produced from compounds based on bismuth, but some researchers also insisted that those organic pollutants could not be fully mineralized and eventually converted into intermediates or metabolites. For instance, Chu et al. [193] found that despite a 97% removal rate being recorded, only 31% of the total organic carbon was eliminated after 6 h of irradiating tetracycline (20 mg/L) with 0.5 g/L of Bi_2WO_6. By using LC-MS/GC-MS, a total of eight intermediates were identified. The primary intermediates were thought to be the by-products of the reaction between photogenerated hydroxyl radicals and holes, which led to the loss of amino, hydroxy, and *N*-methyl groups, as well as to a rearrangement process. Even though several reports have shown the degradation pathways inferred after analysis of the degraded products, these researchers have not reported the toxicity of the by-products, particularly for those that are not fully mineralized. Some of these intermediates may be more toxic than the parent compound. To clarify the transformation and toxicity of the interme-

diates of bismuth-based photocatalysts, more research is required.

Issues, challenges, and potential solutions

There are still some difficulties with several types of nanostructured bismuth-based photocatalysts despite their outstanding performance and widespread application in water remediation. In addition to discussing some current problems and challenges, this article also offers some potential solutions.

1. **Solubility and stability at low pH:** One of the difficulties with some bismuth salts is that they are unstable at low pH values and have low solubility constants, making them insoluble in aqueous solutions. Mineral acids, such as nitric acid or sulfuric acid, usually dissolve these compounds. The bismuth salt has been dissolved by some researchers using strong acids with concentrations as high as 5 M, which may further compromise its stability. The use of a combination of low concentrations of mineral acids and organic acids, such as citric acid or acetic acid, to dissolve the commonly used bismuth salts should be investigated in further studies.
2. **Nature of light source used for photocatalysis:** Several reports have used laboratory-scale UV–visible light lamps or bulbs or solar light simulators as sources of irradiation for the Bi-based photocatalysts during photocatalytic remediation of polluted water. Even though the majority of Bi-based photocatalysts have bandgaps that are suitable for direct sunlight irradiation, very few studies have been performed using this type of illumination. As a result, it is recommended that direct sunlight be used for photocatalysis rather than artificial solar light since it offers a more practical application and uses less energy. The majority of researchers also did not compute or present the actual light intensity that reached the effluent solution during treatment. This is encouraged to make it simple to scale up laboratory reactors to efficient field and industrial treatment units. Additionally, the majority of the studies lack actual photographs and detailed descriptions of the reactors that were used. This merits careful consideration because they offer a reliable basis for comparing photocatalysts.
3. **Multiple pollutants in lab settings and real wastewater:** The majority of studies only use one antibiotic or dye solution, which is far from the truth because wastewater (real effluents) frequently contains a mixture of dyes, dispersing agents, multiple pharmaceuticals, heavy metals, suspended solids, and surfactants. Therefore, the focus should be placed on researching the photocatalytic degradation of real wastewater and multipollutant solutions at the laboratory scale.
4. **Insufficient experimental details:** It has been noted that some researchers fail to provide a thorough account of their experimental procedures. Information such as the initial concentration of the target pollutant, photocatalyst dosage, solution pH, and reactor specifications, is often missing, which makes it difficult to compare their work fairly to that of other researchers.
5. **Instrumental analysis for trace concentration:** To estimate the degree of antibiotic degradation, the majority of researchers used UV–vis spectrophotometers. However, this instrument is less accurate when estimating trace levels of antibiotics, and there is also a significant chance that the antibiotics will oxidise to form more toxic intermediates that cannot be detected by UV–vis spectrophotometers. The percentage of total organic carbon removed from the analyte solution must be measured for fair comparison and an accurate assessment of the degree of degradation because this is an important indicator of how much the antibiotics are being mineralized. Future research should also examine the photocatalyst performance in both trace and concentrated dye solutions when using Bi-based photocatalysts to purify dye-polluted water.
6. **Recovery of powdered photocatalysts and toxicity:** Some of the nanopowder catalysts may escape and be discharged into the environment when nanostructured Bi-based photocatalysts are used to remediate pollutants. The production of reactive oxygen species and radicals might be hazardous to living organisms. There is presently no information on the toxicity of nanostructured Bi-based photocatalysts. Therefore, it is advised to produce magnetically recoverable nanostructured photocatalysts and do additional research on their toxicity.
7. **Recombination rate of photoinduced carriers:** Another problem is the recombination of holes and electrons, which lowers the photocatalytic performance. Tuning the energy bandgap, creating Schottky junctions or type-II heterojunction systems, using the Z-scheme, modifying the morphology, or using surface plasmon resonance are some of the methods used to overcome this particular problem. Future research should concentrate on combining these strategies to create a stable and remarkably exceptional photocatalyst. The majority of the 0-D quantum dot photocatalysts exhibit luminescence and other distinctive characteristics. Therefore, more research should focus on the development and use of low dimensional Bi-based photocatalysts.

Conclusion and Perspectives

Numerous studies have demonstrated that the distinctive physicochemical and optical characteristics and the electronic band

structures of bismuth-based nanostructure photocatalysts yield extraordinary photocatalytic activity under both visible and UV light. Numerous bismuth-based photocatalysts have also been extensively studied for their potential in detecting contaminants in the environment and addressing energy issues. There are still several challenges despite their outstanding photocatalytic performance. Although significant work has gone into improving the photocatalytic activity of bismuth-based photocatalysts, significant constraints regarding their application in the field of photocatalysis cannot be overlooked. In addition to describing problems and recent developments in photocatalysis, this article critically evaluates recently published research on nanostructured bismuth-based photocatalysts specifically for the remediation of water contaminated with textile dye and antibiotics. Researchers working on photocatalysts driven by visible light for efficient treatment of emerging trace contaminants may find the review work to be a useful resource.

Here, we have covered the fundamental workings of the photocatalytic process as well as the specifications for efficient photocatalysts. Outstanding visible-light activity, high stability, the capacity to efficiently separate and transfer photogenerated carriers with a low recombination rate, non-toxicity, adequate reusability, facile separation, and recovery after use are all requirements for a reliable and efficient photocatalyst. $BiFeO_3$, Bi_2WO_6, and Bi_2S_3 are a few of the bismuth-based photocatalysts that have fascinating physicochemical characteristics and favourable bandgap values (1.5–2.8 eV), which enables them to be activated by visible light in contrast to TiO_2 and ZnO semiconductors, which are often used and have wide bandgap values (>3.0 eV). Though some of the bismuth-based photocatalysts have intriguing characteristics, they nevertheless have a few drawbacks, such as rapid charge carrier recombination, delayed charge carrier migration, and low light absorption. Innovative low-energy synthesis techniques, morphological modulation, surface engineering, and bandgap tuning have been used by various groups to reduce these limitations. In this review, recent methods for creating extremely effective Bi-based photocatalysts are explored, including the creation of hybrid Schottky junctions and Z-scheme heterosystems. The review also looks at other operational parameters affecting the photocatalytic processes of Bi-based compounds used in water treatment. Although the majority of the experiments with Bi-based photocatalysts have used solar light simulators at the laboratory level, more thorough research into the use of direct sunlight and larger reactors with full specifications is advised to scale up its use and commercialization. This review is expected to pave the way for scientists to further develop Bi-based nanomaterials for the use in other processes, such as pollution sensing, photovoltaic systems, green energy harvesting and conversion, and catalytic systems other than photocatalytic processes.

ORCID® iDs

Akeem Adeyemi Oladipo - https://orcid.org/0000-0003-3715-5922
Faisal Suleiman Mustafa - https://orcid.org/0000-0003-0685-0025

References

1. Drinking-water. https://www.who.int/news-room/fact-sheets/detail/drinking-water (accessed Feb 1, 2023).
2. Boretti, A.; Rosa, L. *npj Clean Water* **2019,** *2,* 15. doi:10.1038/s41545-019-0039-9
3. World Water Assessment Programme (Nations Unies), The United Nations World Water Development Report 2018. United Nations Educational, Scientific and Cultural Organization: New York, United States, 2018; https://www.unwater.org/publications/world-water-development-report-2018 (accessed Feb 3, 2023).
4. Oladipo, A. A.; Mustafa, F. S.; Ezugwu, O. N.; Gazi, M. *Chemosphere* **2022,** *300,* 134532. doi:10.1016/j.chemosphere.2022.134532
5. Oladipo, A. A.; Ifebajo, A. O.; Vaziri, R. Green Adsorbents for Removal of Antibiotics, Pesticides and Endocrine Disruptors. In *Green Adsorbents for Pollutant Removal;* Crini, G.; Lichtfouse, E., Eds.; Environmental Chemistry for a Sustainable World, Vol. 19; Springer International Publishing: Cham, Switzerland, 2018; pp 327–351. doi:10.1007/978-3-319-92162-4_10
6. Abu Hasan, H.; Muhammad, M. H.; Ismail, N. I. *J. Water Process Eng.* **2020,** *33,* 101035. doi:10.1016/j.jwpe.2019.101035
7. Pan, Z.; Song, C.; Li, L.; Wang, H.; Pan, Y.; Wang, C.; Li, J.; Wang, T.; Feng, X. *Chem. Eng. J.* **2019,** *376,* 120909. doi:10.1016/j.cej.2019.01.188
8. Cui, H.; Huang, X.; Yu, Z.; Chen, P.; Cao, X. *RSC Adv.* **2020,** *10,* 20231–20244. doi:10.1039/d0ra02979c
9. Peng, H.; Guo, J. *Environ. Chem. Lett.* **2020,** *18,* 2055–2068. doi:10.1007/s10311-020-01058-x
10. Berillo, D.; Al-Jwaid, A.; Caplin, J. *Polymers (Basel, Switz.)* **2021,** *13,* 1073. doi:10.3390/polym13071073
11. Oladipo, A. A.; Gazi, M.; Ifebajo, A. O.; Oladipo, A. S.; Ahaka, E. O. Photocatalytic degradation of toxic pesticides. In *Photocatalysts in Advanced Oxidation Processes for Wastewater Treatment;* Fosso-Kankeu, E.; Pandey, S.; Ray, S. S., Eds.; Wiley: Chicago, 2020; pp 93–138. doi:10.1002/9781119631422.ch4
12. Miklos, D. B.; Remy, C.; Jekel, M.; Linden, K. G.; Drewes, J. E.; Hübner, U. *Water Res.* **2018,** *139,* 118–131. doi:10.1016/j.watres.2018.03.042
13. Garrido-Cardenas, J. A.; Esteban-García, B.; Agüera, A.; Sánchez-Pérez, J. A.; Manzano-Agugliaro, F. *Int. J. Environ. Res. Public Health* **2020,** *17,* 170. doi:10.3390/ijerph17010170
14. Babu, D. S.; Srivastava, V.; Nidheesh, P. V.; Kumar, M. S. *Sci. Total Environ.* **2019,** *696,* 133961. doi:10.1016/j.scitotenv.2019.133961
15. Priyadarshini, M.; Das, I.; Ghangrekar, M. M.; Blaney, L. *J. Environ. Manage.* **2022,** *316,* 115295. doi:10.1016/j.jenvman.2022.115295
16. Tian, K.; Hu, L.; Li, L.; Zheng, Q.; Xin, Y.; Zhang, G. *Chin. Chem. Lett.* **2022,** *33,* 4461–4477. doi:10.1016/j.cclet.2021.12.042
17. Munter, R. *Proc. Est. Acad. Sci., Chem.* **2001,** *50,* 59–80. doi:10.3176/chem.2001.2.01
18. Li, X.; Chen, Y.; Tao, Y.; Shen, L.; Xu, Z.; Bian, Z.; Li, H. *Chem Catal.* **2022,** *2,* 1315–1345. doi:10.1016/j.checat.2022.04.007

19. Oladipo, A. A. *J. Colloid Interface Sci.* **2021,** *591,* 193–202. doi:10.1016/j.jcis.2021.01.080
20. Mustafa, F. S.; Oladipo, A. A.; Gazi, M. *ChemistrySelect* **2022,** *7,* e202200727. doi:10.1002/slct.202200727
21. Ameta, S. C.; Ameta, R., Eds. *Advanced Oxidation Processes for Waste Water Treatment;* Elsevier, Academic Press, 2018. doi:10.1016/c2016-0-00384-4
22. Devendran, P.; Selvakumar, D.; Ramadoss, G.; Sivaramakrishnan, R.; Alagesan, T.; Jayavel, R.; Pandian, K. *Chemosphere* **2022,** *287,* 132091. doi:10.1016/j.chemosphere.2021.132091
23. Kader, S.; Al-Mamun, M. R.; Suhan, M. B. K.; Shuchi, S. B.; Islam, M. S. *Environ. Technol. Innovation* **2022,** *27,* 102476. doi:10.1016/j.eti.2022.102476
24. Kristl, M.; Sinanović, N.; Gyergyek, S.; Kristl, J. *Inorg. Chem. Commun.* **2020,** *112,* 107699. doi:10.1016/j.inoche.2019.107699
25. Devika, S.; Tayade, R. J. *Chemosphere* **2022,** *304,* 135300. doi:10.1016/j.chemosphere.2022.135300
26. Fang, B.; Xing, Z.; Sun, D.; Li, Z.; Zhou, W. *Adv. Powder Mater.* **2022,** *1,* 100021. doi:10.1016/j.apmate.2021.11.008
27. Sharma, S.; Kumar, M. *Mater. Today: Proc.* **2020,** *28,* 168–171. doi:10.1016/j.matpr.2020.01.496
28. Na-Phattalung, S.; Harding, D. J.; Pattanasattayavong, P.; Kim, H.; Lee, J.; Hwang, D.-W.; Chung, T. D.; Yu, J. *J. Phys. Chem. Solids* **2022,** *162,* 110503. doi:10.1016/j.jpcs.2021.110503
29. Ansari, S. A.; Cho, M. H. *Sci. Rep.* **2016,** *6,* 25405. doi:10.1038/srep25405
30. Davis, K.; Yarbrough, R.; Froeschle, M.; White, J.; Rathnayake, H. *RSC Adv.* **2019,** *9,* 14638–14648. doi:10.1039/c9ra02091h
31. Debanath, M. K.; Karmakar, S. *Mater. Lett.* **2013,** *111,* 116–119. doi:10.1016/j.matlet.2013.08.069
32. Karmaoui, M.; Jorge, A. B.; McMillan, P. F.; Aliev, A. E.; Pullar, R. C.; Labrincha, J. A.; Tobaldi, D. M. *ACS Omega* **2018,** *3,* 13227–13238. doi:10.1021/acsomega.8b02122
33. Khan, D.; Rehman, A.; Rafiq, M. Z.; Khan, A. M.; Ali, M. *Curr. Res. Green Sustainable Chem.* **2021,** *4,* 100079. doi:10.1016/j.crgsc.2021.100079
34. Zhu, Z.; Wan, S.; Zhao, Y.; Qin, Y.; Ge, X.; Zhong, Q.; Bu, Y. *Nano Sel.* **2021,** *2,* 187–215. doi:10.1002/nano.202000127
35. Wang, B.; Yang, H.; Xian, T.; Di, L. J.; Li, R. S.; Wang, X. X. *J. Nanomater.* **2015,** *2015,* 146327. doi:10.1155/2015/146327
36. Mustafa, F. S.; Oladipo, A. A. *Chemosphere* **2023,** *312,* 137348. doi:10.1016/j.chemosphere.2022.137348
37. Kumar, R.; Raizada, P.; Verma, N.; Hosseini-Bandegharaei, A.; Thakur, V. K.; Le, Q. V.; Nguyen, V.-H.; Selvasembian, R.; Singh, P. *J. Cleaner Prod.* **2021,** *297,* 126617. doi:10.1016/j.jclepro.2021.126617
38. Gupta, S. M.; Tripathi, M. *Chin. Sci. Bull.* **2011,** *56,* 1639–1657. doi:10.1007/s11434-011-4476-1
39. Irfan, S.; Zhuanghao, Z.; Li, F.; Chen, Y.-X.; Liang, G.-X.; Luo, J.-T.; Ping, F. *J. Mater. Res. Technol.* **2019,** *8,* 6375–6389. doi:10.1016/j.jmrt.2019.10.004
40. Sreedhar, A.; Ta, Q. T. H.; Noh, J.-S. *J. Ind. Eng. Chem. (Amsterdam, Neth.)* **2022,** *115,* 26–47. doi:10.1016/j.jiec.2022.08.013
41. El-Hakam, S. A.; ALShorifi, F. T.; Salama, R. S.; Gamal, S.; El-Yazeed, W. S. A.; Ibrahim, A. A.; Ahmed, A. I. *J. Mater. Res. Technol.* **2022,** *18,* 1963–1976. doi:10.1016/j.jmrt.2022.03.067
42. Li, Z.; Bao, Z.; Yao, F.; Cao, H.; Wang, J.; Qiu, L.; Lv, J.; Sun, X.; Zhang, Y.; Wu, Y. *J. Water Process Eng.* **2022,** *46,* 102599. doi:10.1016/j.jwpe.2022.102599
43. Zhou, G.; Tian, Z.; Sun, H.; Zhang, J.; Zhao, H.; Li, P.; Sun, H. *J. Phys. Chem. Solids* **2020,** *146,* 109577. doi:10.1016/j.jpcs.2020.109577
44. Saison, T.; Chemin, N.; Chanéac, C.; Durupthy, O.; Ruaux, V.; Mariey, L.; Maugé, F.; Beaunier, P.; Jolivet, J.-P. *J. Phys. Chem. C* **2011,** *115,* 5657–5666. doi:10.1021/jp109134z
45. Zheng, Q.; Cao, Y.; Huang, N.; Zhang, R.; Zhou, Y. *Acta Phys.-Chim. Sin.* **2021,** *37,* 2009063. doi:10.3866/pku.whxb202009063
46. Mu, F.; Dai, B.; Zhao, W.; Yang, X.; Zhao, X.; Guo, X. *Chin. Chem. Lett.* **2021,** *32,* 2539–2543. doi:10.1016/j.cclet.2020.12.016
47. Danner, M. C.; Robertson, A.; Behrends, V.; Reiss, J. *Sci. Total Environ.* **2019,** *664,* 793–804. doi:10.1016/j.scitotenv.2019.01.406
48. Kümmerer, K. *Chemosphere* **2009,** *75,* 417–434. doi:10.1016/j.chemosphere.2008.11.086
49. Singer, A. C.; Shaw, H.; Rhodes, V.; Hart, A. *Front. Microbiol.* **2016,** *7,* 1728. doi:10.3389/fmicb.2016.01728
50. Wise, R. *J. Antimicrob. Chemother.* **2002,** *49,* 585–586. doi:10.1093/jac/49.4.585
51. Van Boeckel, T. P.; Gandra, S.; Ashok, A.; Caudron, Q.; Grenfell, B. T.; Levin, S. A.; Laxminarayan, R. *Lancet Infect. Dis.* **2014,** *14,* 742–750. doi:10.1016/s1473-3099(14)70780-7
52. Browne, A. J.; Chipeta, M. G.; Haines-Woodhouse, G.; Kumaran, E. P. A.; Hamadani, B. H. K.; Zaraa, S.; Henry, N. J.; Deshpande, A.; Reiner, R. C., Jr.; Day, N. P. J.; Lopez, A. D.; Dunachie, S.; Moore, C. E.; Stergachis, A.; Hay, S. I.; Dolecek, C. *Lancet Planet. Health* **2021,** *5,* E893–E904. doi:10.1016/s2542-5196(21)00280-1
53. aus der Beek, T.; Weber, F.-A.; Bergmann, A.; Hickmann, S.; Ebert, I.; Hein, A.; Küster, A. *Environ. Toxicol. Chem.* **2016,** *35,* 823–835. doi:10.1002/etc.3339
54. Managaki, S.; Murata, A.; Takada, H.; Tuyen, B. C.; Chiem, N. H. *Environ. Sci. Technol.* **2007,** *41,* 8004–8010. doi:10.1021/es0709021
55. Segura, P. A.; Takada, H.; Correa, J. A.; El Saadi, K.; Koike, T.; Onwona-Agyeman, S.; Ofosu-Anim, J.; Sabi, E. B.; Wasonga, O. V.; Mghalu, J. M.; dos Santos, A. M., Junior.; Newman, B.; Weerts, S.; Yargeau, V. *Environ. Int.* **2015,** *80,* 89–97. doi:10.1016/j.envint.2015.04.001
56. Madikizela, L. M.; Tavengwa, N. T.; Chimuka, L. *J. Environ. Manage.* **2017,** *193,* 211–220. doi:10.1016/j.jenvman.2017.02.022
57. Agunbiade, F. O.; Moodley, B. *Environ. Toxicol. Chem.* **2016,** *35,* 36–46. doi:10.1002/etc.3144
58. European Commission. *Technical guidance document in support of Commission Directive 93/67/EEC on risk assessment for new notified substances and Commission Regulation (EC) No 1488/94 on risk assessment for existing substances. Part I*; Part II/Chapter 3: Environmental Risk Assessment. Luxembourg , 1996; https://op.europa.eu/en/publication-detail/-/publication/c78cc899-c742-11e6-a6db-01aa75ed71a1/language-en/format-PDF/source-280068741.
59. Molander, L.; Ågerstrand, M.; Rudén, C. *Regul. Toxicol. Pharmacol.* **2009,** *55,* 367–371. doi:10.1016/j.yrtph.2009.08.009
60. Singer, A. C.; Shaw, H.; Rhodes, V.; Hart, A. *Front. Microbiol.* **2016,** *7,* 1–22. doi:10.3389/fmicb.2016.01728

61. Zhou, L.; Li, S.; Li, F. *Environ. Res.* **2022,** *215,* 114188. doi:10.1016/j.envres.2022.114188
62. Javaid, A.; Latif, S.; Imran, M.; Hussain, N.; Rajoka, M. S. R.; Iqbal, H. M. N.; Bilal, M. *Chemosphere* **2022,** *291,* 133056. doi:10.1016/j.chemosphere.2021.133056
63. Ding, C.; He, J. *Appl. Microbiol. Biotechnol.* **2010,** *87,* 925–941. doi:10.1007/s00253-010-2649-5
64. Dickinson, A. W.; Power, A.; Hansen, M. G.; Brandt, K. K.; Piliposian, G.; Appleby, P.; O'Neill, P. A.; Jones, R. T.; Sierocinski, P.; Koskella, B.; Vos, M. *Environ. Int.* **2019,** *132,* 105117. doi:10.1016/j.envint.2019.105117
65. Ellepola, N.; Ogas, T.; Turner, D. N.; Gurung, R.; Maldonado-Torres, S.; Tello-Aburto, R.; Patidar, P. L.; Rogelj, S.; Piyasena, M. E.; Rubasinghege, G. *Ecotoxicol. Environ. Saf.* **2020,** *188,* 109892. doi:10.1016/j.ecoenv.2019.109892
66. Brain, R. A.; Hanson, M. L.; Solomon, K. R.; Brooks, B. W. Aquatic Plants Exposed to Pharmaceuticals: Effects and Risks. In *Reviews of Environmental Contamination and Toxicology;* Whitacre, D. M., Ed.; Springer: New York, NY, 2008; Vol. 192, pp 67–115. doi:10.1007/978-0-387-71724-1_3
67. Gothwal, R.; Shashidhar, T. *Clean: Soil, Air, Water* **2015,** *43,* 479–489. doi:10.1002/clen.201300989
68. Lellis, B.; Fávaro-Polonio, C. Z.; Pamphile, J. A.; Polonio, J. C. *Biotechnol. Res. Innovation* **2019,** *3,* 275–290. doi:10.1016/j.biori.2019.09.001
69. Mani, S.; Bharagava, R. N. Exposure to crystal violet, its toxic, genotoxic and carcinogenic effects on environment and its degradation and detoxification for environmental safety. In *Reviews of environmental contamination and toxicology;* de Voogt, P., Ed.; Springer International Publishing: Cham, Switzerland, 2016; Vol. 237, pp 71–104. doi:10.1007/978-3-319-23573-8_4
70. Kishor, R.; Purchase, D.; Saratale, G. D.; Saratale, R. G.; Ferreira, L. F. R.; Bilal, M.; Chandra, R.; Bharagava, R. N. *J. Environ. Chem. Eng.* **2021,** *9,* 105012. doi:10.1016/j.jece.2020.105012
71. Franceschini, F.; Jagdale, P.; Bartoli, M.; Tagliaferro, A. *Curr. Opin. Environ. Sci. Health* **2022,** *26,* 100345. doi:10.1016/j.coesh.2022.100345
72. Subhiksha, V.; Kokilavani, S.; Sudheer Khan, S. *Chemosphere* **2022,** *290,* 133228. doi:10.1016/j.chemosphere.2021.133228
73. Ajiboye, T. O.; Oyewo, O. A.; Onwudiwe, D. C. *Surf. Interfaces* **2021,** *23,* 100927. doi:10.1016/j.surfin.2021.100927
74. Lin, Z.; Yang, Z.; Huang, J. *Beilstein J. Nanotechnol.* **2022,** *13,* 745–762. doi:10.3762/bjnano.13.66
75. Cadenbach, T.; Benitez, M. J.; Morales, A. L.; Costa Vera, C.; Lascano, L.; Quiroz, F.; Debut, A.; Vizuete, K. *Beilstein J. Nanotechnol.* **2020,** *11,* 1822–1833. doi:10.3762/bjnano.11.164
76. Ao, M.; Liu, K.; Tang, X.; Li, Z.; Peng, Q.; Huang, J. *Beilstein J. Nanotechnol.* **2019,** *10,* 1412–1422. doi:10.3762/bjnano.10.139
77. Wu, S.; Xu, Z.; Zhang, J.; Zhu, M. *Sol. RRL* **2021,** *5,* 2100668. doi:10.1002/solr.202100668
78. Hofmann, P. *Prog. Surf. Sci.* **2006,** *81,* 191–245. doi:10.1016/j.progsurf.2006.03.001
79. Wang, F.; Tang, R.; Yu, H.; Gibbons, P. C.; Buhro, W. E.; Louis, S. *Chem. Mater.* **2008,** *20,* 3656–3662. doi:10.1021/cm8004425
80. Hoffman, C. A.; Meyer, J. R.; Bartoli, F. J.; Di Venere, A.; Yi, X. J.; Hou, C. L.; Wang, H. C.; Ketterson, J. B.; Wong, G. K. *Phys. Rev. B* **1993,** *48,* 11431–11434. doi:10.1103/physrevb.48.11431
81. Qi, J.; Shi, D.; Zhao, J.; Jiang, X. *J. Phys. Chem. C* **2008,** *112,* 10745–10753. doi:10.1021/jp801735g
82. Song, S.; Xing, Z.; Zhao, H.; Li, Z. *Green Energy Environ.* **2022,** in press. doi:10.1016/j.gee.2022.04.004
83. Sirimanne, P. M.; Takahashi, K.; Sonoyama, N.; Sakata, T. *Sol. Energy Mater. Sol. Cells* **2002,** *73,* 175–187. doi:10.1016/s0927-0248(01)00123-4
84. Walsh, A.; Yan, Y.; Huda, M. N.; Al-Jassim, M. M.; Wei, S.-H. *Chem. Mater.* **2009,** *21,* 547–551. doi:10.1021/cm802894z
85. Ran, Z.; Wang, X.; Li, Y.; Yang, D.; Zhao, X.-G.; Biswas, K.; Singh, D. J.; Zhang, L. *npj Comput. Mater.* **2018,** *4,* 14. doi:10.1038/s41524-018-0071-1
86. Amiri-Shookoh, F.; Aliabad, H. A. R.; Tavakoli-Anbaran, H. *Indian J. Phys.* **2022,** 2458. doi:10.1007/s12648-022-02458-1
87. Irfan, S.; Khan, S. B.; Lam, S. S.; Ong, H. C.; Aizaz Ud Din, M.; Dong, F.; Chen, D. *Chemosphere* **2022,** *302,* 134750. doi:10.1016/j.chemosphere.2022.134750
88. Mittal, S.; Garg, S.; Bhandari, H.; Sharma, V. *Inorg. Chem. Commun.* **2022,** *144,* 109834. doi:10.1016/j.inoche.2022.109834
89. Safi, R.; Shokrollahi, H. *Prog. Solid State Chem.* **2012,** *40,* 6–15. doi:10.1016/j.progsolidstchem.2012.03.001
90. Ponraj, C.; Vinitha, G.; Daniel, J. *Environ. Nanotechnol. Monit. Manage.* **2017,** *7,* 110–120. doi:10.1016/j.enmm.2017.02.001
91. Wang, X.; Lin, Y.; Ding, X.; Jiang, J. *J. Alloys Compd.* **2011,** *509,* 6585–6588. doi:10.1016/j.jallcom.2011.03.074
92. Liu, Z.; Qi, Y.; Lu, C. *J. Mater. Sci.: Mater. Electron.* **2010,** *21,* 380–384. doi:10.1007/s10854-009-9928-x
93. Bharathkumar, S.; Sakar, M.; Balakumar, S. *J. Phys. Chem. C* **2016,** *120,* 18811–18821. doi:10.1021/acs.jpcc.6b04344
94. Li, S.; Lin, Y.-H.; Zhang, B.-P.; Nan, C.-W.; Wang, Y. *J. Appl. Phys.* **2009,** *105,* 056105. doi:10.1063/1.3080131
95. Xue, Z.; Wang, T.; Chen, B.; Malkoske, T.; Yu, S.; Tang, Y. *Materials* **2015,** *8,* 6360–6378. doi:10.3390/ma8095310
96. Xing, H.; Gao, S.; Zhang, J.; Xu, Y.; Du, H.; Zhu, Z.; Wang, J.; Yao, Y.; Zhang, S.; Ren, L. *J. Alloys Compd.* **2021,** *854,* 157281. doi:10.1016/j.jallcom.2020.157281
97. Nazir, A.; Latif, S.; Adil, S. F.; Kuniyil, M.; Imran, M.; Hatshan, M. R.; Kanwal, F.; Shaik, B. *Materials* **2022,** *15,* 213. doi:10.3390/ma15010213
98. Jiang, Y.; Xing, C.; Chen, Y.; Shi, J.; Wang, S. *Environ. Sci. Pollut. Res.* **2022,** *29,* 57656–57668. doi:10.1007/s11356-022-19806-7
99. Dumitru, R.; Ianculescu, A.; Păcurariu, C.; Lupa, L.; Pop, A.; Vasile, B.; Surdu, A.; Manea, F. *Ceram. Int.* **2019,** *45,* 2789–2802. doi:10.1016/j.ceramint.2018.07.298
100. Sharmin, F.; Basith, M. A. *J. Alloys Compd.* **2022,** *901,* 163604. doi:10.1016/j.jallcom.2021.163604
101. Xiang, Y.; Ju, P.; Wang, Y.; Sun, Y.; Zhang, D.; Yu, J. *Chem. Eng. J.* **2016,** *288,* 264–275. doi:10.1016/j.cej.2015.11.103
102. Chen, T.; Liu, L.; Hu, C.; Huang, H. *Chin. J. Catal.* **2021,** *42,* 1413–1438. doi:10.1016/s1872-2067(20)63769-x
103. Orimolade, B. O.; Idris, A. O.; Feleni, U.; Mamba, B. *Environ. Pollut.* **2021,** *289,* 117891. doi:10.1016/j.envpol.2021.117891
104. Zhang, L.; Wang, H.; Chen, Z.; Wong, P. K.; Liu, J. *Appl. Catal., B* **2011,** *106,* 1–13. doi:10.1016/j.apcatb.2011.05.008
105. Saison, T.; Gras, P.; Chemin, N.; Chanéac, C.; Durupthy, O.; Brezová, V.; Colbeau-Justin, C.; Jolivet, J.-P. *J. Phys. Chem. C* **2013,** *117,* 22656–22666. doi:10.1021/jp4048192

106. Yi, H.; Qin, L.; Huang, D.; Zeng, G.; Lai, C.; Liu, X.; Li, B.; Wang, H.; Zhou, C.; Huang, F.; Liu, S.; Guo, X. *Chem. Eng. J.* **2019,** *358,* 480–496. doi:10.1016/j.cej.2018.10.036
107. Liu, X.; Gu, S.; Zhao, Y.; Zhou, G.; Li, W. *J. Mater. Sci. Technol.* **2020,** *56,* 45–68. doi:10.1016/j.jmst.2020.04.023
108. Zhao, Y.; Wang, Y.; Liu, E.; Fan, J.; Hu, X. *Appl. Surf. Sci.* **2018,** *436,* 854–864. doi:10.1016/j.apsusc.2017.12.064
109. Kaur, A.; Kansal, S. K. *Chem. Eng. J.* **2016,** *302,* 194–203. doi:10.1016/j.cej.2016.05.010
110. Zhu, F.; Lv, Y.; Li, J.; Ding, J.; Xia, X.; Wei, L.; Jiang, J.; Zhang, G.; Zhao, Q. *Chemosphere* **2020,** *252,* 126577. doi:10.1016/j.chemosphere.2020.126577
111. Huang, C.; Chen, L.; Li, H.; Mu, Y.; Yang, Z. *RSC Adv.* **2019,** *9,* 27768–27779. doi:10.1039/c9ra04445k
112. Wang, J.-j.; Tang, L.; Zeng, G.-m.; Zhou, Y.-y.; Deng, Y.-c.; Fan, C.-z.; Gong, J.-l.; Liu, Y.-n. *Trans. Nonferrous Met. Soc. China* **2017,** *27,* 1794–1803. doi:10.1016/s1003-6326(17)60202-4
113. Lai, M. T. L.; Lai, C. W.; Lee, K. M.; Chook, S. W.; Yang, T. C. K.; Chong, S. H.; Juan, J. C. *J. Alloys Compd.* **2019,** *801,* 502–510. doi:10.1016/j.jallcom.2019.06.116
114. Shad, N. A.; Zahoor, M.; Bano, K.; Bajwa, S. Z.; Amin, N.; Ihsan, A.; Soomro, R. A.; Ali, A.; Imran Arshad, M.; Wu, A.; Iqbal, M. Z.; Khan, W. S. *Inorg. Chem. Commun.* **2017,** *86,* 213–217. doi:10.1016/j.inoche.2017.10.022
115. Liang, L.; Tursun, Y.; Nulahong, A.; Dilinuer, T.; Tunishaguli, A.; Gao, G.; Abulikemu, A.; Okitsu, K. *Ultrason. Sonochem.* **2017,** *39,* 93–100. doi:10.1016/j.ultsonch.2017.03.054
116. Wang, S.; Yang, H.; Wang, X.; Feng, W. *J. Electron. Mater.* **2019,** *48,* 2067–2076. doi:10.1007/s11664-019-07045-5
117. Pramila, S.; Ranganatha, V. L.; Soundarya, T. L.; Ramu, R.; Nagaraju, G.; Mallikarjunaswamy, C. *J. Cluster Sci.* **2022,** *33,* 2233–2248. doi:10.1007/s10876-021-02147-9
118. Wang, L.; Wang, Z.; Zhang, L.; Hu, C. *Chem. Eng. J.* **2018,** *352,* 664–672. doi:10.1016/j.cej.2018.07.028
119. Batool, M.; Nazar, M. F.; Awan, A.; Tahir, M. B.; Rahdar, A.; Shalan, A. E.; Lanceros-Méndez, S.; Zafar, M. N. *Nano-Struct. Nano-Objects* **2021,** *27,* 100762. doi:10.1016/j.nanoso.2021.100762
120. Zhang, Z.; Wang, W.; Shang, M.; Yin, W. *J. Hazard. Mater.* **2010,** *177,* 1013–1018. doi:10.1016/j.jhazmat.2010.01.020
121. Tian, N.; Hu, C.; Wang, J.; Zhang, Y.; Ma, T.; Huang, H. *Coord. Chem. Rev.* **2022,** *463,* 214515. doi:10.1016/j.ccr.2022.214515
122. Lin, X.; Liu, Z.; Guo, X.; Liu, C.; Zhai, H.; Wang, Q.; Chang, L. *Mater. Sci. Eng., B* **2014,** *188,* 35–42. doi:10.1016/j.mseb.2014.06.005
123. Phu, N. D.; Hoang, L. H.; Chen, X.-B.; Kong, M.-H.; Wen, H.-C.; Chou, W. C. *J. Alloys Compd.* **2015,** *647,* 123–128. doi:10.1016/j.jallcom.2015.06.047
124. Wang, Y.; Jiang, W.; Luo, W.; Chen, X.; Zhu, Y. *Appl. Catal., B* **2018,** *237,* 633–640. doi:10.1016/j.apcatb.2018.06.013
125. Narenuch, T.; Senasu, T.; Chankhanittha, T.; Nanan, S. *Molecules* **2021,** *26,* 5624. doi:10.3390/molecules26185624
126. Chen, F.; Yang, Q.; Wang, Y.; Yao, F.; Ma, Y.; Huang, X.; Li, X.; Wang, D.; Zeng, G.; Yu, H. *Chem. Eng. J.* **2018,** *348,* 157–170. doi:10.1016/j.cej.2018.04.170
127. Yan, M.; Yan, Y.; Wu, Y.; Shi, W.; Hua, Y. *RSC Adv.* **2015,** *5,* 90255–90264. doi:10.1039/c5ra13684a
128. Chen, M.; Dai, Y.; Guo, J.; Yang, H.; Liu, D.; Zhai, Y. *Appl. Surf. Sci.* **2019,** *493,* 1361–1367. doi:10.1016/j.apsusc.2019.04.160
129. Kumar, A.; Kumar, A.; Sharma, G.; Al-Muhtaseb, A. H.; Naushad, M.; Ghfar, A. A.; Stadler, F. J. *Chem. Eng. J.* **2018,** *334,* 462–478. doi:10.1016/j.cej.2017.10.049
130. Qin, H.; Wang, K.; Jiang, L.; Li, J.; Wu, X.; Zhang, G. *J. Alloys Compd.* **2020,** *821,* 153417. doi:10.1016/j.jallcom.2019.153417
131. Gan, H.; Yi, F.; Zhang, H.; Qian, Y.; Jin, H.; Zhang, K. *Chin. J. Chem. Eng.* **2018,** *26,* 2628–2635. doi:10.1016/j.cjche.2018.02.017
132. Abraham, S. D.; David, S. T.; Bennie, R. B.; Joel, C.; Kumar, D. S. *J. Mol. Struct.* **2016,** *1113,* 174–181. doi:10.1016/j.molstruc.2016.01.053
133. Gao, Y.; Wang, L.; Li, Z.; Li, C.; Cao, X.; Zhou, A.; Hu, Q. *Mater. Lett.* **2014,** *136,* 295–297. doi:10.1016/j.matlet.2014.08.026
134. Raza, W.; Haque, M. M.; Muneer, M.; Harada, T.; Matsumura, M. *J. Alloys Compd.* **2015,** *648,* 641–650. doi:10.1016/j.jallcom.2015.06.245
135. Ma, Y.; Bian, Y.; Tan, P.; Shang, Y.; Liu, Y.; Wu, L.; Zhu, A.; Liu, W.; Xiong, X.; Pan, J. *J. Colloid Interface Sci.* **2017,** *497,* 144–154. doi:10.1016/j.jcis.2017.03.010
136. Zhang, Y.; Sun, X.; Yang, G.; Zhu, Y.; Si, H.; Zhang, J.; Li, Y. *Mater. Sci. Semicond. Process.* **2016,** *41,* 193–199. doi:10.1016/j.mssp.2015.08.040
137. Phuruangrat, A.; Dumrongrojthanath, P.; Ekthammathat, N.; Thongtem, S.; Thongtem, T. *J. Nanomater.* **2014,** *2014,* 138561. doi:10.1155/2014/138561
138. Sun, D.; Li, J.; He, L.; Zhao, B.; Wang, T.; Li, R.; Yin, S.; Feng, Z.; Sato, T. *CrystEngComm* **2014,** *16,* 7564–7574. doi:10.1039/c4ce00596a
139. Huang, Y.; Zhang, X.; Zhang, K.; Lu, P.; Zhang, D. *J. Nanopart. Res.* **2018,** *20,* 328. doi:10.1007/s11051-018-4431-z
140. Josephine, A. J.; Dhas, C. R.; Venkatesh, R.; Arivukarasan, D.; Christy, A. J.; Monica, S. E. S.; Keerthana, S. *Mater. Res. Express* **2020,** *7,* 015036. doi:10.1088/2053-1591/ab653f
141. Karnan, T.; Selvakumar, S. A. S.; Adinaveen, T.; Suresh, J. *Int. J. Sci. Eng. Res.* **2016,** *7,* 266.
142. Siddique, M.; Khan, N. M.; Saeed, M. *Z. Phys. Chem.* **2019,** *233,* 595–607. doi:10.1515/zpch-2018-1225
143. Liu, Z.; Wang, H.; Duan, J.; Hou, B. *Ceram. Int.* **2022,** *48,* 24777–24787. doi:10.1016/j.ceramint.2022.05.127
144. Shao, W.; Wang, H.; Zhang, X. *Dalton Trans.* **2018,** *47,* 12642–12646. doi:10.1039/c8dt02613k
145. Qiu, Y.; Lu, J.; Yan, Y.; Niu, J. *J. Hazard. Mater.* **2022,** *422,* 126920. doi:10.1016/j.jhazmat.2021.126920
146. Mustafa, F. S.; Oladipo, A. A. *J. Water Process Eng.* **2021,** *42,* 102132. doi:10.1016/j.jwpe.2021.102132
147. Shen, J.; Xue, J.; Chen, Z.; Ni, J.; Tang, B.; He, G.; Chen, H. *J. Mater. Sci.* **2018,** *53,* 4848–4860. doi:10.1007/s10853-017-1885-9
148. Irfan, S.; Rizwan, S.; Shen, Y.; Tomovska, R.; Zulfiqar, S.; Sarwar, M. I.; Nan, C.-W. *RSC Adv.* **2016,** *6,* 114183–114189. doi:10.1039/c6ra23674j
149. Zhang, J.; Zhu, K.; Zhu, Y.; Qin, C.; Liu, L.; Liu, D.; Wang, Y.; Gan, W.; Fu, X.; Hao, H. *Chem. Phys. Lett.* **2020,** *750,* 137483. doi:10.1016/j.cplett.2020.137483
150. Lv, X.; Yan, D. Y. S.; Lam, F. L.-Y.; Ng, Y. H.; Yin, S.; An, A. K. *Chem. Eng. J.* **2020,** *401,* 126012. doi:10.1016/j.cej.2020.126012
151. Zhong, X.; Zhang, K.-X.; Wu, D.; Ye, X.-Y.; Huang, W.; Zhou, B.-X. *Chem. Eng. J.* **2020,** *383,* 123148. doi:10.1016/j.cej.2019.123148
152. Liu, F.; Liang, J.; Chen, L.; Tong, M.; Liu, W. *J. Mol. Liq.* **2019,** *275,* 807–814. doi:10.1016/j.molliq.2018.11.119

153. Liu, Z.; Liu, J.; Wang, H.; Cao, G.; Niu, J. *J. Colloid Interface Sci.* **2016,** *463,* 324–331. doi:10.1016/j.jcis.2015.10.028
154. Yu, C.; He, H.; Fan, Q.; Xie, W.; Liu, Z.; Ji, H. *Sci. Total Environ.* **2019,** *694,* 133727. doi:10.1016/j.scitotenv.2019.133727
155. Zeng, L.; Zhe, F.; Wang, Y.; Zhang, Q.; Zhao, X.; Hu, X.; Wu, Y.; He, Y. *J. Colloid Interface Sci.* **2019,** *539,* 563–574. doi:10.1016/j.jcis.2018.12.101
156. Low, J.; Yu, J.; Jaroniec, M.; Wageh, S.; Al-Ghamdi, A. A. *Adv. Mater. (Weinheim, Ger.)* **2017,** *29,* 1601694. doi:10.1002/adma.201601694
157. Oladipo, A. A. *J. Water Process Eng.* **2021,** *40,* 101932. doi:10.1016/j.jwpe.2021.101932
158. Azalok, K. A.; Oladipo, A. A.; Gazi, M. *Chemosphere* **2021,** *268,* 128844. doi:10.1016/j.chemosphere.2020.128844
159. Azalok, K. A.; Oladipo, A. A.; Gazi, M. *J. Photochem. Photobiol., A* **2021,** *405,* 112976. doi:10.1016/j.jphotochem.2020.112976
160. Shen, H.; Liu, G.; Zhao, Y.; Li, D.; Jiang, J.; Ding, J.; Mao, B.; Shen, H.; Kim, K.-S.; Shi, W. *Fuel* **2020,** *259,* 116311. doi:10.1016/j.fuel.2019.116311
161. He, F.; Zhu, B.; Cheng, B.; Yu, J.; Ho, W.; Macyk, W. *Appl. Catal., B* **2020,** *272,* 119006. doi:10.1016/j.apcatb.2020.119006
162. Oladipo, A. A.; Ifebajo, A. O.; Gazi, M. *Appl. Catal., B* **2019,** *243,* 243–252. doi:10.1016/j.apcatb.2018.10.050
163. Chae, S. Y.; Lee, C. S.; Jung, H.; Joo, O.-S.; Min, B. K.; Kim, J. H.; Hwang, Y. J. *ACS Appl. Mater. Interfaces* **2017,** *9,* 19780–19790. doi:10.1021/acsami.7b02486
164. Li, S.; Lin, Y.-H.; Zhang, B.-P.; Li, J.-F.; Nan, C.-W. *J. Appl. Phys.* **2009,** *105,* 054310. doi:10.1063/1.3091286
165. Low, J.; Jiang, C.; Cheng, B.; Wageh, S.; Al-Ghamdi, A. A.; Yu, J. *Small Methods* **2017,** *1,* 1700080. doi:10.1002/smtd.201700080
166. Shen, S.; Zhang, H.; Xu, A.; Zhao, Y.; Lin, Z.; Wang, Z.; Zhong, W.; Feng, S. *J. Alloys Compd.* **2021,** *875,* 160071. doi:10.1016/j.jallcom.2021.160071
167. Chava, R. K.; Son, N.; Kang, M. *Chemosphere* **2022,** *300,* 134570. doi:10.1016/j.chemosphere.2022.134570
168. Yadav, M.; Garg, S.; Chandra, A.; Hernadi, K. *J. Colloid Interface Sci.* **2019,** *555,* 304–314. doi:10.1016/j.jcis.2019.07.090
169. Sharma, S.; Ibhadon, A. O.; Francesconi, M. G.; Mehta, S. K.; Elumalai, S.; Kansal, S. K.; Umar, A.; Baskoutas, S. *Nanomaterials* **2020,** *10,* 910. doi:10.3390/nano10050910
170. Wang, W.; Han, Q.; Zhu, Z.; Zhang, L.; Zhong, S.; Liu, B. *Adv. Powder Technol.* **2019,** *30,* 1882–1896. doi:10.1016/j.apt.2019.06.006
171. Shi, Z.; Zhang, Y.; Shen, X.; Duoerkun, G.; Zhu, B.; Zhang, L.; Li, M.; Chen, Z. *Chem. Eng. J.* **2020,** *386,* 124010. doi:10.1016/j.cej.2020.124010
172. Zhuang, X.; Li, X.; Yang, Y.; Wang, N.; Shang, Y.; Zhou, Z.; Li, J.; Wang, H. *Water* **2020,** *12,* 2273. doi:10.3390/w12082273
173. Wen, X.-J.; Qian-Lu; Lv, X.-X.; Sun, J.; Guo, J.; Fei, Z.-H.; Niu, C.-G. *J. Hazard. Mater.* **2020,** *385,* 121508. doi:10.1016/j.jhazmat.2019.121508
174. Zhao, Y.; Liang, X.; Wang, Y.; Shi, H.; Liu, E.; Fan, J.; Hu, X. *J. Colloid Interface Sci.* **2018,** *523,* 7–17. doi:10.1016/j.jcis.2018.03.078
175. Chen, F.; Huang, H.; Zhang, Y.; Zhang, T. *Chin. Chem. Lett.* **2017,** *28,* 2244–2250. doi:10.1016/j.cclet.2017.09.017
176. Imam, S. S.; Adnan, R.; Mohd Kaus, N. H. *Colloids Surf., A* **2020,** *585,* 124069. doi:10.1016/j.colsurfa.2019.124069
177. Lam, S.-M.; Sin, J.-C.; Mohamed, A. R. *Mater. Sci. Semicond. Process.* **2016,** *47,* 62–84. doi:10.1016/j.mssp.2016.02.019
178. Li, Z.; Shen, Y.; Yang, C.; Lei, Y.; Guan, Y.; Lin, Y.; Liu, D.; Nan, C.-W. *J. Mater. Chem. A* **2013,** *1,* 823–829. doi:10.1039/c2ta00141a
179. Li, Z.; Shen, Y.; Guan, Y.; Hu, Y.; Lin, Y.; Nan, C.-W. *J. Mater. Chem. A* **2014,** *2,* 1967–1973. doi:10.1039/c3ta14269h
180. Wang, X.; Mao, W.; Zhang, J.; Han, Y.; Quan, C.; Zhang, Q.; Yang, T.; Yang, J.; Li, X.; Huang, W. *J. Colloid Interface Sci.* **2015,** *448,* 17–23. doi:10.1016/j.jcis.2015.01.090
181. Mohamed, H. E. A.; Sone, B. T.; Khamlich, S.; Coetsee-Hugo, E.; Swart, H. C.; Thema, T.; Sbiaa, R.; Dhlamini, M. S. *Mater. Today: Proc.* **2021,** *36,* 328–335. doi:10.1016/j.matpr.2020.04.119
182. Li, Y.-F.; Zhang, M.; Guo, D.-L.; He, F.-X.; Li, Y.-Z.; Wang, A.-J. *J. Nanomater.* **2014,** *2014,* 347061. doi:10.1155/2014/347061
183. Huang, K.-T.; Yeh, S.-B.; Huang, C.-J. *ACS Appl. Mater. Interfaces* **2015,** *7,* 21021–21029. doi:10.1021/acsami.5b07362
184. An, L.; Wang, G.; Cheng, Y.; Zhao, L.; Gao, F.; Tian, Y. *Res. Chem. Intermed.* **2015,** *41,* 7449–7461. doi:10.1007/s11164-014-1836-x
185. Mendoza-Mendoza, E.; Nuñez-Briones, A. G.; Ysiwata-Rivera, A. P.; Moral-Rodríguez, A. I.; García-Cerda, L. A.; Peralta-Rodríguez, R. D.; Rodríguez-Hernández, J.; Rodríguez-López, J. L. *Water, Air, Soil Pollut.* **2020,** *231,* 219. doi:10.1007/s11270-020-04566-2
186. Souza, J. S.; Hirata, F. T. H.; Corio, P. *J. Nanopart. Res.* **2019,** *21,* 35. doi:10.1007/s11051-019-4476-7
187. Wang, Z.; Cai, X.; Xie, X.; Li, S.; Zhang, X.; Wang, Z. *Sci. Total Environ.* **2021,** *764,* 142879. doi:10.1016/j.scitotenv.2020.142879
188. Chen, M.; Huang, Y.; Chu, W. *Chin. J. Catal.* **2019,** *40,* 673–680. doi:10.1016/s1872-2067(19)63285-7
189. Anwar, K.; Naqvi, F. K.; Beg, S.; Haneef, S. *J. Mol. Struct.* **2023,** *1272,* 134183. doi:10.1016/j.molstruc.2022.134183
190. Huang, D.; Li, J.; Zeng, G.; Xue, W.; Chen, S.; Li, Z.; Deng, R.; Yang, Y.; Cheng, M. *Chem. Eng. J.* **2019,** *375,* 121991. doi:10.1016/j.cej.2019.121991
191. Qin, K.; Zhao, Q.; Yu, H.; Xia, X.; Li, J.; He, S.; Wei, L.; An, T. *Environ. Res.* **2021,** *199,* 111360. doi:10.1016/j.envres.2021.111360
192. Niu, J.; Zhang, L.; Li, Y.; Zhao, J.; Lv, S.; Xiao, K. *J. Environ. Sci.* **2013,** *25,* 1098–1106. doi:10.1016/s1001-0742(12)60167-3
193. Chu, X.; Shan, G.; Chang, C.; Fu, Y.; Yue, L.; Zhu, L. *Front. Environ. Sci. Eng.* **2016,** *10,* 211–218. doi:10.1007/s11783-014-0753-y

BEILSTEIN JOURNAL OF NANOTECHNOLOGY

Titania nanoparticles for photocatalytic degradation of ethanol under simulated solar light

Evghenii Goncearenco[1], Iuliana P. Morjan[1], Claudiu Teodor Fleaca[1], Florian Dumitrache[1], Elena Dutu[1], Monica Scarisoreanu[*1,§], Valentin Serban Teodorescu[2], Alexandra Sandulescu[3], Crina Anastasescu[3] and Ioan Balint[3]

Full Research Paper

Open Access

Address:
[1]National Institute for Lasers, Plasma and Radiation Physics, Atomistilor Str., No. 409, 077125, Bucharest-Magurele, Romania, [2]National Institute of Materials Physics, Atomistilor Str., No. 405A, 077125, Bucharest-Magurele, Romania and [3]Romanian Academy, Inst. Phys. Chem. Ilie Murgulescu, 202 Spl. Independentei, 060021, Bucharest, Romania

Email:
Monica Scarisoreanu[*] - monica.scarisoreanu@inflpr.ro

* Corresponding author
§ Tel.: +4021-4574489; fax: +4021-4574243

Keywords:
ethanol; H_2 production; laser pyrolysis; photocatalyst; TiO_2 nanoparticles

Beilstein J. Nanotechnol. **2023,** *14,* 616–630.
https://doi.org/10.3762/bjnano.14.51

Received: 31 January 2023
Accepted: 02 May 2023
Published: 22 May 2023

This article is part of the thematic issue "Nanomaterials for photocatalysis and applications in environmental remediation and renewable energy".

Guest Editor: V. V. Pham

Abstract

TiO_2 nanoparticles were synthesized by laser pyrolysis from $TiCl_4$ vapor in air in the presence of ethylene as sensitizer at different working pressures (250–850 mbar) with and without further calcination at 450 °C. The obtained powders were analyzed by energy-dispersive X-ray spectroscopy, X-ray photoelectron spectroscopy, X-ray diffractometry, and transmission electron microscopy. Also, specific surface area and photoluminescence with optical absorbance were evaluated. By varying the synthesis parameters (especially the working pressure), different TiO_2 nanopowders were obtained, whose photodegradation properties were tested compared to a commercial Degussa P25 sample. Two series of samples were obtained. Series "a" includes thermally treated TiO_2 nanoparticles (to remove impurities) that have different proportions of the anatase phase (41.12–90.74%) mixed with rutile and small crystallite sizes of 11–22 nm. Series "b" series represents nanoparticles with high purity, which did not require thermal treatment after synthesis (ca. 1 atom % of impurities). These nanoparticles show an increased anatase phase content (77.33–87.42%) and crystallite sizes of 23–45 nm. The TEM images showed that in both series small crystallites form spheroidal nanoparticles with dimensions of 40–80 nm, whose number increases with increasing the working pressure. The photocatalytic properties have been investigated regarding the photodegradation of ethanol vapors in Ar with 0.3% O_2 using P25 powder as reference under simulated solar light. During the irradiation H_2 gas production has been detected for the samples from series "b", whereas the CO_2 evolution was observed for all samples from series "a".

Introduction

Semiconductor materials are widely used, from electronic components to substances that catalyze decomposition processes. They have a bandgap that varies from one material to another. Titanium dioxide is a semiconductor material and has been investigated, at first, for solar cells [1-4] and as optoelectronic component [5-7]. In recent years, it has been found that TiO_2 shows a high photocatalytic efficiency in the decomposition of pollutant substances such as dye wastewater [8-11], soiling [12], and harmful organic materials [13-15]. Also, TiO_2 powders show promising results for the decomposition of ethanol in various environments [16-18]. Moreover, investigations have shown the possibility for applying TiO_2 in hydrogen production by water decomposition [19-23]. Given the TiO_2 bandgap, it is considered a low-efficiency material in photo-driven water splitting, because only 3% of the solar light can be used. Different approaches were tried to reduce the bandgap [24] by doping with, for example, nitrogen [17].

Recent investigations have shown a possible application of TiO_2 for the photocatalytic production of hydrogen from water with the aid of sacrificial agents, such as methanol, ethanol, or glycols [21,22]. There are many studies carried out in gas and liquid phases concerning the photodegradation of ethanol through TiO_2-based materials, targeting both hydrogen production [25,26] and the photocatalytic oxidation of ethanol to CO_2 [27,28]. Hydrogen production and depollution via ethanol photodegradation are of great interest because ethanol is an inexpensive compound and can be produced by biomass. However, it can be also largely found as pollutant in air and wastewater emerging from industrial activities.

There are several pathways to convert ethanol to hydrogen, namely thermochemical, hydrothermal electrochemical, and photochemical methods [25]. Ethanol obtained from biomass is a renewable resource, and hydrogen has a high energy content and does not produce greenhouse gases by burning. Hence, it is an ideal combustible for the future [25].

TiO_2 has some advantages over commonly used catalytic Pt- or Pt-doped materials. It is inexpensive, non-toxic, stable in different solvents and under irradiation, and it can be doped with different elements according to specific necessities. TiO_2 can crystalize in three different crystallographic structures, namely anatase, rutile, and brookite [29,30]. The differences in crystal structure are reflected in direct or indirect electron transitions. The bandgaps of anatase and rutile differ only by 0.2 eV, but can influence significantly the creation of electron–hole pairs, resulting in an increase of the photocatalytic activity. Anatase has a higher decomposition efficiency than rutile [14,31], while the highest photocatalytic activity has been found in mixed anatase/rutile TiO_2 [13,32]. One possible explanation is that the difference in the crystal structure and chemical bonding results in different ionization potentials and electron affinities. Exploiting these differences could promote the fabrication of new devices with higher efficiency in electron–hole separation [33].

There are a lot of methods to obtain TiO_2 powder, from chemical reactions in solvents [34-36] to simple oxidation at high temperatures [37]. Every method has its particular yield and productivity, which are in some cases extremely low compared to a continuous flow method such as laser pyrolysis which, in the case of the studied powders, allows for a productivity of 1 g/h with the possibility of upscaling to an industrial level by increasing the reaction area. Another point is to find the ratio between anatase and rutile that yields the highest photocatalytic activity. Thus, the main scope of this study is to find the best process parameters for the pyrolysis synthesis of TiO_2 powders. Another part is to obtain powders with specific mixtures of the crystallographic phases (anatase/rutile) that yield the highest photocatalytic decomposition of ethanol as harmful compound in gaseous or liquid media, that is air and wastewater.

Results and Discussion

Powder characterization

The main chemical reaction of the $TiCl_4$ precursor in laser pyrolysis in the presence of synthetic air can be described as:

$$TiCl_4 + O_2 \rightarrow TiO_2 + 2Cl_2. \quad (1)$$

The raw TiO_2 powders contain some carbon (from the decomposition of the ethylene sensitizer) and chlorine impurities, whose amount it is greatly diminished by calcination in air at 450 °C for 5 h. To certify this, a composition investigation by energy-dispersive X-ray spectroscopy (EDS) has been done. Calcined TiO_2 powders contain titanium and oxygen and small traces of impurities (ca. 1%). The compositions of all calcined powder samples are presented in Table 1. Theoretically, the ratio between O and Ti should be 2:1. However, because of impurities and crystal structure imperfections (point defects), there are some deviations. The small oxygen deficiency observed even after calcination is related to remaining chlorine impurities and Ti^{3+} ions that resisted calcination.

Phase composition and crystallites sizes of the TiO_2 powders were investigated. The X-ray diffractograms of the obtained powders are presented in Figure 1. The calcined TiO_2 nanopowders show both anatase and rutile phases, corresponding to ICDD database powder diffraction files (PDFs) no. #04-002-2751 and #04-008-7850, respectively.

Table 1: Composition of the obtained TiO_2 powders.

Sample	Ti [atom %]	O [atom %]	Impurities [atom %]
TO-250-a	33.91	65.06	1.03
TO-450-a	33.72	65.14	1.14
TO-650-a	33.21	65.39	1.40
TO-850-a	33.91	65.31	0.78
TO-250-b	34.50	64.21	1.29
TO-450-b	32.49	67.01	0.50
TO-650-b	33.75	65.60	0.65
TO-850-b	33.01	65.71	1.28

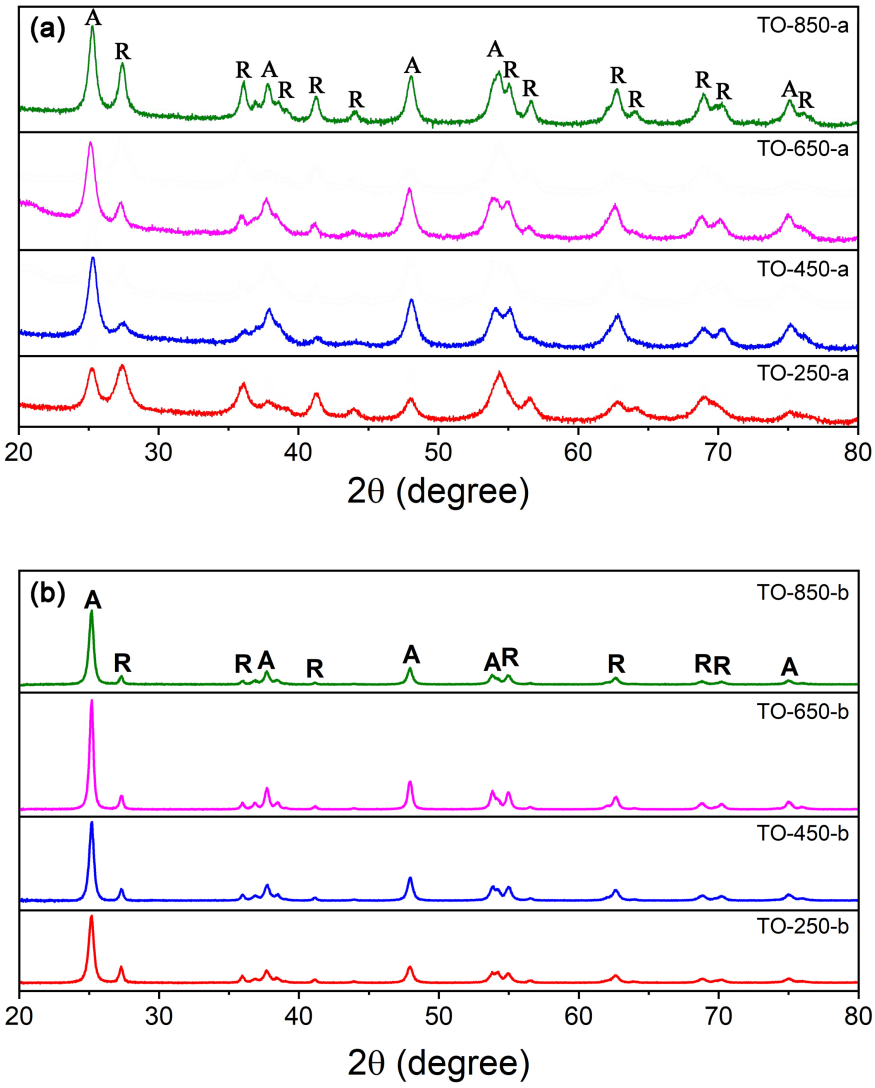

Figure 1: X-ray diffractograms of the TiO_2 powders: (a) samples of series "a" and (b) samples of series "b" (R: rutile, A: anatase).

The ratio between anatase and rutile phases has been calculated using the equations from Spurr and Myers [38], and the medium crystallite diameter has been calculated via the Scherrer equation [39]. Both parameters are presented in Table 2. The anatase crystal structure is dominant for the sample TO-450-a, and this dominance decreases with increasing synthesis pres-

sure. An exception is TO-250-a, that is, the sample synthesized at the lowest pressure and in the presence of the highest C_2H_4 sensitizer flow (120 sccm). Here, the rutile crystal structure is the main constituent. The crystallite size increases for both phases from 14 nm and 11 nm to 22 nm for anatase and rutile, respectively, with increasing pressure in the reaction chamber.

Table 2: The ratios between anatase and rutile and the crystallite sizes in the powders.

Sample	Anatase [%]	$d_{cryst.}$ [nm]	Rutile [%]	$d_{cryst.}$ [nm]
TO-250-a	41.12	14	58.88	11
TO-450-a	90.74	16	9.26	11
TO-650-a	84.21	16	15.79	18
TO-850-a	64.87	22	35.13	22
TO-250-b	77.33	23	22.67	35
TO-450-b	83.30	26	16.70	37
TO-650-b	86.22	33	13.78	40
TO-850-b	87.42	25	12.58	45

The TEM analysis reveals that the TiO_2 crystallites tend to arrange in bigger spherical particles (Figure 2a,b). This tendency is more pronounced as the pressure in the reaction chamber increases. The average particles sizes for TO-250-a, TO-450-a, TO-650-a, and TO-850-a nanopowders are 17.3, 17.0, 15.5, and 22.0 nm, respectively. These values are in good agreement with the mean crystallites size calculated from XRD investigations.

The number of the bigger particles (60–70 nm) in the TO-850-a powder increases, possibly due to enhanced coalescence in the laser pyrolysis flame at the highest working pressure. Similarly, in the "b" series, the nanoparticles contain crystallites with an average size of 20–25 nm and spherical particles with dimensions between 40 and 80 nm. The biggest spheres of the "b" series were identified in sample TO-450-b (Figure 2c). The highest number of spheres compared to the total number of particles are in sample TO-850-b (7.6%) and the fewest in sample TO-250-b (1.9%).

The HRTEM images (Figure 3) show the crystal structure of the TO-850-a powder with point defects and some residual impurities at the particle surface. The interplanar distance of 0.32 nm (Figure 3, right) corresponds to the *c* axis of the rutile phase (2.96 Å from XRD measurements).

The specific surface areas of series "a" of TiO_2 powders obtained with increasing pressure in the reaction chamber are 78.0, 82.7, 89.9, and 57.9 m^2/g, respectively. The correlation between specific surface area and particle/crystallite size is most obvious when comparing the TO-850-a sample with those synthesized at lower pressures. When the average particle size increases, the surface area diminishes.

X-ray photoelectron spectroscopy (XPS) analysis was performed, and the spectral alignment of the binding energy (BE) scale was referenced to adventitious carbon at 284.8 eV [40,41]. Figure 4a shows the full survey scans of TO-250-a, TO-850-b, and commercial TiO_2 (Degussa P25) samples, indicating the presence of the expected elements Ti, O, and C. The high-resolution XPS spectra of the C 1s, O 1s, and Ti 2p regions of TO-250-a, TO-850-b, and P25 are indicated in Figure 4b–d. The carbon region consists of three singlets with maxima located at 284.8, 286.1, and 289 eV (see Figure 4b). The highest peak located at 284.8 eV originates from the C=C bond, followed by the oxidized carbon forms C–O–C/C–OH (286.1 eV) and O–C–O (289 eV), which probably formed during the synthesis [42]. No C 1s peak at ca. 281 eV (Ti–C bond) was observed, suggesting that carbon does not modify the TiO_2 phase [43]. Figure 4c shows the Ti 2p peaks, where the Ti^{4+} $2p_{3/2}$ and

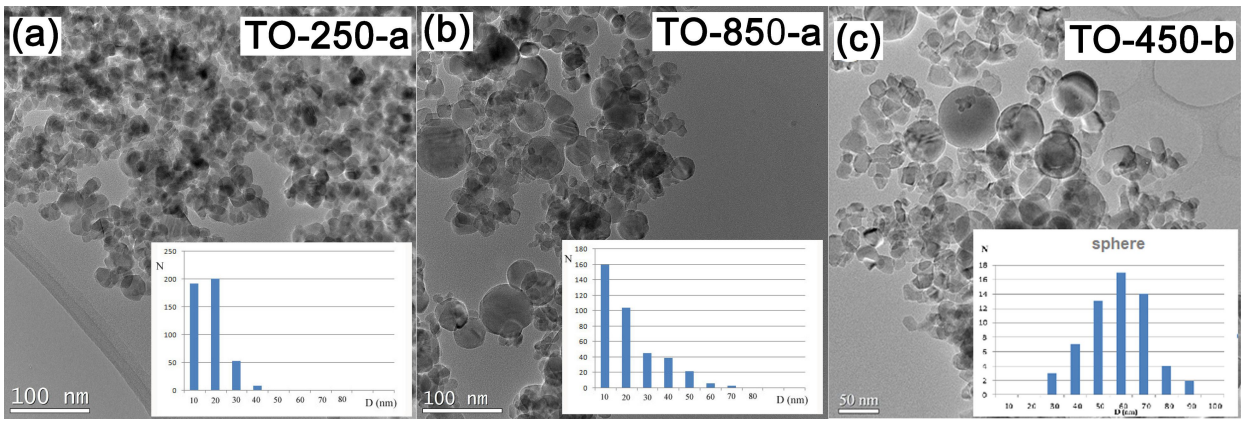

Figure 2: TEM images and the particle distributions: (a) TO-250-a, (b) TO-850-a, and (c) TO-450-b.

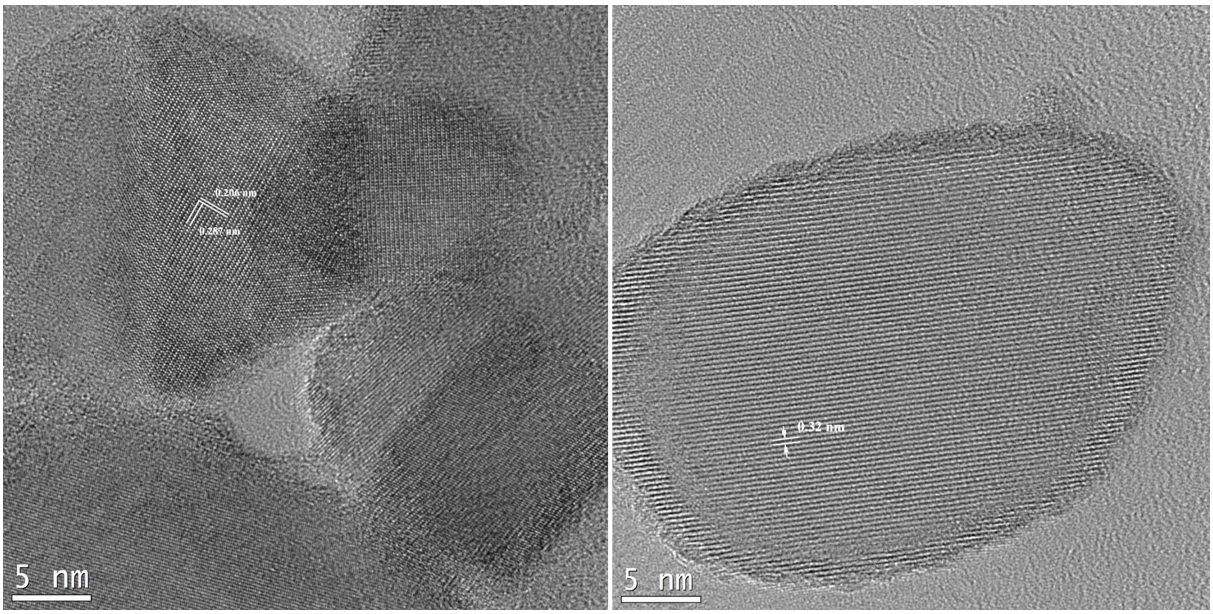

Figure 3: The HRTEM images of the TO-850-a powder.

Ti^{4+} $2p_{1/2}$ spin–orbital doublets centered at 459.4 and 464.5 eV correspond to Ti^{4+}–O bonds in TiO_2 [44-47]. The binding energy difference between Ti^{4+} $2p_{1/2}$ and Ti^{4+} $2p_{3/2}$ is 5.8 eV, which is similar to the values reported in previous studies [48,49]. The O 1s spectra of pure P25, TO-250-a, and TO-850-b nanoparticles are shown in Figure 4d and were fitted with two peaks. The peaks at binding energies of 529.9 and 530.5 eV are attributed, respectively, to oxygen bound to Ti^{4+} and the adsorption of –OH on the surface [50,51]. The XPS results do not show differences between the two series of samples and do not indicate changes regarding the variation of the nanoparticle surfaces according to the value of the working pressure. Since XPS analysis is a surface measurement and the samples were calcined in air, the possibility to identify the presence of Ti^{3+} species and oxygen vacancies is small, but we do not exclude the possibility that these defects are located on the TiO_2 surface and that the concentration of defects is below the detection limit of XPS [52,53]. Another explanation would be this: The surface depth sensitivity of XPS is known to be 5–10 nm compared to 1 µm in PL. Hence, this technique provides more details about the species located on the surface and even subsurface [54]. The complementary results regarding our samples are presented below.

One of the most crucial parts in understanding catalytic behavior is the determination of the bandgap value and of shallow donor or acceptor levels, which are localized in the vicinity of the conduction and the valence bands. There are two ways to obtain such knowledge, that is, from optical and luminescence measurements. The former gives us information about electron transitions from the lower to the higher energy levels and the latter about the recombination between free electrons and holes.

The optical properties of the TiO_2 powders has been investigated by absorbance measurements. Figure 5 presents an example of these measurements of both sample series. In the case of the TiO_2 material, it is known that it can have two types of transitions, namely direct and indirect transitions, which are related to the crystal structure.

To distinguish these two types of transition, it is common to use the Tauc plot [55-58], where the absorbance coefficient is multiplied with the photon energy and plotted as an exponential function of the photon energy. The value of the exponent depends on the transition type. For indirect transitions it is 0.5 (Figure 6a), for direct transitions it is 2 (Figure 6b) [55,56]. We presume that in our samples no forbidden transitions occur. The absorbance coefficient was calculated using the following equation [58,59]:

$$\alpha = 2.303\frac{\text{absorbance}}{d}, \tag{2}$$

where d is the thickness of the measured sample.

The bandgap values for bulk anatase and rutile are 3.2 and 2.95 eV, respectively [33,57,60,61]. All calculated bandgap values are listed in Table 3. Our values are slightly higher due

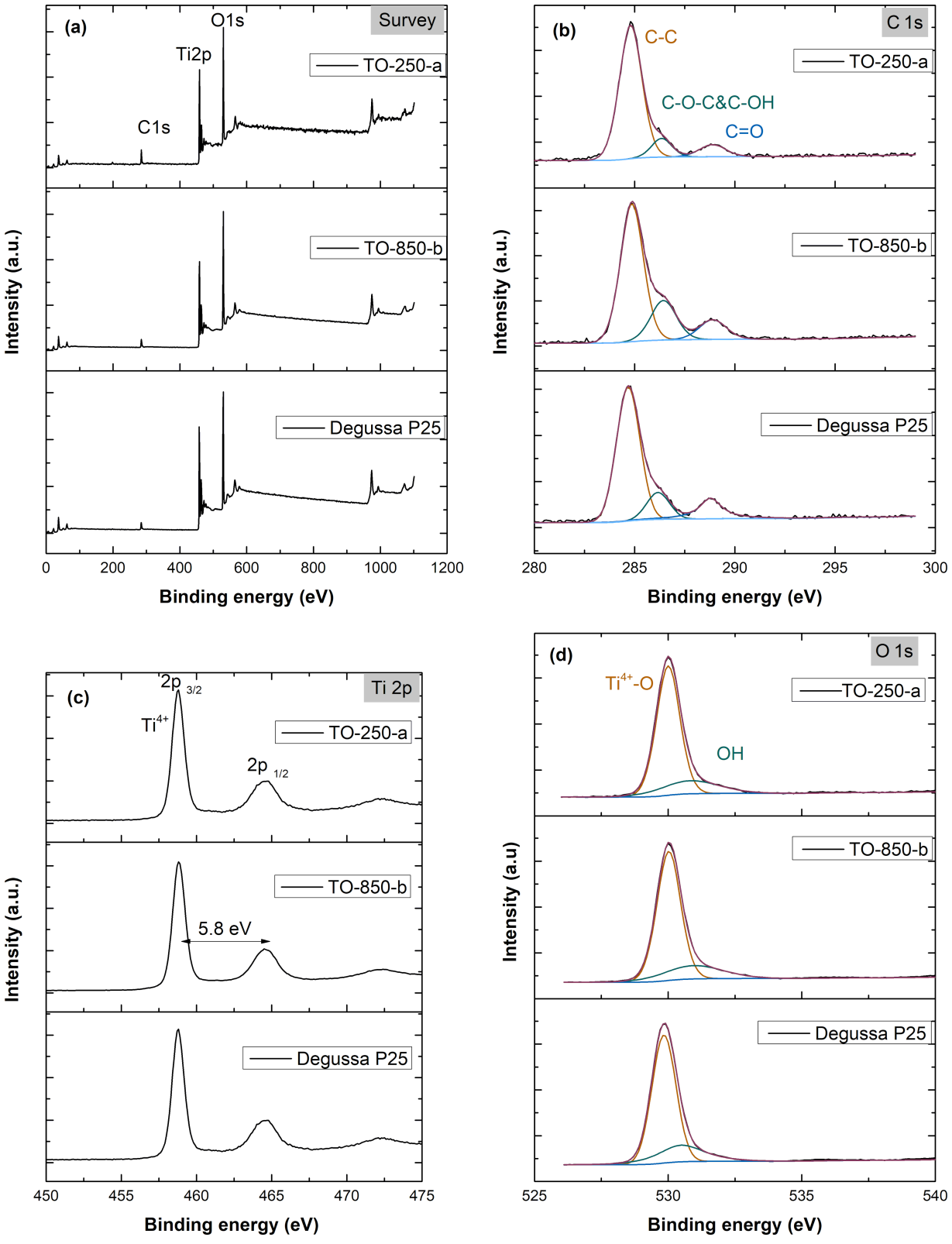

Figure 4: XPS spectra of TO-250-a, TO-850-b, and P25 samples: (a) survey spectra; (b–d) high-resolution XPS spectra of (b) C 1s, (c) Ti 2p, and (d) O 1s core lines.

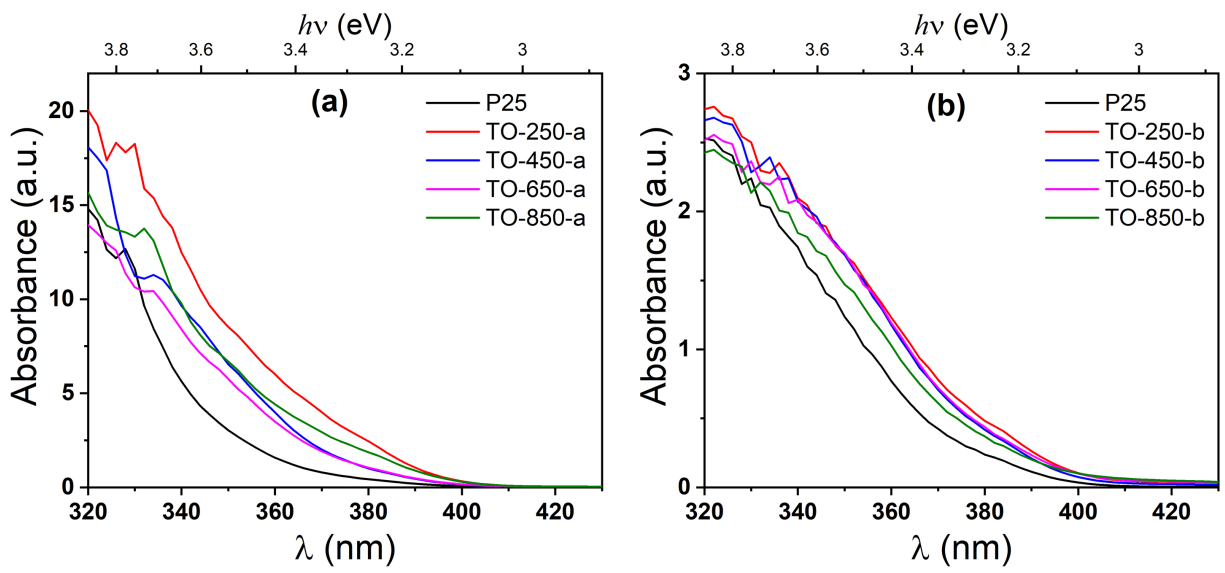

Figure 5: Absorbance of the TiO_2 samples at room temperature.

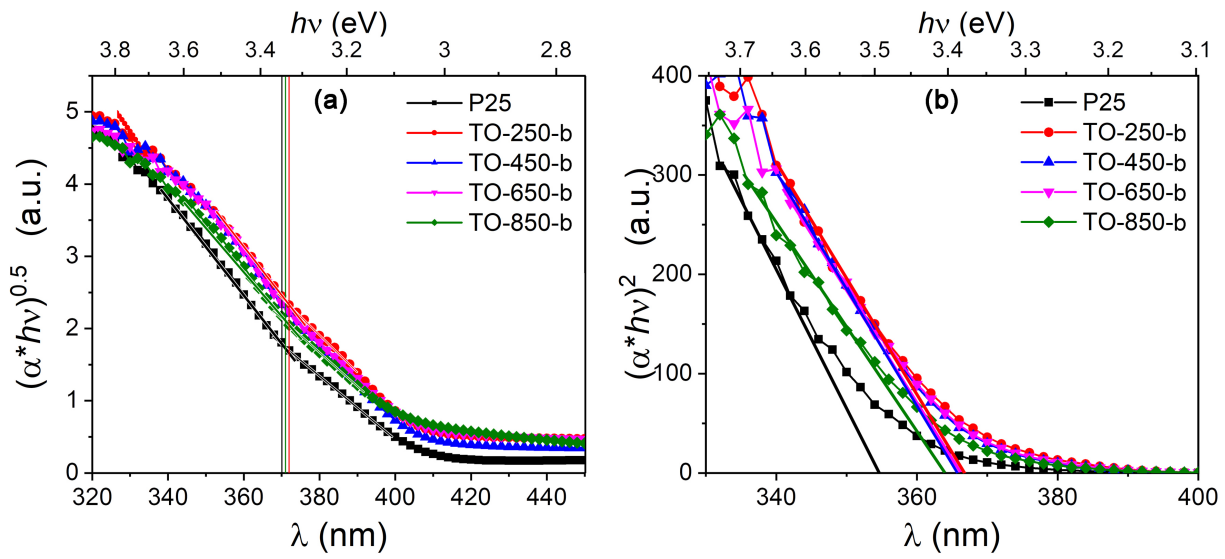

Figure 6: Example of the calculated (a) indirect and (b) direct transitions from sample series “b”.

to the blueshift with reduction of the size of the powder particles [62,63]. Indirect transitions are more common in both sample groups. The valence bands are the same in P25 and our TiO_2 powders, indirect transitions have almost the same values for all measured samples, and the differences among the values could be due to calculus errors. In the case of direct transitions, the values obtained in our powders are smaller. A possible explanation is the smaller volume of the particles with anatase crystal structure or the formation of shallow donor levels near the conduction band [64,65].

Photoluminescence (PL) spectra at 260 nm excitation wavelength are presented in Figure 7. The most important band is the band located at 400 nm (3.10 eV), but there are some other bands at 450 nm (2.75 eV), 465 nm (2.66 eV), and 500 nm (2.48 eV). The band at 400 nm is complex, and its maximum shifts depending on the intensity of each component. For example, the maximum of the 400 nm band of the TO-250-a and TO-450-b samples are shifted to lower energies, which is caused by the more intense PL component in the region of longer wavelengths. Other PL

Table 3: Calculated bandgap values.

	Indirect		Direct	
Sample	Series “a” [eV]	Series “b” [eV]	Series “a” [eV]	Series “b” [eV]
P25	3.03	3.35	3.64	3.49
TO-250	3.00	3.33	3.49	3.37
TO-450	3.07	3.37	3.50	3.38
TO-650	3.05	3.32	3.52	3.37
TO-850	3.00	3.34	3.50	3.40

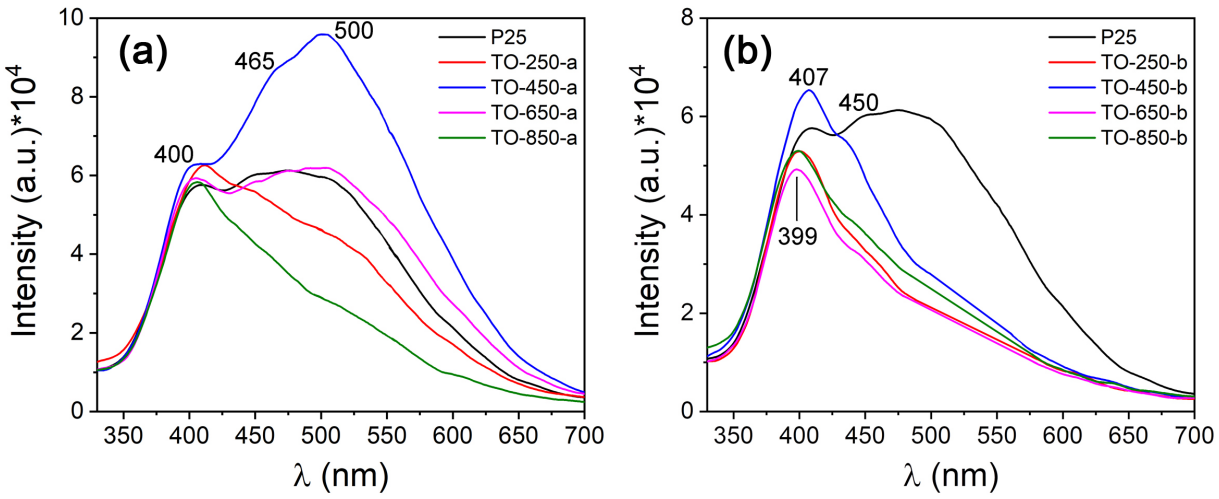

Figure 7: Photoluminescence of the TiO_2 powders under λ_{exc} = 260 nm at room temperature: (a) samples of series “a” and (b) samples of series “b”.

bands represent the recombination probability at energy levels located more deeply in the forbidden bandgap. Some of them could be donor levels, for example chlorine atoms [66], but most probably they are acceptor levels created by titanium vacancies [67,68].

Band-to-band transitions have not been detected as separate PL bands, taking into account the obtained bandgap values from the optical properties. But, they are surely a part of the complex PL band at 400 nm, the resolution of which into the components requires another investigation. Oxygen and titanium vacancies have been found. These points defects are created most probably at the surface of the powder particles because in the HRTEM figures we do not see any dislocation or other crystal structure modification inside the particles. Another explanation is that photons emitted from the depth of the particles are reabsorbed in the superficial zone and are then reemitted. There is also a high probability that free electrons are trapped by donor levels (V_O) [65,67] and that recombination processes are taking place at that level. This also applies to free holes trapped at acceptor levels [68], which cannot escape as easily as electrons from the donor level.

Generation of hydroxyl radicals

Reactive oxygen species are usually involved in the photodegradation of organic compounds. For example, the hydroxyl radical (•OH) is a strong oxidizer. The generation of (•OH) over the samples under simulated solar light irradiation (AM 1.5) has been evaluated according to the PL emission from 451 nm, attributable to the presence of umbelliferone, a derivative of coumarin resulting from the interaction with photogenerated hydroxyl radicals.

Despite the fact that radical trapping was performed in aqueous solution, it can be indicative for the ability of the catalyst surface to generate hydroxyl radicals in the present investigated system. The main reactions leading to (•OH) formation are the following:

$$h^+ + \text{ -OH (surface hydroxy group)} \rightarrow {}^{\bullet}OH \quad (3)$$

or

$$\begin{aligned} &O_2 + e^- \rightarrow \left(O_2^-\right)_{ads} \text{ (on catalyst surface),} \\ &\left(O_2^-\right)_{ads} + 2H^+ + e^- \rightarrow H_2O_2 \rightarrow 2\,{}^{\bullet}OH. \end{aligned} \quad (4)$$

Figure 8 shows a significant ability of TO-250-a, TO-450-a, TO-650-a, TO-850-a, and P 25 catalysts to generate •OH, indicating a presumable activity for CO_2 generation. In contrast, the samples of series "b" are almost inactive. Only TO-450-b can produce hydroxyl radicals.

Photocatalytic performance of the nanopowders

These experiments have been conducted in environments with low oxygen concentration. Ethanol vapors play a double role here, that is, they generate hydrogen by photodehydrogenation and also undergo oxidation to carbon dioxide and water under the action of simulated sunlight in the presence of oxygen. The main intermediate product in the process of hydrogen photogeneration is acetaldehyde as intermediate, which can be further oxidized to CO_2 and H_2O, according to the following chemical equations:

$$C_2H_5OH \rightarrow CH_3CHO + H_2, \quad (5)$$

$$CH_3CHO + 2.5O_2 \rightarrow 2CO_2 + H_2O. \quad (6)$$

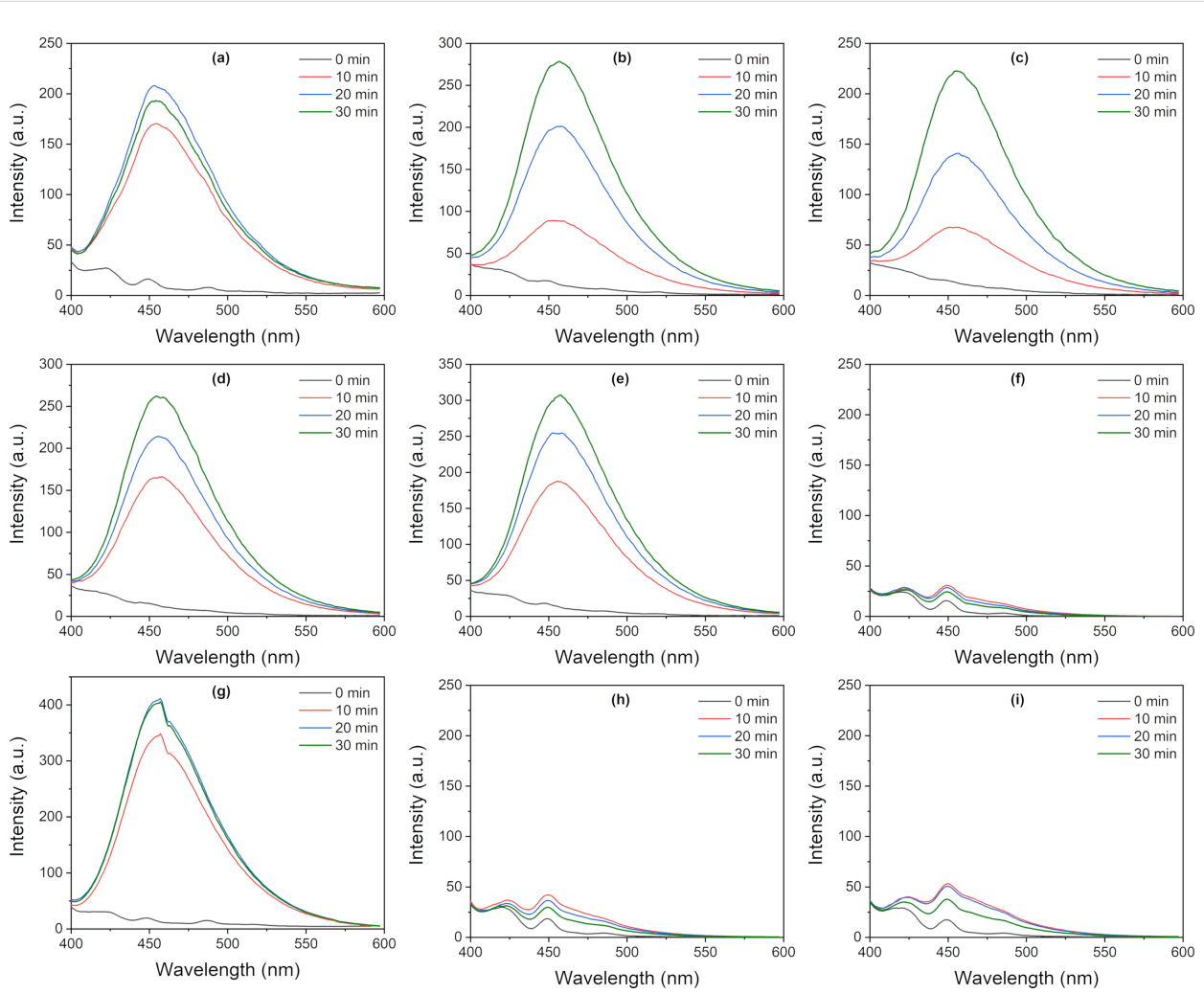

Figure 8: Generation of hydroxyl radicals under simulated solar irradiation over the investigated catalysts as a function of the time. The emission at 451 nm is characteristic to the presence of umbelliferone: (a) P25, (b) TO-250-a, (c) TO-450-a, (d) TO-650-a, (e) TO-850-a, (f) TO-250-b, (g) TO-450-b, (h) TO-650-b, and (i) TO-850-b.

Hydrogen generation

As can be seen in Figure 9, the H_2 generation performance of the tested titania nanoparticles greatly differs. The TO-850-b sample exhibits the highest activity for H_2 photogeneration, reaching 5 µmol H_2 after 3 h of reaction. The entire sequence of TO-250-b, TO-450-b, and TO-650-b catalysts proves to have a higher activity for H_2 generation than TO-250-a, TO-450-a, and TO-650-a, which are quite close to P 25 in terms of an almost insignificant H_2 production. This clear difference between the two catalysts series can be related to structural characteristics providing different densities of photogenerated charges (electrons) to react with protons available at the surface.

Carbon dioxide evolution

The photo-oxidative conversion of ethanol to CO_2 (and water) under simulated sunlight irradiation is depicted in Figure 10, revealing the different kinds of behavior of the sample series "a" and "b". All samples of series "a" show a significant activity regarding the mineralization of ethanol in the gas phase. The highest activity was measured for TO-250-a, which generated around 70 µmol CO_2 after 3 h. All catalysts of this series exhibit a higher activity than P25. Also, an increase of the CO_2 formation rate after the first hour of irradiation can be observed, probably due to the mineralization of the previously generated intermediates. The catalysts of the series "b" are less active than

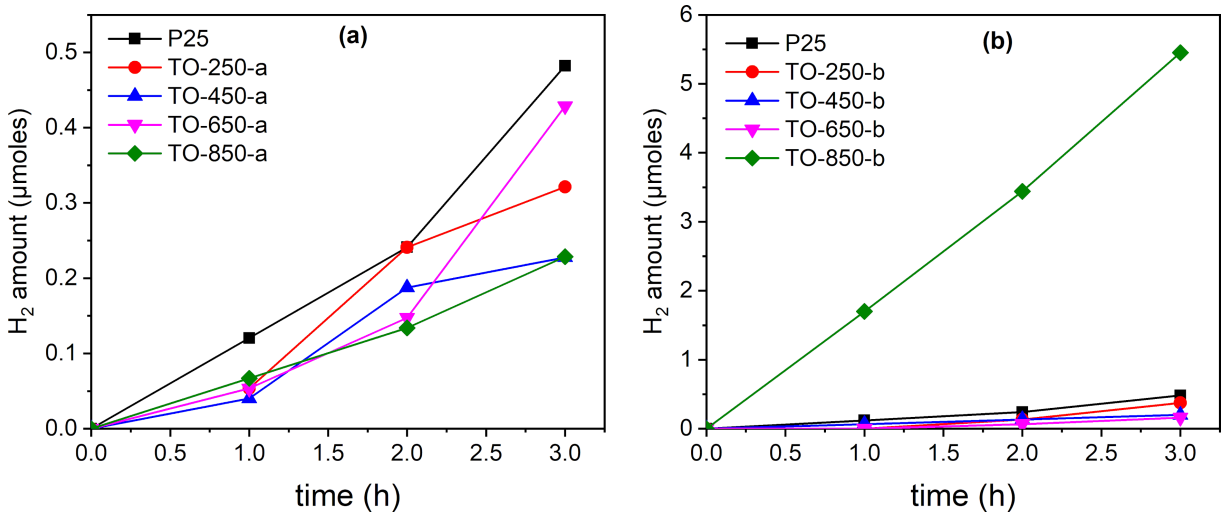

Figure 9: Photocatalytic H_2 evolution from C_2H_5OH vapors over both catalyst series under simulated solar light irradiation: (a) series "a" and (b) series "b".

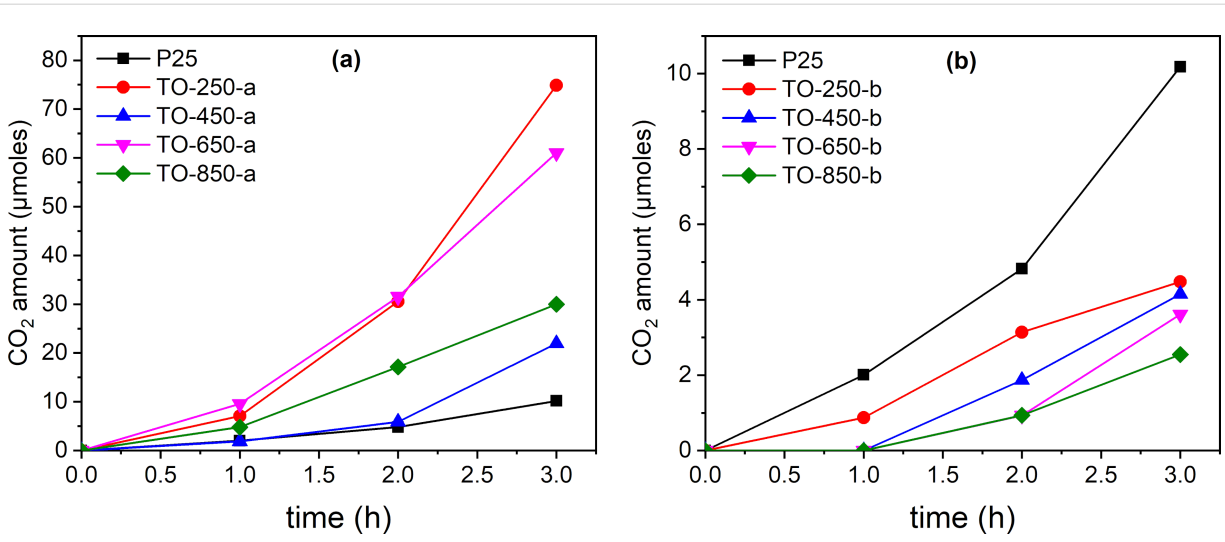

Figure 10: Photocatalytic CO_2 evolution from C_2H_5OH vapor over TiO_2 under simulated solar light irradiation: (a) series "a" and (b) series "b".

P 25 regarding the mineralization to CO_2. A very good correlation can be established between these results and Figure 8 illustrating the hydroxyl radical formation. It is obvious that all catalysts of the first series generate high amounts of hydroxyl radicals and, consequently, trigger ethanol photomineralization. It should be noted that the TO-450-b sample also produced hydroxyl radicals and shows a straight increase of CO_2 formation after 1 h of irradiation. Probably, a longer irradiation time would be beneficial for ethanol photomineralization over this sample. Also, TO-650-b shows a linear increase of activity after 2 h of irradiation.

Figure 11 is illustrative for the different kinds of behavior of the two catalyst series regarding ethanol photodegradation. For the ethanol photodegradation carried out over the TO-250-a, TO-450-a, TO-650-a, and TO-850-a catalysts, the formation rate of CO_2 is significantly higher than the formation rate of H_2. This indicates a potential use for depollution since TiO_2 is an environmentally friendly, non-toxic, and inexpensive material. More than that, these tests used solar light, which is a regenerable energy source. The investigated TiO_2-based catalysts lead to ethanol photomineralization under simulated solar light, indicating an efficient use of UV light from the solar spectrum, but also the presence of optically and catalytically active defects in the structure of the catalysts.

Figure 11 shows also a lower CO_2 formation rate for the second catalyst series with a simultaneously increasing H_2 formation rate, especially for TO-850-b. From this perspective, it might be interesting to consider these catalysts for use and further modification regarding H_2 production. Table 4 shows an increase of acetaldehyde formation for the catalyst series "b" relative to series "a", especially for TO-850-b. This observation is in line with the highest hydrogen production obtained by using this catalyst.

Table 4: Comparative formation of acetaldehyde after 180 min of irradiation over the investigated catalysts.

Time reaction (min)	Amount of CH_3CHO [µmol]								
	P25	TO-250-a	TO-450-a	TO-650-a	TO-850-a	TO-250-b	TO-450-b	TO-650-b	TO-850-b
0	0	0	0	0	0	0	0	0	0
30	36.29	14.30	4.74	4.65	8.52	50.20	23.00	50.00	50.30
60	65.11	31.42	20.00	11.67	18.00	84.50	41.90	60.00	87.20
90	76.72	42.11	26.00	16.80	26.19	90.40	53.40	63.00	106.00
120	87.19	52.40	39.87	21.80	38.00	92.40	56.00	71.00	111.00
150	92.20	62.41	40.46	27.00	50.00	97.00	59.00	74.00	113.00
180	97.67	71.07	42.00	36.80	55.00	90.00	63.00	80.00	114.00

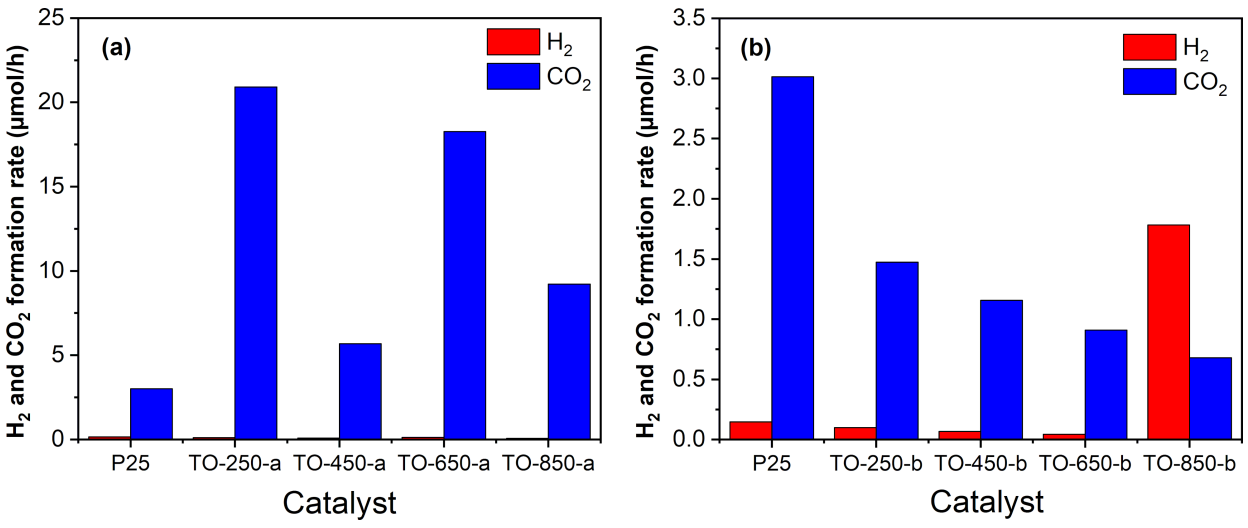

Figure 11: Comparative H_2/CO_2 formation rate over titania nanopowders in ethanol vapor environments: (a) series "a" and (b) series "b".

Conclusion

This study describes the photocatalytic degradation of ethanol vapors under simulated solar light and low oxygen concentration using TiO_2 nanoparticles obtained by laser pyrolysis. The final products are CO_2, H_2O, and H_2. The average particle sizes are between 15 and 22 nm with anatase being the predominant crystalline phase and rutile being a minor fraction. An exception to this is the sample synthesized at the lowest pressure without supplementary air flow. Two series of samples were tested in ethanol photodegradation experiments, observing that all samples from series "a" have a higher photocatalytic activity towards the oxidation of ethanol to CO_2 than the reference sample Degussa P25, especially the small nanoparticles obtained at the lowest pressure (250 mbar). In contrast, the larger nanoparticles obtained in the "b" series at the highest pressure (850 mbar) contribute to a slight improvement regarding the production of H_2, compared to the commercial reference sample. The ethanol photodegradation under simulated solar light leads to valuable results concerning different TiO_2 functional properties depending on the synthesis conditions. Also, a potential application both for the degradation of organic compounds and the production of hydrogen has been revealed.

Materials and Methods

Laser pyrolysis was used to obtain powder of TiO_2 in a similar manner as described in our previous studies [69,70]. The laser radiation was generated by a continuous CO_2 laser with 10.55 µm wavelength and maximum power of 450 W. Ethylene was used to absorb the infrared laser radiation and transfer the energy to the precursor molecules, thus playing the role of a sensitizer. The reaction took place in the volume delimited by the orthogonally intersection of the laser beam with the precursor flow (Figure 12).

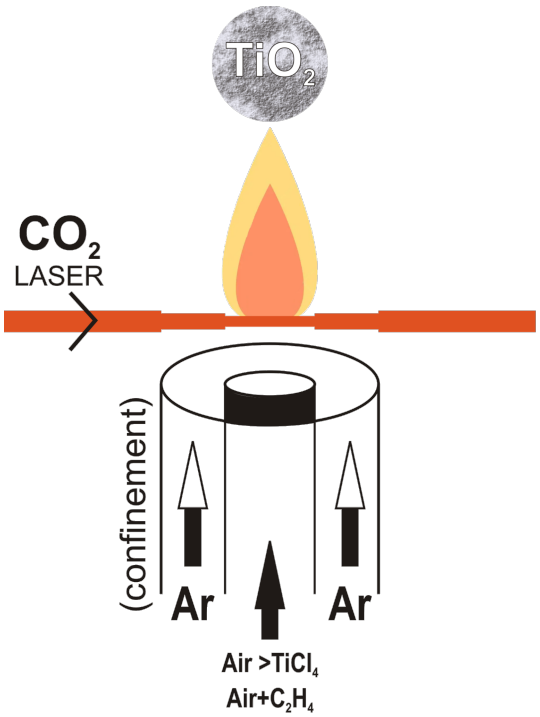

Figure 12: Schematic representation of the laser pyrolysis method.

The precursors were injected through the central nozzle. The reactive flow was a mixture of synthetic air (Siad 99.99% purity) as oxidizer, C_2H_4 (Siad 99.5% purity) as sensitizer, and $TiCl_4$ vapor (Aldrich 98% purity) as Ti precursor. Synthetic air was used as carrier of gaseous $TiCl_4$ from a liquid reservoir (via a bubbler) and as oxidizer (Table 5). The co-axial flow of Ar (Siad 99.98% purity) confined the inner reactive flow after passing through an external annular inlet. The powder collection time was ca. 1 h. The first powders (denominated as series "a") were further calcined at 450 °C for 5 h in order to minimize the traces of carbon from ethylene decomposition and of chlorine from $TiCl_4$. Because the flow of entrained precursor vapors diminished with increasing pressure of the carrier gas, in

Table 5: Process parameters of laser pyrolysis synthesis of titania nanoparticles.

Sample	$\Phi_{Ar(conf.)}$ [sccm]	Φ_{air} [sccm]	$\Phi_{air \rightarrow TiCl_4}$ [sccm]	$\Phi_{C_2H_4}$ [sccm]	*P* [mBar]	Laser power [W]
TO-250-a	1800	—	80	120	250	450
TO-450-a	1800	100	120	100	450	450
TO-650-a	1800	200	160	80	650	450
TO-850-a	2000	200	200	60	850	450
TO-250-b	2000	200	300	50	250	450
TO-450-b	2000	200	300	50	450	450
TO-650-b	2000	200	300	50	650	450
TO-850-b	2000	200	300	50	850	450

the first series of experiments we increased the carrier gas flow at higher pressures to not reduce the $TiCl_4$ flow too much. Also, a supplementary air flow was used in these experiments, with the exception of those at the lowest pressure. Also, in this first series of experiments, we gradually decreased the C_2H_4 sensitizer flow with increasing pressure in order to maintain a stable burning flame. The process conditions were further modified (by enhancing the air carrier flow and diminishing the C_2H_4 flow and employing the same carrier and supplementary air and ethylene flows at all pressures) in order to obtain higher-purity TiO_2 nanoparticles that do not require post-synthesis treatment. These samples were grouped in the second batch of samples, that is, in series "b".

The elemental composition of the TiO_2 powders was estimated by EDS performed inside a scanning electron microscope, FEI Quanta Inspect S, at 15 kV in high vacuum. The crystalline structures and phase concentrations were determined from X-ray diffraction (XRD) patterns, measured by an X-ray diffractometer Panalytical X'Pert MPD theta–theta, and the morphological properties were determined by transmission electron microscopy (TEM), high-resolution transmission electron microscopy (HRTEM), and selected-area electron diffraction (SAED) measurements using a JEM ARM 200F analytical microscope (Jeol, Japan). The specific surface area was measured using a BET flowing gas surface area analyzer, Horiba SA-9600, with a 30% N_2/70% He gas mixture. Photoluminescence measurements were carried out using a Horiba Flourolog-3. The excitation source was a xenon lamp at λ_{exc} = 260 nm. All samples have been irradiated at room temperature and under the same conditions. Diffuse reflectance UV–vis measurements were performed by using a spectrophotometer Perkin Elmer Lambda 35 with an integrating sphere in the 200–1100 nm range. The measured reflectance data were converted to absorption data using the Kubelka–Munk function $F(R)$.

For the XPS analyses we employed an ESCALAB Xi+ (Thermo SCIENTIFIC Surface Analysis) apparatus with an Al Kα radiation source ($h\nu$ = 1486.2 eV) using the C 1s level (284.4 eV) as the energy reference. The superficial chemical compositions as well as the oxidation states were found from the XPS spectra by using the "Avantage" software, version 5.978.

ROS identification

Trapping of •OH radicals was performed with 10 mM coumarin (Merck) solution and 0.001 g suspended catalyst exposed to simulated solar irradiation. The formation of a fluorescent compound, namely umbelliferone, was monitored with a Carry Eclipse fluorescence spectrometer, slits set to 10 nm in excitation and emission, λ_{exc} = 330 nm.

The experimental procedure for photocatalytic tests started with dispersing a uniform layer of 0.01 g of titania photocatalyst nanopowder on an area of about 3.6 cm^2. This photoactive surface was subsequently exposed to simulated sunlight. Ethanol (7.2 μL) was injected into the photoreactor with a volume of about 120 cm^3 containing 0.3% O_2 in Ar. The temperature inside the photoreactor was maintained constant at 18 °C with a cryostat. The AM 1.5 solar light (1000 W/m^2) was provided by a Peccell L01 solar simulator. For each test, 200 μL gas samples were taken from the photoreactor every 30 min and analyzed with two gas chromatographs equipped with either a flame ionization detector (FID, Agilent 7890A) or a thermal conductivity detector (TCD, Buck Scientific, model 910). The total time of a photocatalytic test was 180 min. The photoreactor works thus under static conditions, which differs from the dynamic conditions used by other researchers where a continuous flow of ethanol vapors (mixed with water vapors) was employed via bubbling [18,71].

Funding

This work was supported by Romanian Ministry of Research, Innovation and Digitalization under Romanian National Nucleu Program LAPLAS VII – contract no. 30N/2023 and CNCS-UEFISCDI, contract number 31TE/2022 Project.

ORCID® iDs

Iuliana P. Morjan - https://orcid.org/0000-0001-8108-8478

References

1. Frank, A. J.; Kopidakis, N.; van de Lagemaat, J. *Coord. Chem. Rev.* **2004,** *248,* 1165–1179. doi:10.1016/j.ccr.2004.03.015
2. Nazeeruddin, M. K.; Grätzel, M. *Compr. Coord. Chem. II* **2003,** *9,* 719–758. doi:10.1016/b0-08-043748-6/09025-3
3. Elsaeedy, H. I.; Qasem, A.; Yakout, H. A.; Mahmoud, M. *J. Alloys Compd.* **2021,** *867,* 159150. doi:10.1016/j.jallcom.2021.159150
4. van der Zanden, B.; Goossens, A.; Schoonman, J. *Synth. Met.* **2001,** *121,* 1601–1602. doi:10.1016/s0379-6779(00)01503-4
5. Chaudhari, C.; Gautam, D. K. *Opt. Commun.* **2000,** *181,* 61–69. doi:10.1016/s0030-4018(00)00741-0
6. Ivanova, T.; Harizanova, A. *Solid State Ionics* **2001,** *138,* 227–232. doi:10.1016/s0167-2738(00)00798-0
7. Ferhati, H.; Djeffal, F. *Optik (Munich, Ger.)* **2016,** *127,* 7202–7209. doi:10.1016/j.ijleo.2016.05.047
8. Ollis, D. F. *C. R. Acad. Sci., Ser. IIc: Chim.* **2000,** *3,* 405–411. doi:10.1016/s1387-1609(00)01169-5
9. Fujishima, A.; Zhang, X.; Tryk, D. A. *Surf. Sci. Rep.* **2008,** *63,* 515–582. doi:10.1016/j.surfrep.2008.10.001
10. Paz, Y. *Appl. Catal., B* **2010,** *99,* 448–460. doi:10.1016/j.apcatb.2010.05.011
11. Rachna; Rani, M.; Shanker, U. *J. Environ. Manage.* **2019,** *248,* 109340. doi:10.1016/j.jenvman.2019.109340

12. Mokhtarifar, M.; Kaveh, R.; Bagherzadeh, M.; Lucotti, A.; Pedeferri, M.; Diamanti, M. V. *ACS Appl. Mater. Interfaces* **2020,** *12,* 29671–29683. doi:10.1021/acsami.0c06792
13. Micek-Ilnicka, A.; Ogrodowicz, N.; Filek, U.; Kusior, A. *Catal. Today* **2021,** *380,* 84–92. doi:10.1016/j.cattod.2021.04.021
14. Zhang, W.; Huang, Y.; Liu, P.; Zhao, Y.; Wu, H.; Guan, M.; Zhang, H. *Mater. Sci. Semicond. Process.* **2014,** *17,* 124–128. doi:10.1016/j.mssp.2013.08.014
15. Singh, J.; Lee, B.-K. *J. Environ. Manage.* **2016,** *170,* 88–96. doi:10.1016/j.jenvman.2016.01.015
16. Li, J.; Kazakov, A.; Dryer, F. L. *J. Phys. Chem. A* **2004,** *108,* 7671–7680. doi:10.1021/jp0480302
17. Halasi, G.; Ugrai, I.; Solymosi, F. *J. Catal.* **2011,** *281,* 309–317. doi:10.1016/j.jcat.2011.05.016
18. Xing, C.; Zhang, Y.; Liu, Y.; Wang, X.; Li, J.; Martínez-Alanis, P. R.; Spadaro, M. C.; Guardia, P.; Arbiol, J.; Llorca, J.; Cabot, A. *Nanomaterials* **2021,** *11,* 1399. doi:10.3390/nano11061399
19. Ochiai, T.; Fujishima, A. *J. Photochem. Photobiol., C* **2012,** *13,* 247–262. doi:10.1016/j.jphotochemrev.2012.07.001
20. Wang, R.; Hashimoto, K.; Fujishima, A.; Chikuni, M.; Kojima, E.; Kitamura, A.; Shimohigoshi, M.; Watanabe, T. *Nature* **1997,** *388,* 431–432. doi:10.1038/41233
21. Shirai, K.; Sugimoto, T.; Watanabe, K.; Haruta, M.; Kurata, H.; Matsumoto, Y. *Nano Lett.* **2016,** *16,* 1323–1327. doi:10.1021/acs.nanolett.5b04724
22. Wang, Q.; Domen, K. *Chem. Rev.* **2020,** *120,* 919–985. doi:10.1021/acs.chemrev.9b00201
23. Tachibana, Y.; Vayssieres, L.; Durrant, J. R. *Nat. Photonics* **2012,** *6,* 511–518. doi:10.1038/nphoton.2012.175
24. Tao, J.; Luttrell, T.; Batzill, M. *Nat. Chem.* **2011,** *3,* 296–300. doi:10.1038/nchem.1006
25. Nanda, S.; Rana, R.; Zheng, Y.; Kozinski, J. A.; Dalai, A. K. *Sustainable Energy Fuels* **2017,** *1,* 1232–1245. doi:10.1039/c7se00212b
26. Romero Ocaña, I.; Beltram, A.; Delgado Jaén, J. J.; Adami, G.; Montini, T.; Fornasiero, P. *Inorg. Chim. Acta* **2015,** *431,* 197–205. doi:10.1016/j.ica.2015.01.033
27. Muggli, D. S.; McCue, J. T.; Falconer, J. L. *J. Catal.* **1998,** *173,* 470–483. doi:10.1006/jcat.1997.1946
28. Yu, Z.; Chuang, S. S. C. *J. Catal.* **2007,** *246,* 118–126. doi:10.1016/j.jcat.2006.11.022
29. Ohno, T.; Sarukawa, K.; Tokieda, K.; Matsumura, M. *J. Catal.* **2001,** *203,* 82–86. doi:10.1006/jcat.2001.3316
30. Balachandran, U.; Eror, N. G. *J. Solid State Chem.* **1982,** *42,* 276–282. doi:10.1016/0022-4596(82)90006-8
31. Xu, M.; Gao, Y.; Martinez Moreno, E.; Kunst, M.; Muhler, M.; Wang, Y.; Idriss, H.; Woll, C. *Phys. Rev. Lett.* **2011,** *106,* 138302. doi:10.1103/physrevlett.106.138302
32. Sarngan, P. P.; Lakshmanan, A.; Sarkar, D. *Chemosphere* **2022,** *286,* 131692. doi:10.1016/j.chemosphere.2021.131692
33. Scanlon, D. O.; Dunnill, C. W.; Buckeridge, J.; Shevlin, S. A.; Logsdail, A. J.; Woodley, S. M.; Catlow, C. R. A.; Powell, M. J.; Palgrave, R. G.; Parkin, I. P.; Watson, G. W.; Keal, T. W.; Sherwood, P.; Walsh, A.; Sokol, A. A. *Nat. Mater.* **2013,** *12,* 798–801. doi:10.1038/nmat3697
34. Zumeta, I.; Ayllón, J. A.; González, B.; Domenech, X.; Vigil, E. *Sol. Energy Mater. Sol. Cells* **2009,** *93,* 1728–1732. doi:10.1016/j.solmat.2009.05.022
35. Zumeta, I.; González, B.; Espinosa, R.; Ayllón, J. A.; Vigil, E. *Semicond. Sci. Technol.* **2004,** *19,* L52–L55. doi:10.1088/0268-1242/19/5/l03
36. Avril, L.; Bourgeois, S.; Simon, P.; Domenichini, B.; Zanfoni, N.; Herbst, F.; Imhoff, L. *Thin Solid Films* **2015,** *591,* 237–244. doi:10.1016/j.tsf.2015.06.007
37. Chen, X.; Huang, L.; Jiao, Y.; Wang, S.; An, Q.; Bao, Y.; Geng, L. *Mater. Lett.* **2021,** *286,* 129230. doi:10.1016/j.matlet.2020.129230
38. Spurr, R. A.; Myers, H. *Anal. Chem. (Washington, DC, U. S.)* **1957,** *29,* 760–762. doi:10.1021/ac60125a006
39. Patterson, A. L. *Phys. Rev.* **1939,** *56,* 978–982. doi:10.1103/physrev.56.978
40. Gengenbach, T. R.; Major, G. H.; Linford, M. R.; Easton, C. D. *J. Vac. Sci. Technol., A* **2021,** *39,* 013204. doi:10.1116/6.0000682
41. Jacquemin, M.; Genet, M. J.; Gaigneaux, E. M.; Debecker, D. P. *ChemPhysChem* **2013,** *14,* 3618–3626. doi:10.1002/cphc.201300411
42. Peñas-Garzón, M.; Abdelraheem, W. H. M.; Belver, C.; Rodriguez, J. J.; Bedia, J.; Dionysiou, D. D. *Sep. Purif. Technol.* **2021,** *275,* 119169. doi:10.1016/j.seppur.2021.119169
43. Zhao, L.; Chen, X.; Wang, X.; Zhang, Y.; Wei, W.; Sun, Y.; Antonietti, M.; Titirici, M.-M. *Adv. Mater. (Weinheim, Ger.)* **2010,** *22,* 3317–3321. doi:10.1002/adma.201000660
44. Chi, M.; Sun, X.; Lozano-Blanco, G.; Tatarchuk, B. J. *Appl. Surf. Sci.* **2021,** *570,* 151147. doi:10.1016/j.apsusc.2021.151147
45. Panda, A. B.; Mahapatra, S. K.; Barhai, P. K.; Das, A. K.; Banerjee, I. *Appl. Surf. Sci.* **2012,** *258,* 9824–9831. doi:10.1016/j.apsusc.2012.06.037
46. Liu, G.; Yang, H. G.; Wang, X.; Cheng, L.; Lu, H.; Wang, L.; Lu, G. Q. (Max).; Cheng, H.-M. *J. Phys. Chem. C* **2009,** *113,* 21784–21788. doi:10.1021/jp907749r
47. Di Valentin, C.; Pacchioni, G.; Selloni, A. *J. Phys. Chem. C* **2009,** *113,* 20543–20552. doi:10.1021/jp9061797
48. Kar, P.; Zeng, S.; Zhang, Y.; Vahidzadeh, E.; Manuel, A.; Kisslinger, R.; Alam, K. M.; Thakur, U. K.; Mahdi, N.; Kumar, P.; Shankar, K. *Appl. Catal., B* **2019,** *243,* 522–536. doi:10.1016/j.apcatb.2018.08.002
49. Mahdi, N.; Kumar, P.; Goswami, A.; Perdicakis, B.; Shankar, K.; Sadrzadeh, M. *Nanomaterials* **2019,** *9,* 1186. doi:10.3390/nano9091186
50. Ishfaq, M.; Rizwan Khan, M.; Bhopal, M. F.; Nasim, F.; Ali, A.; Bhatti, A. S.; Ahmed, I.; Bhardwaj, S.; Cepek, C. *J. Appl. Phys.* **2014,** *115,* 174506. doi:10.1063/1.4874942
51. Bharti, B.; Kumar, S.; Lee, H.-N.; Kumar, R. *Sci. Rep.* **2016,** *6,* 32355. doi:10.1038/srep32355
52. Krishna, D. N. G.; Philip, J. *Appl. Surf. Sci. Adv.* **2022,** *12,* 100332. doi:10.1016/j.apsadv.2022.100332
53. Mascaretti, L.; Russo, V.; Zoppellaro, G.; Lucotti, A.; Casari, C. S.; Kment, Š.; Naldoni, A.; Li Bassi, A. *J. Phys. Chem. C* **2019,** *123,* 11292–11303. doi:10.1021/acs.jpcc.9b01727
54. Toney, J. E. Photoluminescence Spectroscopy. *Characterization of Materials,* 2nd ed.; John Wiley & Sons, 2002. doi:10.1002/0471266965.com058
55. Tauc, J. *Mater. Res. Bull.* **1968,** *3,* 37–46. doi:10.1016/0025-5408(68)90023-8
56. Tauc, J.; Grigorovici, R.; Vancu, A. *Phys. Status Solidi* **1966,** *21,* 627. doi:10.1002/pssb.19660150224
57. Lance, R. Optical Analysis of Titania: Bandgaps of Brookite, Rutile and Anatase. Bachelors thesis, Oregon State University, USA, 2018.
58. Makuła, P.; Pacia, M.; Macyk, W. *J. Phys. Chem. Lett.* **2018,** *9,* 6814–6817. doi:10.1021/acs.jpclett.8b02892

59. Mayerhöfer, T. G.; Pahlow, S.; Popp, J. *ChemPhysChem* **2020,** *21,* 2029–2046. doi:10.1002/cphc.202000464
60. Reyes-Coronado, D.; Rodríguez-Gattorno, G.; Espinosa-Pesqueira, M. E.; Cab, C.; de Coss, R.; Oskam, G. *Nanotechnology* **2008,** *19,* 145605. doi:10.1088/0957-4484/19/14/145605
61. Kim, D.-H.; Kim, W.-S.; Kim, S.; Hong, S.-H. *ACS Appl. Mater. Interfaces* **2014,** *6,* 11817–11822. doi:10.1021/am501656r
62. Ehfros, A. L.; Ehfros, A. L. *Fiz. Tekh. Poluprovodn. (S.-Peterburg)* **1982,** *16,* 1209–1214.
63. Singh, M.; Goyal, M.; Devlal, K. *J. Taibah Univ. Sci.* **2018,** *12,* 470–475. doi:10.1080/16583655.2018.1473946
64. Abdullah, S. A.; Sahdan, M. Z.; Nafarizal, N.; Saim, H.; Bakri, A. S.; Cik Rohaida, C. H.; Adriyanto, F.; Sari, Y. *J. Phys.: Conf. Ser.* **2018,** *995,* 012067. doi:10.1088/1742-6596/995/1/012067
65. Reckers, P.; Dimamay, M.; Klett, J.; Trost, S.; Zilberberg, K.; Riedl, T.; Parkinson, B. A.; Brötz, J.; Jaegermann, W.; Mayer, T. *J. Phys. Chem. C* **2015,** *119,* 9890–9898. doi:10.1021/acs.jpcc.5b01264
66. Sun, M.; Liu, H.; Sun, Z.; Li, W. *J. Environ. Chem. Eng.* **2020,** *8,* 104168. doi:10.1016/j.jece.2020.104168
67. Nowotny, J.; Alim, M. A.; Bak, T.; Idris, M. A.; Ionescu, M.; Prince, K.; Sahdan, M. Z.; Sopian, K.; Mat Teridi, M. A.; Sigmund, W. *Chem. Soc. Rev.* **2015,** *44,* 8424–8442. doi:10.1039/c4cs00469h
68. He, J.; Behera, R. K.; Finnis, M. W.; Li, X.; Dickey, E. C.; Phillpot, S. R.; Sinnott, S. B. *Acta Mater.* **2007,** *55,* 4325–4337. doi:10.1016/j.actamat.2007.04.005
69. Scarisoreanu, M.; Ilie, A. G.; Goncearenco, E.; Banici, A. M.; Morjan, I. P.; Dutu, E.; Tanasa, E.; Fort, I.; Stan, M.; Mihailescu, C. N.; Fleaca, C. *Appl. Surf. Sci.* **2020,** *509,* 145217. doi:10.1016/j.apsusc.2019.145217
70. Ilie, A. G.; Scarisoreanu, M.; Dutu, E.; Dumitrache, F.; Banici, A.-M.; Fleaca, C. T.; Vasile, E.; Mihailescu, I. *Appl. Surf. Sci.* **2018,** *427,* 798–806. doi:10.1016/j.apsusc.2017.08.041
71. Kumaravel, V.; Imam, M. D.; Badreldin, A.; Chava, R. K.; Do, J. Y.; Kang, M.; Abdel-Wahab, A. *Catalysts* **2019,** *9,* 276. doi:10.3390/catal9030276

License and Terms